Mining gut microbes for brain medicines p. 570

Robotic flight inspired by mosquitoes pp. 586 & 634

Hayabusa2 collects a sample of asteroid Ryugu p. 654

Science

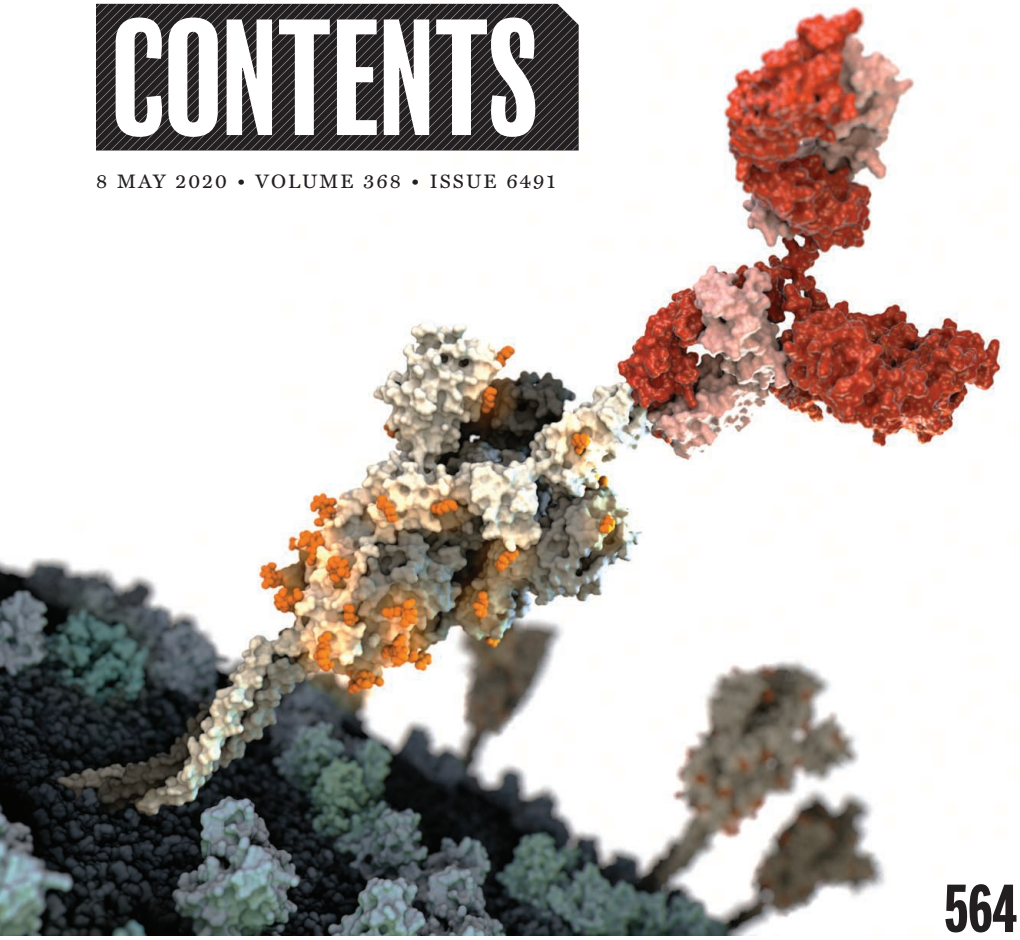
$15
8 MAY 2020
SPECIAL ISSUE
sciencemag.org

AAAS

EARLY LIFE IMMUNOLOGY

CONTENTS

8 MAY 2020 • VOLUME 368 • ISSUE 6491



564

NEWS

IN BRIEF

558 News at a glance

IN DEPTH

561 NIH move to ax bat coronavirus grant draws fire
Controversy comes amid global calls for China to allow independent probe of virus origins *By M. Wadman and J. Cohen*

562 Children's role in pandemic is still a puzzle
Some countries reopen schools, hoping it won't accelerate transmission
By G. Vogel and J. Couzin-Frankel

564 The race is on for antibodies that stop the new coronavirus
Mass-produced immune proteins may far precede a vaccine *By J. Cohen*
PODCAST

566 Ape researchers mobilize to save primates from coronavirus
Past respiratory epidemics raise fears of infection in apes
By A. Gibbons

566 Without fossil fuels, reactors churn out chemicals
Prospects brighten for making fertilizer, plastics with solar and wind power
By R. F. Service

567 Paperwork mistakes ensnare health data expert
Georgia Tech professor faces sentencing—and may lose her job—for mishandling grant *By J. Mervis*

FEATURES

570 Meet the psychobiome
Mounting evidence that gut bacteria influence the nervous system inspires efforts to mine the microbiome for brain drugs
By E. Pennisi

INSIGHTS

POLICY FORUM

574 In pursuit of open science, open access is not enough
Preventing monopolies in knowledge infrastructure is the next battleground for publishers and research institutions
By C. Aspesi and A. Brand

577 Harnessing multiple models for outbreak management
Expert elicitation methods and a structured decision-making framework will help account for risk and uncertainty *By K. Shea* et al.

PERSPECTIVES

580 Tree planting is not a simple solution
Tree planting must be carefully planned and implemented to achieve desired outcomes
By K. D. Holl and P. H. S. Brancalion
PODCAST

582 Quantum resonances near absolute zero
Ultralow-energy atom-molecule collisions reveal quasi-bound state quantum resonances *By T. Yang and X. Yang*
REPORT p. 626

583 Closing the science gap in 3D metal printing
X-ray imaging and modeling reveal how metal powders absorb energy and can create defects *By A. T. Polonsky and T. M. Pollock*
REPORT p. 660

584 Sending copper where it is needed most
Elesclomol improves survival in a mouse model of Menkes disease *By S. Lutsenko*
REPORT p. 620

586 Drones become even more insect-like
Mosquitoes' exceptional sensitivity to sound and airflow inspires new collision avoidance technology
By J. Young and M. Garratt
REPORT p. 634

587 Toward artificial photosynthesis
Microfluidics lights the way to a synthetic plant-like cell *By N. J. Gaut and K. P. Adamala*
REPORT p. 649

589 The challenge of early detection in cancer
Tumor growth dynamics and the timing of metastasis impose limits on cancer screening
By N. Pashayan and P. D. P. Pharoah

591 Katherine Johnson (1918–2020)
Groundbreaking U.S. space program mathematician *By S. M. Malcom*

BOOKS *ET AL.*

592 A field guide to existential risk
A pandemic isn't the only peril for which we're unprepared *By S. Jerabek*

593 The secret lives of birds
A science writer weaves a vivid portrait of avian culture, communication, and care
By B. C. Klump

GRAPHIC: V. ALTOUNIAN/*SCIENCE*; (IMAGES) W. SURYA *ET AL.*, *BIOCHIM. BIOPHYS. ACTA* 1860, 1309 (2018); D. WRAPP *ET AL.*, *SCIENCE* 367, 1260 (2020); E. O. SAPHIRE *ET AL.*, *SCIENCE* 293, 1155 (2001); M. D. HARTMANN, *PROC. NATL. ACAD. SCI. U.S.A.* 106, 16950 (2009); ORIENTATIONS OF PROTEINS IN MEMBRANES DATABASE

Published by AAAS



SPECIAL SECTION

EARLY LIFE IMMUNOLOGY

INTRODUCTION

598 The immune system's first steps

REVIEWS

600 Prenatal development of human immunity *J.-E. Park* et al.

604 Microbial–host molecular exchange and its functional consequences in early mammalian life *S. C. Ganal-Vonarburg* et al.

608 Contributions of maternal and fetal antiviral immunity in congenital disease *L. J. Yockey* et al.

612 Vaccination strategies to enhance immunity in neonates *T. R. Kollmann* et al.

ON THE COVER



Illustrated mosaic of a mother with child, assembled from various immune cell types. The developing immune system interacts with and is influenced by several factors, including the mother's cells (and her commensal microbiota) in utero and after birth. This special issue celebrates recent advances in early life immunology, which will help inform strategies to combat both childhood infections and immune disorders in later life. See page 598.
Illustration: Charis Tsevis

LETTERS

594 Research opportunities in pandemic lockdown
By R. Saraswat and D. A. Saraswat

595 The inherent challenges of classifying senescence
By A. Zhavoronkov

595 Response
By S. R. G. Calimport et al.

596 Technical Comment abstracts

RESEARCH

IN BRIEF

616 From *Science* and other journals

RESEARCH ARTICLES

619 Coronavirus
Quantifying SARS-CoV-2 transmission suggests epidemic control with digital contact tracing *L. Ferretti* et al.
RESEARCH ARTICLE SUMMARY; FOR FULL TEXT: DX.DOI.ORG/10.1126/SCIENCE.ABB6936

620 Biomedicine
Elesclomol alleviates Menkes pathology and mortality by escorting Cu to cuproenzymes in mice *L. M. Guthrie* et al.
PERSPECTIVE p. 584

REPORTS

626 Ultracold chemistry
Imaging the onset of the resonance regime in low-energy NO-He collisions
T. de Jongh et al.
PERSPECTIVE p. 582

630 Coronavirus
A highly conserved cryptic epitope in the receptor binding domains of SARS-CoV-2 and SARS-CoV
M. Yuan et al.

634 Bioinspired robots
Aerodynamic imaging by mosquitoes inspires a surface detector for autonomous flying vehicles
T. Nakata et al.
PERSPECTIVE p. 586

638 Coronavirus
An investigation of transmission control measures during the first 50 days of the COVID-19 epidemic in China
H. Tian et al.

642 Colloids
Emergence of complexity in hierarchically organized chiral particles
W. Jiang et al.

649 Synthetic biology
Light-powered CO_2 fixation in a chloroplast mimic with natural and synthetic parts
T. E. Miller et al.
PERSPECTIVE p. 587

654 Asteroids
Sample collection from asteroid (162173) Ryugu by Hayabusa2: Implications for surface evolution *T. Morota* et al.

660 3D printing
Controlling interdependent meso-nanosecond dynamics and defect generation in metal 3D printing *S. A. Khairallah* et al.
PERSPECTIVE p. 583

665 Chemical physics
Intermolecular vibrational energy transfer enabled by microcavity strong light–matter coupling
B. Xiang et al.

DEPARTMENTS

551 Editorial
Combination prevention for COVID-19
By Myron S. Cohen and Lawrence Corey

553 Editorial
Beat COVID-19 through innovation
By Pierre Azoulay and Benjamin Jones

674 Working Life
A Ph.D. on hold—indefinitely
By Kara Fikrig

Science Staff 550
New Products 669
Science Careers 670

SCIENCE (ISSN 0036-8075) is published weekly on Friday, except last week in December, by the American Association for the Advancement of Science, 1200 New York Avenue, NW, Washington, DC 20005. Periodicals mail postage (publication No. 484460) paid at Washington, DC, and additional mailing offices. Copyright © 2020 by the American Association for the Advancement of Science. The title SCIENCE is a registered trademark of the AAAS. Domestic individual membership, including subscription (12 months): $165 ($74 allocated to subscription). Domestic institutional subscription (51 issues): $2148; Foreign postage extra: Air assist delivery: $98. First class, airmail, student, and emeritus rates on request. Canadian rates with GST available upon request, GST #125488122. Publications Mail Agreement Number 1069624. **Printed in the U.S.A.**
Change of address: Allow 4 weeks, giving old and new addresses and 8-digit account number. **Postmaster:** Send change of address to AAAS, P.O. Box 96178, Washington, DC 20090–6178. **Single-copy sales:** $15 each plus shipping and handling available from backissues.sciencemag.org; bulk rate on request. **Authorization to reproduce** material for internal or personal use under circumstances not falling within the fair use provisions of the Copyright Act can be obtained through the Copyright Clearance Center (CCC), www.copyright.com. The identification code for *Science* is 0036-8075. *Science* is indexed in the *Reader's Guide to Periodical Literature* and in several specialized indexes.

PHOTO: KHUNCHOOO7/SHUTTERSTOCK

Published by AAAS

Science AAAS

Editor-in-Chief Holden Thorp, hthorp@aaas.org

Executive Editor Monica M. Bradford

Editors, Research Valda Vinson, Jake S. Yeston **Editor, Insights** Lisa D. Chong

DEPUTY EDITORS Julia Fahrenkamp-Uppenbrink (UK), Stella M. Hurtley (UK), Phillip D. Szuromi, Sacha Vignieri **SR. EDITORIAL FELLOW** Andrew M. Sugden (UK) **SR. EDITORS** Gemma Alderton (UK), Caroline Ash (UK), Brent Grocholski, Pamela J. Hines, Paula A. Kiberstis, Marc S. Lavine (Canada), Steve Mao, Ian S. Osborne (UK), Beverly A. Purnell, L. Bryan Ray, H. Jesse Smith, Keith T. Smith (UK), Jelena Stajic, Peter Stern (UK), Valerie B. Thompson, Brad Wible, Laura M. Zahn **ASSOCIATE EDITORS** Michael A. Funk, Priscilla N. Kelly, Tage S. Rai, Seth Thomas Scanlon (UK), Yury V. Suleymanov **LETTERS EDITOR** Jennifer Sills **LEAD CONTENT PRODUCTION EDITORS** Harry Jach, Lauren Kmec **CONTENT PRODUCTION EDITORS** Amelia Beyna, Jeffrey E. Cook, Chris Filiatreau, Julia Katris, Nida Masiulis, Suzanne M. White **SR. EDITORIAL COORDINATORS** Carolyn Kyle, Beverly Shields **EDITORIAL COORDINATORS** Aneera Dobbins, Joi S. Granger, Jeffrey Hearn, Lisa Johnson, Maryrose Madrid, Ope Martins, Shannon McMahon, Jerry Richardson, Hilary Stewart (UK), Alana Warnke, Alice Whaley (UK), Anita Wynn **PUBLICATIONS ASSISTANTS** Jeremy Dow, Alexander Kief, Ronmel Navas, Brian White **EXECUTIVE ASSISTANT** Jessica Slater **ASI DIRECTOR, OPERATIONS** Janet Clements (UK) **ASI SR. OFFICE ADMINISTRATOR** Jessica Waldock (UK)

News Editor Tim Appenzeller

NEWS MANAGING EDITOR John Travis **INTERNATIONAL EDITOR** Martin Enserink **DEPUTY NEWS EDITORS** Elizabeth Culotta, Lila Guterman, David Grimm, Eric Hand (Europe), David Malakoff **SR. CORRESPONDENTS** Daniel Clery (UK), Jon Cohen, Jeffrey Mervis, Elizabeth Pennisi **ASSOCIATE EDITORS** Jeffrey Brainard, Catherine Matacic **NEWS REPORTERS** Adrian Cho, Jennifer Couzin-Frankel, Jocelyn Kaiser, Kelly Servick, Robert F. Service, Erik Stokstad, Paul Voosen, Meredith Wadman **INTERNS** Eva Frederick, Rodrigo Perez Ortega **CONTRIBUTING CORRESPONDENTS** Warren Cornwall, Ann Gibbons, Mara Hvistendahl, Sam Kean, Eli Kintisch, Kai Kupferschmidt (Berlin), Andrew Lawler, Mitch Leslie, Eliot Marshall, Virginia Morell, Dennis Normile (Shanghai), Elisabeth Pain (Careers), Charles Piller, Michael Price, Tania Rabesandratana (Barcelona), Emily Underwood, Gretchen Vogel (Berlin), Lizzie Wade (Mexico City) **CAREERS** Donisha Adams, Rachel Bernstein (Editor), Katie Langin (Acting Editor) **COPY EDITORS** Julia Cole (Senior Copy Editor), Cyra Master (Copy Chief) **ADMINISTRATIVE SUPPORT** Meagan Weiland

Creative Director Beth Rakouskas

DESIGN MANAGING EDITOR Marcy Atarod **GRAPHICS MANAGING EDITOR** Alberto Cuadra **PHOTOGRAPHY MANAGING EDITOR** William Douthitt **WEB CONTENT STRATEGY MANAGER** Kara Estelle-Powers **SENIOR DESIGNER** Chrystal Smith **DESIGNER** Christina Aycock **GRAPHICS EDITOR** Nirja Desai **INTERACTIVE GRAPHICS EDITOR** Xing Liu **SENIOR SCIENTIFIC ILLUSTRATORS** Valerie Altounian, Chris Bickel **SCIENTIFIC ILLUSTRATOR** Alice Kitterman **SENIOR GRAPHICS SPECIALISTS** Holly Bishop, Nathalie Cary **SENIOR PHOTO EDITOR** Emily Petersen **PHOTO EDITOR** Kaitlyn Dolan

Chief Executive Officer and Executive Publisher Sudip Parikh

Publisher, Science Family of Journals Bill Moran

DIRECTOR, BUSINESS SYSTEMS AND FINANCIAL ANALYSIS Randy Yi **DIRECTOR, BUSINESS OPERATIONS & ANALYSIS** Eric Knott **DIRECTOR OF ANALYTICS** Enrique Gonzales **MANAGER, BUSINESS OPERATIONS** Jessica Tierney **SENIOR BUSINESS ANALYST** Cory Lipman, Meron Kebede **FINANCIAL ANALYST** Alexander Lee **ADVERTISING SYSTEM ADMINISTRATOR** Tina Burks **SENIOR SALES COORDINATOR** Shirley Young **DIGITAL/PRINT STRATEGY MANAGER** Jason Hillman **QUALITY TECHNICAL MANAGER** Marcus Spiegler **ASSISTANT MANAGER DIGITAL/PRINT** Rebecca Doshi **SENIOR CONTENT SPECIALISTS** Steve Forrester, Jacob Hedrick, Antoinette Hodal, Lori Murphy **DIGITAL PRODUCTION MANAGER** Lisa Stanford **CONTENT SPECIALIST** Kimberley Oster **ADVERTISING PRODUCTION OPERATIONS MANAGER** Deborah Tompkins **DESIGNER, CUSTOM PUBLISHING** Jeremy Huntsinger **SR. TRAFFIC ASSOCIATE** Christine Hall **SPECIAL PROJECTS ASSOCIATE** Sarah Dhere

ASSOCIATE DIRECTOR, BUSINESS DEVELOPMENT Justin Sawyers **GLOBAL MARKETING MANAGER** Allison Pritchard **DIGITAL MARKETING MANAGER** Aimee Aponte **JOURNALS MARKETING MANAGER** Shawana Arnold **MARKETING ASSOCIATES** Tori Velasquez, Mike Romano, Ashley Hylton **DIGITAL MARKETING SPECIALIST** Asleigh Rojanavongse **SENIOR DESIGNER** Kim Huynh

DIRECTOR AND SENIOR EDITOR, CUSTOM PUBLISHING Sean Sanders **ASSISTANT EDITOR, CUSTOM PUBLISHING** Jackie Oberst

DIRECTOR, PRODUCT & PUBLISHING DEVELOPMENT Chris Reid **DIRECTOR, BUSINESS STRATEGY AND PORTFOLIO MANAGEMENT** Sarah Whalen **ASSOCIATE DIRECTOR, PRODUCT MANAGMENT** Kris Bishop **SR. PRODUCT ASSOCIATE** Robert Koepke **DIGITAL PRODUCT STRATEGIST** Michael Hardesty **SPJ ASSOCIATE** Samantha Bruno Fuller

DIRECTOR, INSTITUTIONAL LICENSING Iquo Edim **ASSOCIATE DIRECTOR, RESEARCH & DEVELOPMENT** Elisabeth Leonard **MARKETING MANAGER** Kess Knight **SENIOR INSTITUTIONAL LICENSING MANAGER** Ryan Rexroth **INSTITUTIONAL LICENSING MANAGER** Marco Castellan **MANAGER, AGENT RELATIONS & CUSTOMER SUCCESS** Judy Lillibridge **SENIOR OPERATIONS ANALYST** Lana Guz **FULFILLMENT COORDINATOR** Melody Stringer **SALES COORDINATOR** Josh Haverlock

DIRECTOR, GLOBAL SALES Tracy Holmes **US EAST COAST AND MID WEST SALES** Stephanie O'Connor **US WEST COAST SALES** Lynne Stickrod **US SALES MANAGER, SCIENCE CAREERS** Claudia Paulsen-Young **US SALES REP, SCIENCE CAREERS** Tracy Anderson **ASSOCIATE DIRECTOR, ROW** Roger Goncalves **SALES REP, ROW** Sarah Lelarge **SALES ADMIN ASSISTANT, ROW** Bryony Cousins **DIRECTOR OF GLOBAL COLLABORATION AND ACADEMIC PUBLISHING RELATIONS, ASIA** Xiaoying Chu **ASSOCIATE DIRECTOR, INTERNATIONAL COLLABORATION** Grace Yao **SALES MANAGER** Danny Zhao **MARKETING MANAGER** Kilo Lan **ASCA CORPORATION, JAPAN** Kaoru Sasaki (Tokyo), Miyuki Tani (Osaka) **COLLABORATION/CUSTOM PUBLICATIONS/JAPAN** Adarsh Sandhu

DIRECTOR, COPYRIGHT, LICENSING AND SPECIAL PROJECTS Emilie David **RIGHTS AND LICENSING COORDINATOR** Jessica Adams **RIGHTS AND PERMISSIONS ASSOCIATE** Elizabeth Sandler **CONTRACTS AND LICENSING ASSOCIATE** Lili Catlett

---

MAIN HEADQUARTERS
Science/AAAS
1200 New York Ave. NW
Washington, DC 20005

SCIENCE INTERNATIONAL
Clarendon House
Clarendon Road
Cambridge, CB2 8FH, UK

SCIENCE CHINA
Room 1004, Culture Square
No. 59 Zhongguancun St.
Haidian District, Beijing, 100872

SCIENCE JAPAN
ASCA Corporation
Sibaura TY Bldg. 4F, 1-14-5
Shibaura Minato-ku
Tokyo, 108-0073 Japan

EDITORIAL
science_editors@aaas.org

NEWS
science_news@aaas.org

INFORMATION FOR AUTHORS
sciencemag.org/authors/science-information-authors

REPRINTS AND PERMISSIONS
sciencemag.org/help/reprints-and-permissions

MEDIA CONTACTS
scipak@aaas.org

MULTIMEDIA CONTACTS
SciencePodcast@aaas.org
ScienceVideo@aaas.org

INSTITUTIONAL SALES AND SITE LICENSES
sciencemag.org/librarian

PRODUCT ADVERTISING & CUSTOM PUBLISHING
advertising.sciencemag.org/products-services
science_advertising@aaas.org

CLASSIFIED ADVERTISING
advertising.sciencemag.org/science-careers
advertise@sciencecareers.org

JOB POSTING CUSTOMER SERVICE
employers.sciencecareers.org
support@sciencecareers.org

MEMBERSHIP AND INDIVIDUAL SUBSCRIPTIONS
sciencemag.org/subscriptions

MEMBER BENEFITS
aaas.org/membercentral

AAAS BOARD OF DIRECTORS
CHAIR Steven Chu
PRESIDENT Claire M. Fraser
PRESIDENT-ELECT Susan G. Amara
TREASURER Carolyn N. Ainslie
CHIEF EXECUTIVE OFFICER Sudip Parikh
BOARD Cynthia M. Beall, Rosina M. Bierbaum, Ann Bostrom, Stephen P.A. Fodor, S. James Gates, Jr., Laura H. Greene, Kaye Husbands Fealing, Maria M. Klawe, Robert B. Millard, Alondra Nelson, William D. Provine

BOARD OF REVIEWING EDITORS (Statistics board members indicated with **(S)**)

Adriano Aguzzi, *U. Hospital Zürich*
Takuzo Aida, *U. of Tokyo*
Leslie Aiello, *Wenner-Gren Foundation*
Judith Allen, *U. of Manchester*
Sebastian Amigorena, *Institut Curie*
James Analytis, *U. of California, Berkeley*
Paola Arlotta, *Harvard U.*
Johan Auwerx, *EPFL*
David Awschalom, *U. of Chicago*
Clare Baker, *U. of Cambridge*
Nenad Ban, *ETH Zürich*
Franz Bauer, *Pontificia Universidad Católica de Chile*
Ray H. Baughman, *U. of Texas at Dallas*
Peter Bearman, *Columbia U.*
Carlo Beenakker, *Leiden U.*
Yasmine Belkaid, *NIAID, NIH*
Philip Benfey, *Duke U.*
Gabriele Bergers, *VIB*
Bradley Bernstein, *Mass. General Hospital*
Alessandra Biffi, *Harvard Med. School*
Peer Bork, *EMBL*
Chris Bowler, *École Normale Supérieure*
Ian Boyd, *U. of St. Andrews*
Emily Brodsky, *U. of California, Santa Cruz*
Ron Brookmeyer, *U. of California, Los Angeles* **(S)**
Christian Büchel, *UKE Hamburg*
Dennis Burton, *Scripps Research*
Carter Tribley Butts, *U. of California, Irvine*
György Buzsáki, *New York U. School of Med.*
Blanche Capel, *Duke U.*
Annmarie Carlton, *U. of California, Irvine*
Nick Chater, *U. of Warwick*
Zhijian Chen, *UT Southwestern Med. Ctr.*
Ib Chorkendorff, *Denmark TU*
James J. Collins, *MIT*
Robert Cook-Deegan, *Arizona State U.*
Alan Cowman, *Walter & Eliza Hall Inst.*
Carolyn Coyne, *U. of Pittsburgh*
Roberta Croce, *VU Amsterdam*
Jeff L. Dangl, *U. of North Carolina*
Tom Daniel, *U. of Washington*
Chiara Daraio, *Caltech*
Nicolas Dauphas, *U. of Chicago*
Frans de Waal, *Emory U.*
Claude Desplan, *New York U.*
Sandra Díaz, *Universidad Nacional de Córdoba*
Ulrike Diebold, *TU Wien*
Hong Ding, *Inst. of Physics, CAS*
Jennifer Dionne, *Stanford U.*
Dennis Discher, *U. of Penn.*
Gerald Dorn, *Washington U. in St. Louis*
Jennifer A. Doudna, *U. of California, Berkeley*
Bruce Dunn, *U. of California, Los Angeles*
William Dunphy, *Caltech*
Christopher Dye, *U. of Oxford*
Todd Ehlers, *U. of Tübingen*
Jennifer Elisseeff, *Johns Hopkins U.*
Tim Elston, *U. of North Carolina*
Andrea Encalada, *U. San Francisco de Quito*
Nader Engheta, *U. of Penn.*
Karen Ersche, *U. of Cambridge*
Barry Everitt, *U. of Cambridge*
Vanessa Ezenwa, *U. of Georgia*
Michael Feuer, *The George Washington U.*
Toren Finkel, *U. of Pittsburgh Med. Ctr.*
Gwenn Flowers, *Simon Fraser U.*
Peter Fratzl, *Max Planck Inst. Potsdam*
Elaine Fuchs, *Rockefeller U.*
Eileen Furlong, *EMBL*
Jay Gallagher, *U. of Wisconsin*
Daniel Geschwind, *U. of California, Los Angeles*
Karl-Heinz Glassmeier, *TU Braunschweig*
Ramon Gonzalez, *U. of South Florida*
Elizabeth Grove, *U. of Chicago*
Nicolas Gruber, *ETH Zürich*
Hua Guo, *U. of New Mexico*
Kip Guy, *U. of Kentucky College of Pharmacy*
Taekjip Ha, *Johns Hopkins U.*
Christian Haass, *Ludwig Maximilians U.*
Sharon Hammes-Schiffer, *Yale U.*
Wolf-Dietrich Hardt, *ETH Zürich*
Louise Harra, *U. College London*
Jian He, *Clemson U.*
Carl-Philipp Heisenberg, *IST Austria*
Ykä Helariutta, *U. of Cambridge*
Janet G. Hering, *Eawag*
Hans Hilgenkamp, *U. of Twente*
Kai-Uwe Hinrichs, *U. of Bremen*
Lora Hooper, *UT Southwestern Med. Ctr.*
Fred Hughson, *Princeton U.*
Randall Hulet, *Rice U.*
Auke Ijspeert, *EPFL*
Akiko Iwasaki, *Yale U.*
Stephen Jackson, *USGS and U. of Arizona*
Kai Johnsson, *EPFL*
Peter Jonas, *IST Austria*
Matt Kaeberlein, *U. of Washington*
William Kaelin Jr., *Dana-Farber Cancer Inst.*
Daniel Kammen, *U. of California, Berkeley*
V. Narry Kim, *Seoul Nat. U.*
Robert Kingston, *Harvard Med. School*
Nancy Knowlton, *Smithsonian Institution*
Etienne Koechlin, *École Normale Supérieure*
Alexander L. Kolodkin, *Johns Hopkins U.*
Julija Krupic, *U. of Cambridge*
Thomas Langer, *Max Planck Inst. Cologne*
Mitchell A. Lazar, *U. of Penn.*
Ottoline Leyser, *U. of Cambridge*
Wendell Lim, *U. of California, San Francisco*
Jianguo Liu, *Michigan State U.*
Luis Liz-Marzán, *CIC biomaGUNE*
Jonathan Losos, *Washington U. in St. Louis*
Ke Lu, *Chinese Acad. of Sciences*
Christian Lüscher, *U. of Geneva*
Jean Lynch-Stieglitz, *Georgia Inst. of Tech.*
Fabienne Mackay, *U. of Melbourne*
Anne Magurran, *U. of St. Andrews*
Oscar Marín, *King's College London*
Charles Marshall, *U. of California, Berkeley*
Christopher Marx, *U. of Idaho*
Geraldine Masson, *CNRS*
C. Robertson McClung, *Dartmouth College*
Rodrigo Medellín, *U. Nacional Autónoma de México*
Graham Medley, *London School of Hygiene & Tropical Med.*
Jane Memmott, *U. of Bristol*
Baoxia Mi, *U. of California, Berkeley*
Edward Miguel, *U. of California, Berkeley*
Tom Misteli, *NCI, NIH*
Yasushi Miyashita, *U. of Tokyo*
Alison Motsinger-Reif, *NIEHS, NIH* **(S)**
Daniel Nettle, *Newcastle U.*
Daniel Neumark, *U. of California, Berkeley*
Beatriz Noheda, *U. of Groningen*
Helga Nowotny, *Vienna Science, Research & Tech. Fund*
Rachel O'Reilly, *U. of Birmingham*
Harry Orr, *U. of Minnesota*
Pilar Ossorio, *U. of Wisconsin*
Andrew Oswald, *U. of Warwick*
Isabella Pagano, *Istituto Nazionale di Astrofisica*
Margaret Palmer, *U. of Maryland*
Elizabeth Levy Paluck, *Princeton U.*
Jane Parker, *Max Planck Inst. Cologne*
Giovanni Parmigiani, *Dana-Farber Cancer Inst.* **(S)**
Samuel Pfaff, *Salk Inst. for Biological Studies*
Julie Pfeiffer, *UT Southwestern Med. Ctr.*
Matthieu Piel, *Institut Curie*
Kathrin Plath, *U. of California, Los Angeles*
Martin Plenio, *Ulm U.*
Katherine Pollard, *U. of California, San Francisco*
Elvira Poloczanska, *Alfred-Wegener-Inst.*
Julia Pongratz, *Ludwig Maximilians U.*
Philippe Poulin, *CNRS*
Jonathan Pritchard, *Stanford U.*
Félix A. Rey, *Institut Pasteur*
Trevor Robbins, *U. of Cambridge*
Joeri Rogelj, *Imperial College London*
Amy Rosenzweig, *Northwestern U.*
Mike Ryan, *U. of Texas at Austin*
Mitinori Saitou, *Kyoto U.*
Shimon Sakaguchi, *Osaka U.*
Miquel Salmeron, *Lawrence Berkeley Nat. Lab*
Nitin Samarth, *Penn. State U.*
Jürgen Sandkühler, *Med. U. of Vienna*
Alexander Schier, *Harvard U.*
Wolfram Schlenker, *Columbia U.*
Susannah Scott, *U. of California, Santa Barbara*
Rebecca Sear, *London School of Hygiene & Tropical Med.*
Vladimir Shalaev, *Purdue U.*
Jie Shan, *Cornell U.*
Beth Shapiro, *U. of California, Santa Cruz*
Jay Shendure, *U. of Washington*
Steve Sherwood, *U. of New South Wales*
Brian Shoichet, *U. of California, San Francisco*
Robert Siliciano, *Johns Hopkins U. School of Med.*
Lucia Sivilotti, *U. College London*
Alison Smith, *John Innes Centre*
Richard Smith, *U. of North Carolina* **(S)**
Mark Smyth, *QIMR Berghofer*
Pam Soltis, *U. of Florida*
John Speakman, *U. of Aberdeen*
Tara Spires-Jones, *U. of Edinburgh*
Allan C. Spradling, *Carnegie Institution for Science*
V. S. Subrahmanian, *Dartmouth College*
Ira Tabas, *Columbia U.*
Sarah Teichmann, *Wellcome Sanger Inst.*
Rocio Titiunik, *Princeton U.*
Shubha Tole, *Tata Inst. of Fundamental Research*
Wim van der Putten, *Netherlands Inst. of Ecology*
Reinhilde Veugelers, *KU Leuven*
Bert Vogelstein, *Johns Hopkins U.*
Kathleen Vohs, *U. of Minnesota*
David Wallach, *Weizmann Inst. of Science*
Jane-Ling Wang, *U. of California, Davis* **(S)**
David Waxman, *Fudan U.*
Jonathan Weissman, *U. of California, San Francisco*
Chris Wikle, *U. of Missouri* **(S)**
Terrie Williams, *U. of California, Santa Cruz*
Ian A. Wilson, *Scripps Research* **(S)**
Yu Xie, *Princeton U.*
Jan Zaanen, *Leiden U.*
Kenneth Zaret, *U. of Penn. School of Med.*
Jonathan Zehr, *U. of California, Santa Cruz*
Xiaowei Zhuang, *Harvard U.*
Maria Zuber, *MIT*

Science serves as a forum for discussion of important issues related to the advancement of science by publishing material on which a consensus has been reached as well as including the presentation of minority or conflicting points of view. Accordingly, all articles published in *Science*—including editorials, news and comment, and book reviews—are signed and reflect the individual views of the authors and not official points of view adopted by AAAS or the institutions with which the authors are affiliated.

Published by AAAS

EDITORIAL

Combination prevention for COVID-19

The coronavirus disease 2019 (COVID-19) pandemic has produced the fear and disorder inevitably provoked by emerging pathogens. As such, it should also inspire consideration of our experience with HIV over the past 40 years. As with HIV, the road to reducing infections with severe acute respiratory syndrome coronavirus 2 (SARS-CoV-2, the cause of COVID-19), and attendant morbidity and mortality, requires medical and nonmedical strategies. The most important lesson learned from tackling HIV is to use a combination of prevention strategies.

The first step to stopping the spread of SARS-CoV-2 has already been taken—behavioral changes. This reflects a rapid but imperfect understanding of the transmission of this virus. At the beginning of the AIDS epidemic, changes in sexual behavior, condom promotion, and government interventions (closing "hotspots" of HIV transmission such as bathhouses) made a difference. For SARS-CoV-2, masks and gloves, hand hygiene, and "shelter in place" mandates have already demonstrated benefits. More efficient behavioral intervention requires better understanding of the rules governing SARS-CoV-2 transmission. What are the risks from exposure to respiratory droplets, airborne virus, and surface contamination? What concentration of SARS-CoV-2 is required for transmission? Evidence suggests that SARS-CoV-2 transmission is greatest very early in infection prior to development of symptoms—the same lessons learned from HIV. Given this rule of transmission, biomedical prevention strategies that provide reliable protection become essential. And as has proven true for HIV, directing prevention to people at the highest risk for SARS-CoV-2 infection or the worst disease outcomes will be an important consideration.

Historically, antiviral therapies that reduce the severity of infection have preceded the development of biomedical approaches to prevent onward transmission (although interruption of viral replication also offers a prevention benefit). The first HIV treatment, azidothymidine (AZT), extended life by up to 18 months, providing hope that HIV infection could be transformed from a death sentence to a treatable disease. Reduced risk of mother-to-child transmission by AZT was the first biomedical prevention against HIV transmission. This success was the precursor to "pre-exposure prophylaxis." AZT also launched research focused on "treatment as prevention" where antiviral agents reduce the HIV viral load to a point where infected people no longer transmit. This approach, which uses combinations of powerful antiretroviral agents, is now the mainstay of HIV prevention worldwide.

For SARS-CoV-2, we have leapt into a cacophony of clinical trials of drug candidates with differing degrees of plausibility. Preliminary results from a large randomized controlled trial show that the antiviral drug remdesivir substantially reduced the duration of hospitalization for COVID-19. To date, COVID-19 testing results have been used primarily for patient isolation, contact tracing, and quarantine. But effective therapies will lend great urgency for the universal availability of rapid and reliable testing for SARS-CoV-2 infection, so that treatment can be provided when indicated.

Long-acting antiviral agents and monoclonal antibodies that neutralize SARS-CoV-2 may become important nonvaccine pharmacologic tools for prevention. Antiviral agents that prevent replication of SARS-CoV-2 could be used as pre-, peri-, or postexposure prophylaxis. Several different potent monoclonal antibody combinations designed to treat and prevent SARS-CoV-2 will enter clinical trials in June 2020.

> "HIV has taught us that multiple concomitant prevention strategies are essential."

Ultimately, a safe and effective vaccine is crucial for preventing COVID-19. Vaccine efforts started immediately after the discovery of SARS-CoV-2. Numerous vaccine candidates have been identified, and early-phase vaccine studies of several are underway. Proof of vaccine efficacy will require large trials with 6000 to 12,000 participants or more in each study. Because SARS-CoV-2 is moving around the planet, clinical research teams must prepare for trials where incident infections occur (a sufficient "attack rate"). We cannot predict the time of availability or degree of efficacy of a SARS-CoV-2 vaccine with precision, but most trials in development are designed to demonstrate 60 or 70% prevention efficacy, not 100% protection.

HIV has taught us that multiple concomitant prevention strategies are essential. Behavioral changes to reduce SARS-CoV-2 spread must be accepted as the "new normal." The COVID-19 toolbox must include safe and effective interventions whose values have been proven through robust scientific methods honed over decades. Ongoing research in each prevention domain must be sustained. We simply cannot depend on any single "magic bullet."

–Myron S. Cohen and Lawrence Corey

Myron S. Cohen is a professor in the Department of Medicine, Division of Infectious Diseases, and The Institute for Global Health and Infectious Diseases at the University of North Carolina at Chapel Hill, Chapel Hill, NC, USA. mscohen@med.unc.edu

Lawrence Corey is a professor in the Vaccine and Infectious Disease Division at the Fred Hutchinson Cancer Research Center, Seattle, WA, and a Professor of Laboratory Medicine and Medicine at the University of Washington, Seattle, WA, USA. lcorey@fredhutch.org

10.1126/science.abc5798

Published by AAAS

EDITORIAL

Beat COVID-19 through innovation

As coronavirus disease 2019 (COVID-19) has spread, public health and economic well-being are increasingly in conflict. Governments are prioritizing public health, but the current solution—social isolation—is costly as commerce remains shut down. Restarting economies could rekindle the pandemic and cause even worse human suffering. Innovation can help societies escape the untenable choice between public and economic health. The world needs effective vaccines, therapies, or other solutions. But how do we achieve these solutions, and achieve them quickly?

Innovation policy can accelerate advances, with high returns. In the United States, COVID-19 has reduced gross domestic product (GDP) by ~30%. What if additional investment in research and development (R&D) could bring forward an effective vaccine by just 1 day? If this investment costs less than the daily loss in GDP ($18 billion in the United States alone), it would pay for itself. Even large incremental funding to support R&D will be miniscule in scale compared to the $2.8 trillion the U.S. government is spending to compensate for the economic shutdown.

What principles should guide government innovation policy to battle COVID-19? It is critical to support many independent avenues of research. Outcomes from R&D investments are uncertain. Many avenues will be dead ends, so many different paths—each corresponding to an independent effort—should be pursued. Consider funding 10,000 such efforts. Even if each had only a 0.1% chance of producing an advance in prevention, treatment, or infection control, the probability of at least five such advances would be 97%. By contrast, if efforts crowd into only a few prospects, the odds of collective failure can become overwhelming.

This innovative push must draw widely on talent. Research talent is plentiful, but many laboratories and teams are now shuttered and dispersed by the pandemic. Private investment gravitates toward marketable solutions, but key insights are likely to come from asking "why" questions (for example, basic research into the pathophysiology of the disease) and not simply from "shovel ready" drug development projects. Moreover, good ideas often come from unexpected corners. Useful solutions may be discovered outside biomedicine, including through engineering disciplines and information technology.

What would a bold innovation policy agenda look like? In the United States, funding for R&D must be fortified, as recently called for by the Task Force on American Innovation and 17 other organizations. Also, a principal investigator already receiving public funding should be able to receive immediate support to work on COVID-19 with minimal application burden and decisions within 1 week. The National Institutes of Health (NIH) has taken some first steps with emergency procedures to supplement existing grants, but these efforts need to draw on additional labs and talent, and to accelerate review. The marginal investment through the NIH, at $3 billion, appears modest in size, equating to the U.S. GDP loss in just 4 hours. Globally, researchers with relevant expertise are essential workers; they should have access to their labs and additional resources to engage in the COVID-19 battle.

Government support for private sector R&D should be delivered at great speed. A "Pandemic R&D Program" could deploy loans that are forgivable later, based on actual investment in COVID-19–related innovations, thus ensuring that financial constraints do not slow down solutions. More support could come through supplementing the R&D tax credit system, which already exists in the United States and other countries.

> "COVID-19 presents... a brutal choice between economic and public health."

In June 1940, the U.S. government created the National Defense Research Committee (NDRC), composed of eminent scientists and innovators in the public and private sectors, with the mandate to achieve innovations related to the war effort. This leadership structure drove the rapid development of numerous technologies, including weapons systems but also antimalarial drugs and penicillin manufacturing. A COVID-19 Defense Research Committee could similarly be empowered to coordinate and fund solutions to the pandemic. This group would track R&D efforts, create a public clearinghouse documenting the avenues pursued, fund innovations and the scaling of successful advances, and streamline bureaucracy. The new vaccine effort, Operation Warp Speed, moves in this direction. But we also need efforts beyond vaccines.

COVID-19 presents the world with a brutal choice between economic and public health. Innovation investments are essential to avoiding that choice—yet tiny in cost compared to current economic losses and other emergency programs. Even the slight acceleration of advances will bring massive benefits.

–Pierre Azoulay and Benjamin Jones

Pierre Azoulay is a professor at the Sloan School of Management at the Massachusetts Institute of Technology, Cambridge, MA, USA, and a research associate at the National Bureau of Economic Research, Cambridge, MA, USA. pazoulay@mit.edu

Benjamin Jones is a professor at the Kellogg School of Management at Northwestern University, Evanston, IL, USA, and a research associate at the National Bureau of Economic Research, Cambridge, MA, USA. bjones@kellogg.northwestern.edu

10.1126/science.abc5792

Published by AAAS

NEWS



Physicians, nurses, and police officers in Mumbai, India, are showered with flower petals by helicopter on 3 May to thank them for handling the country's COVID-19 cases.

IN BRIEF

Edited by **Erik Stokstad**

DISPATCHES FROM THE PANDEMIC

NIH funds new COVID-19 tests

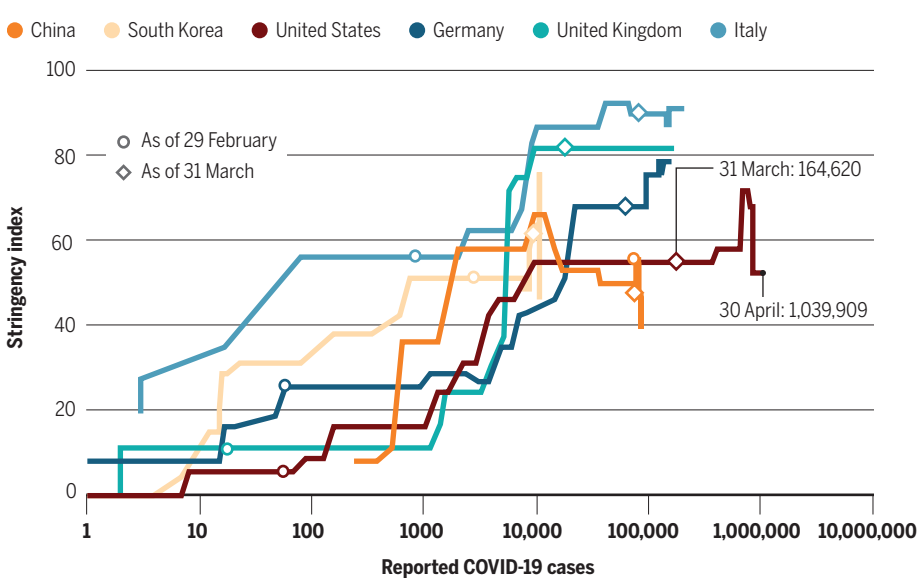
DIAGNOSTICS | The U.S. National Institutes of Health (NIH) has announced a $1.5 billion initiative to speed breakthroughs in diagnostic tests for the virus that causes COVID-19. Proposals can use any technology to detect an active infection and will be evaluated for their likely success in improving testing performance—qualities such as speed, reliability, and accuracy—and ease of use, for example by detecting the virus in saliva or exhaled breath. NIH is already accepting proposals and expects to approve roughly 100 diagnostics projects for up to three rounds of development, officials said last week. NIH anticipates backing a handful of those projects to full commercial development. The program aims to increase the U.S. capacity for testing up to 100-fold by late summer. But Alan Wells, a diagnostics expert at the University of Pittsburgh Medical Center, is skeptical. "I don't care how much money you give me; I'm not going to have 10 million tests a week by November."

Stringency of U.S. response lags

POLICY | The United States leads the world in COVID-19 cases, but its policy response lags far behind many other countries, according to an analysis by University of Oxford researchers. The Oxford COVID-19 Government Response Tracker project has charted the "stringency" of governments' responses to the pandemic since January. The composite score, updated regularly, is based on various social distancing policies, including closing schools and restricting travel. The Oxford group is also tracking progress on steps needed to safely lift official lockdowns, such as adequate capacity to detect and isolate all cases of COVID-19 regardless of severity. As of 1 May, no

Behind the curve

The "stringency" of social distancing policies in the United States lagged behind other nations from 1 January to 30 April. Even when reported U.S. infections exceeded 160,000 on 31 March, for example, it continued to impose laxer restrictions than other nations that had reached similar numbers.



CREDITS: (PHOTO) RAJANISH KAKADE/AP PHOTO; (GRAPHIC) X. LIU/*SCIENCE*; (DATA) OXFORD COVID-19 GOVERNMENT RESPONSE TRACKER

Published by AAAS

country had satisfied the criteria recommended by the World Health Organization. Only about 20 are close, the researchers said, and that group does not include the United States, where several states last week began to ease their lockdowns.

Museums seek pandemic artifacts

HISTORY OF SCIENCE | The COVID-19 pandemic is a long way from being history, but museums in multiple countries are already interested in preserving images, publications, and artifacts chronicling the outbreak. Curators hope to document daily life during the lockdown by preserving masks, information signs, and other pandemic paraphernalia. The five member institutions of the Science Museum Group in the United Kingdom have launched a search for items related to COVID-19 research, medical treatment, and the public health response. Those museums began their hunt in March, before they closed for social distancing, and have taken care not to distract health care workers, according to a statement released last week. The Smithsonian Institution's National Museum of American History, meanwhile, is developing its own plan for amassing a pandemic collection. Have something to donate? You can reach Science Museum Curators at scmobjectenquiries@sciencemuseum.ac.uk and the Smithsonian at inquiry@si.edu.

Antiviral drug shows promise

CLINICAL RESEARCH | The experimental drug remdesivir accelerated recovery from COVID-19 in the first large, carefully controlled clinical trial of patients hospitalized with the disease. Remdesivir, made by Gilead Sciences, cripples a viral enzyme. Patients who received the drug recovered from COVID-19 in an average of 11 days versus 15 in patients who received a placebo, according to the National Institute of Allergy and Infectious Diseases, the trial's sponsor. The patients treated with remdesivir also had a lower mortality rate—8% versus 11.6% for the placebo—but this trend did not reach statistical significance. The study began on 21 February and enrolled 1063 patients at 68 sites in the United States, Europe, and Asia. "It's a promising signal, but we do not need to get hyperexcited—this is not a home run," says Carlos del Rio, an infectious disease clinician at Emory University, which participated in the trial. On 1 May, the U.S. Food and Drug Administration authorized emergency use of remdesivir for severe cases.

SCIENCEMAG.ORG/TAGS/CORONAVIRUS
Read additional *Science* coverage of the pandemic.

ENVIRONMENTAL SCIENCE

Northern Europe braces for drought

Northern Europe is facing a drought for the third year in a row. In April, across much of Germany, no measurable rain fell until the last few days of the month. In the Netherlands, 2020 is on track to be worse than the record-setting drought year of 1976. In the Czech Republic, authorities are warning of the worst drought in 500 years. Meteorologists are hoping for rain, but even a wet summer won't be enough to relieve the stress on the region's forests, German experts said at a press briefing on 5 May. Because the soil is so dry, heavy rains run off and can't replenish groundwater supplies. With climate change expected to increase temperature and dryness, farmers and foresters should plant crops and tree species that are better suited to long-term dry and hot conditions, they said.

Epstein's Harvard ties detailed

#METOO | Harvard University maintained a campus office for disgraced financier Jeffrey Epstein after his 2008 conviction on sex charges involving a minor, according to a report the university released on 1 May. It estimates Epstein made more than 40 visits to the office maintained for him by quantitative biologist Martin Nowak, whose Program for Evolutionary Dynamics received $6.5 million from Epstein before the conviction. In 2008, Harvard prohibited researchers from accepting further donations from him. But the report says Epstein introduced Nowak and George Church, a geneticist at Harvard Medical School, to donors who between 2010 and 2015 gave them $7.5 million and $2 million, respectively. (The donors deny that Epstein directed their donations.) In 2013, the report says, several faculty members asked Harvard to consider accepting Epstein donations again, but their request was declined.

AI can't be named inventor

ARTIFICIAL INTELLIGENCE | A computer program cannot be named an inventor, the U.S. Patent and Trademark Office affirmed last week. The office denied a final appeal by patent lawyers with the international Artificial Inventor Project (AIP) to name DABUS, an artificial intelligence program developed by researcher Stephen Thaler. It was listed as inventor in a pair of patent applications for interlocking canisters and a flashing beacon, both filed in 2018. The language in U.S. patent laws and federal regulations assumes an inventor is a person, the patent office noted in its ruling, which followed similar decisions in Europe and the United Kingdom. On its website, AIP argues that interpretation forces humans to falsely take credit for conceptions made by machine.

Nearest black hole found

ASTRONOMY | The closest black hole to Earth has been found 1000 light-years away—just down the road in galactic terms. Only a few dozen black holes in our galaxy have revealed themselves by gorging on gas and dust that glow in x-rays. But theorists think hundreds of millions more are hidden from view, simply because they emit no light. In recent years, astronomers have found candidates by looking for stars that wobble, pulled by an invisible orbiting companion. Using this technique, researchers studying the nearby system HR 6819, which consists of two binary stars, this week announced a third partner—a black hole weighing four times the mass of the Sun. The next nearest confirmed black hole is three times farther.

Polymath Robert May dies

IN MEMORIUM | Robert May, a physicist whose career spanned ecology, math, and public policy, has died at age 84. Raised in Australia, May began his career studying superconductivity at the University of Sydney. Later, at Princeton University and the University

Published by AAAS

of Oxford, he made major contributions in epidemiology and population ecology, including showing how, contrary to intuition, diverse ecosystems can be unstable. May served as a blunt-spoken science adviser to the U.K. government from 1995 to 2000, when controversy over genetically modified crops was rife and during an outbreak of mad cow disease. May was president of the Royal Society from 2000 to 2005, and he served for 10 years on the U.K. Committee on Climate Change.

THREE QS

A forensics sequel

A 5-year-old initiative to bring greater statistical rigor to crime laboratory analysis of fingerprints, shoeprints, and other forensic evidence has won $20 million in funding from the National Institute of Standards and Technology to continue its work for another 5 years. The Center for Statistics and Applications in Forensic Evidence (CSAFE) includes more than 60 researchers from six universities. Director Alicia Carriquiry, a statistician at Iowa State University, told *Science* about her vision for the center's second chapter.

Q: What has changed since the center launched?
A: I think the community of practitioners has come to understand that, first of all, we're not here to tell them they're doing everything wrong. We're here to see whether we can help them do their job better, and develop tools for them to use.

Q: Which advances make you proudest?
A: We've built enormous databases that are carefully constructed, very well documented, and searchable, and we've put all these data in the public domain. For example, one of the databases has 250,000 images of the bottoms of shoes. We have some pretty good algorithms to look at the question of source—do these two pieces of evidence have a common source? CSAFE 2.0 is going to try to start some serious piloting [in forensic labs].

Q: Could forensic scientists eventually take charge of their own statistics?
A: We can always dream! At the very least, you want forensic scientists to be cognizant of issues such as uncertainty, the need to measure variability … and the notion of probability. If we get to the point where you may not understand how to do statistics, but you understand why statistics is important, I think that would be a good place.

Did cattle semen revive disease?

ANIMAL HEALTH | An epidemic of bluetongue disease that has been ravaging European sheep and cattle since 2015 may have been caused by infected semen used in cattle breeding. The livestock virus mysteriously turned up in Europe for the first time in 2006, sparking an outbreak that cost farmers billions of euros until vaccinations ended it 4 years later. But the disease re-emerged in 2015. Now, researchers report in *PLOS Biology* that the genome of the virus currently circulating is remarkably like some samples collected before 2010. Because the virus mutates when it circulates, that similarity suggests the virus was frozen for years—most likely in semen. EU regulations require that semen be tested for bluetongue when it is shipped between countries, but not when used domestically.

Genes trace ancient Andeans

ANCIENT DNA | The most comprehensive study of ancient human DNA from South America paints a broad picture of genetic continuity in the face of cultural change. An international team studied DNA from the remains of 89 individuals who lived between 9000 and 500 years ago and were part of the Inca, Moche, and other ancient societies in South America. The researchers found that people of the Central Andes—what is primarily Peru today—became isolated 9000 years ago and remained genetically distinct. Even during the rise and fall of several cultures over the past 2000 years, this group, centered in the Andean highlands, was not replaced by new groups, the team reports this week in *Cell*. That genetic stability contrasts with tumultuous events in Eurasia at this time, where genetic studies have found evidence of repeated invasions and replacements.



Red-sided garter snakes hang out after emerging from hibernation.

PHOTO: HUW CORDEY/MINDEN PICTURES

ANIMAL BEHAVIOR

A common snake buddies up

Snakes and other reptiles are considered solitary creatures that come together for mating and hibernating but not much else. Garter snakes tend to be a lot more social, comparative psychologists have discovered. Some of these harmless American serpents are extroverts and prefer large groups, whereas others tend to be loners, Noam Miller and his graduate student Morgan Skinner at Wilfrid Laurier University reported last month in *Behavioral Ecology and Sociobiology*. And many individual garter snakes have "friends"—snakes they spend much of their time with—the pair found. Because snakes are difficult to track in the wild, Skinner monitored young eastern garter snakes (*Thamnophis sirtalis sirtalis*) in an enclosure, tracking how they arranged themselves after he reshuffled their positions twice a day. The social structures of the snakes "are in some ways surprisingly similar to those of mammals, including humans," Skinner says.

Published by AAAS



IN DEPTH

Researchers with the EcoHealth Alliance and the Wuhan Institute of Virology took samples from bats in southern China in order to identify viruses that might harm humans.

COVID-19

NIH move to ax bat coronavirus grant draws fire

Controversy comes amid global calls for China to allow independent probe of virus origins

By **Meredith Wadman** *and* **Jon Cohen**

The research community is reacting with alarm and anger to the National Institutes of Health's (NIH's) abrupt decision to kill a grant that helped support research in China on how coronaviruses—such as the one causing the current COVID-19 pandemic—move from bats to humans.

The unusual 24 April move occurred shortly after President Donald Trump alleged—without providing evidence—that the pandemic virus had escaped from a Chinese laboratory supported by the NIH grant, and vowed to end the funding. The episode came as calls mounted for China to allow an independent investigation, perhaps led by the United Nations. "The whole world wants the exact origin of the virus to be clarified," German Minister of Foreign Affairs Heiko Maas said on 4 May.

Many scientists are skeptical of the laboratory escape theory, and the Chinese virologist at the heart of the allegation rejects the idea. Critics of NIH's decision, meanwhile, say it represents an unacceptable intrusion of politics into the agency's grants process and possibly violated its rules.

"This is a horrible precedent" and "the most counterproductive thing I could imagine" given the work's relevance to understanding the current pandemic and preventing futures ones, says Gerald Keusch, a former director of NIH's Fogarty International Center who is now at Boston University. Other researchers note that work done on the canceled grant allowed testing of the antiviral drug remdesivir, which is showing promise in treating COVID-19.

NIH would not comment on why it canceled the grant to the EcoHealth Alliance, a nonprofit in New York City that runs global research collaborations. But in emails reviewed by *Science*, Michael Lauer, NIH's deputy director for extramural research, suggested the Wuhan Institute of Virology (WIV), a partner on the grant, had not "taken all appropriate precautions to prevent the release of pathogens." He also wrote that the grant did not "align" with NIH priorities. But NIH offered no support for either statement, and Lauer called claims that the pandemic virus had escaped from WIV just "allegations."

The termination disrupts a long-standing collaboration. For 15 years, the grant's principal investigator, EcoHealth Alliance President Peter Daszak, has collaborated with Shi Zhengli, a leading WIV virologist, to study bat coronaviruses. In 2014, the National Institute of Allergy and Infectious Diseases awarded the alliance a $3.1 million, 5-year grant. About $600,000 went to Shi to collect blood, urine, and other samples from bats in China and to sequence viruses found in them, with the goal of identifying coronaviruses that might infect humans. (Shi's team has amassed some 15,000 samples from bats.) The funding enabled blood testing of people who live near bat caves in southern China, revealing that nearly 3% of them had been infected with coronaviruses originating in bats.

Science's COVID-19 coverage is supported by the Pulitzer Center.

The project also produced research tools, including genetic sequences of two coronaviruses that have now been used to test remdesivir. "Our work on remdesivir absolutely would not have moved forward" without the alliance's research, says virologist Mark Denison of Vanderbilt University, who launched the studies that led to the drug's current use.

In 2019, the grant was renewed after receiving an outstanding score from peer reviewers. The researchers received an additional $292,000, none of which went to Shi, Daszak says. The team planned to do more human, wildlife, and lab-based studies to pinpoint hot spots in southern China where the risk is highest for a bat coronavirus to jump to humans. "The reason our grant was renewed for 5 years is because our work is so important," Daszak says.

PHOTO: ECOHEALTH ALLIANCE

Published by AAAS

Shi's work has already shed light on the pandemic's origins. In January, her team published the genetic sequence of a bat virus it collected that shares 96.2% of its genome with SARS-CoV-2, the pandemic coronavirus. The finding suggests SARS-CoV-2 originated in bats, although researchers widely believe it most likely jumped to another mammal before infecting humans.

Among some policymakers and media, however, the finding fed speculation that SARS-CoV-2 had been engineered by scientists at WIV, or was a collected virus that escaped from that laboratory. On 14 April, the speculation mounted after a column in *The Washington Post* reported that U.S. Department of State officials had, in 2018, raised concerns about safety at WIV's then-new biosafety level 4 (BSL-4) laboratory, designed to handle the most dangerous pathogens. The multicampus WIV also has separate, lower containment BSL-2 and BSL-3 laboratories where Shi did her grant-funded work, Daszak says. But after a reporter erroneously informed Trump that NIH had funded work at the BSL-4 lab, he replied: "We will end that grant very quickly."

One week later, Lauer emailed Daszak that NIH was ending the alliance's grant "for convenience." Asked by *Science* to explain the phrase, NIH pointed to a Grants Policy Statement that says it can unilaterally cancel a grant "to protect the public health and welfare from the effects of a serious deficiency."

Administrators familiar with NIH believe the agency might have broken regulations governing grant disbursal, which allow the midstream cancellation of an award for just a few reasons, such as malfeasance.

Virologist Dennis Carroll, who recently retired as director of the emerging threats division of the U.S. Agency for International Development, says he saw the cables on the safety of WIV's BSL-4 lab when he was at the U.S. embassy in Beijing, and doesn't "place an enormous amount of weight on the observations" because they were made by diplomats, not scientists. If any problems were "of substance," he adds, NIH would have "needed to take serious steps" because it funded work at WIV. (There is no public indication NIH took any action.)

Other researchers say there is no evidence that SARS-CoV-2 escaped from WIV, although they concede the scenario can't be completely ruled out. They note that research suggests the bat virus Shi described, although 96.2% similar to the pandemic virus, evolved in bats at least 20 years ago, meaning it would have taken decades to evolve into the pandemic virus had it escaped from a laboratory. On 1 May, the Office of the Director of National Intelligence said the intelligence community "concurs with the wide scientific consensus that the COVID-19 virus was not manmade or genetically modified," but was still "rigorously" examining whether it spread from infected animals or a lab accident in Wuhan.

Shi has said that virus didn't come from her work. "The closest progenitor of COVID-19 virus is still mysterious and it's definitely not from my lab or any other labs," she told *Science* on 18 April. "It's a shame to make the science so complicated."

The Chinese government has rejected assertions that it bears responsibility for the pandemic—and has suggested that the virus originated in the United States. The government says it has launched investigations into the origins of the virus, but has provided few details and has placed restrictions on scientists in China who are studying the question. "They're not helping themselves," says James Le Duc, director of Galveston National Laboratory, where he runs a BSL-4 lab.

"The closest progenitor of COVID-19 virus is still mysterious and it's definitely not from my lab ..."
Shi Zhengli, Wuhan Institute of Virology

China is facing growing pressure to allow an independent investigation. On 1 May, the World Health Organization's (WHO's) Emergency Committee of expert advisers recommended a probe that would involve "field missions" to China and perhaps inlcude the World Organisation for Animal Health and the U.N. Food and Agriculture Organization.

Others have made similar recommendations. "It would seem entirely reasonable and sensible that the world would want to have an independent assessment of how this all occurred, so we can learn the lessons and prevent it from happening again," Australian Prime Minister Scott Morrison said on 23 April in urging a WHO probe.

WHO is not involved in studies in China, says spokesperson Tarik Jasarevic, but it "would be keen to work with international partners and at the invitation of the Chinese government to participate in investigation around the animal origins" of the virus.

Daszak, meanwhile, says he is trying to engage NIH about the future of his group's work. He says he asked on 27 April to speak with Lauer, but had not heard back as of 5 May, when *Science* went to press. ■

With reporting by Kai Kupferschmidt, David Malakoff, Dennis Normile, and John Travis.

COVID-19

Children's role in pandemic is still a puzzle

Some countries reopen schools, hoping it won't accelerate transmission

By **Gretchen Vogel** *and* **Jennifer Couzin-Frankel**

For families eager for schools to throw open their doors, the tale of a 9-year-old British boy who caught COVID-19 in the French Alps in January offers a glimmer of hope. The youngster, infected by a family friend, suffered only mild symptoms; he enjoyed ski lessons and attended school before he was diagnosed. Astonishingly, he did not transmit the virus to any of 72 contacts who were tested. His two siblings escaped infection even though other germs spread readily among them: In the weeks that followed, all three had influenza and a common cold virus.

The story could be a bizarre outlier—or a tantalizing clue. Several studies of COVID-19 hint that children are less likely to catch the novel coronavirus and don't often transmit it to others. A recent survey of the literature couldn't find a single example of a child younger than 10 passing the virus on to someone else, for example.

Relying on those encouraging if scant data—and the reassuring indications that very few children get severely ill from COVID-19—some governments are beginning to reopen schools. Denmark sent children up to age 11 back on 15 April, and Germany welcomed back mostly older children on 29 April. Some Israeli schools reopened on 3 May; the Netherlands the Canadian province of Quebec plan to reopen many primary schools on 11 May. Most schools are resuming with reduced class sizes, shortened school days, and extra hand washing.

Ending school closures has clear benefits for children's education and mental health—not to mention their parents' well-being—but scientists disagree about the risks. Some worry that even if children transmit less efficiently than adults, they may make up for it by their far more expansive web of contacts, especially at school. "From the data we have so far, it

Published by AAAS



Children are back in class in Copenhagen, Denmark, but must be seated at a safe distance from each other.

PHOTO: THIBAULT SAVARY/AFP VIA GETTY IMAGES

is very dangerous to open schools and day cares at the moment," says Marco Ajelli, an epidemiologist at the Bruno Kessler Foundation in Trento, Italy. Several new studies now underway aim to better gauge the risk, including one announced on 4 May by the U.S. National Institutes of Health (NIH) that will follow 2000 families for 6 months. "We need this information to safely plan for return to school and work and play," says Catherine Birken, a pediatrician and researcher at the Hospital for Sick Children in Toronto. "Without it, we're completely in the dark."

As parents and teachers know all too well, children excel at catching and sharing germs, from influenza to common colds, even when they don't feel very sick themselves. "Respiratory viruses really like children," says Isabella Eckerle, a virologist at Geneva University Hospitals.

Could COVID-19 be different? The evidence so far is mixed. Researchers in Iceland, one of the few countries to conduct mass screening, turned up no infections in 848 children under the age of 10 without significant symptoms, compared with an infection rate of nearly 1% in ages 10 and older. A U.S. analysis of nearly 150,000 infected people found that just 1.7% were younger than 18. But a study of 391 cases and almost 1300 close contacts in Shenzhen, China, reported that children were just as likely to be infected as adults. Eckerle cautions that some of these data come from surveys done after shutdowns were put in place. "They were collected in an artificial situation," she says. Children "weren't going to the playground and were not going to school."

Several studies suggest children who do get sick with COVID-19 are just as infectious as ailing adults. Researchers have detected the same amounts of viral RNA in nose or throat swabs from sick children as in those from older patients. Finding RNA does not always mean a person is infectious; it can also come from noninfectious viral remnants. But in a 1 May preprint, Eckerle's team reported that 12 out of 23 children sick with COVID-19 had virus in their nose or throat able to attack and infect human cells, a rate similar to adults.

Far less is known about the risk posed by infected children with few or no symptoms. But there's at least one example of a child who didn't appear sick and was nevertheless a virus factory: In February, doctors in Singapore described a 6-month-old baby, infected without apparent symptoms, whose coronavirus levels were on par with those of sick adults.

Real-life studies of how often children transmit COVID-19 are scarce. Researchers at the Dutch National Institute for Public Health and the Environment (RIVM) looked carefully at how the disease spread in 54 households, together comprising 123 adults and 116 children aged 16 or younger. They didn't find a single family in which a child was the first patient. This study, too, began only after schools closed, says RIVM epidemiologist Susan van den Hof, but additional evidence comes from Dutch contact tracing studies: Of 43 contacts of infected children and teens who were followed, none became infected.

Critics have noted these numbers, posted on RIVM's website, are too small to be statistically significant. But combined with other studies, Van den Hof says, "The data all seem to be pointing in the same direction: that there is not as much transmission from children." That helped convince the Dutch government to reopen elementary schools—and allow children's sport teams to practice—starting next week.

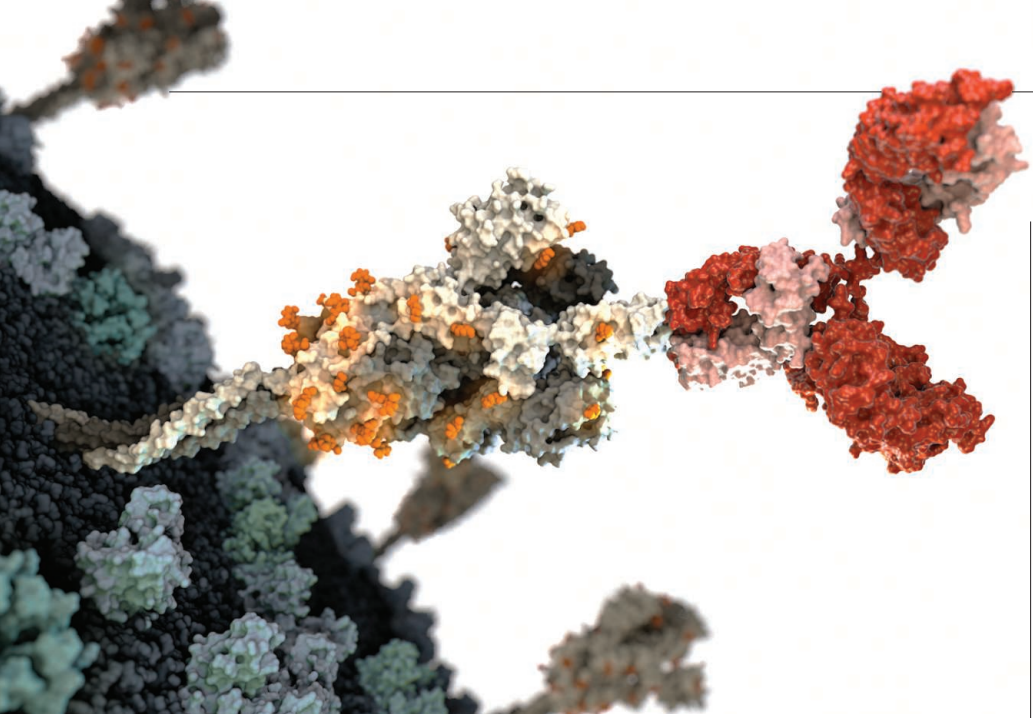
Ajelli, who thinks such moves premature, teamed with colleagues in China to estimate the effects of school closures and other social distancing measures in Shanghai and Wuhan, China. Based on contact surveys, which ask subjects how many other people they typically meet during school or workdays and on the weekend, the team found that children have approximately three times as many contacts as adults. Although they were only one-third as likely to be infected, keeping children at home helped curb China's outbreaks, the team concludes in a paper published online by *Science* on 29 April. Reopening schools will likely accelerate transmission, Ajelli cautions.

To pinpoint the role of children, Birken and her colleague Jonathon Maguire at St. Michael's Hospital, also in Toronto, plan to scrutinize transmission as it happens. They have begun to recruit 1000 families, all of them part of an ongoing children's health study in the region, for weekly nasal swabs, symptom checklists, and queries about day-to-day family life. Were children biking with friends? Did parents go to the grocery store? Birken also hopes to see what happens as school closures and other restrictions are lifted. The NIH study has a similar setup and draws from existing pediatric research projects in 11 cities. Another study is ongoing in the Netherlands.

"Doing studies as schools reopen will be really important," says infectious disease specialist Susan Coffin of the Children's Hospital of Philadelphia, who is planning one herself in her hometown. It would include regular testing of children, staff, and teachers, along with other members of students' households. Coffin hopes to trace contacts and sequence the virus from individual patients, which can help clarify who transmitted it to whom.

Even without those efforts, daily case numbers could soon provide a reality check. If children are ample virus spreaders after all, cases could surge in a matter of weeks in the countries reopening their schools. If they aren't, parents and policymakers will heave a sigh of relief and more countries may follow. "Everyone is looking at each other," Van den Hof says, "to see what will happen." ■

Published by AAAS



An antibody (orange) bound to the surface spike protein of SARS-CoV-2 can block infection.

COVID-19

The race is on for antibodies that stop the new coronavirus

Mass-produced immune proteins may outpace a vaccine

By **Jon Cohen**

One of the first people to be diagnosed with COVID-19 in the United States hopes a legacy of her nightmare—the antibodies it left in her blood—will lead to a drug that can help others infected with the novel coronavirus that has now killed more than 250,000 people worldwide.

Early this year, the woman had just learned of the outbreak in Wuhan, China, when she flew to Beijing to celebrate the Lunar New Year with her elderly parents and extended family. A brother from Wuhan joined the gathering on 23 January, catching one of the last flights out before the city went into a lockdown. Days later, her father developed a fever, but the family wasn't concerned. "My dad always has some fever in the winter," says the woman, a researcher who asked to be called Dr. X to protect her privacy. On 28 January, her brother also developed a fever.

The next day, on her scheduled flight home, a nervous Dr. X wore a mask, brought disinfectant wipes and cleaned everything she touched, and didn't accept any food or drinks from flight attendants. "I treated myself as a potential infectious source."

Her husband picked her up at the airport, wearing a mask. With the car windows rolled down, they drove to an emergency room to request a coronavirus test. "I didn't have a fever, so they didn't really take me seriously," she says. But coincidentally, her brother texted as she waited to be seen: He had COVID-19. So she received a test. Days later, after she quarantined herself, developed mild COVID-19 symptoms, and then rebounded, the result came back positive.

By then, her brother and father had both been hospitalized. The brother recovered after 12 days, but her father, a retired scientist in his 80s, went from a ventilator to extracorporeal membrane oxygenation, an artificial lung of sorts. The novel coronavirus, SARS-CoV-2, ultimately infected all seven family members who had gathered for the New Year celebration.

Dr. X could not help her sick family members, but her eagerness to do something grew. She knew that in China, plasma from recovered people, which contains antibodies to the virus, was showing promise as a treatment. Her doctor told her about a project, a collaboration between Vanderbilt University and AstraZeneca, to develop something safer and more powerful. It aims to go beyond the mishmash of antibodies in convalescent plasma and pull out the equivalent of a guided missile: an antibody that "neutralizes" the infectivity of SARS-CoV-2 by binding to the so-called spike protein that enables it to enter human cells. Once one or several neutralizing antibodies have been identified, antibody-producing B cells can be engineered to make them in quantity. These so-called monoclonal antibodies could treat or even prevent COVID-19.

The Vanderbilt-AstraZeneca team is far from the only group trying to identify or engineer monoclonals against SARS-CoV-2. Unlike the many repurposed drugs now being tested in COVID-19 patients, including the modestly effective remdesivir, the immune proteins specifically target this virus. Whereas some groups hope to sieve a neutralizing antibody (a "neut") from the blood of a survivor like Dr. X, others are trying to produce neuts in mice by injecting them with the spike protein. Still others aim to reengineer an existing antibody or even create one directly from DNA sequences.

Many researchers are optimistic that antibodies will, relatively quickly, prove their worth as a preventive or remedy that buys the world time until a vaccine arrives—if it does. "We've got at least 50—and probably more we don't know about—companies and academic labs that are all racing horses," says immunologist Erica Ollmann Saphire of the La Jolla Institute for Immunology, who leads an effort to coordinate and evaluate candidate monoclonals. Regeneron Pharmaceuticals, which developed a cocktail of three monoclonal antibodies that worked against the Ebola virus—a notoriously difficult disease to treat—may be out of the gates first with a candidate monoclonal drug entering clinical trials as soon as next month.

Saphire says many questions remain. "We need a sense of the landscape: What are the most effective antibodies against this virus? If we need a cocktail of two, what is the most effective combination?" she asks. "And you might want a very different kind of antibody to prevent infection versus treating an established one."

John Mascola, an immunologist at the U.S. National Institute of Allergy and Infectious Diseases (NIAID), adds that some antibodies may have nonneutralizing, immune-boosting properties. "The field doesn't know very much about protective immunity to SARS-CoV-2," Mascola says. "So there's a little bit of scientific guesswork here."

On a practical level, monoclonals are relatively difficult to make and administer; they have to be given by intravenous drip or injected, and they have traditionally been niche medicines available mainly in wealthy countries. "Monoclonals may well have a very important role," says Jeremy Farrar, head of the Wellcome Trust charity and an

CREDITS: (ILLUSTRATION) V. ALTOUNIAN/*SCIENCE*; (IMAGES) W. SURYA *ET AL.*, *BIOCHIM. BIOPHYS. ACTA* 1860 1309 (2018); D. WRAPP *ET AL.*, *SCIENCE*, 367, 6483, 1260 (2020); E. O. SAPHIRE *ET AL.*, *SCIENCE*, 293, 5532, 1155 (2001); M. D. HARTMANN, *PNAS*, 106, 40, 16950 (2009); ORIENTATIONS OF PROTEINS IN MEMBRANES DATABASE

Published by AAAS

infectious disease specialist. "The big questions will be the capacity to manufacture at scale, distribute, and the cost."

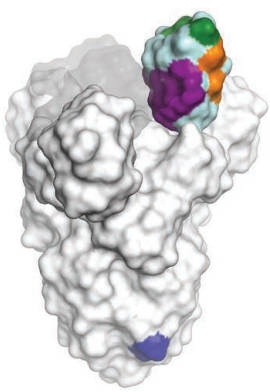
On 7 March, Dr. X visited the Vanderbilt lab led by James Crowe to donate blood. "I couldn't really help my dad," the woman says. "It was too late. So I want to make sure that fewer people have to go through what my family has gone through."

Her father died 9 days later.

FROM EBOLA TO COVID-19

Although monoclonal antibodies to treat cancer and autoimmune diseases are a booming business, few for infectious diseases have come to market so far. Regeneron's monoclonal cocktail for Ebola offers an example of their power. It proved its worth during an outbreak in the Democratic Republic of the Congo (DRC) last year and could be approved soon by the U.S. Food and Drug Administration. And a single monoclonal developed by an NIAID team that included Mascola thwarted Ebolavirus in the same DRC study. No other Ebola treatments—including drugs and convalescent plasma—had worked.

Treating millions of people worldwide with a monoclonal isn't far-fetched, Crowe says. "In the past, fully human antibodies were difficult to isolate and expensive to produce," he notes. But it's getting easier and cheaper. "In the next 5 years, antibodies will become the principal tool used as a medical countermeasure in the event of an epidemic," he predicts.



The receptor-binding domain (top) at the tip of SARS-CoV-2's spike protein can be blocked by antibodies targeting several different areas (colors).

IMAGE: N. WU AND M. YUAN

It generally takes weeks before an infected person's B cells begin to pump out neuts. Because of the lag, Crowe's team—one of four funded by the Pentagon's Defense Advanced Research Projects Agency (DARPA) to discover monoclonals for emerging infectious threats—sought out early U.S. COVID-19 patients, including Dr. X. The team isolated antibody-producing B cells from the volunteers and used the spike protein, linked to a magnetic bead, as bait for the tiny percentage that produce neuts against SARS-CoV-2.

When they initially bled Dr. X, some 6 weeks after she became infected, those special B cells were only faintly detectable. En route to the airport on a Sunday morning to fly home, Dr. X stopped in the lab for yet another bleed, and they finally struck gold.

A second DARPA-funded group, Canada's AbCellera Biologics, uses a version of spike that Mascola and co-workers engineered as neut bait. To isolate single B cells, copies are placed in 200,000 fluid-filled chambers of a device the size of a credit card. From blood of an early U.S. COVID-19 case in Seattle who had severe disease, AbCellera found 500 candidate antibodies against spike. It whittled them down to 24 leads, selecting those that retain their shape when mass produced and stick longest to the viral protein. (Antibodies bounce on and off their targets.)

Regeneron has similarly bled recovered COVID-19 patients, but it is also injecting spike into mice equipped with human genes for antibody production. From a pool of human- and mouse-derived antibodies, the company plans to select two that neutralize a broad range of SARS-CoV-2 variants. Regeneron is aiming for a pair of antibodies that bind to nonoverlapping sites on spike, Christos Kyratsous, vice president of research at Regeneron, says. This type of antibody cocktail provides an insurance policy against the emergence of mutant strains of SARS-CoV-2 that resist the treatment. "It's unlikely that both sites [on spike] are going to change at the same time," Kyratsous says.

AstraZeneca, in addition to screening blood from recovered patients and spike-injected mice, is sifting through a massive library of essentially random antibodies created with a method involving viruses called phages. Most groups assume that effective antibodies must target the very tip of the spike, its so-called receptor-binding domain (RBD). But Mark Esser, an AstraZeneca vice president, says, "We have found interesting antibodies that bind to other parts of the spike protein."

Research groups are also searching for leads from other coronavirus diseases such as severe acute respiratory syndrome (SARS). Vir Biotechnology has found an antibody in a recovered SARS survivor from 2003 that neutralizes SARS-CoV-2. This antibody binds to a region of the RBD that is "highly conserved" between the two coronaviruses, Vir reported in an April preprint.

The company went on to modify the antibody to make it more potent. One modification slows the antibody degradation to give it a longer effective life; another improves the so-called vaccinal effect, which summons T cells—another arm of the immune system—to help destroy infected cells.

Jacob Glanville, an immunologist and computer scientist who runs Distributed Bio, has designed neuts for SARS-CoV-2 in a computer, drawing on genetic sequences and structures of ones known to thwart the SARS virus in cells and even mice. "I'm basically able to get a freebie ride on [past] research in a very brief period," Glanville says.

With molecular modeling software, Glanville mutated the antibodies to the SARS virus into billions of variants. And using phages as well, Glanville's group created a still larger library of antibodies. The researchers then sorted through what Glanville calls "this vast mutational space" for antibodies predicted to bind to SARS-CoV-2 spike, identifying 50 leads they are testing in vitro. They soon hope to select the best 13 candidates.

Glanville says the aim is to find antibodies that can potently neutralize a broad range of coronaviruses. "The exercise here is to approve one drug that will protect us from this current outbreak but also will enable us to have a tool at our disposal immediately when the next coronavirus outbreak takes place." That way, he says, "We don't have to play this game every time."

THE BURDEN OF CHOICE

With so many COVID-19 monoclonals being developed, "How do you know what is really best and why?" Saphire asks. The Coronavirus Immunotherapy Consortium she leads, funded by $1.7 million from the Bill & Melinda Gates Foundation, is organizing a large-scale, blinded, side-by-side evaluation of candidate monoclonals in test tube studies that gauge their ability to thwart SARS-CoV-2 infection of human cells. The consortium also plans to compare lead candidates in animal models, but needs funding for that costly endeavor.

A doctor in northern Italy who recovered from COVID-19 and has, like Dr. X, contributed his own plasma to AstraZeneca's antibody hunt, stresses that it's far from a given that monoclonals will work. "We don't know the role of neutralizing antibodies in this disease," says the doctor, who asked not to be named because of his hospital's concerns about publicity. He is also personally familiar with the cost and scarcity of existing monoclonal drugs: His hospital has already had difficulty obtaining immune-calming monoclonals for COVID-19 patients who were having dangerously strong immune reactions to the virus.

A COVID-19 vaccine could, in the long run, do away with the global need for SARS-CoV-2 monoclonals. But Mene Pangalos, AstraZeneca's executive vice president of pharmaceutical R&D, stresses that prospect doesn't concern the company. That would be "fantastic," he says. "It's important for one of us to solve this pandemic so that we can all get back to some semblance of normality." ■

Published by AAAS

COVID-19

Ape researchers mobilize to save primates from coronavirus

Past respiratory epidemics raise fears of infection in apes

By **Ann Gibbons**

Seven years ago, a respiratory virus swept through 56 chimpanzees in a community at Kibale National Park in Uganda, where researchers have studied chimp behavior for 33 years. More than 40 apes were sickened; five died. "Chimpanzees looked like limp dolls on the forest floor," recalls disease ecologist Tony Goldberg of the University of Wisconsin, Madison. "It was just horrendous."

The culprit? Rhinovirus C, a human common cold virus, according to samples from a dead infant chimp. Goldberg is "100% certain" the virus came from a human, perhaps a tourist, researcher, or villager.



Six-year-old Amina, in Uganda, lost her mother to a respiratory virus.

Human respiratory viruses are already the leading cause of death in chimp communities at Kibale and at Gombe Stream National Park in Tanzania, where Jane Goodall worked, according to a study led by Goldberg. Now, researchers are gearing up to protect apes as well as local people from COVID-19. Last week, hundreds of researchers, conservationists, and veterinarians gathered virtually to share strategies in back-to-back webinars held by the Ape Alliance and the African Primatological Society. They are already cordoning off preserves, working with locals to reduce contact with apes, and wearing masks in the forest.

The ape form of the receptor that the new coronavirus uses to enter cells (the angiotensin-converting enzyme 2, or ACE2, receptor) is identical to the human one, so it's likely apes can be infected, according to an 11 April preprint on bioRxiv. If the virus gets into ape communities, flattening the curve will be all but impossible. "Gorillas can't social distance," says primatologist Tara Stoinski at the Dian Fossey Gorilla Fund.

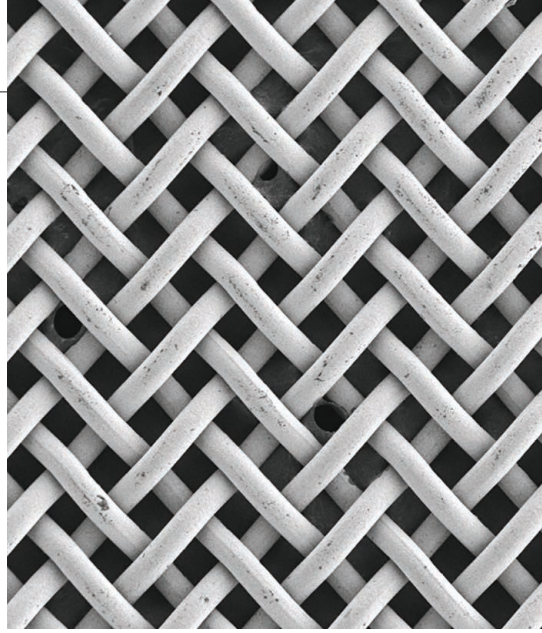
The virus would hit already depleted populations. Among chimps at Taï National Park in Côte d'Ivoire, researchers have detected repeated outbreaks of viruses and strep since 1999. Each time a respiratory virus swept through, about one-quarter of the chimps died, says primatologist Roman Wittig of the Max Planck Institute for Evolutionary Anthropology. Those deaths, plus poaching and habitat loss, have shrunk the Taï forest chimp population from 3000 in 1999 to 300–400 today, he says.

Among mountain gorillas, respiratory viruses cause up to 20% of sudden deaths, according to a February report in *Frontiers in Public Health*. Half the world's 1063 mountain gorillas live at Bwindi Impenetrable National Park in Uganda, where 40,000 tourists visit every year. The February study found that more than 98% of the observed tourist groups got closer to the gorillas than the mandated 7 meters, and that sick tourists tried to hide their illnesses, Bwindi veterinarian Gladys Kalema-Zikusoka said in a webinar.

African governments have already stopped all ape-related tourism. At Bwindi, Kalema-Zikusoka trained 130 Ugandan Wildlife Authority rangers on how to keep coronavirus from gorillas and monitor the apes for illness. At Taï and Kibale, researchers who observe the apes quarantine for up to 14 days, wear masks, and keep their distance, among other actions. And researchers at Taï can send chimps' feces to be tested for COVID-19.

To keep people out of the forest and reduce hunting, some researchers are offering goats to local people or helping farmers grow cash crops like coffee. In Lomami National Park in the Democratic Republic of the Congo, researchers had to chase a female bonobo to train her to stay out of a village, primatologist Jo Thompson, director of the Lukuru Wildlife Research Project in the DRC, said in a webinar.

If apes do sicken and become too weak to climb into their sleeping nests in trees, researchers may sleep nearby to protect them from leopards or poachers, Wittig says. But there are no plans to treat sick animals. ■



MATERIALS SCIENCE

Without fossil fuels, reactors churn out chemicals

Prospects brighten for making fertilizer, plastics with solar and wind power

By **Robert F. Service**

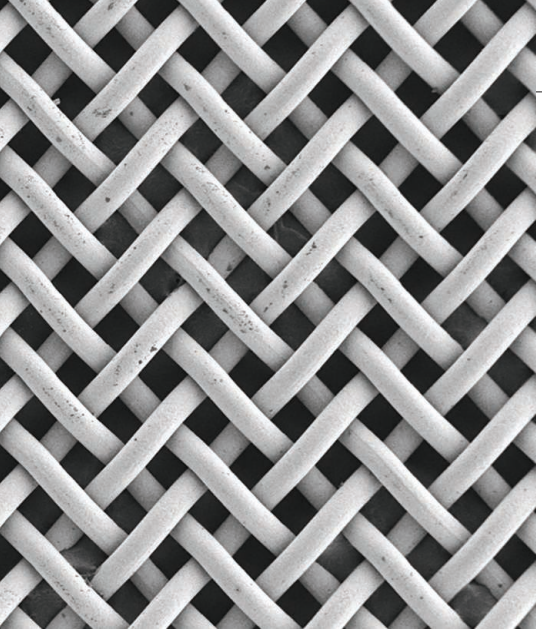
As windmills and solar panels multiply, the supply of renewable electricity sometimes exceeds demand. Chemists would like to put the excess to work making commodity chemicals, such as the raw materials for fertilizer and plastics, which are now produced with heat, pressure, and copious fossil fuels. The electrochemical cells that can harness renewable electricity to make these compounds have been too slow to be practical. Now, two groups report redesigning the cells to achieve a dramatic speedup—perhaps enough to put green industrial chemistry within reach.

"In the future, electrons to molecules will be a major part of how we do chemical synthesis," says Etosha Cave, chief scientific officer of Opus 12, a startup aiming to turn renewable energy into chemicals. "These two papers help push that vision forward."

One research group uses carbon dioxide (CO_2) as its starting material to make ethanol, a fuel, and ethylene, a starting point

IMAGES: (LEFT TO RIGHT) JEREMY CLIFT; N. LAZOUSKI *ET AL*., *NATURE CATALYSIS*, 4 MAY 2020

Published by AAAS



A stainless steel mesh is at the heart of an electrically powered device that synthesizes ammonia.

for plastics; the other turns nitrogen (N_2) into ammonia (NH_3), a key component in fertilizer. Both owe their progress to advances in the catalyst-coated electrodes that drive chemical reactions between gases and liquids.

In theory, turning CO_2 into hydrocarbons such as ethanol and ethylene is simple: Just add energy to the CO_2 so it can steal hydrogen atoms from water. But the reactions are tricky. They take place in electrolyzers, which consist of two electrodes separated by a liquid electrolyte. At one electrode, the anode, water splits into oxygen, electrons, and hydrogen ions, or protons. The protons then migrate through the electrolyte to the cathode, where they react with CO_2, which is fed in separately, to make the hydrocarbons.

In current electrolyzers, the cathode typically consists of a 3D carbon mesh dotted with tiny copper catalyst particles. Their "gas diffusion" design allows CO_2 gas that infiltrates the mesh to interact with all the catalyst particles simultaneously. One side of the mesh is also in contact with the liquid electrolyte, which helps ferry protons over from the anode. But water in the electrolyte can also infiltrate the pores, blocking CO_2 gas from reaching the catalyst particles.

Coating the electrode with a water-repellent, fluorine-rich polymer can help. That and other improvements have resulted in electrolyzers that efficiently convert a modest input of electricity into hydrocarbons. But only about 40% of the product compounds have two carbon atoms, as ethylene and ethanol do. Much of the rest is methane, which has one carbon and is less valuable.

Now, researchers led by Ye Wang, a chemist at Xiamen University, report that adding fluorine to the standard copper catalyst on their gas diffusion electrode changes the pathway of the reactions, so that up to 85% of the resulting products are valuable two-carbon compounds.

The setup can also handle 1600 milliamps of current per square centimeter of catalyst, twice the throughput of the previous record holder, the researchers reported on 20 April in *Nature Catalysis*. "[It's] definitely in the range where someone will be interested in commercializing the technology," says Karthish Manthiram, a chemical engineer at the Massachusetts Institute of Technology.

Manthiram reported parallel improvements in an electrochemical process for making NH_3 using N_2 from air and hydrogen (H_2). The H_2, made by splitting water in a separate cell, is fed into a second electrolyzer, where it splits into protons and electrons at the anode. The protons pass through a liquid electrolyte made of an organic solvent that the team spikes with lithium to speed transfer of hydrogen to nitrogen. At the cathode, a three-step chemical process takes place: Piped-in N_2 splits into individual nitrogen atoms, which react with the lithium to make lithium nitride. The lithium nitride then reacts with protons and electrons coming from the anode to make NH_3, regenerating the lithium.

Manthiram's team couldn't use a porous carbon cathode because the liquid electrolyte would flood the electrode, blocking N_2 gas from the catalyst particles. So the researchers replaced the carbon cathode with a stainless steel mesh, which repels the organic electrolyte and allows N_2 in.

The setup churned out ammonia nearly five times as fast as the previous record, the group reported this week in *Nature Catalysis*. Its efficiency for transferring electrons from water to NH_3 is 40%, the highest ever achieved with an electrolyzer.

That still doesn't rival the performance of fossil fuel–based plants, which can make ammonia with up to 80% energy efficiency—an even more stringent measure than transferring electrons—but "it's absolutely great," says Matteo Cargnello, a chemical engineer at Stanford University. Lauren Greenlee, a chemical engineer at the University of Arkansas, Fayetteville, agrees: "I think people will really jump on this" in search of further improvements.

With oil prices crashing because of price wars and the coronavirus pandemic, companies will likely continue to rely on fossil fuels to produce ammonia, ethanol, and other commodity chemicals in the near future. But as researchers continue to improve electricity-based production methods, even cheap fossil fuels may ultimately prove no match for surplus green energy. ■

SCIENTIFIC COMMUNITY

Paperwork mistakes ensnare health data expert

Georgia Tech professor faces sentencing—and may lose her job—for mishandling grant

By **Jeffrey Mervis**

Eva Lee is in high demand for her ability to crunch massive amounts of health care data. Government and public health officials fighting the COVID-19 pandemic are clamoring to use software that the Georgia Institute of Technology systems engineering professor began to develop nearly 2 decades ago to maximize the use of limited health resources. And Lee's participation in a group of U.S. scientists who raised an early alarm about the pandemic has drawn national media attention.

In spite of the acclaim, Lee's future is in jeopardy. On 21 May, she is scheduled to be in a federal court in Atlanta learning her punishment for mishandling a National Science Foundation (NSF) grant that supported her research. The judge's sentence, which follows her guilty plea in December 2019 to charges of providing false information to NSF, is likely to trigger a review by Georgia Tech officials that could lead to her dismissal.

"I thought the plea would let me go back to work," says Lee, whose plight has led dozens of colleagues to pen letters urging the federal government and the university to show leniency. But her case is a sobering reminder that, although institutions are responsible for ensuring that grants are properly managed, individual scientists can face serious consequences if they don't follow the rules.

Over the years, Lee has received more than $10 million in grants from multiple U.S. government agencies to develop optimization models for improving health care. Yet it's one of the smallest of those awards—an NSF grant of $240,000 over 5 years—that has gotten her into so much trouble. That

Published by AAAS

grant supported her continued participation in the Center for Health Organization Transformation (CHOT), a multisite project launched in 2008 by NSF's Industry-University Collaborative Research Centers program. Companies pay $50,000 a year to help shape the center's research agenda and use its findings.

Lee's research has helped improve care for thousands of patients, including those at Grady Memorial Hospital in Atlanta, which cut emergency room waiting times by half and nearly eliminated postsurgical infections among cardiac patients. "Her model … gave me the data I needed to make the case for needed improvements," says Michael Wright, a former senior vice president for operations at Grady.

In 2014, NSF renewed CHOT, which is based at Texas A&M University, College Station, for 5 more years. But Lee says Georgia Tech, which had handled the grant's paperwork during its first phase, left her to oversee that task in its second phase.

To meet NSF's rules, she had to document that Georgia Tech was receiving a total of at least $175,000 from at least three companies. But an investigation done by NSF's Office of Inspector General (OIG) found that she made up the numbers. "I had no idea what [the industry partners] were contributing," she admits. "I knew that it was well over the limit. So I just put down $50,000 for each one."

Lee also admitted to OIG that when she needed the signature of a Georgia Tech administrator on annual reports to NSF, she simply lifted it from previous documents. Lee told investigators that she assumed the signature was still valid.

In addition, Lee confessed that she had manipulated the process used to set the center's research priorities. Members of its Industrial Advisory Board (IAB) vote on those priorities after hearing pitches from each research team. But in an interview with OIG in April 2019, Lee "admitted that she [had] voted on behalf of IAB members."

Based on its investigation, NSF's OIG concluded Lee's behavior represented "a significant departure from accepted practices." Her punishment, handed down in September 2019, was a 3-year ban as a reviewer or consultant on NSF grant proposals.

But that didn't end matters. Lee was also the target of a federal investigation for aggravated identify theft for the purloined signature, and fraud for the incorrect information sent to NSF. (The U.S. attorney's office has declined to say why it decided to prosecute Lee.) If convicted, she would face a minimum of 2 years in prison. But after Lee's guilty plea to two lesser charges—filing a false statement to NSF and lying to OIG—the U.S. attorney promised to ask District Court Judge Steve Jones to impose 8 months of home confinement instead.

Lee's lawyer, Buddy Parker, says the sentence should be no more than 6 months' probation, citing her services to public health and the nature of her offense. "Dr. Lee stole no monies from NSF," he says.



"I just want to get back to my students and my research."

Eva Lee, Georgia Institute of Technology

"She stole no monies from Georgia Tech." Parker also decries what he calls "an abandonment … of prosecutorial discretion" and the government's refusal to agree to an out-of-court settlement.

Lee and Parker are equally upset with Georgia Tech's behavior. One week after NSF interviewed her, Lee was suspended with pay, banned from campus, and denied access to her research data and her Georgia Tech email. Parker accuses the university of trying to cover up its own mistakes. Its program office "for over 3 years failed to support Dr. Lee in the administrative work with NSF," Parker asserts. But Georgia Tech "disagrees" with that claim and disputes the idea "that she was left on her own," says W. Blair Meeks, the university's assistant vice president for external communications.

Lee's friends and colleagues don't excuse her errors, but they also don't seem surprised. Her personality and circumstances likely played a role in her predicament, they surmise.

"She's flat-out brilliant. … She also wants to help people," says Rice University mathematician Richard Tapia, a National Medal of Science winner and her graduate adviser in the 1990s. But Lee can have difficulty with some everyday tasks, he says. "She has trouble tying her shoelaces, she can't operate a copying machine. … She makes a lot of administrative mistakes. So do I," Tapia says. "Fortunately, I have someone whose job is to save me. But Eva doesn't."

Mark Plausnitz, a Georgia Tech biochemical engineering professor who has known Lee for 20 years, says he's been able to use resources within his department to employ an assistant to help with the necessary paperwork on his grants. But he says Lee, who is in a different department in the engineering school, "doesn't have the benefit of someone like that."

Georgia Tech, like all large research universities, has an office responsible for managing external grants. But faculty members can't always count on getting the help they need from that office, Plausnitz says. Lee says program staff were "extremely helpful" during the first phase of her grant, but not the second phase. And without that help, she says, she cut corners.

Lee's prolonged separation from campus has wreaked havoc on her lab, which 1 year ago included 15 Ph.D. students, 10 master's students, and 40 undergraduates, she says. That separation could become permanent if the university exercises its authority to dismiss a faculty member who has committed a felony.

"We are not doing interviews about this because Dr. Lee has not been sentenced and she is undergoing employment review," Meeks said when asked about Lee's prospects. "We do not want to disrupt either process."

With her fate in the balance, Lee has been working long hours from home, consulting with government officials and public health scientists on the pandemic. "I just want to get back to my students and my research," she says. ■

PHOTO: VILLAR LOPEZ/EFE/NEWSCOM

Published by AAAS



Newly isolated bacteria grown on agar plates or their products could act as "psychobiotics."

MEET THE PSYCHOBIOME

Mounting evidence that gut bacteria influence the nervous system inspires efforts to mine the microbiome for brain drugs

By **Elizabeth Pennisi**, *in Cambridge, Massachusetts; Photography by* **Ken Richardson**

Katya Gavrish is searching for new brain drugs in a seemingly unlikely place: human stool samples. An earnest and focused microbiologist who trained in Russia and loves classical music, she's standing in front of a large anaerobic chamber in a lab at Holobiome, a small startup company here. She reaches into the glass-fronted chamber through Michelin Man–like sleeves to begin to dilute the sample inside. That's the first step toward isolating and culturing bacteria that Gavrish and her Holobiome colleagues hope will produce new treatments for depression and other disorders of the brain and nervous system.

The eight-person company plans to capitalize on growing evidence from epidemiological and animal studies that link gut bacteria to conditions as diverse as autism, anxiety, and Alzheimer's disease. Since its founding a mere 5 years ago, Holobiome has created one of the world's largest collections of human gut microbes. The company's CEO, Phil Strandwitz, cannot yet say exactly what form the new treatments will take. But the targeted ailments include depression and insomnia, as well as constipation, and visceral pain like that typical of irritable bowel syndrome—conditions that may have neurological as well as intestinal components. Strandwitz, a mild-mannered Midwesterner with a Ph.D. in microbiology, isn't prone to visionary statements, but neither is he short on ambition: He predicts the first human trial will start within 1 year.

The allure is simple: Drug development for neuropsychiatric disorders has lagged

Published by AAAS

for decades, and many existing drugs don't work for all patients and cause unwanted side effects. A growing number of researchers see a promising alternative in microbe-based treatments, or "psychobiotics," a term coined by neuropharmacologist John Cryan and psychiatrist Ted Dinan, both at University College Cork. "This is a really young and really exciting field with a huge amount of potential," says Natalia Palacios, an epidemiologist at the University of Massachusetts, Lowell, who is looking into connections between gut microbes and Parkinson's disease.

Some researchers prefer a less hurried approach focused on understanding the underlying biology. But Holobiome and a few other companies are eager to cash in on the burgeoning, multibillion-dollar market that has already sprung up for other microbial therapies, which aim to treat conditions including intestinal disorders, allergies, and obesity. Those companies are pushing ahead despite many unresolved questions about how psychobiotic therapies might actually work and the potential dangers of moving too fast. "There's a gold rush mentality," says Rob Knight, a microbiologist at the University of California (UC), San Diego.

OVER THE PAST 20 YEARS, the recognition that the microbes living inside us outnumber our body's own cells has turned our view of ourselves inside out. The gut microbiome, as it's known, weighs about 2 kilograms—more than the 1.4-kilogram human brain—and may have just as much influence over our bodies. Thousands of species of microbes (not only bacteria but also viruses, fungi, and archaea) reside in the gut. And with as many as 20 million genes among them, those microbes pack a genomic punch that our measly 20,000 genes can't match. Gut bacteria can make and use nutrients and other molecules in ways the human body can't—a tantalizing source of new therapies.

The brain is the newest frontier, but it's one with an old connection to the gut. The ancient Greeks, for example, believed mental disorders arose when the digestive tract produced too much black bile. And long before microbes were discovered, some philosophers and physicians argued that the brain and gut were partners in shaping human behavior. "What probably happens is that our brain and our gut are in constant communication," says Cryan, who over the past decade has helped drive efforts to decode those communications.

Epidemiological researchers have turned up intriguing connections between gut and brain disorders. For example, many people with irritable bowel syndrome are also depressed, people on the autism spectrum tend to have digestive problems, and people with Parkinson's are prone to constipation.

Researchers have also noticed an increase in depression in people taking antibiotics—but not antiviral or antifungal medications that leave gut bacteria unharmed. Last year, Jeroen Raes, a microbiologist at the Catholic University of Leuven, and colleagues analyzed the health records of two groups—one Belgian, one Dutch—of more then 1000 people participating in surveys of their types of gut bacteria. People with depression had deficits of the same two bacterial species, the authors reported in April 2019 in *Nature Microbiology*.

Researchers see ways in which gut microbes could influence the brain. Some may secrete messenger molecules that travel though the blood to the brain. Other bacteria may stimulate the vagus nerve, which runs from the base of the brain to the organs in the abdomen. Bacterial molecules might relay signals to the vagus through recently discovered "neuropod" cells that sit in the lining of the gut, sensing its biochemical milieu, including microbial compounds. Each cell has a long "foot" that extends outward to form a synapselike connection with nearby nerve cells, including those of the vagus.

Indirect links may also exist. Increasingly, researchers see inflammation as a key factor in disorders such as depression and autism. Gut bacteria are key to proper immune system development and maintenance, and studies show that having the wrong mix of microbes can derail that process and promote inflammation. And microbial products may influence what are known as enteroendocrine cells, which reside in the lining of the gut and release hormones and other peptides. Some of those cells help regulate digestion and control insulin production, but they also release the neurotransmitter serotonin, which escapes the gut and travels throughout the body.

It takes guts

Bacterial residents of the intestines may influence neurons and the brain through several routes.



Substances secreted by microbes into the gut may infiltrate **blood vessels** for a direct ride to the brain.



Microbes prompt **neuropod cells** in the gut lining to stimulate the vagus nerve, which connects directly to the brain.



More indirectly, microbes activate **enteroendocrine cells** in the gut lining, which send hormones throughout the body.



Even more indirectly, gut microbes influence **immune cells** and **inflammation**, which can affect the brain.

GRAPHIC: V. ALTOUNIAN/*SCIENCE*

Although the mechanisms remain elusive, animal studies by Cryan and others have bolstered the idea that gut microbes can influence the brain. Rats and mice given fecal transplants from people with Parkinson's, schizophrenia, autism, or depression often develop the rodent equivalents of those problems. Conversely, giving those animals fecal transplants from healthy people sometimes relieves their symptoms. The presence or absence of certain microbes in young mice affects how the mice respond to stress as adults, and other mouse studies have pointed to a role for microbes in the development of the nervous system.

At their lab, Cryan, Dinan, and their colleague Gerard Clarke think the amino acid tryptophan, which some gut bacteria produce, could be a causal link. Microbes or the body's own cells can convert tryptophan into serotonin, a neurotransmitter implicated in depression and other psychiatric disorders. Cells also turn tryptophan into a substance called kynurenine, which reacts further to form products that can be toxic to neurons. Changes in the microbiome might tip the production of those various substances in a way that impairs mental health, Cryan says. Research has shown, for example, that people with depression convert tryptophan into kynurenine more readily than into serotonin.

Cryan's group has amassed scores of papers and reviews that have helped solidify the case for microbial effects on several psychological and neurological disorders. But teasing effective fixes out of those links will be difficult, Clarke says: "It is one thing to know that a particular aspect of host physiology is influenced by our gut microbes and quite another to bend this influence to our will."

Clarke's group collaborates and consults with many companies and has tested some potential psychobiotics for stress manage-

Published by AAAS



ment in healthy volunteers. But he sees a long road to treatments. "It will be important to understand better and more precisely the mechanisms at play."

HOLOBIOME ISN'T AS PATIENT. Strandwitz founded the company in 2015 while still a graduate student in Kim Lewis's microbiology lab at Northeastern University. "He very politely told me that he would join the lab only if I helped him start a company once he graduated," recalls Lewis, who is famous for discovering and working to commercialize new antibiotics from soil microbes. Lewis agreed, but he figured it would be 10 years or more before Strandwitz would have his own company. Lewis was wrong: It only took 4 years.

At Northeastern, Strandwitz learned what he calls the "art of cultivation" from Gavrish, who was working with Lewis on isolating soil microbes. At the time, only about 25% of gut bacteria could be grown in the lab. Gavrish, who specializes in isolating and describing new microbial species, taught Strandwitz to manipulate nutrients and use antibiotics to give slow-growing, picky bacteria a chance to survive in culture instead of being outcompeted by more aggressive species. He began to track down growth factors to keep recalcitrant species going. Now, Strandwitz says, "We have in culture about 70%" of the known human gut microbes. If true, it's a figure few other labs can match.

One growth factor Strandwitz identified turned out to be the key to launching his entrepreneurial dreams. He and colleagues isolated a bacterium that couldn't survive on typical culture media and required an amino acid called gamma-aminobutyric acid (GABA) to thrive. GABA is a neurotransmitter that inhibits neural activity in the brain, and its misregulation has been linked to depression and other mental health problems.

The researchers reasoned that if this gut microbe had to have GABA, some other microbe must be making it. Such GABA producers might be a psychobiotic gold mine. Strandwitz and colleagues began to add gut microbes one at a time to petri dishes containing the GABA eater. If the GABA eater thrived, the scientists would know they'd found a GABA producer. They discovered such producers among three groups of bacteria, including *Bactereroides*. They quickly filed a patent for packaging those bacteria—or their products—to treat people with depression or other mental disorders.

Before publishing those findings, the group teamed up with researchers at Weill Cornell Medicine who were doing a brain scan study of 23 people diagnosed with depression. They found that people with fewer *Bacteroides* bacteria had a stronger pattern of hyperactivity in the prefrontal cortex, which some researchers have associated with severe depression. The collaboration reported its findings on 10 December 2018 in *Nature Microbiology*, along with the discovery of GABA-producing bacteria.

Holobiome further discovered that the bacteria produce GABA in the rat digestive tract, which may increase GABA levels in the brain. And it found that GABA eaters reduced learned helplessness—a symptom of depression—in those animals. One of Strandwitz's co-authors, microbial ecologist Jack Gilbert at UC San Diego, is also testing the therapeutic potential of GABA-producing bacteria in rats. His group and Holobiome have both observed that treated

PHOTO: KEN RICHARDSON

Published by AAAS



At Holobiome, Stephen Skolnick tests whether bacterial cells can make GABA, an important neurotransmitter.

rats are more likely to stay longer on an uncomfortably warm surface—a test of visceral pain tolerance—perhaps because elevated GABA calms them. The findings are unpublished, but they've persuaded Gilbert to investigate whether those bacteria can also reduce anxiety in rats. "It's clear they do have a neuromodulatory effect," he says.

GABA is too big to reach the brain by slipping across the blood-brain barrier, a cellular defense wall that limits the size and types of molecules that can get into the brain from blood vessels. Instead, the molecule may act through the vagus nerve or the enteroendocrine cells. Some researchers might question why bacteria would be any more beneficial than GABA-boosting drugs. But Strandwitz says the bacteria may do more than simply boost GABA. He notes that they produce molecules that may have other effects on the brain and body, thereby addressing other symptoms of depression.

He and Gilbert are unfazed by those uncertainties. "If we can show an influence, without any side effects, I don't see any reason for not going forward with clinical trials," Gilbert says.

At Holobiome, Strandwitz and colleagues have identified and ranked 30 promising GABA-producing bacteria, including the ones Gilbert is testing. Now, the company is enlisting an outside manufacturer to figure out which GABA-producing bacteria are best suited to produce in large enough quantities to test in people. The researchers hope to complete regulatory and ethical reviews in time to start human trials by early 2021. "We've been able to progress at this rate because we know our microbiology," Strandwitz says. The initial target conditions are insomnia and irritable bowel syndrome with constipation.

Ultimately, Holobiome does not know whether its best products will be a single bacterial species, a group of species, or a compound made by bacteria. "For now, live bugs work the best," Strandwitz says. He suggests a consortium of bacteria that includes a wider range of species than typical probiotics will be more versatile and able to treat multiple aspects of, say, depression.

> **"It is one thing to know that a particular aspect of host physiology is influenced by our gut microbes and quite another to bend this influence to our will."**
>
> **Gerard Clarke**, University College Cork

HOLOBIOME IS ALREADY LOOKING beyond GABA producers. Thousands of newly isolated microbes wait in frozen vials at the company's headquarters for their psychobiotic potential to be explored. "Whenever we see someone publishes a new paper on the microbiome, we can check if we have those bacteria and replicate the experiments," says Holobiome's Stephen Skolnick, who recently joined the company.

A key tool for those experiments is a "gut simulator," a series of flasks connected by tubing, with several portals for adding microbes and for monitoring what's happening inside. By allowing a mock microbiome to develop from different combinations of bacteria, sometimes with mammalian cells in the mix, the researchers can investigate newly isolated microbes and their products. If the scientists see promise, they can quickly pivot to thinking about additional products to develop.

Skolnick took the lead on obtaining a patent for Holobiome's use of queuine—a vitaminlike molecule only produced by certain gut microbes—to improve mental well-being. The body converts queuine into building blocks for neurotransmitters such as dopamine, serotonin, and melatonin. Whether adding queuine producers or the molecule itself to the gut might help people with mental illness isn't clear, but Strandwitz says he's excited about the idea.

"It's been amazing to witness the tremendous growth in the microbiome gut-brain field," says UC Los Angeles biologist Elaine Hsiao. Like Strandwitz, she is an enthusiast, having helped start two companies to develop microbial therapies for several disorders, including epilepsy and autism.

Other researchers fear entrepreneurship is outracing science. Knight says venture capitalists are funding startups developing almost any microbiome-based therapies. Some concepts are "very promising and are supported by a lot of evidence," he says, but others aren't, and they're still getting money. Knight says investors see an opportunity in eager patients. (Raes says he gets almost daily emails from depressed people seeking help.)

Microbial therapies won't necessarily meet the same standards of efficacy as regular drugs. To be marketed as a pharmaceutical, a treatment has to pass muster with the U.S. Food and Drug Administration, or its equivalent in other countries, through clinical trials that prove its effectiveness against specific diseases. Most microbiome treatments so far are marketed as probiotics, for which regulatory thresholds are lower, at least in the United States—as are limits on the health claims that a manufacturer can make. Holobiome is developing both types of products.

The field still faces considerable scientific questions, too. Besides the correlative nature of much of the research and the usual questions of whether animal studies will translate to humans, there's also the sheer complexity of the human microbiome, says Beatriz Peñalver Bernabé, a systems reproductive biologist at the University of Illinois, Chicago. "I don't think that it will be 'one thing fits all.' We will need to look for specific strains and dosages for different people." And, she adds, new theories and models are needed to predict how those strains will affect the individual's particular microbiome community.

Despite the obstacles, Gavrish remains confident that some strains she's growing in the anaerobic chamber will lead to treatments. After all, she says, the connection between gut microbes and the human brain has deep evolutionary roots. "I truly believe you can harness the power of a million years of signaling by gut bacteria to help people." ■

Published by AAAS



ILLUSTRATION: DAVIDE BONAZZI/SALZMANART

SCIENTIFIC PUBLISHING

In pursuit of open science, open access is not enough

Preventing monopolies in knowledge infrastructure is the next battleground for publishers and research institutions

By **Claudio Aspesi**[1] *and* **Amy Brand**[2,3]

After decades of debate on the feasibility of open access (OA) to scientific publications, we may be nearing a tipping point. A number of recent developments, such as Plan S, suggest that OA upon publication could become the default in the sciences within the next several years. Despite uncertainty about the long-term sustainability of OA models, many publishers who had been reluctant to abandon the subscription business model are showing openness to OA (*1*). Although more OA can mean more immediate, global access to scholarship, there remains a need for practical, sustainable models, for careful analysis of the consequences of business model choices, and for "caution in responding to passionate calls for a 'default to open'" (*2*). Of particular concern for the academic community, as subscription revenues decline in the transition to OA and some publishers prioritize other sources of revenue, is the growing ownership of data analytics, hosting, and portal services by large scholarly publishers. This may enhance publishers' ability to lock in institutional customers through combined offerings that condition open access to journals upon purchase of other services. Even if such "bundled" arrangements have a near-term benefit of increasing openly licensed scholarship, they may run counter to long-term interests of the academic community by reducing competition and the diversity of service offerings. The healthy functioning of the academic community, including fair terms and conditions from commercial partners, requires that the global marketplace for data analytics and knowledge infrastructure be kept open to real competition.

Published by AAAS



BUNDLED METRICIZATION

The bundling of journals (often using undisclosed pricing models) has historically worked well for commercial journal publishers, often at the expense of academic libraries (e.g., conditioning access to high-demand scientific literature on the purchase of resources for which there is little or no demand) (*3*). Exemplifying a different form of bundling, many publishers are actively negotiating transformative "read-and-publish" agreements with libraries and consortia, in which payment terms for access to journals and author fees for publishing in OA journals are bundled into a single contract (*4*). Such transformative deals may accelerate the transition to OA, but discounted article processing charges also have the potential to influence where researchers opt to publish their work, contravening basic principles of academic freedom.

As OA continues to gain ground, some publishers are seeking to protect their profitability by accelerating investment in research infrastructure and data analytics, and by bundling these and other offerings with journal access. For example, Elsevier announced a controversial framework agreement in late 2019 with several Dutch academic and funding bodies that ties a presumed zero increase in spending for content access with prefunded open access for affiliated authors and a commitment to partner on the development of new research intelligence tools and services. Although the details are not public, the implication is that these universities are contributing institutional metadata for Elsevier product development in exchange for OA publication by their researchers (*5*). Ownership of the data may remain with the universities, though it is unclear whether they maintain perpetual access rights to analyses based on that data (*6*).

Bundling of access and analytics is worrisome in light of the ways in which scholarly publishers are positioning themselves, largely through the acquisition of existing commercial and nonprofit technology companies, to compete with stand-alone vendors of analytics products to provide decision-support tools to university administrators. Consider that vendors of analytics-only services, unable to combine their services with price breaks on content access or article processing charges, could be disadvantaged, increasing the probability that data analytics will become a monopolistic or highly concentrated oligopolistic market. At the same time, shifting revenue growth among commercial providers from content to data analytics could generate deflationary pressure on the revenues of pure journal publishers, starving them of the capital needed to compete effectively and innovate.

Given how our established metrics already influence the academic ecosystem, the risks for universities and academic freedom could extend well beyond excessive spending and reduced competition. The use of data to inform institutional decision-making is of course, in principle, a laudable goal, and inclusion of a range of commercial interests in the development of analytics can provide useful skills and insights to advance such efforts. That said, the metricization of the academic community and the spread of data analytics are not without concern to researchers, who are among those most affected by the use of quantitative measures but with the least control over whether and how algorithms are applied and their outputs interpreted. Indeed, rigid models for assessing productivity are often less helpful in the promotion review process than qualitative assessments of their work.

The impact factor, widely recognized within the academic community as problematic but nonetheless central in many academic appointment and promotion decisions, serves as a cautionary tale: an algorithm created to rank journal quality morphed into a universal academic metric largely because of its widespread availability. So too, the senior leadership of many academic institutions around the world is preoccupied with university rankings, regardless of their validity. The proliferation of algorithms for comparing productivity within standard academic disciplines across individuals, departments, institutions, and nations has the potential to exacerbate bias and exert an abundance of control over core decision processes, such as resource allocation and career advancement decisions. Without a competitive market fostering alternative measures, leading academic institutions may be more prone to optimize for the same limited indicators of excellence and set the same research investment priorities.

PORTALS AND PLATFORMS

Longer term, we are also concerned about the potential rise of new discipline portals, or enhanced full-text databases. Organizing information within a particular subject domain into a searchable index is by no means new to scholarly publishing. Indeed, the first abstracting and indexing services date back to the early days of digitization. Whereas bibliographic databases typically contain only metadata, keywords, and abstracts, full-text databases contain complete documents, creating the potential for augmented discovery services through artificial intelligence (AI)–powered mining and analysis of full-text.

From the researcher's perspective, full-featured subject portals may make good sense. Systematic collections of research data and publications, conference proceedings, discussion threads, relevant events, and perhaps even media coverage and job postings could become natural destinations for scholars in many disciplines. One reason such robust disciplinary portals have thus far failed to become widespread is the cost, considering the expense involved in creating a platform that is truly comprehensive in coverage, reliably curated and cross-indexed, and kept up to date. For example, the tremendous resources of the Chan Zuckerberg Initiative (CZI) made it possible to create the AI-powered Meta platform that CZI acquired in 2017 and that indexes

[1]Independent Consultant, Zurich, Switzerland. [2]The MIT Press, Cambridge, MA, USA. [3]Knowledge Futures Group, Cambridge, MA, USA. Email: amybrand@mit.edu

Published by AAAS

and links to more resources in the life sciences than any competitor.

A larger historic barrier to full-text portals has been the fragmentation of scientific content. As long as most articles sit behind paywalls, it is challenging (although not impossible) for any one publisher to secure access to a critical mass of content with the requisite legal rights. The comprehensive adoption of OA and less restrictive Creative Commons licenses changes this dynamic and makes it easier to imagine how a large publisher or funder, with the scale to invest in the technology, could layer onto full-text aggregations functions such as collaboration platforms, data hosting, literature and dataset search and linkage, open reviews, proceedings and discussion threads, faculty news, job searches, and perhaps other activities of learned societies. Whereas basic service tiers might be free to researchers, premium tiers and institutional contracts could command high prices.

At the same time, access to the data and information exchanged by participants would provide the operator with valuable insights into both past and predicted future productivity of departments and individual faculty, potentially leading to new "information arbitrage" markets. With the rise in biological and medical research intelligence, the biomedical arena is likely to produce the first robust portals, and others would no doubt follow. However useful such portals may be, the potential benefits must be weighed against the potential costs of highly concentrated control of the market. Minimal or nonexistent competition is likely to result in less favorable terms for subscribing institutions, whether on price, user privacy, or overall service quality.

How likely is this outcome? Although fully open and not a multipurpose portal, Meta is a good indication of what's technically possible when it comes to automated sourcing, analyzing, and connecting of published content. On the commercial side, one initiative that aims to aggregate multiple data sources is Elsevier's Entellect. In 2019, Elsevier also launched a new PracticeUpdate community focused on advanced melanoma (*7*) to supplement the other medical communities it has hosted over the past several years. Looking beyond the life sciences, the company signed a "content integration" agreement during the same year with the Society of Petroleum Engineers (*8*). These are just some of the ways in which one organization can establish the building blocks of a subject portal strategy.

Developing portals across multiple disciplines would enable economies of scale in building and running the underlying software and in selling institutional subscriptions, potentially leading to even greater consolidation. It is hard to imagine more than a handful of enterprises being able to afford the upfront investment required to build and maintain these platforms. Once established, it would be difficult for new entrants to gain sufficient scale to compete, increasing the risk of monopoly control and pricing.

A COMMUNITY BEHOLDEN

We have highlighted some admittedly "worst case" scenarios, but we suggest that certain preventive measures could help ensure a robust and diversified ecosystem for data analytics and academic infrastructure and are worth pursuing even if the worst case does not come to fruition. If it doesn't invest in alternative solutions, the academic community may find itself beholden to a small number of vendors for managing communities, data flows, research assessment, and learned society communications, all within digital silos that could hinder the growth of cross-disciplinary collaboration and discovery. In response to these concerns, the Scholarly Publishing and Academic Resources Coalition (SPARC) outlined a number of practical steps that university leaders should consider (*9*). Among the steps proposed: ensure that appropriate institutional policies and personnel are in place to manage research data and faculty productivity analysis; diversify the infrastructure ecosystem by investing in community-owned solutions and stronger cross-institution partnerships; and actively partner with research funders and learned societies in these efforts.

> **"...diversify the infrastructure ecosystem by investing in community-owned solutions..."**

The relationship between academic institutions and learned societies is complex. Many faculty are members or leaders of learned societies, and some serve on the editorial boards of society journals. Learned societies have been among the least enthusiastic supporters of OA, stemming from concerns about the loss of the journal subscription revenues that subsidize their operations. Many societies copublish with large publishers, and if the transition to OA results in a revenue decline, societies could choose to partner with subject portal providers as one way to replace lost revenues. To offer an alternative path to sustainability, institutional leaders would be wise to involve learned societies in the development of community-owned infrastructures and consortia. Compensating societies for applying their disciplinary expertise and convening power to these efforts could provide them with new sources of revenue.

Even if monopolistic subject portals never come to pass, the possibility remains that a small number of companies will own most of the critical data assets, analytics, and platforms used by the scientific community. There have long been a limited number of academic journal hosting platforms, and in recent years most of these services have been acquired by publishers (e.g., Wiley's purchase of Atypon and SAGE Publishing's purchase of Global Village Publishing) or private equity firms (e.g., Accel-KKR's large stake in HighWire Press). Taylor & Francis's acquisition of F1000 Research is a recent example of market consolidation in the OA publishing platform space, but several open-source hosting and workflow solutions have begun to emerge (*10*), leading to welcome diversity in the technology choices of new OA publishers. Most of these solutions, though, lack solid plans for long-term growth and sustainability.

A first step to support competition and avoid monopolistic consolidation would be to engage in efforts to model consortial funding for and ownership of these and other noncommercial platforms. Universities should step up to invest in home-grown research infrastructures and cross-institution consortia, with the goals of establishing competition, sustaining best-in-breed open alternatives, and perhaps eventually providing a suite of services that can substitute for all-in-one commercial workflow solutions. Open, community-owned discovery and analytics services such as lens.org, along with Stanford Libraries' home-grown analytics solution RIALTO, merit further attention from academic leadership, as do grassroots efforts to develop indicators of excellence focused on humanities and social sciences (e.g., HuMetricsHSS). So does the widespread use of altmetric indicators in journal publishing and the growing adoption of open standards like the CRediT taxonomy, which links standardized roles to author names in multiauthored publications, providing a qualitative indicator of researcher contribution.

University leaders should be poised to revisit the lessons of past collective efforts to learn from what did and did not work, to design effective and durable collaborations going forward. There is much to be

Published by AAAS

learned, for example, from the long-standing success of the arXiv e-print repository in the fields of physics, mathematics, and computer science, fueled by a combination of grants, in-kind support, and institutional memberships.

The struggle for control over information and knowledge looms large. When Berners-Lee created the World Wide Web, his intention was to enable researchers to share their work. Not only have our research communication tools and practices thus far fallen short of the decentralization that the Web made possible, but the evolution of the Web itself also reminds us that making vast amounts of linked data readily accessible to third parties can trigger a number of unintended consequences. The dominance of a limited number of social networks, shopping services, and search engines shows us how internet platforms based on data and analytics can tend toward monopoly. In the research information space, contracts are being negotiated establishing de facto terms and conditions for how data analytics services are being provided. Learned societies are being wooed. Research assessment metrics are being proposed. Building blocks for establishing discipline portals are being assembled. The time for the academic community to act in coordination is now. ■

REFERENCES AND NOTES

1. Press release, 8 April 2020; https://group.springernature.com/gp/group/media/press-releases/springer-nature-plan-s/17877246.
2. K. Smith, Three Questions with Don Waters. *Council on Library and Information Resources* (*CLIR*) *Newsletter* 131 (2019); https://www.clir.org/2019/10/clir-issues-131/.
3. T. C. Bergstrom, P. N. Courant, R. P. McAfee, M. A. Williams, *Proc. Natl. Acad. Sci. U.S.A.* **111**, 9425 (2014).
4. L. Hinchliffe, Transformative Agreements: A Primer. *The Scholarly Kitchen* (23 April 2019); https://scholarlykitchen.sspnet.org/2019/04/23/transformative-agreements/.
5. Leaked document on Elsevier negotiations sparks controversy, *ScienceGuide* (2019); www.scienceguide.nl/2019/11/leaked-document-on-elsevier-negotiations-sparks-controversy/.
6. B. Upton, Dutch universities agree 'new way of working' with Elsevier. Research Professional News. 12 December 2019; www.researchprofessionalnews.com/rr-news-europe-infrastructure-2019-12-dutch-universities-agree-new-way-of-working-with-elsevier/.
7. Elsevier Launches PracticeUpdate, a Free Information Portal for Physicians; www.elsevier.com/about/press-releases/clinical-solutions/elsevier-launches-practiceupdate,-a-free-information-portal-for-physicians.
8. Elsevier and Society of Petroleum Engineers Collaboration will Empower Geoscientists to Make More Informed and Confident Decisions; www.prnewswire.com/news-releases/elsevier-and-society-of-petroleum-engineers-collaboration-will-empower-geoscientists-to-make-more-informed-and-confident-decisions (2019).
9. SPARC Roadmap for Action (2019); https://sparcopen.org/our-work/roadmap-for-action/.
10. J. W. Maxwell *et al.*, Mind the Gap: A Landscape Analysis of Open Source Publishing Tools and Platforms, posted July 2019; https://mindthegap.pubpub.org/.

ACKNOWLEDGMENTS

We thank several anonymous reviewers. C.A. is a paid consultant to SPARC and was the lead author of (*9*).

10.1126/science.aba3763

SCIENCE AND DECISION-MAKING: COVID-19

Harnessing multiple models for outbreak management

Expert elicitation methods and a structured decision-making framework will help account for risk and uncertainty

By **Katriona Shea[1], Michael C. Runge[2], David Pannell[3], William J. M. Probert[4], Shou-Li Li[5], Michael Tildesley[6], Matthew Ferrari[1]**

The coronavirus disease 2019 (COVID-19) pandemic has triggered efforts by multiple modeling groups to forecast disease trajectory, assess interventions, and improve understanding of the pathogen. Such models can often differ substantially in their projections and recommendations, reflecting different policy assumptions and objectives, as well as scientific, logistical, and other uncertainty about biological and management processes (*1*). Disparate predictions during any outbreak can hinder intervention planning and response by policy-makers (*2, 3*), who may instead choose to rely on single trusted sources of advice, or on consensus where it appears. Thus, valuable insights and information from other models may be overlooked, limiting the opportunity for decision-makers to account for risk and uncertainty and resulting in more lives lost or resources used than necessary. We advocate a more systematic approach, by merging two well-established research fields. The first element involves formal expert elicitation methods applied to multiple models to deliberately generate, retain, and synthesize valuable individual model ideas and share important insights during group discussions, while minimizing various cognitive biases. The second element uses a decision-theoretic framework to capture and account for within- and between-model uncertainty as we evaluate actions in a timely manner to achieve management objectives.

EXPERT ELICITATION AND JUDGMENT

Formal methods for elicitation of information from individuals were developed to harness the collective knowledge of many minds while avoiding the frailties of individual experts (e.g., overconfidence) and the problems that arise in group interactions, such as agreeing with field "leaders" (dominance effects), focusing on suggestions raised early in the process to the detriment of other ideas (starting-point bias, groupthink, anchoring), the dominating effects of "loud voices," and overly rapid adoption of early ideas that might, on more careful consideration, be incorrect (*4, 5*). In these formal methods, idea generation and idea evaluation are deliberately separated, allowing a fuller range of possibilities to be explored and a wide range of uncertainties to be assessed. As one example, in the IDEA protocol for expert elicitation (*6*), once experts are clear about the questions, they individually provide initial best estimates and ranges, receive feedback on how their estimates compare with others, discuss the results, and then provide a final individual estimate. Some protocols, including IDEA, are designed to work remotely—an essential requirement in the present COVID-19 context.

To harness both the creativity of individuals and the insights of groups, variations on the Delphi method (developed by the RAND Corporation in the 1950s and included within the IDEA protocol) and the Nominal Group Technique (*7*) involve both independent and interactive stages in an iterative elicitation process (*8, 9*). The expert judgment literature shows that a failure to manage the elicitation process well can lead to generation of biased information and overconfidence (*4, 5*). Expert judgment approaches have been used for elicitation from individual experts in a wide range of relevant settings, such as development of clinical guidelines (*8*), and in conservation and ecology (*9*).

MULTIPLE MODELS

There are a number of existing approaches for dealing with multiple models in weather and climate research (*10*), fisheries (*11*), and disease forecasting (*2, 12*). Such forecasting efforts generally focus on statisti-

[1]Department of Biology, The Pennsylvania State University, University Park, PA, USA. [2]U.S. Geological Survey, Patuxent Wildlife Research Center, Laurel, MD, USA. [3]University of Western Australia, Perth WA 6009, Australia. [4]Big Data Institute, Li Ka Shing Centre for Health Information and Discovery, University of Oxford, Oxford, UK. [5]State Key Laboratory of Grassland Agro-ecosystems, Center for Grassland Microbiome, and College of Pastoral, Agriculture Science and Technology, Lanzhou University, Lanzhou, People's Republic of China. [6]Zeeman Institute for Systems Biology and Infectious Disease Epidemiology Research, Mathematics Institute and School of Life Sciences, University of Warwick, Coventry CV47AL, UK. Email: k-shea@psu.edu

Published by AAAS

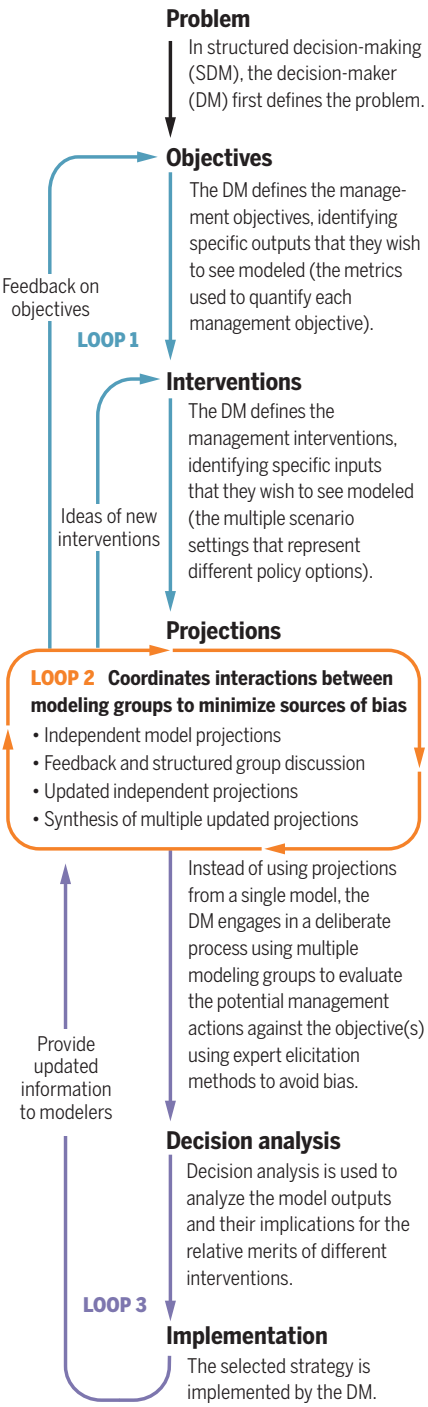
cal averaging of model outputs (ensemble averaging, super-ensemble modeling) and are growing in popularity and impact. A few multiple-model protocols also address optimal management (*1, 3, 13, 14*), specifically asking "what should we do to most increase the benefits or reduce the costs?", instead of "what will happen?" In the current COVID-19 outbreak, there has been unprecedented sharing of data and models in curated discussion groups, on preprint servers, and in working groups coordinated by policy agencies such as the World Health Organization (WHO) and the U.S. Centers for Disease Control and Prevention (CDC). These efforts save duplication of research and allow for rapid dissemination of new information, and are essential in a crisis.

Unfortunately, there is a downside to rapid sharing. Poor, as well as good, information may spread rapidly; a failure to prevent this leads to bias. If premature consensus is reached, models predicated on poor assumptions will inevitably propagate bias. Such propagation of initial bias is well documented in the elicitation literature (*4, 5*) and is clearly a potential concern in an epidemiological context.

MODELING-GROUP ELICITATION

We present an elicitation process for multiple modeling groups based on a modified-Delphi approach to expert elicitation (*6*) embedded in a structured decision-making (SDM) process (*15*). The overall process is coordinated by the decision-maker (DM)—for instance, the public health policy agency with authority to act. The adoption of a formal protocol for SDM (see the figure for an overview of the SDM process) allows us to assess the same set of actions in different models to address key objectives in a timely manner, and with an appropriate expression of uncertainty to enable risk-based decision-making. We expand the SDM approach in loop 2 of the figure to explicitly involve multiple modeling groups in a modified Delphi expert elicitation process. In general overview, the modeling groups initially work alone, then together (coordinated by the DM), and finally alone again.

The DM first outlines the process, and the required information, for the modeling groups. This includes description of the management objective and associated metrics (e.g., minimization of total morbidity or mortality) and of the potential management interventions. Note that projecting spatial spread or caseload trajectory under some baseline scenario of no action is still a management intervention ("do nothing"). Thus, efforts to forecast and to assess interventions should be fully integrated and presented consistently. The DM also provides instructions about how within-model uncertainty should be documented (e.g., provide a full probability distribution of outcomes—not just a mean value—for intervention-objective projections, and document sources of variation). Uncertainty may be structural (e.g., should asymptomatic carriers be modeled explicitly?), or parametric with respect to the biology (e.g., what is the expected time between sequential cases in a chain of transmission?), or it may relate to the interventions (e.g., what is the expected impact of social distancing?). The DM must also provide background information and access to current relevant data, information on intervention efficacy (if known), and guidance on data curation.



The DM next must assemble modeling groups for the elicitation process. In the current COVID-19 outbreak, hundreds of research groups around the world are assisting national and international agencies with forecasts and management recommendations. Any type of new or existing model that encapsulates a scientific research group's best understanding of the situation effectively represents a hypothesis about the system, and should be eligible; however, restrictive criteria may be applied with justification in some situations (*3*). To constructively participate, all groups must agree to examine how the interventions of interest meet the DM's stated objectives. However, if some models cannot assess all interventions (e.g., if nonspatial models cannot address spatially explicit interventions), incomplete results may nevertheless be informative (*14*).

During a first round of analysis, individual modeling groups, working independently, project the outcomes for each of the interventions, capturing their own within-model uncertainty. The DM invites a first report of results in a short period of time; this may be facilitated by providing a template format for model outputs. The DM then compiles and compares the results, provides feedback to the individual groups about their projections, and provides results (anonymized, to reduce peer pressure) from all participants to the whole group.

All the modeling groups then participate in a formal, structured discussion to compare results, assess common features, discuss what caused differences, identify valuable information that might not have been available to all groups, generate important insights about the nature of the disease and its dynamics, and identify important insights to share. This structured discussion is an important step, allowing modelers and the DM to assess why models disagree.

After these discussions, individual modeling groups, again working independently, update their models and projections based on the insights from the whole-group discussion. All groups have the opportunity to revise and rerun their models, using their judgments and data, taking account of the all-group discussion to the extent they think it is warranted, but not asking for consensus. The DM then compiles the second round of results, reporting both the central tendencies and the uncertainties within and across models. The Round 2 results are also then

GRAPHIC: N. CARY/*SCIENCE*

Published by AAAS

combined into an ensemble projection for each management strategy (*1*, *14*). For example, an ensemble projection for different "reopening" scenarios could show the best estimate of COVID-19 case load across models, for different policies for reinstating social interaction, including full expression of the uncertainty captured by the model set.

The full set of results can then be used to guide policy deliberation. Two particular techniques from the field of decision analysis are relevant here: first, risk analysis (which assesses the probability of poor outcomes for different interventions, and judges the tolerability of such risk) (*15*); and second, value of information analysis (which estimates the value to the DM of resolving one or more uncertainties prior to the implementation of a decision) (*13*). Central to these approaches is the recognition that projections may be wrong; by documenting uncertainty, a DM can evaluate which interventions may be most robust to uncertainty and can allocate research effort to reduce the most consequential uncertainty.

Two rounds of modeling (instead of one) are key to the modeling-group elicitation process. Current sharing of early ideas through preprint servers and curated discussion groups permits communication of independent ideas that might otherwise not be shared; however, broad sharing also runs the risk of losing independent idea generation (*3*). The Round 1 projections, undertaken before the groups start collaborating with each other, are essential to avoid starting-point bias and groupthink, by encouraging independent idea generation and creative thinking. Asking modeling teams to formally review collective results and determine the reasons for differences in model projections highlights key uncertainties and helps modeling groups to detect flaws in their assumptions or modeling approach. Nevertheless, the inclusion of a second, postdiscussion round of modeling need not delay the DM from taking action: The first round of results can be used for initial policy recommendations if time is of the essence.

There are major advantages to embedding the model group elicitation process in a structured decision-making framework (*15*), relative to the ad hoc decision processes that are often employed. First, one iteration of the whole elicitation process can be used by the DM to decide on an initial course of action to meet a clearly stated objective. Second, an important advance with expert elicitation is to elicit a relatively unbiased and full expression of uncertainty. The process provides policy-makers with two crucial pieces of information: a sense of the central tendency of the projections across models, and an understanding of the underlying uncertainty, as captured by the range of projections for different interventions. The results can be analyzed to identify which uncertainties most strongly affect the choice of action. It may be that one intervention is ranked best by all models despite uncertainty, or it may be that the top-ranked intervention is highly sensitive to a particular uncertainty, indicating the need for research on that particular factor. Third, if the outbreak is ongoing, and if models disagree (so that uncertainty is an impediment to choosing a course of action), and if new information on dynamics or management outcomes can be incorporated into the process, an adaptive management (AM) approach, involving management with a plan for learning, is warranted (*13*).

It is also possible for policy-makers to tailor the degree to which the elicitation exercise itself feeds into targeted research or management decisions. Scientists can contribute to the process by providing input on new or better-specified objectives to policy-makers and by providing suggestions for additional or modified interventions for the whole group to assess. For example, in loop 1, if a policy-maker requests advice on the optimal intervention to "control" a disease, modeling groups may demonstrate that a more precise objective statement is needed (e.g., while zero cases equates to zero deaths, a small outbreak of COVID-19 in a nursing home may lead to more deaths than a large outbreak in a university setting; reducing caseload and mortality are not equivalent objectives). Similarly, in the 2014 Ebola outbreak, model forecasts ranged wildly, yet a focus on minimizing the number of cases brought surprising consensus on the best approach to intervention (*1*). In loop 1, modeling work by one group may also suggest potentially fruitful interventions that all groups could evaluate (e.g., earlier intervention triggers than proposed by the DM, or previously unconsidered interventions).

The proposed process encourages a healthy conversation between scientists and decision-makers and engenders a stronger integration of science and policy, enabling policy agencies to more effectively achieve their management goals. Furthermore, it helps the DM to embrace uncertainty, rather than hastening to a premature consensus that could derail or deflect management efforts (*9*).

Adoption of elicitation methods for multiple modeling groups should be relatively straightforward; all structures to support and facilitate such a process are already in place [e.g., the "forecasting challenges" exemplified by (*4, 12*), and channels for communication between DMs and modeling groups]. Thus, additional costs of this approach relative to traditional approaches should be minimal. A strength of this approach is that individual modeling groups may preserve their autonomy and unilaterally conduct additional analyses and publish their work independently, as before, yet gain additional benefits from being involved formally in the group exercise, both in terms of access to information and feedback, and in terms of contributing to the greater good. As a result, high participation of modeling groups should be achievable. We suggest that this strategy will prompt better outbreak management outcomes for similar effort by deliberately leveraging more value from the modeling process. As such, the risks and stresses inherent in implementing the approach are also minimized and should not be deterrents.

Leveraging the contributions of multiple modeling groups is likely to pay dividends in preventing morbidity and death. In short, managing any disease, including a disease outbreak, requires that policy objectives be well defined, the decision-making process be carefully structured, and multiple contributing modeling groups be handled in a manner that shares knowledge while avoiding bias. Intertwining expert judgment methods with multiple model comparisons, in a planned and deliberate manner, will thus increase the benefits derived from multiple groups' efforts to model outbreaks. ■

REFERENCES AND NOTES

1. S. L. Li *et al.*, *Proc. Natl. Acad. Sci. U.S.A.* **114**, 5659 (2017).
2. C. J. Carlson, E. Dougherty, M. Boots, W. Getz, S. J. Ryan, *Sci. Rep.* **8**, 4921 (2018).
3. S. den Boon *et al.*, *BMC Med.* **17**, 163 (2019).
4. P. E. Tetlock, D. Gardner, Superforecasting: The Art and Science of Prediction (Random House, 2016).
5. M. A. Burgman, Trusting Judgements: How to Get the Best out of Experts (Cambridge Univ. Press, 2015).
6. V. Hemming, M. A. Burgman, A. M. Hanea, M. F. McBride, B. C. Wintle, *Methods Ecol. Evol.* **9**, 169 (2018).
7. A. Delbecq, A. Van de Ven, *J. Appl. Behav. Sci.* **7**, 466 (1971).
8. M. K. Murphy *et al.*, *Health Technol. Assess.* **2**, 1 (1998).
9. M. C. Runge, S. J. Converse, J. E. Lyons, *Biol. Conserv.* **144**, 1214 (2011).
10. T. N. Krishnamurti *et al.*, *Science* **285**, 1548 (1999).
11. S. C. Anderson *et al.*, *Fish Fish.* **18**, 732 (2017).
12. C. Viboud *et al.*, *Epidemics* **22**, 13 (2018).
13. K. Shea, M. J. Tildesley, M. C. Runge, C. J. Fonnesbeck, M. J. Ferrari, *PLOS Biol.* **12**, e1001970 (2014).
14. W. J. M. Probert *et al.*, *Epidemics* **15**, 10 (2016).
15. R. Gregory *et al.*, Structured Decision Making: A Practical Guide for Environmental Management Choices (Wiley-Blackwell, 2012).

ACKNOWLEDGMENTS

M.F., M.T., and K.S. are supported by an award from the NSF Ecology and Evolution of Infectious Diseases (EEID) program. K.S. is supported by an NSF COVID-19 Rapid Response Research (RAPID) award. K.S. is supported by the Huck Institutes for the Life Sciences at The Pennsylvania State University. W.J.M.P. is funded by the Li Ka Shing Foundation. The authors thank E. Howerton and C. Viboud. Any use of trade, firm, or product names is for descriptive purposes only and does not imply endorsement by the U.S. Government.

10.1126/science.abb9934

Published by AAAS

PERSPECTIVES

ECOLOGY

Tree planting is not a simple solution

Tree planting must be carefully planned and implemented to achieve desired outcomes

By **Karen D. Holl**[1] *and* **Pedro H. S. Brancalion**[2]



This mixed-species tree-planting project is part of a larger-scale initiative to restore 15 million hectares of Brazil's Atlantic Forest.

PHOTO: HOLL *ET AL.*

A plethora of articles suggest that tree planting can overcome a host of environmental problems, including climate change, water shortages, and the sixth mass extinction (*1*–*3*). Business leaders and politicians have jumped on the tree-planting bandwagon, and numerous nonprofit organizations and governments worldwide have started initiatives to plant billions or even trillions of trees for a host of social, ecological, and aesthetic reasons. Well-planned tree-planting projects are an important component of global efforts to improve ecological and human well-being. But tree planting becomes problematic when it is promoted as a simple, silver bullet solution and overshadows other actions that have greater potential for addressing the drivers of specific environmental problems, such as taking bold and rapid steps to reduce deforestation and greenhouse gas emissions.

These ambitious tree-planting efforts (examples in supplementary table S1) are mostly well intentioned and have numerous potential benefits, such as conserving biodiversity, improving water quality, providing shade in urban areas, and sequestering carbon (*1*, *3*). Nonetheless, the widespread obsession over planting trees can lead to negative consequences, which depend strongly on both how and where trees are planted (see the table). For example, whereas tree planting often enhances floral and faunal diversity, planting trees in historic grasslands and savannas can harm native ecosystems and species (*4*). Likewise, trees are often suggested as an important income source for small landholders but may increase social inequity and dispossess local people from land if tree-planting programs are imposed by governments and external investors without stakeholder engagement (*5*). Repeatedly, top-down reforestation projects have failed because the planted trees are not maintained, farmers use the land for livestock grazing, or the land is recleared.

The massive Chinese government Grain-for-Green tree-planting program, which cost an estimated $66 billion, illustrates a number of these trade-offs. The program is credited with increasing tree cover by 32% and reducing soil erosion by 45% in southwestern China over a 10- to 15-year period (*6*). But like many large-scale reforestation programs, most new tree cover is composed of one or a few non-native species that have much lower biodiversity than native forests (*6*). Moreover, large-scale tree planting in the semiarid Loess Plateau in central China has reduced river runoff and in turn the amount of water available for human activities, owing to the large amount of water transpired by rapidly growing trees (*7*). Most of the trees for this program were planted in former agricultural land, resulting in a 24% decrease in cropland. During the same time period, native forest cover decreased by 7% (*6*). This illustrates a major overarching concern about tree planting, which is the displacement of agriculture from the land being reforested to areas occupied by native forests, thus resulting in further deforestation (*8*).

Reforestation projects can be an important component of ensuring the well-being of the planet in coming decades, but only if they are tailored to the local socioecological context and consider potential trade-offs. To achieve the desired outcomes, tree-planting efforts must be integrated as one piece of a multifaceted approach to address complex environmental problems; be carefully planned to consider where and how to most effectively realize specific project goals; and include a long-term commitment to land protection, management, and funding.

The first priority to increase the overall number of trees on the planet must be to reduce the current rapid rate of forest clearing and degradation in many areas of the world. The immediate response of the G7 nations to the 2019 Amazon fires was to offer funding to reforest these areas, rather than to address the core issues of enforcing laws, protecting lands of indigenous people,

[1]Environmental Studies Department, University of California, Santa Cruz, CA 95064, USA. [2]Department of Forest Sciences, "Luiz de Queiroz" College of Agriculture, University of São Paulo, Piracicaba, SP, 13418-900, Brazil. Email: kholl@ucsc.edu

Published by AAAS

and providing incentives to landowners to maintain forest cover. The simplistic assumption that tree planting can immediately compensate for clearing intact forest is not uncommon. Nonetheless, a large body of literature shows that even the best-planned restoration projects rarely fully recover the biodiversity of intact forest, owing to a lack of sources of forest-dependent flora and fauna in deforested landscapes, as well as degraded abiotic conditions resulting from anthropogenic activities (*9*).

Tree planting is not a substitute for taking rapid and drastic actions to reduce greenhouse gas emissions. Certainly, planting trees in formerly forested lands is one of the best options to offset a portion of anthropogenic carbon emissions, but increasing global tree cover will only constitute a fraction of the carbon reductions needed to keep temperature increases below 1.5° to 2°C (*4*). Potential carbon sequestration estimates of increasing tree cover range more than 10-fold, depending on assumptions about the rate of carbon uptake, the amount of land considered appropriate for reforestation, and how long those trees remain on the land (*2*, *3*, *10*). Moreover, much uncertainty remains about how much carbon trees will sequester in the future, given that increasing drought and temperatures from climate change can lead to substantial tree mortality either directly or indirectly through feedback loops involving fire and insect outbreaks (*11*). Conversely, some high-latitude areas that were unsuitable for trees may become favorable in the future.

Maximizing the benefits of tree planting requires balancing multiple ecological and social goals to prioritize where to increase tree cover regionally and globally. Some global maps estimate potential land area for reforestation without factoring in that people need places to live, produce food, and extract natural resources (*12*). Large-scale reforestation may be feasible in some areas, particularly those in public ownership, but reforestation will mostly occur in multiuse landscapes. Several recent studies suggest that prioritizing forest restoration on the basis of criteria, such as past land use, potential for natural regrowth of forest, conservation value, and opportunity cost from other land uses, can increase feasibility and improve reforestation success (*13*). For example, choosing appropriate locations for tree planting in the Brazilian Atlantic Forest biome can triple conservation gains and halve costs (*14*). Large-scale planning is more likely to result in successful reforestation projects over the long term and prevent deforestation elsewhere. But recognizing competing land uses means that the actual land area feasible for reforestation is much lower than the amount proposed by some ambitious global reforestation maps and national commitments (*12*).

Contrasting tree-planting outcomes

Tree-planting efforts can have both negative and positive ecological and social outcomes depending on whether the location-specific pros and cons of different alternatives are rigorously evaluated, and projects are comprehensively planned in consultation with all stakeholders.

Unintended negative effects

- Reduced water supply
- Destruction of native grasslands and spread of invasive tree species
- Increased social inequity
- Displacement of farmland
- Increased deforestation

Potential beneficial outcomes

- Greater carbon and water storage
- Reduced soil erosion
- Increased landscape connectivity and native biodiversity
- Provision of food, wood, and shade
- Income generation

Successful tree planting requires careful planning at the project level, which starts by working with all stakeholders to clearly identify project goals. People plant trees for many different reasons, such as restoring forest, sequestering carbon, providing income from timber harvesting, or improving water quality. A single tree-planting project may achieve multiple goals, but it is rarely possible to simultaneously maximize them all, because goals often conflict, and prioritizing one goal may result in other undesirable outcomes. Clear goals are key to being able to evaluate whether the project was successful and to selecting the most cost-effective way to increase the number of trees. For example, if a primary project goal is to restore historically forested habitat, simply allowing the forest to regrow naturally often results in the establishment of more trees at a much lower cost than actively planting trees, particularly in locations with nearby seed sources and less-intensive previous land use. By contrast, if the goal is to provide landowners with fruit trees or species with valuable timber, then plantations of non-native species may be the most suitable approach. Many additional questions must be addressed prior to project implementation, such as potential unintended consequences of tree planting, which species to plant, how landowners will be compensated for lost income, and who is responsible for maintaining trees over the long term.

Most projects set targets of how many trees to plant (table S1), rather than how many survive over time or, more importantly, whether the desired benefits are achieved. By contrast, most tree-planting goals, such as carbon sequestration and providing timber and nontimber forest products to landowners, require decades to achieve. This short-term view has resulted in large expenditures on tree-planting efforts that have failed. For example, approximately $13 million were spent to plant mangrove trees in Sri Lanka following the Indian Ocean tsunami in 2004, yet monitoring of 23 restoration planting sites five or more years later found that more than 75% of the sites had <10% tree survival because of poor project planning and lack of seedling maintenance (*15*).

Hence, successful tree-planting projects require a multiyear commitment to maintaining trees, monitoring whether project goals have been achieved, and providing funding for corrective actions if they are not. Using this adaptive management approach will certainly increase the price tag of tree planting, but it is money better spent than simply planting trees that mostly do not survive.

To realize the potential benefits of increasing tree cover, it is essential that tree-planting projects include thorough goal setting, community involvement, planning, and implementation, and that the time scale for maintenance and monitoring is sufficient. Otherwise the extensive human energy and financial resources invested in tree planting are likely to be wasted and have undesirable consequences, thus undermining the potential of this activity to deliver the expected environmental benefits that are critically needed for humans and nature in this time of rapid global change. ■

REFERENCES AND NOTES

1. W. D. Newmark *et al.*, *Proc. Natl. Acad. Sci. U.S.A.* **114**, 9635 (2017).
2. J.-F. Bastin *et al.*, *Science* **365**, 76 (2019).
3. B. W. Griscom *et al.*, *Proc. Natl. Acad. Sci. U.S.A.* **114**, 11645 (2017).
4. J. W. Veldman *et al.*, *Science* **366**, eaay7976 (2019).
5. A. Scheidel, C. Work, *Land Use Policy* **77**, 9 (2018).
6. F. Hua *et al.*, *Biol. Conserv.* **222**, 113 (2018).
7. X. Feng *et al.*, *Nat. Clim. Chang.* **6**, 1019 (2016).
8. P. Meyfroidt *et al.*, *Proc. Natl. Acad. Sci. U.S.A.* **107**, 20917 (2010).
9. M. Curran *et al.*, *Ecol. Appl.* **24**, 617 (2014).
10. S. Fuss *et al.*, *Environ. Res. Lett.* **13**, 063002 (2018).
11. W. R. L. Anderegg *et al.*, *Nat. Clim. Chang.* **3**, 30 (2013).
12. R. Delzeit *et al.*, *Science* **366**, 316 (2019).
13. P. H. S. Brancalion *et al.*, *Sci. Adv.* **5**, eaav3223 (2019).
14. B. B. N. Strassburg *et al.*, *Nat. Ecol. Evol.* **3**, 62 (2019).
15. K. A. S. Kodikara *et al.*, *Restor. Ecol.* **25**, 705 (2017).

ACKNOWLEDGMENTS

We thank R. Chazdon, A. Kulikowski, F. Joyce, J. Lesage, M. Loik, J. L. Reid, and K. Ross for helpful comments.

SUPPLEMENTARY MATERIALS

science.sciencemag.org/content/368/6491/580/suppl/DC1

10.1126/science.aba8232

Published by AAAS

ULTRACOLD CHEMISTRY

Quantum resonances near absolute zero

Ultralow-energy atom-molecule collisions reveal quasi-bound state quantum resonances

By **Tiangang Yang**[1] *and* **Xueming Yang**[1,2]

Modeling atomic and molecular collisions precisely requires knowing the details of the key elementary processes that dictate their outcomes. Understanding the quantum nature of atomic and molecular collisions is essential, especially in the low–collisional energy region, where quantum effects are most prominent. Among these features are collision resonances, which are in essence transiently trapped quantum states (*1*–*3*). Their transient nature makes them inherently difficult to probe experimentally. On page 626 of this issue, de Jongh *et al*. (*4*) report a combined experimental and theoretical dynamics study on the resonances in the NO + He collision, a benchmark system for the inelastic collision energy transfer process, at very low collision energies (*4*). Collision resonances are attributed to quasi-bound quantum states with a, more accurate potential energy surface (PES) for NO-He.

To observe these resonances, de Jongh *et al*. measured quantum state-to-state integral and different cross sections (event probabilities) of the inelastic NO(j = ½f) + He → NO(j = ½e) + He collision, where j is the near-degenerate doublet rotational levels f and e of the ground electronic and vibrational state of NO. These doublet states differ in symmetry, and the collision with He deexcites the slightly higher-energy upper f state to the lower-energy e state. These states were measured by using a high-resolution velocity map imaging technique in the collision energy range of 0.2 to 8.5 cm^{-1}, corresponding to an extremely low-temperature range from 0.3 to 12.3 K.

The extremely low collision energy was achieved by using the Stark decelerated molecular beam of NO(j = ½f) and a cryogenic He beam. It improves the study on this collision by the same group (*5*) and allows detailed investigation of inelastic collision dynamics in the onset regime of individual partial-wave resonances. These resonances arise from collisions with different orbital angular momentum (ℓ) partial waves, associated with the colliding molecular partners and which only a few experiments can directly access. A number of distinct peaks were observed in the state-to-state integral cross sections and assigned to quantum resonances arising from quasi-bound states on adiabatic potentials with $\ell_{res} \geq 2$. The lowest $\ell_{res} = 2$ resonance observed is characterized by nearly equal contributions of outgoing partial waves with $\ell_{out} = 0$ (s-wave) and $\ell_{out} = 1$ (p-wave).

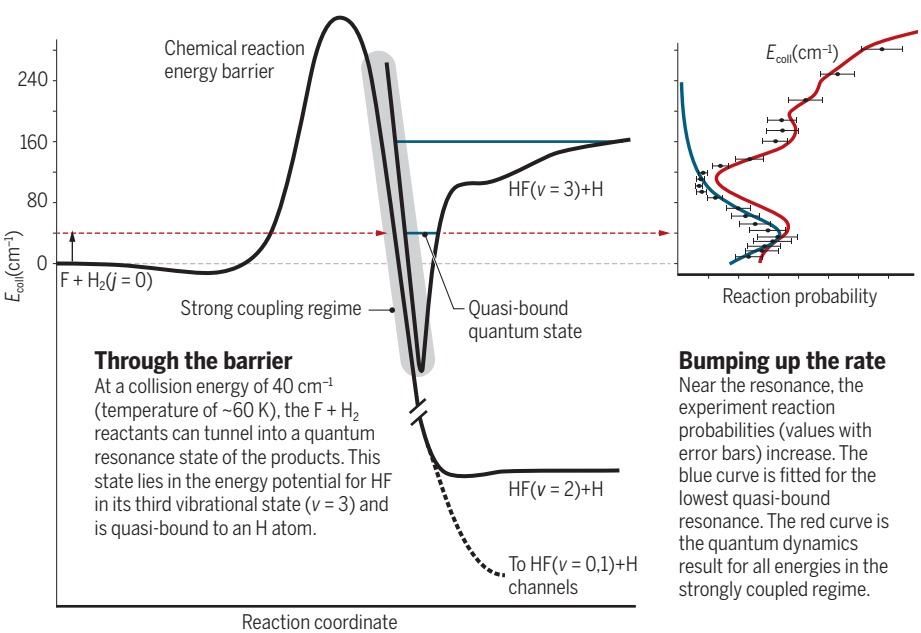
Accurate quantum dynamics calculations are in excellent agreement with experimental results. Particularly interesting is that the resonances could only be accurately described with a new NO-He PES at the CCSDT(Q) level (coupled clusters singles, doubles, triples, and quadruples), demonstrating the exceptionally high level of the resonance model, characterized by both experiment and theory, for this benchmark inelastic collision system. The collision resonances are attributed to the quasi-bound quantum states on the PES. This combined experimental and theoretical study sets a standard for inelastic scattering study of atom-diatom collisions at temperatures near the absolute zero.

Inelastic collision resonances are nevertheless not specific to the NO + He system; such resonances could also exist in many other inelastic collision systems at very low collision energy. In addition to inelastic scattering processes, resonances also exist in chemical reactive collisions in the low–collisional energy regime. An important benchmark for reaction resonances is the F + H_2 → HF + H reaction, which is a major source of HF formation in interstellar clouds. Understanding the HF formation mechanism through this reaction at temperatures near 0 K has astrophysical implications as it can help determine hydrogen column density in space.

The F + H_2 reaction has a substantial reaction barrier (629 cm^{-1}), so product formation should be negligible at low temperatures near absolute zero. However, rate measurements of the F + H_2 reaction by using the CRESU technique (reaction kinetics in uniform supersonic flow) showed pronounced chemical reactivity at

Resonance-enhanced reactivity

For a high reaction barrier, rates should be almost zero at low collision energies corresponding to low temperatures. However, reaction rates can be boosted over an energy window by tunneling into a quasi-bound excited state of the products, as shown for the F + H_2 reaction (*7*).



Through the barrier
At a collision energy of 40 cm^{-1} (temperature of ~60 K), the F + H_2 reactants can tunnel into a quantum resonance state of the products. This state lies in the energy potential for HF in its third vibrational state (v = 3) and is quasi-bound to an H atom.

Bumping up the rate
Near the resonance, the experiment reaction probabilities (values with error bars) increase. The blue curve is fitted for the lowest quasi-bound resonance. The red curve is the quantum dynamics result for all energies in the strongly coupled regime.

[1]Department of Chemistry, College of Science, Southern University of Science and Technology, 1088 Xueyuan Road, Shenzhen 518055, China. [2]State Key Laboratory of Molecular Reaction Dynamics, Dalian Institute of Chemical Physics, Chinese Academy of Sciences, Dalian, Liaoning 116023, China. Email: xmyang@dicp.ac.cn; yangxm@sustech.edu.cn

GRAPHIC: V. ALTOUNIAN/*SCIENCE*

Published by AAAS

temperatures as low as 11 K (*6*). A more recent detailed crossed-beams study on this reaction in the collision energy range of 9.8 to 282 cm^{-1} showed that the reaction resonance peak at the energy around −40 cm^{-1} on the product side is responsible for the enhanced reactivity (see the figure) near 0 K (*7*). Because of this resonance-enhanced quantum tunneling through the reaction barrier, the rate was substantially enhanced at temperatures approaching 0 K. The quasi-bound resonance detected in the crossed-beams study was also in good agreement with the negative-ion photodetachment spectroscopic results (*8*).

The study by de Jongh *et al.* is among advances made recently in the study of quantum resonances in atomic and molecular collisions at temperatures near absolute zero. Experimental breakthroughs have mainly been enabled by emerging molecular-beam methods and better detection techniques. Strong interplay between experiment and theory has also enhanced our understanding of transient resonances in collisions to a level of spectroscopic accuracy. Dynamics studies of atomic and molecular collisions are particularly important to the understanding of energy transfer and chemical reaction processes in gas-phase systems. Such studies affect the understanding of physical and chemical processes in a wide range of systems, including terrestrial and planetary atmospheres, interstellar clouds, gas-phase lasers, semiconductor processing, plasmas, and combustion processes. ■

“...the resonances could only be accurately described with a new NO-He PES at the CCSDT(Q) level...demonstrating the exceptionally high level of the resonance model...”

REFERENCES AND NOTES

1. S. Chefdeville *et al.*, *Science* **341**, 1094 (2013).
2. T. Wang *et al.*, *Chem. Soc. Rev.* **47**, 6744 (2018).
3. H. Yang *et al.*, *Science* **363**, 261 (2019).
4. T. de Jongh *et al.*, *Science* **368**, 626 (2020).
5. S. N. Vogels *et al.*, *Science* **350**, 787 (2015).
6. M. Tizniti *et al.*, *Nat. Chem.* **6**, 141 (2014).
7. T. Yang *et al.*, *Nat. Chem.* **11**, 744 (2019).
8. J. B. Kim *et al.*, *Science* **349**, 510 (2015).

ACKNOWLEDGMENTS

X.Y. acknowledges support by National Natural Science Foundation of China (grant 21688102), Chinese Academy of Sciences (grant XDB17010000). T.Y. thanks support from Shenzhen City (grant C19543101).

10.1126/science.abb8020

3D PRINTING

Closing the science gap in 3D metal printing

X-ray imaging and modeling reveal how metal powders absorb energy and can create defects

By **Andrew T. Polonsky** *and* **Tresa M. Pollock**

Additive manufacturing [three-dimensional (3D) printing] methodologies for high–melting point metallic materials are being used in the advanced aerospace and biomedical sectors to fabricate high-value and geometrically complex parts in moderate production volumes. One barrier to more widespread applications is the gaps in the understanding of the processes that occur during the layer-by-layer buildup by beam heating and melting of powder or wire layers. For example, the absorption of energy in powder layers that are only a few particles thick is poorly understood. On page 660 of this issue, Khairallah *et al.* (*1*) used in situ x-ray synchrotron observations of powder dynamics coupled to thermal and hydrodynamic flow modeling to study energy absorption at the scale of powder particles. The presence of the powder, relative to a flat plate without powder, improves absorptivity at low laser power, but as power approaches 200 W, the details of the powder become far less important.

In powder-bed printing, overlapping linear scans or repeated spot melts with electron or laser beams in preselected patterns form a layer of the part. The process is repeated for hundreds or thousands of layers to build up an object (see the figure, left). Ideally, the print process parameters are adjusted continuously to achieve the desired material structure in zones of the printed part. In a recent demonstration, collections of small equiaxed crystals (“grains”) were printed in a background structure of large columnar crystals (*2*).

At a macroscopic level, the power supplied by the laser, the beam shape, the scan velocity and pulse duration, and the scan pattern must be tuned to achieve favorable local melting conditions. For example, printing a simple cube 2.5 cm on each edge would typically require roughly 3 to 6 km of linear track melting, or 5 million to 30 million individual spot melts. Along this print path, the physics of laser energy absorption, powder particle motion, melting, vaporization, fluid flow, heat transfer, mass transfer of alloy constituent elements, nucleation of the solid, buildup of residual stress, and evolution of the solid-state structure of the material must be predicted and controlled to ensure reproducible printing of high-quality objects (*3*–*6*).

The final properties of a material are controlled by the structure of the material derived from processing (printing) parameters as well as the size, distribution, and character of processing-induced defects. Connecting processing physics to structure and defect formation is challenging, given the complex dynamics of the powder particles. In the vicinity of the melting event, the intense heating of the powder and underlying print substrate by the laser beam creates vapor plumes that can cause particles to “recoil” away from the heated region (*7*).

For example, a short melt track through a 50-μm-thick powder layer of a cobalt-nickel alloy (*8*) that was placed on top of a sheet of the same alloy can be formed (see the figure, left). The sheet is composed primarily of one large grain that exhibits continued growth through the melted layer, except in a region at the top of the melt track where new crystallites formed because of the arrival of a powder particle on the top of the melt pool. A 3D tomographic dataset (*9*) (see the figure, right) shows that the arrival of the powder particle results in nucleation of multiple crystals of different orientations (indicated by differences in color). The physics that produce this unusual powder particle trajectory and the implications for this disturbance in structure for the next printed layer are not well understood.

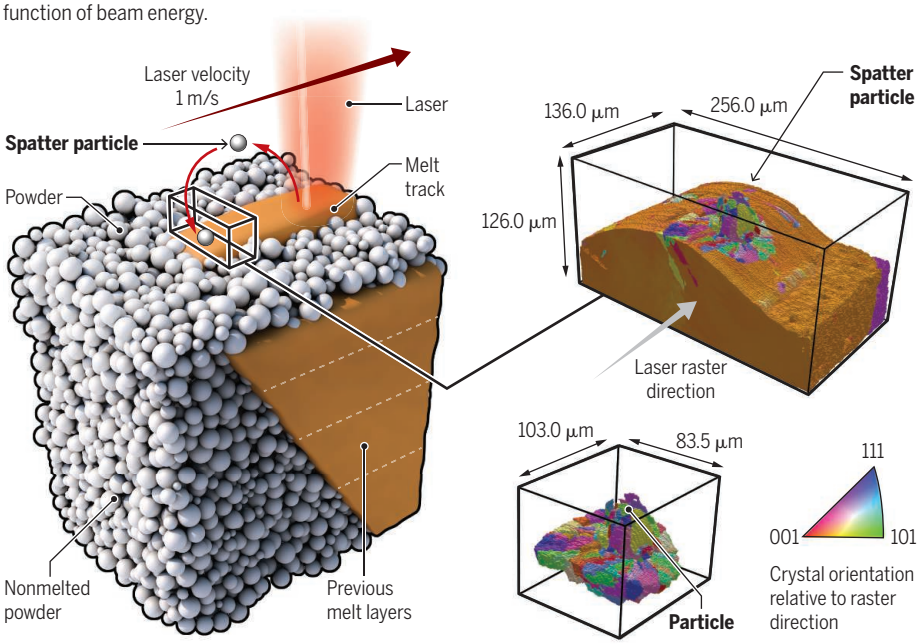
Khairallah *et al.* studied such powder dynamics in relation to the formation of defects in stainless steel. A specific concern during printing is the ejection of “spatter,” that is, liquid droplets or entrained powder particles that undergo expulsion from the melt pool and appear as the sparks or smoke in videos of metal 3D printing. The authors observed spatter events and associated powder dynamics at high resolution

Materials Department, University of California, Santa Barbara, CA, USA. Email: tresap@ucsb.edu

Published by AAAS

Metal-particle physics

Three-dimensional printing of metal powders requires energetic laser- or electron-beam melting that can also move particles. Khairallah *et al*. used x-ray imaging and modeling to understand particle movement as a function of beam energy.



From powder to part
A moving laser beam locally melts the powder bed to build up a part layer by layer. Depending on process parameters, spatter can be ejected and land in melted regions, as shown.

When the spatter lands
A spatter particle lands on the top of a single-track melt pool during solidification and initiates a secondary solidification front with different grain orientations from the point of impact of the particle.

during printing in a high-energy synchrotron imaging environment. To connect the observed dynamics to the physics of defect formation, Khairallah *et al*. modeled a "presintered" powder bed, where particles undergo preliminary fusing with their neighbors during laser-beam preheating (*10*). Presintered beds can reduce powder motion in electron-beam additive manufacturing but have received limited attention in process modeling.

The high-resolution, multiphysics model reveals the role of spatter particles on top of the presintered bed. Khairallah *et al*. show several previously unknown effects that arise from the interaction of the laser beam with spatter that deposited or is in motion. Interaction of the laser beam with previously deposited spatter produces fluctuations in the melt pool depth, which increases the probability that, at low laser power, defects will form through a lack of powder fusion. Also, depending on their location relative to the scanning beam, spatter particles may be broken up, resulting in multiplication of the number of defect sites. In addition, spatter particles in motion may shadow the laser beam, interfering with deposition of laser energy and resulting in pore formation.

With this detailed knowledge of the physics gained from simulations and synchrotron imaging, Khairallah *et al*. developed a macroscopic model to map out the expulsion regime as a function of laser power and laser scan speed. This "upscaling" of the physics for the full range of complex phenomena that occur during 3D printing of metals will ultimately build the confidence needed to use these technologies as reliable, full-production tools. Such understanding will also enable design of new alloys specifically tuned to the physics of the metal 3D printing process, expanding the presently very limited suite of printable metallic materials. ■

REFERENCES AND NOTES

1. S. A. Khairallah *et al.*, *Science* **368**, 660 (2020).
2. R. R. Dehoff *et al.*, *Mater. Sci. Technol.* **31**, 931 (2015).
3. W. E. King *et al.*, *Appl. Phys. Rev.* **2**, 041304 (2015).
4. D. D. Gu, W. Meiners, K. Wissenbach, R. Poprawe, *Int. Mater. Rev.* **57**, 133 (2012).
5. T. DebRoy *et al.*, *Prog. Mater. Sci.* **92**, 112 (2018).
6. S. S. Babu *et al.*, *Metall. Mater. Trans.* **49**, 3764 (2018).
7. A. Klassen, T. Scharowsky, C. Korner, *J. Phys. D Appl. Phys.* **47**, 275303 (2014).
8. C. A. Stewart, S. P. Murray, A. Suzuki, T. M. Pollock, C. G. Levi, *Mater. Des.* **189**, 108445 (2020).
9. M. P. Echlin, M. Straw, S. Randolph, J. Filevich, T. M. Pollock, *Mater. Charact.* **100**, 1 (2015).
10. C. L. A. Leung *et al.*, *Mater. Des.* **174**, 107792 (2019).

ACKNOWLEDGMENTS

We acknowledge the support of Office of Naval Research (ONR) grant N00014-18-1-2794.

10.1126/science.abb4938

BIOMEDICINE

Sending copper where it is needed most

Elesclomol improves survival in a mouse model of Menkes disease

By **Svetlana Lutsenko**

Copper (Cu) is an essential component of human physiology, and it is indispensable for normal brain development. Cells use Cu in many processes, including respiration, formation of myelin sheath, immune responses, wound healing, and synthesis of neurotransmitters (*1*). A sophisticated network of Cu-transporting proteins retrieves Cu from dietary sources, transfers Cu across biological membranes, and distributes it within cells and tissues (*2*). The key component of this network, Cu-transporting adenosine triphosphatase 1 (ATP7A), is inactivated in Menkes disease (MNKD). This causes Cu deficit in the brain, neurodegeneration, and early death. Cu supplementation is ineffective in treating MNKD patients because Cu cannot reach many cellular destinations, especially the brain, without functional transporters. On page 620 of this issue, Guthrie *et al*. (*3*) show that a small Cu-binding molecule, elesclomol, can overcome this problem, improving Cu delivery to the brain and alleviating mortality of ATP7A-deficient mice.

Cu is a fascinating metal. Its malleability, attractive color, and conductivity make Cu a metal of choice for many applications. The role of Cu in human physiology is much less appreciated. This is largely because the daily dietary requirements for Cu are low (only 1 to 2 mg per day) and the genetic disorders of Cu homeostasis are relatively rare. The discovery in 1993 of genes associated with MNKD (*ATP7A*) and Wilson's disease (*ATP7B*, which causes a buildup of Cu in the body) highlighted the role of Cu balance in human physiology and revealed the existence of proteins responsible for Cu transport and distribution (*4*–*7*). The list of Cu-handling proteins as well as disorders associated with Cu imbalance has been growing.

Department of Physiology, Johns Hopkins University School of Medicine, Baltimore, MD 21205, USA.
Email: lutsenko@jhmi.edu

GRAPHIC: C. BICKEL/*SCIENCE*

Published by AAAS

MNKD and Wilson's disease illustrate negative consequences of either Cu deficiency or Cu overload, respectively, and the challenges associated with treatment of these disorders. MNKD and Wilson's disease are caused by inactivating mutations in similar Cu-transporting proteins, which have tissue-specific functions. ATP7A facilitates Cu export from the intestine into the blood for further utilization including Cu import to the brain, whereas ATP7B exports excess Cu from the liver for removal in bile. These functions are essential for human life.

ATP7A also plays an equally important role within cells: It transports Cu from the cytosol into the lumen of specialized cellular compartments (trans-Golgi network, vesicles, and secretory granules), where Cu is used to activate various Cu-dependent enzymes (see the figure). Loss of ATP7A activity causes systemic Cu deficiency, poor temperature control, abnormal formation of connective tissues and vasculature, demyelination of neurons, seizures, developmental delay, and death at the age of 3 to 4 years. Inactivation of ATP7B is also debilitating: It leads to Cu overload in tissues, liver disease, and neurological and psychiatric abnormalities. In both cases, restoring proper distribution of Cu within cells and tissues remains a major challenge.

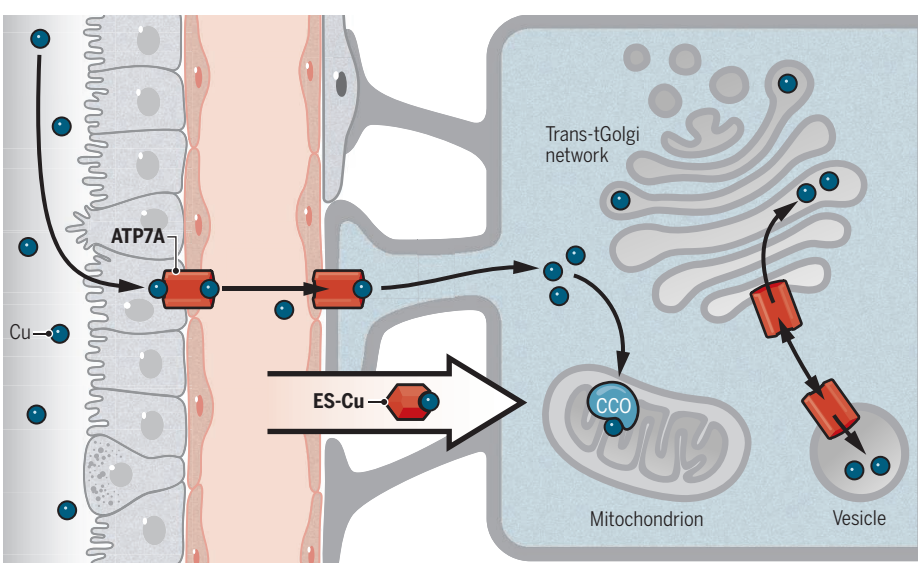
MNKD is especially difficult to treat and, currently, there is no cure. Early diagnosis followed by prompt Cu supplementation with Cu-histidine complex may prolong patients' lives and improve motor skills and neurodevelopment (*8*). Cu-histidine is delivered intravenously and has to cross many biological barriers to reach Cu-dependent proteins within the central nervous system. In the absence of ATP7A, this process is inefficient, and Cu-histidine–treated MNKD patients die before reaching adulthood. Promising progress has been made toward gene therapy for MNKD (*9*), but safe gene transfer to neonatal brain remains a future goal. Furthermore, gene transfer is typically targeted to specific tissues, leaving others "uncorrected." Small molecules are less tissue specific and may facilitate broad balancing of Cu throughout the body. Using mouse models of Cu deficiency, Guthrie *et al.* found that the small molecule elesclomol can carry Cu through various biological membranes and facilitate delivery to Cu-dependent enzymes, especially in mitochondria.

Mitochondria are distinctly sensitive to Cu imbalance and their functions are often compromised in Cu-associated disorders (*10*, *11*). In MNKD, an essential mitochondrial metabolic protein, cytochrome c oxidase (CCO), exhibits reduced activity. Mitochondrial dysfunction contributes to neurodegeneration in MNKD (*12*) and restoring CCO activity is necessary for successful treatment. Using a mouse model of MNKD, Guthrie *et al.* showed that treatment with elesclomol increased CCO activity, improved oxygen consumption by mitochondria, normalized brain structures, improved neurologic functions, and markedly decreased mortality. A slight improvement of poor pigmentation and curly whiskers (both reflections of Cu deficiency in cellular compartments outside mitochondria) suggests that elesclomol-Cu facilitates Cu distribution throughout the cell. Many important Cu-dependent enzymes are located within the cells' secretory pathway, and their activity is greatly diminished in MNKD patients and animal models of the disease. Even partial recovery of their activity is consequential, because it helps to restore production of neurotransmitters, vasculature formation, and other processes. The authors show that elesclomol acts as a Cu shuttle—in a complex with Cu—and it does not appear to have obvious toxic effects in mice.

Guthrie *et al.* offer convincing evidence that it is possible for a small molecule to carry Cu through complex biological barriers and improve Cu metabolism in tissues. It is important to note that, over time, Cu delivered by elesclomol is metabolized and additional Cu-elesclomol delivery is needed to maintain Cu-dependent enzymes in the brain. The rate of Cu entry into the brain is relatively high at the early stages of brain development, but it drops substantially in adult animals. It remains unclear whether Cu supplied during early brain development is sufficient to sustain brain function in adult life. Further studies are also needed to determine whether, in addition to Cu transfer to mitochondria, more efficient Cu transport to the trans-Golgi network and other cellular destinations can be achieved. This could also be important for Wilson's disease. Cu-dependent enzymes that undergo functional maturation inside the trans-Golgi network and various granules critically contribute to brain regulatory and signaling functions and should not be overlooked in a search for therapeutic approaches for MNKD and other diseases of Cu imbalance. Elesclomol offers a starting point toward developing a vehicle for delivery of Cu where it is needed most. ■

Elesclomol facilitates membrane transfer of copper

Copper (Cu)–transporting adenosine triphosphatase 1 (ATP7A) exports Cu from the gut into the bloodstream and facilitates Cu entry through the blood-brain barrier (BBB) into the brain parenchyma. Within cells, ATP7A transports Cu into the trans-Golgi network and vesicles. In *Atp7a*-deficient mice, elesclomol binds Cu (ES-Cu) and transfers Cu through biological membranes to mitochondria, activating cytochrome c oxidase (CCO).



GRAPHIC: A. KITTERMAN/*SCIENCE*

REFERENCES AND NOTES

1. I. F. Scheiber *et al.*, *Prog. Neurobiol.* **116**, 33 (2014).
2. S. Lutsenko, *Metallomics* **8**, 840 (2016).
3. L. M. Guthrie *et al.*, *Science* **368**, 620 (2020).
4. J. F. Mercer *et al.*, *Nat. Genet.* **3**, 20 (1993).
5. C. Vulpe *et al.*, *Nat. Genet.* **3**, 7 (1993).
6. P. C. Bull *et al.*, *Nat. Genet.* **5**, 327 (1993).
7. R. E. Tanzi *et al.*, *Nat. Genet.* **5**, 344 (1993).
8. S. G. Kaler, *J. Trace Elem. Med. Biol.* **28**, 427 (2014).
9. M. R. Haddad *et al.*, *Mol. Ther. Methods Clin. Dev.* **10**, 165 (2018).
10. A. Członkowska *et al.*, *Nat. Rev. Dis. Primers* **4**, 21 (2018).
11. N. Zakery *et al.*, *Metallomics* **9**, 1501 (2017).
12. S. Zlatic *et al.*, *Neurobiol. Dis.* **81**, 154 (2015).

ACKNOWLEDGMENTS

This work was supported by National Institutes of Health grant R01 GM101502 to S.L.

10.1126/science.abb6662

Published by AAAS



Researchers are adapting a wide range of technologies inspired by nature to create and control ever-smaller flying drones.

PHOTO: MICHAEL JACKSON-RAND

ENGINEERING

Drones become even more insect-like

Mosquitoes' exceptional sensitivity to sound and airflow inspires new collision avoidance technology

By **John Young** *and* **Matthew Garratt**

Evolutionary pressures in the animal kingdom have, over the course of several hundred million years, produced a diverse array of creatures highly adapted to survival within their own niche environments. Such adaptations coincide with optimized and efficient materials, body structure, and behavior. Humans have long drawn inspiration from nature in the creation of new technologies—for example, the earliest attempts at flight based on emulation of birds—and many benefits stem from the study of processes, materials, methods, and organizational structures of living organisms. On page 634 of this issue, Nakata *et al.* (*1*) exemplify the bioinspired design methodology through their investigation of the sound- and airflow-sensing capabilities of the southern house mosquito *Culex quinquefasciatus* and subsequent creation of a small quad-copter drone with an autonomous collision avoidance system based on the same sensing principles. The sensor displays compelling advantages in weight, power, and deployability over existing technology.

Drones in various forms have become ubiquitous, operating in fields as disparate as sports broadcasting, pipe and power line inspection, ocean temperature monitoring, and food delivery. The imperative for small, maneuverable, and autonomous aerial drones has led designers to pursue innovative solutions for reduced weight, more efficient locomotion, lower power requirements, higher endurance, and faster, more robust sensing and navigation. Insects, with at least 10 million species on Earth, represent half of all known species of living organisms (*2*) and provide a rich resource from which to draw inspiration.

Nature has at its disposal many tools that human designers seek to emulate in the design of aerial vehicles as small as 20 mm in length and as little as 0.1 g in mass (*3*, *4*). Much of nature's advantage over what engineers can achieve is in the realm of materials and growth versus manufacturability. Natural materials are generally multifunctional, with surface properties at the micrometer or nanometer scale that can provide optical signaling, camouflage, adhesion, drag reduction, hydrophobicity, or hydrophilicity (*2*). Wings and other structures are flexible, with veins, membranes, and otherwise spatially varying stiffness shaped to respond passively to airflow for maximum aerodynamic advantage (*5*), and may be neatly folded for protection when not in use (*6*). Structural stiffness may be tuned to allow resonant actuation with low energy expenditure, and flexibility and regrowth provide for damage tolerance, self-healing, and adaptation to changes in body configuration (such as loss of a wing or a leg).

Mechanical sensors such as hairs may be distributed over the entire insect body to provide global rather than point measurements of airflow or proprioception. Such

School of Engineering and Information Technology, University of New South Wales, Canberra, ACT 2610, Australia. Email: j.young@adfa.edu.au; m.garratt@adfa.edu.au

Published by AAAS

sensors allow for more precise locomotion control strategies. Muscles provide linear actuation that, when coupled with levers, pivots, and pneumatic inflation of hollow flexible structures, allows easily scalable production of a wide range of kinematics for flying, crawling, swimming, climbing, jumping, perching, and hanging. Such is the utility of natural actuators that roboticists are now emulating them in so-called "soft robotics" or using them directly in biohybrid designs, which create interfaces between living cells and artificial components (*7*, *8*).

Other concepts stem from neurological and behavioral adaptation, inspiring algorithms for swarming, passive sensing and communication (to prevent jamming), attitude and altitude control, and collision avoidance. Robots, in general, have a number of sensing modalities for collision avoidance, including radar, laser rangefinders, and stereo vision. These types of sensors tend to have a minimum size and shape, making it difficult or impossible to integrate them into small aerial vehicles for which weight and size are critical limitations (*9*). In addition, systems based on vision are generally computationally very expensive because they require matching of features across images to create disparity maps (using either multiple cameras or robot motion between images to detect structures in the environment). In either case, current hardware and algorithms cannot reliably provide vision-based navigation on low-power processors at the high speeds required for onboard flight control of small drones (*10*). Furthermore, optical systems using visible light do not work at night, and systems that emit radiation, such as radar and laser rangers, might be restricted in their use around humans to avoid eye damage or other adverse health effects.



New drone technology mimics the collision avoidance mechanism used by *Culex quinquefasciatus*.

PHOTO: ARNAV RAY / ISTOCK.COM

The work of Nakata *et al*. showcases a simple, reliable, and passive technique for avoiding obstacles at close range, inspired by hearing in mosquitoes. Insect hearing is accomplished by means of tympanal organs (e.g., beetles and locusts) or Johnston's organs (e.g., flies, bees, and mosquitoes) (*11*). The latter are found in the pedicel segment at the base of the antennae and are shaped somewhat like upturned umbrellas, with the spokes connected to sensory neurons. Johnston's organs can distinguish among gravitational, mechanical, and acoustic signals and are exceptionally sensitive to air displacement and acoustic particle velocity (that is, the speed of a notional parcel of air as the sound wave passes through it). Thus, mosquitoes are able to sense flight speed as well as motions on the order of millionths of their body length (*12*).

To assess changes in the airflow around the insect induced by its flapping wings, Nakata *et al*. first conducted computational fluid dynamics calculations on a dynamic model of a mosquito in free flight and in proximity to walls or the ground. They found that the *Culex* Johnston's organ is sensitive enough to detect these changes, and proposed a mechanism for the mosquito's observed collision avoidance behavior in the absence of visual cues. They then repeated the process experimentally with a palm-sized 27-g commercial drone and demonstrated functional collision avoidance with a sensor module responsive to changes in pressure at 10 locations around the drone. Once the pressure thresholds that indicate surface or ground proximity were established for the vehicle, the device operated with essentially no computer processing, making it simple and robust. Moreover, the concept can be implemented on a scale suited for current or future smaller drones that can operate indoors and in highly cluttered environments. This method, which scientists are now using in the pursuit of microscale flight, joins the list of human design tools that insects have been using for millions of years. ■

REFERENCES AND NOTES

1. T. Nakata *et al*., *Science* **368**, 634 (2020).
2. T. B. H. Schroeder, J. Houghtaling, B. D. Wilts, M. Mayer, *Adv. Mater.* **30**, 1705322 (2018).
3. K. Y. Ma, P. Chirarattananon, S. B. Fuller, R. J. Wood, *Science* **340**, 603 (2013).
4. Y. Chen *et al*., *Nature* **575**, 324 (2019).
5. J. Young, S. M. Walker, R. J. Bomphrey, G. K. Taylor, A. L. R. Thomas, *Science* **325**, 1549 (2009).
6. S.-M. Baek, S. Yim, S.-H. Chae, D.-Y. Lee, K.-J. Cho, *Sci. Robot.* **5**, eaaz6262 (2020).
7. M. Hassanalian, A. Abdelkefi, *Prog. Aerosp. Sci.* **91**, 99 (2017).
8. L. Ricotti *et al*., *Sci. Robot.* **2**, eaaq0495 (2017).
9. X. Yang *et al*., *IEEE Trans. Intell. Transp. Syst.* 10.1109/TITS.2019.2955598 (2019).
10. H. D. Escobar-Alvarez, M. Ohradzansky, J. Keshavan, B. N. Ranganathan, J. S. Humbert, *IEEE Trans. Robot.* **35**, 1220 (2019).
11. G. L. Fain, *Sensory Transduction* (Oxford Univ. Press, ed. 2, 2019).
12. R. J. Bomphrey, T. Nakata, N. Phillips, S. M. Walker, *Nature* **544**, 92 (2017).

10.1126/science.abb0064

SYNTHETIC BIOLOGY

Toward artificial photosynthesis

Microfluidics lights the way to a synthetic plant-like cell

By **Nathaniel J. Gaut** *and* **Katarzyna P. Adamala**

The creation of a fully artificial living cell would signify progress in both understanding current life and the development of synthetic organisms. A crucial component of any living organism is energy generation: the means to power its internal machinery. Because of their relative simplicity, catabolic reactions are the classical means for providing carbon and energy to synthetic cells, and much work has been done in optimizing which energy substrates work best for particular reactions (*1*). Despite robust success using small-molecule energy sources, the possibility of designing anabolic mechanisms that can harvest virtually limitless energy from light is very alluring yet remains unrealized. On page 649 of this issue, Miller *et al*. (*2*) leverage the capacity of microfluidics to combine natural and artificial biological networks to achieve photosynthetic anabolic reactions on a microscale level.

Attempts at placing a series of complex reactions in a single, in vitro, cell-free protein expression platform generally have been plagued by low fidelity, irreproducibility, and small sample sizes. Within the past few decades, engineering of microfluidics to create artificial biological membranes has allowed these issues to be addressed (*3*). Microfluidic techniques allow for performing experiments in miniature cell culture systems in which cells and all reactants are exposed to dynamic fluid flow at the micrometer scale. The approach allows for the control of fluids through microchannels to change environmental conditions and provides opportunity for analyzing every cell separately (instead of looking at bulk cultures). Microfluidic barcoding (*4*) and screening (*5*) methods allow for easy synthesis and visualization of droplets (microscopic artificial "containers") in a high-throughput manner. The rise of microfluidics has allowed milestone improvements in synthetic biology research through tighter reaction component

Department of Genetics, Cell Biology, and Development, University of Minnesota, Minneapolis, MN, USA.
Email: kadamala@umn.edu

Published by AAAS

titration and a virtually limitless sample size (because each droplet acts as its own discrete reaction compartment).

The development of a synthetic liposome harboring functional adenosine triphosphate (ATP) synthase and bacteriorhodopsin to establish a proton gradient, and thus driving ATP synthesis, was a remarkable advancement in artificial photosynthesis (*6*). This system encompasses the basic function of photosynthesis: using light to synthesize an energy carrier molecule. An earlier study demonstrated encapsulation of these two protein complexes, purified separately, to harvest light energy and drive a variety of life-essential processes in liposomes, including high-energy molecule synthesis, carbon fixation, and actin polymerization (*7*). Both of those projects represent groundbreaking advancements toward creating light-powered artificial bioreactors as well as understanding the requirements for a photosynthetic system. However, more work is needed to realize a fully artificial photosynthetic cell.

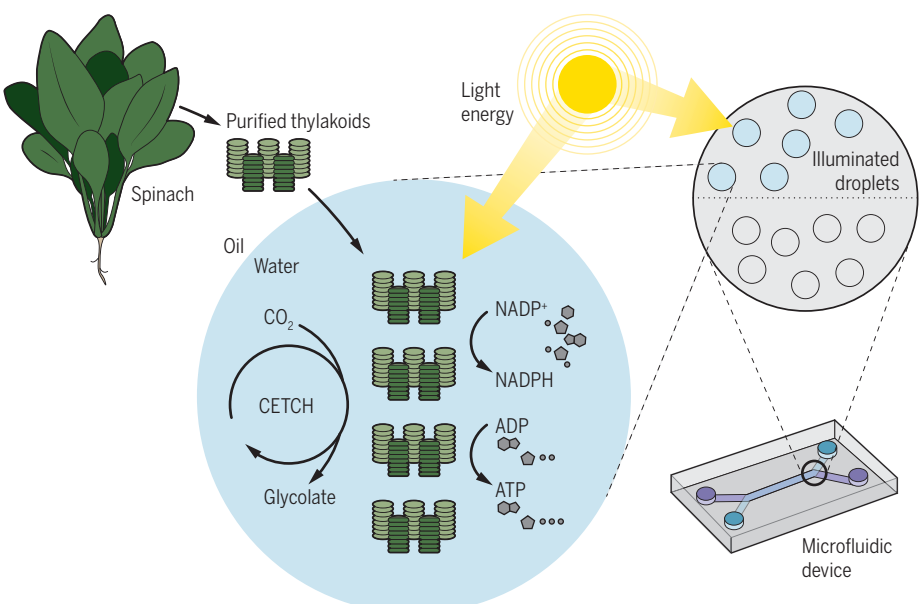
In this study by Miller *et al.*, membranes from thylakoids (compartments where the light-dependent reactions of photosynthesis take place) were isolated from the spinach plant (*Spinacia oleracea*) and encapsulated within water-in-oil droplets along with the 16 enzymes composing the crotonyl-coenzyme A (CoA)/ethylmalonyl-CoA/hydroxybutyryl-CoA (CETCH) pathway (see the figure). The CETCH pathway is a synthetic cycle for the continuous fixation of CO_2, designed to complement the six naturally occurring carbon fixation pathways for use in in vitro models (*8*). The resulting encapsulated system uses light energy to produce the multicarbon molecule glycolate from CO_2 while also phosphorylating adenosine diphosphate (ADP) to ATP, thereby successfully reconstituting an essential photosynthetic plant anabolic pathway. This design is validated experimentally by measuring an increase in ATP, reduced nicotinamide adenine dinucleotide phosphate (NADPH), and glycolate production upon illumination. Looking to expand this technology toward an easier bulk production method, the authors turned toward microfluidics to create thousands of water-in-oil droplets in an automated way. Using this scaled-up method of droplet production, they engineered precise control of the reaction conditions and visualized the reaction progression by imaging NADPH fluorescence. This advancement marks an important step toward the development of a synthetic plant-like cell.

Potential future challenges in this area include further inclusion of plant enzymes to incorporate the light-dependent or light-independent reactions that are essential to plant metabolism. This could be as simple as coupling this technology with the quasi–light-dependent synthetic system mentioned above (*6*, *7*) or an independently developed reaction network that more closely borrows from pathways found in nature. Additionally, coupling this technology with one of the cell-free protein expression platforms, PURE (protein synthesis using recombinant elements) (*9*) or TXTL (whole-cell transcription-translation system) (*10*) would be a step toward a self-replicating system powered by endogenously expressed light-harvesting complexes. Using more complex microfluidics methods would enable encapsulation within a phospholipid bilayer membrane (liposomes are a monolayer lipid), resulting in better mimics of natural cells with the capacity for environmental interaction using natural transmembrane signaling tools (*11*). Combining energy generation with existing uses of cell-free and synthetic cell technologies would create a very powerful tool for biotechnology (*12*).

Miller *et al.* demonstrate a major advancement in synthetic biology and a crucial milestone toward the construction of a self-sustaining synthetic cell. The ability to harvest light energy and fix CO_2 into multicarbon compounds creates an essential foundation for technologies that will find use in many other areas, from small-molecule or drug synthesis in artificial bioreactors to development of an artificial biological system for sequestering environmental carbon. As we become better able to redesign and reconstruct natural biology, there will be many great leaps such as that achieved by Miller and colleagues in both understanding basic biological concepts as well as developing biotechnological innovations. ■

A technological approach to semisynthetic photosynthesis

Thylakoids (where photosynthesis occurs) are purified from spinach, situated within oil-in-water droplets along with the 16 CETCH enzymes. When hit with light, the underlying reactions are triggered. This could be used in applications such as solar-powered bioreactors and engineering cells.



CETCH, crotonyl-coenzyme A (CoA)/ethylmalonyl-CoA/hydroxybutyryl-CoA; $NADP^+$, nicotinamide adenine dinucleotide phosphate; NADPH, reduced form of $NADP^+$; ADP, adenosine diphosphate: ATP, adenosine triphosphate.

GRAPHIC: MELISSA THOMAS BAUM/*SCIENCE*

REFERENCES AND NOTES

1. H. C. Kim, D. M. Kim, *J. Biosci. Bioeng.* **108**, 1 (2009).
2. T. E. Miller *et al.*, *Science* **368**, 649 (2020).
3. D. N. Breslauer *et al.*, *Mol. Biosyst.* **2**, 97 (2006).
4. C. M. Svensson *et al.*, *Small* **15**, 1 (2019).
5. A. Kulesa, J. Kehe, J. E. Hurtado, P. Tawde, P. C. Blainey, *Proc. Natl. Acad. Sci. U.S.A.* **115**, 6685 (2018).
6. S. Berhanu *et al.*, *Nat. Commun.* **10**, 1325 (2019).
7. K. Y. Lee *et al.*, *Nat. Biotechnol.* **36**, 530 (2018).
8. T. Schwander *et al.*, *Science* **354**, 900 (2016).
9. Y. Shimizu *et al.*, *Methods* **36**, 299 (2005).
10. Z. Z. Sun *et al.*, *J. Vis. Exp.* **79**, e50762 (2013).
11. D. Carugo *et al.*, *Sci. Rep.* **6**, 25876 (2016).
12. F. Villarreal, C. Tan, *Front. Chem. Sci. Eng.* **11**, 58 (2017).

10.1126/science.abc1226

Published by AAAS

CANCER

The challenge of early detection in cancer

Tumor growth dynamics and the timing of metastasis impose limits on cancer screening

By **Nora Pashayan**[1] *and* **Paul D. P. Pharoah**[2]

The chances of survival for a patient with cancer are substantially improved if the disease is diagnosed and treated at an early clinical stage (*1*). This underpins the promise of early detection to improve prognosis. Longer survival time may reflect later death, but it may also reflect advancement of time of diagnosis or increased diagnosis of indolent tumors with no shift in time of death (*2*). Despite several decades of research, only a handful of early detection tests have been shown to reduce cancer-specific mortality. This benefit comes at a cost: the diagnosis and treatment of cancers that otherwise never would have been diagnosed in the lifetime of the patient. Further research is needed to improve cancer early detection methods, but fundamental issues surrounding tumor growth dynamics and the timing of metastasis make early detection challenging.

An early detection test could be applied in symptomatic patients to reduce the time between presentation and diagnosis. It could also be applied as a "screening" test in apparently healthy individuals to identify those with asymptomatic cancer. It is in the context of screening that early detection is discussed. After malignant transformation, a cancer is small, asymptomatic, and undetectable. As it grows, it might be detectable by an early detection test before becoming symptomatic and clinically diagnosable. Cancer cells may metastasize at any point, but only a small proportion will grow into macroscopic metastases (*3*). The majority of deaths from cancer result from widespread metastatic disease (*4*). Given that cancer mostly occurs in the elderly, mortality from another cause may intervene at any time.

A tumor that has not metastasized at the time of diagnosis can be completely removed and cured by surgery. A tumor that has metastasized may also be curable by a combination of surgery and systemic therapy, but some will be incurable. The probability of achieving a systemic cure may depend on the volume of metastatic disease at the time of treatment. The ideal scenario for early detection is that a tumor that would have metastasized before it is clinically detectable is detected early, before the metastasis occurs, so that the cancer can be cured. An alternative scenario is a case in which detection by screening occurs after the tumor has metastasized, but the earlier diagnosis of metastasis means that it is more likely to be curable with systemic treatment.

The potential for screening to detect a tumor before metastasis has occurred depends on factors including the tumor's growth rate and the relationship between tumor size and metastatic potential (*5*) (see the figure). Additionally, there is dependence on screening factors including the threshold size at which tumors can be detected and the frequency of screening. The growth rate of tumors of the same tissue of origin in different individuals varies widely, from almost static to fast-growing. Most human tumors have a preclinical period of at least several years, grow at a constant rate for a prolonged period, and often metastasize before the tumor is clinically detectable (*6*). A tumor develops its own blood supply once it is 1 to 2 mm in diameter, so it is assumed that the earliest distant, or blood-borne, metastasis can occur when the tumor has reached 1 mm in diameter. The probability of the occurrence of metastasis increases with the size of the tumor at diagnosis (*7*, *8*), and fast-growing tumors are more likely to metastasize than slow-growing tumors (*7*, *9*). Screening is less likely to detect the tumors that are most likely to metastasize because they are growing faster.

The impact of tumor growth on the potential for screening can be illustrated for breast cancer because there are good data describing both primary tumor and metastasis growth and because there are data on screening by mammography to detect early disease. The tumor volume doubling time (TVDT) is a measure of the tumor growth rate. In breast cancers, it varies from 30 days to more than a year with a median of 150 days (*6*, *9*) and metastasis doubling time is usually about half that of the primary tumor (*9*). If early detection could advance the diagnosis sufficiently, the chance of metastasis having occurred at the time of diagnosis would be reduced and the chance of surgical cure increases. Screening would also need to be offered more frequently to detect fast-growing tumors. However, a tumor with a TVDT of 50 days would take just 6 months to grow from the current limit of detection by mammography (~5 mm in diameter) to a tumor large enough to be diagnosed clinically (2 cm). It seems unlikely that a population-based screening program with a screening interval of less than 1 year would be feasible. Therefore, an effective, annual screening test for such tumors would need to be able to detect even smaller tumors. The same tumor would take 16 months to grow from 2 mm to 2 cm, but currently available technology is not sensitive enough to detect such small lesions.

Detecting a tumor at a smaller size increases the likelihood of detection before metastasis has occurred. However, not all individuals whose cancer is detected earlier by screening benefit from early detection and some are harmed. For example, if metastasis has already occurred at the time of screen detection, the metastasis might be too small to be diagnosed, appropriate systemic treatment would not be given, and the chance of cure is reduced. Harm may also arise from an increase in the burden of overdiagnosis and overtreatment. Overdiagnosis refers to the detection of cancers that would not have become clinically apparent during an individual's lifetime in the absence of screening. Overdiagnosis occurs with detection of either nonprogressive cancer or slow-growing cancer that would take longer than the remaining lifetime of the patient to progress to a clinical diagnosis of cancer. Treatment of overdiagnosed cancer does not yield survival benefits but causes emotional and physical harm. If new tests do not distinguish progressive from nonprogressive cancers, then early detection will likely increase the incidence of cancer without a comparable reduction in cancer-specific mortality.

Detection of smaller tumors could be achieved by screening at shorter intervals. Given the heterogeneity of tumor growth rates, more frequent screening would subject a proportion of the population to unnecessary testing and its consequences, including investigation of false test results. Tailoring screening frequency to the tumor growth

[1]Department of Applied Health Research, University College London, London, UK. [2]Department of Oncology and Department of Public Health and Primary Care, University of Cambridge, Cambridge, UK. Email: pp10001@medschl.cam.ac.uk

Published by AAAS

rates would optimize the benefit-harm trade-off of screening.

The potential of early detection to reduce cancer-specific mortality depends critically on tumor growth rates, metastasis growth rates, and the probability that a tumor has metastasized at different points of the growth curve. The relationship of metastasis probability to tumor size has important implications for early detection. Many new imaging technologies are being developed, but it seems unlikely that imaging would be able to detect very small tumors, and so the potential for imaging as a modality for early detection will depend on the probability of early metastasis for different cancers. Historical studies with long-term follow-up of the occurrence of distant metastasis in different types of cancer patients treated by primary surgery without systemic therapy would provide such data. Incorporating such data into multiscale computational modeling platforms that can simulate tumor growth for individualized prediction would inform individualized screening strategies.

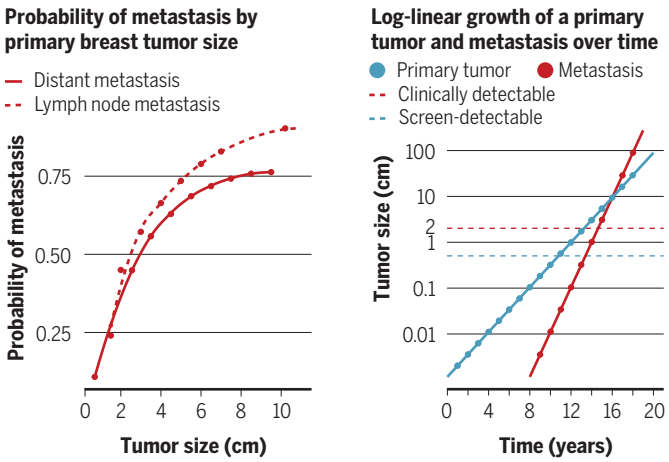
Blood-based tests, often called liquid biopsies, which detect circulating tumor-derived factors such as circulating tumor cells (CTCs) (*10*) and circulating tumor DNA (ctDNA) (*11*), have shown potential in early diagnosis. The sensitivity of these tests for detecting small tumors is currently too low for use in cancer screening. This may change with technical improvements, but the underlying biology of ctDNA may still limit its potential for early detection. Tumors release DNA into the bloodstream during apoptosis, but the avoidance of programmed cell death is a hallmark of cancer, and those tumors most likely to metastasize early may be least likely to shed DNA into the circulation. Indeed, preliminary modeling studies suggest that tumor growth dynamics influence ctDNA amounts and that a slower-growing tumor is associated with a higher ctDNA burden than a faster-growing tumor of the same size (*12*). Given that growth dynamics are an important factor in determining the likely effectiveness of early detection, the balance between earlier detection by liquid biopsy and overdiagnosis (and consequent overtreatment) is difficult to predict. Liquid biopsies may also be limited if they are not cancer site–specific. After an abnormal blood test, the site of origin of cancer needs to be identified, and imaging will probably be required prior to further investigation such as biopsy. Ultimately, determining the effectiveness of liquid biopsies for early detection will depend on empirical studies. Even if the sensitivity of liquid biopsies to detect small primary tumors cannot be improved, their application may prove to be in diagnosing metastasis of small tumors detected by other modalities.

Neoplastic cells in a tumor are heterogeneous, and there is some evidence that only a subpopulation of tumor cells can initiate metastasis (*13*). Testing screen-detected tumors for potential markers of metastasis-forming cells to decide which tumors to treat could reduce overtreatment and improve prognosis. Computational models that can simulate the change in markers of cancer progression and forecast patient-specific cancer progression trajectories could personalize screening strategies and inform when and in whom to initiate treatment (*14*).

The benefit-harm trade-off from early detection will be maximized by taking into account the heterogeneity of tumor growth kinetics. Consequently, basic research in typical tumor and metastasis growth patterns of cancers at different sites is required. Other priorities in early detection research are methods to identify the small tumors that have the potential to metastasize early and the development of tests to detect occult metastasis at the time of early diagnosis. The ultimate challenge for early detection is to demonstrate an improvement in outcome. Proxy outcomes, such as demonstrating that the application of an early detection test increases the proportion of early-stage tumors in all newly diagnosed tumors (known as stage shift) or demonstrating that patients with screen-detected tumors have a longer survival time after diagnosis, are insufficient. An apparent survival benefit of earlier detection may not necessarily lead to prolongation of life because of lead-time bias and length-time bias. Lead-time bias can occur under two scenarios: A screen-detected tumor would have been detected clinically before metastasis had occurred; alternatively, an incurable metastasis has already occurred at the time the tumor is detected by screening. In both cases, there is no resulting improvement in long-term outcome. Length-time bias is the preferential detection of slower-growing tumors by screening (*15*). Therefore, randomized controlled trials are needed to establish improvement in health outcomes of different early detection modalities. Clinical trials are expensive and take many years to complete, and, given the number of early detection tests being developed, it will not be possible to carry out trials for all of them. Perhaps the most important need is for the research community to establish a strategy for rapidly triaging new tests that are least likely to be effective in order to focus efforts on those with the most potential. ■

Tumor growth dynamics in early detection

Tumor growth dynamics determine whether metastasis is present at the time of currently available screening tests. Mammographic screening can detect tumors that are 5 mm in diameter, and clinically detectable tumors are at least 2 cm in diameter. A typical breast tumor has a tumor volume doubling time (TVDT) of 150 days and will have been growing for 8 years before it is large enough to metastasize (>1 mm), but it will be another 3 years before it is big enough to be detected by mammography. [Based on (*6*–*8*)]



GRAPHIC: X. LIU/*SCIENCE*

REFERENCES AND NOTES

1. J. Broggio, S. John, *Cancer Survival in England: Adult, Stage at Diagnosis and Childhood—Patients Followed up to 2018* (UK Office for National Statistics, 2019).
2. A. B. Mariotto *et al.*, *J. Natl. Cancer Inst. Monogr.* **2014**, 145 (2014).
3. R. A. Weinberg, *Carcinogenesis* **29**, 1092 (2008).
4. M. B. Sporn, *Lancet* **347**, 1377 (1996).
5. M. Hakama, A. Auvinen, N. E. Day, A. B. Miller, *J. Med. Screen.* **14**, 174 (2007).
6. S. Friberg, S. Mattson, *J. Surg. Oncol.* **65**, 284 (1997).
7. S. Koscielny *et al.*, *Br. J. Cancer* **49**, 709 (1984).
8. V. Sopik, S. A. Narod, *Breast Cancer Res. Treat.* **170**, 647 (2018).
9. S. Koscielny, M. Tubiana, A. J. Valleron, *Br. J. Cancer* **52**, 515 (1985).
10. M. Poudineh, E. H. Sargent, K. Pantel, S. O. Kelley, *Nat. Biomed. Eng.* **2**, 72 (2018).
11. X. Cai, F. Janku, Q. Zhan, J. B. Fan, *Trends Genet.* **31**, 564 (2015).
12. S. Avanzini *et al.*, bioRxiv 2020.02.12.946228 (13 February 2020).
13. S. Koscielny, M. Tubiana, *Nat. Rev. Cancer* **10**, 156 (2010).
14. R. Walker *et al.*, *Appl. Immunohistochem. Mol. Morphol.* **27**, 270 (2019).
15. S. K. Plevritis, *Math. Biosci.* **171**, 155 (2001).

ACKNOWLEDGMENTS

P.D.P.P. receives salary support from the National Health Service (NHS) in the East of England through the Clinical Academic Reserve.

10.1126/science.aaz2078

Published by AAAS

RETROSPECTIVE

Katherine Johnson (1918–2020)

Groundbreaking U.S. space program mathematician

By **Shirley M. Malcom**

Katherine Johnson, a mathematician for NASA and its predecessor agency, passed away on 24 February at age 101. She and women like her worked unseen for decades to ensure America's success in the space race. The 2016 movie *Hidden Figures* finally brought her story to light. The recognition of Katherine's contributions to aeronautics and to America's ventures into space is well deserved, as she and her African American colleagues did vital work while facing Jim Crow barriers in nearly every aspect of their lives.

Katherine, the youngest child of Joshua and Joylette Coleman, was born on 26 August 1918, in White Sulphur Springs, West Virginia. The state had been part of the Union during the Civil War, but in every way that mattered it was part of the segregated South. Where the Colemans lived, education for Black children only extended through grade school, so Joshua rented a house more than 100 miles away to give his children the opportunity to attend the laboratory school at West Virginia Collegiate Institute (later West Virginia State College), a historically Black public land-grant institution established by the second Morrill Act. In 1933, at the age of 15, Katherine enrolled as a college freshman. She graduated summa cum laude in 1937 with a double major in mathematics and French.

Following the path often taken by Black, college-educated women of her generation, Katherine became a teacher. The possibility of using her education in mathematics in any other career was unimaginable, although her professor did encourage and prepare her to pursue graduate study. An opportunity for graduate work came along when she was among those selected to integrate all-White West Virginia University after a Supreme Court decision mandated equal access to graduate educational opportunities. However, after one summer at the university in 1940, Katherine chose not to continue. Recently married, she stepped away to assume the role of wife and mother.

In 1952, through family, Katherine learned of and seized an opportunity to apply her mathematical skills at the Langley Aeronautical Laboratory, a research center of the National Advisory Committee for Aeronautics (NACA, NASA's predecessor). During World War II and the ensuing Cold War, NACA needed the skills of female mathematicians ("human computers") to support the work of their engineers. With executive orders urging desegregation, the all-Black West Area computing group came onboard, joining the all-White East Area computing group in providing that mathematical power.

At that time, women in government experienced economic inequality—in title, salary, and limited opportunities for promotion. Meanwhile, Black Americans in the segregated South faced educational, social, and economic inequities. And yet, on the strength of her mathematical abilities, Katherine was considered an equal within the community of engineers and scientists with whom she worked. Margot Lee Shetterly, author of the book on which the *Hidden Figures* movie was based, referred to this paradox as a "triumph of meritocracy."



PHOTO: NASA/DONALDSON COLLECTION/GETTY IMAGES

The Soviet Union's successful launch of Sputnik in 1957 led to a blistering pace of work for the engineers, scientists, and mathematicians charged with bolstering American pride in space. Long hours and the agency's demand for results were layered atop increasing family responsibilities. Katherine's husband, James Goble, had died in 1956, leaving her carrying the added weight of single parenting.

In 1959, she married Jim Johnson and published her first research report under the name Katherine G. Johnson. That report and her subsequent work developing precise trajectory calculations for NASA's early human spaceflights were essential to establishing the United States as the leading spacefaring nation. Electronic computers were just being introduced into the space program, and their results were not always reliable. The human computers were there to backstop the machines. In the early 1960s, she worked on lunar orbits. Her contribution was crucial in helping to realize President Kennedy's goal of landing a man on the Moon.

I never had the privilege of meeting Katherine, except in the pages of Shetterly's book, which provides incredible insight into the gifted and confident yet understated mathematician whom astronaut John Glenn was prepared to trust with his life. I attended a panel at the 2017 Emerging Researchers National Conference featuring Shetterly; her father, Robert B. Lee III, a former Langley climate scientist; and "hidden figure" and aeronautical engineer Christine Darden. The panelists' discussions provided insight into NASA's early days and the contributions of pioneering minority and female mathematicians and engineers, pieces of the early history and public face of the agency that had been missing until recently. The 950 attendees at that session included students from 52 historically Black colleges and universities. Katherine's experience of being the first, the only, or among the few who looked like her in a given professional setting was strikingly familiar to us. We were all moved by the stories of triumph over adversity.

In 2015 Katherine was awarded the Presidential Medal of Freedom by President Obama. In 2016 she received a Silver Snoopy Award from astronaut Leland Melvin and a NASA Group Achievement Award. In November 2019, by way of bipartisan legislation, Johnson and other hidden figures of NASA were honored with Congressional Gold Medals.

The girl who loved to count became the woman whose aptitude and passion for mathematics helped propel the space ambitions of the United States. Katherine's story and those of other hidden figures have been embraced in popular culture and by those of us working to diversify science, technology, engineering, and mathematics. But there are other lessons to be learned: Her story demonstrates why we must work to provide excellent education and opportunities for all. It also elucidates the importance of policy interventions and laws in sustaining those opportunities. Katherine Johnson earned her place in the pantheon of America's space heroes; she and the other women who contributed to the country's path to the heavens are hidden no more. ■

10.1126/science.abc1546

STEMM Equity Achievement (SEA) Change, American Association for the Advancement of Science, Washington, DC, USA. Email: smalcom@aaas.org

Published by AAAS



A ballistic missile with a simulated warhead is launched at the Vandenberg Air Force Base in 2017.

PHOTO: IAN DUDLEY/UNITED STATES AIR FORCE

THREAT ASSESSMENT

A field guide to existential risk

A pandemic isn't the only peril for which we're unprepared

By **Stepan Jerabek**

On 16 July 1945, in a desert near Socorro, New Mexico, the U.S. Army conducted a test of the first nuclear weapon. The code name for the experiment, "Trinity," was coined by J. R. Oppenheimer and inspired by one of his favorite poems, John Donne's Holy Sonnet XIV, "Batter my heart, three-person'd God." Oppenheimer was also among the observers who witnessed the detonation. While watching the mushroom cloud after the explosion, a verse from the Hindu scripture the *Bhagavad Gita* crossed his mind: "Now I am become Death, the destroyer of worlds."

Earth was not destroyed in the summer of 1945, nor after. But we can only achieve long-term security if we put deliberate efforts into the reduction of existential risks, writes Toby Ord in *The Precipice*. He argues that with the Trinity test, society entered a new era—the Precipice—in which we are capable of endangering our own future.

Ord, a philosopher at the University of Oxford's Future of Humanity Institute (FHI), begins the book with an overview of civilization's journey from early settlements to modern society. Over time, we progressed through a number of major technological revolutions to achieve unprecedented power and welfare. According to Ord, this could be just the beginning of our story. He presents strong moral arguments for why it would be reasonable to make safeguarding our future a top priority. Currently, he notes, "humanity spends more on ice cream every year than on ensuring that the technologies we develop do not destroy us."

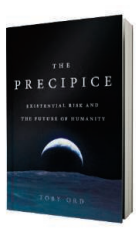
It is in society's best interest to prevent existential catastrophes by reducing threats that Ord broadly classifies into three categories: natural risks, anthropogenic risks, and future risks. His goal is not merely to aggregate research findings but to assign a quantitative estimate to individual threats with regard to their potential to cause an existential catastrophe.

Although the fossil record can provide us with useful hints for how to assess certain risks, we must rely, in some cases, on expert opinions. In such situations, especially when the stakes are very high, Ord advocates using a Bayesian statistics approach. He first sets the a priori probability of the threat (on the basis of prior knowledge or an estimate about the likelihood of an event) and then updates it in the light of available scientific evidence. This method allows some space for subjectivity, but it also enables comparison across different risks.

According to Ord's analysis, natural perils such as asteroids and supervolcanic eruptions represent only a minor existential risk over the next century, especially when compared with the profound anthropogenic risks that we already face. Despite an 80% reduction in the number of nuclear warheads since the mid-1980s, for example, he argues that it is crucial that we continue the disarmament process and increase maintenance and security standards for remaining facilities.

Some of our biggest perils, however—namely, pandemics and unaligned artificial intelligence (AI)—lie ahead. The intentional development of a novel virus with the "right balance" of virulence and contagion would be challenging, but Ord urges serious consideration of the possibility that some entity might weaponize known pathogens or that such pathogens could accidentally be unleashed from the laboratory. And it would be even more difficult to mitigate the risk posed by an extremely powerful AI that is not aligned with human values. [This particular threat is discussed in more detail in *Superintelligence*, written by Ord's FHI colleague Nick Bostrom (*1*).]

Existential risks are often positively correlated; if we succumb to one threat, we are more vulnerable to another. Nevertheless, Ord remains an optimist who believes that we can fulfill our long-term potential. He summarizes specific policy and research recommendations in an appendix, advocating, for example, to restart the Intermediate-Range Nuclear Forces Treaty and to increase the annual budget of the Biological Weapons Convention ($1.4 million in 2019, less than the average annual budget of a single McDonald's restaurant). Given the significance of this material, the book would have benefited from a full chapter with a deeper analysis of current policy and future strategies to prevent a cataclysm.



The Precipice: Existential Risk and the Future of Humanity
Toby Ord
Hachette, 2020.
480 pp.

I urge caution against setting our action threshold to the level of a global catastrophe, which could distort the way we prioritize our next decisions. But Ord's map of the existential risk landscape is an engaging read for anyone who wants to learn more about this important and interdisciplinary research. ■

The reviewer is at the Department of Genetics, Harvard University, Boston, MA 02115, USA.
Email: stepan_jerabek@hms.harvard.edu

REFERENCES AND NOTES

1. N. Bostrom, *Superintelligence: Paths, Dangers, Strategies* (Oxford Univ. Press, 2014).

10.1126/science.abc1235

Published by AAAS

ORNITHOLOGY

The secret lives of birds

A science writer weaves a vivid portrait of avian culture, communication, and care

By **Barbara C. Klump**

From tales of dazzling plumage to anecdotes about almost unfathomable mimicry, Jennifer Ackerman's *The Bird Way: A New Look at How Birds Talk, Work, Play, Parent, and Think* is a walk through the mysteries, wonders, and peculiarities of the avian world. Thematically grouped into five parts (talk, work, play, love, and parent), the book discusses important aspects of every bird's life.

"There is the mammal way and there is the bird way," writes Ackerman in the book's opening line, quoting a scientist's pithy distinction from which the title is drawn. But there is no such thing as a singular "bird way." Indeed, for every aspect of bird life—be it foraging, the establishment and maintenance of social systems, or parental care—much about the "bird way" varies across species.

Stories of remarkable animal behaviors are often stories about attributes and abilities we once believed made humans special. Think of tool use, culture, and the theory of mind, for example. In *The Bird Way*, Ackerman explores birds that are capable of sophisticated behaviors, from crows that manufacture their own hook tools; to raptors that some scientists believe intentionally start fires to flush out prey; to hummingbirds that remember not only where but also when they visited nectar-filled flowers, returning only after the flowers have had time to replenish their stores. Given some of our less-inspired human endeavors—introducing kudzu to control erosion, for example—"it would seem," Ackerman pointily observes, "that our species can be fairly inept at using the past to plan for the future."

Much of our knowledge about the avian world is rooted in research focused on birds in the temperate zones of Europe and North America. But as more work is conducted in other parts of the world, behaviors that were once thought to be typical—for example, that only males sing complex songs at dawn and dusk and defend their territories exclusively during the short breeding season—might not be the norm after all. "Welcome to Australia," Ackerman writes at one point, "land of avian outlaws." Here, we find bell miners that call all day long and year-round; male and female whipbirds that duet so seamlessly they sound like a single bird calling; and birds that defend their territory in all seasons.

The book follows researchers around the world, taking the reader on adventures and relating mishaps that will be only too familiar to field biologists. Some projects that Ackerman describes are entirely observational, whereas others use new technological approaches to reveal details that hide in plain sight, such as the body flips performed by male black manakins that are simply too fast for the human eye to perceive.



A New Caledonian crow uses a twig as a tool.

Finding food is arguably one of the main tasks in a bird's everyday life. What birds eat and the way they acquire food are as variable as we can imagine. In Costa Rica, for example, antbirds take advantage of raiding ants, which flush out hidden arthropods during their voracious feeding frenzies, leaving a veritable buffet for the antbirds in their wake. But the various antbird species are not just scavengers. Among them are specialists—the ocellated antbird, for example—that track the locations of multiple ant colonies, noting their state (raiding or stationary), and seem to be able to share this information with others.

Parental care is another area where birds employ just about every strategy imaginable. The Australian brush turkey, for example, meticulously conducts daily temperature checks inside its huge nest, called a mound, and will adjust surface materials to maintain optimum temperature for the development of its eggs yet offers no care once its offspring have hatched. Meanwhile in Panama, unrelated pairs of greater ani will build a communal nest and divide the labor of incubating and raising their young.

At times, an evolutionary arms race plays out; consider the cuckoo, which lays its eggs in other species' nests. It has long been known that as the cuckoos' eggs evolve to more closely mimic those laid by their hosts, the hosts are adapting too, improving their ability to discriminate between eggs. In Australia, some hosts have a different strategy: Although they are unable to discriminate between eggs, they have learned to tell their own young from a cuckoo chick (which, in turn, can look like, and learn to mimic the begging calls of, the host species' young).

The avian world is full of wonders, and Ackerman's excitement and love for it are evident in her writing. Her superb storytelling paints a rich picture that engages the reader's imagination, making sometimes-hard-to-grasp research accessible. ■

The Bird Way: A New Look at How Birds Talk, Work, Play, Parent, and Think
Jennifer Ackerman
Penguin Press, 2020. 368 pp.



The reviewer is at the Cognitive and Cultural Ecology Group, Max Planck Institute of Animal Behavior, 78315 Radolfzell, Germany. Email: bklump@ab.mpg.de

10.1126/science.abb6671

PHOTO: ANDY COMINS

Published by AAAS



LETTERS

Edited by **Jennifer Sills**

Research opportunities in pandemic lockdown

To minimize the spread of coronavirus disease 2019 (COVID-19), countries such as India have mandated lockdowns of all but essential services. Many research projects have been interrupted because scientists cannot access their equipment or workspace. However, with almost all industrial businesses shuttered, scientists have an opportunity to collect vital data.

Despite India's stringent laws preventing untreated effluent discharge in rivers and streams (*1*), a substantial fraction of industrial waste ends up in nearby water bodies or groundwater (*2*). Therefore, while industries are operating as usual, it is impossible to collect baseline data. Environmental quality data dating from before industrialization are rarely available. Sediments deposited before the industrialization, often used as baseline data, are marred by physical and chemical changes that have taken place over time (*3*). With the complete shutdown of industrial operations, the effluent discharge is negligible. The water quality of nearby streams, if tested systematically during the lockdown period, could serve as a baseline against which scientists can subsequently track the point source of water pollution.

The lockdown is also a unique opportunity to assess the effect of anthropogenic activities on air quality, atmospheric greenhouse gas concentration, and its influence on global temperature. Several countrywide containment measures (*4*) have substantially reduced greenhouse gas emissions and thus improved the air quality (*5*). The power generation in India has decreased by as much as 26.5% during the countrywide lockdown, including a 33% decrease of coal-based power generation (*6*). The total diesel consumption by Indian railways [usually close to 24 x 10^8 liters/year, with passenger transport accounting for more than half (*7*)] has also dropped, as all passenger trains have been halted. With limited train service, the nitrogen oxide and carbon dioxide emissions they normally produce (*7*) have surely decreased. In addition to these changes, domestic and international flights and vehicular traffic have drastically decreased (*8*). India has likely substantially reduced anthropogenic greenhouse gas emissions as well as particulate matter concentration in the atmosphere. The effect of this short-term but substantially reduced anthropogenic emissions on global temperature, if quantified, could provide a rare data point for global climate simulation models. Researchers could also use this time to explore the effect of these disruptions on the onset, strength, and spatial coverage of precipitation during the forthcoming summer monsoon season.

Although large-scale manual data collection by multiple researchers is neither advised nor feasible, scientists should coordinate efforts in key target areas to take advantage of this opportunity. The countrywide lockdowns in India and elsewhere—and the likely delay in the resumption of full industrial operations—provide a rare opportunity to collect a wealth of data that would otherwise be impossible to obtain.

Rajeev Saraswat[1]* and Divya Atri Saraswat[2]
[1]Micropaleontology Laboratory, Geological

The Yamuna River has seen a visible reduction in pollution since India's COVID-19 lockdown began.

PHOTO: AMAL KSHINDUSTAN TIMES/GETTY IMAGES

Published by AAAS

Oceanography Division, National Institute of Oceanography, Goa, India. [2]Department of Paediatrics, Goa Medical College, Goa, India. *Corresponding author. Email: rsaraswat@nio.org

REFERENCES AND NOTES

1. Ministry of Environment, Forest, and Climate Change, Government of India, "Environment (Protection) Amendment Rules" (2017); http://moef.gov.in/wp-content/uploads/2017/11/Petcoke.pdf.
2. ENVIS Centre on Hygiene, Sanitation, Sewage Treatment Systems, and Technology, "National status of waste water generation and treatment" (2019); www.sulabhenvis.nic.in/Database/STST_wastewater_2090.aspx.
3. P. J. Hanson, D. W. Evans, D. R. Colby, *Mar. Environ. Res.* **36**, 237 (1993).
4. "Annexure to Ministry of Home Affairs Order No. 40-3/2020-D" (2020); www.mha.gov.in/sites/default/files/Guidelines_0.pdf.
5. United Space in Europe, "Air pollution drops in India following lockdown" (2020); www.esa.int/Applications/Observing_the_Earth/Copernicus/Sentinel-5P/Air_pollution_drops_in_India_following_lockdown.
6. Power System Operation Corporation Limited, Government of India, National Load Despatch Centre, "Daily Reports" (2020); https://posoco.in/reports/daily-reports/daily-reports-2019-20/.
7. S. K. Annadanam, S. H. Kota, J. Clean. Prod. **213**, 610 (2019).
8. Ministry of Home Affairs, Government of India, Order No. 40-3/2020-DM-I(A) (2020).

Published online 30 April 2020
10.1126/science.abc3372

The inherent challenges of classifying senescence

In the Policy Forum "To help aging populations, classify organismal senescence" (1 November 2019, p. 576), S. R. G. Calimport *et al.* call for classification of senescence as a disease and propose a classification methodology. Unfortunately, their call to action comes a year after the publication of the 11th International Classification of Diseases (ICD) (*1*). The next revision of the ICD is expected in 2028 or later, and much progress needs to be made in basic research and clinical trials before including senescence would be possible.

Calimport *et al.*'s assertion that aging-related diseases can be classified using current information overestimates our understanding of senescence. Multiple studies suggest that aging starts in utero (*2*) and staging of most senescence processes will require massive longitudinal studies in humans and animals. Furthermore, the first clinical trials targeting aging, such as Targeting Aging with Metformin (TAME), are under discussion, and no aging biomarker consensus or hierarchical structuring has yet emerged (*3*, *4*).

Staging senescence at the tissue-specific level for the purposes of preventative intervention may be a model for private or national health care plans and systems; however, these plans do not require these processes to be classified in the ICD with the individual codes. In addition to providing a general disease framework, ICD codes are used internationally to standardize burden of disease reports and assess cause of death. The concept of staging senescence does not fit the current ICD framework. The addition would likely require a new international initiative to develop a comprehensive set of biomarkers and interventions for senescence and longevity, as well as a set of recommendations for reducing the burden of senescence and aging-associated diseases.

Pharmaceutical companies are already working on the interventions targeting the common biological pathways implicated in aging to deliver therapeutics against age-related diseases within the traditional health care paradigm. To accelerate drug development efforts focused on aging as a disease in the pharmaceutical industry, we need to demonstrate that basic research into whether aging is a biological process disease can yield valuable targets or interventions that demonstrate efficacy in treating or preventing age-related diseases.

Alex Zhavoronkov
Insilico Medicine, Hong Kong Science and Technology Park, Hong Kong; Buck Institute for Research on Aging, Novato, CA 84945, USA; The Biogerontology Research Foundation, London, UK. Email: alex@insilicomedicine.com

REFERENCES AND NOTES

1. A. Zhavoronkov, B. Bhullar, *Front. Genet.* **6**, 326 (2015).
2. B. J. Allison *et al.*, *FASEB* **30**, 5 (2016).
3. J. N. Justice *et al.*, *Cardiovasc. Endocrinol. Metab.* **7**, 80 (2018).
4. American Federation for Aging Research, "TAME trial" (2020); www.afar.org/research/TAME/.

COMPETING INTERESTS

A.Z. is the founder and CEO of Insilico Medicine, a Hong Kong-based artificial intelligence company focused on drug discovery and aging research. He is also an adviser to Haut.AI Ltd., an Estonia-based artificial intelligence company focused on artificial intelligence for skin care and aging research. He is a director and co-founder of Deep Longevity, Inc., an artificial intelligence company focused on aging biomarkers. He is an adviser to the All Party Parliamentary Group (APPG) for Longevity in the UK. He is the seed investor in Retrotope, Inc., a California-based drug discovery company focused on age-related diseases. He may be associated with other startup companies in aging research as an adviser or through investments in Longenesis.

10.1126/science.aba0833

Response

Zhavoronkov questions the timing of our Policy Forum's publication in relation to the release and adoption of the International Classification of Diseases (ICD) 11, but the World Health Organization accepts ICD submissions

2020
SCIENTIFIC CONFERENCES
Presenting the most significant research on cancer etiology, prevention, diagnosis, and treatment

Tumor Heterogeneity: From Single Cells to Clinical Impact
Conference Cochairs: Nicholas E. Navin, Kornelia Polyak, Alexander K. Shalek, and Charles Swanton
September 10-13, 2020
Philadelphia, PA

CRI-ENCI-AACR Sixth International Cancer Immunotherapy Conference: Translating Science into Survival
Conference Cochairs: Özlem Türeci, E. John Wherry, and Jedd D. Wolchok
September 14-17, 2020 | New York, NY

13th Biennial Ovarian Cancer Research Symposium
Conference Cochairs: Douglas A. Levine, Ursula A. Matulonis, Barbara Norquist, and Kunle Odunsi
September 26-28, 2020 | Seattle, WA

Pancreatic Cancer
Conference Cochairs: Dafna Bar-Sagi, Elizabeth M. Jaffee, Ben Z. Stanger, and Brian M. Wolpin
September 29-October 2, 2020
Philadelphia, PA

Myeloma and Plasma Cell Dyscrasias
Conference Cochairs: Kenneth C. Anderson and Irene Ghobrial
October 2-5, 2020 | Boston, MA

13th AACR Conference on The Science of Cancer Health Disparities in Racial/Ethnic Minorities and the Medically Underserved
Conference Chair: John D. Carpten
October 2-5, 2020 | Miami, FL

Advances in Breast Cancer Research
Conference Cochairs: Jason Carroll, Jenny C. Chang, and Jane E. Visvader
October 9-12, 2020 | San Diego, CA

Epigenetics and Metabolism
Conference Cochairs: Chi Van Dang, Kimberly Stegmaier, Craig B. Thompson, and Matthew G. Vander Heiden
October 15-18, 2020 | Baltimore, MD

AACR American Association for Cancer Research
Learn more and register at
AACR.org/Calendar

Published by AAAS

and updates on a rolling basis across the review and maintenance phases, and it is regularly revised, versioned, and updated (*1*). Zhavoronkov also posits that senescence cannot be added to ICD without substantial further research. We challenge this view: Given the World Health Organization's decision-making history, classification and staging consensus, development, and submissions to ICD are needed now.

Organismal senescence at the organ level has already been classified in the ICD as "intrinsic aging of the skin" and "photoaging of the skin," with an accompanying staging scale for aging skin (*2*). It is therefore entirely feasible to classify organismal senescence across the organs and tissues of the body, along with all other aging-related diseases and disorders. Our Policy Forum cites the substantial literature that already exists for such an effort [e.g., (*3*, *4*)].

We agree with Zhavoronkov that there is still much to learn about aging-related diseases. However, many diseases within the ICD were not comprehensively understood before classification. Our understanding of skin aging increased after classification (*5*) as a result of improved recognition and further study. Alzheimer's disease was recognized as a leading cause of death only after its inclusion in ICD-9 led to improved epidemiology and statistics (*6*). If diseases and disorders are identifiable, distinct, and associated with a substantial body of knowledge, they should be classified.

In contrast to Zhavoronkov, we see a place for staging senescence in the ICD framework. It is common for diseases to be classified and staged before the approval of clinical biomarkers. An initial staging of organismal senescence could be achieved for all organs based on macroscopic and histologic measures, similar to the Glogau scale for skin (*5*). Longitudinal studies in animals and humans will be required, as Zhavoronkov states, to further develop the staging of organismal senescence across organs for clinical endpoints and precision medicines. Organismal senescence may be a continuous process that begins early in life, but the ICD classification should be able to distinguish between early age-related degenerative change and any initial processes of organismal development.

Zhavoronkov is correct that severity staging systems do not require ICD approval. However, "severity scale value" may be appended in the ICD for statistical purposes. Staging systems are usually developed and maintained by international disease-specific medical societies. We would welcome the development of international initiatives to develop a comprehensive set of staging systems, biomarkers, and interventions for senescence and aging-related diseases.

Stuart R. G. Calimport*, Barry L. Bentley, Claire E. Stewart, Graham Pawelec, Angelo Scuteri, Manlio Vinciguerra, Cathy Slack, Danica Chen, Lorna W. Harries, Gary Marchant, G. Alexander Fleming, Michael Conboy, Adam Antebi, Gary W. Small, Jesus Gil, Edward G. Lakatta, Arlan Richardson, Clifford Rosen, Karoly Nikolich, Tony Wyss-Coray, Lawrence Steinman, Thomas Montine, João Pedro de Magalhães, Judith Campisi, George Church
*Corresponding author. Email: stuart.calimport07@alumni.imperial.ac.uk
Author affiliations are available at www.sciencemag.org/content/366/6465/576/suppl/DC1.

REFERENCES AND NOTES

1. WHO, Geneva, "ICD revision process: Beta phase and finalization" (WHO, 2013), www.who.int/classifications/icd/revision/icdrevisionprocess.pdf.
2. R. G. Glogau, *Semin. Cutan. Med. Surg.* **15**, 134 (1996).
3. C. López-Otín *et al.*, *Cell* **153**, 1194 (2013).
4. D. Muñoz-Espín, M. Serrano, *Nat. Rev. Mol. Cell Biol.* **15**, 482 (2014).
5. P. S. Peres *et al.*, *J. Photochem. Photobiol. B.* **10**, 93 (2011).
6. A. M. Miniño, S. L. Murphy, J. Xu, K. D. Kochanek, *Natl. Vital Stat. Rep.* **59**, 1 (2011).

COMPETING INTERESTS

In addition to the competing interests listed at www.sciencemag.org/content/366/6465/576/suppl/DC1, C.E.S. is chair of the British Society for Research on Ageing, and L.W.H. has a priority GB patent filed (PCT/GB2019/052125).

10.1126/science.abb4073

TECHNICAL COMMENT ABSTRACTS

Comment on "A noninteracting low-mass black hole–giant star binary system"

Ed P. J. van den Heuvel and Thomas M. Tauris

Thompson *et al.* (Reports, 1 November 2019, p. 637) interpreted the unseen companion of the red giant star 2MASS J05215658+4359220 as most likely a black hole. We argue that if the red giant's mass is ~1 solar mass, its companion can be a close binary consisting of two main-sequence stars. This would explain why no x-ray emission is detected from the system.

Full text: dx.doi.org/10.1126/science.aba3282

Response to Comment on "A noninteracting low-mass black hole–giant star binary system"

Todd A. Thompson, Christopher S. Kochanek, Krzysztof Z. Stanek, Carles Badenes, Tharindu Jayasinghe, Jamie Tayar, Jennifer A. Johnson, Thomas W.-S. Holoien, Katie Auchettl, Kevin Covey

Van den Heuvel and Tauris argue that if the red giant star in the system 2MASS J05215658+4359220 has a mass of 1 solar mass ($M_\odot$), then its unseen companion could be a binary composed of two 0.9 $M_\odot$ stars, making a triple system. We contend that the existing data are most consistent with a giant of mass $3.2^{+1.0}_{-1.0}$ $M_\odot$, implying a black hole companion of $3.3^{+2.8}_{-0.7}$ $M_\odot$.

Full text: dx.doi.org/10.1126/science.aba4356

Where Science Gets Social.

AAAS.ORG/COMMUNITY

AAAS' Member Community is a one-stop destination for scientists and STEM enthusiasts alike. It's "Where Science Gets Social": a community where facts matter, ideas are big and there's always a reason to come hang out, share, discuss and explore.

Member COMMUNITY AAAS

Published by AAAS

Cite as: E. P. J. van den Heuvel, T. M. Tauris, *Science* 10.1126/science.aba3282 (2020).

Comment on "A noninteracting low-mass black hole–giant star binary system"

Ed P. J. van den Heuvel[1]* and Thomas M. Tauris[2,3]

[1]Anton Pannekoek Institute for Astronomy, University of Amsterdam, 1098 XH Amsterdam, Netherlands. [2]Aarhus Institute of Advanced Studies, Aarhus University, 8000 Aarhus C, Denmark. [3]Department of Physics and Astronomy, Aarhus University, 8000 Aarhus C, Denmark.

*Corresponding author. Email: e.p.j.vandenheuvel@uva.nl

Thompson *et al.* (Reports, 1 November 2019, p. 637) interpreted the unseen companion of the red giant star 2MASS J05215658+4359220 as most likely a black hole. We argue that if the red giant's mass is ~1 solar mass, its companion can be a close binary consisting of two main-sequence stars. This would explain why no x-ray emission is detected from the system.

Thompson *et al.* (*1*) argue that the invisible companion in a 83-day orbit around the red giant star 2MASS J05215658+4359220 is most likely a black hole with a mass of $3.3^{+2.8}_{-0.7}$ solar masses ($M_\odot$). If this companion were a normal nondegenerate star, its light would have been detectable in the spectral energy distribution (SED) of the red giant, but it was not.

This approach assumes a normal single unseen companion star. However, in wide binaries, the companion can itself be a closer binary composed of two normal stars with an orbital period on the order of a few days. Such hierarchical triple systems are quite common (*2*). The luminosity L of a main-sequence star depends strongly on its mass M ($L \sim M^{3.5}$), so the luminosity of a close binary consisting of two stars of equal mass is smaller than that of a single star with their combined mass by a factor of ~6. The light of such a binary companion might be undetectable in the SED of the red giant.

Thompson *et al.* argue that the red giant most likely has a mass of 3.2 $M_\odot$, but they show that its high carbon-to-nitrogen ratio [C/N] is consistent with a lower mass of 1 $M_\odot$ (*1*). Spectroscopic determination of a red giant's mass from model atmospheres can be uncertain by a factor of 3 (*3*), which would allow for a red giant mass of ~1 $M_\odot$.

For the higher red giant mass, the companion is $3.3^{+2.8}_{-0.7}$ $M_\odot$. If it were a close binary, the binary components would be ~1.65 $M_\odot$ each, which would have been detectable in the SED of the red giant (*1*). In this case, a black hole companion is the only remaining possibility.

In the alternative case of a 1 $M_\odot$ red giant, the mass of the unseen companion is ≥1.8 $M_\odot$ (*1*), so the companion could be a very close binary of two main-sequence stars of ~0.9 $M_\odot$ each, which would be of spectral type K0-4V with 0.44 solar luminosities ($L_\odot$) (*4*). Their combined luminosity would be less than 0.5% of the >200 $L_\odot$ luminosity of the red giant, which is undetectable.

Such a triple star system is expected to be dynamically stable if the ratio between the semimajor axis of the outer star and that of the inner binary is ≳3.0 (*5*). Using Kepler's third law, the upper limit on the orbital period of the inner binary is ~20 days. This would be consistent with a wide range of possible binaries, including very close systems of K-type main-sequence stars. These are common, and often they have a distant third companion (*6*).

A black hole that accretes matter from the red giant's wind would form an accretion disc, which might be detectable in x-ray emission. The physics of accretion of neutron stars and black holes is very similar. In both cases, the accreting object becomes a strong x-ray source. There are 13 known red-giant x-ray binaries, known as symbiotic x-ray binaries (*7*, *8*). Six of them are regularly pulsating x-ray sources (*8*), showing that neutron stars accreting from the winds of red giants produce sources with x-ray luminosities $L_x = 10^{32}$ to 10^{36} erg s^{-1}. We expect similar values for accreting black holes. As Thompson *et al.* show, using Bondi-Hoyle accretion (*9*), for typical red giant wind velocities, the black hole in the 3.2 $M_\odot$ giant case will capture 1% of the total red giant mass-loss rate.

The wind mass-loss rate of red giants is given by

$$\dot{M}_w = 4\times10^{-13}\eta_R LRM^{-1}\, M_\odot \text{ year}^{-1} \quad (1)$$

(*10*), where η_R is the efficiency parameter for wind mass loss and L, R, and M are the luminosity, radius, and mass of the

giant in solar units. Observations of red giant wind mass loss (*11*) show that $\eta_R = 0.477 \pm 0.070$. Applying the nominal values for 2MASS J05215658+4359220, $L = 331\ L_\odot$, $R = 30\ R_\odot$ (*1*), and, assuming the x-ray energy release $\Delta U = 0.1\ mc^2$ for a mass m accreted onto a black hole, we obtain $L_x = 2.5 \times 10^{34}$ erg s^{-1} for a $3.2\ M_\odot$ giant with a $3.3\ M_\odot$ black hole. Thompson *et al.* find a lower expected value of $L_x = 1.4 \times 10^{33}$ erg s^{-1}. Such x-ray luminosities would be easily detectable, but no x-ray emission from the system is observed.

We consider a $1\ M_\odot$ red giant with a close-binary companion to be more consistent with the observational constraints on this system, as it does not produce detectable light, nor x-ray emission, and the high [C/N] abundance ratio is normal for a $1\ M_\odot$ red giant (*1*). A $3.2\ M_\odot$ red giant with a companion black hole would make this system unusual on three independent accounts: (i) The [C/N] ratio of the giant would be unusually high for giants of this mass; (ii) it has a black hole of unusual mass; and (iii) an explanation must be found for the lack of x-ray emission.

We conclude that the unseen companion of 2MASS J05215658 might not be a black hole.

REFERENCES

1. T. A. Thompson, C. S. Kochanek, K. Z. Stanek, C. Badenes, R. S. Post, T. Jayasinghe, D. W. Latham, A. Bieryla, G. A. Esquerdo, P. Berlind, M. L. Calkins, J. Tayar, L. Lindegren, J. A. Johnson, T. W.-S. Holoien, K. Auchettl, K. Covey, A noninteracting low-mass black hole–giant star binary system. *Science* 366, 637–640 (2019). doi:10.1126/science.aau4005 Medline
2. S. A. Rappaport, K. Deck, A. Levine, T. Borkovits, J. Carter, I. El Mellah, R. Sanchis-Ojeda, B. Kalomeni, Triple-star candidates among the *Kepler* binaries. *Astrophys. J.* **768**, 33–51 (2013). doi:10.1088/0004-637X/768/1/33
3. J. R. Auman, Model Atmospheres of Late-Type Stars. *Astrophys. J.* **157**, 799–826 (1969). doi:10.1086/150114
4. G. Torres, J. Andersen, A. Giménez, Accurate masses and radii of normal stars: Modern results and applications. *Astron. Astrophys. Rev.* **18**, 67–126 (2010). doi:10.1007/s00159-009-0025-1
5. S. Mikkola, in *Multiple Stars Across the H-R Diagram*, S. Hubrig, M. Petr-Gotzens, A. Tokovinin, Eds. (Springer, 2008), pp. 11–20.
6. A. Tokovinin, Comparative statistics and origin of triple and quadruple stars. *Mon. Not. R. Astron. Soc.* **389**, 925–938 (2008). doi:10.1111/j.1365-2966.2008.13613.x
7. R. H. D. Corbet, J. L. Sokoloski, K. Mukai, C. B. Markwardt, J. Tueller, A Comparison of the Variability of the Symbiotic X-Ray Binaries GX 1+4, 4U 1954+31, and 4U 1700+24 from *Swift* BAT and *RXTE* ASM Observations. *Astrophys. J.* **675**, 1424–1435 (2008). doi:10.1086/526337
8. L. R. Yungelson, A. G. Kuranov, K. A. Postnov, Wind-accreting symbiotic X-ray binaries. *Mon. Not. R. Astron. Soc.* **485**, 851–860 (2019). doi:10.1093/mnras/stz467
9. K. Davidson, J. P. Ostriker, Neutron-Star Accretion in a Stellar Wind: Model for a Pulsed X-Ray Source. *Astrophys. J.* **179**, 585–598 (1973). doi:10.1086/151897
10. D. Reimers, Circumstellar absorption lines and mass loss from red giants. *Mem. Soc. R. Sci. Liege* **8**, 369–382 (1975).
11. I. McDonald, A. A. Zijlstra, Mass-loss on the red giant branch: The value and metallicity dependence of Reimers' η in globular clusters. *Mon. Not. R. Astron. Soc.* **448**, 502–521 (2015). doi:10.1093/mnras/stv007

ACKNOWLEDGMENTS

We thank A. M. van den Heuvel for drawing our attention to the paper by Thompson *et al.*, and T. Thompson for kind and helpful explanations and efficient exchange of ideas on 2MASS J05215658+4359220. **Funding:** T.M.T. acknowledges an AIAS-COFUND Senior Fellowship funded by the European Union's Horizon 2020 Research and Innovation Programme (grant no. 754513) and the Aarhus University Research Foundation. **Author contributions:** E.P.J.v.d.H. and T.M.T. interpreted the results, analyzed the system, and wrote the manuscript together. **Competing interests:** We declare no competing interests. **Data and materials availability:** There are no new data in this comment.

23 November 2019; accepted 12 March 2020
Published online 8 May 2020
10.1126/science.aba3282

Cite as: T. A. Thompson *et al.*, *Science* 10.1126/science.aba4356 (2020).

Response to Comment on "A noninteracting low-mass black hole–giant star binary system"

Todd A. Thompson[1,2]*, Christopher S. Kochanek[1,2], Krzysztof Z. Stanek[1,2], Carles Badenes[3,4], Tharindu Jayasinghe[1,2], Jamie Tayar[5], Jennifer A. Johnson[1,2], Thomas W.-S. Holoien[6], Katie Auchettl[2,7,8]†, Kevin Covey[9]

[1]Department of Astronomy, The Ohio State University, Columbus, OH 43210, USA. [2]Center for Cosmology and AstroParticle Physics, The Ohio State University, Columbus, OH 43210, USA. [3]Department of Physics and Astronomy and Pittsburgh Particle Physics, Astrophysics and Cosmology Center (PITT PACC), University of Pittsburgh, Pittsburgh, PA 15260, USA. [4]Institut de Ciències del Cosmos, Universitat de Barcelona, E08028 Barcelona, Spain. [5]Institute for Astronomy, University of Hawai'i, Honolulu, HI 96822, USA. [6]Observatories of the Carnegie Institution for Science, Pasadena, CA 91101, USA. [7]Department of Physics, The Ohio State University, Columbus, OH 43210, USA. [8]DARK, Niels Bohr Institute, University of Copenhagen, 2100 Copenhagen, Denmark. [9]Department of Physics and Astronomy, Western Washington University, Bellingham, WA 98225, USA.

*Corresponding author. Email: thompson.1847@osu.edu

†Present address: School of Physics, University of Melbourne, Parkville, VIC 3010, Australia.

Van den Heuvel and Tauris argue that if the red giant star in the system 2MASS J05215658+4359220 has a mass of 1 solar mass ($M_\odot$), then its unseen companion could be a binary composed of two 0.9 $M_\odot$ stars, making a triple system. We contend that the existing data are most consistent with a giant of mass $3.2^{+1.0}_{-1.0}$ $M_\odot$, implying a black hole companion of $3.3^{+2.8}_{-0.7}$ $M_\odot$.

Van den Heuvel and Tauris (*1*) posit that the red giant star in the system 2MASS J05215658+4359220 (*2*) could have a mass of $M_{\rm giant} \approx 1\ M_\odot$, and that the unobserved companion could be a normal stellar binary system composed of two 0.9 $M_\odot$ stars. This hypothesis is inconsistent with the measured luminosity L and effective temperature $T_{\rm eff}$. The latter was established by three independent and consistent measurements: (i) the optical spectra, (ii) the near-infrared spectra, and (iii) the fit to the giant's spectral energy distribution (SED). The luminosity was determined from two independent methods: (i) the observed SED combined with the measured distance, and (ii) the stellar radius (R) as inferred from the giant's projected rotational velocity ($v \sin i$) combined with $T_{\rm eff}$. Both methods yield consistent L for $\sin i \approx 1$. Given these data and their uncertainties, and acknowledging the inherent systematic uncertainties in comparing with evolutionary models, we disfavored $M_{\rm giant} \approx 1\ M_\odot$ and obtained a best-fitting value of $M_{\rm giant} \approx 3.2^{+1.0}_{-1.0}\ M_\odot$ (2σ uncertainties) (*2*).

Van den Heuvel and Tauris assert that "Spectroscopic determination of a red giant's mass from model atmospheres can be uncertain by a factor of 3." However, we do not determine the mass from the logarithm of the stellar gravitational acceleration ($\log g$) alone, using $10^{\log g} = GM_{\rm giant}/R^2$, but instead from fitting L, $T_{\rm eff}$, and $\log g$ to evolutionary models. Even ignoring the constraint on $\log g$, the combination of L and $T_{\rm eff}$ is inconsistent with $M_{\rm giant} \approx 1\ M_\odot$. The mass obtained from $M_{\rm giant} = R^2 10^{\log g}/G$ is consistent with our best-fitting $M_{\rm giant}$, but it is not the origin of our final reported mass.

Van den Heuvel and Tauris argue that because x-ray emission is seen in symbiotic x-ray binary systems, it should be seen in 2MASS J05215658+4359220 if the unseen companion is a black hole. We do not find this argument convincing. First, the expected x-ray emission depends on the mass-loss rate of the giant, which is uncertain. In particular, some studies have found values of the mass-loss rate normalization lower than those used by van den Heuvel and Tauris (*3*, *4*). Second, the expected accretion rate is strongly dependent on the assumed giant wind velocity, which is not well constrained for this system. Third, the expected x-ray emission depends on the radiative efficiency of the accretion and the nature of the accretor. We estimated the accretion rate and found that the system may be in the radiatively inefficient regime (*2*), implying low x-ray luminosity. In addition, the dichotomy between the x-ray luminosities of neutron star– and black hole–hosting galactic x-ray binaries in quiescence may result from the presence of an event horizon for black holes, whereas neutron stars have surfaces (*5*–*7*). The lack of x-ray emission observed in 2MASS J05215658+4359220 may then be used to argue for a black hole companion instead of a neutron star. The x-ray emission in the symbiotic x-ray binary systems discussed by van

den Heuvel and Tauris is often explained using a settling accretion flow model relevant to neutron stars and not black holes [(*8*), section 2].

Van den Heuvel and Tauris state that "the [C/N] ratio of the giant would be unusually high for giants of this mass" and that "the high [C/N] abundance ratio is normal for a 1 $M_\odot$ red giant." Although the measured abundance ratio is somewhat unusual for a ~3 $M_\odot$ giant in our comparison sample, whether it is unusual enough to outweigh the well-measured values of L and $T_{\rm eff}$ is debatable. Above 3 $M_\odot$, we found that 1 out of 18 stars (about 6%) have high [C/N] (*2*). Although the observation of [C/N] ≈ 0.0 for 2MASS J05215658+4359220 might be used to argue that $M_{\rm giant}$ ≈ 1 $M_\odot$ in the absence of any other information, the additional information provided by L and $T_{\rm eff}$ indicates a substantially more massive star when compared to evolutionary models with a variety of metallicities (*2*). Given the star-spotted, rapidly rotating nature of the giant, we cannot exclude systematic uncertainties in the determination of both the [C/N] abundance ratio and the metallicity. The latter affects the fitting of the giant to evolutionary models (*2*). Systematic uncertainties of ±0.1 to 0.3 dex for C, ±0.2 dex for N, and ±0.1 dex for Fe have been found by comparing APOGEE abundances to other determinations (*9*).

The proposal by van den Heuvel and Tauris is also inconsistent with the limits on ellipsoidal variability derived from the optical light curve [(*2*), section 1.5.5 of supplementary materials]. This is because their proposed system would have lower total mass but the same orbital period, so the semimajor axis would be smaller relative to the radius of the giant, and the mass ratio would shift to be more dominated by the putative binary companion. These limits on ellipsoidal variability could be avoided if the distance to the system is smaller, so that the giant star has lower luminosity and smaller radius, while keeping sin i ≈ 1, but the required change in distance is inconsistent with the parallax uncertainties, and the observed v sin i would then no longer be consistent with the stellar radius.

We conclude that the hypothesis of van den Heuvel and Tauris is inconsistent with the measurements of L, $T_{\rm eff}$, log g, and v sin i and that the low x-ray luminosity may be accommodated by a black hole companion.

REFERENCES

1. E. P. J. van den Heuvel, T. M. Tauris, Comment on "A noninteracting low-mass black hole–giant star binary system". *Science* **368**, eaba3282 (2020).
2. T. A. Thompson, C. S. Kochanek, K. Z. Stanek, C. Badenes, R. S. Post, T. Jayasinghe, D. W. Latham, A. Bieryla, G. A. Esquerdo, P. Berlind, M. L. Calkins, J. Tayar, L. Lindegren, J. A. Johnson, T. W.-S. Holoien, K. Auchettl, K. Covey, A noninteracting low-mass black hole–giant star binary system. *Science* **366**, 637–640 (2019). doi:10.1126/science.aau4005 Medline
3. A. Miglio, K. Brogaard, D. Stello, W. J. Chaplin, F. D'Antona, J. Montalbán, S. Basu, A. Bressan, F. Grundahl, M. Pinsonneault, A. M. Serenelli, Y. Elsworth, S. Hekker, T. Kallinger, B. Mosser, P. Ventura, A. Bonanno, A. Noels, V. Silva Aguirre, R. Szabo, J. Li, S. McCauliff, C. K. Middour, H. Kjeldsen, Asteroseismology of old open clusters with Kepler: Direct estimate of the integrated red giant branch mass-loss in NGC 6791 and 6819. *Mon. Not. R. Astron. Soc.* **419**, 2077–2088 (2012). doi:10.1111/j.1365-2966.2011.19859.x
4. J. Choi, A. Dotter, C. Conroy, M. Cantiello, B. Paxton, B. D. Johnson, MESA Isochrones And Stellar Tracks (MIST). I. Solar-scaled models. *Astrophys. J.* **823**, 102 (2016). doi:10.3847/0004-637X/823/2/102
5. K. Menou, A. A. Esin, R. Narayan, M. R. Garcia, J.-P. Lasota, J. E. McClintock, Black Hole and Neutron Star Transients in Quiescence. *Astrophys. J.* **520**, 276–291 (1999). doi:10.1086/307443
6. M. R. Garcia, J. E. McClintock, R. Narayan, P. Callanan, D. Barret, S. S. Murray, New Evidence for Black Hole Event Horizons from *Chandra*. *Astrophys. J.* **553**, L47–L50 (2001). doi:10.1086/320494
7. J. E. McClintock, R. Narayan, G. B. Rybicki, On the Lack of Thermal Emission from the Quiescent Black Hole XTE J1118+480: Evidence for the Event Horizon. *Astrophys. J.* **615**, 402–415 (2004). doi:10.1086/424474
8. L. R. Yungelson, A. G. Kuranov, K. A. Postnov, Wind-accreting symbiotic X-ray binaries. *Mon. Not. R. Astron. Soc.* **485**, 851–860 (2019). doi:10.1093/mnras/stz467
9. H. Jönsson, C. Allende Prieto, J. A. Holtzman, D. K. Feuillet, K. Hawkins, K. Cunha, S. Mészáros, S. Hasselquist, J. G. Fernández-Trincado, D. A. García-Hernández, D. Bizyaev, R. Carrera, S. R. Majewski, M. H. Pinsonneault, M. Shetrone, V. Smith, J. Sobeck, D. Souto, G. S. Stringfellow, J. Teske, O. Zamora, APOGEE Data Releases 13 and 14: Stellar Parameter and Abundance Comparisons with Independent Analyses. *Astrophys. J.* **156**, 126 (2018). doi:10.3847/1538-3881/aad4f5

ACKNOWLEDGMENTS

T.A.T. thanks K. A. Byram for discussions and support. **Funding:** Supported by NASA grant 80NSSC20K0531 (T.A.T.); PHY 14-30152: Physics Frontier Center/JINA Center for the Evolution of the Elements (JINA-CEE) awarded by NSF, Scialog Scholar grant 24216 from the Research Corporation, and NSF grant AST 19-09022 (C.B.); NSF grants AST-1515927, AST-181440, and AST-1907570 (C.S.K. and K.Z.S.); and NASA Hubble Fellowship grant 51424 awarded by the Space Telescope Science Institute, which is operated by the Association of Universities for Research in Astronomy Inc. for NASA under contract NAS5-26555 (J.T.). **Author contributions:** T.A.T. led the interpretation of the system and the writing of the response. C.S.K., K.Z.S., C.B., and T.J. consulted on aspects of the system, including evolutionary model fitting and ellipsoidal variations, and edited the text. J.T. and J.A.J. provided input on the text and on the analysis of the APOGEE spectra and the abundances. T.W.-S.H., K.A., and K.C. participated in readying the text for publication. **Competing interests:** The authors declare that there are no competing interests. **Data and materials availability:** There are no new data.

17 December 2019; accepted 23 April 2020
Published online 8 May 2020
10.1126/science.aba4356



A mother breastfeeds her newborn baby, transferring mucosal and systemic immune memory via her milk.

PHOTO: KHUNCHO007/SHUTTERSTOCK

Published by AAAS

THE IMMUNE SYSTEM'S FIRST STEPS

REVIEWS
Prenatal development of human immunity p. 600
Microbial–host molecular exchange and its functional consequences in early mammalian life p. 604
Contributions of maternal and fetal antiviral immunity in congenital disease p. 608
Vaccination strategies to enhance immunity in neonates p. 612

By **Seth Thomas Scanlon**

In the early 1950s, Peter Medwar and colleagues showed that transplant tolerance could be induced in adult mice by inoculating them in utero with cells from a donor strain. This elegant experiment revealed that the immune system in early life is functionally distinct and responsive to programming that persists into adulthood. Nearly 70 years later, the complexity and developmental trajectory of the fetal–neonatal immune system are much better understood. We have also begun to appreciate that the immune system in early life does not develop in isolation but is instead strongly influenced by maternal cells, commensal microbes, and pathogens.

This special issue surveys recent advances in the field of early life immunology. Review articles highlight distinctive features of human fetal immune system development elucidated by unbiased multi-omics analysis, the impact of commensal metabolites and xenobiotics on immunity before and after birth, how maternal and fetal immune components work together to combat viral infections during pregnancy (and what happens when these mechanisms fail), and the potential of vaccination approaches to boost fetal–maternal immunity and protect neonates against the pathogens that most frequently cause them harm.

These discoveries should inform future public health initiatives and draw renewed attention to the vulnerability of children in early life, laying the groundwork for vaccination strategies to target pathogens that cause congenital and neonatal infections as well as therapies to treat disorders such as stillbirth and prematurity. Evidence is also mounting that immune system programming that starts in early life may influence the risk of developing conditions such as allergic, autoimmune, reproductive, and neuropsychiatric disorders in later life, further underscoring the translational implications of this kind of research.

Published by AAAS

REVIEW

Prenatal development of human immunity

Jong-Eun Park[1]*, Laura Jardine[2]*, Berthold Gottgens[3,4], Sarah A. Teichmann[1,5]†, Muzlifah Haniffa[1,2,6]†

The blood and immune systems develop in parallel during early prenatal life. Waves of hematopoiesis separated in anatomical space and time give rise to circulating and tissue-resident immune cells. Previous observations have relied on animal models, which differ from humans in both their developmental timeline and exposure to microorganisms. Decoding the composition of the human immune system is now tractable using single-cell multi-omics approaches. Large-scale single-cell genomics, imaging technologies, and the Human Cell Atlas initiative have together enabled a systems-level mapping of the developing human immune system and its emergent properties. Although the precise roles of specific immune cells during development require further investigation, the system as a whole displays malleable and responsive properties according to developmental need and environmental challenge.

Animal model systems have provided fundamental evidence that shapes our understanding of developmental hematopoiesis. Studies performed in mouse, zebrafish, and chicken have established that blood and immune system development occur across distinct anatomical sites (Fig. 1). The first blood cells are extraembryonic, developing in close association with endothelial cells of the yolk sac (*1*). Embryonic hematopoietic stem cells (HSCs), capable of repopulating an adult host in transplant assays, originate from the aorta gonad mesonephros (AGM) region (*2*). The fetal liver and bone marrow (BM) are subsequently seeded by both yolk sac–derived progenitors and AGM-derived HSCs (*3*). However, developmental timelines are not chronologically identical between species. For example, mouse fetal thymus is notably immature compared with human thymus, which supports complete naïve T cell differentiation in utero (*4*). Furthermore, some population-defining markers are poorly conserved, making it difficult to directly apply findings from animal studies to humans. Increasingly, the influence of maternofetal microbial exposure on the fetal immune development is recognized, and both commensal and pathogenic microbial repertoire differs among species (see accompanying reviews). Studies directed at human immune development have been hampered by tissue access and experimental limitations, but single-cell multi-omics technologies have expedited new findings. In this review, we discuss how these technologies have provided an unprecedented view of early life immunity. We describe key insights into how immune development is layered across time and space and explain how immune cells both prepare the fetus for antigen challenge and adopt noncanonical roles in development.

[1]Wellcome Sanger Institute, Wellcome Genome Campus, Hinxton, Cambridge CB10 1SA, UK. [2]Biosciences Institute, Newcastle University, Faculty of Medical Sciences, Newcastle upon Tyne NE2 4HH, UK. [3]Department of Haematology, University of Cambridge, Cambridge CB2 2XY, UK. [4]Wellcome and MRC Cambridge Stem Cell Institute, University of Cambridge, Cambridge CB2 2XY, UK. [5]Department of Physics/Cavendish Laboratory, University of Cambridge, JJ Thomson Ave., Cambridge CB3 0HE, UK. [6]Department of Dermatology and NIHR Newcastle Biomedical Research Centre, Newcastle Hospitals NHS Foundation Trust, Newcastle upon Tyne NE2 4LP, UK.
*These authors contributed equally to this work.
†Corresponding author. Email: st9@sanger.ac.uk (S.A.T.); m.a.haniffa@newcastle.ac.uk (M.H.)

From single cells to system-level development

The challenge of unraveling blood and immune system development in the prenatal human requires a high-performance tool kit. Single-cell RNA sequencing (scRNA-seq) has emerged as a powerful tool for the systematic understanding of the immune system, permitting an unbiased identification of cell state and the resolution of complex mixtures of cells (*5*). Droplet-based scRNA-seq methods, such as 10X, are now scalable to the extent that whole organs can be adequately sampled. For example, our group has profiled single cells from yolk sac and liver to reconstruct early hematopoiesis, from thymus to capture T cell development, and from skin and kidney to elucidate the seeding of peripheral organs (*4*, *6*). Computational techniques have permitted comparison of cell states across tissues and prediction of critical receptor ligand interactions that shape immune cell fate in specific tissues (*7*). Correlation with imaging techniques—for example, in situ transcriptomics—has allowed comprehensive characterization of tissue microenvironments (*4*, *7*–*9*). Developmental trajectories have been inferred within single tissues, as cells are captured at varying stages of differentiation and by integrating samples from a range of gestational ages. This tool kit is beginning to provide a comprehensive overview of early immune development. Meanwhile, considerable challenges remain in tracing the origin of specific immune cells to distinct waves of hematopoiesis. Advances in single-cell DNA sequencing combined with analytical techniques to track distinct clones may bring us closer to this goal.

The developing immune system in space and time

In this section, we follow human immune system development across space and time. We begin by discussing cell types as they first emerge in the yolk sac or fetal liver, before considering the thymus as a key site of T cell development. This cannot be an exhaustive description of immune composition because about 40 immune cell states have been identified in these tissues to date. Instead, we focus on how single-cell multi-omics approaches have advanced our understanding of the human fetal immune system (Fig. 2).

Yolk sac and AGM

An analysis of the human embryonic yolk sac demonstrates the presence of HSC-like progenitors, macrophages, mast cells (MCs), natural killer (NK) cell progenitors, and innate lymphoid cell (ILC) progenitors alongside megakaryocytes and erythroid cells from four postconception weeks (PCW) (*6*).

Macrophage origin has been intensively studied because tissue macrophages arise independently from HSCs and self-renew under homeostatic conditions in mouse models (*10*). Tissue-resident macrophages in the liver, lung, brain, and epidermis were shown by fate mapping to arise from yolk sac hematopoiesis through the erythromyeloid progenitor (*11*, *12*). Although the yolk sac contribution is retained in some tissues (e.g., the liver, brain, and epidermis), macrophages are gradually replaced by HSC-derived monocytes at other sites (e.g., the gut, lung, and heart). This process depends in part on how "open" the niche remains to circulating cells (*10*). In the mouse, the precise contributions of the first versus second waves of yolk sac hematopoiesis and whether the macrophages arise from a monocyte intermediate remain unresolved (*10*). In human fetal development, tissue-specific macrophages are observed from the earliest time points sampled (*6*, *13*, *14*). Single-cell dissection of human AGM revealed a distinct hemogenic endothelial population that gives rise to macrophages (*13*). By 6 PCW, the embryonic pancreas is laden with macrophages, microglia accompany the developing brain, and Hofbauer cells line the placenta (*7*, *14*, *15*). Identification of these cells in appreciable numbers before the onset of fetal liver hematopoiesis at 6 to 9 PCW lends support to yolk sac or AGM-derived macrophages seeding peripheral tissues. Attempts to use transcriptional similarity between yolk sac macrophages and fetal liver macrophages to parse tissue macrophage ontogeny are not sufficiently reliable owing to environmentally related gene expression after tissue residency. However, these profiles have allowed characterization of macrophage diversity essential for development, for example, erythroid island macrophages providing support for erythropoiesis

and Kupffer cells with prominent scavenging function in the fetal liver (*6*).

In parallel to macrophages, fate-mapping studies have demonstrated that tissue MCs arise from both yolk sac and HSC-derived precursors in mouse and that patterns of yolk sac MC retention are tissue specific (*16*, *17*). In human development, a clear MC signature is present in both the yolk sac and fetal liver (*6*). Connective tissue MCs in fetal skin and kidney are closely related to fetal liver MCs by single-cell gene expression profile (*6*). This early dedication by the embryo to MC production is puzzling. The best-characterized function of MCs is their participation in allergic responses on immunoglobulin E (IgE) binding via the high-affinity IgE receptor (*18*). Liver and yolk sac MCs appear ill prepared for this task, because neither expresses the IgE receptor alpha subunit gene (*FCER1A*) (*6*). Early MC production may occur to equip developing mucosal sites and connective tissues with resident immune cells or to provide a pool of pathogen-associated molecular pattern–responsive innate effectors. However, additional functions in supporting angiogenesis are predicted. In mice, embryonic skin MCs express genes involved in vascular and neural patterning (*6*, *16*). In adult mammals, MCs support both physiological and inflammatory angiogenesis (*18*). The role of MCs in prenatal vascular development warrants further investigation.

NK cells, ILC progenitors, and their common lymphoid progenitors can be identified from yolk sac and fetal liver single-cell transcriptome (*6*, *19*). In later stages, they are found as more diverse and differentiated cells in multiple fetal organs (*9*, *20*). In contrast to the maternal decidual NK cells whose role during pregnancy has been well characterized (*7*, *21*), our understanding of fetal NK cell function to date is limited. Although fetal NK cells are considered to be immature and hyporeactive compared with adult NK cells, they already possess killer activity (*22*, *23*). Moreover, fetal or infant NK cells resemble their adult counterparts at several levels, suggesting that they are poised to respond when the right stimuli, such as viral infections, are present (*23*). Concordantly, NK cells are abundant in infant intestines, are equipped with cytolytic granules, and display superior degranulation activity compared with adult intestinal NK cells (*20*). In addition to NK cells, other ILCs have been shown to be enriched in the fetus compared with infants (*24*). Among them, innate lymphoid tissue inducer (LTi) cells play a critical role in the formation of secondary lymphoid organs (*25*, *26*). By interacting with stromal cells, LTi cells induce positive feedback to recruit additional LTi cells as well as other immune cells, generating a lymphoid environment (*27*). Thus, innate lymphocytes develop very early in the human embryo and are involved in both tissue protection and remodeling.

This earliest wave of hematopoiesis in the yolk sac displays dedication to immune cells with structural and physiological roles alongside equipping the embryo with a basic repertoire of innate immune effectors. The precise roles of these cells in tissue development and the checkpoints that prevent damaging immune responses in utero require further investigation.

Liver and BM

Definitive HSCs can generate the full complement of erythroid, megakaryocyte, myeloid, and lymphoid cell lineages in fetal liver, but neutrophils remain absent until BM hematopoiesis is established (*28*).

In contrast to macrophages, monocytes and dendritic cells (DCs) are considered HSC-dependent populations. In the mouse, both are traceable to a clonogenic precursor in BM named the macrophage-DC progenitor (*29*). In human development, the first signs of

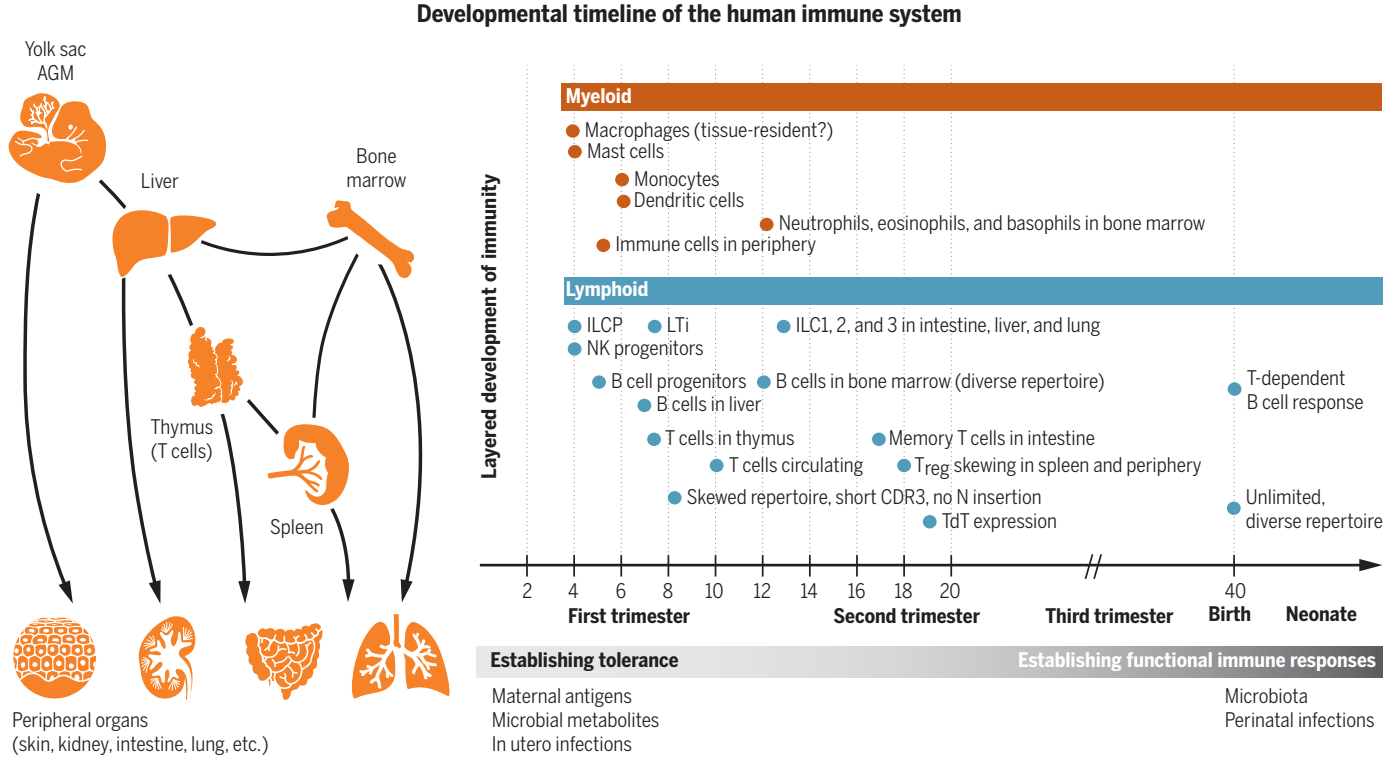


Fig. 1. Temporal and spatial development of the human immune system. The development of blood and immune systems during early human life occurs over several anatomical sites. The major site of hematopoiesis changes from the extraembryonic yolk sac to the intraembryonic AGM, liver, and BM. T cell differentiation and maturation are confined to the thymus. Immune cells seed other lymphoid or peripheral organs—including lymph nodes, skin, intestine, kidney, and lung—and adapt to the respective organ environment. Diverse immune cell types develop and mature at different gestational stages, which is necessary to establish tolerance and functional response based on developmental needs. This prepares the developing embryo and fetus for antigen exposure during pregnancy and after birth. ILCP, ILC precursor; CDR3, complementary-determining region 3; TdT, terminal deoxynucleotidyl transferase.

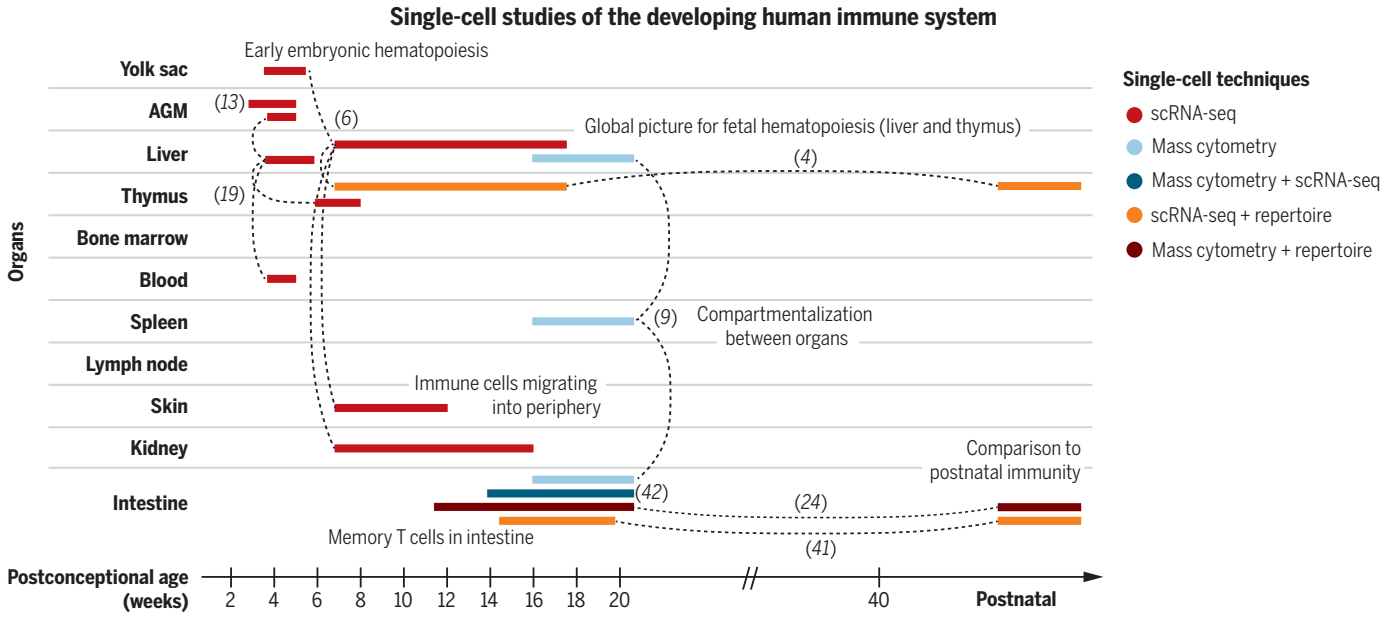


Fig. 2. Overview of single-cell studies detailing the developing human immune system. Diverse single-cell methods (depicted in color) have been applied to generate a comprehensive atlas of human immune system development. In many studies, multiple organs have been sampled together to investigate the migration, adaptation, and compartmentalization of immune cells. (Studies are indicated by the reference number, and dotted lines link the different organs sampled in each study.)

DC production are seen in the fetal liver from around 6 PCW (*6*). Conventional DC1, DC2, and plasmacytoid DCs are found in fetal tissues—including the lung, spleen, skin, and thymus—from 12 PCW and are relatively abundant compared with adult tissue DCs (*30*). Fetal DCs, like their adult counterparts, are capable of migrating, responding to Toll-like receptor ligation, and stimulating T cell proliferation and activation (*30*). Fetal DCs have the particular capacity to induce regulatory T cell differentiation, promote T cell interleukin-4 production, and inhibit T cell tumor necrosis factor–α (TNFα) production via arginase 2 (*30*). Thus, DCs play an important role in maintaining tolerance during fetal life.

The B cell lineage is first observed in the fetal liver from 7 PCW in the form of B cell precursors; mature B cells are present only after 9 PCW (*6*). This has been attributed partly to the change in HSC-intrinsic potential to generate B cells and the liver microenvironment support for B cell differentiation (*6*). At mid-gestation, the BM becomes the major source of B cells, and mature B cells are abundantly enriched in spleen (*31*). Although fetal B cells achieve diverse repertoire from early stages (*24*, *32*), the formation of germinal centers is attenuated until antigen exposure after birth, which is accompanied by active somatic hypermutation (*33*). Comparing intestinal B cells from second-trimester fetuses to infants with single-cell mass cytometry combined with B cell receptor repertoire analysis nicely demonstrated that fetal intestinal B cells are primarily follicular and transitional B cells, whereas plasma B cells are enriched in infants (*24*).

Another interesting aspect of B cell development that has been intensively studied in the mouse model is the tiered development of innate-like B-1 cells, which predominate in early gestation and are followed by conventional B-2 cells (*34*). However, the precise identity of human B-1–like cells has not yet been resolved (*35*). Future studies to generate a single-cell atlas of human fetal BM and spleen will provide a better view on human B cell ontology, highlighting organ-specific differences in the niche factors that support B cell differentiation.

"The clinical implications of fetal immune development and function reach far beyond life in utero."

Thymus and peripheral organs

The thymus provides an environment essential for T cell development. Early lymphoid progenitors originating from the fetal liver migrate into the thymus at 8 PCW, where they develop into naïve T cells (*36*).

Development and maturation of the thymus are mediated by an interplay between thymic stromal cells and immune compartments, which has been largely studied in mouse models. Comprehensive single-cell transcriptome profiling of cellular constituents of developing human thymus showed extensive communication between thymic epithelial cells, mesenchymal cells, early thymic progenitors, developing and mature T cells, and other immune cells (*4*, *19*). The proportion of each cell population also shows coordinated change across development, further proving the importance of harmony between multiple cell types for organ maturation (*4*).

Single-cell studies on fetal liver and thymus revealed detailed molecular signatures accounting for the transition from early thymic progenitors into naïve T cells (*4*, *6*, *19*). Hu and colleagues focused on the molecular profile of thymus-seeding progenitors (*19*). Our group extended this analysis toward later stages in development (*4*). Together, these findings revealed a continuous trajectory from early thymic progenitors developing into multiple mature T cell types.

Naïve T cells egress from the thymus and migrate into other tissues. Circulating T cells are observed at 10 to 11 PCW after functional thymic development (*37*). The absence or presence of microorganisms in the fetal environment remains a matter of debate (see accompanying reviews). Although a healthy pregnancy is most likely sterile, noninherited maternal alloantigens and microbial by-products may potentially activate the fetal immune system. To avoid damaging alloreactivity, the fetus needs to maintain tolerogenic immunity. Consequently, naïve T cells generated from the fetus are more likely to acquire a regulatory T cell fate compared with adult naïve T cells (*38*). Fetal regulatory T cells suppress the proliferation and cytokine secretion of other fetal T cells that are potentially self-reactive (*39*).

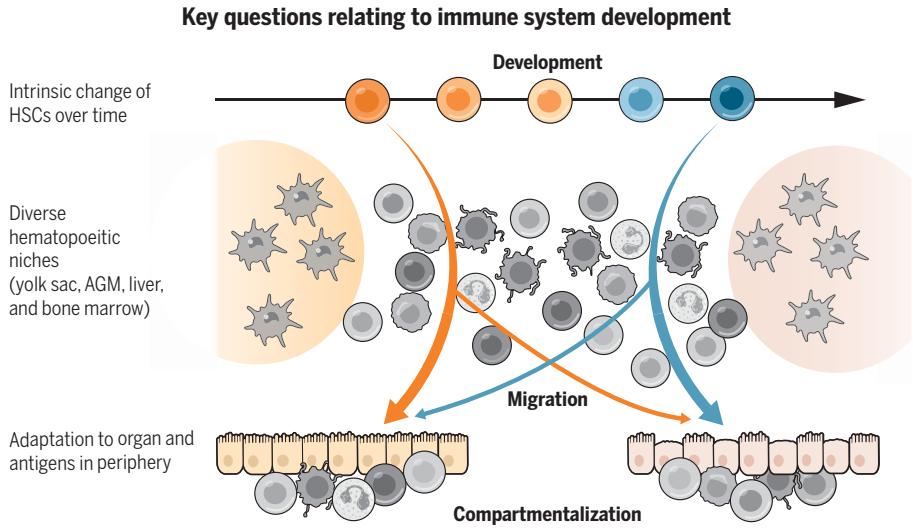


Fig. 3. Key questions to be addressed in future studies of immune system development. The diagram depicts pertinent questions relating to the developing immune system. How do the HSCs change in their potential throughout development? How do diverse hematopoietic niches differ from each other? What determines the migration of immune cells to the target organs, and how do they adapt to a new tissue environment? Single-cell profiling and spatial profiling techniques are now providing answers to these questions by assessing the immune system as a whole and identifying emergent properties of the collective.

Memory T cells have been identified in the fetal intestine, highlighting the potential of fetal T cells to respond to foreign antigens (*9*, *24*, *40*, *41*). Studies on intestinal $CD4^+$ T cells by single-cell techniques combined with repertoire sequencing identified the existence of memory T cell populations and regulatory T cells with the signature of clonal expansion, highlighting the balance between activation and suppression of adaptive immune response in the fetus (*24*, *42*). Intestinal $CD4^+$ T cells can also play a role in promoting development, as shown for the case of moderate TNFα expression (*41*). Thus, fetal adaptive immunity is substantially more mature than previously expected. Active areas of future research on the fetal immune system include the antigenic cues underlying fetal T cell activation and the roles they play in fetal development and protection.

Through this snapshot of fetal immune development across time and space, we note the emergence of both innate and adaptive immune cells with distinctive properties compared with their adult counterparts. Among the components missing from this overview are neutrophils. Current evidence suggests that around one-third of fetal BM cells are neutrophils or their precursors at 10 to 13 PCW, increasing to two-thirds at 21 PCW (*43*). Infants born prematurely or small for gestational age have lower circulating neutrophil counts, lower neutrophil reserve, and higher mortality from sepsis (*44*). Understanding how the fetal neutrophil compartment operates will provide insights into how early-life immune defense can be supported.

Conclusion

Multi-omics suspension and spatial-based technologies have provided ideal platforms to dissect and reconstruct the developing immune system (*4*, *6*, *9*, *13*, *19*, *24*, *41*, *42*). Many areas of uncertainty remain to be unraveled (Fig. 3). How do hematopoietic progenitors change throughout development? How do different tissue niches such as yolk sac, liver, BM, thymus, and spleen affect the progenitor populations and developing immune cells? How do immune cells migrate to and adapt in peripheral nonlymphoid tissues? How does the immune system communicate, learn, and form memory for future encounters?

Completion of the developing immune atlas by focusing on the organs and time points that are currently missing, extending the analyses for comparison with the adult immune cells, and system and cross-species comparisons will provide further knowledge about how the human immune system evolved and is established and sustained. The clinical implications of fetal immune development and function reach far beyond life in utero. Fetal-specific hematopoietic progenitor cells are now recognized as likely cells of origin for blood cancers, including Down syndrome–associated acute megakaryoblastic leukemia, juvenile myelomonocytic leukemia, and infant acute lymphoblastic leukemia. Early-onset primary immunodeficiencies with impaired response to pathogen challenge and/or autoimmunity may also be influenced by developmental cues and changes. In these settings, aberrant hematopoiesis also results in abnormal immune function. The biological insights from in-depth understanding of the developing immune system promise to revolutionize stem cell transplantation and tissue engineering for immunotherapy and regenerative medicine in the near future.

REFERENCES AND NOTES

1. W. His, *Lecithoblast und angioblast der wirbelthiere. Histogenetische studien* (BG Teubner, 1900), vol. 26.
2. E. Dzierzak, A. Medvinsky, *Development* **135**, 2343–2346 (2008).
3. P. G. Holt, C. A. Jones, *Allergy* **55**, 688–697 (2000).
4. J.-E. Park *et al.*, *Science* **367**, eaay3224 (2020).
5. M. Efremova, R. Vento-Tormo, J.-E. Park, S. A. Teichmann, K. R. James, *Annu. Rev. Immunol.* **38**, annurev-immunol-090419-020340 (2020).
6. D.-M. Popescu *et al.*, *Nature* **574**, 365–371 (2019).
7. R. Vento-Tormo *et al.*, *Nature* **563**, 347–353 (2018).
8. M. Asp *et al.*, *Cell* **179**, 1647–1660.e19 (2019).
9. N. Li *et al.*, *Front. Immunol.* **10**, 1932 (2019).
10. F. Ginhoux, M. Guilliams, *Immunity* **44**, 439–449 (2016).
11. E. Gomez Perdiguero *et al.*, *Nature* **518**, 547–551 (2015).
12. G. Hoeffel *et al.*, *Immunity* **42**, 665–678 (2015).
13. Y. Zeng *et al.*, *Cell Res.* **29**, 881–894 (2019).
14. L. Banaei-Bouchareb, M. Peuchmaur, P. Czernichow, M. Polak, *J. Endocrinol.* **188**, 467–480 (2006).
15. D. A. Menassa, D. Gomez-Nicola, *Front. Immunol.* **9**, 1014 (2018).
16. R. Gentek *et al.*, *Immunity* **48**, 1160–1171.e5 (2018).
17. Z. Li *et al.*, *Immunity* **49**, 640–653.e5 (2018).
18. M. Krystel-Whittemore, K. N. Dileepan, J. G. Wood, *Front. Immunol.* **6**, 620 (2016).
19. Y. Zeng *et al.*, *Immunity* **51**, 930–948.e6 (2019).
20. A. F. Sagebiel *et al.*, *Nat. Commun.* **10**, 975 (2019).
21. B. Fu *et al.*, *Immunity* **47**, 1100–1113.e6 (2017).
22. M. A. Ivarsson *et al.*, *J. Clin. Invest.* **123**, 3889–3901 (2013).
23. L. S. Angelo, L. H. Bimler, R. Nikzad, K. Aviles-Padilla, S. Paust, *Front. Immunol.* **10**, 469 (2019).
24. S. F. Stras *et al.*, *Dev. Cell* **51**, 357–373.e5 (2019).
25. K. Hoorweg *et al.*, *J. Immunol.* **195**, 4257–4263 (2015).
26. T. Cupedo *et al.*, *Nat. Immunol.* **10**, 66–74 (2009).
27. S. A. van de Pavert, R. E. Mebius, *Nat. Rev. Immunol.* **10**, 664–674 (2010).
28. W. B. Slayton *et al.*, *Early Hum. Dev.* **53**, 129–144 (1998).
29. D. K. Fogg *et al.*, *Science* **311**, 83–87 (2006).
30. N. McGovern *et al.*, *Nature* **546**, 662–666 (2017).
31. C. Nuñez *et al.*, *J. Immunol.* **156**, 866–872 (1996).
32. E. Rechavi *et al.*, *Sci. Transl. Med.* **7**, 276ra25 (2015).
33. S. Weller *et al.*, *J. Exp. Med.* **205**, 1331–1342 (2008).
34. E. Montecino-Rodriguez, K. Dorshkind, *Immunity* **36**, 13–21 (2012).
35. I. Sanz *et al.*, *Front. Immunol.* **10**, 2458 (2019).
36. B. F. Haynes, C. S. Heinly, *J. Exp. Med.* **181**, 1445–1458 (1995).
37. B. F. Haynes, M. E. Martin, H. H. Kay, J. Kurtzberg, *J. Exp. Med.* **168**, 1061–1080 (1988).
38. J. E. Mold *et al.*, *Science* **330**, 1695–1699 (2010).
39. J. Michaëlsson, J. E. Mold, J. M. McCune, D. F. Nixon, *J. Immunol.* **176**, 5741–5748 (2006).
40. X. Zhang *et al.*, *Sci. Transl. Med.* **6**, 238ra72 (2014).
41. R. R. C. E. Schreurs *et al.*, *Immunity* **50**, 462–476.e8 (2019).
42. N. Li *et al.*, *Nat. Immunol.* **20**, 301–312 (2019).
43. E. Kelemen, W. Calvo, T. M. Fliedner, *Atlas of Human Hemopoietic Development* (Springer, 2013).
44. A. Olin *et al.*, *Cell* **174**, 1277–1292.e14 (2018).

ACKNOWLEDGMENTS

We thank J. Eliasova for graphical images. **Funding:** We acknowledge funding from the Wellcome Human Cell Atlas Strategic Science Support (WT211276/Z/18/Z). M.H. is funded by Wellcome (WT107931/Z/15/Z), the Lister Institute for Preventive Medicine, and the NIHR Newcastle Biomedical Research Centre. S.A.T. is funded by Wellcome (WT206194), ERC Consolidator and EU MRG-GRammar awards, and the Chan Zuckerberg Initiative (CZF2019-002445). B.G. is a Wellcome Investigator (206328/Z/17/Z) and is also supported by core funding from Wellcome and MRC to the Cambridge Stem Cell Institute. L.J. is funded by an NIHR Academic Clinical Lectureship. J.-E.P. is supported by an EMBO Advanced Fellowship (ALTF 623-2019). **Competing interests:** In the past 3 years, S.A.T. has consulted for Biogen, GenenTech, and Roche and is a member of the ForeSite Labs Scientific Advisory Board.

10.1126/science.aaz9330

CREDIT: N.CARY/*SCIENCE*

REVIEW

Microbial–host molecular exchange and its functional consequences in early mammalian life

Stephanie C. Ganal-Vonarburg[1], Mathias W. Hornef[2], Andrew J. Macpherson[1]*

Molecules from symbiotic microorganisms pervasively infiltrate almost every organ system of a mammalian host, marking the initiation of microbial–host mutualism in utero, long before the newborn acquires its own microbiota. Starting from in utero development, when maternal microbial molecules can penetrate the placental barrier, we follow the different phases of adaptation through the life events of birth, lactation, and weaning, as the young mammal adapts to the microbes that colonize its body surfaces. The vulnerability of early-life mammals is mitigated by maternal detoxification and excretion mechanisms, the protective effects of maternal milk, and modulation of neonatal receptor systems. Host adaptations to microbial exposure during specific developmental windows are critical to ensure organ function for development, growth, and immunity.

Living organisms are constrained by the thermodynamic boundaries of obtaining and using sufficient energy within the available environment to construct their cellular and noncellular biomass during mammalian fetal and neonatal development. The consumption of plant, animal, and other xenobiotic material that is partly metabolized by microorganisms in the maternal and neonatal gastrointestinal tract improves energy harvesting for growth but exposes the developing mammal to a wide range of chemicals. Although it is possible for mammals to live in the absence of a microbiota, analytic techniques using isotopically labeled intestinal bacteria have revealed that normally even systemic organ systems and potentially the fetus are promiscuously bathed by molecules synthesized either by microbes on mucous membranes, or by dietary intake, but which cannot be generated by host metabolism itself (*1*, *2*). Here, we examine the potential impact of exposure to microbial constituents and other xenobiotics in early life, from fetal development to the early postnatal period.

Maternal exposure to microbial metabolites and xenobiotics

Mice may be bred in aseptic "germ-free" conditions in isolators with normal fecundity, development, and life span provided that their food is fortified with micronutrients. Vitamin K, for example, is usually produced by bacteria and must be given as a dietary supplement to germ-free mice for normal blood clotting (*3*). The microbiota triggers extensive adaptations in every organ system (*3*), either through sensing of the live microbes at body surfaces or through signaling from microbial metabolites that reach host tissues. Colonized animals are less susceptible to opportunistic infections through the competitive protective effect of the microbiota. Maturation that drives the adaptive and innate immune systems allows scalable responses to later pathogen challenges (*4*). In addition to the functional adaptations that occur in mucous membranes exposed to the microbial biomass, there are also extensive long-range effects on the neural, cardiovascular, hepatic, endocrine, adipose, and skeletal systems.

Although many of these pervasive adaptations can be recovered by colonizing an adult germ-free animal, there are also precise developmental time windows that require microbial colonization for normal immune development and the assembly of a healthy microbiota (*5*). The question is whether such windows are exclusively postnatal, as the young mammal acquires its own microbiota, or whether the molecular diaspora from the mother's microbiota is also important for antenatal development.

Maternal nutrition is clearly an important factor for development in early life. The energy requirements of the fetus and neonate benefit from the mother's microbiota, which optimizes her overall nutritional state by providing vitamins and essential amino acids, detoxifying xenobiotics, and breaking down otherwise indigestible foods (*6*). Bacterial folate positively influences embryonic and fetal development, and short-chain fatty acid microbial metabolites are important to sustain maternal intestinal barrier integrity (*6*).

Effects of the microbiota are mainly studied by comparing germ-free and colonized mice. To understand the specific effects of a maternal microbiota alone, transitory colonization systems have been used, so the mother is only colonized for a short time in pregnancy but delivers germ-free pups (Fig. 1). This approach has been combined with nonradioactive isotope labeling of the transitory bacteria to trace the penetration of microbial molecules into the mother and her offspring. The model shows that maternal microbial metabolites drive the development of her pups' innate immune system and maturation of the intestinal epithelium (*7*). One of the receptors for the chemical signals involved is the aryl hydrocarbon receptor (AhR), which is essential for normal immune function (*8*).

There are poorly understood differences in how different microbes metabolize dietary xenobiotics, drugs, or environmental contaminants (*9*), because microbial genes are mainly annotated by inference from sequence homologies, or their function is unknown. There are also fundamental differences between how eukaryotes and prokaryotes handle xenobiotic (bio)chemicals. The mammalian host generally detoxifies xenobiotic metabolites through the addition of polar functional groups (-OH, epoxide, -SH, or -NH_2), followed by the addition of additional polar head groups (glucuronyl, acetyl, methyl, and sulfonyl), which make the resultant polar molecule susceptible to renal elimination. By contrast, microbial metabolism has evolved to break molecules for carbon sources and/or dispose of reducing equivalents using hydrolases, lyases, reductases, group transfer, or radical chemistry (*9*, *10*). An important unmet need is to understand how far exposure to natural xenobiotics, whether sourced directly from the diet or taken in artificially high amounts as food

Box 1. Is the developing fetus sterile?

The healthy fetus is enclosed in utero by the amniotic membrane and receives blood from the placenta. It has long been thought to be completely sterile, but this notion has been challenged by recent studies that reported a very small microbial biomass in placental tissue, cord blood, or meconium. However, methodological challenges, contradictory results, and our current immunological understanding cast doubts on the interpretation of these findings (*18*). The detection of very small amounts of bacterial DNA may be confounded by laboratory or reagent contaminants. Furthermore, viable bacteria are transiently found in the bloodstream of healthy neonates following minor trauma common during birth. Additionally, bacterial profiles described vary substantially, with taxa from the oral or the skin microbiota that are potential contaminants. Because placental tissue has no lumen, colonizing bacteria would be subject to immune elimination. Finally, cesarean section and sterile fostering of fully colonized experimental animals generate germ-free neonates. Pathogenic bacteria that successfully resist antimicrobial destruction are expected to provoke an inflammatory reaction predisposing to premature birth.

[1]Universitätsklinik für Viszerale Chirurgie und Medizin, Inselspital, Bern University Hospital, Department for BioMedical Research (DBMR), University of Bern, Murtenstrasse 35, 3008 Bern, Switzerland. [2]Institute for Medical Microbiology, RWTH University Hospital, Pauwelsstrasse 30, D-52074 Aachen, Germany.
*Corresponding author. Email: andrew.macpherson@dbmr.unibe.ch

supplements, may show idiosyncratic effects on the fetus or neonate after metabolism by the mother's intestinal microbes. This is ethically difficult, as animal models do not precisely mirror human development mechanisms or the human microbiota composition.

The maternal–fetal interface

Placentation and antenatal hematopoiesis

The basis for antenatal exposure of the developing fetus to circulating microbial metabolites and xenobiotics is the placental interface between the maternal and fetal bloodstream (*6*). Mice and humans have a hemochorial placenta, in which the fetal trophoblast invades the uterine tissue and the endothelium of the maternal blood vessels. A vascular labyrinth starts to form as the fetal umbilical arteries invade the maternal decidua on embryonic day 12.5 (E12.5) in mice (within the first trimester in humans), progressing to an efficient interface between the maternal and fetal vascular systems for respiratory gas exchange, nutrient transfer, excretion, and some detoxification. This provides only a limited barrier to molecular transfer, and non-ionized molecules of relative molecular mass $M_r < 500$ reach the fetal circulation by passive diffusion. Fetal organ systems and immunity are developing in parallel. In mice, primitive hematopoiesis begins in the yolk sac at E7, and hematopoietic stem cells are found in the fetal liver and thymus starting from E10.5 (*6*).

Placental and maternal handling of xenobiotics

The potential risks of the limited placental barrier became apparent through the thalidomide disaster, when a synthesized xenobiotic taken in early pregnancy caused nonhereditary phocomelia (grossly underdeveloped or missing limbs) in babies (*6*). To regulate key compound classes, the placenta has a series of transport proteins, which help to coordinate maternofetal nutrient, excretory, and xenobiotic exchange (*11*). Multidrug resistance protein 1 (MDR1, P-glycoprotein, ABCB1) is an adenosine 5′-triphosphate (ATP)–dependent transporter of xenobiotics present on trophoblast cells, hepatocytes, intestinal epithelial cells, and renal tubular cells. Overall, this transporter helps to protect the fetus from xenobiotics as shown by the occurrence of cleft palate deformities in globally MDR1-deficient mouse fetuses where the dam was administered a polycyclic antihelminth analog (*12*). Two additional transporters (ABCG5 and ABCG8) expressed in the placenta, liver, and intestine are known to limit the uptake of plant-derived sterols, which are themselves subject to microbiota metabolism. Female mice that are globally *Abcg5* deficient exhibit cardiomyopathy, thrombocytopenia, and infertility (*13*). How far selective placental expression of any of these transporters contributes to regulating fetal exposure to maternal microbial metabolites remains unclear.

Environmental toxins, such as dioxins and dioxin-like compounds, are metabolized through the cytochrome P450 superfamily of enzymes, such as Cyp1a1, which are induced through the AhR. High AhR expression is found in the placenta, the liver, and in mucous membranes. Although small amounts of AhR ligands derived from food and the microbiota are beneficial to fetal development and postnatal immune function, toxic amounts are restricted through overall AhR-dependent activation of Cyp1a1 in intestinal, hepatic, and placental tissues (*14*). Limiting fetal xenobiotic exposure is therefore generally a function of a triple layer consisting of maternal intestine, liver, and placenta. Failure to protect the fetus or neonate from exposure to maternal microbial metabolites, as well as other ingested chemicals, may have lasting developmental consequences and predispose these children to metabolic and immunological diseases.

The microbiota potentially affects the biochemical environment of the fetus and neonate in a variety of ways

Effects of microbiota metabolites can be categorized according to whether the chemicals are synthesized endogenously by the microbiota or whether they are secondary metabolites of compounds that are taken as food, pharmaceuticals, or as environmental contaminants. Each of these categories can alter the composition and biomass of the microbiota, as well as generate different portfolios of xenobiotic chemical exposures according to the metabolic capacity of various taxa present [reviewed in (*15*)]. The general effects of dysbiosis on adult (maternal) intestinal, metabolic, and immune functions have been considered in numerous reviews.

Endogenous microbial compounds

Many endogenous microbial compounds are recognized by innate pattern recognition receptors. Comparisons of adult germ-free and colonized mice indicate steady-state penetration of host tissues by Toll-like receptor (TLR) ligands [e.g., lipopolysaccharide (LPS) or flagellin] and NOD ligands, which have been linked to important maturation processes in the host immune system (*16*, *17*). Although we believe that the developing fetus and the placenta are sterile (*18*) (box 1), stable isotope–labeling studies show that there is rather promiscuous penetration of most classes of endogenous microbial compounds into the adult host, especially from bacteria in the lower small intestine (*2*), and these are likely to reach the placenta.

Central nervous system alterations resulting from antenatal LPS exposure have long-term behavioral consequences in rodent models.

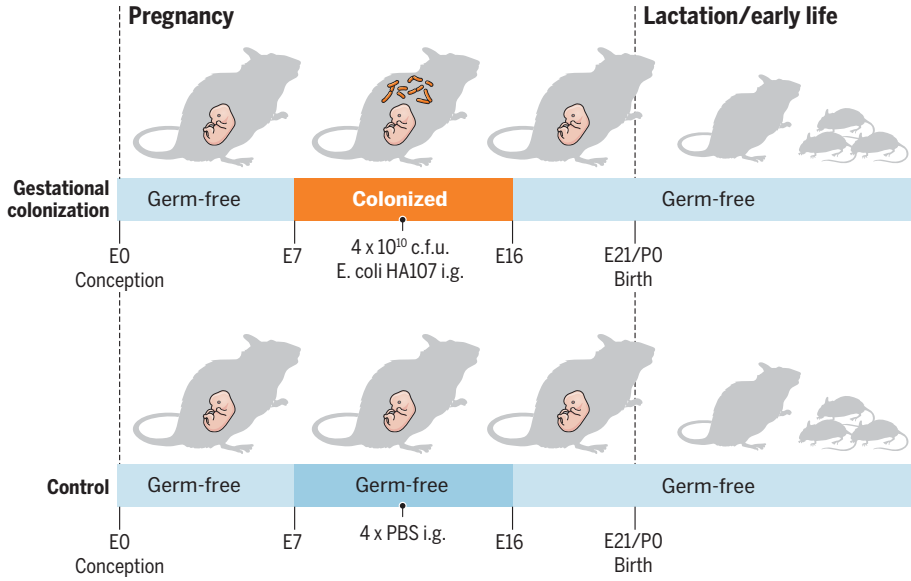


Fig. 1. Experimental model of reversible gestational colonization. The auxotrophic *Escherichia coli* HA107 strain, which is deficient in the synthesis of two bacterial-specific amino acids, meso-diaminopimelic acid and D-alanine, can be used to study the effect of the maternal microbiota on offspring development in the absence of an endogenous microbiota in the offspring. This strain is unable to replicate within the murine germ-free intestine where meso-diaminopimelic acid and D-alanine are absent. If germ-free pregnant dams are treated with HA107, they are transiently colonized but return to germ-free status before giving birth and will thus deliver germ-free pups. This experimental setup has been used to study the effect of maternal microbiota only during pregnancy on developmental processes in the offspring (*7*). i.g., intragastric; c.f.u., colony-forming units; PBS, phosphate-buffered saline.

CREDIT: KELLIE HOLOSKI/*SCIENCE*

However, doses have been used that simulate intrauterine infections, leaving open the question of whether there are also effects from the steady-state penetration of LPS in the healthy pregnant female. Microglia are extensively branched with longer dendrites in adult germ-free mice, whereas microglial immune activation is greater in colonized animals and those treated with LPS during postnatal compared to fetal life (*19*). Therefore, the barriers of the intestine and the placenta coupled with early-life insensitivity to LPS signaling presumably provide protection against steady-state antenatal exposure. Damage to the intestinal barrier (through alcohol intake or parasitic infection) can increase LPS exposure at the maternal–fetal interface (*20*). LPS and glutamyl-diaminopimelic acid (binding TLR4 and NOD1, respectively) induce inflammation at the maternal–fetal interface and can be a risk factor for preterm birth (*21*).

Diet-derived xenobiotics that are metabolized by commensal microbiota

Extensive literature is available on various dietary components and how these can potentially be metabolized by the maternal microbiota possibly with effects on early-life development (table S1). These compounds are mainly plant-synthesized polycyclics (including flavones, isoflavones, and anthraquinones), terpenes, and polyols. Although there is little or no direct epidemiologic evidence either for or against relevant effects on a human fetus, some compounds are consumed in high amounts—for example, with the intention of influencing the gender of human babies.

In other cases, there is clearer evidence for clinically important effects. Retinoids in the maternal diet, whose availability in the intestine is directly regulated by microbial taxa, such as *Clostridia* (*22*), can affect the number of lymphoid tissue inducer cells in the fetus and thus development of secondary lymphoid organs in the offspring (*23*), as well as the induction of oral tolerance in models of allergy (*24*).

Microbes found in the large intestine, such as Bacteroides species, ferment dietary fibers to short-chain fatty acids (SCFAs). These contribute to host immune maturation, either by activating G protein–coupled receptors (GPCRs) on the surface of immune cells, or through inhibition of lysine deacetylases. In a murine model of asthma, feeding female pregnant mice a fiber-rich diet limited inflammatory airway responses and the development of asthma in their offspring through the production of SCFAs (*25*). Similarly, maternal dietary fiber fermentation during pregnancy and lactation can induce the differentiation of regulatory T cells in the offspring (*26*).

Bile acids have a distinctive position in the portfolio of maternal microbial metabolites that affect the fetus. Bile acid pools are generally increased through maternal hepatic synthesis in late pregnancy, and secondary bile acids are formed by microbial metabolism in the maternal gastrointestinal tract. In addition to lipid solubilization in the postnatal intestine, bile acids are known to exert metabolic and growth effects through the GPCR TGR5 and the farnesyl X nuclear receptor (FXR). The fetus is exposed to bile acids both from its own synthesis and from maternal transfer, although renal excretion depends on the mother. Solute transport proteins of the SLC21, SCL22, and ABCG2 classes are expressed in the placenta and may regulate fetal exposure to bile acid metabolites (*27*).

Nuclear receptors, including the AhR, FXR, pregnane X receptor, constitutive androstane receptor, and vitamin D receptor, can bind diet-derived ligands and are likely to detect different maternal microbial compound classes (*28*). They can direct transcriptional activity through epigenetic mechanisms (histone modifications or DNA methylation) and may be of special importance during in utero development, which constitutes the most active period for epigenetic DNA imprinting in a mammal's lifetime.

Birth and postnatal effects

Postnatal colonization with microbes and lactation

The neonate's body surfaces are colonized at birth, exposing the offspring to microbes and

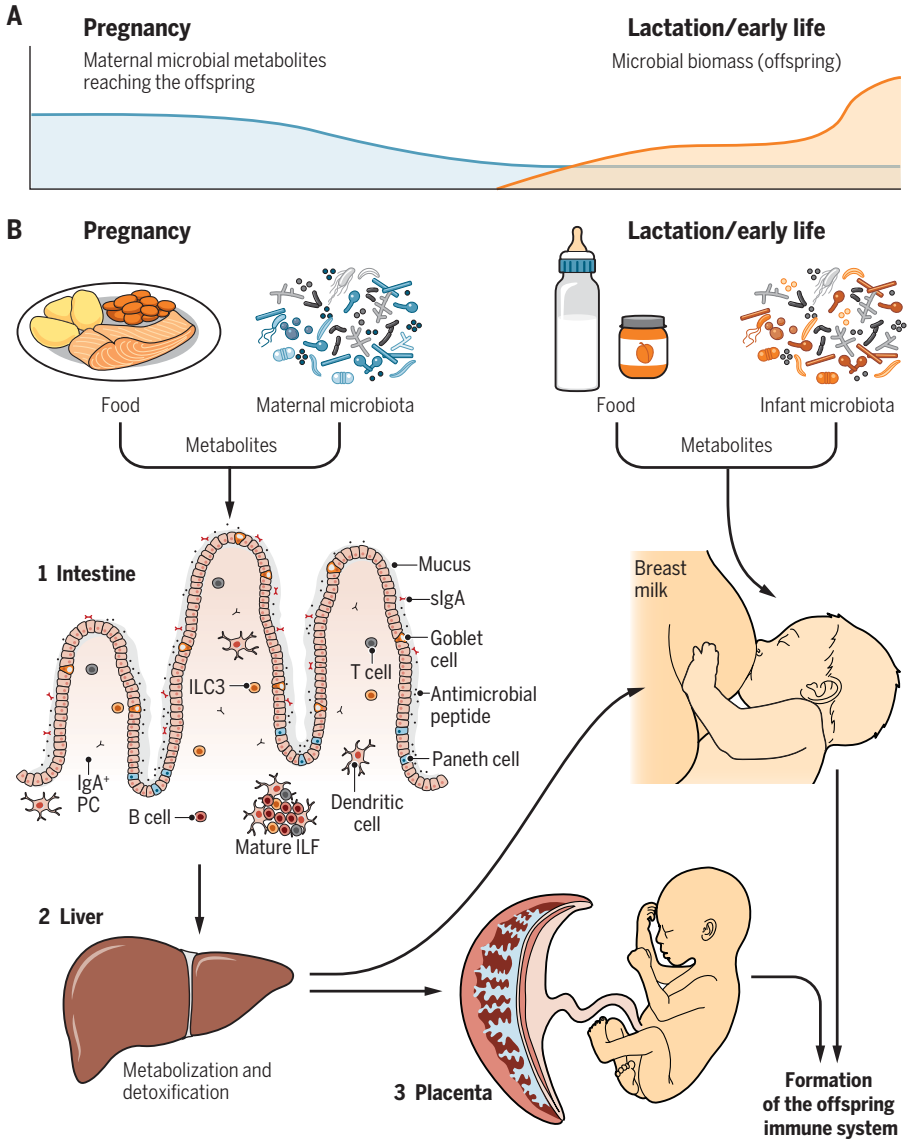


Fig. 2. Host barriers for exposure of the developing fetus and neonate to microbiota-derived metabolites. (**A**) Schematic view of the extent of exposure of the developing fetus or offspring to metabolites originating from or metabolized by the maternal microbiota in comparison to the biomass of microbes colonizing the offspring itself after birth. (**B**) A triple barrier consisting of the intestinal epithelial lining, the detoxifying liver, and the placental barrier partially protects the developing fetus from exposure to maternal bacterial and dietary metabolites. After birth, exposure to those metabolites continues through breast-feeding, further shaping the offspring's endogenous microbiota and immunity.

CREDIT: KELLIE HOLOSKI/*SCIENCE*

their molecular diaspora without maternal intestinal or placental barriers. Maternal microbial molecules still reach the neonate through breast milk, although direct microbial exposure now becomes far more important.

Breast milk shapes the unstable early-life intestinal microbiota through secretory antibodies (*29*), milk oligosaccharides (*30*), or milk proteins, including lactalbumin and lactoferrin. Because the antibody repertoire of maternal milk is shaped by the mother's own microbiota and her previous exposure to pathogens, breast-feeding is an efficient way to transfer mucosal and systemic immune memory from mother to offspring. Once the offspring starts to consume solid food, these protective effects of milk disappear, leaving endogenous microbes to stimulate a "weaning reaction" in a critical developmental window in the young mammal (*31*).

Postnatal colonization and the innate immune system

As in adults, stromal and immune cells of the fetus and neonate express a series of innate immune receptors and antimicrobial effector molecules, allowing them to mount potent and protective immune responses upon infection. However, neonates are also susceptible to inappropriate inflammation upon encounter of microbial stimuli from commensal bacteria, as in the pathogenesis of necrotizing enterocolitis (NEC), a devastating immune-mediated disease in preterm neonates (*32*).

Different mechanisms modulate the innate immune system to control the fetal–postnatal transition. Most of these perinatal changes appear to be developmentally regulated and largely independent of the microbiota, probably reflecting the unreliable presence of microbial stimuli early after birth (*33*). Age-dependent differences exist for the expression of individual receptors and the anatomical distribution of antimicrobial peptides in mice and humans, but mechanistic insight into the functional role of the changes remains limited (*34*, *35*). For example, decreased prenatal expression of TLR4 by the human intestinal epithelium or repressed TLR4 signal transduction in neonatal murine epithelium may help to prevent inflammation upon early postnatal colonization (*36*–*38*). By contrast, enhanced expression of the flagellin receptor TLR5 by the murine neonatal epithelium contributes to the selection of a beneficial gut microbiota (*34*). Similarly, human blood monocytes undergo postnatal reprogramming through stimulation with the endogenous TLR4 ligands S100A8 and S100A9 to avoid hyperinflammation and promote immune homeostasis (*39*). Finally, maternally derived factors in amniotic fluid and breast milk modulate innate immune recognition and mucosal translocation of microbial stimuli to restrict their proinflammatory activity during the immediate postnatal period (*31*, *40*). For example, breast milk–derived secretory immunoglobulin A with affinity to enteric bacteria increases bacterial diversity and protects against the development of NEC in preterm neonates (*41*).

Thus, neonatal innate immunity is not simply less developed or immature. Rather, it is highly adapted and finely tuned to facilitate the fetal–postnatal transition of rapidly increasing microbial biomass and the development of long-term host microbial mutualism.

Postnatal colonization and adaptive immunity

The full maturation of the adaptive immune system occurs predominantly at weaning, when the young host is exposed to new antigens through higher intestinal microbial and food antigen loads. The intestinal mucosa acquires antigen-experienced T cells and activated plasma cells in a microbiota-dependent process (*3*). Antenatal B and T cell development in the fetal liver shifts to the bone marrow and thymus, respectively, and naïve B and T cells migrate into the secondary lymphoid tissues.

The extent to which the preweaning microbiota contributes to the trajectory of B and T cell repertoire development between early life and adulthood is not yet fully understood, although premature diversification appears to be a disadvantage for later immune responses that depend on natural antibodies and can potentially bias the adult B cell repertoire (*42*). Maternal milk immunoglobulins, themselves shaped by the composition of the maternal microbiota as well as neonatal T regulatory cells, delay the onset of secretory antibody production (*43*) and mucosal T helper cell maturation (*44*, *45*) in the offspring.

The process of development of some lymphocytes requires the presence of microbiota during a critical time window prior to weaning. Mice that are germ free until weaning have increased serum IgE concentrations and excessive intestinal mucosal natural killer T cells (*5*). Mucosal associated innate T (MAIT) cells, absent in germ-free mice, only efficiently seed tissues in response to microbiota-derived riboflavins in the first few weeks of life (*46*). Mucosal regulatory T cells require microbiota before weaning, limiting later susceptibility to colitis or allergic airway inflammation (*5*, *47*).

Conclusions

In this Review, we have considered the impact of the microbiota on the early-life mammal. In fetal life, this comes mainly from penetration of molecules synthesized by maternal intestinal microbes or microbial metabolism of food substances (Fig. 2). Our knowledge of these effects at physiological levels of metabolite penetration remains very limited, and the epigenetic and signaling mechanisms involved have primarily been studied thus far in the context of toxicology. After birth, adaptations occur mainly to contain the impact of the rapidly increasing endogenous neonatal microbial biomass and its molecular diaspora. It is clear that there are age-dependent modulations of signaling to innate receptor ligands and that maternal antibodies can shield the neonatal immune system from premature repertoire diversification and shape the composition of the early-life microbiota.

REFERENCES AND NOTES

1. E. Holmes, J. V. Li, T. Athanasiou, H. Ashrafian, J. K. Nicholson, *Trends Microbiol.* **19**, 349–359 (2011).
2. Y. Uchimura *et al.*, *Immunity* **49**, 545–559.e5 (2018).
3. K. Smith, K. D. McCoy, A. J. Macpherson, *Semin. Immunol.* **19**, 59–69 (2007).
4. A. J. Macpherson, N. L. Harris, *Nat. Rev. Immunol.* **4**, 478–485 (2004).
5. T. Gensollen, S. S. Iyer, D. L. Kasper, R. S. Blumberg, *Science* **352**, 539–544 (2016).
6. A. J. Macpherson, M. G. de Agüero, S. C. Ganal-Vonarburg, *Nat. Rev. Immunol.* **17**, 508–517 (2017).
7. M. Gomez de Agüero *et al.*, *Science* **351**, 1296–1302 (2016).
8. B. Stockinger, P. Di Meglio, M. Gialitakis, J. H. Duarte, *Annu. Rev. Immunol.* **32**, 403–432 (2014).
9. K. N. Lam, M. Alexander, P. J. Turnbaugh, *Cell Host Microbe* **26**, 22–34 (2019).
10. N. Koppel, V. Maini Rekdal, E. P. Balskus, *Science* **356**, eaag2770 (2017).
11. A. A. Houde *et al.*, *Epigenetics* **8**, 1289–1302 (2013).
12. G. R. Lankas, L. D. Wise, M. E. Cartwright, T. Pippert, D. R. Umbenhauer, *Reprod. Toxicol.* **12**, 457–463 (1998).
13. T. H. Chase *et al.*, *Blood* **115**, 1267–1276 (2010).
14. L. Stejskalova, P. Pavek, *Curr. Pharm. Biotechnol.* **12**, 715–730 (2011).
15. M. J. Barratt, C. Lebrilla, H. Y. Shapiro, J. I. Gordon, *Cell Host Microbe* **22**, 134–141 (2017).
16. C. Iwamura, N. Bouladoux, Y. Belkaid, A. Sher, D. Jankovic, *Blood* **129**, 171–176 (2017).
17. J. Z. Oh *et al.*, *Immunity* **41**, 478–492 (2014).
18. M. C. de Goffau *et al.*, *Nature* **572**, 329–334 (2019).
19. A. Castillo-Ruiz *et al.*, *Brain Behav. Immun.* **67**, 218–229 (2018).
20. E. A. McDonald *et al.*, *Am. J. Trop. Med. Hyg.* **99**, 495–501 (2018).
21. I. Cardenas *et al.*, *J. Immunol.* **187**, 980–986 (2011).
22. M. Grizotte-Lake *et al.*, *Immunity* **49**, 1103–1115.e6 (2018).
23. S. A. van de Pavert *et al.*, *Nature* **508**, 123–127 (2014).
24. M. Turfkruyer *et al.*, *Mucosal Immunol.* **9**, 479–491 (2016).
25. A. N. Thorburn *et al.*, *Nat. Commun.* **6**, 7320 (2015).
26. A. Nakajima *et al.*, *J. Immunol.* **199**, 3516–3524 (2017).
27. S. McIlvride, P. H. Dixon, C. Williamson, *Mol. Aspects Med.* **56**, 90–100 (2017).
28. M. Venkatesh *et al.*, *Immunity* **41**, 296–310 (2014).
29. E. W. Rogier *et al.*, *Proc. Natl. Acad. Sci. U.S.A.* **111**, 3074–3079 (2014).
30. M. R. Charbonneau *et al.*, *Cell* **164**, 859–871 (2016).
31. Z. Al Nabhani *et al.*, *Immunity* **50**, 1276–1288.e5 (2019).
32. J. Zhao *et al.*, *Proc. Natl. Acad. Sci. U.S.A.* **105**, 7528–7533 (2008).
33. A. H. Lee *et al.*, *Nat. Commun.* **10**, 1092 (2019).
34. M. Fulde *et al.*, *Nature* **560**, 489–493 (2018).
35. N. Iram *et al.*, *Development* **139**, 4210–4219 (2012).
36. S. C. Gribar *et al.*, *J. Immunol.* **182**, 636–646 (2009).
37. C. Chassin *et al.*, *Cell Host Microbe* **8**, 358–368 (2010).
38. D. N. Nguyen *et al.*, *Am. J. Pathol.* **188**, 2629–2643 (2018).
39. T. Ulas *et al.*, *Nat. Immunol.* **18**, 622–632 (2017).
40. E. LeBouder *et al.*, *J. Immunol.* **176**, 3742–3752 (2006).
41. K. P. Gopalakrishna *et al.*, *Nat. Med.* **25**, 1110–1115 (2019).
42. M. Vono *et al.*, *Cell Rep.* **28**, 1773–1784.e5 (2019).
43. N. L. Harris *et al.*, *J. Immunol.* **177**, 6256–6262 (2006).
44. M. A. Koch *et al.*, *Cell* **165**, 827–841 (2016).
45. N. Torow *et al.*, *Nat. Commun.* **6**, 7725 (2015).
46. M. G. Constantinides *et al.*, *Science* **366**, eaax6624 (2019).
47. K. A. Knoop *et al.*, *Sci. Immunol.* **2**, eaao1314 (2017).

ACKNOWLEDGMENTS

Funding: This work was supported by funding from ERC (HHMM Neonates) to A.J.M., Collaborative Research Center CRC1382 to M.W.H., and Peter Hans Hofschneider Professorship to S.C.G.-V.
Competing interests: The authors have no competing interests.

SUPPLEMENTARY MATERIALS

science.sciencemag.org/content/368/6491/604/suppl/DC1
Table S1
References (*48*–*89*)

10.1126/science.aba0478

REVIEW

Contributions of maternal and fetal antiviral immunity in congenital disease

Laura J. Yockey[1,2]*, Carolina Lucas[1]*, Akiko Iwasaki[1,3,4]†

Viral infections during pregnancy can have devastating consequences on pregnancy outcomes, fetal development, and maternal health. In this review, we examine fetal and maternal immune defense mechanisms that mediate resistance against viral infections and discuss the range of syndromes that ensue when such mechanisms fail, from fetal developmental defects to establishment of chronic infection. Further, we highlight the role of maternal immune activation, or uncontrolled inflammation triggered by viral infections during pregnancy, and its potential downstream pathological effects, including tissue damage and fetal demise. Insights into the respective contributions of direct viral toxicity versus fetal and maternal immune responses that underlie the pathogenesis of congenital disease will guide future treatment strategies.

Antiviral immune responses must be carefully balanced to maximize elimination of the pathogen and minimize damage to the host. Infections during pregnancy pose a distinct threat to both the mother and fetus, as the need to defend against the pathogens may conflict with mechanisms that maintain tolerance to the developing allogeneic fetus or disrupt normal developmental programs. Consequently, multiple defense pathways in the mother and fetus have evolved to protect against these threats. Despite these pathways, an expanding collection of "TORCH" pathogens (Box 1) are able to overcome these barriers and cause congenital infections. Common disease manifestations associated with classic TORCH syndrome include microcephaly, hearing loss, ocular abnormalities, hepatosplenomegaly, placental insufficiency, and fetal loss (*1*). The burden of congenital infection remains high: Cytomegalovirus (CMV), for example, infects up to 1 to 5% of infants worldwide and is the leading cause of long-term pediatric disabilities (*2*, *3*). In addition, maternal viral infection, even in the absence of transmission, can result in long-term consequences for the newborn, including abnormal neuropsychiatric development in the case of influenza and abnormal immune system development in the case of HIV-1 (*4*, *5*). Infection during pregnancy can also lead to more severe disease or prolonged infection for the mother (*6*).

In this review, we cover resistance mechanisms used by the fetus and maternal–fetal interface that prevent viral infections. We also examine how, when these mechanisms fail, viral infection and antiviral responses can lead to disruption of placental and fetal development and consequent congenital diseases. Finally, we highlight some gaps in the field toward the development of effective prevention and therapeutics for congenital infections.

Box 1. TORCH pathogens comprise *Toxoplasma gondii*, "other," rubella virus, CMV, and herpes simplex virus (HSV) (*7*).

The "other" category includes syphilis, parvovirus B19, Coxsackievirus, varicella zoster virus (VZV), HIV, Zika virus (ZIKV), hepatitis B virus (HBV), and hepatitis E virus (HEV). Other pathogens with the potential to cause pregnancy complications and perinatal infection include chikungunya virus (CHIKV), human papillomavirus (HPV), Ebola virus, gonorrhea, chlamydia, and group B streptococcus.

[1]Department of Immunobiology, Yale University School of Medicine, New Haven, CT 06520, USA. [2]Vincent Center for Reproductive Biology, Massachusetts General Hospital, Boston, MA 02114, USA. [3]Department of Molecular, Cellular and Developmental Biology, Yale University, New Haven, CT 06512, USA. [4]Howard Hughes Medical Institute, Chevy Chase, MD 20815, USA.
*These authors contributed equally to this work.
†Corresponding author. Email: akiko.iwasaki@yale.edu

Routes and timing of viral infection during pregnancy

In this section, we briefly discuss some of the consequences of viral infection during pregnancy and some of the changes that occur during pregnancy that may dictate susceptibility to infection. The timing of viral infection during pregnancy influences disease outcome in the fetus, potentially because of viral tropism, fetal developmental stages, and dynamic immune changes during pregnancy (Fig. 1).

There are several routes through which viruses may reach the fetus (*7*, *8*). A virus may reach fetal blood vessels in the villous tree from maternal blood to floating villi or from the maternal decidua basalis to anchoring villi. Viruses may also reach the fetus through the amniotic sac from the parietal decidua or the cervix (Fig. 1A, arrows). Maternal blood does not interface with the chorionic villi until the beginning of the second trimester, so the virus likely reaches the fetus from the anchoring villi or parietal decidua before then (*8*).

Early pregnancy

During the first trimester (0 to 13 weeks), placental development and organogenesis occur, making the fetus particularly susceptible to severe disease. Among viral infections during early pregnancy associated with severe outcomes, HSV, HPV, and CMV may affect placental development, leading to spontaneous pregnancy loss or preterm birth (*9*–*11*) (Fig. 1).

Pregnancy is accompanied by dynamic changes in the immune cell composition and cytokine expression at the maternal–fetal interface. During the first trimester, implantation and placenta development is accompanied by increased inflammatory cytokine expression and accumulation of immune cells at the decidua (*6*). In the second trimester (14 to 26 weeks), the maternal–fetal interface is dominated by a more "anti-inflammatory" phenotype. This includes a shift toward M2-like macrophages, decidual natural killer (NK) cells, and regulatory T cells that may be important for maintaining tolerance and normal fetal growth (*6*). Given these tightly regulated immune changes that occur during pregnancy, dysregulation of these responses in the setting of an antiviral immune response may affect normal placental and fetal development.

In addition to affecting the placenta and maternal–fetal interface, several viruses are capable of crossing the placental barrier and reaching the fetus; the most common include VZV, rubella, CMV, HSV, and ZIKV (Fig. 1). Fetal growth restriction, which can be mediated by both placental and fetal factors, is another common outcome and is associated with parvovirus B19, CMV, HBV, VZV, ZIKV, and HIV-1 (*1*). Some viruses, such as VZV and rubella, affect many different organ systems. However, the most common systems affected during early pregnancy infections are the central nervous and hematologic systems, which continue to develop through the second trimester (Fig. 1) (*1*).

Late pregnancy and peripartum infection

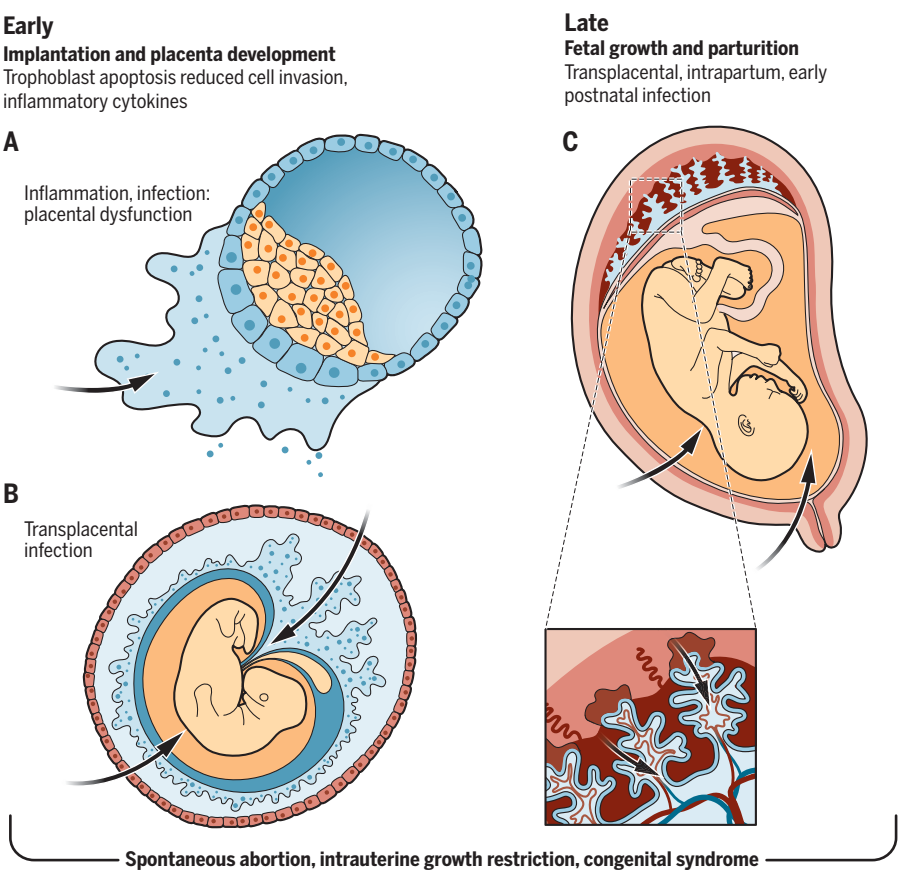
Infections by certain viruses during the third trimester (weeks 27 to 40) and peripartum period can lead to high rates of neonatal mortality or lifelong infections (Fig. 1). Primary maternal infections with HSV or CMV are correlated with a high risk of vertical transmission, particularly during late pregnancy or perinatal periods, when infection may occur through ingestion or aspiration of cervicovaginal secretions during delivery or breastfeeding (*9*–*11*). Infections with VZV, Ebola, Lassa, and HEV increase maternal and fetal mortality during late pregnancy; VZV and HEV infections are linked to ~30% infant mortality, with maternal mortality reaching 20% in HEV infections (*3*, *12*). Vertical infection with CHIKV occurs at delivery in about half of pregnancies with viremia, resulting in newborn encephalitis in 50% of cases (*13*)

(Fig. 1). Additionally, transmission of HBV and HCV, which can occur during all three trimesters, can lead to chronic infection of the infant (*1*). The vertical transmission rates of HIV-1, which typically occurs in the intrapartum and postpartum period, often also result in chronic infection, although antiretroviral therapy has substantially reduced transmission rates (*14*). Nevertheless, even uninfected HIV-exposed infants can suffer delayed growth, increased susceptibility to infections, and increased mortality (*4*). This heightened susceptibility to infection is accompanied by altered immune profiles of the infant, including decreased T cell counts, increases in activated T cells, and decreased neutrophil numbers. The mechanisms underlying these altered newborn immune responses are not well understood but may be caused by increased maternal inflammation or increased risk of maternal infection (*4*). Thus, chronic maternal viral infections can affect the fetus even in the absence of infection.

As new viruses emerge, determining their effects on pregnancy and the best management for pregnant patients is an important concern. A recent example is coronavirus disease 2019 (COVID-19), caused by severe acute respiratory syndrome–coronavirus 2 (SARS-CoV-2). Members of the coronavirus family, including the SARS-CoV and the Middle East respiratory syndrome (MERS-CoV) coronaviruses, are associated with severe pneumonia and can pose serious health risks to pregnant women and cause neonatal complications (*15*). There are limited data about clinical complications and vertical transmission of pregnant woman with COVID-19, although major symptoms overlap with those observed in nonpregnant individuals; these include fever, cough, lymphopenia, coagulopathy, and pulmonary infiltrate. Available studies mostly include women who developed COVID-19 in late pregnancy and thus viral RNA could not be detected in the neonatal throat swabs or breast milk (*16*). In addition, the coagulopathy seen during SARS-CoV2 infection may contribute to hypertensive complications including preeclampsia in pregnant patients with COVID-19. Given the limited availability of studies from earlier pregnancy stages and the small sample size of available studies, further analyses are urgently needed for a better understanding of maternal–fetal transmission of SARS-CoV-2 and its role in pregnancy complications.

Antiviral resistance mechanisms during pregnancy

The placenta and maternal–fetal interfaces are equipped with specialized mechanisms to protect the fetus from infection. The observation that most viral infections of the mother are not transmitted to the fetus supports their effectiveness in most cases (*7*). The innate and



D

VIRUS	TIMING OF INFECTION	MAJOR ROUTE OF INFECTION	SEQUELAE OF VIRAL INFECTION DURING PREGNANCY
HSV-2	A B C	Intrapartum	Microcephaly and intracranial calcifications/ eye defects/ miscarriage
HPV	A	in utero (ascending)	Miscarriage
CMV	A B C	In utero (transplacental)	Microcephaly and intracranial calcifications/learning disabilities/ abnormal long-term neurodevelopment/auditory defects
Varicella	B C	In utero (transplacental)	Microcephaly and intracranial calcifications/seizures, psychomotor defects/eye defects/ increased maternal and neonatal mortality
Rubella	B	In utero (transplacental)	Microcephaly and intracranial calcifications/learning disabilities/ abnormal long-term neurodevelopment/eye defects/auditory defects/hematologic and cardiac defects/miscarriage and stillbirth
Zika	A B C	In utero (transplacental)	Microcephaly and intracranial calcifications/learning disabilities/ abnormal long-term neurodevelopment/eye defects/miscarriage
Ebola	A B C	In utero (transplacental)	Increased maternal mortality/ miscarriage and stillbirth
HIV	B C	Intrapartum	Learning disabilities/abnormal long-term neurodevelopment/ chronic infection of fetus/ neonate
HCV	B C	Intrapartum	Chronic infection of fetus/neonate
HEV	C	In utero (transplacental)	Increased maternal mortality/ miscarriage, stillbirth, and neonatal mortality
Lassa	B C	In utero (transplacental)	Increased maternal mortality/miscarriage, stillbirth, and neonatal death
CHIKV	C	Intrapartum	Encephalitis and hematologic and cardiac defects
Parvovirus B19	A B C	In utero (transplacental)	Learning disabilities/abnormal long-term neurodevelopment/hematologic and cardiac defects (including hydrops fetalis)/ miscarriage

Fig. 1. Overview of congenital viral infections by routes and timing of infection. (**A** and **B**) Early pregnancy. (**C**) Late pregnancy. Arrows indicate potential routes of viral infection. (**D**) Table showing the routes and timing of infection and congenital disease by different viruses. The most common timing of infection is highlighted in blue.

CREDIT: KELLIE HOLOSKI/*SCIENCE*

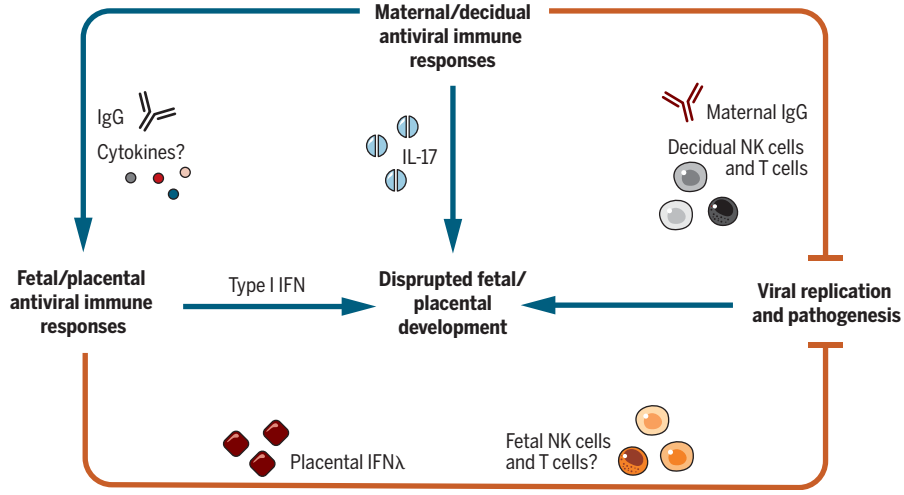


Fig. 2. Potential contributors to viral infection–mediated abnormal fetal development. Shown is a conceptual model of the potential contributions of maternal and fetal immune responses, as well as direct viral effects on disrupted fetal development. Maternal and fetal immune responses are also important for limiting viral replication. Specific examples are shown.

adaptive immune responses at the maternal–fetal interface and within the fetus need to limit infection without interfering with fetal development (Fig. 2). Thus, they provide some examples of specific antiviral mechanisms.

At the interface between the maternal blood and fetal blood of the chorionic villi, the syncytiotrophoblasts form a formidable barrier to infection (Fig. 3). These cells create a physical barrier through cell–cell fusion and constitutive expression of type III interferons (IFNs), exosomes, and antimicrobial peptides, which confer antiviral resistance in a paracrine manner (*8*, *17*). In the chorionic villi, fetal macrophages or Hofbauer cells undergo robust proliferation during viral infection and other nonviral villitis. Many viruses, including CMV, ZIKV, HSV, and Coxsackie virus, have been detected within Hofbauer cells (*18*). It is not clear whether Hofbauer cells limit viral spread or primarily serve as a site for viral replication. Maternal immunoglobulin G (IgG) also accumulates in the villous core, providing another potential barrier to infection (*19*). At the interface of the uterus and placenta, the decidua or maternal-derived lining of the uterus, is composed of 40% immune cells, including NK cells, macrophages, and T cells (*20*). Although these decidual immune cells generally have a less inflammatory phenotype than their counterparts in the blood, there is evidence for antiviral activity of decidual NK cells (dNKs) and CD8 T cells against HIV-1 (*21*) and CMV (*22*, *23*). For example, ex vivo experiments have shown that dNKs produce IFN-γ to limit HIV replication in decidual macrophages, and dNKs can produce perforin and induce cytotoxicity in human CMV (HCMV)–infected fibroblasts (*21*, *23*). These viral infections also alter the cytokine profiles of dNK cells, potentially affecting their baseline functions in mediating normal placental development.

If a virus surpasses the defenses of the decidua and placenta to reach the fetus, the fetus has the potential to develop innate and adaptive antiviral responses. Potential antiviral effector cells develop early during pregnancy (see accompanying reviews in this issue). For example, fetal NK cells are found in the liver as early as 6 weeks of gestation and show evidence of cytotoxicity as early as 9 weeks (*24*). CMV-specific T cells and IgM responses are present in CMV-infected fetal blood, indicating the ability to develop an antigen-specific response (*24*). CMV-specific $CD8^+$ T cells from infected newborns and fetuses can induce perforin-dependent lysis of infected cells, and they also produce granzyme and antiviral cytokines including IFN-γ and tumor necrosis factor-alpha (TNF-α) (*25*). Further functional evidence is needed to better understand the effectiveness of fetal immune responses in controlling viral replication or contributing to congenital disease in vivo. Variable fetal immune responses could be one reason why only a certain percentage of infected fetuses develop symptoms (*7*). Further, protection from intrauterine infection would help to explain why these immune responses develop so early in fetal development.

Mechanisms of virus- versus immune-mediated fetal damage

Even in the absence of transplacental transmission, viral infections can affect fetal development because of inflammatory responses in the placenta or infection-induced systemic changes in the pregnant mother, including metabolic alterations. In this section, we will focus on some of the molecular mechanisms by which viruses and immune responses to viruses affect placental and fetal development (Fig. 2).

Direct virus infection and damage

Direct virus damage, induced by killing or altered function of the infected cell by the virus, leads to severe complications during pregnancy. Infection of trophoblast cells by HSV or CMV can result in apoptosis and reduced cell invasion (*9*–*11*). HPV can also infect the extravillous trophoblast, causing abnormal placental pathology, spontaneous pregnancy loss, or preterm birth (*26*). Zika NS1 alters the surface glycosaminoglycans of placental endothelial cells, leading to increased vascular permeability and potential placental dysfunction (*27*). Such direct viral toxicity could contribute to placental abnormalities, as well as preterm birth, intrauterine growth restriction, and spontaneous miscarriage.

VZV, rubella, CMV, HSV, and ZIKV are all capable of infecting fetal neurons and neuronal precursors. In newborns, neuronal HSV infection results in apoptosis and neurologic damage (*28*). CMV-infected fetal brains present with white matter abnormalities, brain local necrosis, and hemorrhage. Neurological damage includes brain calcifications, microcephaly, and occipital horn anomalies (*2*). ZIKV can directly infect cortical neuron progenitors, as well as mature neurons and glial cells, resulting in cell death, neuroinflammation, and cortical thinning in postnatal brains (*29*, *30*). In newborn mouse models, CHIKV encephalopathy was associated with brain swelling and with the presence of virus in the cerebrospinal fluid, although it remains undetermined whether this was direct virus toxicity or inflammation-induced damage (*31*, *32*).

Maternal and fetal innate immune activation

Epidemiological studies have linked viral infection during pregnancy to an increased risk of psychiatric disorders in the adult offspring, including schizophrenia and autism spectrum disorders (ASDs), as well as neurological symptoms such as cerebral palsy (*5*, *33*). Infection-induced inflammation per se can cause disorders in the newborn, including ASD. The current widely used maternal immune activation (MIA) murine model is based on administration of a double-stranded RNA viral mimic, polyinosinic:polycytidylic acid (poly I:C), around midgestation in mice, which leads to behavioral symptoms resembling schizophrenia, depression, and ASD (*34*, *35*). One of the mechanisms of MIA-induced brain damage is a direct action of interleukin-17 (IL-17) from maternal T helper 17 (T_H17) cells on developing fetal cortical neurons (*36*). IL-17 receptor alpha signaling in a population of developing neurons of the somatosensory cortex (S1DZ neurons) results in increased

CREDIT: KELLIE HOLOSKI/*SCIENCE*

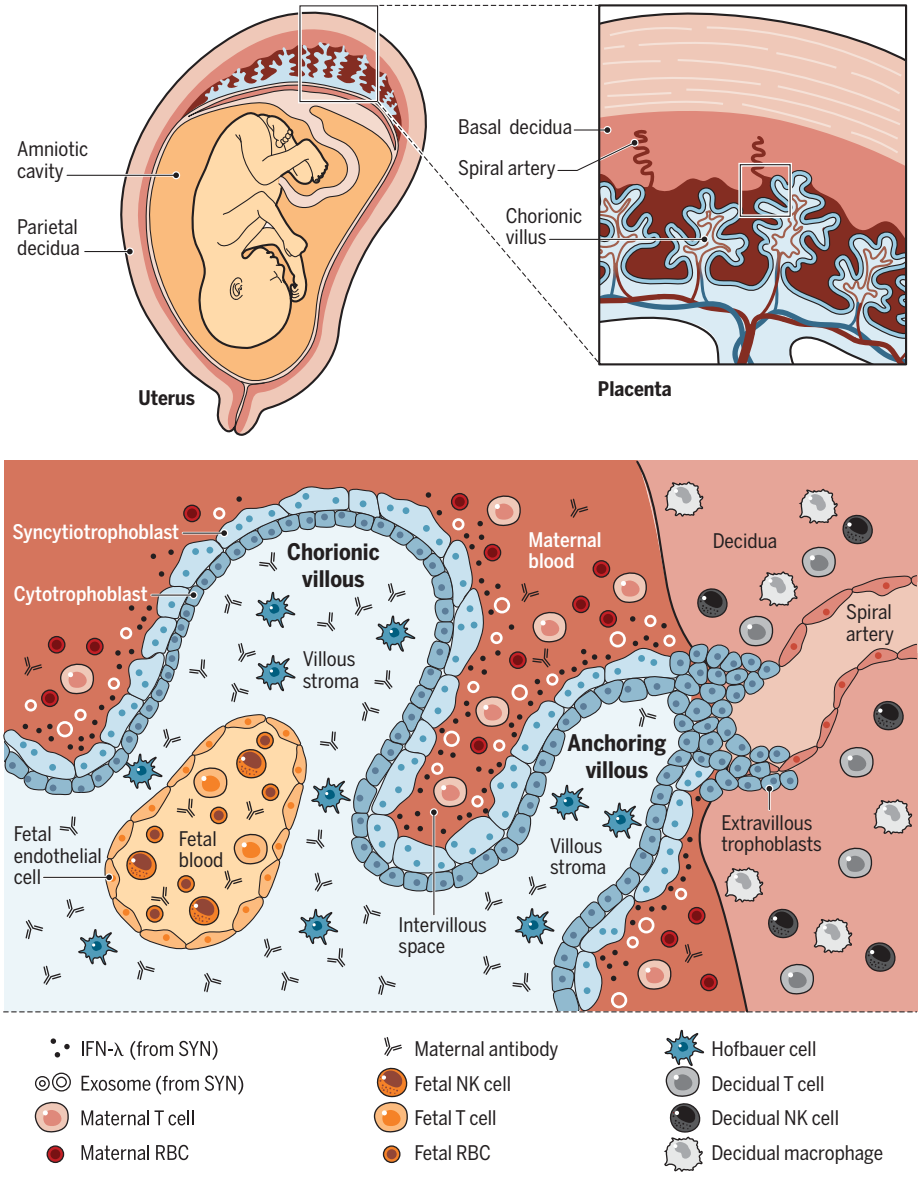


Fig. 3. Layers of defenses at maternal–fetal interfaces. Shown is an illustration of antiviral defenses at potential routes of infection: the chorionic villus, which is the interface between the maternal blood and fetal blood, and the anchoring villus, which is a connection between the decidua and villus.

neuronal activity and altered behavior (*37*). In addition to IL-17, mouse models of herpesvirus infection (MHV-68) showed that even in the absence of direct fetal infection, fetal inflammatory cytokines including IL-1β, IFN-γ, and TNF-α are elevated (*38*). Increased expression of proinflammatory cytokines are also observed in the human placenta after infection with CMV and other viral infections (*39*). The exact role of these cytokines in fetal brain development remains unknown.

Mouse models of ZIKV infection provide an excellent example of a host antiviral response inducing the termination of pregnancy. Type I IFN receptor signaling in the fetus, but not the mother, interferes with placental development, resulting in decreased fetal weight and fetal resorption that are independent of viral burden (*40*). The cellular mechanism by which the type I IFN response affects placental development has recently been elucidated. IFN-stimulated IFN-induced transmembrane (IFITM) molecules, which normally interfere with the viral fusion process, block fusion of cytotrophoblast to form multinucleated syncytiotrophoblasts, the cells of the placenta that interface with maternal blood (*41*, *42*). This cell fusion process is mediated by coopted retroviral envelope proteins called syncytins, which are necessary for placentation. This IFN-mediated disruption of pregnancy may be an evolutionarily adaptive "quality control" mechanism to minimize maternal investment early in a potentially unsuccessful pregnancy. However, it could also be an incidental consequence of antiviral responses interfering with the dependence on viral proteins for placentation.

The toxic impacts of type I IFNs in the developing fetus have been previously implicated in Aicardi–Goutières (AGS) syndrome, a genetic disease that leads to type I IFN overexpression caused by impaired nucleic acid metabolism (*43*). AGS patients suffer clinical symptoms very similar to congenital infections, which is known as pseudo-TORCH syndrome. Thus, AGS serves as a proof of principle for the toxic effects of dysregulated fetal immune responses on human development.

Current therapies and future directions

For women who have been exposed to a viral infection during pregnancy, current therapies focus on limiting viral replication. For example, hyperimmunoglobulin is recommended after exposure to VZV (*3*), and antiretroviral therapy is effective at preventing HIV transmission from mother to fetus (*1*). For many other viruses, this strategy is limited by the general lack of effective antiviral therapies. A better mechanistic understanding of how viral infection disrupts fetal development will be crucial to designing future therapies that limit congenital diseases. In cases where immune responses mediate damage to the fetus, insights into molecular pathways that lead to viral control versus pathology will guide more targeted therapies against the latter. Some ongoing questions include: (i) During maternal infection with TORCH pathogens, what factors (maternal, fetal, and viral) determine whether a fetus will be infected and develop long-term sequelae? (ii) What role do the immune cells at the maternal–fetal interface, including Hofbauer cells and decidual immune cells, play in limiting viral spread, propagating viral infection (in the mother and fetus), and exacerbating disease? How do viral infections affect the normal developmental functions of these immune cells? (iii) Do fetal immune responses effectively control viral replication? Evolutionarily, how have in utero viral infections shaped fetal immune development both to limit immunopathology and control infection? (iv) Beyond IFNs, how do fetal antiviral immune responses mediate some of the diseases associated with congenital viral infection? (v) In addition to antibodies (see accompanying reviews in this issue), how do maternal immune responses reach and influence fetal development and viral control? (vi) How will emerging viral infections affect the short- and long-term health of both mother and fetus?

Given the distinct cell types at the maternal–fetal interface and the dynamic nature of fetal development, exploring viral–maternal–fetal tripartite interactions has the potential to reveal unexpected insights into developmental biology, immunology, and virology. In particular,

CREDIT: KELLIE HOLOSKI/*SCIENCE*

viral infections could be a functional probe with which to better understand immunological changes during pregnancy and fetal development. Principles learned while studying viral infections during pregnancy, such as the impacts on placental development and brain development, could then be applied to gaining a better understanding of the pathogenesis of other common nonviral pregnancy complications and congenital diseases.

REFERENCES AND NOTES

1. N. Neu, J. Duchon, P. Zachariah, *Clin. Perinatol.* **42**, 77–103 (2015).
2. S. Manicklal, V. C. Emery, T. Lazzarotto, S. B. Boppana, R. K. Gupta, *Clin. Microbiol. Rev.* **26**, 86–102 (2013).
3. K. M. Bialas, G. K. Swamy, S. R. Permar, *Clin. Perinatol.* **42**, 61–75 (2015).
4. B. Abu-Raya, T. R. Kollmann, A. Marchant, D. M. MacGillivray, *Front. Immunol.* **7**, 383 (2016).
5. B. J. S. al-Haddad *et al.*, *Am. J. Obstet. Gynecol.* **221**, 549–562 (2019).
6. G. Mor, P. Aldo, A. B. Alvero, *Nat. Rev. Immunol.* **17**, 469–482 (2017).
7. L. Pereira, *Annu. Rev. Virol.* **5**, 273–299 (2018).
8. N. Arora, Y. Sadovsky, T. S. Dermody, C. B. Coyne, *Cell Host Microbe* **21**, 561–567 (2017).
9. T. Liu *et al.*, *Int. J. Clin. Exp. Med.* **8**, 17248–17260 (2015).
10. D. J. Schust, A. B. Hill, H. L. Ploegh, *J. Immunol.* **157**, 3375–3380 (1996).
11. N. Nørskov-Lauritsen *et al.*, *J. Med. Virol.* **36**, 162–166 (1992).
12. M. T. Pérez-Gracia, B. Suay-García, M. L. Mateos-Lindemann, *Rev. Med. Virol.* **27**, e1929 (2017).
13. P. Gérardin *et al.*, *PLOS Negl. Trop. Dis.* **8**, e2996 (2014).
14. H. B. Bernstein, A. D. Wegman, *Clin. Obstet. Gynecol.* **61**, 122–136 (2018).
15. D. Di Mascio *et al.*, *Am. J. Obstet. Gynecol. MFM* 10.1016/j.ajogmf.2020.100107 (2020).
16. L. Chen *et al.*, *N. Engl. J. Med.* 10.1056/NEJMoa2002032 (2020).
17. A. Bayer *et al.*, *Cell Host Microbe* **19**, 705–712 (2016).
18. L. Reyes, T. G. Golos, *Front. Immunol.* **9**, 2628 (2018).
19. T. Takizawa, C. L. Anderson, J. M. Robinson, *J. Immunol.* **175**, 2331–2339 (2005).
20. N. Jabrane-Ferrat, *Front. Immunol.* **10**, 1397 (2019).
21. H. Quillay *et al.*, *Retrovirology* **13**, 39 (2016).
22. A. van der Zwan *et al.*, *Proc. Natl. Acad. Sci. U.S.A.* **115**, 385–390 (2018).
23. J. Siewiera *et al.*, *PLOS Pathog.* **9**, e1003257 (2013).
24. E. Rechavi, R. Somech, *Best Pract. Res. Clin. Obstet. Gynaecol.* **60**, 35–41 (2019).
25. A. Marchant *et al.*, *J. Clin. Invest.* **111**, 1747–1755 (2003).
26. T. L. Slatter *et al.*, *Mod. Pathol.* **28**, 1369–1382 (2015).
27. H. Puerta-Guardo *et al.*, *J. Infect. Dis.* **221**, 313–324 (2020).
28. S. H. James, D. W. Kimberlin, *Infect. Dis. Clin. North Am.* **29**, 391–400 (2015).
29. C. Li *et al.*, *Cell Stem Cell* **19**, 120–126 (2016).
30. H. Tang *et al.*, *Cell Stem Cell* **18**, 587–590 (2016).
31. T. Couderc *et al.*, *PLOS Pathog.* **4**, e29 (2008).
32. D. Ramful *et al.*, *Pediatr. Infect. Dis. J.* **26**, 811–815 (2007).
33. R. Vigneswaran, S. J. Aitchison, H. M. McDonald, T. Y. Khong, J. E. Hiller, *BMC Pregnancy Childbirth* **4**, 1 (2004).
34. S. E. Smith, J. Li, K. Garbett, K. Mirnics, P. H. Patterson, *J. Neurosci.* **27**, 10695–10702 (2007).
35. H. T. Ito, S. E. Smith, E. Hsiao, P. H. Patterson, *Brain Behav. Immun.* **24**, 930–941 (2010).
36. G. B. Choi *et al.*, *Science* **351**, 933–939 (2016).
37. Y. Shin Yim *et al.*, *Nature* **549**, 482–487 (2017).
38. I. Cardenas *et al.*, *J. Immunol.* **185**, 1248–1257 (2010).
39. G. M. Scott *et al.*, *J. Infect. Dis.* **205**, 1305–1310 (2012).
40. L. J. Yockey *et al.*, *Sci. Immunol.* **3**, eaao1680 (2018).
41. A. Zani *et al.*, *J. Biol. Chem.* **294**, 19844–19851 (2019).
42. J. Buchrieser *et al.*, *Science* **365**, 176–180 (2019).
43. Y. J. Crow, N. Manel, *Nat. Rev. Immunol.* **15**, 429–440 (2015).

ACKNOWLEDGMENTS

Funding: This work was supported by the National Institutes of Health (grants AI054359, R01EB000487, R01AI127429, and R21AI131284 to A.I.). A.I. is an Investigator of the Howard Hughes Medical Institute. C.L. is a Pew Latin American Fellow. **Competing interests:** The authors declare no competing interests.

10.1126/science.aaz1960

REVIEW

Vaccination strategies to enhance immunity in neonates

Tobias R. Kollmann[1]*†, Arnaud Marchant[2]*†, Sing Sing Way[3]†

Neonates are particularly susceptible to infection. This vulnerability occurs despite their responsiveness to most vaccines. However, current vaccines do not target the pathogens responsible for most of the severe neonatal infections, and the time it takes to induce protective pathogen-specific immunity after vaccination limits protection in the first days to weeks of life. Alternative strategies include using vaccines to broadly stimulate neonatal immunity in a pathogen-agnostic fashion or vaccinating women during pregnancy to induce protective antibodies that are vertically transferred to offspring within their window of vulnerability. Protection may be further improved by integrating these approaches, namely vaccinating the neonate under the cover of vertically transferred maternal immunity. The rationale for and knowledge gaps related to each of these alternatives are discussed.

Infectious morbidity and mortality are highest in the first weeks after birth (*1*, *2*). This vulnerability is not unexpected, given the predominantly naïve phenotype of neonatal immune cells and distinctive immunological challenges at birth, which require discrimination between not only innocuous self-antigens and noninherited maternal antigens but also the wide assortment of foreign antigens associated with primary commensal colonization (*3*, *4*). Susceptibility to severe infection likely reflects a combination of these physiological constraints.

Vaccination remains one of the most cost-effective ways of preventing infection. Vaccines against poliomyelitis, hepatitis B, tuberculosis, tetanus, pertussis, diphtheria, *Haemophilus influenzae* type b (Hib), rotavirus, and measles are administered to millions of infants, preventing an estimated 2.5 million deaths each year (*5*). Although vaccination has clearly benefited older infants and children, it has been considerably less effective in the first month of life (*1*, *2*). The World Health Organization recommends vaccination against tuberculosis, hepatitis B, and polio as soon as possible after birth (<24 hours) to accelerate priming of protective immune components. Likewise, maternal vaccination protects against infection by certain pathogens through vertically transferred immunity (*6*). However, emerging evidence shows that neonatal infections in lower- and middle-income regions are caused by a diversity of pathogens (Fig. 1). A recent meta-analysis identified *Staphylococcus aureus*, *Klebsiella*, and *Escherichia coli* spp. as the dominant causes of bacteremia and sepsis in neonates (infants younger than 28 days) in sub-Saharan Africa (*7*). *Ureaplasma* spp. and Group B *Streptococcus* were most frequently identified among cases of suspected early onset sepsis (infants 3 days or younger) in South Africa (*8*), whereas respiratory syncytial virus (RSV) and *Ureaplasma* spp. were the most commonly identified pathogens in cases of possible serious bacterial infection in infants younger than 60 days in Southeast Asia (*9*). Notably, none of these pathogens are covered by vaccines currently in clinical use (Fig. 1). Furthermore, the inciting pathogen was not identified in >70% of cases of clinically suspected infection, despite the use of cutting-edge diagnostic approaches (*8*, *9*). Although some of these undiagnosed cases may not be bona fide infections, the proportion of causative pathogens missed by vaccination is still likely to be greater than currently appreciated. Thus, alternative strategies to enhance early life immunity against a wide variety of pathogens are needed. We summarize the principles underpinning vaccination of neonates and their mothers, including increasingly recognized pathogen-agnostic benefits, which highlight the need to consider the mother–newborn dyad as one immunological unit to optimally enhance early life immunity.

Pathogen-specific immunity after neonatal vaccination

The neonate is often inappropriately considered "immature" and therefore presumed unable to respond to vaccination. Dampened antibody responses to T cell–independent polysaccharide antigens of encapsulated bacterial pathogens, including Hib and pneumococcus, until 2 years of age correlate with reduced marginal-zone B cells. Nonetheless, the conjugation to protein carriers activates T cells, resulting in robust protective antibody responses even in neonates (*10*). Similarly, diphtheria–tetanus–whole cell pertussis and some acellular pertussis vaccine formulations have been described to elicit reduced responses in neonates compared with older infants (*11*). However, monovalent acellular pertussis vaccines administered to neonates induce strong primary responses and do not induce tolerance to vaccine boosters (*12*). Compared with older infants, neonates are just as, if not more, responsive to vaccines currently included in neonatal immunization programs, namely bacillus Calmette-Guérin (BCG) vaccine, oral polio vaccine (OPV), and hepatitis B vaccine (*13*, *14*). The serological response of the neonate is also robust in response to other vaccines not currently licensed for neonatal administration, for example, those targeting rotavirus, diphtheria, and tetanus (*10*).

Even live vaccines have an outstanding safety record in neonates. Disseminated BCG infection is exceptionally rare (<1 per one million vaccine recipients) and almost exclusively occurs in infants with underlying immune deficiency (*15*). Vaccine-associated polio primarily occurs in underimmunized populations, which facilitate person-to-person spread, persistence, and eventual reversion into a more virulent phenotype. Vaccine-associated polio is expected to further decline with reformulation of trivalent to bivalent OPV (*16*). Furthermore, evidence of similar rates of infection by non–vaccine-targeted pathogens in older children regardless of prior cumulative vaccine exposure argues against the misconception that vaccines may overload and weaken the immune system (*17*). Thus, neonates are exceedingly capable of responding robustly and safely to most vaccines.

Given that neonates are capable of robust vaccine responses, why have current vaccination programs not lead to mortality reductions in neonates that are comparable to those in older infants and children? First, current vaccines administered to neonates do not specifically target the pathogens that cause severe infection in the first weeks of life (Fig. 1). Although tuberculosis, hepatitis B, and polio can be acquired within the first weeks after birth, these infections clinically manifest mostly outside of the neonatal period. For pathogens that do cause severe infection in the first weeks after birth, such as RSV, *Ureaplasma*, and several other bacteria, vaccines are either unavailable or have not yet been tested in neonates. Second, priming a protective adaptive immune response in predominantly naïve neonatal cells often takes weeks (*18*), whereas infections can cause morbidity and mortality within the first few days after birth (*1*, *2*) (Fig. 2A). This discordance between when infections occur and the time it takes to prime protective pathogen-specific immunity makes strategies aimed at inducing protective neonatal adaptive immune components challenging. To more effectively protect against infections manifesting in the neonatal period, alternative strategies, such as boosting resistance through non–pathogen-specific (i.e., pathogen-agnostic) approaches

[1]Systems Vaccinology, Telethon Kids Institute, Nedlands, WA 6009, Australia. [2]Institute for Medical Immunology, Université libre de Bruxelles, 6041 Charleroi, Belgium. [3]Center for Inflammation and Tolerance and Division of Infectious Disease, Cincinnati Children's Hospital, Cincinnati, OH 45229, USA.
*These authors contributed equally to this work.
†Corresponding author. Email: tobias.kollmann@telethonkids.org.au (T.R.K.); arnaud.marchant@ulb.be (A.M.); singsing.way@cchmc.org (S.S.W.)



Fig. 1. Current maternal and neonatal vaccines do not cover most pathogens associated with severe infection in early life. Relative proportion of each pathogen, represented by the size of each segment, identified in recent studies of suspected sepsis in early life (*7*–*9*). The top pathogens from each study are shown, covering >90% of cases in which a pathogen was identified. Age range (in days) and number of neonates are shown for each study.

and/or promoting transfer of pathogen-specific maternal immunity, must be considered.

Pathogen-agnostic protection after neonatal vaccination

Accumulating evidence shows that live vaccines can broadly enhance host resilience against infection beyond their specific pathogen target (*19*, *20*). A recent meta-analysis encompassing >6000 low–birth weight neonates attributed an additional 38% reduction in neonatal mortality to BCG vaccine administered at birth, beyond protection against tuberculosis (*21*). A separate study including >7000 neonates showed a 40% reduction in mortality when OPV was administered with BCG vaccine within the first 2 days of life (*22*). These pathogen-agnostic protective effects appear to be fast-acting, because substantial reduction in overall neonatal mortality can be identified within the first 3 days after BCG vaccine administration (*21*), in contrast to the weeks required to achieve pathogen-specific immunity. Enhanced serological responsiveness to other vaccines in neonates administered BCG vaccine at birth further highlights the broad immunostimulatory effects of BCG vaccination (*23*).

Mechanisms by which live vaccines confer pathogen-agnostic protective effects have not been established, but they likely include cross-reactive T cells (e.g., heterologous immunity) or activation of innate immune components (e.g., trained immunity) (*19*, *20*). Another unresolved question is whether pathogen-agnostic protective effects primed by live vaccines are restricted to the neonatal period. Analysis of >15,000 children in rural Guinea-Bissau showed that mortality reductions associated with BCG vaccine scarring were limited to children vaccinated within the first 4 weeks of life, with the most pronounced effect observed among those vaccinated within the first week of life (*24*). Although a distinctive window of opportunity in the neonatal period could be inferred from these data, this pathogen-agnostic protection has also been shown for older infants administered other live vaccines (*25*, *26*). An expanded window of plasticity for pathogen-agnostic immunity is supported by similar reductions in childhood mortality associated with live attenuated measles vaccine administered after 4 months of age (*27*). Given that pathogen-agnostic approaches have the potential to confer broad and fast protection to the neonate—bypassing each of the drawbacks associated with current pathogen-specific strategies for neonatal immunization—establishing protective mechanisms is an important next step.

Pathogen-specific immunity after vaccinating mothers

Multiple adaptations occur during pregnancy to accommodate growth and avert rejection of the semiallogeneic fetus. These tolerogenic adaptations are likely anatomically confined and/or restricted to cells with fetal specificity, because the response to vaccines administered during pregnancy is largely comparable to that of nonpregnant women (*28*). Vertically transferred maternal antibodies protect offspring in the early postnatal period (*6*). An important distinction between vaccination of mothers and neonatal immunization is the transient nature of the protective benefits conferred by non-self-renewing antibodies that functionally persist in infants only for several months, thereby deferring infection until the consequences are less severe (Fig. 2B).

Vaccination during pregnancy has already been shown to be effective for several important pathogens. For example, tetanus vaccination of pregnant women reduces neonatal mortality from tetanus by >90% (*29*). Protection of infants against respiratory illness and confirmed influenza infection ranges from 30 to 60% when mothers are vaccinated during pregnancy (*30*). Protective efficacy against pertussis in the first 2 to 3 months of life is ~90% after maternal vaccination (*31*). In light of these considerable benefits, developing vaccines for pregnant women that target other neonatal pathogens should be prioritized.

Maternal antibodies transferred across the placenta are almost exclusively immunoglobulin G (IgG), the levels of which exponentially increase in fetal tissues during the final weeks of gestation. Transfer is coordinated by binding to Fc receptors expressed by trophoblasts, macrophages, and endothelial cells, with preferential transfer of some isotypes (*32*). The accelerated transfer of maternal antibodies in later gestation means that immunity primed by maternal vaccination is drastically different for preterm infants. IgG levels are also reduced among small-for-gestational-age infants, as well as infants born to mothers with chronic infections, such as HIV or placental malaria (*33*). Maternal IgA and IgG antibodies are also transferred through

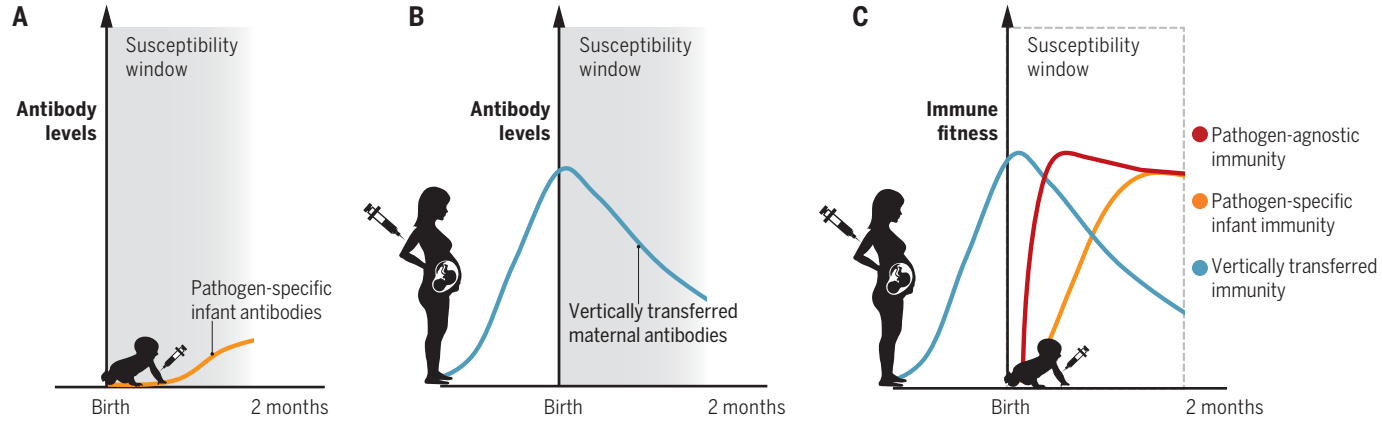


Fig. 2. Tempo of immunity provided by vaccination at birth compared with vaccination during pregnancy in relation to the neonatal window of infection susceptibility. (**A**) Antibody levels primed by neonatal vaccination increase with delayed tempo, which offers suboptimal protection during the early life window of susceptibility. (**B**) Maternal immunization provides high levels of pathogen-specific antibodies at birth and is an effective strategy for narrowing the window of susceptibility to specific pathogens. (**C**) Combining maternal vaccination with pathogen-agnostic and pathogen-specific benefits of neonatal vaccination may contribute equally to optimal neonatal immune fitness and efficiently close the early life window of susceptibility.

breastfeeding, and increased levels of both isotypes can be detected in breastmilk after vaccination during pregnancy (*28*). Optimal protection of neonates will require establishing the molecular determinants of antibodies transferred through breastmilk and whether they functionally complement placentally transferred antibodies.

Although vaccination during pregnancy raises concerns regarding safety, the vaccines currently administered to pregnant women have excellent safety profiles. There is no evidence of increased pregnancy complications with inactivated vaccines adjuvanted with alum or oil-based emulsions (*34*). Live attenuated vaccines, however, are currently not recommended during pregnancy. Nonetheless, analysis after their inadvertent administration suggests that they are safe. Rubella virus vaccine administration to >3500 pregnant women with documented serological susceptibility did not cause congenital rubella syndrome, and only one case of asymptomatic virus shedding was reported (*35*). Administration of OPV or yellow fever vaccine in outbreak settings did not cause increased rates of growth retardation, congenital anomalies, or pregnancy complications in women vaccinated during pregnancy (*34*). One potential exception is smallpox vaccination; But even in this case, the largest meta-analysis (including >12,000 pregnant women) showed only marginally increased (relative risk: 1.3) incidence of congenital defects, with a similar incidence of other complications, including spontaneous abortion, stillbirth, and preterm birth (*36*). Thus, most live vaccines appear to be safe during pregnancy.

Linking the mother–newborn dyad

Chronic maternal infection with a variety of pathogens can affect infant health independently from pathogen transmission (*37*), along with the tempo and quality of immune development (*38*). HIV-exposed but uninfected infants have reduced levels of maternal antibodies and show increased susceptibility to severe infection by unrelated pathogens compared with infants not exposed to HIV (*39*). Cord blood cells from neonates born to mothers with chronic hepatitis B virus infection produce increased antimicrobial cytokines after stimulation with various bacterial pathogens (*40*). These phenotypic changes in neonatal immune cells may reflect stimulation by antigens transferred in utero, with evidence of both activating and tolerogenic impacts on fetal immune components (*41*, *42*). Maternal programming of neonatal immunity also persists after birth by way of cells, cytokines, and antibodies acquired through breastfeeding (*43*) and by maternal cells that establish microchimerism (*44*). Thus, immune fitness, defined as resistance to severe infection, is dominantly influenced by maternal immunological experience.

Vertical transfer of maternal antibodies is teleologically conserved, and enriched for glycosylated antibodies that promote antimicrobial activity in neonates (*6*, *32*, *33*, *45*). Vertically transferred immunity can also dominantly influence the response of offspring to vaccination. High-titer maternal antibodies have often been associated with diminished primary antibody response of infants to vaccines (*46*, *47*). A classical study prompted by increased symptomatic measles infection among children immunized before their first birthday showed a muted serological response in children with high-titer pre-vaccination antibodies and increased responsiveness in children with reduced pre-vaccine titers (*48*). Interference of infant serological response is also observed for other live and inactivated vaccines, although the reduction magnitude is variable between studies and individual vaccines (*33*, *49*, *50*).

Interference by preexisting antibodies is not specific to infants and instead likely reflects control of excessive antibody production classically described in adults (*51*). Masking of immunodominant epitopes, regulation of B cell activation and germinal center maturation, and B cell inhibition through FcγRIIB cross-linking are potential mechanisms (*52*, *53*). The priming of memory B cells is much less sensitive to the presence of high titers of preexisting antibodies, because infant responses to vaccine boosters are consistently preserved with primary vaccination under the cover of high titers of maternal antibodies (*54*–*56*). T cell priming also appears to be intact, because the presence of antibodies affects neither proliferation nor effector cytokine production (*57*, *58*). Thus, interference is generally restricted to the primary serological response of offspring to vaccination. However, the clinical implications remain uncertain, because memory B and T cell responses primed by vaccination of neonates under the cover of maternal immunity remain intact.

Vaccination during early infancy under the cover of maternal immunity may in fact prime responses that are more protective, especially considering the aforementioned pathogen-agnostic protective benefits of live vaccines. A 78% reduction in mortality was shown for infants administered live attenuated measles vaccine at 4.5 months of age in the presence of maternal measles antibodies at the time of vaccination (*27*). The reduction of infant mortality associated with BCG vaccination in the neonatal period is further enhanced among infants born to mothers with prior BCG priming (*59*). A more balanced response by vertically transferred innate and adaptive maternal factors including antibodies, cytokines, cells, or metabolites likely explains these enhanced protective benefits. Considering this potential to enhance antimicrobial host defense, further narrowing the window of neonatal susceptibility against a wide range of pathogens will likely require

stimulating pathogen-agnostic and pathogen-specific immunity by neonatal immunization under the cover of maternal immunity (Fig. 2C).

Outlook

Neonatal infection is a complex, multifaceted problem with many critical dimensions yet to be defined. The pathogens associated with neonatal infections in low-to-middle income areas have only recently been systemically evaluated using modern diagnostic tools (*8*, *9*) (Fig. 1). The wide range of identified bacteria and viruses with varying virulence, combined with the large fraction of cases where a specific pathogen was not identified, suggests that complex immunological perturbations in the neonatal period drive clinical sepsis. Future diagnostic and treatment strategies will need to go beyond current approaches, which are narrowly focused on specific inciting pathogens. Likewise, designing vaccines that target the mother–newborn dyad implies knowledge of how mother and child are immunologically linked. However, current knowledge of how human pregnancy is sustained remains rudimentary. The necessity for specific molecules and immune cell subsets in maintaining maternal–fetal tolerance has almost exclusively been established using preclinical pregnancy models (rodents), which do not recapitulate the more prolonged gestational length and in utero accumulation of fetal adaptive immune components observed in humans (*60*).

Despite our present ignorance, vaccines that prime pathogen-specific immunity in the maternal–fetal dyad clearly work. We are on the brink of eradicating poliomyelitis with vaccines administered to neonates. Eliminating neonatal tetanus is also within reach by way of maternal vaccination. Boosted pathogen-agnostic immunity primed by live vaccines also shows promise, with nearly 40% reductions in overall infant mortality (*21*, *22*, *52*). These successes clearly highlight the protective potential of neonatal and maternal immune components. Enhanced protection will likely require previously unexplored strategies that combine vaccination of mothers and their newborns to simultaneously stimulate pathogen-agnostic and pathogen-specific immunity (Fig. 2C). Physicians are instructed to first "do no harm." This instills a reflexive reluctance to deviate from the status quo. Unfortunately, the current status quo is that nearly half of under-age-5 mortality occurs in neonates, and a large fraction of these deaths are due to infection. Perhaps actively excluding pregnant mothers and newborns from vaccine research is inadvertently causing even more harm. The priority should be to protect these vulnerable populations through research, not from it.

REFERENCES AND NOTES

1. H. Wang *et al*., *Lancet* **384**, 957–979 (2014).
2. T. Wardlaw, D. You, L. Hug, A. Amouzou, H. Newby, *Reprod. Health* **11**, 82 (2014).
3. T. R. Kollmann, B. Kampmann, S. K. Mazmanian, A. Marchant, O. Levy, *Immunity* **46**, 350–363 (2017).
4. S. Elahi *et al*., *Nature* **504**, 158–162 (2013).
5. C. A. MacLennan, A. Saul, *Proc. Natl. Acad. Sci. U.S.A.* **111**, 12307–12312 (2014).
6. F. M. Munoz, D. J. Jamieson, *Obstet. Gynecol.* **133**, 739–753 (2019).
7. U. Okomo *et al*., *Lancet Infect. Dis.* **19**, 1219–1234 (2019).
8. S. C. Velaphi *et al*., *PLOS ONE* **14**, e0214077 (2019).
9. S. K. Saha *et al*., *Lancet* **392**, 145–159 (2018).
10. A. Saso, B. Kampmann, *Semin. Immunopathol.* **39**, 627–642 (2017).
11. L. W. Sauer, *Ill. Med. J.* **97**, 73–76 (1950).
12. N. Wood *et al*., *JAMA Pediatr.* **172**, 1045–1052 (2018).
13. M. O. Ota *et al*., *Vaccine* **22**, 511–519 (2004).
14. F. J. Mateen, R. T. Shinohara, R. W. Sutter, *Vaccine* **31**, 2517–2524 (2013).
15. J. M. Grange, *Commun. Dis. Public Health* **1**, 84–88 (1998).
16. L. R. Platt, C. F. Estívariz, R. W. Sutter, *J. Infect. Dis.* **210** (suppl. 1), S380–S389 (2014).
17. J. M. Glanz *et al*., *JAMA* **319**, 906–913 (2018).
18. S. K. Burchett *et al*., *J. Infect. Dis.* **165**, 813–818 (1992).
19. L. C. J. de Bree *et al*., *Semin. Immunol.* **39**, 35–43 (2018).
20. H. S. Goodridge *et al*., *Nat. Rev. Immunol.* **16**, 392–400 (2016).
21. S. Biering-Sørensen *et al*., *Clin. Infect. Dis.* **65**, 1183–1190 (2017).
22. N. Lund *et al*., *Clin. Infect. Dis.* **61**, 1504–1511 (2015).
23. M. O. Ota *et al*., *J. Immunol.* **168**, 919–925 (2002).
24. L. Storgaard *et al*., *Clin. Infect. Dis.* **61**, 950–959 (2015).
25. F. Shann, *Trans. R. Soc. Trop. Med. Hyg.* **109**, 5–8 (2015).
26. S. R. Newcomer *et al*., *Pediatr. Infect. Dis. J.* **39**, 247–253 (2020).
27. P. Aaby *et al*., *BMJ* **307**, 1308–1311 (1993).
28. A. Marchant *et al*., *Lancet Infect. Dis.* **17**, e197–e208 (2017).
29. H. Blencowe, J. Lawn, J. Vandelaer, M. Roper, S. Cousens, *Int. J. Epidemiol.* **39** (suppl. 1), i102–i109 (2010).
30. S. A. Madhi *et al*., *N. Engl. J. Med.* **371**, 918–931 (2014).
31. G. Amirthalingam *et al*., *Lancet* **384**, 1521–1528 (2014).
32. C. R. Wilcox, B. Holder, C. E. Jones, *Front. Immunol.* **8**, 1294 (2017).
33. G. G. Fouda, D. R. Martinez, G. K. Swamy, S. R. Permar, *Immunohorizons* **2**, 14–25 (2018).
34. B. Keller-Stanislawski *et al*., *Vaccine* **32**, 7057–7064 (2014).
35. J. Hofmann *et al*., *J. Med. Virol.* **61**, 155–158 (2000).
36. M. L. Badell *et al*., *Obstet. Gynecol.* **125**, 1439–1451 (2015).
37. N. Dauby, T. Goetghebuer, T. R. Kollmann, J. Levy, A. Marchant, *Lancet Infect. Dis.* **12**, 330–340 (2012).
38. T. Goetghebuer *et al*., *Clin. Infect. Dis.* **68**, 1193–1203 (2019).
39. C. Evans, C. E. Jones, A. J. Prendergast, *Lancet Infect. Dis.* **16**, e92–e107 (2016).
40. M. Hong *et al*., *Nat. Commun.* **6**, 6588 (2015).
41. C. R. Wilcox, C. E. Jones, *Front. Immunol.* **9**, 1548 (2018).
42. Y. Tian, C. F. Kuo, O. Akbari, J. H. Ou, *Immunity* **44**, 1204–1214 (2016).
43. A. Laouar, *Trends Immunol.* **41**, 225–239 (2020).
44. J. M. Kinder, I. A. Stelzer, P. C. Arck, S. S. Way, *Nat. Rev. Immunol.* **17**, 483–494 (2017).
45. M. F. Jennewein *et al*., *Cell* **178**, 202–215.e14 (2019).
46. S. Niewiesk, *Front. Immunol.* **5**, 446 (2014).
47. C. A. Siegrist, *J. Pediatr.* **153**, 305–307 (2008).
48. P. Albrecht, F. A. Ennis, E. J. Saltzman, S. Krugman, *J. Pediatr.* **91**, 715–718 (1977).
49. M. Voysey *et al*., *JAMA Pediatr.* **171**, 637–646 (2017).
50. K. M. Edwards, *Vaccine* **33**, 6469–6472 (2015).
51. J. W. Uhr, G. Möller, *Adv. Immunol.* **8**, 81–127 (1968).
52. M. Vono *et al*., *Cell Rep.* **28**, 1773–1784.e5 (2019).
53. D. Kim, D. Huey, M. Oglesbee, S. Niewiesk, *Blood* **117**, 6143–6151 (2011).
54. K. Maertens *et al*., *Vaccine* **34**, 3613–3619 (2016).
55. F. M. Munoz *et al*., *JAMA* **311**, 1760–1769 (2014).
56. S. A. Halperin *et al*., *Clin. Infect. Dis.* **67**, 1063–1071 (2018).
57. H. A. Gans *et al*., *J. Infect. Dis.* **190**, 83–90 (2004).
58. H. A. Gans *et al*., *J. Immunol.* **162**, 5569–5575 (1999).
59. M. L. T. Berendsen *et al*., *J. Pediatric Infect. Dis. Soc.* 10.1093/jpids/piy142 (2019).
60. J. E. Mold, J. M. McCune, *Adv. Immunol.* **115**, 73–111 (2012).

ACKNOWLEDGMENTS

We thank C. B. Wilson for his inspirational mentoring and pioneering contributions defining the field of early life immunology. We are indebted to contributions by numerous investigators in this field and apologize that many important references were unable to be discussed due to space constraints. **Funding:** T.R.K. is supported by NIH/NIAID U19AI118608 and Telethon Kids and Perth Children's Hospital Foundation. A.M. is research director at the Fonds de la Recherche Scientifique, F.R.S.-FNRS, Belgium. S.S.W. is supported through NIH grants DP1AI131080, R01AI120202, R01AI124657, and U01AI144673; the HHMI Faculty Scholar's Program; the Burroughs Wellcome Fund; and the March of Dimes Foundation Ohio Collaborative. **Competing interests:** The authors have no competing interests to declare.

10.1126/science.aaz9447

RESEARCH

IN *SCIENCE* JOURNALS

Edited by
Michael Funk



COLLOIDS

Complex chiral particles

Synthetic colloids are usually smooth, but nature can produce micrometer-scale particles with intricate structure and shape, such as the coccoliths produced by algae. Jiang *et al*. controlled the self-assembly of gold–cysteine nanoplatelets into a variety of chiral, hierarchically organized colloidal particles by changing the chiral fraction of cysteine and the nucleation temperature. Organic cations created electrostatic repulsions that favored edge assembly of the nanoplatelets, which in turn could create surfaces bearing twisted spikes. —PDS *Science*, this issue p. 642

False-color scanning electron microscopy image of cysteine-coated gold nanoplatelets

CORONAVIRUS

Targeting the SARS-CoV-2 spike

The surface of severe acute respiratory syndrome–coronavirus 2 (SARS-CoV-2) is decorated with trimeric spikes that bind to host cell receptors. These spikes also illicit an antibody response, so understanding antibody recognition may aid in vaccine design. Yuan *et al*. determined the structure of CR3022, a neutralizing antibody obtained from a convalescent SARS-CoV–infected patient, in complex with the receptor-binding domain of the SARS-CoV-2 spike. The antibody binds to an epitope conserved between SARS-CoV-2 and SARS-CoV that is distinct from the receptor-binding site. CR3022 likely binds more tightly to SARS-CoV because its epitope contains a glycan not present in SARS-CoV-2. Structural modeling showed that the epitope is only revealed when at least two of the three spike proteins are in a conformation competent to bind the receptor. —VV

Science, this issue p. 630

VACCINES

Sharpening focus for anti-RSV antibodies

Respiratory syncytial virus (RSV) is a paramyxovirus that infects lung epithelial cells, causing potentially severe infections in young children and elderly and immunocompromised persons. Although an effective RSV vaccine remains a major unmet medical need, previous work has identified a stabilized prefusion (pre-F) conformation of the RSV fusion protein as a preferred immunogen for eliciting neutralizing antibodies. Swanson *et al*. constructed a multimeric vaccine featuring a central ferritin core connected to eight trimeric pre-F spikes bearing engineered glycans that mask poorly neutralizing epitopes. This self-assembling nanoparticle vaccine induced stronger neutralizing antibody responses than pre-F trimers in both mice and nonhuman primates. These studies pave the way toward initiating clinical trials to test this vaccine's ability to protect vulnerable human populations from RSV-associated disease. —IRW

Sci. Immunol. **5**, eaba6466 (2020).

CHEMICAL PHYSICS

Atypical vibrational interactions

Vibrational energy transfer (VET) between solute molecules is generally unfavorable in liquids because of weak intermolecular forces. Xiang *et al*. measured the two-dimensional infrared spectrum of a molecular mixture, $W(CO)_6$ and $W(^{13}CO)_6$, with saturated concentrations in a binary solvent embedded in an optical microcavity. This experiment showed that the VET between the asymmetric stretch vibrations of two solute molecules is enhanced via polaritonic intermediate states formed by a strong coupling with the cavity mode. The efficiency is modulated by the cavity lifetime, which provides an

IMAGE: JIANG *ET AL.*

Published by AAAS

opportunity to control the VET process in the liquid phase. This could lead to various practical implementations. —YS

Science, this issue p. 665

ASTEROIDS

Collecting a sample of asteroid Ryugu

The Hayabusa2 spacecraft recently traveled to the nearby carbonaceous asteroid Ryugu to collect samples and return them to Earth for laboratory analysis. Morota *et al*. describe Hayabusa2's first sample collection, taken during a brief touchdown on Ryugu's surface. Close-up images and video taken during the sampling process allowed the authors to investigate the surface colors and morphology on a small scale. Relating these to the surface craters and stratigraphy constrains the evolution of Ryugu. The authors conclude that the asteroid experienced a prior period of strong solar heating caused by changes in its orbit. The sample is expected to arrive on Earth in December 2020. —KTS

Science, this issue p. 654

SEPSIS

The vaccine that keeps on giving

Bacille-Calmette-Guérin (BCG) is a vaccine often given to infants in countries with a high incidence of tuberculosis infection. However, emerging evidence suggests that this tuberculosis vaccine may have additional beneficial effects for the infants. Following on previous observations of reduced neonatal mortality in BCG-vaccinated infants, Brook *et al*. performed a systematic study of mouse models and human infants in multiple countries. The authors demonstrated that BCG given during the neonatal period protected infants from death due to sepsis, possibly because of the rapid increase in neutrophils driven by the vaccine. —YN

Sci. Transl. Med. **12**, eaax4517 (2020).

CORONAVIRUS

The most effective interventions

By 23 February 2020, China had imposed a national emergency response to restrict travel and impose social distancing measures on its populace in an attempt to inhibit the transmission of severe acute respiratory syndrome–coronavirus 2 (SARS-CoV-2). However, which measures were most effective is uncertain. Tian *et al*. performed a quantitative analysis of the impact of control measures between 31 December 2019 and 19 February 2020, which encompasses the Lunar New Year period when millions of people traveled across China for family visits. Travel restrictions in and out of Wuhan were too late to prevent the spread of the virus to 262 cities within 28 days. However, the epidemic peaked in Hubei province on 4 February 2020, indicating that measures such as closing citywide public transport and entertainment venues and banning public gatherings combined to avert hundreds of thousands of cases of infection. It is unlikely that this decline happened because the supply of susceptible people was exhausted, so relaxing control measures could lead to a resurgence. —CA

Science, this issue p. 638



An infant bearing a small scar from the BCG vaccine, which provides direct protection from tuberculosis and some nonspecific protection from sepsis

PHOTOS (FROM LEFT): SCIENCE PHOTO LIBRARY/ALAMY STOCK PHOTO; STEVECOLEIMAGES/GETTY IMAGES

IN OTHER JOURNALS

Edited by **Caroline Ash** *and* **Jesse Smith**



MATERIALS SCIENCE

Beat the heat! Stop the smoking!

Polyurethane foams are widely used in upholstered furniture and mattresses but pose a fire hazard because they can be highly flammable. Flame and heat retardants are used to make these materials safer, but they can have issues regarding cost or toxicity. Fahami *et al*. show that three common, inexpensive materials can be used to make a flame retardant. Foams were coated with chitosan-stabilized mica and then poly(acrylic acid)-stabilized mica in a layer-by-layer process with repeated cycling to build up thicker coatings to open cell foams. They found that the coated foams resisted dripping when exposed to heat and would self-extinguish during a 10-second torch test. Further, when exposed to a heat test, the coatings reduced the release of volatile components and smoke from the foam. —MSL

ACS Appl. Mater. Interfaces **12**, 19938 (2020).

An inexpensive, nontoxic flame retardant for the polyurethane foams often used in furniture can be made from specially treated mica.

LUNG DISEASE

Odd stem cells obstruct breath

Chronic obstructive pulmonary disease (COPD) is a progressive lung disease characterized by inflammation, fibrosis, and excessive secretion of mucus. About 250 million people have COPD and it is a leading cause of death worldwide. Rao *et al*. identified three different stem cell variants in the lung fluid of COPD patients and hypothesized that these cells might play a pathogenic role. To test this, they injected the variant cells into the lungs of mice and found that the animals indeed

Published by AAAS

POLLINATION

Floral recovery from accidents

Plants in the field layer may be susceptible to damage, with their stems bent or twisted by wind, falling objects, or trampling. For flowers specialized to attract insect pollinators, such accidents can cause changes in orientation that could decrease the chances of successful pollination. In experiments with a range of herbaceous species, Armbruster and Muchhala compared the postinjury responses of bilaterally symmetrical flowers with those of radially symmetrical flowers. Bilateral flowers mostly showed the ability to correct their position though reorientation of the floral stem or the floral sexual organs themselves, resulting in restoration of pollination efficiency. Few radially symmetrical flowers showed the same ability because their orientation had little effect on pollination accuracy. —AMS

New Phytol. 10.1111/nph.16482 (2020).



Flowers with an asymmetrical structure, like this pelargonium, will reorientate to encourage pollinators if their stems become damaged.

PHOTO: W. SCOTT ARMBRUSTER

developed many signature features of COPD. Patients with COPD currently receive treatment for their symptoms, not for the disease. These new results raise the possibility that the variant stem cells, or the factors they secrete, could be valuable therapeutic targets. —PAK

Cell 10.1016/j.cell.2020.03.047 (2020).

CELL BIOLOGY

Stress relief

How can tissues maintain functional integrity during exposure to high levels of mechanical stress? Specifically, how does a cell's nucleus cope? Heterochromatin can dynamically rearrange its epigenetic state and architecture when stressed, which alters the mechanical properties of chromatin and the nucleus to mitigate DNA damage. Using mice, Nava *et al*. combined stem cell biology and mechanobiology to study epidermal stem cells and skin tissue that might be expected to experience stretching. Mechanical strain on epithelial sheets triggered stem cell nucleus deformation, which induced calcium release from the endoplasmic reticulum via Piezo1 channels. Calcium signaling altered the architecture, epigenetics, and mechanical state of heterochromatin to dissipate mechanical energy and minimize DNA damage. Stem cells subjected to continuous mechanical stress over longer periods of time became aligned perpendicular to the direction of strain to redistribute mechanical stress. —SMH

Cell 10.1016/j.cell.2020.03.052 (2020).

GALAXIES

Missing gas cooling in distant galaxies

Gas in galaxies is heated by ultraviolet light from hot stars, which must be balanced by cooling to maintain the gas temperature. In nearby galaxies, cooling is mostly through a [C II] line at 158 micrometers. It's unclear whether this applies in the distant Universe, when star formation was more intense, less carbon was available, and gas may have been hotter. McKinney *et al*. searched for the [C II] line in six galaxies at redshift ~2. They detected [C II] in only one source, finding that the line is generally weaker than expected from indirect measurements of the galaxies' ultraviolet heating. Therefore, something else must dominate gas cooling in these distant galaxies. —KTS

Astrophys. J. **892**, 119 (2020).

SCIENTIFIC WORKFORCE

Does diversity breed innovation?

If diversity breeds innovation, and innovation is predictive of success, do underrepresented scientists generate more novel innovations? To compare minority and majority scholars' rates of scientific novelty, Hofstra *et al*., used machine learning to analyze a population of ~1.2 million U.S. doctoral recipients to identify scientific innovations, investigate the rates at which these innovations get taken up by others, and examine the impact these innovations have on scientific careers. Results show that rewards are similar for low-impact innovation; however, as impact novelty increases, minority contributions become devalued and are taken up at lower rates. This study reveals a stratified system in which minorities need to innovate at higher levels to achieve similar levels of career success, further stressing the critical need to address biases in research evaluation and publication. —MMc

Proc. Natl. Acad. Sci. U.S.A. **117**, 9284 (2020).

AGRICULTURE

Food shares for all

Although local crop yields may vary, food exchange between human populations mitigates that variability. O'Dwyer analyzed mathematical models of exchange to predict effects on human population stability. When food is broadly scarce, as in times of drought, some patterns of food exchange help to maintain human populations, whereas others are destabilizing and lead to depopulation. Balanced reciprocity results in population stability across a range of agricultural productivity scenarios, whereas resource pooling does not. Thus, the pattern of food exchange that a society falls into may be a factor in determining their long-term stability. —PJH

One Earth **2**, 269 (2020).

Published by AAAS

ALSO IN *SCIENCE* JOURNALS

Edited by **Michael Funk**

CLIMATE

Challenges in tree-planting programs

Numerous tree-planting projects have been launched globally, but will they really help to improve environmental conditions? In a Perspective, Holl and Brancalion discuss the issues with tree-planting projects, including reforestation with non-native species, limited recovery of biodiversity, competing land uses, and lack of long-term management to ensure survival of planted trees. Although tree planting can be beneficial, there are numerous challenges to be overcome before this practice can be shown to improve the environment. —GKA

Science, this issue p. 580

CANCER

Tracking growth dynamics

Very few screening tests have increased the survival of individuals diagnosed with cancer. In a Perspective, Pashayan and Pharoah discuss the importance of understanding tumor growth dynamics, especially when metastases are seeded from the primary tumor. Metastasis is the major cause of mortality from cancer, so the ability to detect tumors before metastases arise is an important challenge. In particular, many tests based on imaging can only detect tumors of a certain size and others cannot discriminate which will progress, potentially causing harm. It is important to develop screening tests that can account for growth dynamics to identify individuals with tumors that are most likely to spread and cause mortality. —GKA

Science, this issue p. 589

CORONAVIRUS

Instantaneous contact tracing

New analyses indicate that severe acute respiratory syndrome–coronavirus 2 (SARS-CoV-2) is more infectious and less virulent than the earlier SARS-CoV-1, which emerged in China in 2002. Unfortunately, the current virus has greater epidemic potential because it is difficult to trace mild or presymptomatic infections. As no treatment is currently available, the only tools that we can currently deploy to stop the epidemic are contact tracing, social distancing, and quarantine, all of which are slow to implement. However imperfect the data, the current global emergency requires more timely interventions. Ferretti *et al*. explored the feasibility of protecting the population (that is, achieving transmission below the basic reproduction number) using isolation coupled with classical contact tracing by questionnaires versus algorithmic instantaneous contact tracing assisted by a mobile phone application. For prevention, the crucial information is understanding the relative contributions of different routes of transmission. A phone app could show how finite resources must be divided between different intervention strategies for the most effective control. —CA

Science, this issue p. 619

BIOMEDICINE

Elesclomol rescues Menkes disease mice

Menkes disease results from loss-of-function mutations in the P-type copper-transporting adenosine triphosphatase ATP7A. Children diagnosed with Menkes present with connective tissue abnormalities and neurodegenerative changes that result in death caused by severe copper deficiency, typically before 3 years of age. In the brain, lack of copper impairs cytochrome c oxidase (complex IV) in the electron transport chain, which leads to progressive neurological injury in Menkes patients. No treatment exists for Menkes disease because of the difficulty in supplying the brain with copper using traditional hydrophilic copper complexes such as copper histidine. Guthrie *et al*. developed a treatment involving the drug elesclomol that successfully alleviated disease symptoms in a mouse model of Menkes disease (see the Perspective by Lutsenko). —SMH

Science, this issue p. 620; see also p. 584

ULTRACOLD CHEMISTRY

Ultracold molecular collision dynamics

Ultracold collision dynamics are of great importance in understanding the quantum nature of chemical interactions, but achieving the ultracold regime for molecules is challenging. Traditional techniques based on alternative routes to assemble the ultracold atomic constituents are only able to produce a type of ultracold molecules that cannot probe state-selective dynamics. Using Stark deceleration and velocity map–imaging techniques, de Jongh *et al*. achieved the ultracold regime directly for a nitric oxide–helium system and measured the state-to-state cross sections for inelastic scattering with high precision (see the Perspective by Yang and Yang). The observed scattering resonances confirmed high sensitivity to the underlying interaction potential because only the most accurate electronic structure theory could reproduce their structure. —YS

Science, this issue p. 626; see also p. 582

3D PRINTING

Circumventing spatter

Laser powder bed fusion is an additive manufacturing technique that laser-melts powder layer by layer to build a three-dimensional (3D) part. Khairallah *et al*. used experiments and a multiphysics model to determine the origin of the melt spatter and defect formation that degrade the properties of built parts (see the Perspective by Polonsky and Pollock). Informed modulation of laser power is important to avoid disturbing the powder bed and creating laser shadowing. This reduces pore formations and leads to more uniform properties of 3D-printed parts. —BG

Science, this issue p. 660; see also p. 583

BIOINSPIRED ROBOTS

Sensing surfaces like a mosquito

Although sonar or lidar are used by autonomous vehicles to detect nearby objects, these approaches incur significant equipment and signal-processing costs. Nakata *et al*. show that mosquitos detect surfaces using the flow fields caused by the movement of their own wings (see the Perspective by Young and Garratt). Near surfaces, there are small changes in the pressure and velocity that mosquitos can detect using their sensitive antennae. The authors translated this process into a simple, low-cost approach for detecting surfaces near a flying quadcopter. —MSL

Science, this issue p. 634; see also p. 586

SYNTHETIC BIOLOGY

Hybrid approach catches light

Plant chloroplasts enclose two major photosynthetic processes: light reactions, which generate the energy carriers adenosine

Published by AAAS

triphosphate and reduced nicotinamide dinucleotide phosphate (NADPH), and dark reactions, which use these molecules to fix carbon dioxide and build biomass. Miller *et al*. appropriated natural components, thylakoid membranes from spinach, for the light reactions and showed that these could be coupled to a synthetic enzymatic cycle that fixes carbon dioxide within water-in-oil droplets. The composition of the droplets could be tuned and optimized and the metabolic activity monitored in real time by NADPH fluorescence (see the Perspective by Gaut and Adamala). These chloroplast-mimicking droplets bring together natural and synthetic components in a small space and are amenable to further functionalization to perform complex biosynthetic tasks. —MAF

Science, this issue p. 649; see also p. 587

PAIN

Chaperones put the brakes on opioids

Until alternatives to opioids are developed, keeping opioid doses low but effective may be key to limiting their adverse effects. Duron *et al*. found that inhibitors of the chaperone protein Hsp90 enhanced the efficacy of systemically administered opioids in mice. In sensory neuron–rich regions of the spine, Hsp90 attenuated the activity of a kinase-regulated protein synthesis pathway required for the antinociceptive effects of opioids. In mice, blocking Hsp90 in the spine, but not in the brain or periphery, made opioids more effective at dampening sensitivity to heat and touch. —LKF

Sci. Signal. **13**, eaaz1854 (2020).

NEUROSCIENCE

A model to study HSV-Alzheimer's link

Herpes simplex virus type I (HSV-1) infection has been linked to the development of Alzheimer's disease (AD) in various ways, but direct evidence of a causal link has been missing, even for in vitro models. Cairns *et al*. used a human induced neural stem cell three-dimensional tissue model and demonstrated that infection with HSV-1 reproduces some features seen in AD patient brain tissues, such as large fibrillar plaques, gliosis, and neuroinflammation. Treatment with an antiviral drug diminished the observed phenotype. This model may be valuable for future mechanistic and therapeutic studies considering the link between HSV infection and AD. —LV

Sci. Adv. 10.1126/sciadv.aay8828 (2020).

Published by AAAS

RESEARCH ARTICLE SUMMARY

CORONAVIRUS

Quantifying SARS-CoV-2 transmission suggests epidemic control with digital contact tracing

Luca Ferretti*, Chris Wymant*, Michelle Kendall, Lele Zhao, Anel Nurtay, Lucie Abeler-Dörner, Michael Parker, David Bonsall†, Christophe Fraser†‡

INTRODUCTION: Coronavirus disease 2019 (COVID-19), caused by severe acute respiratory syndrome–coronavirus 2 (SARS-CoV-2), has clear potential for a long-lasting global pandemic, high fatality rates, and incapacitated health systems. Until vaccines are widely available, the only available infection prevention approaches are case isolation, contact tracing and quarantine, physical distancing, decontamination, and hygiene measures. To implement the right measures at the right time, it is of crucial importance to understand the routes and timings of transmission.

RATIONALE: We used key parameters of epidemic spread to estimate the contribution of different transmission routes with a renewal equation formulation, and analytically determined the speed and scale for effective identification and contact tracing required to stop the epidemic.

RESULTS: We developed a mathematical model for infectiousness to estimate the basic reproductive number R_0 and to quantify the contribution of different transmission routes. To parameterize the model, we analyzed 40 well-characterized source-recipient pairs and estimated the distribution of generation times (time from infection to onward transmission). The distribution had a median of 5.0 days and standard deviation of 1.9 days. We used published parameters for the incubation time distribution (median 5.2 days) and the epidemic doubling time (5.0 days) from the early epidemic data in China.

The model estimated R_0 = 2.0 in the early stages of the epidemic in China. The contributions to R_0 included 46% from presymptomatic individuals (before showing symptoms), 38% from symptomatic individuals, 10% from asymptomatic individuals (who never show symptoms), and 6% from environmentally mediated transmission via contamination. Results on the last two routes are speculative. According to these estimates, presymptomatic transmissions alone are almost sufficient to sustain epidemic growth.

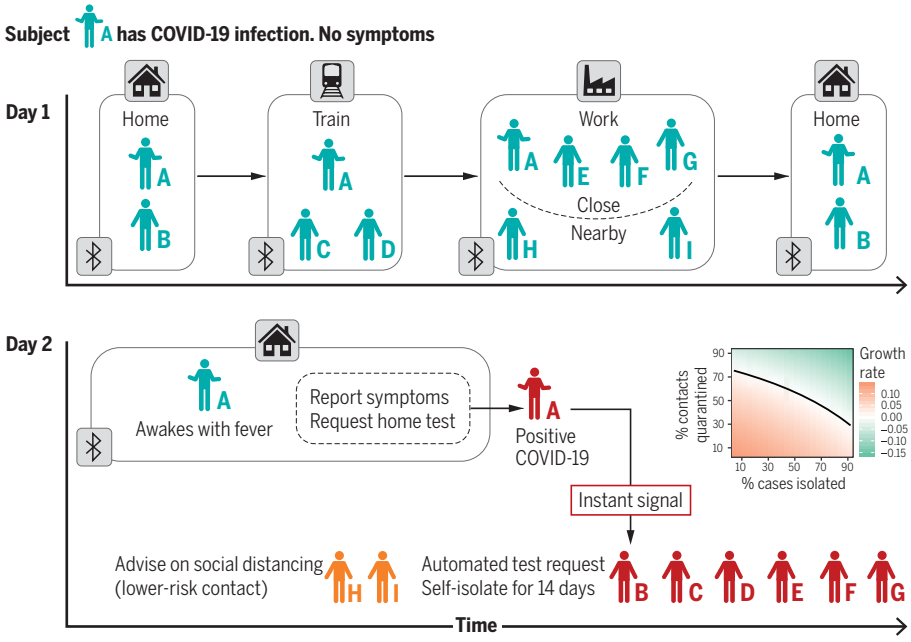
To estimate the requirements for successful contact tracing, we determined the combination of two key parameters needed to reduce R_0 to less than 1: the proportion of cases who need to be isolated, and the proportion of their contacts who need to be quarantined. For a 3-day delay in notification assumed for manual contact tracing, no parameter combination leads to epidemic control. Immediate notification through a contact-tracing mobile phone app could, however, be sufficient to stop the epidemic if used by a sufficiently high proportion of the population.

We propose an app, based on existing technology, that allows instant contact tracing. Proximity events between two phones running the app are recorded. Upon an individual's COVID-19 diagnosis, contacts are instantly, automatically, and anonymously notified of their risk and asked to self-isolate. Practical and logistical factors (e.g., uptake, coverage, R_0 in a given population) will determine whether an app is sufficient to control viral spread on its own, or whether additional measures to reduce R_0 (e.g., physical distancing) are required. The performance of the app in scenarios with higher values of R_0 can be explored at https://bdi-pathogens.shinyapps.io/covid-19-transmission-routes/.

ON OUR WEBSITE

Read the full article at https://dx.doi.org/10.1126/science.abb6936

CONCLUSION: Given the infectiousness of SARS-CoV-2 and the high proportion of transmissions from presymptomatic individuals, controlling the epidemic by manual contact tracing is infeasible. The use of a contact-tracing app that builds a memory of proximity contacts and immediately notifies contacts of positive cases would be sufficient to stop the epidemic if used by enough people, in particular when combined with other measures such as physical distancing. An intervention of this kind raises ethical questions regarding access, transparency, the protection and use of personal data, and the sharing of knowledge with other countries. Careful oversight by an inclusive advisory body is required. ■



Instant contact tracing can reduce the proportion of cases that need to be isolated and contacts who need to be quarantined to achieve control of an epidemic. Subject A becomes symptomatic after having had contact with other people in different settings the day before. Contacts are notified and quarantined where needed. In the inset, the green area indicates the success rates needed to control an epidemic with R_0 = 2 (i.e., negative growth rates after isolating cases and quarantining their contacts).

The list of author affiliations is available in the full article online.
*These authors contributed equally to this work.
†These authors contributed equally to this work.
‡Corresponding author. Email: christophe.fraser@bdi.ox.ac.uk
This is an open-access article distributed under the terms of the Creative Commons Attribution license (https://creativecommons.org/licenses/by/4.0/), which permits unrestricted use, distribution, and reproduction in any medium, provided the original work is properly cited.
Cite this article as L. Ferretti *et al.*, *Science* **368**, eabb6936 (2020). DOI: 10.1126/science.abb6936

RESEARCH ARTICLE

CORONAVIRUS

Quantifying SARS-CoV-2 transmission suggests epidemic control with digital contact tracing

Luca Ferretti[1]*, Chris Wymant[1]*, Michelle Kendall[1], Lele Zhao[1], Anel Nurtay[1], Lucie Abeler-Dörner[1], Michael Parker[2], David Bonsall[1,3]†, Christophe Fraser[1,4]†‡

The newly emergent human virus SARS-CoV-2 (severe acute respiratory syndrome–coronavirus 2) is resulting in high fatality rates and incapacitated health systems. Preventing further transmission is a priority. We analyzed key parameters of epidemic spread to estimate the contribution of different transmission routes and determine requirements for case isolation and contact tracing needed to stop the epidemic. Although SARS-CoV-2 is spreading too fast to be contained by manual contact tracing, it could be controlled if this process were faster, more efficient, and happened at scale. A contact-tracing app that builds a memory of proximity contacts and immediately notifies contacts of positive cases can achieve epidemic control if used by enough people. By targeting recommendations to only those at risk, epidemics could be contained without resorting to mass quarantines ("lockdowns") that are harmful to society. We discuss the ethical requirements for an intervention of this kind.

Coronavirus disease 2019 (COVID-19) is a rapidly spreading infectious disease caused by severe acute respiratory syndrome–coronavirus 2 (SARS-CoV-2), a betacoronavirus, which has now established a global pandemic. Around half of infected individuals become reported cases, and with intensive care support, the case fatality rate is approximately 2% (*1*). More concerning is that the proportion of cases requiring intensive care support is 5%, and patient management is complicated by requirements to use personal protective equipment and engage in complex decontamination procedures (*2*). Fatality rates are likely to be higher in populations older than in Hubei province (such as in Europe) and in low-income settings where critical care facilities are lacking (*3*). The public health cost of failing to achieve sustained epidemic suppression has been estimated as 250,000 lives lost in the next few months in Great Britain, and 1.1 to 1.2 million in the United States, even with the strongest possible mitigation action to "flatten the curve" (*4*). Even modest outbreaks will see fatality rates climb as hospital capacity is overwhelmed, and the indirect effects caused by compromised health care services have yet to be quantified.

No treatment is currently available, and vaccines are not expected to be sufficiently widely available to control the epidemic within the coming year. The only approaches that we currently have available to stop the epidemic are those of classical epidemic control, such as case isolation, contact tracing and quarantine, physical distancing, and hygiene measures.

The basic reproduction number R_0 is the typical number of infections caused by an individual in the absence of widespread immunity. Once immunity becomes widespread, the effective reproduction number R will become lower than R_0; once R is less than 1, the population has herd immunity and the epidemic declines. Immunity can only safely be obtained by vaccination. Here we use the term "sustained epidemic suppression" to mean a reduction of R to less than 1 by changing nonimmunological conditions of the population that affect transmission, such as social contact patterns.

The biological details of transmission of betacoronaviruses are known in general terms: These viruses can pass from one individual to another through exhaled droplets (*5*), aerosol (*6*), contamination of surfaces (*7*), and possibly through fecal-oral contamination (*8*). Here, we compare different transmission routes that are more closely aligned to their implications for prevention. Specifically, we propose four categories:

1) Symptomatic transmission: direct transmission from a symptomatic individual, through a contact that can be readily recalled by the recipient.

2) Presymptomatic transmission: direct transmission from an individual that occurs before the source individual experiences noticeable symptoms. (Note that this definition may be context-specific—for example, based on whether it is the source or the recipient who is asked whether the symptoms were noticeable.)

3) Asymptomatic transmission: direct transmission from individuals who never experience noticeable symptoms. This can only be established by follow-up, as single–time point observation cannot fully distinguish asymptomatic from presymptomatic individuals.

4) Environmental transmission: transmission via contamination, and specifically in a way that would not typically be attributable to contact with the source in a contact survey (i.e., this does not include transmission pairs who were in extended close contact, but for whom in reality the infectious dose passed via the environment instead of more directly). These could be identified in an analysis of spatial movements.

We acknowledge that boundaries between these categories may be blurred, but defined broadly these categories have different implications for prevention, responding differently to classical measures of case isolation and quarantining contacts (*9*, *10*) [for a specific application to COVID-19, see below (*11*)].

Evidence exists for each of these routes of transmission: symptomatic (*12*), presymptomatic (*13*), asymptomatic (*14*), and environmental (*12*). For prevention, the crucial information is the relative frequency of different routes of transmission so as to allocate finite resources between different intervention strategies.

Li *et al.* (*12*) presented self-reported data on exposure for the first 425 cases in Wuhan; some of these recorded visits to the Huanan Seafood Wholesale Market. The generalizability of transmission in that setting to other settings is highly uncertain, as this large-scale event seeded the epidemic in the absence of any knowledge about the disease. After closure of the Huanan Seafood Wholesale Market on 1 January 2020, of 240 cases with no exposure to any wet market, 200 individuals (83%) reported no exposure to an individual with respiratory symptoms. Inaccurate recall may explain some responses, including failing to notice symptoms that were exceptional at a time before awareness of the disease began, but it is unlikely to be as much as 83% of them, implying that many individuals were infected by nonsymptomatic individuals.

The situation in Singapore at first glance appears different, because unlike in Wuhan, many individuals were linked to an identified symptomatic source. However, the main difference is that the linkage was retrospective, such that linkage could be established even if transmission occurred before a case was symptomatic. As of 5 March 2020, there were 117 cases, of which 25 were imported. By devoting considerable resources, including police investigation, 75 of the 92 cases of local transmission were traced back to their presumed exposure, either to a known case or to a location linked to spread (*15*). Linking cases via a location generally includes the possibility of environmentally

[1]Big Data Institute, Li Ka Shing Centre for Health Information and Discovery, University of Oxford, Oxford, UK. [2]Wellcome Centre for Ethics and the Humanities and Ethox Centre, University of Oxford, Oxford, UK. [3]Oxford University NHS Trust, University of Oxford, Oxford, UK. [4]Wellcome Centre for Human Genetics, University of Oxford, Oxford, UK.
*These authors contributed equally to this work. †These authors contributed equally to this work.
‡Corresponding author. Email: christophe.fraser@bdi.ox.ac.uk

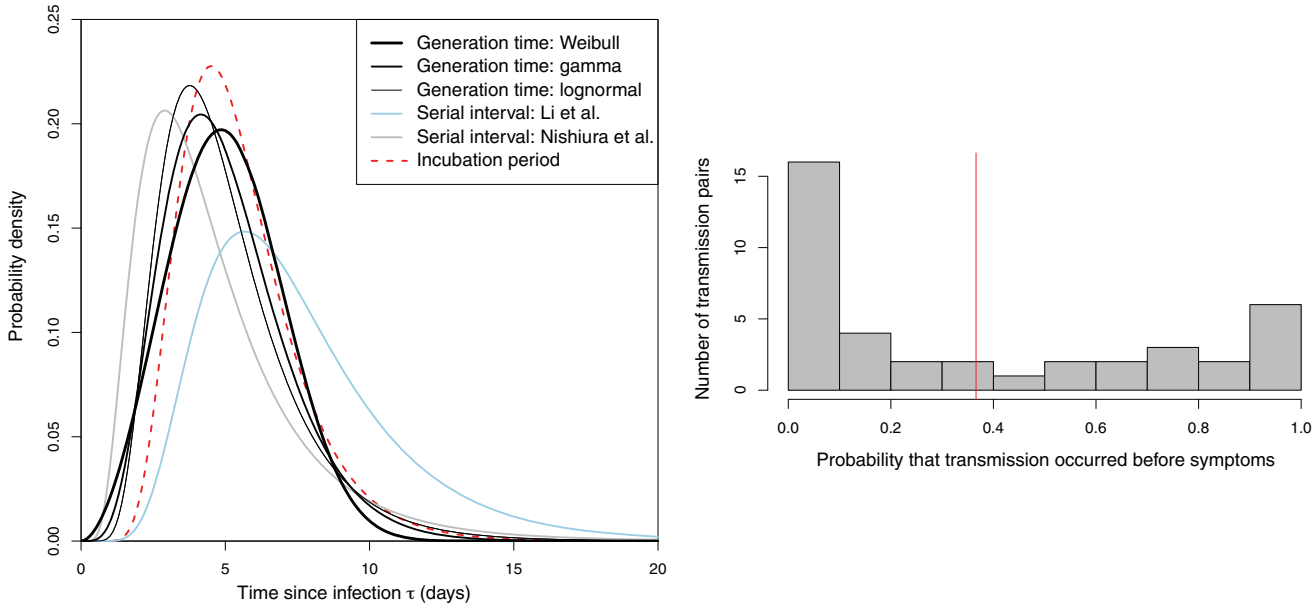


Fig. 1. Quantifying transmission timing in 40 transmission pairs. Left: Our inferred generation time distributions, in black; thicker lines denote higher support for the corresponding functional form, with the Weibull distribution being the best fit. For comparison, we also include the serial interval distributions previously reported by Li *et al*. (*12*) (light blue) and Nishiura *et al*. (*22*) (gray) and the incubation period distribution we used here, from Lauer *et al*. (*21*) (dashed red line). Right: Distribution of the posterior probability of presymptomatic transmission for each of the 40 transmission pairs. The red vertical line shows the mean probability.

mediated transmission. Therefore, the large fraction of traceable transmission in Singapore does not contradict the large fraction without symptomatic exposure in Wuhan. However, it does suggest that transmission from asymptomatic, rather than presymptomatic, individuals is not a major driver of spread. Although serological surveys are currently lacking, other lines of evidence suggest that the scenario of many asymptomatic infections for each symptomatic one is unlikely. Testing of 1286 close contacts of confirmed cases found that among 98 individuals testing positive, only 20% did not have symptoms at first clinical assessment (*16*). Among 634 individuals testing positive onboard the Diamond Princess cruise ship, the proportion of individuals without symptoms was found to be 52%; the proportion who were asymptomatic (rather than presymptomatic) was estimated as 18% (*17*). Testing of passengers onboard six repatriation flights from Wuhan suggests that 40 to 50% of infections were not identified as cases (*4*, *18*). Viral loads of mild cases have been found to be less than those of severe cases by a factor of 60 (*19*), and it is likely that the viral loads of asymptomatic individuals are lower still, with possible implications for infectiousness and diagnosis.

The most accurate and robust quantification of the relative frequency of routes of transmission would be a well-designed prospective cohort study with detailed journal and phylogenetic investigations. However, the current global emergency requires timely estimates using imperfect data sources. We performed a detailed analysis of the timing of events in defined transmission pairs, derived the generation time distribution, and attributed a probability for each pair that transmission was presymptomatic. We also fit a mathematical model of infectiousness through the four routes discussed above over the course of infection. This allowed us to calculate R_0, estimate the proportion of transmission from different routes, and make predictions about whether contact tracing and isolation of known cases would be enough to prevent spread of the epidemic.

Estimating SARS-CoV-2 transmission parameters

We used the exponential growth rate of the epidemic, r, from the early stages of the epidemic in China, such that the effect of control measures discussed later will be relative to the early stages of an outbreak, exemplified by baseline contact patterns and environmental conditions in Hubei during that period. We note that this assumption is implicit in many estimates of R_0. The epidemic doubling time T_2 is equal to $\log_e(2)/r$. We used the value r = 0.14 per day (*20*), corresponding to a doubling time of 5.0 days.

The incubation period is defined as the time between infection and onset of symptoms. It is estimated as the time between exposure and report of noticeable symptoms. We used the incubation period distribution calculated in (*21*). The distribution is lognormal with a mean of 5.5 days, a median of 5.2 days, and a standard deviation of 2.1 days, and is included with our results in Fig. 1.

The generation time is defined for source-recipient transmission pairs as the time between the infection of the source and the infection of the recipient. Because time of infection is generally not known, the generation time is often approximated by the serial interval, which is defined as the time between the onset of symptoms of the source and the onset of symptoms of the recipient. We did not take that approach here; instead, we directly estimated the generation time distribution from 40 source-recipient pairs. These pairs were manually selected according to high confidence of direct transmission inferred from publicly available sources at the time of writing (March 2020), and with known time of onset of symptoms for both source and recipient. We combined dates of symptom onset with intervals of exposure for both source and recipient (when available) and the above distribution of incubation times, and from these we inferred the distribution of generation times. The distribution is best described by a Weibull distribution (Akaike information criterion = 148.4, versus 149.9 for gamma and 152.3 for lognormal distribution) with mean and median equal to 5.0 days and standard deviation of 1.9 days, shown in the left panel of Fig. 1. We also show the results of a sensitivity analysis to different functional forms, as well as two previously published serial interval distributions (*12*, *22*). Uncertainty in the fit of the distribution is

Table 1. Parameters of the infectiousness model.

Name	Symbol	Description	Central value	Uncertainty	Source
Parameters directly calculated from data					
Doubling time	T_2	The time taken for the epidemic to double in size during the early uncontrolled phase of expansion	5.0 days	95% CI: 4.2–6.4	(*20*)
Incubation period (two parameters)	$s(\tau)$	Lognormal meanlog Lognormal sdlog	1.644 0.363	95% CI: 1.495–1.798 95% CI: 0.201–0.521	(*21*)
Generation time (two parameters)	$w(\tau)$	Weibull shape Weibull scale	2.826 5.665	95% CI: 1.75–4.7 95% CI: 4.7–6.9	This paper
Parameters with Bayesian priors informed by anecdotal reports or indirect evidence					
Proportion asymptomatic	P_a	The proportion of infected individuals who are asymptomatic	0.4	Prior = beta (α = 1.5, β = 1.75) Mode = 0.4 Mean = 0.46	Media reports (Diamond Princess)
Relative infectiousness of asymptomatics	x_a	The ratio of infectiousness of asymptomatic individuals to infectiousness of symptomatic individuals	0.1	Prior = beta (α = 1.5, β = 5.5) Mode = 0.1 Mean = 0.21	Observation of few missing links in Singapore outbreak to date [suggestion from (*19*)]
Fraction of all transmission that is environmentally mediated	R_E/R_0	Self-explanatory	0.1	Prior = beta (α = 1.5, β = 5.5) Mode = 0.1 Mean = 0.21	Anecdotal observation that many infections can be traced to close contacts once detailed tracing is completed
Environmental infectiousness	$E(l)$	Rate at which a contaminated environment infects new people after a time lag l	3	Box function (0, n) days, prior for n = gamma (shape = 4, rate = 1) Mode = 3 Mean = 4	(*39*); variety of values for many different surfaces

shown in fig. S1. Our distribution is robust with respect to the choice of transmission events (fig. S2). Correlation in the uncertainty between the inferred mean and standard deviation is shown in fig. S3. The distribution of serial intervals for these pairs is shown in fig. S4. The countries from which the transmission pair data were obtained are shown in fig. S5.

For each of the 40 transmission pairs, we estimated the posterior probability that transmission was presymptomatic (i.e., occurred before the onset of symptoms in the infector). We used a Bayesian approach with an uninformative prior (i.e., transmission before or after symptoms equally likely). The 40 probabilities inferred are shown in the right panel of Fig. 1; the mean probability is 37% [95% confidence interval (CI), 27.5 to 45%], which can be interpreted as the fraction of presymptomatic transmission events out of presymptomatic plus symptomatic transmission events. This mean probability over all pairs is close to our prior, but the bimodal distribution of individual probabilities in Fig. 1 shows that these are typically far from the prior (i.e., the data are strongly informative). Uncertainty in the value of this fraction is shown in fig. S6. The value does not depend significantly on the choice of prior (figs. S7 and S8), on the functional form of the distribution of generation times (figs. S9 and S10), or on the choice of transmission events (fig. S11).

A general mathematical model of SARS-CoV-2 infectiousness

We used a mathematical formalism (*23*) that describes how infectiousness varies as a function of time since infection, τ, for a representative cohort of infected individuals. This includes heterogeneity between individuals, and averages over those individuals who infect few others and those who infect many. This average defines the function $\beta(\tau)$. Infectiousness may change with τ as a result of changing disease biology (notably viral shedding) and/or changing contact with others. The area under the β curve is the reproduction number R_0.

We decomposed $\beta(\tau)$ into four contributions that reflect our categorization above, namely asymptomatic transmission, presymptomatic transmission, symptomatic transmission, and environmental transmission. The area under the curve of one of these contributions gives the mean total number of transmissions over one full infection, via that route—asymptomatic, presymptomatic, symptomatic, or environmental—which we define to be R_A, R_P, R_S, and R_E, respectively. The sum of these is R_0.

The mathematical form for $\beta(\tau)$ is

$$\beta(\tau) = \underbrace{P_a x_a \beta_s(\tau)}_{\text{asymptomatic}} + \underbrace{(1-P_a)[1-s(\tau)]\beta_s(\tau)}_{\text{presymptomatic}} + \underbrace{(1-P_a)s(\tau)\beta_s(\tau)}_{\text{symptomatic}} + \underbrace{\int_{l=0}^{\tau} \beta_s(\tau-l)E(l)dl}_{\text{environmental}}$$

where $\beta_s(\tau)$ is the infectiousness of an individual currently either symptomatic or presymptomatic, at age of infection τ. Other parameters in this expression, and those feeding into it indirectly, are listed in Table 1. A detailed discussion of this expression, including its assumptions, is found in the supplementary materials. The priors chosen for parameters not directly calculated from data are shown in fig. S12. The infectiousness model result using central values of all parameters is shown in Fig. 2.

By drawing input parameter sets from the uncertainties shown in Table 1, we quantified our uncertainty in R_0 and its four contributions. The resulting values are shown in Table 2, and their underlying distributions are shown in

fig. S13. Two-dimensional distributions showing correlations in uncertainty are shown in fig. S14. The estimate of $R_P/(R_P + R_S)$ obtained by this method is 0.55 (CI, 0.37 to 0.72), which is larger than the estimate of 0.37 (CI, 0.28 to 0.45) from our analysis of the 40 transmission pairs but with overlapping uncertainty.

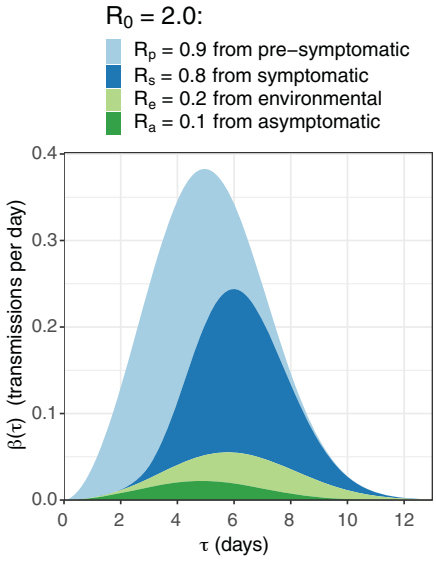


Fig. 2. Our model of infectiousness. The average infectiousness (rate of infecting others), β, is shown as a function of the amount of time since infection, τ. The total colored area found between two values of τ is the number of transmissions expected in that time window. The total colored area over all values of τ is the number of transmissions expected over the full course of one infection (i.e., the basic reproduction number R_0). The different colors indicate the contributions of the four routes of transmission, so that the total area of one color over all values of τ is the average number of transmissions via that route over the whole course of infection: R_P, R_S, R_E, and R_A for presymptomatic, symptomatic, environmentally mediated, and asymptomatic transmission, respectively. Note that the colors are stacked on top of one another (i.e., the lower colors are not in front, and the higher colors are not behind and partially obscured). Values are rounded to one decimal place. Stopping the spread of disease requires reduction of R to less than 1: blocking transmission, from whatever combination of colors and values of τ we can achieve, such that the total area is halved.

We define θ as the fraction of all transmissions that do not come from direct contact with a symptomatic individual: $1 - (R_S/R_0)$. This corresponds to the θ of (*9*) in the case where there is only presymptomatic and symptomatic transmission. From Table 2, this is 0.62 (CI, 0.50 to 0.92). The value of θ observed during an exponentially growing epidemic will be distorted when the timings of the different contributions to transmission occur at different stages of the infection, as a result of overrepresentation of recently infected individuals. This effect can be calculated through use of the renewal equation, as was recently done to calculate the distribution of time from onset of COVID-19 symptoms to recovery or death (*20*) (see supplementary materials). We calculated the θ that would be observed with the early exponential growth seen in China as 0.68 (CI, 0.56 to 0.92). The correction due to the epidemic dynamics is small relative to parameter uncertainties.

We developed our mathematical model of infectiousness into a web application where users can test the effect of alternative parameter combinations (*24*).

Modeling case isolation and contract tracing with quarantine

We modeled the combined impact of two interventions: (i) isolating symptomatic individuals, and (ii) tracing the contacts of symptomatic cases and quarantining them. These interventions aim to stop the spread of the virus by reducing the number of transmissions from both symptomatic individuals and their contacts (who may not be symptomatic) while minimizing the impact on the larger population. In practice, neither intervention will be successful or possible for 100% of individuals. The success rate of these interventions determines the long-term evolution of the epidemic. If the success rates are high enough, the combination of isolation and contact tracing/quarantining could bring R below 1 and therefore effectively control the epidemic.

An analytical mathematical framework for the combined impact of these two interventions on an epidemic was previously derived in (*9*). In the supplementary materials, we solve these equations using our infectiousness model above—that is, quantifying how the SARS-CoV-2 epidemic is expected to be controlled (or not) by case isolation and the quarantining of traced contacts. Our results are shown in Fig. 3. The black line shows the threshold for epidemic control: Combined success rates in the region to the upper right of the black line are sufficient to reduce R to less than 1. The x axis is the success rate of case isolation, which can be thought of either as the fraction of symptomatic individuals isolated (assuming perfect prevention of transmission upon isolation) or the degree to which the infectiousness of symptomatic individuals is reduced (assuming all of them are isolated). The y axis is the success rate of contact tracing; similarly, this can be thought of as the fraction of all contacts traced (assuming perfectly successful quarantine upon tracing) or the degree to which infectiousness of contacts is reduced (assuming all of them are traced). These results for intervention effectiveness, and their dependence on all parameters in our combined analysis, can be explored through the same web interface as for our model of infectiousness (*24*).

Delays in these interventions make them ineffective at controlling the epidemic (Fig. 3): Traditional manual contact-tracing procedures are not fast enough for SARS-CoV-2. However, a delay between confirming a case and finding that person's contacts is not inevitable. Specifically, this delay can be avoided by using a mobile phone app.

Epidemic control with instant digital contact tracing

A mobile phone app can make contact tracing and notification instantaneous upon case confirmation. By keeping a temporary record of proximity events between individuals, it can immediately alert recent close contacts of diagnosed cases and prompt them to self-isolate.

Table 2. R_0 and its components.

	Presymptomatic	Symptomatic	Environmental	Asymptomatic	Total R_0
Absolute	Point estimate: 0.9 Uncertainty median: 0.7 CI: 0.2–1.1	Point estimate: 0.8 Uncertainty median: 0.6 CI: 0.2–1.1	Point estimate: 0.2 Uncertainty median: 0.4 CI: 0.0–1.3	Point estimate: 0.1 Uncertainty median: 0.2 CI: 0.0–1.2	Point estimate: 2.0 Uncertainty median: 2.1 CI: 1.7–2.5
Fraction of R_0	Point estimate: 0.47 Uncertainty median: 0.35 CI: 0.11–0.58	Point estimate: 0.38 Uncertainty median: 0.28 CI: 0.09–0.49	Point estimate: 0.1 by assumption Uncertainty median: 0.19 CI: 0.02–0.56	Point estimate: 0.06 Uncertainty median: 0.09 CI: 0.00–0.57	1 by definition

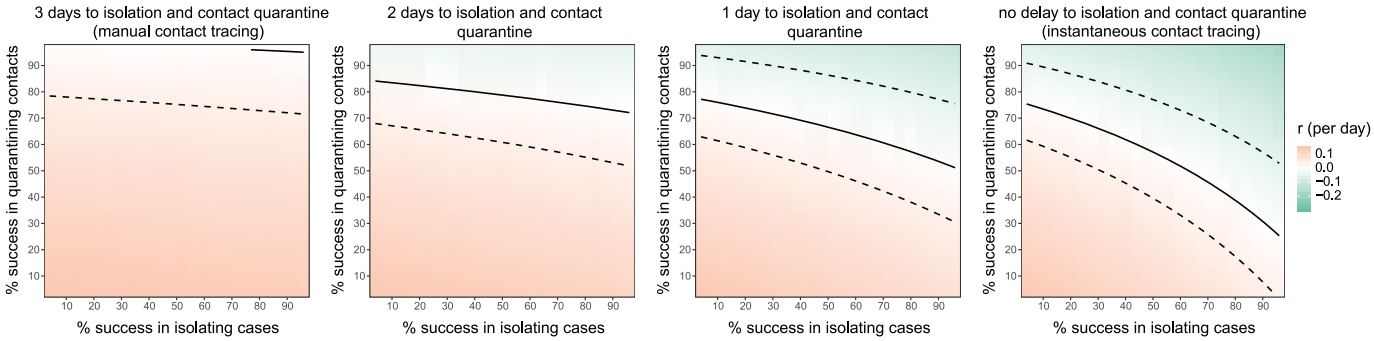


Fig. 3. Quantifying intervention success. Heat map plot shows the exponential growth rate of the epidemic r as a function of the success rate of instant isolation of symptomatic cases (x axis) and the success rate of instant contact tracing (y axis). Positive values of r (red) imply a growing epidemic; negative values of r (green) imply a declining epidemic, with greater negative values implying faster decline. The solid black line shows $r = 0$ (i.e., the threshold for epidemic control). The dashed lines show uncertainty in the threshold due to uncertainty in R_0 (see figs. S15 to S17). The different panels show variation in the delay associated with the intervention, from initiation of symptoms to case isolation and quarantine of contacts.

Apps with similar aims have been deployed in China. Public health policy was implemented using an app that was not compulsory but was required to move between quarters and into public spaces and public transport. The app allows a central database to collect data on user movement and coronavirus diagnosis and displays a green, amber, or red code to relax or enforce restrictions on movement. The database is reported to be analyzed by an artificial intelligence algorithm that issues the color codes (*25*). The app is a plug-in for the WeChat and Alipay apps and has been generally adopted.

Mainland China outside of Hubei province received substantially more introductions from Wuhan than did any other locality, following mass movements of people around the Chinese New Year and the start of the Wuhan lockdown (*26*). Despite this, sustained epidemic suppression has been achieved in China: Fewer than 150 new cases have been reported each day from 2 March to 22 April, down from thousands each day at the height of the epidemic. South Korea has also achieved sustained epidemic suppression—8 new cases on 23 April, down from a peak of 909 on 29 February—and is also using a mobile phone app for recommending quarantine. Both the Chinese and South Korean apps have come under public scrutiny over issues of data protection and privacy.

With our result in Fig. 3 implying the need for extremely rapid contact tracing, we set out to design a simple and widely acceptable algorithm from epidemiological first principles, using common smartphone functionality. The method is shown in Fig. 4. The core functionality is to replace a week's work of manual contact tracing with instantaneous signals transmitted to and from a central server. Coronavirus diagnoses are communicated to the server, enabling recommendation of risk-stratified quarantine and physical distancing measures in those now known to be possible contacts, while preserving the anonymity of the infected individual. Tests could be requested by symptomatic individuals through the app.

The simple algorithm can easily be refined to be more informative—for example, quarantining areas if local epidemics become uncontrolled, quarantining whole households, or performing second- or third-degree contact tracing if case numbers are rising, which would result in more people being preemptively quarantined. Algorithmic recommendations can also be manually overridden where public health officials gather more specific evidence. The app can serve as the central hub of access to all COVID-19 health services, information, and instructions, and as a mechanism to request food or medicine deliveries during self-isolation.

In the context of a mobile phone app, Fig. 3 paints an optimistic picture. There is no delay between case confirmation and notification of contacts; thus, the delay for the contact quarantine process is the period from an individual experiencing symptoms to their contacts entering quarantine. The delay between symptom development and case confirmation will decrease with faster testing protocols, and indeed could become instant if presumptive diagnosis of COVID-19 based on symptoms were accepted in high-prevalence areas. The delay between contacts being notified and entering quarantine should be minimal with high levels of public understanding, as should the delay for case isolation. The efficacy of contact tracing (the y axis of Fig. 3) is the square of the proportion of the population using the app, multiplied by the probability of the app detecting infectious contacts, multiplied by the fractional reduction in infectiousness resulting from being notified as a contact.

Ethical considerations

Successful and appropriate use of the app relies on it commanding well-founded public trust and confidence. This applies to the use of the app itself and of the data gathered. There are strong, well-established ethical arguments recognizing the importance of achieving health benefits and avoiding harm. These arguments are particularly strong in the context of an epidemic with the potential for loss of life on the scale possible with COVID-19. Requirements for the intervention to be ethical and capable of commanding the trust of the public are likely to comprise the following: (i) oversight by an inclusive and transparent advisory board, which includes members of the public; (ii) the agreement and publication of ethical principles by which the intervention will be guided; (iii) guarantees of equity of access and treatment; (iv) the use of a transparent and auditable algorithm; (v) integrating evaluation and research in the intervention to inform the effective management of future major outbreaks; (vi) careful oversight of and effective protections around the uses of data; (vii) sharing of knowledge with other countries, especially low- and middle-income countries; and (viii) ensuring that the intervention involves the minimum imposition possible and that decisions in policy and practice are guided by three moral values: equal moral respect, fairness, and the importance of reducing suffering (*27*). It is noteworthy that the algorithmic approach we propose avoids the need for coercive surveillance, because the system can have very large impacts and achieve sustained epidemic suppression even with partial uptake. People should be democratically entitled to decide whether to adopt this platform. The intention is not to impose the technology as a permanent change to society, but we believe that under these pandemic circumstances it is necessary and justified to protect public health.

Discussion

In this study, we estimated key parameters of the SARS-CoV-2 epidemic, using an analytically solvable model of the exponential phase of spread and of the impact of interventions. Our

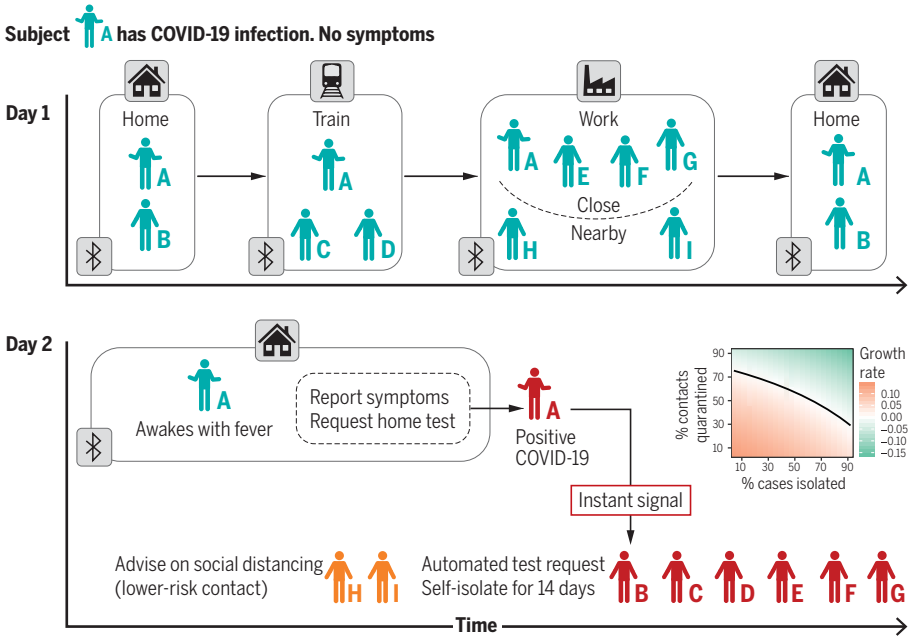


Fig. 4. A schematic of app-based COVID-19 contact tracing. Contacts of individual A (and all individuals using the app) are traced using low-energy Bluetooth connections with other app users. Individual A requests a SARS-CoV-2 test (using the app) and that person's positive test result triggers an instant notification to individuals who have been in close contact. The app advises isolation for the case (individual A) and quarantine of the individual's contacts.

estimate of R_0 is lower than many previous published estimates, for example (*12*, *28*, *29*). These studies assumed SARS-like generation times; however, the emerging evidence for shorter generation times for COVID-19 implies a smaller R_0. This means that a smaller fraction of transmissions need to be blocked for sustained epidemic suppression ($R < 1$). However, it does not mean that sustained epidemic suppression will be easier to achieve, because each individual's transmissions will occur in a shorter window of time after infection, and a greater proportion of them will occur before the warning sign of symptoms. Specifically, our approaches suggest that between one-third and one-half of transmissions occur from presymptomatic individuals. This is in line with estimates of 48% of transmission being presymptomatic in Singapore and 62% in Tianjin, China (*30*), and 44% in transmission pairs from various countries (*31*). Our infectiousness model suggests that the total contribution to R_0 from presymptomatics is 0.9 (CI, 0.2 to 1.1), almost enough to sustain an epidemic on its own. For SARS, the corresponding estimate was almost zero (*9*), immediately telling us that different containment strategies will be needed for COVID-19.

Transmission occurring rapidly and before symptoms, as we have found, implies that the epidemic is highly unlikely to be contained solely by isolating symptomatic individuals. Published models (*9*–*11*, *32*) suggest that in practice, manual contact tracing can only improve on this to a limited extent: It is too slow, and personnel limitations prevent it from being scaled up once the epidemic grows beyond the early phase. Using mobile phones to measure infectious disease contact networks has been proposed previously (*33*–*35*). Considering our quantification of SARS-CoV-2 transmission, we suggest that this approach, with a mobile phone app implementing instantaneous contact tracing, could reduce transmission enough to achieve $R < 1$ and sustained epidemic suppression, thereby stopping the virus from spreading further. We have developed a web interface to explore the uncertainty in our modeling assumptions (*24*). This will also serve as an ongoing resource as new data become available and as the epidemic evolves.

We included environmentally mediated transmission and transmission from asymptomatic individuals in our general mathematical framework. However, given current data, the relative importance of these transmission routes remains speculative. Cleaning and decontamination are being deployed to varying levels in different settings, and improved estimates of their relative importance would help to inform this as a priority. Asymptomatic infection has been widely reported for COVID-19 [e.g., (*14*)], unlike for SARS, where this was very rare (*36*). We argue that the reports from the early outbreak in Singapore imply that even if asymptomatic infections are common, onward transmission from this state is probably uncommon, because forensic reconstruction of the transmission networks closed down most missing links. There is an important caveat to this: The Singapore outbreak at that stage was small and has not implicated children. There has been widespread speculation that children could be frequent asymptomatic carriers and potential sources of SARS-CoV-2 (*37*, *38*).

We calibrated our estimate of the overall amount of transmission based on the epidemic growth rate observed in China not long after the epidemic started. Growth in Western European countries so far appears to be faster, implying either shorter intervals between individuals becoming infected and transmitting onward, or a higher R_0. We illustrate the latter effect in figs. S18 and S19. If this is an accurate picture of viral spread in Europe and not an artifact of early growth, epidemic control with only case isolation and quarantining of traced contacts appears implausible in this case, requiring near-universal app usage and near-perfect compliance. The app should be one tool among many general preventive population measures such as physical distancing, enhanced hand and respiratory hygiene, and regular decontamination.

An app-based intervention could be more powerful than our analysis here suggests, however. The renewal equation mathematical framework we use, although well adapted to account for realistic infectiousness dynamics, is not well adapted to account for the benefits of recursion over the transmission network. Once they have been confirmed as cases, individuals identified by tracing can trigger further tracing, as can their contacts, and so on. This effect was not modeled in our analysis here. If testing capacity is limited, individuals who are identified by tracing may be presumed confirmed upon onset of symptoms, because the prior probability of them being positive is higher than for the index case, accelerating the algorithm further without compromising specificity. With fast enough testing, even index cases diagnosed late in infection could be traced recursively to identify recently infected individuals, both before they develop symptoms and before they transmit. Improved sensitivity of testing in early infection could also speed up the algorithm and achieve rapid epidemic control.

The economic and social impact caused by widespread lockdowns is severe. Individuals on low incomes may have limited capacity to remain at home, and support for people in quarantine requires resources. Businesses will lose confidence, causing negative feedback cycles in the economy. Psychological impacts may be lasting. Digital contact tracing could play a critical role in avoiding or leaving lockdown. We have quantified its expected success and laid

out a series of requirements for its ethical implementation. The app we propose offers benefits for both society and individuals, reducing the number of cases and also enabling people to continue their lives in an informed, safe, and socially responsible way. It offers the potential to achieve important public benefits while maximizing autonomy. Specific issues exist for groups within the population that may not be amenable to such an approach, and these could be rapidly refined in policy. Essential workers, such as health care workers, may need separate arrangements.

Further modeling is needed to compare the number of people disrupted under different scenarios consistent with sustained epidemic suppression. But a sustained pandemic is not inevitable, nor is a sustained national lockdown. We recommend urgent exploration of means for intelligent physical distancing via digital contact tracing.

REFERENCES AND NOTES

1. World Health Organization, *Coronavirus Disease 2019 (COVID-19): Situation Report – 36* (25 February 2020); www.who.int/docs/default-source/coronaviruse/situation-reports/20200225-sitrep-36-covid-19.pdf.
2. W.-J. Guan *et al*., Clinical Characteristics of Coronavirus Disease 2019 in China. *N. Engl. J. Med.* 10.1056/NEJMoa2002032 (2020). doi: 10.1056/NEJMoa2002032; pmid: 32109013
3. H. Li *et al*., Age-dependent risks of Incidence and Mortality of COVID-19 in Hubei Province and Other Parts of China. medRxiv 2020.02.25.20027672 [preprint]. 6 March 2020.
4. N. Ferguson *et al*., *Impact of Non-Pharmaceutical Interventions (NPIs) to Reduce COVID-19 Mortality and Healthcare Demand* (16 March 2020); www.imperial.ac.uk/media/imperial-college/medicine/sph/ide/gida-fellowships/Imperial-College-COVID19-NPI-modelling-16-03-2020.pdf.
5. I. T. S. Yu, J. J. Y. Sung, The epidemiology of the outbreak of severe acute respiratory syndrome (SARS) in Hong Kong—What we do know and what we don't. *Epidemiol. Infect.* **132**, 781–786 (2004). doi: 10.1017/S0950268804002614; pmid: 15473139
6. Y. Li, X. Huang, I. T. S. Yu, T. W. Wong, H. Qian, Role of air distribution in SARS transmission during the largest nosocomial outbreak in Hong Kong. *Indoor Air* **15**, 83–95 (2005). doi: 10.1111/j.1600-0668.2004.00317.x; pmid: 15737151
7. J. A. Otter *et al*., Transmission of SARS and MERS coronaviruses and influenza virus in healthcare settings: The possible role of dry surface contamination. *J. Hosp. Infect.* **92**, 235–250 (2016). doi: 10.1016/j.jhin.2015.08.027; pmid: 26597631
8. S. W. X. Ong *et al*., Air, Surface Environmental, and Personal Protective Equipment Contamination by Severe Acute Respiratory Syndrome Coronavirus 2 (SARS-CoV-2) From a Symptomatic Patient. *JAMA* 10.1001/jama.2020.3227 (2020). doi: 10.1001/jama.2020.3227; pmid: 32129805
9. C. Fraser, S. Riley, R. M. Anderson, N. M. Ferguson, Factors that make an infectious disease outbreak controllable. *Proc. Natl. Acad. Sci. U.S.A.* **101**, 6146–6151 (2004). doi: 10.1073/pnas.0307506101; pmid: 15071187
10. C. M. Peak, L. M. Childs, Y. H. Grad, C. O. Buckee, Comparing nonpharmaceutical interventions for containing emerging epidemics. *Proc. Natl. Acad. Sci. U.S.A.* **114**, 4023–4028 (2017). doi: 10.1073/pnas.1616438114; pmid: 28351976
11. J. Hellewell *et al*., Feasibility of controlling COVID-19 outbreaks by isolation of cases and contacts. *Lancet Glob. Health* **8**, e488–e496 (2020). doi: 10.1016/S2214-109X(20)30074-7; pmid: 32119825
12. Q. Li *et al*., Early Transmission Dynamics in Wuhan, China, of Novel Coronavirus-Infected Pneumonia. *N. Engl. J. Med.* **382**, 1199–1207 (2020). doi: 10.1056/NEJMoa2001316; pmid: 31995857
13. Z.-D. Tong *et al*., Potential Presymptomatic Transmission of SARS-CoV-2, Zhejiang Province, China, 2020. *Emerg. Infect. Dis.* **26**, 10.3201/eid2605.200198 (2020). doi: 10.3201/eid2605.200198; pmid: 32091386
14. Y. Bai *et al*., Presumed Asymptomatic Carrier Transmission of COVID-19. *JAMA* 10.1001/jama.2020.2565 (2020). doi: 10.1001/jama.2020.2565; pmid: 32083643
15. Channel News Asia; https://infographics.channelnewsasia.com/covid-19/coronavirus-singapore-clusters.html?cid=FBcna.
16. Q. Bi, Y. Wu *et al*., Epidemiology and Transmission of COVID-19 in Shenzhen China: Analysis of 391 cases and 1,286 of their close contacts. medRxiv 2020.03.03.20028423 [preprint]. 27 March 2020.
17. K. Mizumoto, K. Kagaya, A. Zarebski, G. Chowell, Estimating the asymptomatic proportion of coronavirus disease 2019 (COVID-19) cases on board the Diamond Princess cruise ship, Yokohama, Japan, 2020. *Euro Surveill.* **25**, 2000180 (2020). doi: 10.2807/1560-7917.ES.2020.25.10.2000180; pmid: 32183930
18. R. Verity *et al*., Estimates of the severity of COVID-19 disease. medRxiv 2020.03.09.20033357 [preprint]. 13 March 2020.
19. Y. Liu *et al*., Viral dynamics in mild and severe cases of COVID-19. *Lancet Infect. Dis.* S1473-3099(20)30232-2 (2020). doi: 10.1016/S1473-3099(20)30232-2; pmid: 32199493
20. I. Dorigatti *et al*., *Report 4: Severity of 2019-Novel Coronavirus (nCoV)* (10 February 2020); www.imperial.ac.uk/media/imperial-college/medicine/sph/ide/gida-fellowships/Imperial-College-COVID19-severity-10-02-2020.pdf.
21. S. A. Lauer *et al*., The incubation period of 2019-nCoV from publicly reported confirmed cases: Estimation and application. medRxiv 2020.02.02.20020016 [preprint]. 4 February 2020.
22. H. Nishiura, N. M. Linton, A. R. Akhmetzhanov, Serial interval of novel coronavirus (2019-nCoV) infections. medRxiv 2020.02.03.20019497 [preprint]. 17 February 2020.
23. N. C. Grassly, C. Fraser, Mathematical models of infectious disease transmission. *Nat. Rev. Microbiol.* **6**, 477–487 (2008). doi: 10.1038/nrmicro1845; pmid: 18533288
24. BDI Pathogen Dynamics Group, Digital contact tracing for SARS-COV-2 (2020); https://bdi-pathogens.shinyapps.io/covid-19-transmission-routes/.
25. P. Mozur, R. Zhong, A. Krolik, "In Coronavirus Fight, China Gives Citizens a Color Code, With Red Flags." *New York Times* (1 March 2020); www.nytimes.com/2020/03/01/business/china-coronavirus-surveillance.html.
26. S. Chen, J. Yang, W. Yang, C. Wang, T. Bärnighausen, COVID-19 control in China during mass population movements at New Year. *Lancet* **395**, 764–766 (2020). doi: 10.1016/S0140-6736(20)30421-9; pmid: 32105609
27. Nuffield Council on Bioethics, *Research in Global Health Emergencies: Ethical Issues* (28 January 2020); www.nuffieldbioethics.org/publications/research-in-global-health-emergencies.
28. S. Zhao *et al*., Preliminary estimation of the basic reproduction number of novel coronavirus (2019-nCoV) in China, from 2019 to 2020: A data-driven analysis in the early phase of the outbreak. *Int. J. Infect. Dis.* **92**, 214–217 (2020). doi: 10.1016/j.ijid.2020.01.050; pmid: 32007643
29. T. Zhou *et al*., Preliminary prediction of the basic reproduction number of the Wuhan novel coronavirus 2019-nCoV. *J. Evid. Based Med.* **13**, 3–7 (2020). doi: 10.1111/jebm.12376; pmid: 32048815
30. T. Ganyani *et al*., Estimating the generation interval for COVID-19 based on symptom onset data. medRxiv 2020.03.05.20031815 [preprint]. 8 March 2020.
31. X. He *et al*., Temporal dynamics in viral shedding and transmissibility of COVID-19. medRxiv 2020.03.15.20036707 [preprint]. 18 March 2020.
32. D. Klinkenberg, C. Fraser, H. Heesterbeek, The effectiveness of contact tracing in emerging epidemics. *PLOS ONE* **1**, e12 (2006). doi: 10.1371/journal.pone.0000012; pmid: 17183638
33. M. Salathé *et al*., A high-resolution human contact network for infectious disease transmission. *Proc. Natl. Acad. Sci. U.S.A.* **107**, 22020–22025 (2010). doi: 10.1073/pnas.1009094108; pmid: 21149721
34. E. Yoneki, J. Crowcroft, EpiMap: Towards quantifying contact networks for understanding epidemiology in developing countries. *Ad Hoc Netw.* **13**, 83–93 (2014). doi: 10.1016/j.adhoc.2012.06.003
35. K. A. Nguyen, Z. Luo, C. Watkins, in *Progress in Location-Based Services 2014*, G. Gartner, H. Huang, Eds. (Springer, 2015), pp. 63–78.
36. G. M. Leung *et al*., SARS-CoV antibody prevalence in all Hong Kong patient contacts. *Emerg. Infect. Dis.* **10**, 1653–1656 (2004). doi: 10.3201/eid1009.040155; pmid: 15498170
37. K.-Q. Kam *et al*., A Well Infant with Coronavirus Disease 2019 with High Viral Load. *Clin. Infect. Dis.* ciaa201 (2020). doi: 10.1093/cid/ciaa201; pmid: 32112082
38. X. Lu *et al*., SARS-CoV-2 Infection in Children. *N. Engl. J. Med.* NEJMc2005073 (2020). doi: 10.1056/NEJMc2005073; pmid: 32187458
39. G. Kampf, D. Todt, S. Pfaender, E. Steinmann, Persistence of coronaviruses on inanimate surfaces and their inactivation with biocidal agents. *J. Hosp. Infect.* **104**, 246–251 (2020). doi: 10.1016/j.jhin.2020.01.022; pmid: 32035997
40. The code used for our analyses is available at https://doi.org/10.5281/zenodo.3727255.

ACKNOWLEDGMENTS

We thank W. Probert, A. Akhmetzhanov, A. Ledda, B. Cowling, G. Leung, and Y. Yang for helpful comments. **Funding:** This work was funded by the Li Ka Shing Foundation. A.N. is funded by the ARTIC Network (Wellcome Trust Collaborators Award 206298/Z/17/Z). The funders played no role in study conception or execution. **Author contributions:** Conceptualization: C.F., D.B. Data curation: L.F., C.W., A.N., L.Z. Funding acquisition: C.F., M.P. Investigation: L.F., C.W., M.K., C.F. Methodology: L.F., C.W. Visualization: L.F., C.W., M.K., D.B. Project administration: L.A.-D. Software: M.K. Ethical analysis: M.P., C.F., D.B. Writing, original draft: L.F., C.W., M.P., D.B., C.F. Writing, review, and editing: all authors. **Competing interests:** None declared. **Data and materials availability:** All data are available in the manuscript or the supplementary materials. The code used for our analyses is publicly available at (*40*). This work is licensed under a Creative Commons Attribution 4.0 International (CC BY 4.0) license, which permits unrestricted use, distribution, and reproduction in any medium, provided the original work is properly cited. To view a copy of this license, visit https://creativecommons.org/licenses/by/4.0/. This license does not apply to figures/photos/artwork or other content included in the article that is credited to a third party; obtain authorization from the rights holder before using such material.

SUPPLEMENTARY MATERIALS

science.sciencemag.org/content/368/6491/eabb6936/suppl/DC1
Materials and Methods
Figs. S1 to S21
References (*41*–*45*)

11 March 2020; accepted 27 March 2020
Published online 31 March 2020
10.1126/science.abb6936

RESEARCH ARTICLE

BIOMEDICINE

Elesclomol alleviates Menkes pathology and mortality by escorting Cu to cuproenzymes in mice

Liam M. Guthrie[1], Shivatheja Soma[2], Sai Yuan[3], Andres Silva[2], Mohammad Zulkifli[2], Thomas C. Snavely[2], Hannah Faith Greene[2], Elyssa Nunez[2], Brogan Lynch[2], Courtney De Ville[2], Vinit Shanbhag[4], Franklin R. Lopez[5]*, Arjun Acharya[2], Michael J. Petris[4], Byung-Eun Kim[3], Vishal M. Gohil[2]†, James C. Sacchettini[2]†

Loss-of-function mutations in the copper (Cu) transporter ATP7A cause Menkes disease. Menkes is an infantile, fatal, hereditary copper-deficiency disorder that is characterized by progressive neurological injury culminating in death, typically by 3 years of age. Severe copper deficiency leads to multiple pathologies, including impaired energy generation caused by cytochrome c oxidase dysfunction in the mitochondria. Here we report that the small molecule elesclomol escorted copper to the mitochondria and increased cytochrome c oxidase levels in the brain. Through this mechanism, elesclomol prevented detrimental neurodegenerative changes and improved the survival of the mottled-brindled mouse—a murine model of severe Menkes disease. Thus, elesclomol holds promise for the treatment of Menkes and associated disorders of hereditary copper deficiency.

Copper (Cu) is an essential micronutrient required for numerous critical enzymes, including cytochrome c oxidase (CcO) of the adenosine 5′-triphosphate (ATP)–generating electron transport pathway found in mitochondria (*1*). Paradoxically, Cu possesses inherent toxicity, in part because of its ability to generate hydroxyl radicals in biological systems (*2*). Organisms have evolved highly complex systems of metallochaperones and transporters to safely distribute Cu (*3*, *4*). Mutations that impair the function of any component of Cu transport can influence numerous cellular processes, affecting systems as diverse as energy production (*5*, *6*), catecholamine biosynthesis, and connective tissue maturation—resulting in debilitating, often-fatal human diseases (*7*).

The coordinated efforts of the two major Cu membrane transporters, CTR1 and ATP7A, regulate intracellular Cu levels and directional transport across polarized epithelial layers, such as the intestinal enterocyte lining (*8*) and choroid plexus (*9*). CTR1 affects initial Cu entry, whereas ATP7A facilitates Cu egress from cells.

Mutations in the Cu-transporting adenosine triphosphatase (ATPase), ATP7A, result in Menkes disease—a fatal, X-linked infantile condition with no Food and Drug Administration (FDA)–approved treatment (*10*). Clinical presentations of Menkes include abnormal catecholamine ratios, characteristic kinky hair, hypopigmentation, connective tissue defects, and severe neurodegeneration (*7*, *10*, *11*). In the brain, this Cu deficit causes secondary CcO dysfunction, which leads to progressive neurological injury and death (*12*–*14*). Efforts to restore normal Cu levels and enzyme function by means of parenteral-Cu supplementation using hydrophilic complexes, such as copper histidine (HIS-Cu^{2+}), do not always ameliorate severe neurological pathology in Menkes patients because of poor penetrance and low restoration of neuronal CcO function in the brain (*14*, *15*). We previously reported that elesclomol (ES), a small, highly lipophilic Cu^{2+}-binding molecule, restores mitochondrial function in the context of defective Cu transport in yeast and mammalian cell lines (*16*). A membrane traversing drug like ES, capable of Cu delivery to key cuproenzymes, such as CcO in brain mitochondria, could alleviate the neurodegenerative aspects of Menkes disease. This would be similar to hinokitiol, a lipophilic carrier that restores iron levels in the context of defective membrane transport both in vitro and in vivo (*17*, *18*).

ES restores mitochondrial function in *Ctr1* knockout H9c2 cells and mice

We measured the oxygen consumption rate (OCR)—an indication of electron transport activity—and ATP levels in the Cu importer *Ctr1* knockout (KO) H9c2 rat cardiomyocytes. *Ctr1* KO H9c2 cells exhibited significant reduction in basal OCR and ATP levels. Preincubation with 1 nM of ES restored OCR to 103% (+34%) of wild-type (WT) (2.5 versus 3.7 pM min^{-1} per microgram of protein; $P < 0.001$) (fig. S1A). Similarly, ES treatment increased ATP levels compared with the *Ctr1* KO vehicle (0.74 versus 1.01, $P < 0.001$) (fig. S1B).

Loss of CTR1 results in severe cellular Cu deficiency in mice. $Ctr1^{-/-}$ mice demonstrate lethality in utero (*19*). The cardiac-specific *Ctr1* KO mouse (*20*) exhibits growth retardation, severe hypertrophic cardiomyopathy due to cardiac muscle CcO dysfunction, and death around postnatal day (PND) 12. To assess the ability of ES to escort Cu^{2+} through CTR1-deficient cardiac cellular membranes, we administered subcutaneous ES at 10 mg kg^{-1}. WT mice tolerated ES injections well with favorable tolerability and pharmacokinetics (table S1 and fig. S2). We observed a 100%

[1]Department of Molecular and Cellular Medicine, Texas A&M Health Science Center, College Station, TX 77843, USA. [2]Department of Biochemistry and Biophysics, Texas A&M University, College Station, TX 77843, USA. [3]Department of Animal and Avian Sciences, University of Maryland, College Park, MD 20742, USA. [4]Department of Biochemistry, University of Missouri, Columbia, MO 65211, USA. [5]Texas Veterinary Medicine Diagnostic Laboratory, College Station, TX 77843, USA.
*Present address: Charles River Laboratories, Durham, NC 27703, USA.
†Corresponding author. Email: vgohil@tamu.edu (V.M.G.); sacchett@tamu.edu (J.C.S.)

Table 1. Treatment regime and 10-week survival in the *mo-br* mouse. Dashes indicate a value was not applicable.

		Treatment				Survival		
Cohort	*n*	Exposure (mg kg^{-1})	Total (μg)	ES/HIS (μg)	Cu^{2+} (μg)	Median (days)	Viable mice 10 weeks	Percent (%)
WT vehicle	15	–	–	–	–	–	15	100
WT ES-Cu^{2+}	13	7.25	29	25.02	3.98	–	13	100
mo-br vehicle	9	–	–	–	–	14	0	0
mo-br ES	6	6.25	25.02	25.02	–	16.5	0	0
mo-br ES-Cu^{2+}	27	7.25	29	25.02	3.98	203	22	81.5
mo-br HIS-Cu^{2+}	6	5.83	23.3	19.35	3.98	18	0	0

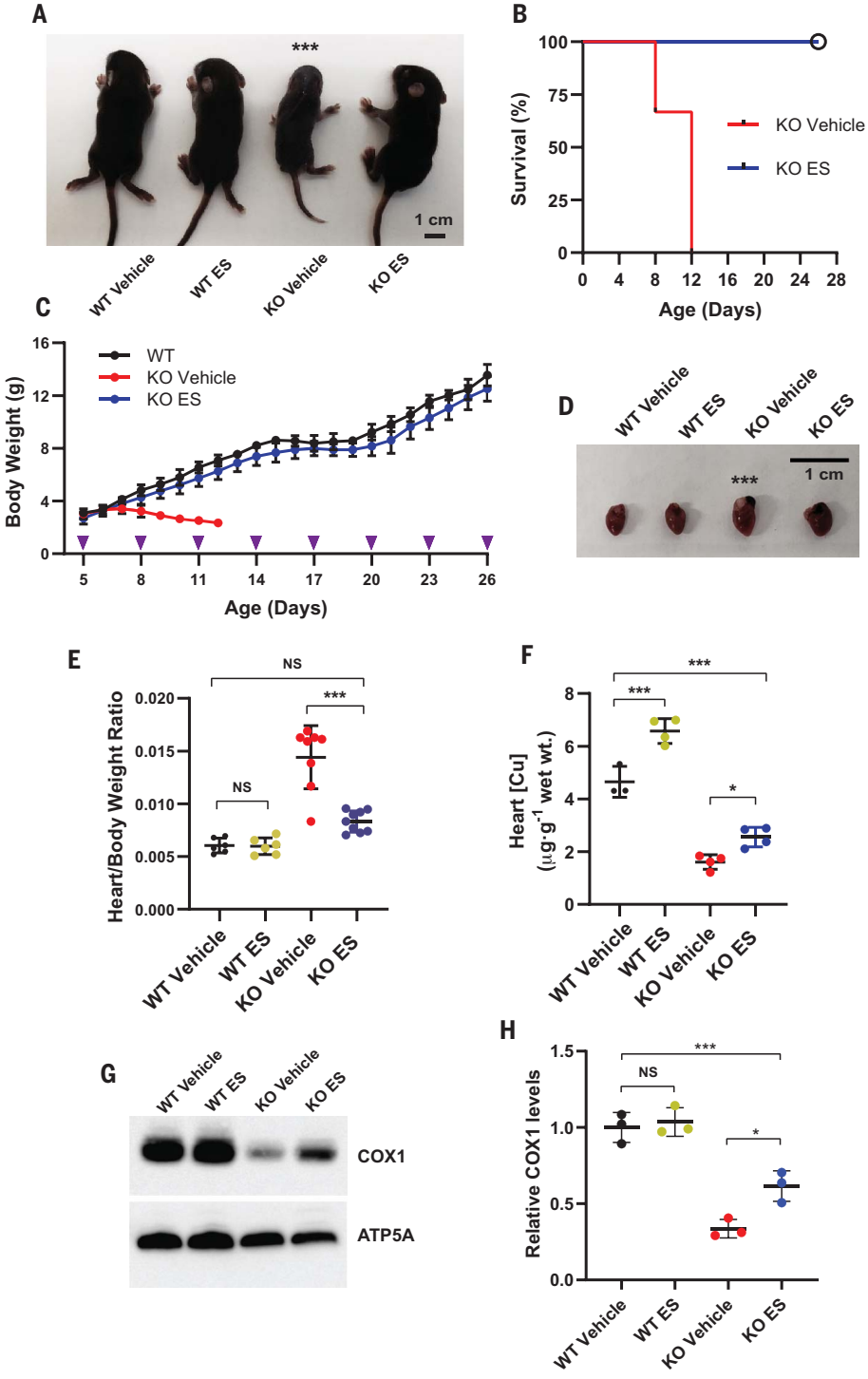


Fig. 1. Effects of ES treatment in cardiac *Ctr1* KO mice. (**A**) Gross appearance of mice at PND 10. Asterisks (***) indicate moribund KO vehicle mouse. (**B**) Kaplan-Meier survival curve. (**C**) Growth curves. WT and WT ES mice exhibited identical growth curves (WT ES omitted for clarity; see fig. S3A). Cohorts consisted of WT vehicle (n = 3 mice), WT ES (n = 7), KO vehicle (n = 3), and KO ES (n = 9). (**D**) Gross appearance of hearts at PND 10. Asterisks (***) indicate hypertrophied KO vehicle mouse heart. (**E**) Heart-to-body weight ratio. Cohorts consisted of n = 6, 6, 8, and 9 animals, respectively. (**F**) Heart [Cu] levels. Cohorts consisted of n = 4 per treatment. (**G**) Heart COX1 levels. (**H**) Quantification of relative COX1 levels. Data are reported as means ± SD with statistical significance assessed by one-way analysis of variance (ANOVA) with Tukey's post hoc test or Welch one-way ANOVA with Tukey's post hoc test. NS, not significant; *P < 0.05; ***P < 0.001. Western blot images in (G) were analyzed with ImageJ software.

26-day survival rate in ES-treated mice whereas those receiving vehicle died between PND 8 and 12 (Fig. 1, A and B). Growth of ES mice was restored to WT pattern with no pronounced deviation from either WT vehicle or WT ES-treated groups (Fig. 1C and fig. S3A).

ES mice demonstrated normalization of total body, heart, and spleen weights at PND 10 (Fig. 1, D and E, and fig. S3, B to D). Cardiac histopathology at PND 10 of vehicle-treated KO mice showed pronounced hypertrophy characterized by increased cell area compared with WT tissue samples (186 versus 87 μm^2, P < 0.01) (fig. S3, E and F). ES treatment ameliorated severe cardiac pathology with a partial reduction in hypertrophy (119 μm^2, P < 0.01) (fig. S3, E and F). Cardiac [Cu] increased with ES treatment from a vehicle KO level of 34 to 55% (1.6 versus 2.6 $\mu g\ g^{-1}$, P = 0.04) (Fig. 1F). The 21% increase in cardiac [Cu] resulted in a 28% increase in COX1, the Cu-containing subunit of CcO (*1*) (Fig. 1, G and H). SOD1, a cuproenzyme highly resistant to Cu depletion (*21*), remained unchanged (fig. S4).

ES alone does not rescue mottled-brindled mice

The mottled-brindled (*mo-br*) mouse phenotypically recapitulates Menkes disease (*22*). *Mo-br* mice possess a 6–base pair (bp) deletion in exon 11 of the mouse *Atp7A* gene, which

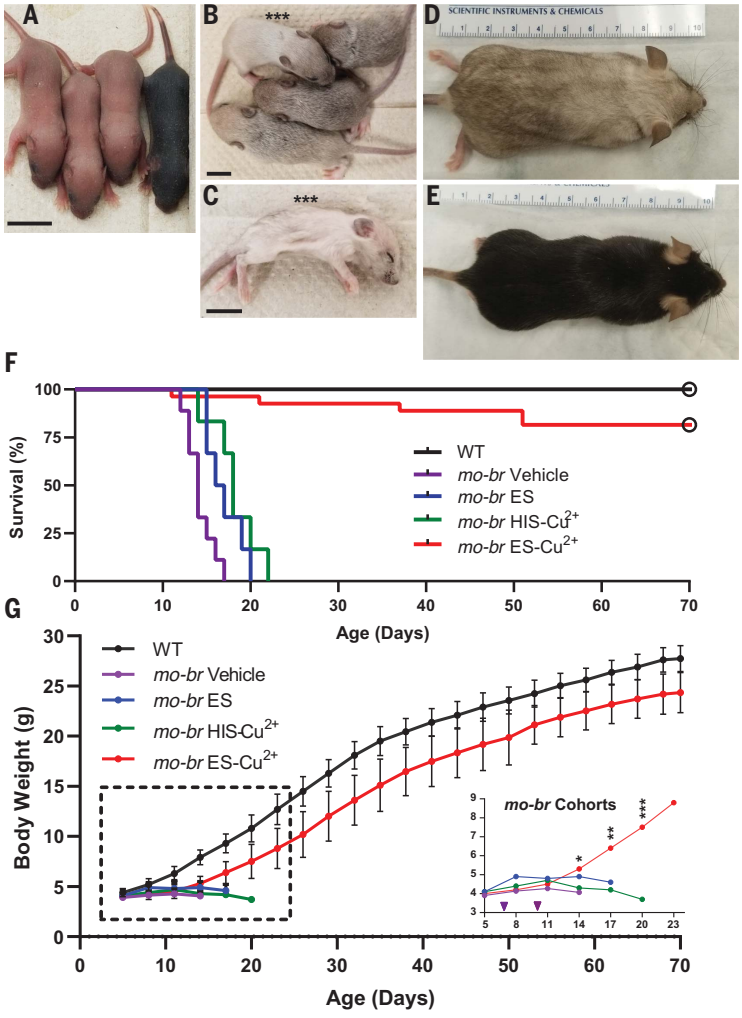


Fig. 2. Effects of ES-Cu^{2+} treatment in *mo-br* mice. (**A**) *Mo-br* hemizygous males and WT littermate at PND 5 before intervention. (**B**) Pigmentation changes in *mo-br* males administered ES-Cu^{2+} compared with vehicle (***) on PND 12. (**C**) Moribund *mo-br* vehicle (***) mouse on PND 14. (**D** and **E**) *Mo-br* ES-Cu^{2+} (D) and WT littermate (E) at PND 70. (**F**) Kaplan-Meier survival curve. All WT mice survived experimental protocol. (**G**) Growth curves of indicated groups: WT and WT ES-Cu^{2+} mice exhibited near identical growth curves (WT ES-Cu^{2+} omitted for clarity; see fig. S8E). Cohorts consisted of WT vehicle (n = 15), WT ES-Cu^{2+} (n = 13), *mo-br* vehicle (n = 9), *mo-br* ES (n = 6), *mo-br* HIS-Cu^{2+} (n = 6), and *mo-br* ES-Cu^{2+} (n = 27). Inset shows a close-up of the curves in the region indicated by the dashed-line box, including the curves of *mo-br* cohorts only. Data are reported as means ± SD with statistical significance assessed by one-way ANOVA test or Welch one-way ANOVA with Tukey's post hoc test. *P < 0.05; **P < 0.01; ***P < 0.001. Scale bars in (A) to (C), 1 cm.

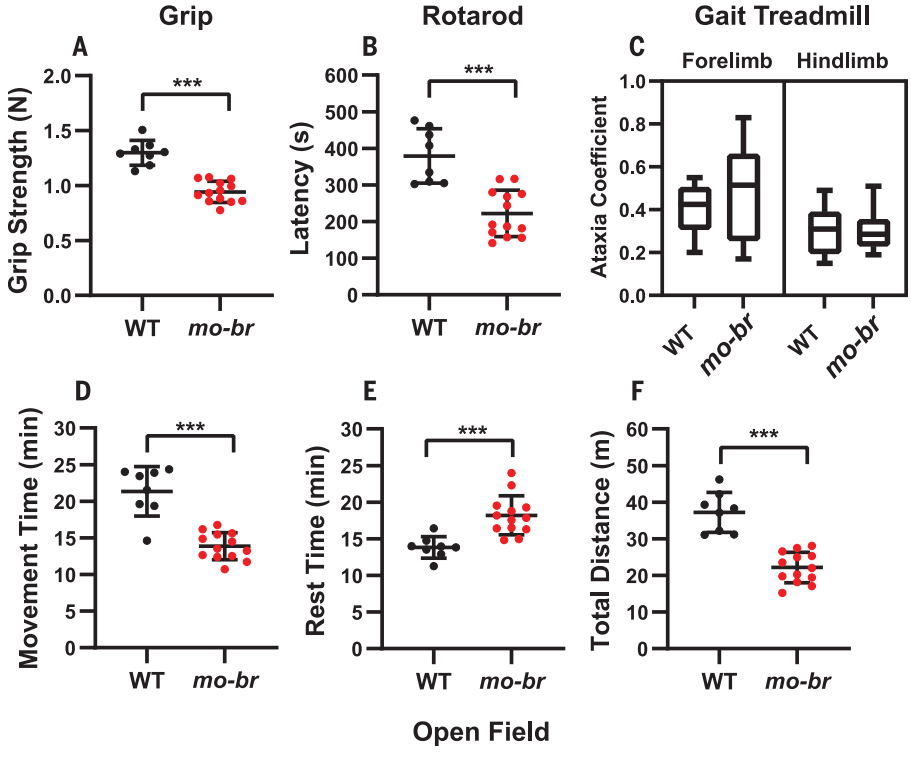


Fig. 3. Neuromotor tests of 10-week-old mice. Mice were assessed by grip strength, rotarod, gait treadmill, and open field at 10 weeks of age. (**A**) Forelimb grip strength. (**B**) Rotarod. (**C**) Gait treadmill. DigiGait-generated ataxia coefficients of shoulder and pelvic girdles were statistically insignificant. (**D** to **F**) Open field: movement time (D), rest time (E), and total distance (F). Cohorts consisted of WT (n = 8) and *mo-br* (n = 13). Data are reported as means ± SD with statistical significance assessed by unpaired t test. ***P < 0.001.

results in an in-frame deletion of Leu^{799} and Ala^{800}. This deletion results in little residual Cu transporting function with severe disease phenotypes, including hypopigmentation, kinky whiskers, growth delay, neurological abnormalities, seizures, and death around PND 14. As with most Menkes patients, the *mo-br* mouse shows little response to treatment with hydrophilic Cu complexes alone (*23*–*25*).

In preliminary studies, we administered ES at 10 mg kg^{-1} of body weight. Unlike the cardiac *Ctr1* KO mice, this pilot study demonstrated no enhanced survival among treated *mo-br* males. This was likely because *mo-br* mice were too deficient in systemic Cu to benefit from ES alone, whereas the cardiac *Ctr1* KO mice possess an elevated serum Cu pool capable of ES-mediated redistribution to deficient cardiomyocytes (*20*). We hypothesized that, by preloading ES with Cu^{2+}, we would address the systemic Cu deficiency and ATP7A-mediated defective transport.

ES-Cu^{2+} complex rescues *mo-br* mice

Menkes disease is characterized by severe neurodegeneration, and therefore any successful treatment must involve a drug that facilitates Cu delivery across the blood-brain barrier or the blood–cerebral spinal fluid barrier (*9*, *10*, *14*). Brain pharmacokinetic studies on PND 7 mice demonstrated high levels of ES in the brain at 201.3 ± 41.7 ng mg^{-1} (fig. S5A), whereas adult exposure, though still significant, was lower at 7.8 ± 5.0 ng mg^{-1} (fig. S5B).

We next administered ES-Cu^{2+} at 3.625 mg kg^{-1} per dose by subcutaneous injection on PND 7 and 10. The total dose of Cu approximated the total amount of Cu (4 μg) in a 4-g WT mouse (*26*). Additional *mo-br* cohorts included vehicle, ES only, and HIS-Cu^{2+}, formulated with an equivalent dose of Cu compared to the ES-Cu^{2+} cohort (Table 1). We selected HIS-Cu^{2+} as a control because of the drug's investigational status for Menkes disease (*14*). ES-Cu^{2+} was well tolerated and exhibited favorable pharmacokinetics (tables S2 to S4 and figs. S6 and S7).

As reported, *mo-br* mice exhibited hypopigmentation with death around PND 14 (Fig. 2, A to C). Within 24 hours, we observed pigment production in ES-Cu^{2+}–treated mice in the immediate vicinity of the injection site (Fig. 2B and fig. S8A). Pigment production indicated increased activity of the secretory pathway cuproenzyme tyrosinase. This was in agreement with the in vitro assessment of an ATP7A KO B16 melanoma cell line, which showed that 1 nM of ES was able to partially rescue tyrosinase activity (fig. S8B). Because tyrosinase requires the action of ATP7A for Cu import into the Golgi complex (*27*), our findings were unexpected and suggest that ES-Cu^{2+} was delivering Cu to cuproenzymes metalated in the Golgi. We also observed that whisker appearance improved from bushy, highly kinked clumps to near-normal by PND 70 in only the ES-Cu^{2+} cohort (fig. S8C), which indicated improved sulfhydryl oxidase activity (*28*).

Mo-br vehicle, ES only, and HIS-Cu^{2+} cohorts developed seizures beginning around PND 11 (movie S1). Seizures increased in severity with subsequent death of all individuals in these groups between PND 14 and 21. We only observed a negligible survival advantage for HIS-Cu^{2+} over vehicle alone (Table 1). ES-Cu^{2+}–treated *mo-br* adult mice did not have seizures and exhibited similar body size to that of their WT siblings (Fig. 2, D and E, and

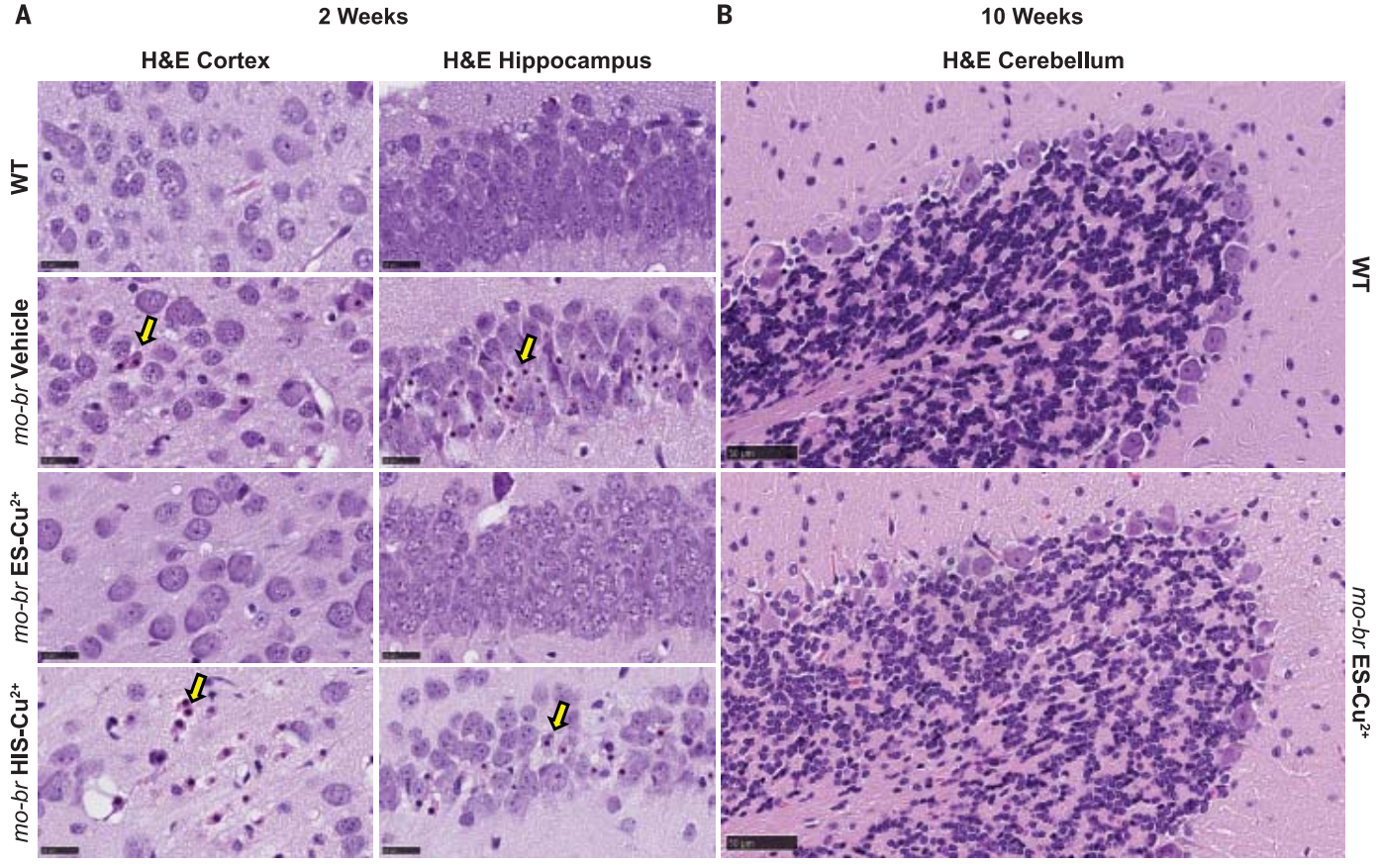


Fig. 4. Neuropathology of 2- and 10-week-old mice. (**A**) Hematoxylin and eosin (H&E)–stained sections of cortex and hippocampus from PND 14 WT and *mo-br* mice, administered vehicle, ES-Cu^{2+}, or HIS-Cu^{2+}. Somatomotor cortical neurons in *mo-br* vehicle and HIS-Cu^{2+} cohorts exhibit marked, diffuse neurodegenerative changes, characterized by numerous pyknotic nuclei with eosinophilic cytoplasm (yellow arrows). In the hippocampus, the pyramidal neuron layer of region CA1 demonstrates degenerative changes including necrotic neurons in vehicle and HIS-Cu^{2+} *mo-br* mice (yellow arrows). (**B**) Cerebellar peduncles from PND 70 WT and *mo-br* ES-Cu^{2+} mice revealed preservation of continuous Purkinje neuron layer. Scale bars in (A), 25 μm. Scale bars in (B), 50 μm.

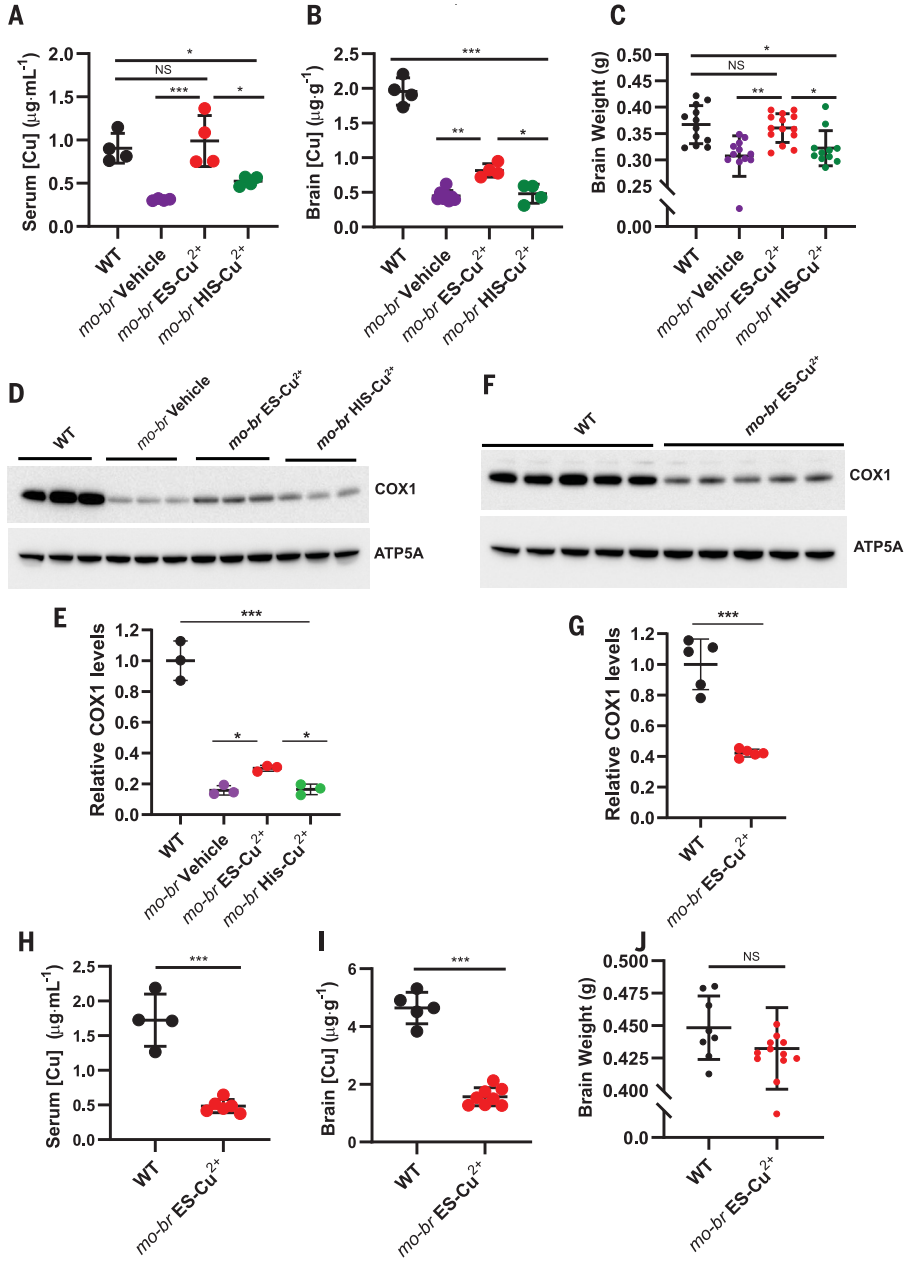


Fig. 5. ES-Cu^{2+} rescues biochemical phenotypes in 2- and 10-week-old *mo-br mice*. (**A**) Serum [Cu] at PND 14 (all cohorts, *n* = 4). (**B**) Brain [Cu] at PND 14 (all cohorts, *n* = 4). (**C**) Brain weights at PND 14 (WT, *n* = 12; *mo-br* Vehicle, *n* = 12; *mo-br* ES-Cu^{2+}, *n* = 14; *mo-br* HIS-Cu^{2+}, *n* = 11). (**D** and **E**) Brain COX1 at PND 14 (all cohorts, *n* = 3). (**F** and **G**) Brain COX1 at PND 70 (all cohorts, *n* = 5). (**H**) Serum [Cu] at PND 70 (WT, *n* = 4; *mo-br* ES-Cu^{2+}, *n* = 6). (**I**) Brain [Cu] at PND 70 (WT, *n* = 5; *mo-br* ES-Cu^{2+}, *n* = 8). (**J**) Brain weights at PND 70 (WT, *n* = 8; *mo-br* ES-Cu^{2+}, *n* = 13). Data are reported as means ± SD with statistical significance assessed by one-way ANOVA or Welch one-way ANOVA with Tukey's post hoc test. NS, not significant; *P < 0.05; **P < 0.01; ***P < 0.001. Western blot images in (D) and (F) were analyzed with ImageJ software.

movie S2). ES-Cu^{2+} increased the survival of *mo-br* mice and successfully rescued 82% of animals at 10 weeks of age with a median survival of 203 days (P < 0.01, log-rank test) (Fig. 2F, fig. S8D, and Table 1). After treatment, ES-Cu^{2+} *mo-br* mice experienced accelerated growth and near normal body weight by week 10 (Fig. 2G and fig. S8E). Histological examination of the livers of WT vehicle and both ES-Cu^{2+}–treated WT and *mo-br* mice demonstrated no pathological changes associated with drug exposure (fig. S9).

Neuromotor assessment of ES-Cu^{2+} rescue

Ten-week-old *mo-br* mice were evaluated by phenotype and neuromotor functional tests. ES-Cu^{2+}–treated *mo-br* mice exhibited hypopigmentation but no other gross abnormalities on observation (Fig. 2, D and E). On a forelimb grip-strength test using a Chatillon force apparatus, ES-Cu^{2+}–treated *mo-br* mice possessed 73% grip strength compared with WT animals (0.94 versus 1.29 N, P < 0.01) (Fig. 3A). On the accelerating rotarod, a test of endurance and motor coordination, ES-Cu^{2+} *mo-br* mice exhibited average latency-to-fall time of 222 s compared with 379 s (P < 0.01) for WT (Fig. 3B). On the gait treadmill, overall ataxic indices for ES-Cu^{2+} *mo-br* mice were statistically insignificant for both pelvic and shoulder girdles compared with WT (Fig. 3C, table S5, and movies S3 and S4). In the open field, *mo-br* mice demonstrated 35% decreased movement time, 24% increased rest time, and traveled 60% of total distance compared with WT (P < 0.01) (Fig. 3, D to F).

Brain histology and biochemical markers of ES-Cu^{2+} therapy

Brain sections of vehicle and HIS-Cu^{2+}–treated mice at 2 weeks of age showed marked, diffuse neurodegeneration of cortical and hippocampal neurons (Fig. 4A and fig. S10A). In the hippocampus, necrotic pyramidal neurons represented 10.5% of 3200 counted cells in vehicle and 4.9% in HIS-Cu^{2+} *mo-br* mice. ES-Cu^{+2} preserved cortical and hippocampal neurons, with hippocampal regions showing no signs of necrosis as characterized by pyknotic nuclei (Fig. 4A). The Purkinje neuron layer in the cerebellum was also preserved. (fig. S10B). At 10 weeks of age, brain structures were preserved with no distinct differences between WT and ES-Cu^{2+}–treated *mo-br* mice (Fig. 4B and fig. S11, A to C).

Two-week-old mice treated with ES-Cu^{2+} showed normalized serum [Cu] (Fig. 5A) with increased brain [Cu] from the vehicle baseline of 22% of WT to 41% (0.45 versus 0.82 μg g^{-1}, P < 0.01) compared with 24% with HIS-Cu^{2+} (0.48 μg g^{-1}) (Fig. 5B). ES-Cu^{2+} proved superior to HIS-Cu^{2+} at delivering Cu to brain tissue (P < 0.01). Necropsy at 2 weeks showed significant decrease in total brain mass in *mo-br* animals treated with vehicle and HIS-Cu^{2+} (−16 and −12%) (Fig. 5C and tables S6 and S7). ES-Cu^{2+}-normalized brain mass was comparable to that of WT littermates (<2% difference between WT and *mo-br* ES-Cu^{2+} cohorts) (Fig. 5C).

Mitochondrial COX1 levels exhibited a 14% improvement with ES-Cu^{2+} intervention (30 versus 16%, P = 0.03) (Fig. 5, D and E). We did not observe any significant correction in COX1 levels in vehicle or HIS-Cu^{2+}–treated mice (17%, P = 0.99) (Fig. 5, D and E). Though overall brain [Cu] in the ES-Cu^{2+} cohort was about half of that in the WT cohort (0.82 versus 1.95 μg g^{-1}), the mitochondria-specific

delivery mechanism of ES-Cu^{2+} could explain the degree of COX1 metalation. We also observed significant improvements in [Cu] and COX1 levels in the hearts of ES-Cu^{2+}–treated *mo-br* mice both at PND 14 and 70 (fig. S12). SOD1 levels remained unchanged (fig. S13).

At 10 weeks, COX1 levels in ES-Cu^{2+} mice were 42% of those in WT mice (Fig. 5, F and G). Serum [Cu] reverted to the earlier-established *mo-br* baseline of 28% of WT (0.48 versus 1.73 μg mL^{-1}) (Fig. 5H). In the brain, Cu levels declined from 41 to 34% of WT (1.57 versus 4.64 μg g^{-1}) (Fig. 5I), but brain weights remained indistinguishable (0.448 versus 0.432 g, $P = 0.23$) (Fig. 5J and table S6).

Discussion

Although deficiencies in Cu transport and processing adversely affect numerous important biological pathways, the most profound pathological changes occur as a result of perturbation of the electron transport chain (*5*, *6*). Specifically, CcO requires Cu for assembly and catalytic activity of two subunits, COX1 and COX2 (*1*). CcO dysfunction secondary to Cu deficiency results in cardiomyopathy, neurodegeneration, and premature death (*13*, *14*). ES at relatively low dose stopped early mortality and conferred near-normal cardiac and brain histology while improving COX1 abundance in Cu-deficient cardiac-specific *Ctr1* KO and *mo-br* mice.

In cardiac *Ctr1* KO mice, affected animals possess elevated serum [Cu] (*20*), which allows for in vivo ES-Cu^{2+} complex formation and redistribution of Cu across CTR1-deficient cardiomyocyte membranes to mitochondria for metalation of CcO without supplementation of exogenous Cu. ES treatment completely reversed the delayed growth and slowed disease progression in these mice. ES-treated mice exhibited improved survival at PND 26. Heart COX1 levels improved from 34% baseline to 66% (+28%) with a corresponding normalization of heart weight and reduced cardiomyocyte area, despite only modest improvement in total tissue Cu levels.

HIS-Cu^{2+} clinical trials for Menkes disease have shown mixed results. Although there were some improvements in survival and clinical markers, these improvements were primarily observed in a subset of patients with mutations that display residual ATP7A activity (*14*, *25*). The *mo-br* mouse, possessing little residual transporter functionality (*22*), only marginally benefits from HIS-Cu^{2+} therapy. In contrast, ES-Cu^{2+} significantly improves total brain tissue [Cu] levels compared with HIS-Cu^{2+}, with improved outcomes for survival, restoration of growth, preservation of neurological structures, tissue Cu delivery, and COX1 abundance. Two doses of ES-Cu^{2+}, equaling ~4 μg of Cu by PND 10, rescued *mo-br* males and improved median survival from 14 to 203 days.

The 14% improvement in brain COX1 level in 2-week-old mice sufficiently preserved key neurological structures, such as cortical and hippocampal neurons. Preservation of brain structures and COX1 persisted past the 2-week assessment. At 10 weeks of age, the ES-Cu^{2+}–treated *mo-br* mice demonstrated normal brain structures and increased COX1 metalation with only small defects in gross neuromotor function, as determined by open field, rotarod, grip strength, and gait treadmill experiments.

Our in vivo results indicate that the mechanism of ES-mediated Cu relocalization may not be limited to the mitochondria. Morphological changes in fur pigmentation and whisker structure indicate improvement in the secretory pathway cuproenzymes tyrosinase and sulfhydryl oxidase, enzymes whose metalation requires ATP7A activity in the Golgi complex. Partial improvement in other secretory pathway cuproenzymes, such as dopamine-β-hydroxylase and lysyl oxidase, could further explain the beneficial effects given the profound deficiency of most Cu-utilizing systems associated with Menkes disease.

Administration of ES or ES-Cu^{2+} complex in a 1:1 stoichiometry and appropriate formulation exhibited good pharmacokinetic properties, low toxicity, and efficacy. Our results indicated that ES corrects defective CTR1 and ATP7A membrane-Cu transport with beneficial, targeted improvement of mitochondrial CcO metalation, owing to the ES-Cu^{2+} complex's mechanism of selective mitochondrial Cu release. The membrane-permeating properties of ES, coupled with its directed release mechanism, make this agent a good candidate for drug repurposing as a Cu courier for disorders affecting metalation of CcO. Our results in cardiac *Ctr1* KO and *mo-br* mice indicate that ES or ES-Cu^{2+} hold promise as a potential, efficacious therapeutic agent for the treatment of hereditary Cu-deficiency disorders.

REFERENCES AND NOTES

1. B. E. Kim, T. Nevitt, D. J. Thiele, *Nat. Chem. Biol.* **4**, 176–185 (2008).
2. L. M. Gaetke, H. S. Chow-Johnson, C. K. Chow, *Arch. Toxicol.* **88**, 1929–1938 (2014).
3. E. D. Harris, *Annu. Rev. Nutr.* **20**, 291–310 (2000).
4. N. J. Robinson, D. R. Winge, *Annu. Rev. Biochem.* **79**, 537–562 (2010).
5. I. Valnot *et al.*, *Am. J. Hum. Genet.* **67**, 1104–1109 (2000).
6. L. C. Papadopoulou *et al.*, *Nat. Genet.* **23**, 333–337 (1999).
7. S. G. Kaler, *Handb. Clin. Neurol.* **113**, 1745–1754 (2013).
8. H. Öhrvik, D. J. Thiele, *Ann. N.Y. Acad. Sci.* **1314**, 32–41 (2014).
9. B. S. Choi, W. Zheng, *Brain Res.* **1248**, 14–21 (2009).
10. S. G. Kaler, *Nat. Rev. Neurol.* **7**, 15–29 (2011).
11. H. Kodama, Y. Murata, M. Kobayashi, *Pediatr. Int.* **41**, 423–429 (1999).
12. M. Sparaco, A. Hirano, M. Hirano, S. DiMauro, E. Bonilla, *Brain Pathol.* **3**, 349–354 (1993).
13. S. Zlatic, H. S. Comstra, A. Gokhale, M. J. Petris, V. Faundez, *Neurobiol. Dis.* **81**, 154–161 (2015).
14. S. G. Kaler *et al.*, *N. Engl. J. Med.* **358**, 605–614 (2008).
15. J. H. Kim *et al.*, *Metab. Brain Dis.* **30**, 75–81 (2015).
16. S. Soma *et al.*, *Proc. Natl. Acad. Sci. U.S.A.* **115**, 8161–8166 (2018).
17. A. S. Grillo *et al.*, *Science* **356**, 608–616 (2017).
18. M. D. Garrick *et al.*, *Biometals* **32**, 745–755 (2019).
19. J. Lee, J. R. Prohaska, D. J. Thiele, *Proc. Natl. Acad. Sci. U.S.A.* **98**, 6842–6847 (2001).
20. B. E. Kim *et al.*, *Cell Metab.* **11**, 353–363 (2010).
21. M. J. Niciu *et al.*, *Neurobiol. Dis.* **27**, 278–291 (2007).
22. A. Grimes, C. J. Hearn, P. Lockhart, D. F. Newgreen, J. F. Mercer, *Hum. Mol. Genet.* **6**, 1037–1042 (1997).
23. A. Donsante *et al.*, *Mol. Ther.* **19**, 2114–2123 (2011).
24. M. R. Haddad *et al.*, *Mol. Ther. Methods Clin. Dev.* **10**, 165–178 (2018).
25. S. G. Kaler, *J. Trace Elem. Med. Biol.* **28**, 427–430 (2014).
26. J. W. Pyatskowit, J. R. Prohaska, *Comp. Biochem. Physiol. C Toxicol. Pharmacol.* **147**, 316–323 (2008).
27. S. R. Setty *et al.*, *Nature* **454**, 1142–1146 (2008).
28. J. M. Gillespie, *Australas. J. Dermatol.* **14**, 127–131 (1973).

ACKNOWLEDGMENTS

We thank H. McGuire and R. McAdams for rodent husbandry and tissue processing assistance; P. Trivedi for optimizing the *mo-br* genotyping protocol; and C. Klemashevich and S. Shankar from Texas A&M University Integrated Metabolomics Analysis Core (IMAC) for mass spectroscopy technical expertise. We thank M. Anguiano from Texas Veterinary Medicine Diagnostics Laboratory (TVMDL) for brain histology technical help. **Funding:** This work was supported by the Chancellor's Research Initiative, Texas A&M University System (J.C.S.), Welch Foundation grants A-0015 (J.C.S.) and A-1810 (V.M.G.), and National Institutes of Health grants R01GM111672 (V.M.G.) and R01DK110195 (B.-E.K.).
Author contributions: L.M.G. established *mo-br* rodent colony, husbandry and breeding, drug formulations, and pharmacokinetics and toxicological (PK/Tox) experiments; developed interventional protocols, efficacy studies, and behavioral studies; and wrote the manuscript. A.S., T.C.S., S.S., M.Z., H.F.G., B.L., C.D.V., and E.N. assisted in husbandry and biological sample processing for PK/Tox, histology, and biochemical experiments. S.S. and M.Z. performed tissue, Cu, and biochemical studies. A.A. synthesized ES-Cu^{2+} complex. V.S. and M.J.P. developed the *ATP7A*$^{-/-}$ B16 melanoma cell line and provided technical expertise. F.R.L. performed histopathology sectioning, generation of digital slide sets, and analysis. S.Y. and B.-E.K. established cardiac *Ctr1* KO rodent colony, husbandry and breeding, efficacy studies, histology, and biochemical studies. V.M.G. and J.C.S. developed the concept of ES drug therapy for hereditary Cu disorders, provided administrative and technical expertise, undertook data analysis, and helped write the manuscript. **Competing interests:** L.M.G., J.C.S., S.S., and V.M.G. are inventors on the patent application PCT/US2019/041571 submitted by Texas A&M University entitled "Compositions for the Treatment of Copper Deficiency and Methods of Use." **Data and materials availability:** All data are available in the main text or the supplementary materials.

SUPPLEMENTARY MATERIALS

science.sciencemag.org/content/368/6491/620/suppl/DC1
Materials and Methods
Supplementary Text
Figs. S1 to S13
Tables S1 to S7
References (*29*–*33*)
MDAR Reproducibility Checklist
Movies S1 to S4

View/request a protocol for this paper from *Bio-protocol*.

18 October 2019; resubmitted 10 February 2020
Accepted 19 March 2020
10.1126/science.aaz8899

REPORT

ULTRACOLD CHEMISTRY

Imaging the onset of the resonance regime in low-energy NO-He collisions

Tim de Jongh[1]*, Matthieu Besemer[1]*, Quan Shuai[1]*, Tijs Karman[2], Ad van der Avoird[1], Gerrit C. Groenenboom[1]†, Sebastiaan Y. T. van de Meerakker[1]†

At low energies, the quantum wave–like nature of molecular interactions results in distinctive scattering behavior, ranging from the universal Wigner laws near 0 kelvin to the occurrence of scattering resonances at higher energies. It has proven challenging to experimentally probe the individual waves underlying these phenomena. We report measurements of state-to-state integral and differential cross sections for inelastic NO-He collisions in the 0.2 to 8.5 centimeter^{-1} range with 0.02 centimeter^{-1} resolution. We studied the onset of the resonance regime by probing the lowest-lying resonance dominated by *s* and *p* waves only. The highly structured differential cross sections directly reflect the increasing number of contributing waves as the energy is increased. Only with CCSDT(Q) level of theory was it possible to reproduce our measurements.

The study of collisions between atoms and molecules at the full quantum level has been an important research goal in chemistry and physics for decades (*1*). To date, the internal rotational and vibrational states of molecules have received the most attention, and a rich variety of experimental methods has been developed to select a single quantum state before the collision and to probe the occupied quantum states of the products (*2*). The wealth of experimental and theoretical state-to-state scattering studies has contributed immensely to our present understanding of molecular interactions (*3*).

Yet in addition to these internal states, the angular momentum associated with the relative motion of the particles is also quantized. It is described by a set of orbital angular momentum states, or partial waves, with integer quantum number ℓ, which takes the values $\ell = 0, 1, 2, \ldots$ with names *s*, *p*, *d*, ...-wave, respectively. The contribution of each partial wave to a scattering cross section describes how the reagents transform into products at the most fundamental state-to-state level and contains all of the information about the scattering event.

The influence of a single partial wave to a collision event is in principle directly encoded in the differential cross sections (DCSs), which can be probed experimentally. For atom-atom collisions, each wave will result in a distinctive angular distribution in which the number of nodes observed in a DCS equals the value of ℓ (*4*). That is, *s*-wave scattering leads to an isotropic DCS, *p*-wave scattering results in a single node, and so on. For molecular systems with anisotropic interactions, multiple partial waves contribute and interfere with each other, resulting in a more complicated DCS pattern from which the partial wave composition cannot be directly discerned. The identification of the partial wave composition of a collision event from experimental observations has therefore remained a formidable challenge (*5*), preventing state-to-state experiments at the full partial-wave level.

The effects of individual partial waves may best be observed in situations in which only a limited number of interfering waves contribute. This number critically depends on the particles' de Broglie wavelengths and, hence, the collision energy (*6*, *7*). If the energy is too high, a large number of waves contribute, so that the collisions may be regarded as semiclassical, and the dynamics can often be described with semiclassical models. There is no hope to disentangle the contribution of individual waves from experimental observations in this regime. By contrast, at energies approaching 0 K, only the lowest allowed partial wave (for most systems, this is the *s*-wave) contributes, leading to universal rules for the energy dependence of collision cross sections in the form of Wigner's threshold laws (*8*). In this "ultracold" regime, the *s*-wave results in DCSs that contain no intrinsic structure; the number of contributing waves is too low to harness information on the interaction potential and collision dynamics from state-to-state experiments.

As the energy is increased from the ultracold limit, the number of contributing partial waves consecutively increases, yielding unprecendented opportunities to directly observe the effect of individual waves on the scattering cross section. The regime is entered where scattering resonances occur in the collision cross sections: When the collision energy becomes resonant with a quasi-bound state supported by the interaction potential, the incident particles are temporarily captured into a quasi-bound long-lived complex (*9*). In a simplified picture, these resonances may be regarded as the orbiting of the atom around the molecule (a shape resonance) or as the transient excitation of the molecule to a state of higher energy (Feshbach resonance). Analogous to Bohr's model of electrons orbiting around an atom's nucleus with given angular momentum, the atom-molecule binary system is stabilized when the collision energy is resonant with a partial wave that fits on the atom's orbit an integer number of times. The corresponding "resonant" partial wave will dominate the scattering process, which appears as a sudden increase in the integral cross section (ICS) at the resonance energy. The resonant wave will dominate the DCS as well, resulting in an angular distribution that fits the value for ℓ from which the resonance originates. Measurements of DCSs at resonances therefore yield the distinctive opportunity to experimentally probe the partial-wave fingerprint of the collision process, revealing the scattering mechanism at the most fundamental state-to-state quantum mechanical level.

Scattering resonances are extremely sensitive to the details of the potential energy surface (PES), in particular at energies just above the ultracold Wigner limit at which only a few waves with $\ell > 0$ start contributing. Their observation has been a quest in molecular physics for decades (*10*); however, it has proven extremely challenging to experimentally reach the low energies to access the relevant energy region and the high-energy resolutions required to scan the energy over the resonances and to probe DCSs (*11*–*15*). In ultracold gases, scattering resonances are routinely induced by tuning external fields to shift bound states into resonance (*16*, *17*), but *s*-wave collisions observed in such experiments invariably result in isotropic DCSs, containing little information about the collision dynamics. To date, only a few experiments have succeeded in directly measuring the energy dependence of state-to-state cross sections near resonances, mostly by using molecular beam methods (*18*). Resonances in ICSs have been observed by using the crossed-beam approach, using a small beam intersection angle (*19*–*23*). Using merged beams, resonances in Penning ionization cross sections of metastable atoms with atomic and molecular partners have been studied at energies down to 0.01 cm^{-1} (*24*–*28*). Measurements of resonance features in state-to-state DCSs for inelastic collisions have recently also become possible by using the Stark deceleration and velocity map imaging techniques

[1]Institute for Molecules and Materials, Radboud University, 6525 AJ Nijmegen, Netherlands. [2]Institute for Theoretical Atomic Molecular and Optical Physics, Center For Astrophysics, Harvard and Smithsonian, Cambridge, MA 02138, USA.
*These authors contributed equally to this work.
†Corresponding author. Email: basvdm@science.ru.nl, gerritg@theochem.ru.nl

(*29*, *30*), although the lowest energy achieved was limited to 13 cm^{-1}, which is typically two to three orders of magnitude too hot to probe individual partial waves. Measurements of state-to-state ICSs and DCSs at energies that approach the ultracold Wigner regime, at which only a few waves contribute, have remained elusive, hampering a detailed view on how molecular collisions evolve from the pure quantum single-partial-wave into the multi-partial-wave regime (*31*).

Here, we report the measurement of state-to-state ICSs and DCSs for inelastic collisions between state-selected NO [$X^2\Pi_{1/2}$, $v = 0, j = 1/2f$, hereafter referred to as ($1/2f$) (*32*)] radicals and He atoms in a crossed-beam experiment at energies between 0.2 and 8.5 cm^{-1}, with an energy resolution of 0.02 cm^{-1}. Three fully resolved partial-wave resonances were observed in the ICS, and the incline of a fourth resonance was observed at the lowest energies. These resonances originated from the lowest-lying quasi-bound states supported by the NO-He interaction potential just above the energetic long-range asymptote. They correspond to values for ℓ that follow a progression from the lowest possible value and probe the onset of the resonance regime at energies connecting to the ultracold Wigner limit. Rapid variations were observed in the highly structured DCSs as the energy was scanned over the resonances, in which the number of nodes observed in the angular distributions directly reflected the increasing value of ℓ as the energy was increased. We found that our measurements of the lowest partial-wave resonances in NO-He could not be reproduced satisfactorily by the most advanced NO-He PES at the CCSD(T) (*33*) level of theory. Good agreement was only obtained with an ab initio PES at the CCSDT(Q) (*33*) level. Such level of precision was previously only needed for high-resolution spectroscopy of bound states probing the PES in the region of the well (*34*) and anticipated for low-energy scattering resonances (*30*). The need for theory at the CCSDT(Q) level as demonstrated here for NO-He collisions illustrates the unprecedented sensitivity of scattering resonances in probing PESs accross their entire energy landscapes.

We used a crossed-molecular-beam apparatus that combines Stark deceleration and velocity map imaging (VMI) (supplementary materials). A packet of NO ($1/2f$) radicals with a computer-controlled velocity and a narrow velocity spread was produced by using the Stark decelerator. A beam of He atoms was produced with a cryogenic valve held at temperatures between 11 and 18 K. Beam intersection angles of 5° and 10° were used to cover the 0.2 to 3 cm^{-1} and 0.8 to 8.5 cm^{-1} energy ranges, respectively. The collision energy resolution ranged from 0.02 cm^{-1} for the lowest collision energies to 0.7 cm^{-1} for the highest energies. The scattered NO radicals were state-selectively detected by using a two-color laser ionization scheme and velocity mapped on a two-dimensional detector. The measurements with a 5° intersection angle were performed by using a VMI detector that offered improved velocity resolution.

We studied collisions that de-excite the NO radicals from the ($1/2f$) to the ($1/2e$) level, which have an energy splitting of 0.01 cm^{-1} (*35*). For ICS measurements, we scanned the collision energy between 0.2 and 8.5 cm^{-1} and observed three prominent resonances in the relative ICS with almost zero scattering probability at energies in between the resonances (Fig. 1A). The incline of a fourth resonance was observed below 1 cm^{-1}. We compared the experimentally obtained relative ICS with theoretical ICSs, convoluted with the experimental resolution, based on two sets of PESs (Fig. 1A

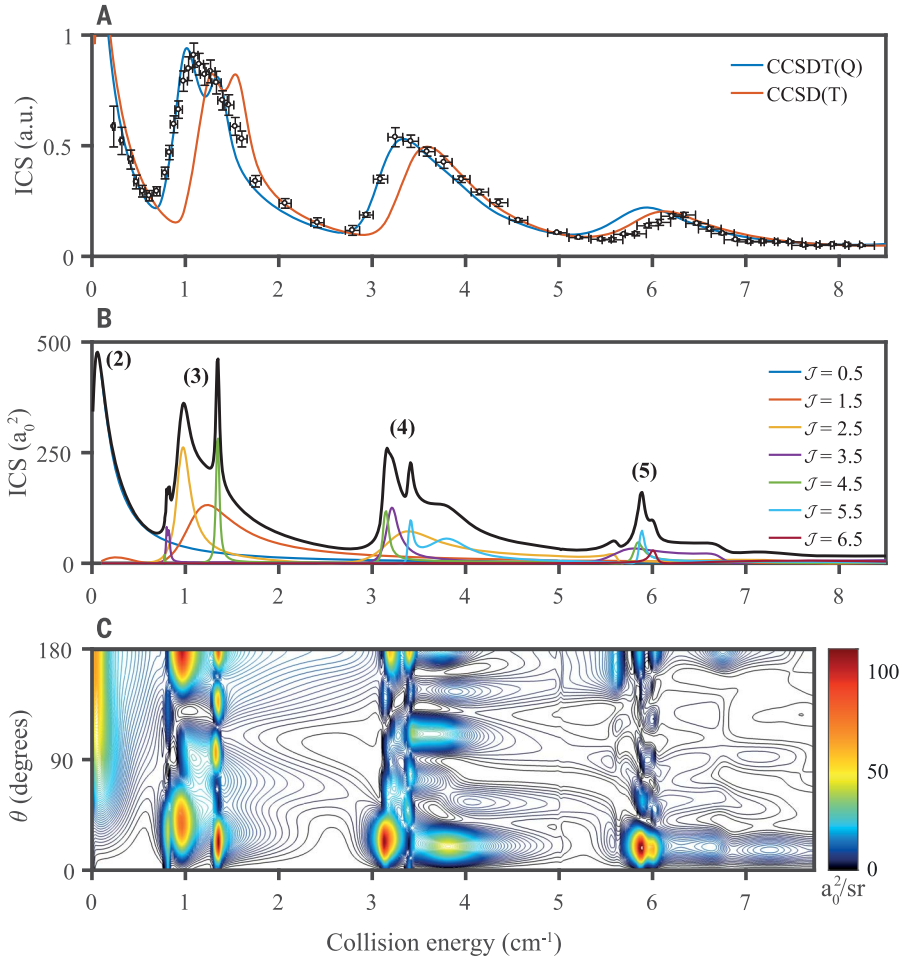


Fig. 1. Collision energy dependence of integral and differential cross sections for inelastic NO-He ($j = 0.5f \rightarrow 0.5e$) collisions. (**A**) Comparison between measured (data points with error bars) and calculated (solid curves) cross sections based on CCSD(T) and CCSDT(Q) potentials. Experimental data are in a.u., arbitrary units. Data were accumulated using a continuous cycle over collision energies. Vertical error bars represent statistical uncertainties at 95% of the confidence interval. Horizontal error bars represent uncertainties in energy calibration. The calculated cross sections were convoluted with the experimental energy resolution. (**B**) Theoretically predicted state-to-state cross section based on the CCSDT(Q) potential (black), together with the contribution of each angular momentum state with quantum number $\mathcal{J}$. The value for the resonant partial wave ℓ_{res} is given in parenthesis. (**C**) Contour plot of theoretically calculated [CCSDT(Q)-potential] DCS as function of collision energy.

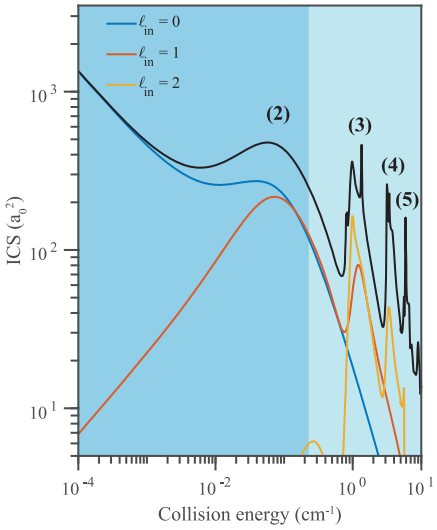


Fig. 2. Logarithmic plot of theoretical ICSs based on the CCSDT(Q)-potential. Included are the contributions of *s*, *p*, and *d* partial waves in the ingoing channel. The value for the resonant partial wave ℓ_{res} is given in parenthesis. The light blue shaded area indicates the energy region probed in our measurements.

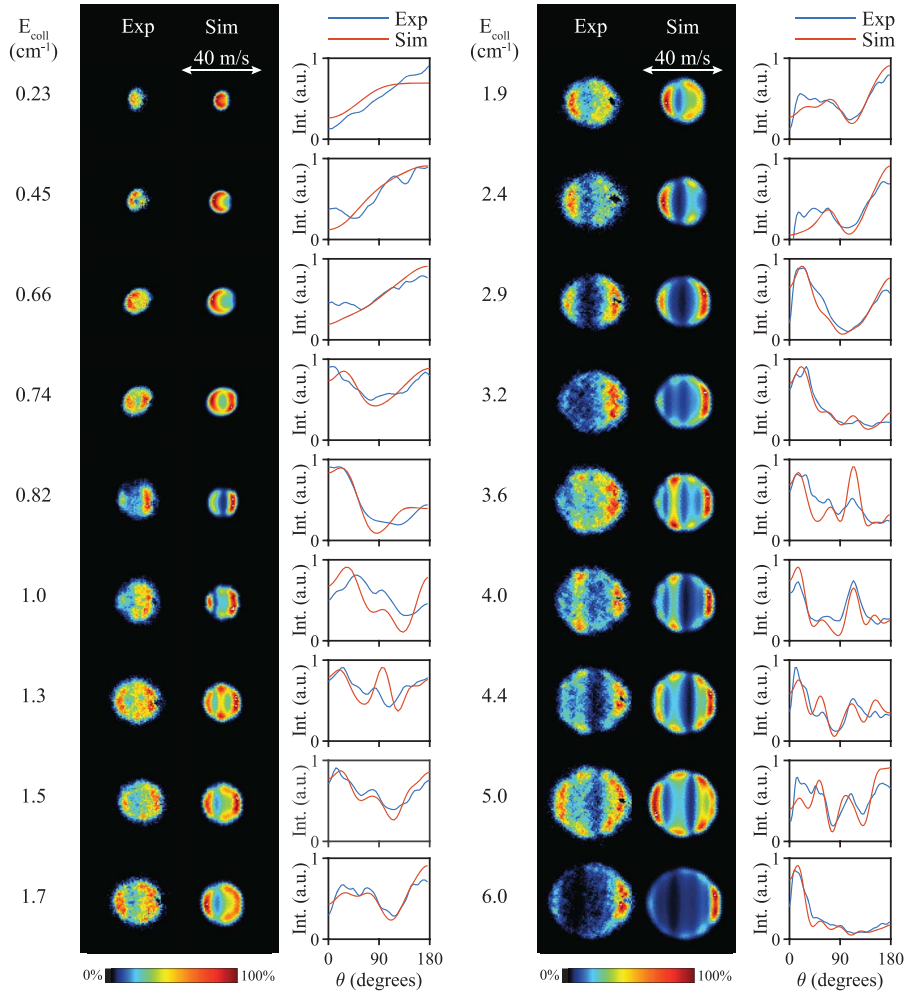


Fig. 3. Experimental and simulated ion images based on the CCSDT(Q) potential at selected collision energies. Exp, experimental; Sim, simulated. The images are presented so that the relative velocity vector is oriented horizontally, with the forward direction on the right side of the image. Small segments of the images around forward scattering are masked owing to imperfect state selection of the NO packet. The angular scattering distributions as derived from the experimental (blue curves) and simulated (red curves) images are shown for each collision energy.

and fig. S6). The first set of potentials was computed at the UCCSD(T)/CBS (*33*) limit by using a complete basis-set extrapolation (CBS) scheme. The second set of PESs were computed at the UCCSDT(Q)/CBS (*33*) level. We refer to the sets as CCSD(T) and CCSDT(Q) potentials, respectively. The CCSDT(Q) potential is deeper than the CCSD(T) potential by about 0.6 cm^{-1} near the well of the potential (table S1) and causes a linear shift of roughly 0.25 cm^{-1} in the position of all the calculated resonances. We found that the CCSDT(Q) corrections were essential to quantitatively describe the lowest-lying resonances, although the resonance observed near 6.5 cm^{-1} was predicted at slightly lower energies by both potentials. We performed several tests to investigate the possible origin of this discrepancy. A few test points computed at the UCCSDTQ(P) (*33*) level suggest that the electron correlation for the UCCSDT(Q) potentials is converged to better than 0.1 cm^{-1}. We also devised a method by which to investigate the sensitivity of the resonances to changes in the PESs; using an *S*-matrix Kohn variational method (*36*, *37*), we isolated a square integrable resonance contribution to the wave function, which allowed us to compute the first-order response to changes in the PES as a simple integral. We tested overall scaling, scaling of the correlation energy alone, the anisotropy of the PESs, or a radial shift (supplementary materials). We found that in all cases, all resonances shift in the same direction by nearly the same amount of energy, implying that it is hard to adjust the position of the highest resonance into closer agreement with the experiment without affecting the lower-lying resonances, even if we admit much larger variations than the expected uncertainty of the potential. With uncertainties in the PESs virtually ruled out as a non-negligible source of error in the resonance positions, we performed three further checks: We investigated (i) the effect of including scalar relativistic effects, (ii) the effect of explicitly including NO zero-point vibrational motion, and (iii) the effect of the diagonal Born-Oppenheimer correction (DBOC). This last test required a modification of the usual DBOC because the two-PESs scattering method already corrected for the dominant non–Born-Oppenheimer couplings. These three checks are discussed in detail in the supplementary materials, and all three were found to have a negligible effect.

We analyzed the partial-wave composition of the resonances from the CCSDT(Q) potentials and expressed them in terms of the total angular momentum with conserved quantum number $\mathcal{J}$, which forms from the coupling of the rotational state of NO with quantum number $j = 0.5$ and the partial-wave quantum numbers ℓ_{in} and ℓ_{out} that represent the relevant partial waves in the ingoing and outgoing channel, respectively: $\mathcal{J} = \ell_{in/out} \pm 0.5$ (Fig. 1B). Each observed resonance feature was found to consist of a set of overlapping resonances, which we could characterize as mostly pure Feshbach resonances (supplementary materials), with a distinctive value for the resonant partial wave ℓ_{res} corresponding to the quasi-bound NO-He state from which the resonance originates. The resonance below 1 cm^{-1} is characterized by the lowest possible value for $\mathcal{J}$ and ℓ_{res} ($\mathcal{J} = 0.5$; $\ell_{res} = 2$), corresponding to the

lowest NO-He quasi-bound state located just above the energetic asymptote of the free NO radical and He atom. Resonances with $\ell_{res} = 0$ or 1 do not exist because these values correspond to real bound states supported by the potential well (fig. S9 and table S4). The $\ell_{res} = 2$ resonance is further characterized by almost equal contributions of outgoing waves, with $\ell_{out} = 0$ (*s*-wave) and $\ell_{out} = 1$ (*p*-wave). From the ICS calculated in an extended energy regime [Fig. 2; the results based on the CCSD(T) potentials are provided in fig. S8], this resonance was found to connect to the pure *s*-wave Wigner regime, where the ICS is proportional to $1/\sqrt{E}$. The series of resonance features found at higher energies follow the progression of $\ell_{res} = 2, 3, 4, 5, \ldots$ and probe the consecutive series of quasi-bound NO-He states supported by the interaction potential.

The underlying partial-wave composition of a resonance was directly reflected in the energy dependence of the DCS. We first analyzed the inherent structure of the DCS by compiling a contour plot of the theoretically predicted DCS versus collision energy (Fig. 1C). We found that at energies in between the resonances, the DCS was rather independent of the collision energy. By contrast, at a resonance, the DCS was observed to change rapidly, following the rapid change of contributing partial waves. At the resonance energies, it was possible to discern the two dominant ingoing and outgoing partial waves ℓ_{in} and ℓ_{out} underlying the resonance from the DCS: The number of nodes observed in the angular distribution equals the highest value of ℓ.

We experimentally probed the energy dependence of the DCS by measuring scattering images at selected energies at which the DCS was predicted to change rapidly with collision energy and compared them with a simulated scattering image based on the CCSDT(Q) potentials and kinematics of the experiment (Fig. 3). At the lowest energies probed, the velocity images were small, but we could still discern structure in the images. For energies up to 0.7 cm^{-1}, we found strong backscattering, which evolved into a forward-backward peaked structure at energies around 0.7 to 0.8 cm^{-1}. The observed distributions arose from the interference of the *s*- and *p*-waves that dominate the scattering at these low energies. For energies greater than 0.8 cm^{-1}, we observed a rich energy dependence of the DCS, with additional peaks and nodes appearing, reflecting the addition of consecutive partial waves as the energy was increased. We extracted angular scattering distributions from the experimental and simulated images and found excellent agreement with the experimental and simulated distributions.

The resonance structures in both the ICS and DCS as reported here were extremely sensitive to the details of the PESs: The small change in well-depth between the CCSD(T) and CCSDT(Q) PESs caused an experimentally observable shift in resonance position. We investigated this sensitivity further by measuring the resonance position found around 1.3 cm^{-1} for collisions of He with ^{14}NO and ^{15}NO (Fig. 4). The isotope effect and associated change in reduced mass, center-of-mass point of the NO-He complex, and rotational constant resulted in a difference in the centrifugal barrier, anisotropy of the potential, and change in energies of the rotational states (fig. S13). Consequently, the resonance position for He collisions with the heavier ^{15}NO radical was found to shift by ~0.18 cm^{-1} to lower energies, primarily caused by a change in the rotational constant and in excellent agreement with theoretical predictions.

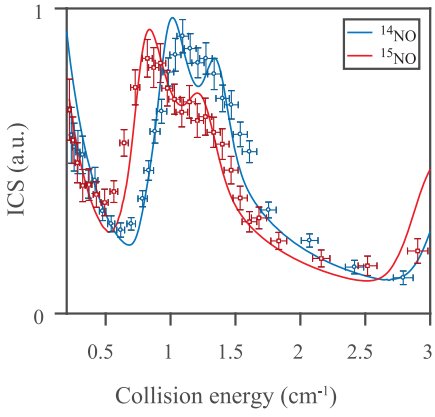


Fig. 4. Measurements of the relative state-to-state ICSs for inelastic (j = 0.5f → j = 0.5e) collisions of $^{14}N^{16}O$ and $^{15}N^{16}O$ with He around the resonance feature at 1 cm^{-1}. Blue data points indicate $^{14}N^{16}O$, and red data points indicate $^{15}N^{16}O$. Shown also are the calculated cross sections from the CCSDT(Q) potential convoluted with the experimental resolution. Vertical error bars represent statistical uncertainties at 95% CI. Horizontal error bars represent uncertainties in energy calibration.

Our joint experimental and theoretical studies of partial-wave resonances for the benchmark NO-He system at energies down to 0.2 cm^{-1} showed that cold collisions in chemically relevant systems can be probed with full quantum-state resolution—at the partial-wave level—and at energies approaching the Wigner regime. Measurements of the collision energy dependence of the ICS and, in particular, the DCSs revealed how molecular collisions transformed from ultracold into hot by subsequently adding a partial wave as the energy is increased, bridging the gap between the ultracold quantum physics and physical chemistry communities. The high resolution with which resonances were probed experimentally required theory beyond the gold-standard CCSD(T) level to obtain quantitative agreement and allowed for the observation of minute isotope shifts in the resonance positions. The energies attained here were lower than the typical interaction energy of a molecule that posseses an electric or magnetic dipole moment with an external electric or magnetic field, respectively, opening up the possibility to tune the collision dynamics with tailored electric or magnetic fields, maintaining the quantum-state preparation of the reagents and the quantum-state resolution of the products. Field control of cold molecular collisions would transform these studies from merely probing nature with the highest possible level of detail into manipulating nature with the highest possible level of control.

REFERENCES AND NOTES

1. R. D. Levine, R. B. Bernstein, *Molecular Reaction Dynamics and Chemical Reactivity* (Oxford Univ. Press, 1987).
2. A. Schiffman, D. W. Chandler, *Int. Rev. Phys. Chem.* **14**, 371–420 (1995).
3. M. Brouard, C. Vallance, *Tutorials in Molecular Reaction Dynamics* (RSC Publishing, 2010).
4. M. McDonald *et al*., *Nature* **535**, 122–126 (2016).
5. W. E. Perreault, N. Mukherjee, R. N. Zare, *Science* **358**, 356–359 (2017).
6. J. L. Bohn, A. M. Rey, J. Ye, *Science* **357**, 1002–1010 (2017).
7. R. Krems, W. Stwalley, B. Friedrich, Eds., *Cold Molecules: Theory, Experiment, Applications* (Taylor and Francis, 2009).
8. E. P. Wigner, *Phys. Rev.* **73**, 1002–1009 (1948).
9. M. T. Bell, T. P. Softley, *Mol. Phys.* **107**, 99–132 (2009).
10. W. Erlewein, M. von Seggern, J. P. Toennies, *Z. Phys.* **211**, 35–50 (1968).
11. C. Naulin, M. Costes, *Int. Rev. Phys. Chem.* **33**, 427–446 (2014).
12. W. Dong *et al*., *Science* **327**, 1501–1502 (2010).
13. T. Yang *et al*., *Science* **347**, 60–63 (2015).
14. J. B. Kim *et al*., *Science* **349**, 510–513 (2015).
15. D. Hauser *et al*., *Nat. Phys.* **11**, 467–470 (2015).
16. J. Weiner, V. S. Bagnato, S. Zilio, P. S. Julienne, *Rev. Mod. Phys.* **71**, 1–85 (1999).
17. G. Quéméner, P. S. Julienne, *Chem. Rev.* **112**, 4949–5011 (2012).
18. J. Jankunas, A. Osterwalder, *Annu. Rev. Phys. Chem.* **66**, 241–262 (2015).
19. S. Chefdeville *et al*., *Phys. Rev. Lett.* **109**, 023201 (2012).
20. M. Lara *et al*., *Phys. Rev. Lett.* **109**, 133201 (2012).
21. S. Chefdeville *et al*., *Science* **341**, 1094–1096 (2013).
22. A. Bergeat, J. Onvlee, C. Naulin, A. van der Avoird, M. Costes, *Nat. Chem.* **7**, 349–353 (2015).
23. A. Bergeat *et al*., *Nat. Chem.* **10**, 519–522 (2018).
24. A. B. Henson, S. Gersten, Y. Shagam, J. Narevicius, E. Narevicius, *Science* **338**, 234–238 (2012).
25. E. Lavert-Ofir *et al*., *Nat. Chem.* **6**, 332–335 (2014).
26. A. Klein *et al*., *Nat. Phys.* **13**, 35–38 (2017).
27. Y. Shagam *et al*., *Nat. Chem.* **7**, 921–926 (2015).
28. J. Jankunas, K. Jachymski, M. Hapka, A. Osterwalder, *J. Chem. Phys.* **142**, 164305 (2015).
29. S. N. Vogels *et al*., *Science* **350**, 787–790 (2015).
30. S. N. Vogels *et al*., *Nat. Chem.* **10**, 435–440 (2018).
31. S. S. Kondov *et al*., *Phys. Rev. Lett.* **121**, 143401 (2018).
32. The labels $X^2\Pi_{1/2}$, v, and j indicate the electronic state, the vibrational state, and rotational state of the NO radical, respectively. Each rotational state of NO possesses two near-degenerate Λ-doublet components, with symmetry labels *e* (lower component) and *f* (upper component), that refer to the total parity of the electronic wave function, exclusive of rotation.
33. The abbreviations CCSD(T), CCSDT(Q), and CCSDTQ(P) denote the level of coupled-cluster (CC) theory used to calculate potential-energy surfaces, which include single (S), double (D), triple (T), quadruple (Q), and quintuple (P) excitations of electrons. The last letter in parenthesis indicates perturbative treatment of the excitation. The prefix letter U stands for unrestricted and further details the implementation of the theoretical methods.
34. P. Jankowski, A. R. W. McKellar, K. Szalewicz, *Science* **336**, 1147–1150 (2012).

35. W. L. Meerts, A. Dymanus, *J. Mol. Spectrosc.* **44**, 320–346 (1972).
36. J. Z. H. Zhang, W. H. Miller, *J. Chem. Phys.* **91**, 1528–1547 (1989).
37. G. C. Groenenboom, D. T. Colbert, *J. Chem. Phys.* **99**, 9681–9696 (1993).
38. T. de Jongh, M. Besemer, Q. Shuai, T. Karman, A. van der Avoird, G. C. Groenenboom, S. Y. T. van de Meerakker, Imaging the onset of the resonance regime in low-energy NO-He collisions online data. DANS (2020); doi:10.17026/dans-x4h-ur6f.

ACKNOWLEDGMENTS

We thank J. Klos for providing us with NO-He PESs at the CCSD(T) level, T. Cremers for developing data acquisition software, and J. Stanton for help with DBOC calculations. We thank N. Janssen and A. van Roij for expert technical support. **Funding:** This work is part of the research program of the Netherlands Organization for Scientific Research (NWO). S.Y.T.v.d.M. acknowledges support from the European Research Council (ERC) under the European Union's Seventh Framework Program (FP7/2007-2013/ERC grant agreement 335646 MOLBIL) and from the ERC under the European Union's Horizon 2020 Research and Innovation Program (grant agreement 817947 FICOMOL). **Author contributions:** The project was conceived by S.Y.T.v.d.M. The experiments, data analysis, and simulations were carried out by T.d.J. and Q.S. Potential energy surfaces and scattering cross sections were calculated by M.B., A.v.d.A., and G.C.G. DBOC calculations for open-shell systems were performed by G.C.G. The *S*-matrix Kohn-variational method was implemented by T.K. All authors were involved in the interpretation of the data, discussed the results, and commented on the manuscript. The paper was written by T.d.J., M.B., and S.Y.T.v.d.M., with contributions from all authors. **Competing interests:** None declared. **Data and materials availability:** All data are available in the main text or the supplementary materials, as well as online at DANS (*38*).

SUPPLEMENTARY MATERIALS

science.sciencemag.org/content/368/6491/626/suppl/DC1
Supplementary Text
Figs. S1 to S13
Tables S1 to S4
References (*39*–*70*)

29 November 2019; accepted 19 March 2020
10.1126/science.aba3990

CORONAVIRUS

A highly conserved cryptic epitope in the receptor binding domains of SARS-CoV-2 and SARS-CoV

Meng Yuan[1]*, Nicholas C. Wu[1]*, Xueyong Zhu[1], Chang-Chun D. Lee[1], Ray T. Y. So[2], Huibin Lv[2], Chris K. P. Mok[2]†, Ian A. Wilson[1,3]†

The outbreak of coronavirus disease 2019 (COVID-19) caused by severe acute respiratory syndrome–coronavirus 2 (SARS-CoV-2) has now become a pandemic, but there is currently very little understanding of the antigenicity of the virus. We therefore determined the crystal structure of CR3022, a neutralizing antibody previously isolated from a convalescent SARS patient, in complex with the receptor binding domain (RBD) of the SARS-CoV-2 spike (S) protein at 3.1-angstrom resolution. CR3022 targets a highly conserved epitope, distal from the receptor binding site, that enables cross-reactive binding between SARS-CoV-2 and SARS-CoV. Structural modeling further demonstrates that the binding epitope can only be accessed by CR3022 when at least two RBDs on the trimeric S protein are in the "up" conformation and slightly rotated. These results provide molecular insights into antibody recognition of SARS-CoV-2.

The ongoing outbreak of coronavirus disease 2019 (COVID-19) originated in China in December 2019 (*1*) and became a global pandemic by March 2020. COVID-19 is caused by a novel coronavirus, severe acute respiratory syndrome–coronavirus 2 (SARS-CoV-2) (*2*). Two other coronaviruses have caused worldwide outbreaks in the past two decades, namely SARS-CoV (2002–2003) and Middle East respiratory syndrome coronavirus (MERS-CoV) (2012–present). The surface spike (S) glycoprotein, which is critical for virus entry through engaging the host receptor and mediating virus-host membrane fusion, is the major antigen of coronaviruses. The S proteins of SARS-CoV-2 and SARS-CoV, which are phylogenetically closely related, have an amino acid sequence identity of ~77% (*3*). Such a high degree of sequence similarity raises the possibility that cross-reactive epitopes may exist.

CR3022, which was previously isolated from a convalescent SARS patient, is a neutralizing antibody that targets the receptor binding domain (RBD) of SARS-CoV (*4*). The immunoglobulin heavy chain variable, diversity, and joining (IGHV, IGHD, and IGHJ) regions are encoded by germline genes IGHV5-51, IGHD3-10, and IGHJ6, and the light chain variable and joining regions (IGKV and IGKJ) are encoded by IGKV4-1 and IGKJ2 (*4*). IgBlast analysis (*5*) indicates that the IGHV of CR3022 is 3.1% somatically mutated at the nucleotide sequence level, which results in eight amino acid changes from the germline sequence, whereas IGKV of CR3022 is 1.3% somatically mutated, resulting in three amino acid changes from the germline sequence (fig. S1). A recent study has shown that CR3022 can also bind to the RBD of SARS-CoV-2 (*6*). This finding provides an opportunity to uncover a cross-reactive epitope. We therefore determined the crystal structure of CR3022 with the SARS-CoV-2 RBD (Fig. 1A) at 3.1-Å resolution (table S1 and fig. S2, A and B) (*7*). CR3022 uses both heavy and light chains (Fig. 1B) as well as all six complementarity-determining region (CDR) loops (Fig. 1C) for interaction with the RBD. The buried surface area on the epitope is 917 Å^2, and SARS-CoV-2 recognition by CR3022 is largely driven by hydrophobic interactions (Fig. 1E). Five out of 11 somatic mutations are found in the paratope region (defined as residues on the antibody buried by RBD) (fig. S2C), implying their likely importance in the affinity maturation process.

Out of 28 residues in the epitope (defined as residues buried by CR3022), 24 (86%) are conserved between SARS-CoV-2 and SARS-CoV (Figs. 1D and 2A). This high sequence conservation explains the cross-reactivity of CR3022. Nonetheless, despite having a high conservation of the epitope residues, CR3022 Fab binds to SARS-CoV RBD [dissociation constant (K_d) = 1 nM] with a much higher affinity than it does to SARS-CoV-2 RBD (K_d = 115 nM) (Table 1 and fig. S3). The difference in binding affinity of CR3022 to SARS-CoV-2 and SARS-CoV RBDs is likely due to the nonconserved residues in the epitope (Fig. 2). The most drastic difference is an additional N-glycosylation site at N370 on SARS-CoV (N357 in SARS-CoV numbering). The N-glycan sequon (N-X-S/T, where X is any amino acid but proline) arises from an amino acid difference at residue 372, where SARS-CoV has a Thr compared with Ala in SARS-CoV-2 (Fig. 2B). Mass spectrometry analysis shows that a complex glycan is indeed present at this N-glycosylation site in SARS-CoV (*8*). An N-glycan at N370 would fit into a groove formed between heavy and light chains (Fig. 2C), which could increase contact and thus binding affinity to CR3022. This result also suggests that the difference in antigenicity between the RBDs of SARS-CoV-2 and SARS-CoV can be at least partially attributed to the N-glycosylation site at residue 370. We tested whether CR3022 was able to neutralize SARS-CoV-2 and SARS-CoV in an in vitro microneutralization assay (*7*). Although CR3022 could neutralize SARS-CoV, it did not neutralize SARS-CoV-2 at the highest concentration tested (400 μg/ml) (fig. S4). This in vitro neutralization result is consistent with lower affinity binding of CR3022 for SARS-CoV-2, although other explanations are also possible, as outlined below.

SARS-CoV-2 uses the same host receptor, angiotensin I–converting enzyme 2 (ACE2), as SARS-CoV (*3*, *9*–*11*). The epitope of CR3022 does not overlap with the ACE2-binding site (Fig. 3A). Structural alignment of the CR3022–SARS-CoV-2 RBD complex with the ACE2–SARS-CoV-2 RBD complex (*11*) further indicates that binding of CR3022 would not clash with ACE2 (*12*). This analysis implies that the neutralization mechanism of CR3022 for SARS-CoV does not depend on direct blocking of receptor binding, which is consistent with the observation that CR3022 does not compete with ACE2 for binding to the RBD (*6*). Unlike CR3022, most known SARS RBD-targeted antibodies compete with ACE2 for binding to RBD (*4*, *13*–*16*). The epitopes of these antibodies are very different from that of CR3022 (Fig. 3B). It has been shown that CR3022 can synergize with other RBD-targeted antibodies to neutralize SARS-CoV (*4*). Although CR3022 itself cannot neutralize SARS-CoV-2 in this in vitro assay, whether CR3022 can synergize with other SARS-CoV-2 RBD-targeted monoclonal antibodies for neutralization remains to be investigated.

Table 1. Binding affinity of CR3022 to recombinant RBD and S protein. Binding affinity is expressed as the nanomolar dissociation constant (K_d).

Target	CR3022 IgG binding affinity (K_d)	CR3022 Fab binding affinity (K_d)
SARS-CoV-2 RBD	<0.1	115 ± 3
SARS-CoV RBD	<0.1	1.0 ± 0.1

[1]Department of Integrative Structural and Computational Biology, The Scripps Research Institute, La Jolla, CA 92037, USA. [2]HKU-Pasteur Research Pole, School of Public Health, Li Ka Shing Faculty of Medicine, The University of Hong Kong, Hong Kong SAR, China. [3]The Skaggs Institute for Chemical Biology, The Scripps Research Institute, La Jolla, CA, 92037, USA.
*These authors contributed equally to this work.
†Corresponding author. Email: ch02mkp@hku.hk (C.K.P.M.); wilson@scripps.edu (I.A.W.)

The recent cryo–electron microscopy (cryo-EM) structures of the homotrimeric SARS-CoV-2 S protein (*17*, *18*) demonstrated that the RBD, as in other coronaviruses (*19*, *20*), can undergo a hinge-like movement to transition between "up" and "down" conformations (Fig. 4A). ACE2 host receptor can only interact with the RBD when it is in the up conformation—the down conformation is inaccessible to ACE2. The epitope of CR3022 is also only accessible when the RBD is in the up conformation (Fig. 4, B and C). However, even when one RBD in the SARS-CoV-2 S protein is in the up conformation, the binding of CR3022 to RBD can still be sterically hindered. Structural alignment of the CR3022–SARS-CoV-2 RBD complex with the SARS-CoV-2 S protein (*17*, *18*) indicates that the CR3022 variable region would clash with the RBD on the adjacent protomer if the latter adopted a down conformation. In addition, the CR3022 variable domain would clash with the S2 domain underneath the RBD, and the CR3022 constant region would clash with the N-terminal domain (Fig. 4D). Although,

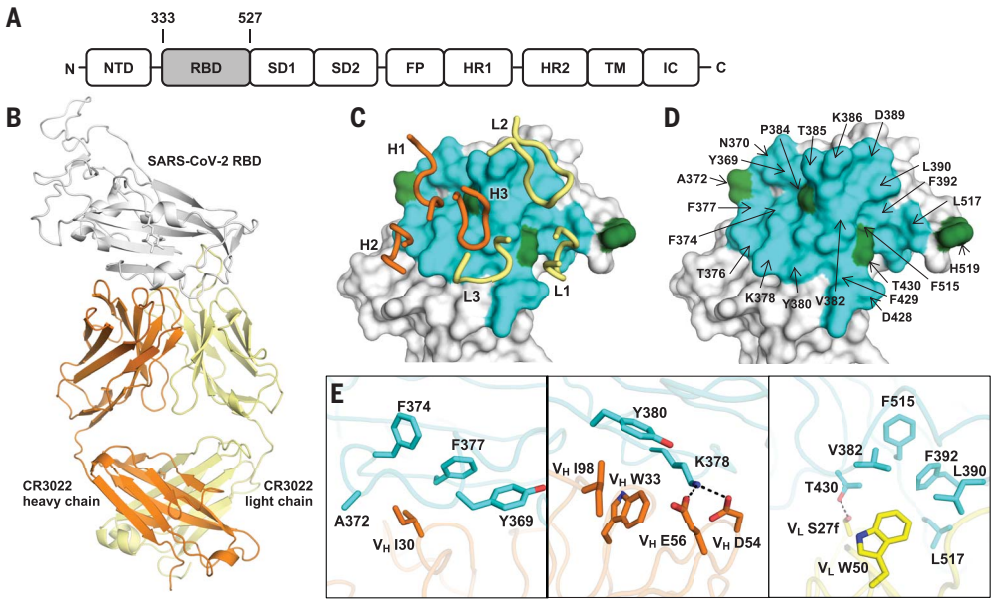


Fig. 1. Crystal structure of CR3022 in complex with SARS-CoV-2 RBD. (**A**) Overall topology of the SARS-CoV-2 spike glycoprotein. NTD, N-terminal domain; RBD, receptor binding domain; SD1, subdomain 1; SD2, subdomain 2; FP, fusion peptide; HR1, heptad repeat 1; HR2, heptad repeat 2; TM, transmembrane region; IC, intracellular domain; N, N terminus; C, C terminus. (**B**) Structure of CR3022 Fab in complex with SARS-CoV-2 RBD. CR3022 heavy chain is orange, CR3022 light chain is yellow, and SARS-CoV-2 RBD is light gray. (**C** and **D**) Epitope residues on SARS-CoV-2 are shown. CDR loops are labeled. Epitope residues that are conserved between SARS-CoV-2 and SARS-CoV are shown in cyan, and those that are not conserved are shown in green. (D) Epitope residues that are important for binding to CR3022 are labeled. Epitope residues are defined here as residues in SARS-CoV-2 RBD with buried surface area > 0 Å^2 after Fab CR3022 binding, as calculated with Proteins, Interfaces, Structures and Assemblies (PISA) (*34*). Single-letter abbreviations for the amino acid residues are as follows: A, Ala; D, Asp; E, Glu; F, Phe; H, His; I, Ile; K, Lys; L, Leu; M, Met; N, Asn; P, Pro; S, Ser; T, Thr; V, Val; W, Trp; and Y, Tyr. (**E**) Several key interactions between CR3022 and SARS-CoV-2 RBD are highlighted. CR3022 heavy chain is orange, CR3022 light chain is yellow, and SARS-CoV-2 RBD is cyan. Hydrogen bonds are represented by dashed lines.

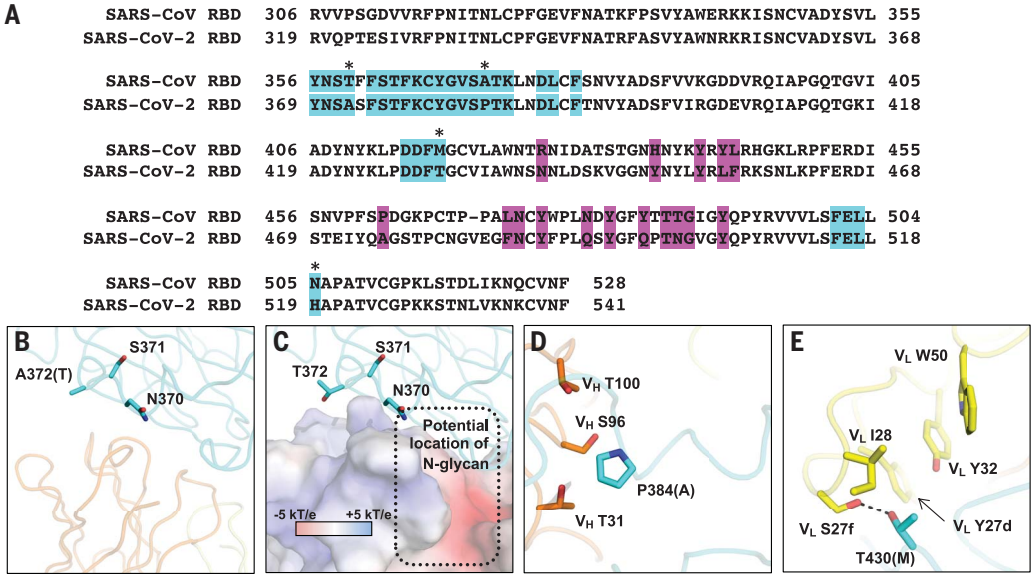


Fig. 2. Conservation of epitope residues. (**A**) Sequence alignment of SARS-CoV-2 RBD and SARS-CoV RBD. CR3022 epitope residues are highlighted in cyan. ACE2-binding residues are highlighted in magenta. Nonconserved epitope residues are marked with asterisks. (**B** to **E**) Interactions between the nonconserved epitope residues and CR3022 are shown. Amino acid variants observed in SARS-CoV are in parentheses. SARS-CoV-2 RBD is cyan, CR3022 heavy chain is orange, and CR3022 light chain is yellow. Residues are numbered according to their positions on the SARS-CoV-2 S protein sequence. (B) Whereas SARS-CoV-2 has an Ala at residue 372, SARS-CoV has Thr, which introduces an N-glycosylation site at residue N370. (C) The potential location of N370 glycan in SARS-CoV RBD is indicated by the dotted box. CR3022 is shown as an electrostatic potential surface presentation with units of kT/e, where e is the charge of an electron, k is the Boltzmann constant, and T is temperature in kelvin. (D) P384 interacts with T31, S96, and T100 of CR3022 heavy chain. Ala at this position in SARS-CoV would allow the backbone to adopt a different conformation when binding to CR3022. (E) T430 forms a hydrogen bond (dashed line) with S27f of CR3022 light chain. Met at this position in SARS-CoV would instead likely insert its side chain into the hydrophobic pocket formed by Y27d, I28, Y32, and W50 of CR3022 light chain.

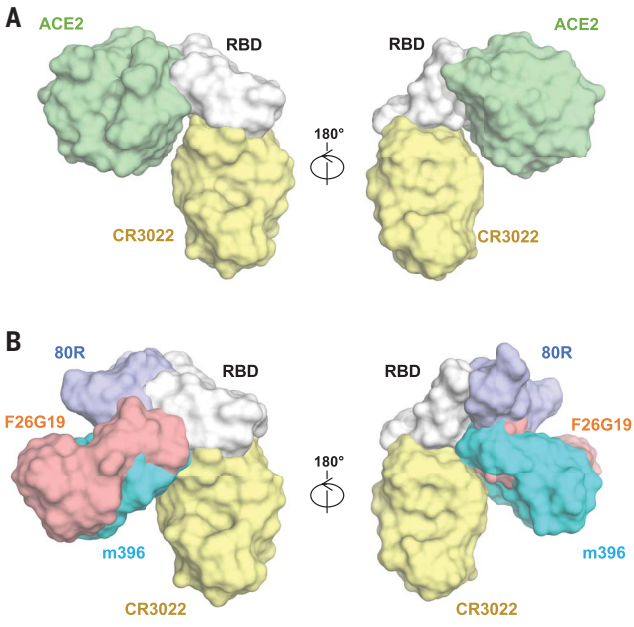


Fig. 3. The relative binding location of CR3022 with respect to receptor ACE2 and other SARS-CoV RBD monoclonal antibodies. (**A**) Structures of CR3022–SARS-CoV-2 RBD complex and ACE2–SARS-CoV-2 RBD complex (*11*) are aligned on the basis of the SARS-CoV-2 RBD. ACE2 is green, RBD is light gray, and CR3022 is yellow. (**B**) Structural superposition of CR3022–SARS-CoV-2 RBD complex, F26G19–SARS-CoV RBD complex [Protein Data Bank (PDB) ID 3BGF] (*35*), 80R–SARS-CoV RBD complex (PDB ID 2GHW) (*36*), and m396–SARS-CoV RBD complex (PDB ID 2DD8) (*16*).

as compared with SARS-CoV-2, the up conformation of the RBD in SARS-CoV has a larger dihedral angle to the horizontal plane of the S protein (fig. S5), the clashes described above would also exist in the SARS-CoV S protein (fig. S6).

For CR3022 to bind to the S protein, the previously described clashes need to be resolved. The clash with the CR3022 variable domain can be partially relieved when the targeted RBD on one protomer of the trimer and the RBD on the adjacent protomer are both in the up conformation (Fig. 4E). SARS-CoV S protein with two RBDs in the up conformation has been observed in cryo-EM studies (*19*, *21*, *22*). Nevertheless, clashes with the N-terminal domain (NTD) and S2 domain would still exist in the "two-up" conformation. Further structural modeling shows that all clashes can be avoided with a slight rotation of the targeted RBD in the "double-up" conformation (Fig. 4F). This conformational change is likely to be physiologically relevant because CR3022 can neutralize SARS-CoV. In addition, our enzyme-linked immunosorbent assay (ELISA)

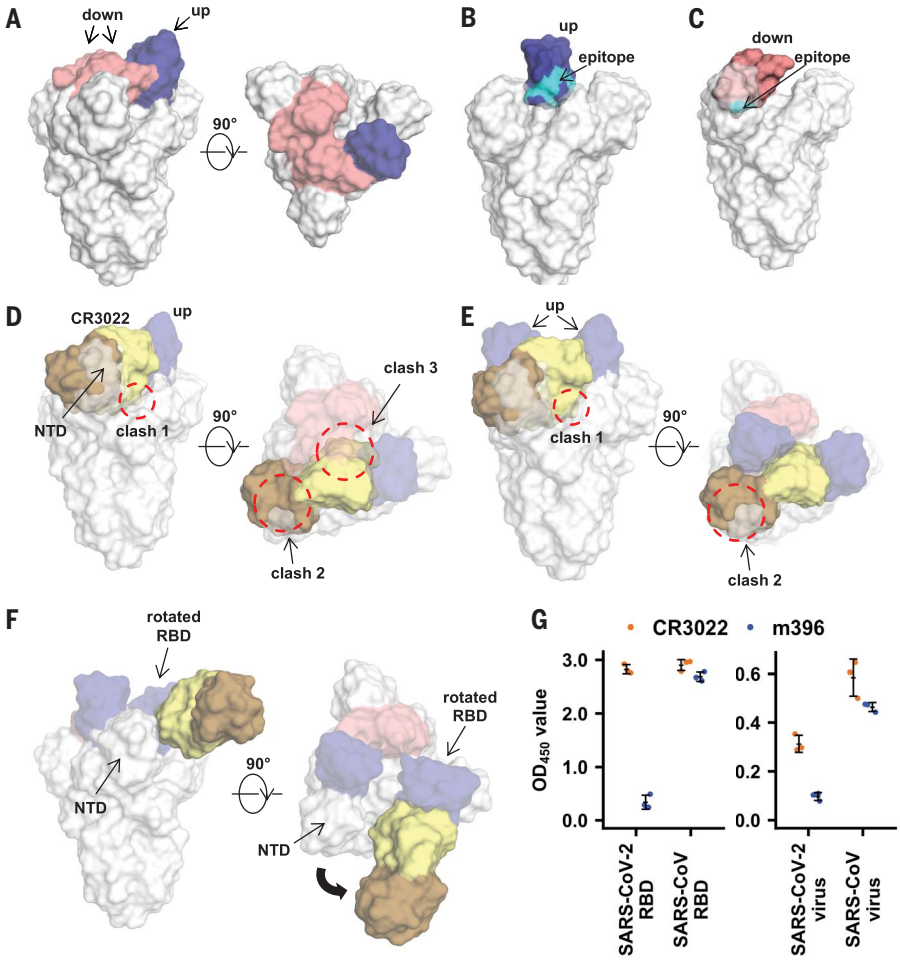


Fig. 4. Model of the binding of CR3022 to the homotrimeric S protein. (**A**) RBD in the S proteins of SARS-CoV-2 and SARS-CoV can adopt either an up conformation (blue) or a down conformation (red). PDB ID 6VSB (cryo-EM structure of SARS-CoV-2 S protein) (*17*) is shown. (**B** and **C**) CR3022 epitope (cyan) on the RBD is exposed in (B) the up conformation but not in (C) the down conformation. (**D**) Binding of CR3022 to single-up conformation would clash (indicated by the red dashed circles) with the S protein. Clash 1: CR3022 variable region (yellow) clashes with the S2 domain. Clash 2: CR3022 constant region (brown) clashes with NTD. Clash 3: CR3022 variable region clashes with the neighboring RBD that is in the down conformation. (**E**) Clash 3 is resolved when the neighboring RBD is in the up conformation (i.e., S protein in double-up conformation). (**F**) All clashes are resolved if the targeted RBD is slightly rotated in the double-up conformation. The curved arrow indicates the change in CR3022 orientation due to the slight rotation of the RBD. Of note, given that the elbow angle between the constant and variable domains of CR3022 is the same as observed in our crystal structure, our model shows that a maximum rotation angle of ~45° for the RBD would avoid all clashes. However, the elbow region of an antibody is known to be highly flexible. Therefore, the rotation angle of the RBD could be much smaller when the spike trimer is bound to CR3022. (**G**) Binding of CR3022 immunoglobulin G (IgG) and m396 IgG to recombinant RBD proteins from SARS-CoV-2 and SARS-CoV (left panel) and to SARS-CoV-2 and SARS-CoV viruses (right panel). Black lines indicate mean ± standard deviation of three technical replicates. OD_{450}, optical density at 450-nm wavelength.

experiment demonstrated that CR3022 is able to interact with the SARS-CoV-2 virus. Although the binding signals of CR3022 and m396, which is a SARS-CoV–specific antibody (*6*, *17*), to SARS-CoV were comparable in ELISA ($P > 0.05$, two-tailed t test) (Fig. 4G, left panel), CR3022 had a significantly higher binding signal to SARS-CoV-2 than did m396 ($P = 0.003$, two-tailed t test) (Fig. 4G, left panel), but not higher than its own binding signal to SARS-CoV, which is consistent with their relative binding to the RBD (Table 1 and fig. S3).

Our study provides insight into how SARS-CoV-2 can be targeted by the humoral immune response, and it reveals a conserved, but cryptic, epitope shared between SARS-CoV-2 and SARS-CoV. Recently, our group and others have identified a conserved epitope on influenza A virus hemagglutinin (HA) that is located in the trimeric interface and is only exposed through protein "breathing" (*23*–*25*), which is somewhat analogous to the epitope of CR3022. Antibodies to this influenza HA trimeric interface epitope do not exhibit in vitro neutralization activity but can confer in vivo protection. Similarly, antibodies to another conserved epitope that partially overlaps with the influenza HA trimeric interface are also non-neutralizing in vitro but protective in vivo (*26*). Examples of antibodies that do not have in vitro neutralization activity but confer in vivo protection have also been reported for influenza virus (*27*), herpesvirus (*28*), cytomegalovirus (*29*), alphavirus (*30*), and dengue virus (*31*). Therefore, although CR3022 does not neutralize SARS-CoV-2 in vitro, it is possible that this epitope can confer in vivo protection. Further study will require suitable animal models, which have yet to be established.

This coronavirus outbreak continues to pose an enormous global risk (*32*, *33*), and the availability of conserved epitopes may allow structure-based design not only of a SARS-CoV-2 vaccine but also of cross-protective antibody responses against future coronavirus epidemics and pandemics. Although a more universal coronavirus vaccine is not the most urgent goal at present, it is certainly worth future consideration, especially as cross-protective epitopes are identified, so that we can be better prepared for the next novel coronavirus outbreak.

REFERENCES AND NOTES

1. C. Huang *et al.*, *Lancet* **395**, 497–506 (2020).
2. Coronaviridae Study Group of the International Committee on Taxonomy of Viruses, *Nat. Microbiol.* **5**, 536–544 (2020).
3. P. Zhou *et al.*, *Nature* **579**, 270–273 (2020).
4. J. ter Meulen *et al.*, *PLOS Med.* **3**, e237 (2006).
5. J. Ye, N. Ma, T. L. Madden, J. M. Ostell, *Nucleic Acids Res.* **41**, W34–W40 (2013).
6. X. Tian *et al.*, *Emerg. Microbes Infect.* **9**, 382–385 (2020).
7. See supplementary materials.
8. Y. Watanabe *et al.*, bioRxiv 2020.02.20.957472 [Preprint]. 21 February 2020; https://doi.org/10.1101/2020.02.20.957472.
9. M. Letko, A. Marzi, V. Munster, *Nat. Microbiol.* **5**, 562–569 (2020).
10. R. Yan *et al.*, *Science* **367**, 1444–1448 (2020).
11. J. Lan *et al.*, bioRxiv 2020.02.19.956235 [Preprint]. 20 February 2020; https://doi.org/10.1101/2020.02.19.956235.
12. ACE2 also forms a dimer when it associates with the amino acid transporter B^0AT1 (*10*). We modeled a CR3022 IgG onto this dimer structure and found no clashes of CR3022 with ACE2 in its dimeric form, where the RBDs would likely come from adjacent trimers on the virus (*10*).
13. J. Sui *et al.*, *Proc. Natl. Acad. Sci. U.S.A.* **101**, 2536–2541 (2004).
14. E. N. van den Brink *et al.*, *J. Virol.* **79**, 1635–1644 (2005).
15. J. D. Berry *et al.*, *J. Virol. Methods* **120**, 87–96 (2004).
16. P. Prabakaran *et al.*, *J. Biol. Chem.* **281**, 15829–15836 (2006).
17. D. Wrapp *et al.*, *Science* **367**, 1260–1263 (2020).
18. A. C. Walls *et al.*, *Cell* **181**, 281–292.e6 (2020).
19. Y. Yuan *et al.*, *Nat. Commun.* **8**, 15092 (2017).
20. M. Gui *et al.*, *Cell Res.* **27**, 119–129 (2017).
21. R. N. Kirchdoerfer *et al.*, *Sci. Rep.* **8**, 15701 (2018).
22. Yuan *et al.* (*19*) observed 56% of the wild-type recombinant SARS-CoV S protein particle in "none-up" conformation and 44% in "single-up" conformation, whereas Kirchdoerfer *et al.* (*21*) found that recombinant SARS-CoV S protein, with Lys^{968}→Pro and Val^{969}→Pro mutations in the S2 domain to stabilize the prefusion conformation, has 58% in single-up, 39% in double-up, and 3% in triple-up conformations. However, it is not known whether the distribution of different conformations of S proteins on virus surface is the same as that of recombinant S protein.
23. S. Bangaru *et al.*, *Cell* **177**, 1136–1152.e18 (2019).
24. A. Watanabe *et al.*, *Cell* **177**, 1124–1135.e16 (2019).
25. G. Bajic *et al.*, *Cell Host Microbe* **25**, 827–835.e6 (2019).
26. J. Lee *et al.*, *Nat. Med.* **22**, 1456–1464 (2016).
27. C. Dreyfus *et al.*, *Science* **337**, 1343–1348 (2012).
28. C. Petro *et al.*, *eLife* **4**, e06054 (2015).
29. A. Bootz *et al.*, *PLOS Pathog.* **13**, e1006601 (2017).
30. C. W. Burke *et al.*, *Viruses* **10**, 147 (2018).
31. E. A. Henchal, L. S. Henchal, J. J. Schlesinger, *J. Gen. Virol.* **69**, 2101–2107 (1988).
32. V. D. Menachery *et al.*, *Nat. Med.* **21**, 1508–1513 (2015).
33. V. D. Menachery *et al.*, *Proc. Natl. Acad. Sci. U.S.A.* **113**, 3048–3053 (2016).
34. E. Krissinel, K. Henrick, *J. Mol. Biol.* **372**, 774–797 (2007).
35. J. E. Pak *et al.*, *J. Mol. Biol.* **388**, 815–823 (2009).
36. W. C. Hwang *et al.*, *J. Biol. Chem.* **281**, 34610–34616 (2006).

ACKNOWLEDGMENTS

We thank H. Tien for technical support with the crystallization robot, J. Matteson for contribution to mammalian cell culture, W. Yu for contribution to insect cell culture, R. Stanfield for assistance with data collection, and A. Ward for discussion. **Funding:** This work was supported by National Institutes of Health grant K99 AI139445 (N.C.W.); a Calmette and Yersin scholarship from the Pasteur International Network Association (H.L.); Bill and Melinda Gates Foundation grant OPP1170236 (I.A.W.); Guangzhou Medical University High-level University Innovation Team Training Program (Guangzhou Medical University released [2017] no. 159) (C.K.P.M.); and National Natural Science Foundation of China (NSFC)/ Research Grants Council (RGC) Joint Research Scheme (N_HKU737/18) (C.K.P.M.). General Medical Sciences and Cancer Institutes Structural Biology Facility at the Advanced Photon Source (APS) has been funded by federal funds from the National Cancer Institute (ACB-12002) and the National Institute of General Medical Sciences (AGM-12006). This research used resources of the APS, a U.S. Department of Energy (DOE) Office of Science User Facility operated for the DOE Office of Science by Argonne National Laboratory under contract DE-AC02-06CH11357. **Author contributions:** M.Y., N.C.W., X.Z., C.K.P.M., and I.A.W. conceived of and designed the study. M.Y., N.C.W., and C.-C.D.L. expressed and purified the proteins. M.Y. and N.C.W. performed biolayer interferometry binding assays. R.T.Y.S., H.L., and C.K.P.M. performed the neutralization and virus-binding experiments. M.Y., N.C.W., and X.Z. collected the x-ray data and determined and refined the x-ray structures. M.Y., N.C.W., and C.K.P.M. analyzed the data. M.Y., N.C.W., and I.A.W. wrote the paper, and all authors reviewed and edited the paper. **Competing interests:** The authors declare no competing interests. **Data and materials availability:** X-ray coordinates and structure factors are deposited in the RCSB Protein Data Bank under ID 6W41. This work is licensed under a Creative Commons Attribution 4.0 International (CC BY 4.0) license, which permits unrestricted use, distribution, and reproduction in any medium, provided the original work is properly cited. To view a copy of this license, visit https://creativecommons.org/licenses/by/4.0/. This license does not apply to figures/photos/artwork or other content included in the article that is credited to a third party; obtain authorization from the rights holder before using such material.

SUPPLEMENTARY MATERIALS

science.sciencemag.org/content/368/6491/630/suppl/DC1
Materials and Methods
Figs. S1 to S6
Tables S1 to S3
References (*37*–*46*)
MDAR Reproducibility Checklist

View/request a protocol for this paper from *Bio-protocol*.

14 March 2020; accepted 1 April 2020
Published online 3 April 2020
10.1126/science.abb7269

BIOINSPIRED ROBOTS

Aerodynamic imaging by mosquitoes inspires a surface detector for autonomous flying vehicles

Toshiyuki Nakata[1,2]*, Nathan Phillips[1]*, Patrício Simões[3], Ian J. Russell[3], Jorn A. Cheney[1], Simon M. Walker[4], Richard J. Bomphrey[1]†

Some flying animals use active sensing to perceive and avoid obstacles. Nocturnal mosquitoes exhibit a behavioral response to divert away from surfaces when vision is unavailable, indicating a short-range, mechanosensory collision-avoidance mechanism. We suggest that this behavior is mediated by perceiving modulations of their self-induced airflow patterns as they enter a ground or wall effect. We used computational fluid dynamics simulations of low-altitude and near-wall flights based on in vivo high-speed kinematic measurements to quantify changes in the self-generated pressure and velocity cues at the sensitive mechanosensory antennae. We validated the principle that encoding aerodynamic information can enable collision avoidance by developing a quadcopter with a sensory system inspired by the mosquito. Such low-power sensing systems have major potential for future use in safer rotorcraft control systems.

At night, in caves, or in otherwise visually compromised environments, animal guidance and control systems must sense and avoid obstacles without relying on optical information. Mechanoreceptors in arthropods are extraordinarily sensitive and diverse (*1*), and insects exploit this fully (*2*), including for the detection of self-induced flows. For example, fields of unidirectional trichoid sensilla are likely a key component of the fused sensory input used by flying insects to monitor their attitude (*3*), and changes in forward speed can be regulated by aerodynamic drag on the antennae (*4*). In insects, antennal motion is detected by the Johnston's organ (JO), an array of chordotonal mechanoreceptors located in the antennal pedicel. The JO can detect fluid flows, gravitational pull, and acoustic stimulation, and it is one of the most sensitive mechanoreceptive organs in the animal kingdom (*5*). Mosquitoes have exceedingly sensitive JOs. The radial organization of their ~12,000 mechanoreceptive units functionally arranged in antiphase pairs (*6*) allows mosquitoes to respond to antennal deflections of ±0.0005° induced by ±11-nm air particle displacements in the acoustic near field (*Toxorhynchites brevipalpis*) (*7*) or to acoustic particle velocities of ~10^{-7} ms^{-1} (*Culex quinquefasciatus*) (*8*).

We took inspiration from such neurophysiological evidence and postulated a sensory mechanism for *C. quinquefasciatus* that can explain recent behavioral experiments showing that mosquitoes avoid surfaces invisible to their compound eyes (*9*). The absence of visual cues indicates that another source of close-range information exists, and we hypothesized that these alternative cues are manifest within interactions between the fluid and antennae or hair structures. Specifically, we propose that mosquitoes can detect changes to their self-induced flow patterns caused by the proximal physical environment. These changes to the downwash flow patterns initially generated by the flapping wings arise as the jets of air impinge on the obstacle's surface. This noncontact, sensory modality for flying insects is somewhat akin to the hydrodynamic imaging capability of the lateral line system in fish (*10*, *11*), which is also fundamentally a fluid-dynamic, pressure-based system. Such a system would be particularly useful for mosquitoes, which must be adept at stealthy landings on hosts (*12*) and depositing eggs over water at night.

We demonstrate how nearby surfaces may be detected by mosquitoes by means of the flow field produced during flapping flight (*13*), which is modulated in response to surfaces at magnitudes sufficient for detection by their mechanosensors. We implemented these governing principles in developing a miniature flying vehicle that operates close to the ground and walls and is fitted with a sensor package that can detect surfaces at distances sufficiently far from collision for effective obstacle avoidance (movie S1).

Mosquito wingbeat kinematics show high wingbeat frequency (wbf), low wingbeat amplitude, and large, rapid spanwise rotations. These features result in unorthodox aerodynamic flows around the wings themselves (*13*) and two concentrated jets of fast-moving air that merge approximately two wing lengths beneath the body. Because of the shallow stroke amplitude, the jets are more focused than the wake of other flying animals; this may help to improve the signal if the interaction of the induced flow with a ground plane is important for collision avoidance. Building on our previous dataset (*13*), we performed further computational fluid dynamics (CFD) simulations at a range of distances from either the ground or a wall plane to quantify the effect on local flows around the mosquito (Fig. 1A and fig. S1). Movie S1 shows flow simulations at infinite altitude (where "infinite" in this case means flight at an altitude far from a surface) and when the jets impinge on a ground plane 10 mm below the mosquito.

Downwash dominates the flow field at higher altitudes. However, at lower altitudes (<10 mm), the downwash velocity progressively decreases and recirculation can be seen in some regions, particularly under the body. To see this effect more clearly, we calculated the wingbeat-averaged pressure deltas for each distance relative to the infinite altitude case (Fig. 1C). The zones with the largest pressure deltas were located below the thorax and, unexpectedly, above the head. The antennae, with their sensitive JO at the base (*7*, *8*), are therefore well placed to measure subtle changes in the vector strength of particle velocity in the anterodorsal region of the head despite being located the farthest from the ground. Flow-sensitive hairs along the hind leg femur, and elsewhere, could also detect changes in flow velocity associated with these pressure changes, especially at the lower altitudes, although hind leg hair sensitivity is an order of magnitude lower (fig. S2). Mosquitoes extend their hind legs toward a surface when landing and backward when flying, which complements the JO in detecting pressure differences caused by ground and wall effects. The antennae of flying insects are self-stimulated both by periodic air movements caused by wingbeats and by tonic flow from translation through the air. Recent mosquito tuning data show two sensitivity peaks in male JOs. One occurs at lower frequencies (centered at ~280 Hz) and is tuned to detect the wbf of females using an acoustic distortion mechanism (*8*). A secondary peak of sensitivity is centered on frequencies similar to those at which males fly (600 to 800 Hz), which would enable a male mosquito to hear its own flight and possibly that of other nearby males (*8*, *14*). Male mosquito JOs are therefore adept at perceiving tiny changes in the direction and magnitude of flow velocity of the type associated with proximity to surfaces, potentially using one sensitivity band to detect females and another for detecting changes to their self-generated flow fields when encountering obstacles. In addition to ground effects, wall surfaces also modulate the flow field (Fig. 1B). Again, changes in pressure distribution can be seen above the head and below the thorax, so both floors and walls could be detected by the same cuticular flow sensors or pressure sensors.

[1]Structure and Motion Laboratory, Royal Veterinary College, Hatfield AL9 7TA, UK. [2]Graduate School of Engineering, Chiba University, Chiba 263-8522, Japan. [3]Pharmacy and Biomolecular Sciences, University of Brighton, Moulsecoomb, Brighton BN2 4GJ, UK. [4]Faculty of Biological Sciences, University of Leeds, Leeds LS2 9JT, UK.
*These authors contributed equally to this work.
†Corresponding author. Email: rbomphrey@rvc.ac.uk

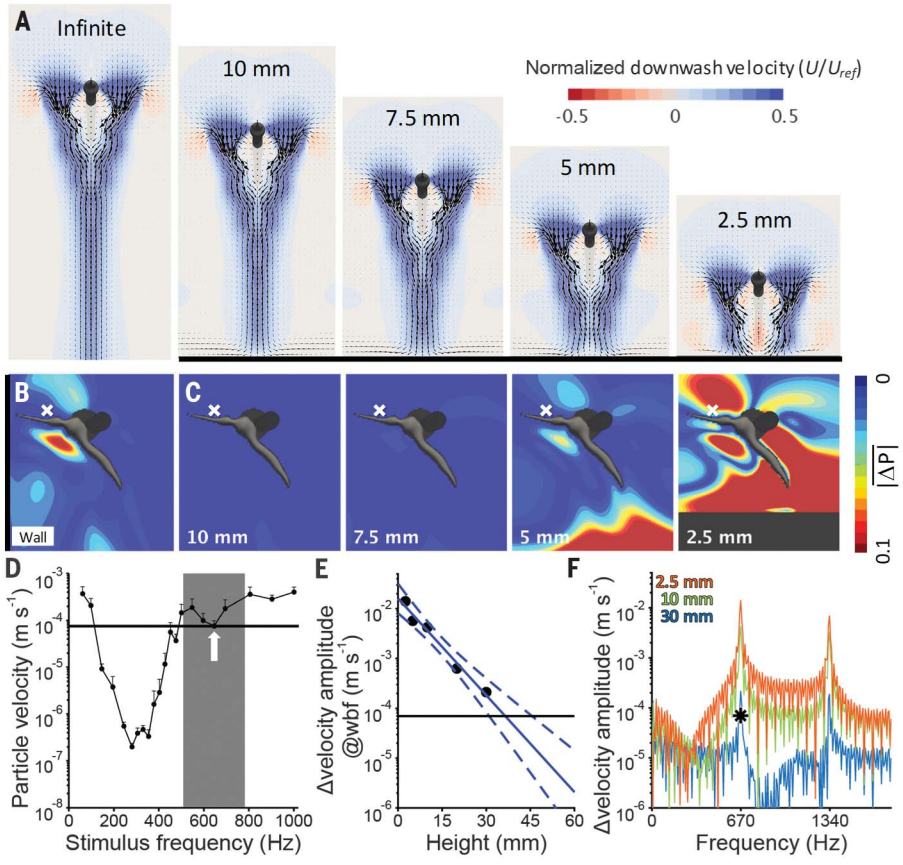


Fig. 1. Velocity and pressure distributions around mosquitoes flying near surfaces. (**A**) Front view of a mosquito hovering at five altitudes measured from the mosquito body with downwash shown in blue and upwash in red. The flow visualization plane is shown at maximum wingspan. A discrete jet from each wing merges in the infinite and high-altitude cases. (**B** and **C**) Side view of a hovering mosquito (gray) and distribution of absolute wingbeat-averaged mean difference in pressure relative to the infinite case $\overline{|\Delta P|}$ (Pa) measured in the sagittal plane. The pressure distribution in free airspace is compared with flight near a wall [(B), where the wall is the left edge of the panel] and at varying altitudes (C); white crosses show monitoring location corresponding to the tip of the antenna. (**D**) Particle velocity detection threshold of the male JO showing a secondary notch of enhanced sensitivity (white arrow) within the male wbf range [see the supplementary materials for electrophysiology methods; also see (*8*)]. Gray shading indicates the range of male wbf's observed during free flight. The JO's secondary notch has a particle velocity sensitivity shown by the solid line. The primary notch at ~200 Hz is used for mating communication and is tuned to tones generated by the male-female wbf distortion product. (**E**) The amplitude of change in velocity magnitude at wbf measured at the antennae increases with proximity to the ground. A straight line of best fit is plotted (blue, with 95% confidence intervals shown as dashed lines) to show the intersection with the JO flow velocity sensitivity at the male wbf alone (solid horizontal line). (**F**) Amplitude of changes in velocity magnitude at the antennae in the frequency domain, calculated as the fast Fourier transform (FFT) at infinite altitude subtracted from the FFT at a given altitude over 50 wingbeat cycles. Differences are always greatest at wbf irrespective of altitude. Asterisk indicates JO particle velocity sensitivity at wbf.

At the male wbf, the JO exhibits a local peak in sensitivity and can detect changes in flow velocities on the order of 10^{-4} ms^{-1} (Fig. 1D and supplementary materials). We include this empirically derived limit in Fig. 1, D to F, where we present the change in flow velocity at the wbf with varying proximity to the ground (Fig. 1E) and the frequency spectrum of the induced flows (Fig. 1F). Flow velocity oscillates less with altitude, and closer proximity to the ground does not cause oscillations in the flow experienced by the JO to deviate from wbf. At higher altitudes, differences in the magnitude of velocity fluctuations at the wbf become less pronounced and, for numerical reasons, CFD will eventually fail to capture the very smallest changes in velocity. There is a considerable computational burden as the fine mesh extends to ever more distant ground planes and the velocity deltas tend to zero; nevertheless, a clear trend can be seen whereby the JO can easily detect changes at low altitude, but with a diminishing response as the altitude increases, until the threshold for detection is not met (Fig. 1E).

The intercept of the CFD-derived velocity changes and the measured sensitivity of the JO predict a maximum surface detection distance in *Culex* mosquitoes of 36.4 mm, or 20.2 wing lengths. This is a conservative estimate because it only considers the content of the flow signature at wbf. This distance predicted for *Culex* males is broadly consistent with egg-laying dipping behavior in female *Anopheles,* which dip to altitudes of 20 to 70 mm above the water surface (*9*). Detection of a ground plane at such distances is far in excess of that which might be expected by the ground effect typically referred to in the aerodynamic literature, where notable improvements in lift and drag force characteristics of wings become negligible beyond an altitude of a single wing length or rotor radius. In our mosquitoes, the negative pressure delta region observed above the head and under the thorax when close to the floor occurred as a result of increasing unsteadiness of the flow in this region, leading to higher peak velocities and lower pressures (Fig. 1C). Conversely, away from surfaces, the flow around the body was relatively steady because the speeds of the wing bases were low.

Mosquitoes are not known to have pressure receptors that could monitor the reflected sound from nearby surfaces in the same manner as echolocating animals. Although we do not rule out the possibility that the JO could detect the reflected particle velocity component of self-induced sounds, it would be less useful than the pressure component because the particle velocities decrease with the inverse cube of distance rather than the inverse square. Moreover, the frequency of the flight tone means that the wavelength of the acoustic signature is relatively large, on the order of 0.5 to 1.0 m, which limits precision in locating a surface. By contrast, typical echolocation in gleaning bats uses frequencies in the tens of kilohertz, giving a superior resolution by two orders of magnitude. Given the relatively large changes in particle velocity induced by each wingbeat that can comfortably be detected by the JO at altitudes of many body lengths, we think that this is a more robust solution to surface detection than echolocation.

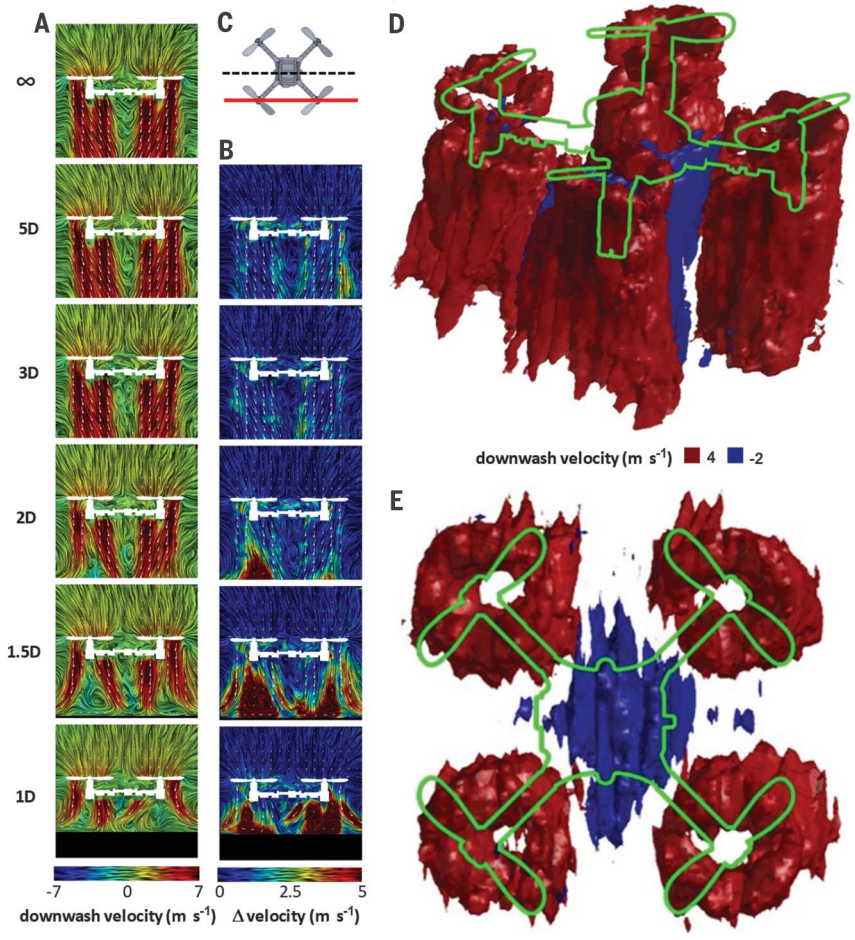


Fig. 2. Quadcopter flow-field characterization. (**A**) Slices showing induced downwash for a quadcopter hovering at a range of altitudes in multiples of rotor diameter (D = 46 mm). Line integral convolution shows instantaneous streamlines and color flood shows vertical velocity. (**B**) Differences in velocity magnitude at a range of altitudes. (**C**) Schematic of the craft showing the particle image velocimetry measurement plane (red) with respect to a center line (dashed). (**D**) Oblique and (**E**) Top view of the three-dimensional flow field at an altitude of 2 D. Four annular jets emanate from the rotors and recirculate under the fuselage (isosurface of downwash and upwash: 4 ms^{-1} in red; −2 ms^{-1} in blue). An outline of the quadcopter is shown in green for reference.

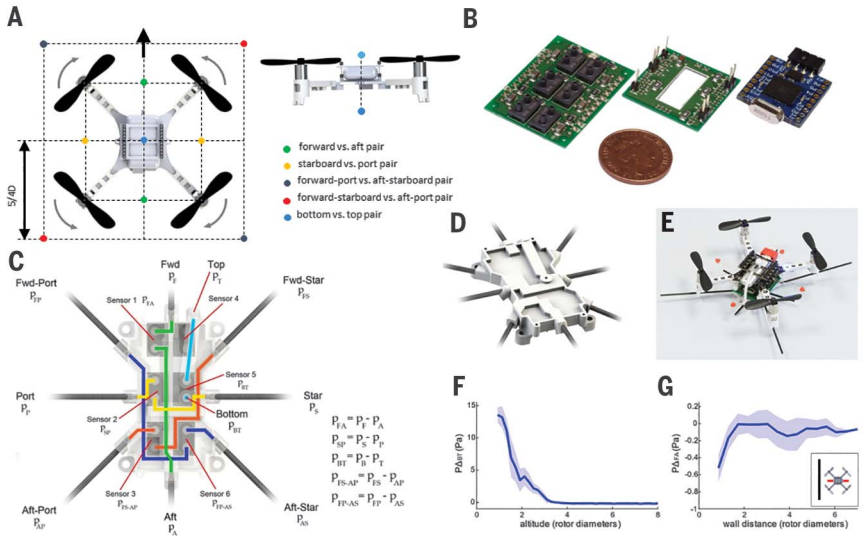


Fig. 3. Bioinspired sensor module. (**A**) Arrangement and placement of five paired pressure probes placed to maximize pressure deltas when close to surfaces. (**B**) Pressure sensor module components comprising the pressure sensor array, adapter printed circuit board, and microcontroller. (**C**) Schematic diagram showing internal routing tracks connecting paired probes (with Fore-Aft in green, Port-Starboard in yellow, ForwardPort-AftStarboard in dark blue, and ForwardStarboard-AftPort in orange, from top to bottom in light blue) to pressure sensors through a tube network shown in (**D**). (**E**) Free-flying prototype of a mosquito-inspired surface detection device. (**F** and **G**) Differential pressure delta with proximity to ground (F) and wall (G); shaded regions indicate 1 SD. Altitude is measured from the plane of the rotor hubs. Wall proximity is measured from the nearest rotor hub.

To show how mechanosensory flow-field monitoring can be used in collision avoidance in autonomous systems, we fitted a small quadcopter platform with a bioinspired sensor that can detect floors and walls using physical principles similar to those described above: specifically, modulation of a deforming flow field. It is lightweight, power-efficient, and stealthy, with no additional emission of light or electromagnetic radiation necessary. It is also applicable to rotorcraft or flappercraft of any scale and can work in conditions that are unsuited to alternative range-finding tools. We instrumented an existing 27 g platform (Crazyflie 2.0, Bitcraze, Sweden) with custom circuits and algorithms to identify obstacle proximity based on pressure sensor readings. The stand-alone sensor module performs reliable obstacle detection up to three rotor diameters away during autonomous flights.

The device, like the mosquito, will be most sensitive if sensors are mounted at locations experiencing the greatest changes in the flow field when approaching surfaces. Nearby

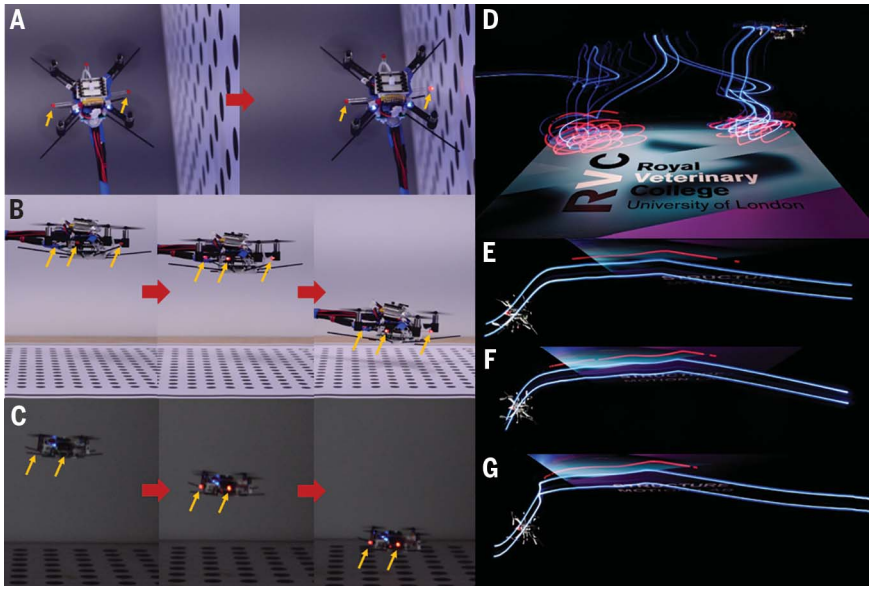


Fig. 4. Demonstration of aerodynamic imaging in a quadcopter. (**A**) Tethered wall proximity test with the wall on the forward side of the quadcopter. Yellow arrows indicate forward and aft red indicator lights. (**B**) Tethered ground proximity test. Yellow arrows indicate red alarm lights illuminating when ground is detected. (**C**) Piloted free-flight test of ground detection. (**D** to **G**) Long-exposure photographs of autonomous test of ground detection. (D) Oblique side view showing perpetual flight lights in blue and detection indicator lights in red. The ground was detected twice. (E to G) Top view of three wall detection trials. A single surface detection indicator light illuminates on one side nearest the wall before the quadcopter moves away from the obstruction. A strobe flash before the end of the exposure captures the quadcopter toward the end of its flight.

surfaces distort the flow field all around the body, making surface detection simple, direct, and robust; however, to determine optimal sensor design, number, and placement, it is necessary to find the most affected regions. We used stereoparticle image velocimetry to measure fluid velocities around the quadcopter at various altitudes and proximities to a wall (Fig. 2 and fig. S3). These flow measurements were used to inform the position of probe tubes relative to the annular jets and regions of recirculation under the control boards. The probes were connected to differential pressure sensors, which are a more accessible solution than particle-velocity probes (Fig. 3 and figs. S4 to S7). Because the dynamic pressure is proportional to the square of flow velocity, the same physical phenomenon underpins the sensing capability. Ground effect could be detected using a pair of probes extending above and below the craft, and the direction of nearby walls could be detected by using paired probes extending fore to aft, laterally, or diagonally. Further detail on the design criteria and the pressure delta thresholds for each proximity condition are detailed in supplementary materials.

This simple model was able to detect both ground and wall effects. Pressure differential increases with surface proximity (Fig. 3, F and G) and with sufficient signal to provide alarm thresholds (tables S1 and S3) for each proximity condition. The complete module weighed just 9.2 g (see table S2 for a detailed mass breakdown).

The device successfully emulated the mosquito model behavior by identifying nearby obstacles during flight. Initially, the quadcopter was flown tethered (Fig. 4, A and B), was then piloted (Fig. 4C), and, finally, flew autonomously using positional feedback from a motion capture system. Ground (Fig. 4D and figs. S9 and S10) and wall (Fig. 4, E to G) planes could be discriminated using appropriately placed sensor combinations monitoring induced flow-field changes. Previous quadcopter studies have detected proximal surfaces by combining measured rotor speeds required for stable hovering with an aerodynamic model of the rotor and the motor speed required to support weight (*15*). Others have detected external flows such as fans emulating the downwash of another vehicle (*16*) or successfully incorporated flight dynamics models of the specific quadcopter platform and used them to infer obstacle proximity by the forces and torques acting on the vehicle (*17*). Our method requires no a priori aerodynamic or rigid body models to function, only basic thresholds. It is therefore a more direct measure of surface proximity and needs little or no processing to function.

REFERENCES AND NOTES

1. F. G. Barth, *A Spider's World: Senses and Behavior* (Springer, 2002).
2. M. C. Göpfert, R. M. Hennig, *Annu. Rev. Entomol.* **61**, 257–276 (2016).
3. G. K. Taylor, H. G. Krapp, in *Advances in Insect Physiology: Insect Mechanics and Control*, J. Casas, S. Simpson, Eds. (Elsevier, 2007), vol. 34, pp. 231–316.
4. T. Roy Khurana, S. P. Sane, *eLife* **5**, e14449 (2016).
5. L. H. Field, T. Matheson, in *Advances in Insect Physiology*, P. D. Evans, Ed. (Elsevier, 1998), vol. 27, pp. 1–228.
6. D. N. Lapshin, D. D. Vorontsov, *J. Exp. Biol.* **222**, jeb208785 (2019).
7. M. C. Göpfert, H. Briegel, D. Robert, *J. Exp. Biol.* **202**, 2727–2738 (1999).
8. P. M. V. Simões, R. A. Ingham, G. Gibson, I. J. Russell, *J. Exp. Biol.* **219**, 2039–2047 (2016).
9. F. Hawkes, G. Gibson, *Parasit. Vectors* **9**, 320 (2016).
10. S. Dijkgraaf, *Biol. Rev. Camb. Philos. Soc.* **38**, 51–105 (1963).
11. M. Yoshizawa, W. R. Jeffery, S. M. van Netten, M. J. McHenry, *J. Exp. Biol.* **217**, 886–895 (2014).
12. F. T. Muijres *et al*., *J. Exp. Biol.* **220**, 3751–3762 (2017).
13. R. J. Bomphrey, T. Nakata, N. Phillips, S. M. Walker, *Nature* **544**, 92–95 (2017).
14. D. N. Lapshin, *Entomol. Rev.* **92**, 605–621 (2012).
15. C. Powers, D. Mellinger, A. Kushleyev, B. Kothmann, V. Kumar, in *Experimental Robotics: The 13th International Symposium on Experimental Robotics*, J. P. Desai, G. Dudek, O. Khatib, V. Kumar, Eds. (Springer, 2013), pp. 289–302.
16. D. W. Yeo, N. Sydney, D. A. Paley, D. Sofge, *J. Guid. Control Dyn.* **40**, 692–701 (2016).
17. C. D. McKinnon, A. P. Schoellig, *Robot. Auton. Syst.* **123**, 103314 (2020).
18. H. Liu, *J. Comput. Phys.* **228**, 439–459 (2009).
19. S. M. Walker, A. L. R. Thomas, G. K. Taylor, *J. R. Soc. Interface* **9**, 1194–1207 (2012).

ACKNOWLEDGMENTS

We thank the RVC flight group, P. Kimber and C. Jones of the Defense Science and Technology Laboratory (Dstl), and N. Short for discussions and H. Liu of Chiba University for permission to use the CFD simulator. **Funding:** This work was funded in part by the Autonomous Systems Underpinning Research (ASUR) program under the auspices of Dstl, the UK Ministry of Defense (R.J.B.), and the Biotechnology and Biological Sciences Research Council (BB/J001244/1 to R.J.B.). S.M.W. was supported by a Royal Society University Research Fellowship. Work at the University of Brighton was funded by the Medical Research Council (MR/N004299/1). P.S. was partly supported by a Rising Stars Award from the University of Brighton. **Author contributions:** R.J.B. conceived the experiments with T.N., N.P., S.M.W., and I.J.R. S.M.W., I.J.R., and P.S. advised on the experimental protocol. N.P. designed and built the quadcopter sensor module. N.P. and J.A.C. built the quadcopter module communication links. I.J.R. and P.S. gathered and processed data for the JO and femoral hairs. R.J.B., T.N., N.P., and S.M.W. wrote the manuscript. All authors contributed to editing the manuscript. **Competing interests:** Some of this work was used to support the filing of patent WO 2019/002892 A1. **Data and materials availability:** All data are available in the main text or the supplementary materials. Mosquito kinematics are available from Bomphrey *et al.* (*13*). The CFD solver (*18*) and kinematics acquisition code (*19*) are described in further detail elsewhere.

SUPPLEMENTARY MATERIALS

science.sciencemag.org/content/368/6491/634/suppl/DC1
Materials and Methods
Figs. S1 to S10
Tables S1 to S3
Caption for Movie S1
References (*20*–*22*)
Movie S1

24 October 2019; accepted 2 April 2020
10.1126/science.aaz9634

CORONAVIRUS

An investigation of transmission control measures during the first 50 days of the COVID-19 epidemic in China

Huaiyu Tian[1]*†, Yonghong Liu[1]*, Yidan Li[1]*, Chieh-Hsi Wu[2]*, Bin Chen[3]*, Moritz U. G. Kraemer[4,5,6], Bingying Li[1], Jun Cai[7], Bo Xu[7], Qiqi Yang[1], Ben Wang[1], Peng Yang[8], Yujun Cui[9], Yimeng Song[10], Pai Zheng[11], Quanyi Wang[8], Ottar N. Bjornstad[12,13], Ruifu Yang[9]†, Bryan T. Grenfell[14,15]†, Oliver G. Pybus[4]†, Christopher Dye[4,16]†

Responding to an outbreak of a novel coronavirus [agent of coronavirus disease 2019 (COVID-19)] in December 2019, China banned travel to and from Wuhan city on 23 January 2020 and implemented a national emergency response. We investigated the spread and control of COVID-19 using a data set that included case reports, human movement, and public health interventions. The Wuhan shutdown was associated with the delayed arrival of COVID-19 in other cities by 2.91 days. Cities that implemented control measures preemptively reported fewer cases on average (13.0) in the first week of their outbreaks compared with cities that started control later (20.6). Suspending intracity public transport, closing entertainment venues, and banning public gatherings were associated with reductions in case incidence. The national emergency response appears to have delayed the growth and limited the size of the COVID-19 epidemic in China, averting hundreds of thousands of cases by 19 February (day 50).

On 31 December 2019—less than a month before the 2020 Spring Festival holiday, including the Chinese Lunar New Year—a cluster of pneumonia cases caused by an unknown pathogen was reported in Wuhan, a city of 11 million inhabitants and the largest transport hub in Central China. A novel coronavirus (*1*, *2*) was identified as the etiological agent (*3*, *4*), and human-to-human transmission of the virus [severe acute respiratory syndrome–coronavirus 2 (SARS-CoV-2)] has been since confirmed (*5*, *6*). Further spatial spread of this disease was of great concern in view of the upcoming Spring Festival (*chunyun*), during which there are typically 3 billion travel movements over the 40-day holiday period, which runs from 15 days before the Spring Festival (Chinese Lunar New Year) to 25 days afterward (*7*, *8*).

Because there is currently neither a vaccine nor a specific drug treatment for coronavirus disease 2019 (COVID-19), a range of public health (nonpharmaceutical) interventions has been used to control the epidemic. In an attempt to prevent further dispersal of COVID-19 from its source, all transport was prohibited in and out of Wuhan city from 10:00 a.m. on 23 January 2020, followed by the whole of Hubei Province a day later. In terms of the population covered, this appears to be the largest attempted cordon sanitaire in human history.

On 23 January, China also raised its national public health response to the highest state of emergency: Level 1 of 4 levels of severity in the Chinese Emergency System, defined as an "extremely serious incident" (*9*). As part of the national emergency response, and in addition to the Wuhan city travel ban, suspected and confirmed cases have been isolated, public transport by bus and subway rail suspended, schools and entertainment venues have been closed, public gatherings banned, health checks carried out on migrants ("floating population"), travel prohibited in and out of cities, and information widely disseminated. Despite all of these measures, COVID-19 remains a danger in China. Control measures taken in China potentially hold lessons for other countries around the world.

Although the spatial spread of infectious diseases has been intensively studied (*10*–*15*), including explicit studies of the role of human movement (*16*, *17*), the effectiveness of travel restrictions and social distancing measures in preventing the spread of infection is uncertain. For COVID-19, SARS-CoV-2 transmission patterns and the impact of interventions are still poorly understood (*6*, *7*). We therefore carried out a quantitative analysis to investigate the role of travel restrictions and transmission control measures during the first 50 days of the COVID-19 epidemic in China, from 31 December 2019 to 19 February 2020 (Fig. 1). This period encompassed the 40 days of the Spring Festival holiday, 15 days before the Chinese Lunar New Year on 25 January and 25 days afterward. The analysis is based on a geocoded repository of data on COVID-19 epidemiology, human movement, and public health (nonpharmaceutical) interventions. These data include the numbers of COVID-19 cases reported each day in each city of China, information on 4.3 million human movements from Wuhan city, and data on the timing and type of transmission control measures implemented across cities of China.

We first investigated the role of the Wuhan city travel ban, comparing travel in 2020 with that in previous years and exploring how holiday travel links to the dispersal of infection across China. During Spring Festival travel in 2017 and 2018, there was an average outflow of 5.2 million people from Wuhan city during the 15 days before the Chinese Lunar New Year.

Table 1. Association between the Wuhan travel ban and COVID-19 dispersal to other cities in China. The dependent variable *Y* is the arrival time (days) of the outbreak in each city.

Covariates	Coefficient	95% CI	*P*
Intercept	25.95	(23.43, 28.48)	<0.01
Longitude (degrees)	−0.03	(−0.05, −0.01)	<0.01
Latitude (degrees)	0.03	(0.01, 0.06)	<0.05
log10 (population)	−0.70	(−1.12, −0.28)	<0.01
log10 (total movements)	−0.12	(−0.22, −0.02)	<0.05
Travel ban (days)	2.91	(2.54, 3.29)	<0.01

[1]State Key Laboratory of Remote Sensing Science, College of Global Change and Earth System Science, Beijing Normal University, Beijing, China. [2]School of Mathematical Sciences, University of Southampton, Southampton, UK. [3]Department of Land, Air and Water Resources, University of California Davis, Davis, CA, USA. [4]Department of Zoology, University of Oxford, Oxford, UK. [5]Harvard Medical School, Harvard University, Boston, MA, USA. [6]Boston Children's Hospital, Boston, MA, USA. [7]Ministry of Education Key Laboratory for Earth System Modeling, Department of Earth System Science, Tsinghua University, Beijing, China. [8]Beijing Center for Disease Prevention and Control, Beijing, China. [9]State Key Laboratory of Pathogen and Biosecurity, Beijing Institute of Microbiology and Epidemiology, Beijing, China. [10]Department of Urban Planning and Design, The University of Hong Kong, Hong Kong. [11]Department of Occupational and Environmental Health Sciences, School of Public Health, Peking University, China. [12]Center for Infectious Disease Dynamics, Department of Biology, Pennsylvania State University, University Park, PA, USA. [13]Department of Entomology, College of Agricultural Sciences, Pennsylvania State University, University Park, PA, USA. [14]Division of International Epidemiology and Population Studies, Fogarty International Center, National Institutes of Health, Bethesda, MD, USA. [15]Department of Ecology and Evolutionary Biology, Princeton University, Princeton, NJ, USA. [16]Oxford Martin School, University of Oxford, Oxford, UK.
*These authors contributed equally to this work.
†Corresponding author. Email: tianhuaiyu@gmail.com (H.T.); christopher.dye@zoo.ox.ac.uk (C.D.); oliver.pybus@zoo.ox.ac.uk (O.G.P.); grenfell@princeton.edu (B.T.G.); ruifuyang@gmail.com (R.Y.)

In 2020, this travel was interrupted by the Wuhan city shutdown, but 4.3 million people traveled out of the city between 11 January and the implementation of the ban on 23 January (Fig. 2A) (*7*). In 2017 and 2018, travel out of the city during the 25 days after the Chinese Lunar New Year averaged 6.7 million people each year. In 2020, the travel ban prevented almost all of that movement and markedly reduced the number of exportations of COVID-19 from Wuhan (*7*, *8*).

The dispersal of COVID-19 from Wuhan was rapid (Fig. 3A). A total of 262 cities reported cases within 28 days. For comparison, the 2009 influenza H1N1 pandemic took 132 days to reach the same number of cities in China (Supplementary materials, materials and methods). The number of cities providing first reports of COVID-19 peaked at 59 per day on 23 January, the date of the Wuhan travel ban.

The total number of cases reported from each province by 30 January, 1 week after the Wuhan shutdown, was strongly associated with the total number of travellers from Wuhan [correlation coefficient (r) = 0.98, $P < 0.01$; excluding Hubei, $r = 0.69$, $P < 0.01$] (Fig. 2, B and C). COVID-19 arrived sooner in those cities that had larger populations and had more travellers from Wuhan (Table 1 and table S1). However, the Wuhan travel ban was associated with a delayed arrival time of COVID-19 in other cities by an estimated 2.91 days [95% confidence interval (CI), 2.54 to 3.29 days] on average (Fig. 3B and Table 1).

This delay provided extra time to prepare for the arrival of COVID-19 in more than 130 cities across China but would not have curbed transmission after infection had been exported to new locations from Wuhan. The timing and implementation of emergency control measures in 342 cities across China are shown in Fig. 1 (figs. S2 and S4). School closure, the isolation of suspected and confirmed patients, plus the disclosure of information were implemented in all cities. Public gatherings were banned and entertainment venues closed in 220 cities (64.3%). Intracity public transport was suspended in 136 cities (39.7%), and intercity travel was prohibited by 219 cities (64.0%). All three measures were applied in 136 cities (table S2).

Cities that implemented a Level 1 response (any combination of control measures) (figs. S2 and S4) preemptively, before discovering any COVID-19 cases, reported 33.3% (95% CI, 11.1 to 44.4%) fewer laboratory-confirmed cases during the first week of their outbreaks (13.0 cases; 95% CI, 7.1 to 18.8, n = 125 cities) compared with cities that started control later (20.6 cases, 95% CI, 14.5 to 26.8, n = 171 cities), with a statistically significant difference between the two groups (Mann-Whitney U = 8197, $z = -3.4$, $P < 0.01$). A separate analysis using regression models shows that among specific control measures, cities that suspended intracity public transport and/or closed entertainment venues and banned public gatherings, and did so sooner, had fewer cases during the first week of their outbreaks (Table 2 and table S3). This analysis provided no evidence that the prohibition of travel between cities, which was implemented after and in addition to the Wuhan shutdown on 23 January, reduced the number of cases in other cities across China. These results are robust to the choice of statistical regression model (table S3).

The reported daily incidence of confirmed cases peaked in Hubei province (including Wuhan) on 4 February (3156 laboratory-confirmed cases, 5.33 per 100,000 population in Hubei) and in all other provinces on 31 January (875 cases, 0.07 per 100,000 population) (fig. S1). The low level of peak incidence per capita, the early timing of the peak, and the subsequent decline in daily case reports suggest that transmission control measures were associated not only with a delay in the growth of the epidemic but also with a marked reduction in the number of cases. By fitting an epidemic model to the time series of cases reported in each province (fig. S3), we estimate that the (basic) case reproduction number (R_0) was 3.15 before the implementation of the emergency response on 23 January (Table 3). As control was scaled-up from 23 January onward (stage 1), the case reproduction number declined to 0.97, 2.01, and 3.05 (estimated as C_1R_0) in three groups of provinces, depending on the rate of implementation in each group (Table 3 and table S4). Once the implementation of interventions was 95% complete everywhere (stage 2), the case reproduction number had fallen to 0.04 on average (C_2R_0), far below the replacement rate ($\ll 1$) and consistent with the rapid decline in incidence (Fig. 4A, Table 3, fig. S5, and table S4).

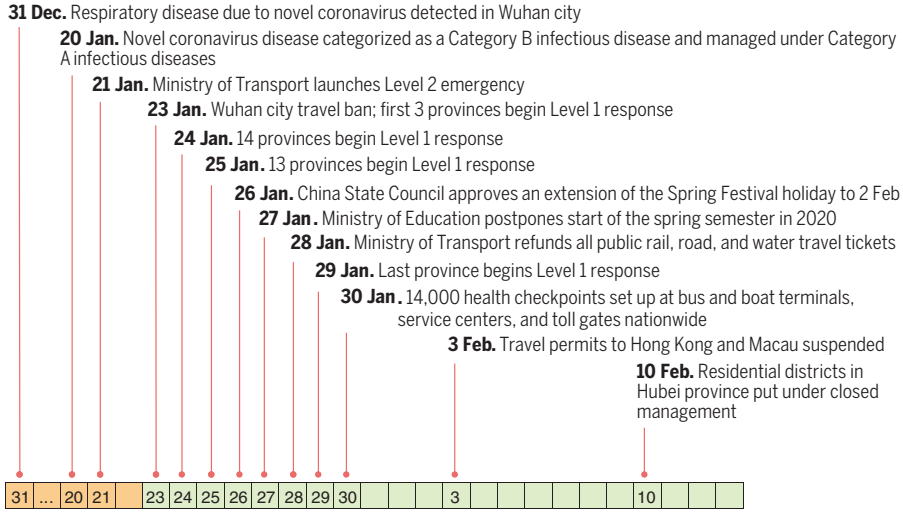


Fig. 1. Dates of discovery of the novel coronavirus causing COVID-19 and of the implementation of control measures in China, from 31 December 2019.

Table 2. Associations between the type and timing of transmission control measures and the number of COVID-19 cases reported in city outbreaks the first week. Data were evaluated by means of a generalized linear regression model.

Covariates	Coefficient	95% CI	*P*
(Intercept)	−9.10	(−9.56, −8.64)	<0.01
Arrival time	0.44	(0.43, 0.46)	<0.01
Distance from Wuhan City (log10)	0.61	(0.49, 0.73)	<0.01
Suspension of intra-city public transport			
Implementation	−3.50	(−4.28, −2.73)	<0.01
Timing	0.11	(0.08, 0.14)	<0.01
Closure of entertainment venues			
Implementation	−2.28	(−2.98, −1.57)	<0.01
Timing	0.09	(0.06, 0.11)	<0.01

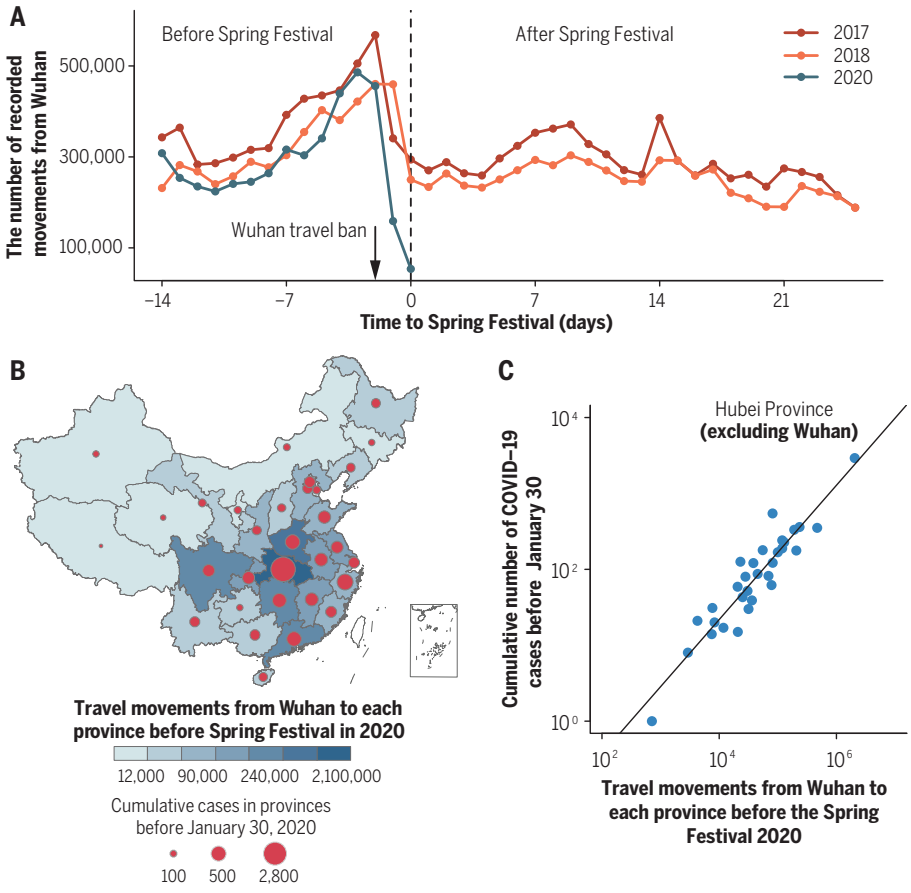


Fig. 2. The dispersal of COVID-19 in China 15 days before and 25 days after the Spring Festival (Chinese Lunar New Year). (**A**) Movement outflows from Wuhan city during Spring Festival travel in 2017, 2018, and 2020. The vertical dotted line is the date of the Spring Festival (Chinese Lunar New Year). (**B**) The number of recorded movements from Wuhan city to other provinces during the 15 days before the Spring Festival in 2020. The shading from light to dark represents the number of human movements from Wuhan to each province. The areas of circles represent the cumulative number of cases reported by 30 January 2020, 1 week after the Wuhan travel ban on 23 January. (**C**) Association between the cumulative number of confirmed cases reported before 30 January and the number of movements from Wuhan to other provinces.

Table 3. Parameter estimates of the SEIR (susceptible-exposed-infectious-recovered) epidemic model. BCI, Bayesian confidence interval; C_{1_high}, Heilongjiang, Shanghai, Tianjin, Zhejiang, and Hubei (excluding Wuhan); C_{1_medium}, Anhui, Beijing, Fujian, Guangdong, Guangxi, Guizhou, Hunan, Jilin, Jiangsu, Jiangxi, Inner Mongolia, Shandong, and Tibet; C_{1_low}, Gansu, Hainan, Hebei, Henan, Liaoning, Ningxia, Qinghai, Shanxi, Shaanxi, Sichuan, Xinjiang, Yunnan, and Chongqing.

Parameter	Definition	Mean	95% BCI
ρ	Reporting proportion	0.002	0.001 to 0.003
R_0	Basic reproduction number	3.15	3.04 to 3.26
$1/\delta$	Mean latent period (days)	4.90	4.32 to 5.47
C_{1_high}	Lower effect of control at the first stage	0.97	0.94 to 0.99
C_{1_medium}	Medium effect of control at the first stage	0.65	0.58 to 0.72
C_{1_low}	Higher effect of control at the first stage	0.31	0.24 to 0.38
C_2	Effect of control at the second stage	0.01	0.001 to 0.03
$1/\gamma$	Infectious period before isolation (days)	5.19	4.51 to 5.86
I_{w0}	Minimum number of cases when none detected	1.12	0.91 to 1.32

On the basis of the fit of the model to daily case reports from each province, and on the preceding statistical analyses, we investigated the possible effects of control measures on the trajectory of the epidemic outside Wuhan city (Fig. 4B). Our model suggests that without the Wuhan travel ban or the national emergency response, there would have been 744,000 (±156,000) confirmed COVID-19 cases outside Wuhan by 19 February, day 50 of the epidemic. With the Wuhan travel ban alone, this number would have decreased to 202,000 (±10,000) cases. With the national emergency response alone (without the Wuhan travel ban), the number of cases would have decreased to 199,000 (±8500). Thus, neither of these interventions would, on their own, have reversed the rise in incidence by 19 February (Fig. 4B). But together and interactively, these control measures offer an explanation of why the rise in incidence was halted and reversed, limiting the number of confirmed cases reported to 29,839 (fitted model estimate 28,000 ± 1400 cases), 96% fewer than expected in the absence of interventions.

This analysis shows that transmission control (nonpharmaceutical) measures initiated during the Chinese Spring Festival holiday, including the unprecedented Wuhan city travel ban and the Level 1 national emergency response, were strongly associated with, although not necessarily the cause of, a delay in epidemic growth and a reduction in case numbers during the first 50 days of the COVID-19 epidemic in China.

The number of people who have developed COVID-19 during this epidemic, and therefore the number of people who were protected by control measures, is not known precisely, given that cases were almost certainly underreported. However, in view of the small fraction of people known to have been infected by 19 February (75,532 cases, 5.41 per 100,000 population), it is unlikely that the spread of infection was halted and epidemic growth reversed because the supply of susceptible people had been exhausted. This implies that a large fraction of the Chinese population remains at risk of COVID-19; control measures may need to be reinstated, in some form, if there is a resurgence of transmission. Further investigations are needed to verify that proposition, and population surveys of infection are needed to reveal the true number of people who have been exposed to this novel coronavirus.

We could not investigate the impact of all elements of the national emergency response because many were introduced simultaneously across China. However, this analysis shows that suspending intracity public transport, closing entertainment venues, and banning public gatherings, which were introduced at different times in different places, were associated with the overall containment of the epidemic.

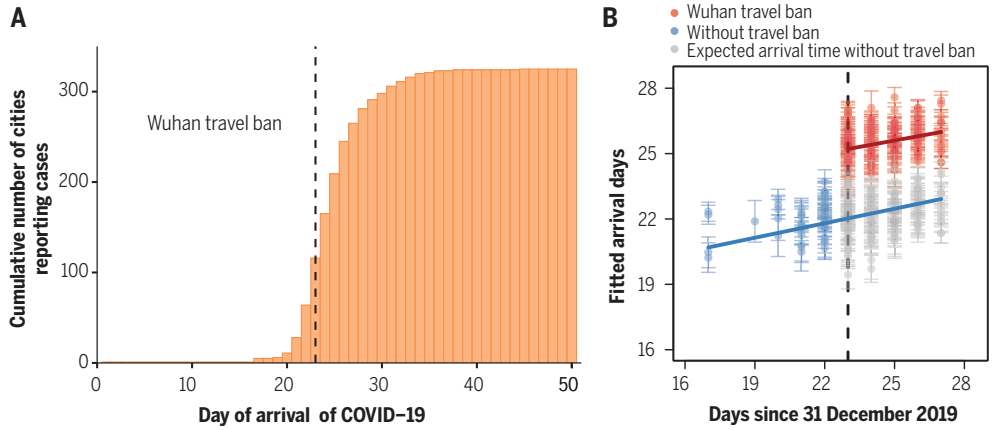


Fig. 3. Spatial dispersal of COVID-19 in China. (**A**) Cumulative number of cities reporting cases by 19 February 2020. Arrival days are defined as the time interval (days) from the date of the first case in the first infected city (Wuhan) to the date of the first case in each newly infected city (a total of 324 cities), to characterize the intercity transmission rate of COVID-19. The dashed line indicates the date of the Wuhan travel ban (shutdown). (**B**) Before (blue) and after (red) the intervention by 30 January 2020, 1 week after the Wuhan travel ban (shutdown). The blue line and points show the fitted regression of arrival times up to the shutdown on day 23 (23 January, vertical dashed line). Gray points show the expected arrival times after day 23, without the shutdown. The red line and points show the fitted regression of delayed arrival times after the shutdown on day 23. Each observation (point) represents one city. Error bars give ±2 standard deviations.

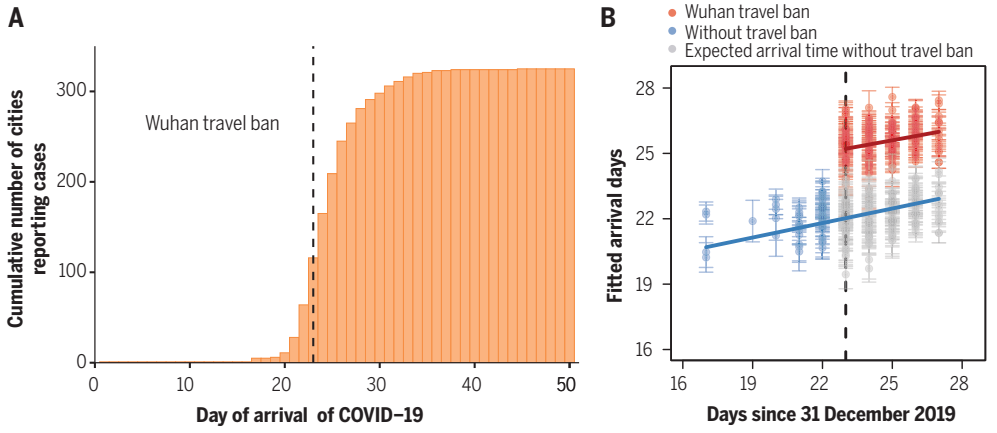


Fig. 4. The role of interventions in controlling the COVID-19 outbreak across China. (**A**) Epidemic model (line) fitted to daily reports of confirmed cases (points) summed across 31 provinces. Hubei excludes Wuhan city. (**B**) Expected epidemic trajectories without the Wuhan travel ban (shutdown), and with (blue) or without (red) interventions carried out as part of the Level 1 national emergency response, with the Wuhan travel ban and with (black) or without (orange) the intervention. Vertical dashed lines in (A) and (B) mark the date of the Wuhan travel ban and the start of the emergency response on 23 January. Shaded regions in (A) and (B) mark the 95% prediction envelopes.

However, other factors are likely to have contributed to control, especially the isolation of suspected and confirmed patients and their contact, and it is not yet clear which parts of the national emergency response were most effective. We did not find evidence that prohibiting travel between cities or provinces reduced the numbers of COVID-19 cases outside Wuhan and Hubei, perhaps because such travel bans were implemented as a response to, rather than in anticipation of, the arrival of COVID-19.

This study has drawn inferences not from controlled experiments but from statistical and mathematical analyses of the temporal and spatial variation in case reports, human mobility, and transmission control measures. With that caveat, control measures were strongly associated with the containment of COVID-19, potentially averting hundreds of thousands of cases by 19 February, day 50 of the epidemic. Whether the means and the outcomes of control can be replicated outside China and which of the interventions are most effective are now under intense investigation as the virus continues to spread worldwide.

REFERENCES AND NOTES

1. N. Zhu *et al.*, *N. Engl. J. Med.* **382**, 727–733 (2020).
2. R. Lu *et al.*, *Lancet* **395**, 565–574 (2020).
3. F. Wu *et al.*, *Nature* **579**, 265–269 (2020).
4. P. Zhou *et al.*, *Nature* **579**, 270–273 (2020).
5. J. Cai *et al.*, *Int. J. Environ. Res. Public Health* **16**, 222 (2019).
6. C. Wang, P. W. Horby, F. G. Hayden, G. F. Gao, *Lancet* **395**, 470–473 (2020).
7. S. Chen, J. Yang, W. Yang, C. Wang, T. Bärnighausen, *Lancet* **395**, 764–766 (2020).
8. M. U. G. Kraemer *et al.*, *Science* eabb4218 (2020).
9. Chinadaily, "Tibet activates highest-level public health alert" (29 January 2020); www.chinadaily.com.cn/a/202001/29/WS5e318a36a3101282172739c1.html.
10. B. T. Grenfell, O. N. Bjørnstad, J. Kappey, *Nature* **414**, 716–723 (2001).
11. D. Brockmann, D. Helbing, *Science* **342**, 1337–1342 (2013).
12. A. Wesolowski *et al.*, *Science* **338**, 267–270 (2012).
13. N. M. Ferguson *et al.*, *Nature* **437**, 209–214 (2005).
14. K. E. Jones *et al.*, *Nature* **451**, 990–993 (2008).
15. D. M. Morens, G. K. Folkers, A. S. Fauci, *Nature* **430**, 242–249 (2004).
16. C. Viboud *et al.*, *Science* **312**, 447–451 (2006).
17. A. Wesolowski *et al.*, *Proc. Natl. Acad. Sci. U.S.A.* **112**, 11887–11892 (2015).
18. H. Tian *et al.*, Code for: An investigation of transmission control measures during the first 50 days of the COVID-19 epidemic in China. *Zenodo* (2020).

ACKNOWLEDGMENTS

We thank the thousands of Centers for Disease Control (CDC) staff and local health workers in China who collected data and continue to work to contain COVID-19 in China and elsewhere. **Funding:** This study was provided by the National Natural Science Foundation of China (81673234), Beijing Natural Science Foundation (JQ18025), Beijing Advanced Innovation Program for Land Surface Science, and Young Elite Scientist Sponsorship Program by CAST (YESS) (2018QNRC001). H.T., M.U.G.K., O.G.P., and C.D. acknowledge support from the Oxford Martin School; H.T. acknowledges support from the Military Logistics Research Program. The funders had no role in study design, data collection and analysis, the decision to publish, or in preparation of the manuscript. **Author contributions:** H.T., P.Z., R.Y., O.G.P., B.T.G., and C.D. designed the study. B.C. and Y.S. collected and processed the Tencent's LBS data. Y.Liu, B.L., B.X., Q.Y., B.W., P.Y., Y.C., and Q.W. collected the statistical data. H.T., Y.Li, C.-H.W., and J.C. conducted the analyses. M.U.G.K., O.N.B.,

R.Y., O.G.P., B.T.G., and C.D. edited the manuscript. H.T. and C.D. wrote the manuscript. All authors read and approved the manuscript. **Competing interests:** All other authors declare no competing interests. **Data and materials availability:** Code and data are available on the following GitHub repository: https://github.com/huaiyutian/COVID-19_TCM-50d_China (*18*).

This work is licensed under a Creative Commons Attribution 4.0 International (CC BY 4.0) license, which permits unrestricted use, distribution, and reproduction in any medium, provided the original work is properly cited. To view a copy of this license, visit https://creativecommons.org/licenses/by/4.0/. This license does not apply to figures/photos/artwork or other content included in the article that is credited to a third party; obtain authorization from the rights holder before using such material.

SUPPLEMENTARY MATERIALS

science.sciencemag.org/content/368/6491/638/suppl/DC1
Materials and Methods
Figs. S1 to S7
Tables S1 to S4
References (*19*–*28*)

View/request a protocol for this paper from *Bio-protocol*.

6 March 2020; accepted 27 March 2020
Published online 31 March 2020
10.1126/science.abb6105

COLLOIDS

Emergence of complexity in hierarchically organized chiral particles

Wenfeng Jiang[1,2,3], Zhi-bei Qu[1,2,3], Prashant Kumar[1,2], Drew Vecchio[1,2], Yuefei Wang[4,5], Yu Ma[1,2,6], Joong Hwan Bahng[7], Kalil Bernardino[8], Weverson R. Gomes[9], Felippe M. Colombari[10], Asdrubal Lozada-Blanco[9], Michael Veksler[1,2], Emanuele Marino[11], Alex Simon[1,2], Christopher Murray[11], Sérgio Ricardo Muniz[12], André F. de Moura[9]*, Nicholas A. Kotov[1,2,4,13,14]*

The structural complexity of composite biomaterials and biomineralized particles arises from the hierarchical ordering of inorganic building blocks over multiple scales. Although empirical observations of complex nanoassemblies are abundant, the physicochemical mechanisms leading to their geometrical complexity are still puzzling, especially for nonuniformly sized components. We report the self-assembly of hierarchically organized particles (HOPs) from polydisperse gold thiolate nanoplatelets with cysteine surface ligands. Graph theory methods indicate that these HOPs, which feature twisted spikes and other morphologies, display higher complexity than their biological counterparts. Their intricate organization emerges from competing chirality-dependent assembly restrictions that render assembly pathways primarily dependent on nanoparticle symmetry rather than size. These findings and HOP phase diagrams open a pathway to a large family of colloids with complex architectures and unusual chiroptical and chemical properties.

Organic-inorganic particles made by or found in living systems often display spiky, reticulated, twisted, and fractal morphologies with nanoscale structural components. They can be referred to as hierarchically organized particles (HOPs) because they possess multiscale levels of organization encompassing both molecular and nanoscale structural units. Although some topological elements of HOP geometry can be replicated in synthetic particles with different degrees of similarity (*1*–*7*), the physical mechanisms responsible for HOP formation remain mysterious. One unanswered question concerns the origin of their complexity, given the highly unfavorable thermodynamics of their templateless self-organization (*8*, *9*). The Gibbs free energy of open structures with nanoscale organization (*10*) should be higher than that of the corresponding random, compact agglomerates (fig. S1). The latter are favored by entropy and enthalpy, and yet complex HOPs spontaneously form in multiple biological and abiological systems. Another question concerns the role of polydispersity of the nanoscale components involved in the self-assembly process. For similar thermodynamic reasons, the wide size distribution should favor disorganized structures, but numerous biological systems defy these expectations.

One mechanism guiding the assembly of nanostructures could be related to the chirality of the constituent building blocks (*11*–*14*) typical for biology. However, chirality-guided self-assembly pathways are typically understood as lock-and-key mechanisms that do not permit structural variability of the components. The thermodynamic preferences of nanoparticle association based on their chirality can also be destroyed by large energy perturbations from size variations (*15*). Nonetheless, the role of chirality in the assembly patterns of building blocks with wide size distribution is worth investigating further because of the many fundamental implications and practical implementations of chiral HOPs.

In the search for appropriate experimental systems, we turned to noble-metal thiolates (*16*, *17*) because they are known to exist as one- and two-dimensional nanostructures with variable surface ligands and strong chiroptical activity (*18*–*21*). We prepared chiral thiolates of gold in the form of nanoplatelets with the amino acid cysteine (Cys) as surface ligands (figs. S2 and S3 and supplementary materials) and developed multiscale computational models (figs. S2, S4, and S5 and tables S1 and S2) that enabled us to evaluate their thermodynamic and optical characteristics. Au-Cys nanoplatelets are uniform in thickness but have a broad lateral size distribution with a dispersity index of 1.36 (fig. S2, B and C). When bearing nonracemic ligands, these particles display circular dichroism (CD) spectra with peaks in the far-ultraviolet (UV) range associated with the Cys ligands and those at the longer wavelengths associated with chirality of nanoplatelets themselves, according to molecular dynamics (MD) and xTB-sTDA calculations (*22*) (figs. S6 to S8 and movie S1).

The tendency of Au-Cys nanocolloids toward randomized agglomeration was mitigated by strong electrostatic repulsion imparted to particles by cetyltrimethylammonium bromide (CTAB). CTA^+ cations increase the electrokinetic zeta potential, ζ, of nanoplatelets from –18.6 mV to +44.7 mV; nanoplatelets serve as nanoscale building blocks for most particles investigated here. Association of the Au-Cys nanoplatelets, induced by high ionic strength (0.5 M NaCl) without CTAB, led to disordered high–molecular mass agglomerates (fig. S9). Without NaCl and CTAB, half-spiked spheroids formed (fig. S10). These spheroids were largely disorganized but their shape was peculiar, revealing consistent symmetry breaking, with one side of the particle being smooth and the other spiky.

Adsorption of CTA^+ on the nanoplatelets increased the electrostatic repulsion, which counteracted the close-range attraction responsible for thermodynamic minima along the high-mass pathway (fig. S1). At some point, the repulsion became strong enough to avoid stochastic agglomeration, switching the process from the high-mass agglomeration pathway to electrostatically frustrated self-assembly (*23*, *24*). With increasing CTA^+ concentration, the high ζ value should make edge-to-edge attachment of the nanoplatelets more favorable than the face-to-face alternative. When $[CTA^+]$ = 0.27 M, the use of pure L- or D-Cys enantiomers (enantiomeric excess $\chi = \pm 100\%$; see supplementary materials) produced HOPs (Fig. 1, A, B, D, and E) with twisted spikes radially organized around a common center (fig. S11); their formation was associated with the growth of strong CD bands in UV-visible and infrared (IR) parts of the spectrum (Fig. 2D and fig. S12). These spiky particles are denoted as Au–L-Cys and Au–D-Cys, respectively, or coccolith-like particles (CLIPs), cumulatively, in reference to their partial resemblance to spiky skeletons produced by microscale algae coccolithophores (e.g., *Syracosphaera anthos HOL*). Despite prior studies (*8*, *10*, *25*), the unique echinate geometry of coccoliths and silicoflagellates remains a biomineralization puzzle. Statistical analysis of 500 Au–L-Cys CLIPs showed that they were highly uniform in size, with a diameter of 3.5 ± 0.3 μm and polydispersity index of 1.02 (Fig. 1, A and B, and fig. S13).

Kayak-shaped HOPs with layered architectures, denoted as Au–DL-Cys, which lack the

[1]Department of Chemical Engineering, University of Michigan, Ann Arbor, MI 48109, USA. [2]Biointerfaces Institute, University of Michigan, Ann Arbor, MI 48109, USA. [3]School of Chemistry and Chemical Engineering, Frontiers Science Center for Transformative Molecules, Shanghai Jiao Tong University, Shanghai 200240, China. [4]Department of Materials Science, University of Michigan, Ann Arbor, MI 48109, USA. [5]School of Chemical Engineering and Technology, Tianjin University, Tianjin 300072, China. [6]School of Stomatology, Lanzhou University, Lanzhou 730000, China. [7]California Institute of Technology, Pasadena, CA 91125, USA. [8]Institute of Chemistry, University of São Paulo, 05508-000 São Paulo, SP, Brazil. [9]Department of Chemistry, Federal University of São Carlos, 13565-905 São Carlos, SP, Brazil. [10]Brazilian Nanotechnology National Laboratory (LNNano), Brazilian Center for Research in Energy and Materials (CNPEM), 13083-970 Campinas, SP, Brazil. [11]Department of Chemistry, University of Pennsylvania, Philadelphia, PA 19104, USA. [12]São Carlos Institute of Physics, University of São Paulo, 13560-970 São Carlos, SP, Brazil. [13]Department of Macromolecular Science and Engineering, University of Michigan, Ann Arbor, MI 48109, USA. [14]Michigan Institute of Translational Nanotechnology (MITRAN), Ypsilanti, MI 48198, USA.
*Corresponding author. Email: moura@ufscar.br (A.F.d.M.); kotov@umich.edu (N.A.K.)

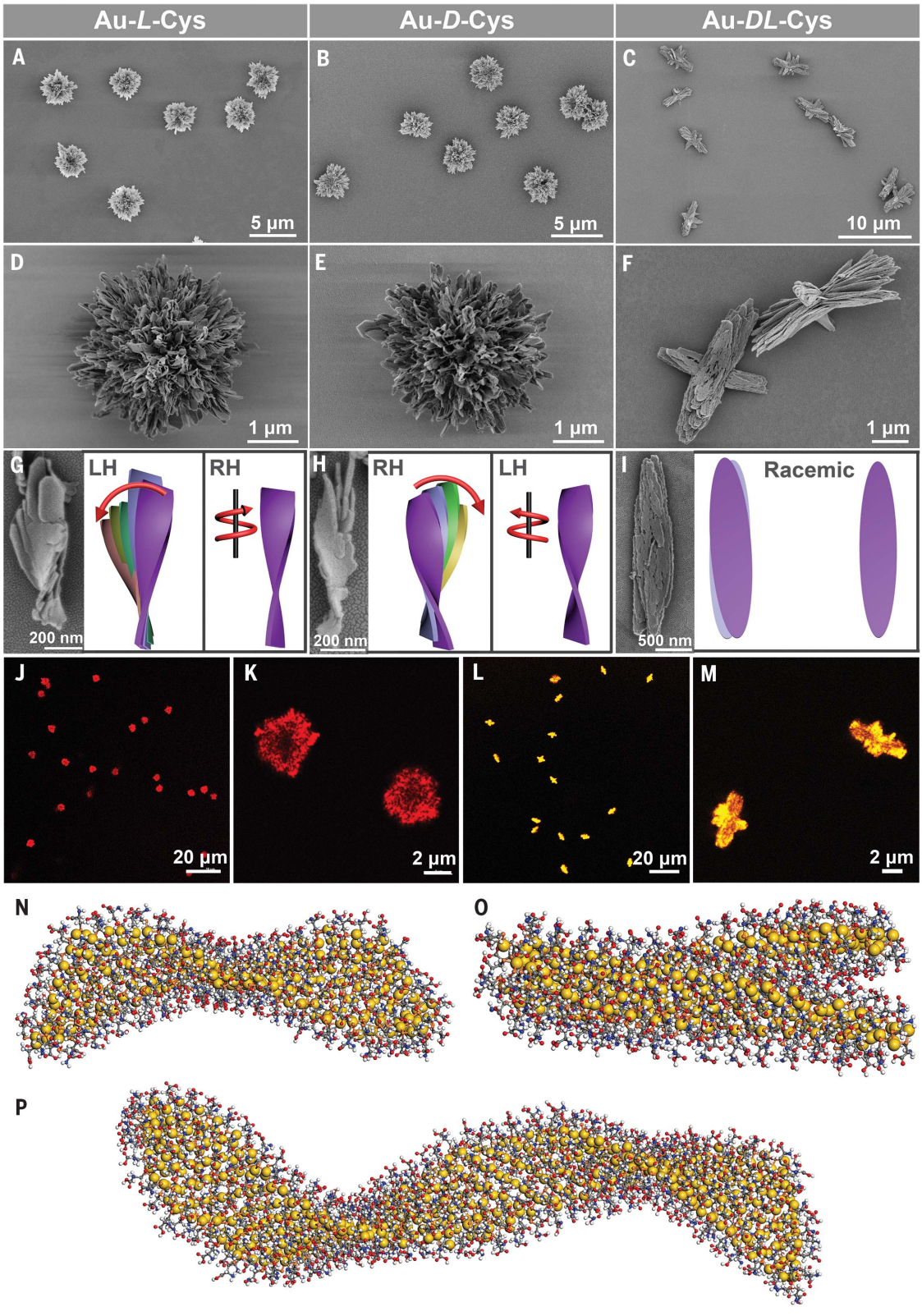


Fig. 1. Gold thiolate hierarchically organized particles (HOPs) with cysteine surface ligands. (**A** to **C**) SEM images of Au–L-Cys and Au–D-Cys coccolith-like particles (CLIPs) [(A) and (B)] and Au–DL-Cys kayak particles (C) with low magnification. (**D** to **F**) Enlarged SEM images of Au–L-Cys and Au–D-Cys CLIPs [(D) and (E)] and Au–DL-Cys (F) kayak particles. (**G** to **I**) SEM images and corresponding schematic illustrations of segments of Au–L-Cys (G), Au–D-Cys (H), and Au–DL-Cys (I). Statistical analysis of SEM images for 100 assembly segments indicates that the pitch of individual nanoribbons in the stacks is 1300 ± 123 nm and their average width is 16 ± 1.8 nm, whereas the average angle between two neighboring nanoribbons in the stack is 7° ± 0.7° and the pitch of nanoribbon stacks is 820 ± 10 nm. (**J** to **M**) Confocal microscopy images of Au–L-Cys CLIPs [(J) and (K)] and Au–DL-Cys kayak particles [(L) and (M)]. (**N** to **P**) Atomistic MD simulation of twisted conformation of Au–L-Cys single sheets of different lengths [(N) and (P)] and their stacks (O). The XRD, XPS, and thermogravimetry data obtained for different HOPs indicate that only Cys molecules are present in the interlamellar spacing between adjacent Au–L-Cys sheets.

spiky geometry but do manifest hierarchical organization (Fig. 1, C and F), were observed when a racemic mixture of Cys (χ = 0%) was used. Au–L-Cys (Fig. 1, J and K), Au–D-Cys (fig. S14, A and B), and Au–DL-Cys (Fig. 1, L and M) possess strong light emission with red and orange colors for χ = ±100% and 0%, respectively. The confocal microscopy images (Fig. 1, J to M, and fig. S14, A and B) obtained using this intrinsic particle emission show geometries consistent with the scanning electron microscopy (SEM) images.

The disassembly of HOPs into twisted nanoribbons by sonication reveals their hierarchical structure, composed of staggered thin

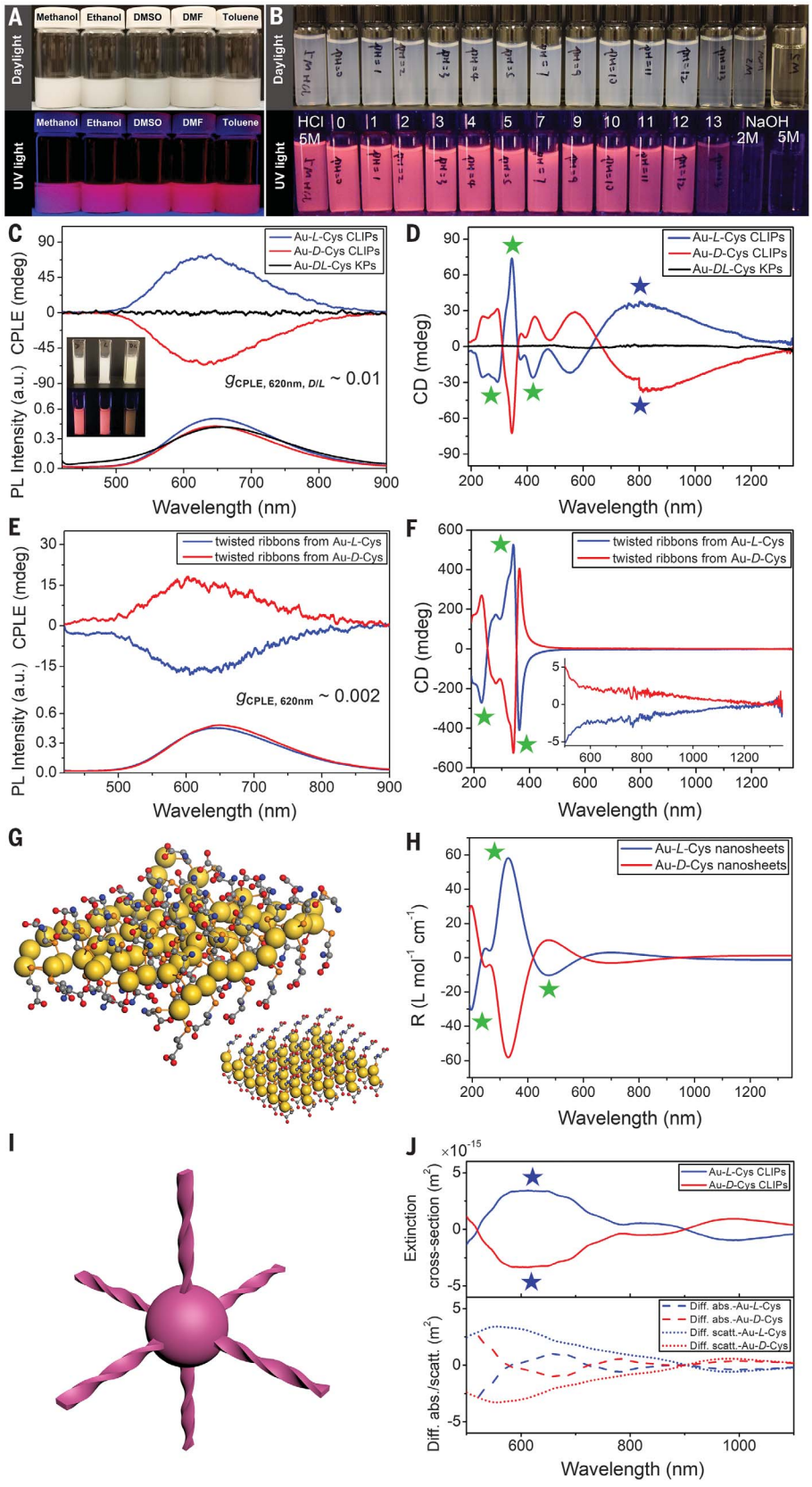


Fig. 2. Chemical and optical properties of Au-Cys CLIPs. (**A**) Dispersions of Au–L-Cys CLIPs in different solvents [methanol, ethanol, dimethyl sulfoxide (DMSO), *N*,*N*-dimethylformamide (DMF), and toluene]. Some sediment forms upon long-term standing; it redisperses upon shaking. (**B**) Stability study of Au–L-Cys dispersions with different pH values or concentrations of HCl or NaOH after 12 hours. Top photograph was taken under daylight illumination; bottom photo was taken under UV light (wavelength 365 nm) irradiation. (**C** and **D**) CPLE (C) and CD (D) spectra of Au–L-Cys CLIPs (blue), Au–D-Cys CLIPs (red), and Au–DL-Cys kayak particles (black). Inset in (C): Photos of Au–L-Cys, Au–D-Cys, and Au–DL-Cys dispersions under daylight (top) and UV light (bottom) illumination. (**E** and **F**) CPLE (E) and CD (F) spectra of Au–L-Cys (blue) and Au–D-Cys (red) after sonication. Inset in (F): The same spectra for the 500- to 1350-nm spectral window to confirm the absence of the CD peaks associated with differential scattering of assembled CLIPs. The helicity of the nanoribbon stacks of Au–L-Cys is left-handed, and therefore the light scattered by Au–L-Cys has left-handed polarization. After disassembly of the stacks into single right-handed nanoribbons, the light passing through these dispersions acquires right-handed circular polarization. (**G** and **H**) The computational model (G) and calculated CD spectra (H) of Au–L-Cys nanoplatelets. The corresponding peaks in the short-wavelength part of the CD spectra of CLIPs and nanoplatelet are marked in (D), (F), and (H) with green stars. (**I** and **J**) The computational model (I) and the differential extinction spectrum (J) for the differential scattering contribution to the chiroptical properties of the CLIPs at long wavelengths. The corresponding signals in the experimental and calculated spectra in (D) and (J) are marked with blue stars.

sheets (Fig. 1, G and H, and fig. S14, C and D). Structural analysis of CLIPs and constituent twisted ribbons by means of x-ray diffraction (XRD), x-ray photoelectron spectroscopy (XPS), thermogravimetric analysis, Fourier-transform infrared spectroscopy, UV-visible spectroscopy, and time-resolved fluorescence imaging yielded results that are consistent with atomically thin layers of gold and sulfur connected by aurophilic bonds (figs. S15 to S18). The x-ray diffraction spacing between the layers is 1.23 nm; it is nearly identical to the thickness of the Au-Cys sheets of 1.26 nm and 1.37 nm, calculated according to MD simulations using either quantum chemical potential energy surfaces (fig. S19) or a classical force field (fig. S2A). The corresponding atomic structure of Au-Cys nanoribbons (fig. S2) forming nanosheets with [010] growth direction along the long axis can be proposed on the basis of density functional theory (DFT) calculations (figs. S4 and S19) and substantiated by small-angle x-ray scattering (SAXS) and XRD data (figs. S3 and S15). The preference of [010] atomic structure over [100] can also be verified for twisted states of the ribbon by coarse-grained models (fig. S5 and movie S2).

The gold-thiolate nanoribbons in Au-L-Cys HOPs are right-handed (RH, twisted clockwise). The stacks of the corresponding nanoribbons are, however, left-handed (LH, twisted counterclockwise, Fig. 1G). The handedness of the nanoribbons and their stacks is inverted (i.e., to LH and RH, respectively) if D-Cys is used instead (Fig. 1H). The twist of individual nanoribbons is reproduced well in atomistic MD models (Fig. 1, N to P). The staggered configuration of the ribbons assembled in a stack originates from the minimization of electrostatic repulsive forces observed previously for gold nanorods (*26*, *27*).

Strong bonding of sulfur atoms to two Au atoms and the spiky geometry associated with the molecular and submicrometer organization of CLIPs leads to chemical properties that are unusual for both colloidal particles and two-dimensional nanostructures. Typical gold thiolates are known to aggregate rapidly and form precipitates (*28*), but this is not the case for CLIPs. The spiky geometry and charged surface ligands allow this type of HOPs to form dispersions in hydrophilic and hydrophobic media with high colloidal stability (Fig. 2A and fig. S20) (*29*). They also display remarkable chemical stability, with both their geometry and bright red luminescence observed from pH 0 to 11 (Fig. 2B and figs. S21 and S22).

The dispersibility and strong luminescence of CLIPs enables elucidation of their chiroptical properties and self-assembly pathways. The spectroscopic measures for different levels of organization in CLIPs are needed as experimental order parameters to understand how self-assembly pathways to complexity depend on the chirality and polydispersity (fig. S1). Unlike small chiral molecules, nanoparticles, and biological and (bio)inorganic nanoassemblies (*30*), HOPs of this type display strong chiroptical activity in absorption, luminescence, and differential scattering simultaneously. Separation of HOPs into structural components by ultrasonication (Fig. 1, G and H, and fig. S14, C and D) as well as a diverse set of computational techniques make possible the comprehensive identification of spectral signatures of all these optical processes.

The CD spectra for CLIPs show nearly perfect mirror symmetry for all the bands. Sharp peaks at 250, 310, 350, and 380 nm (Fig. 2D and fig. S23A) correspond to electronic transitions matching those calculated for model Au–L-Cys nanoplatelets (Fig. 2, G and H, and figs. S7 and S8). The broad 650- to 1350-nm band in Fig. 2D is attributed to the circularly polarized differential scattering (*31*) from the spiky particles (Fig. 2, I and J). Disassembly of these HOPs into nanoribbon stacks (Fig. 2F and fig. S23B) leads to disappearance of the peaks with maxima at 420, 560, and 830 nm, indicating that these bands are specific to the fully assembled CLIPs.

Circularly polarized light emission (CPLE) spectra of Au–L-Cys and Au–D-Cys display mirror-symmetrical strong bands at 620 nm, whereas their racemic counterparts, kayak-like HOPs, are CPLE-silent (Fig. 2C). Emission from HOPs acquires circular polarization by two mechanisms. First, photons are emitted in the circularly polarized state as a result of angstrom-scale chirality of the excited states in the Au-Cys nanosheets (fig. S18). The chirality and a more general case of asymmetry of the different excited states can be visualized by quantum chemical calculations (movie S1). Second, the emitted photons acquire additional circular polarization as the result of scattering on dispersed particles with submicrometer-scale chirality. The second mechanism modifies the polarization of photons emitted by Au-Cys sheets and can revert the polarization rotation of the photons acquired during the emission. The stage of assembly and the geometry of the HOPs affect the contribution of scattering, which results in the variable sign of CPLE spectra. As such, the polarity of the CPLE peak of Au–L-Cys switches from positive (left-handed photons dominate) to negative (right-handed photons dominate) after disassembly of CLIPs into individual ribbons (Fig. 2, C and E, and fig. S24) because CLIPs contribute more of the differential scattering in CPLE. The same is observed for Au–D-Cys and constituent twisted ribbons, albeit with opposite signs of the CPLE peaks. The CD peaks in the 500- to 1200-nm region (Fig. 2, D and F) disappear for the constituent nanoribbons. The positive and negative CPLE peaks are therefore spectroscopic signatures of CLIPs, as was also confirmed by electrodynamics simulations (Fig. 2, I and J).

Combining SEM images and CPLE data, which serve as spectroscopic order parameters for this thermodynamic system, we constructed phase diagrams (Fig. 3, A to C, and fig. S25) and found a diverse spectrum of HOP phases and degrees of organization for different values of χ and the building-block nucleation temperature t_n (see supplementary materials). Besides the CLIPs and kayak particles, χ-t_n diagrams include several other phases with different packing of Au-Cys sheets (Fig. 3B) and CPLE activity (Fig. 3C).

The CPLE peaks mark the evolution of the nanoscale system toward complex HOPs. However, CPLE and other chiroptical characteristics such as optical dissymmetry factor (*g*-factor) have difficulties as general enumerators of complexity because they require similarity in materials and/or geometries of the particles. For example, the *g*-factor of complex porous particles from $BaCO_3$ (*1*), $CaCO_3$ (*3*), or FeSe (*9*) with centrosymmetric geometry is ~0. The *g*-factor of solid particles from gold with noncentrosymmetric geometry is ≥0.2 (*4*), but their complexity can be comparable to that of the previous particles. To address this problem, we enumerated particle complexity using graph theory (GT), extending GT approaches from chemistry (*32*) to nanomaterials (see supplementary materials). We calculated a GT-based complexity index (*CI*) as an augmented valence sum (*33*) with modifications ensuring its applicability across a wide range of self-assembled structures (see supplementary materials). *CI* values for a variety of particles indicate that this parameter adequately ranks them according to information content and structural sophistication (table S3). Note that other common GT indices reveal little or no correlations with particle complexity (table S4).

For typical assemblies of nanoparticles studied earlier, *CI* is in the range of 1.5 to 38.25 (fig. S26 and table S3). Analogous calculations for HOPs with the morphology of reticulated supraparticles, kayak particles, and CLIPs (Fig. 1 and fig. S11) give *CI* values of 6.0, 40.0, and 87.0, respectively (Fig. 4, A to F). Within the knowledge of nanoscale structure available for spiky coccoliths representing one of the complex biological HOPs, their *CI* is 49.0 (Fig. 4, G and H).

Both in the lab and in nature (molecules responsible for biomineralization processes are homochiral), the highest structural complexity is observed for χ = 100%. One might infer that complexity increases as χ increases, which might be compelling given the amazing complexity of biological systems. However, the relationship between χ and *CI* is nonmonotonic, as reflected by the *CI* calculation for different HOP phases (Fig. 3D). For example, supraparticle phases 1 and 2 (SPP 1 and 2), observed for 45% < χ < 70%, have *CI* values of 6 to 20; these are smaller than the *CI* values of both CLIP and kayak-like particles, which may

confirm the initial concerns about the ability of nanoparticle chirality to guide the assembly of complex systems. Nonetheless, the strong dependence of structural complexity on chirality can be substantiated by replacement of L-Cys with achiral thioglycolic acid (TGA; Fig. 4, A and B). With an increasing amount of TGA, Au-thiolate particles gradually lose their organization, transitioning to random agglomerates, porous dumbbells, and spheroidal particles (figs. S27 and S28) with $CI \leq 6$ (Fig. 4). Additionally, Au-S nanoplatelets with chiral penicillamine produce CLIPs with twisted spikes (fig. S29) similar to those from L- and D-Cys, with $CI = 87$.

The relationship between chirality and complexity in this system can be understood in the context of different restrictions on the association

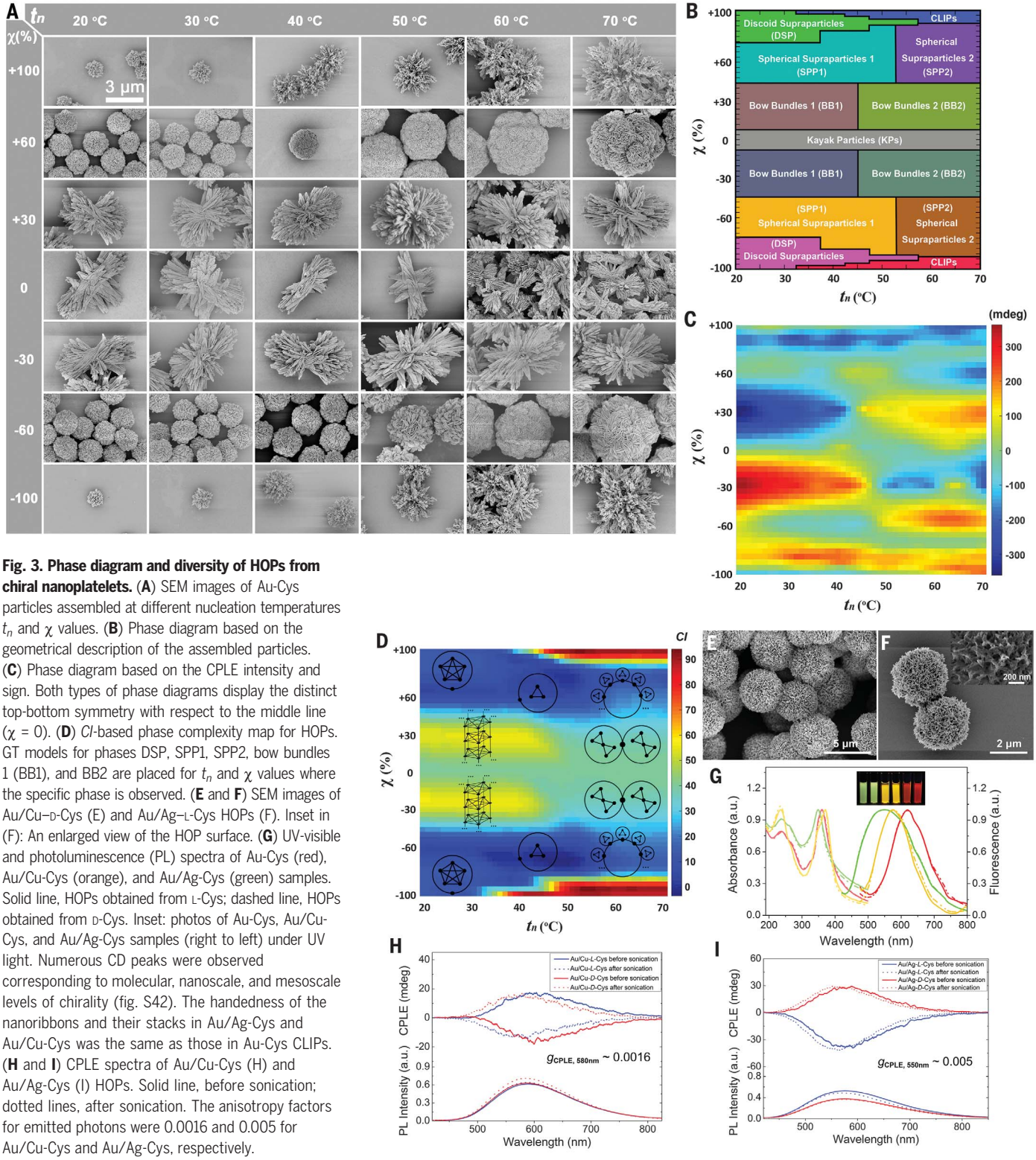


Fig. 3. Phase diagram and diversity of HOPs from chiral nanoplatelets. (**A**) SEM images of Au-Cys particles assembled at different nucleation temperatures t_n and χ values. (**B**) Phase diagram based on the geometrical description of the assembled particles. (**C**) Phase diagram based on the CPLE intensity and sign. Both types of phase diagrams display the distinct top-bottom symmetry with respect to the middle line ($\chi = 0$). (**D**) *CI*-based phase complexity map for HOPs. GT models for phases DSP, SPP1, SPP2, bow bundles 1 (BB1), and BB2 are placed for t_n and χ values where the specific phase is observed. (**E** and **F**) SEM images of Au/Cu–D-Cys (E) and Au/Ag–L-Cys HOPs (F). Inset in (F): An enlarged view of the HOP surface. (**G**) UV-visible and photoluminescence (PL) spectra of Au-Cys (red), Au/Cu-Cys (orange), and Au/Ag-Cys (green) samples. Solid line, HOPs obtained from L-Cys; dashed line, HOPs obtained from D-Cys. Inset: photos of Au-Cys, Au/Cu-Cys, and Au/Ag-Cys samples (right to left) under UV light. Numerous CD peaks were observed corresponding to molecular, nanoscale, and mesoscale levels of chirality (fig. S42). The handedness of the nanoribbons and their stacks in Au/Ag-Cys and Au/Cu-Cys was the same as those in Au-Cys CLIPs. (**H** and **I**) CPLE spectra of Au/Cu-Cys (H) and Au/Ag-Cys (I) HOPs. Solid line, before sonication; dotted lines, after sonication. The anisotropy factors for emitted photons were 0.0016 and 0.005 for Au/Cu-Cys and Au/Ag-Cys, respectively.

patterns for nanoparticles traversing the thermodynamic landscapes (fig. S1). One of the exemplary restrictions is due to electrostatic repulsion (*13*, *23*, *24*). Gradually increasing electrostatic forces in self-assembled structures leads to self-limitation of particle aggregation. Note that electrostatic restrictions result in self-limited particles exceeding 100 nm, and therefore the size variations of individual nanoparticles (2 to 5 nm) become insignificant (fig. S2, B and C). The resulting spheroids, however, have high size uniformity but not high complexity (see SPP1 and SPP2 phases in figs. S25, S27, and S28) with *CI* = 2 to 20.

The complex particle architectures emerge only when restrictions on the assembly size are multiple, anisotropic, and competitive (*13*, *24*, *34*). They may be associated with different types of interactions and can be anisotropic; that is, the restrictions for assembly of Au-Cys nanoplatelets along their normal or in-plane axes can also vary. What is essential is that energy gains and penalties associated with these restrictions on the assembly of building blocks must be comparable. When none of the competing interactions and restrictions dominate, the nanoparticle assembly acquires complex architectures to negotiate these conflicting requirements. In the case of chiral nanoplatelets, anisotropic restrictions associated with electrostatic repulsion are intertwined with those from supramolecular and elastic ones. Surface energy, Frank chiral energy (*34*), and Casimir forces (*35*) contribute to the overall ΔG, but the gains and penalties associated with these interactions may not be sufficiently high to compete with restrictions from other interactions.

The comparable ΔG contribution from multiple interactions and associated restrictions on the assembly patterns force the system to acquire complex geometries. The first-order assessment of energy penalties related to electrostatic, elastic, and supramolecular interactions for two chiral nanoplatelets, based on MD and experimental data, gives a range of 50 to 150 kJ/mol (*36*, *37*). For instance, the energy penalties for twisting nanoribbons (fig. S5 and movie S2) and separating two chiral nanoparticles coated with L-Cys are both ~50 to 60 kJ/mol (*36*).

To better understand how the competitive restrictions can produce the entire spectrum of HOP phases (Fig. 3 and fig. S25) and the origin of nonmonotonous dependence between chirality and complexity, an additional factor needs to be considered. Although the assembly of nanoparticles can be quasi-reversible, the formation of early nanoparticles (i.e., the building blocks) is irreversible. The shape of these building blocks varies for different HOPs. The early particles found at different points on the phase diagram have diverse shapes with twisted, flat, and spheroidal geometries (Fig. 1N and figs. S30 to S33)

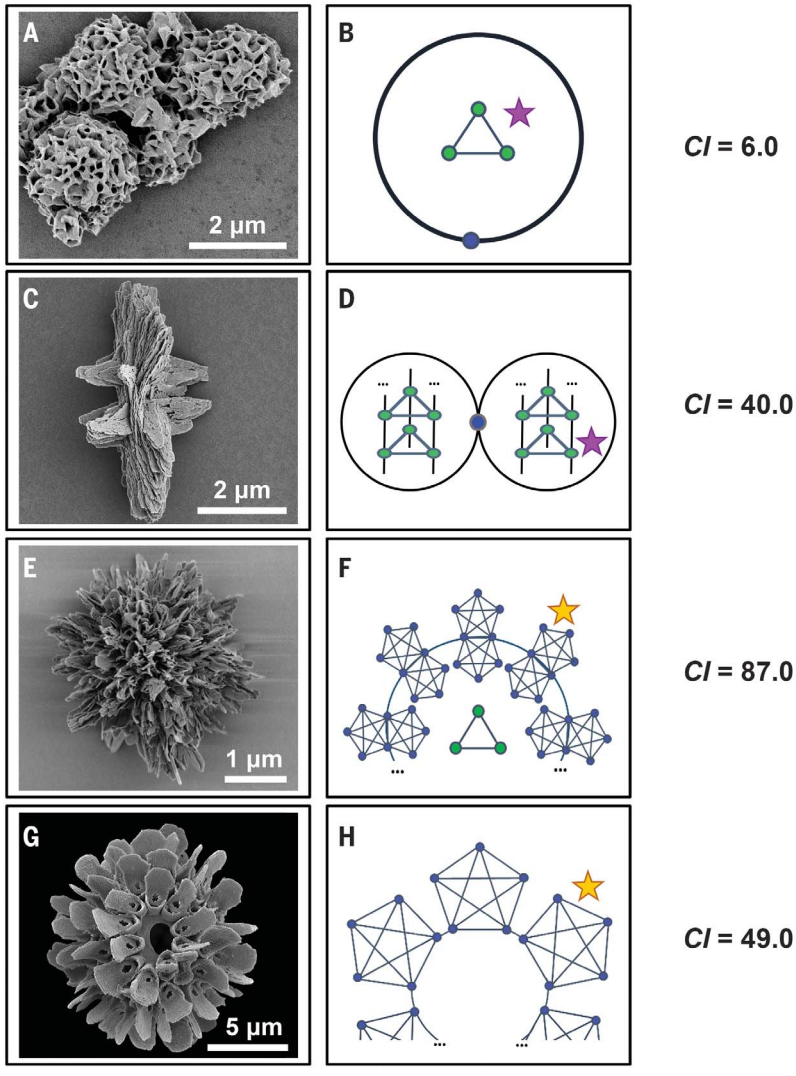


Fig. 4. SEM images of different HOPs, their GT models, and corresponding complexity indexes (*CI*). (**A** and **B**) SEM image of supraparticle Au-thiolate with achiral TGA as surface ligands (A) and its GT model (B). (**C** and **D**) SEM image of the Au–DL-Cys kayak-like particle (C) and its GT model (D). (**E** and **F**) SEM image of the Au–L-Cys CLIP (E) and its GT model (F). (**G** and **H**) SEM image of a skeleton of *Syracosphaera anthos HOL* reproduced from the depository of SEM images of coccoliths found at www.microtax.org (G) and its GT model (H). The graph segments marked with the purple stars in (B) and (D) are minimal topological contracts (MTCs) for the flat Au-S sheets with continuous crystallinity. The graph segments marked with the orange stars in (F) and (H) are the MTC for twisted sheets.

depending on both χ and t_n. When the initial D/L-Au-S nanoplatelets are flat and thin, as for the kayak particles, where χ = 0% (fig. S31A), the elastic energy becomes small. The structure-defining competing restrictions for these particles are electrostatic and supramolecular, related to edge-to-edge and face-to-face attachment of the nanoplatelets. Instead of random agglomerates, uniformly sized ribbons whose widths and stacking heights are restricted by electrostatic repulsion are formed. The kayak-like particles made from them are fairly complex, but *CI* can be increased further when elastic restrictions become more pronounced.

As χ reaches 30 to 60%, chiral asymmetry at the molecular scale increases, but particle dissymmetry and elastic restrictions disappear because the initial building blocks are large, amorphous, and spherical (fig. S32). The nearly isotropic electrostatic repulsion dominates over other restrictions, and so do the spheroidal assemblies with low *CI* represented by the SPP1, SPP2, and discoid supraparticles (DSP) phases. The analogous conclusions can be made from the nanoassemblies made with mixed TGA/Cys surface ligands (fig. S33). When the initial particles are chiral nanoplatelets, electrostatic and elastic restrictions

compete with those supramolecular ones (fig. S34). Consequently, complex HOPs with the highest *CI* emerge.

Finally, one of the key factors driving the formation of self-assembled structures with high complexity from polydispersed building blocks can be particle-particle correlations that favor a specific mutual orientation of nanoparticles, such as stacking of nanoplatelets. The particle-particle correlations can originate from long-range ion correlations (*38*) and criticality of phase transitions (*39*). A phase diagram with numerous phase transitions indicates a possibility of irreversible near-critical states that can enhance interparticle correlation and dominance of particle symmetry over polydispersity (*39*).

The interplay between the different restrictions and the self-assembly pathways toward complex particles can be further visualized in HOPs obtained by doping Au–L-Cys with other coinage metals, such as Cu and Ag (Fig. 3, E and F, and figs. S35 to S38). The possibility for gradual "tuning" of the competitive interactions through doping also offers the opportunity to engineer the HOP complexity. The constituent twisted nanoribbons in Au/Cu and Au/Ag HOPs displayed a pitch of 4 μm and 10 μm, respectively, indicating increased stiffness of the metal-thiolate nanosheets after doping. The elastic restrictions dominate the assembly process, which results in the formation of simple microscale nanosheets to minimize stored mechanical energy. Consequently, a morphological transition from HOPs to long, individual nanoribbons was observed upon increasing the Ag/Au ratio (figs. S38 to S41).

Doping with Cu and Ag also enables the chiroptical properties to be tuned. The emission peaks shifted from red (620 nm) to orange (580 nm) and yellowish-green (550 nm) upon Cu and Ag doping (Cu/Au = 3.3% and Ag/Au = 16.5%; fig. S35), respectively (Fig. 3G and table S5), with concomitant changes in the CD and CPLE spectra (Fig. 3, H and I, and figs. S42 to S44) due to quantum mechanical conjugation of atomic orbitals of the coinage metals with the electronic levels of Au-Cys nanosheets.

Thus, anisotropic electrostatic and elastic interactions place combined restrictions on the assembly pathways of chiral nanoparticles, such that the evolution of multiparticle systems becomes strongly dependent on particle symmetry and asymmetry rather than on particle size (*40*). The described phase diagrams open the door to further studies of phase transitions in systems with high dispersity and may allow comprehensive explorations of the roles of particle chirality and asymmetry in a variety of assembly pathways. The unique optical, chemical, and colloidal properties of some of the HOPs suggest their broad application in asymmetric catalysis and polarization-based optoelectronics. Assembly mechanisms involving those observed for HOPs may help us to understand the origins of the astounding diversity and sophistication of biological nanocomposites.

REFERENCES AND NOTES

1. S.-H. Yu, H. Cölfen, K. Tauer, M. Antonietti, *Nat. Mater.* **4**, 51–55 (2005).
2. A. Gal *et al.*, *Science* **353**, 590–593 (2016).
3. W. Jiang *et al.*, *Nat. Commun.* **8**, 15066 (2017).
4. H. E. Lee *et al.*, *Nature* **556**, 360–365 (2018).
5. L. Zhang, T. Wang, Z. Shen, M. Liu, *Adv. Mater.* **28**, 1044–1059 (2016).
6. Y. Duan *et al.*, *J. Am. Chem. Soc.* **136**, 7193–7196 (2014).
7. X. Liu *et al.*, *Nature* **559**, 593–598 (2018).
8. S. Mann, G. A. Ozin, *Nature* **382**, 313–318 (1996).
9. D. Deng *et al.*, *J. Am. Chem. Soc.* **139**, 16630–16639 (2017).
10. J. J. De Yoreo *et al.*, *Science* **349**, aaa6760 (2015).
11. S. Pieraccini, S. Masiero, A. Ferrarini, G. Piero Spada, *Chem. Soc. Rev.* **40**, 258–271 (2011).
12. P. Duan, H. Cao, L. Zhang, M. Liu, *Soft Matter* **10**, 5428–5448 (2014).
13. T. Gibaud *et al.*, *Nature* **481**, 348–351 (2012).
14. T. Aida, E. W. Meijer, S. I. Stupp, *Science* **335**, 813–817 (2012).
15. T. Shimizu, M. Kogiso, M. Masuda, *Nature* **383**, 487–488 (1996).
16. I. Dolamic, B. Varnholt, T. Bürgi, *Nat. Commun.* **6**, 7117 (2015).
17. C. Noguez, I. L. Garzón, *Chem. Soc. Rev.* **38**, 757–771 (2009).
18. S. Cha, J. Kim, K. Kim, J. Lee, *Chem. Mater.* **19**, 6297–6303 (2007).
19. B. Söptei *et al.*, *Colloids Surf. A* **470**, 8–14 (2015).
20. H. Nie, M. Li, Y. Hao, X. Wang, S. X.-A. Zhang, *Chem. Sci.* **4**, 1852 (2013).
21. C. Li, K. Deng, Z. Tang, L. Jiang, *J. Am. Chem. Soc.* **132**, 8202–8209 (2010).
22. S. Grimme, C. Bannwarth, *J. Chem. Phys.* **145**, 054103 (2016).
23. Y. Xia *et al.*, *Nat. Nanotechnol.* **6**, 580–587 (2011).
24. G. M. Grason, *J. Chem. Phys.* **145**, 110901 (2016).
25. J. R. Young, J. M. Didymus, P. R. Brown, B. Prins, S. Mann, *Nature* **356**, 516–518 (1992).
26. W. Ma *et al.*, *Sci. Rep.* **3**, 1934 (2013).
27. M. Sun *et al.*, *Nat. Commun.* **8**, 1847 (2017).
28. H. Nie *et al.*, *RSC Adv.* **4**, 50521–50528 (2014).
29. J. H. Bahng *et al.*, *Nature* **517**, 596–599 (2015).
30. M. Liu, L. Zhang, T. Wang, *Chem. Rev.* **115**, 7304–7397 (2015).
31. S. R. Kirchner *et al.*, *J. Phys. Chem. C* **122**, 12015–12021 (2018).
32. J.-C. Chambron, C. Dietrich-Buchecker, J.-P. Sauvage, in *Supramolecular Chemistry I—Directed Synthesis and Molecular Recognition* (Springer, 1993), pp. 131–162.
33. M. Randic, D. Plavsic, *Croat. Chem. Acta* **75**, 107–116 (2002).
34. C. Gao *et al.*, *Proc. Natl. Acad. Sci. U.S.A.* **116**, 22030–22036 (2019).
35. E. Marino *et al.*, *J. Phys. Chem. C* **123**, 13451–13457 (2019).
36. W. Feng *et al.*, *Sci. Adv.* **3**, e1601159 (2017).
37. G. I. Guerrero-García, E. González-Tovar, M. Olvera de la Cruz, *Soft Matter* **6**, 2056 (2010).
38. N. Boon, G. I. Guerrero-García, R. van Roij, M. Olvera de la Cruz, *Proc. Natl. Acad. Sci. U.S.A.* **112**, 9242–9246 (2015).
39. M. E. Fisher, *Rep. Prog. Phys.* **30**, 615–730 (1967).
40. Z. B. Qu, W.-J. Feng, Y. Wang, F. Romanenko, N. A. Kotov, *Angew. Chem. Int. Ed.* (2019).

ACKNOWLEDGMENTS

We thank National Laboratory for Scientific Computing, LNCC/MCTI, Brazil (http://sdumont.lncc.br) for the access to the SDumont supercomputer and the Cloud@UFSCar (http://portalcloud.ufscar.br/) for the HPC resources, and the Michigan Center for Materials Characterization (MC)^2 for its assistance with electron microscopy. N.A.K. thanks D. Lioi from Universal Technology Corporation, Wright Patterson Air Force Base, and S. Glotzer of the University of Michigan for insightful discussions. S.R.M. thanks S. Pratavieira and F. Guimarães at IFSC/USP for technical assistance and discussions. **Funding:** Supported by the Vannevar Bush DoD Fellowship to N.A.K. titled "Engineered Chiral Ceramics" ONR N000141812876, NSF project "Energy- and Cost-Efficient Manufacturing Employing Nanoparticles" (NSF 1463474, ONR N000141812876); NSF 1566460 "Nanospiked Particles for Photocatalysis"; NSF grant 1538180; NSF grant DMR-9871177 for funding the JEOL 2010F analytical electron microscope used in this work; and the Brazilian funding agencies CAPES (finance code 001), CNPq, and FAPESP (process 2009/54035-4, 2012/15147-4, 2013/07276-1, 2013/07296-2, and 2017/12063-8). Support for the Dual Source and Environmental X-ray Scattering Facility at the University of Pennsylvania was provided by the Laboratory for Structure and Matter which is funded in part by NSF MRSEC 1720530. Also supported by Office of Naval Research Multidisciplinary University Research Initiative Award ONR N00014-18-1-2497 (E.M. and C.M.); an MEC/PET fellowship (2014–2020) and a CNPq Fellowship of Research Productivity (2020) (A.F.d.M.); and the China Scholarship Council and Shanghai Jiao Tong University (W.J.). **Author contributions:** N.A.K. conceived the project. W.J. and N.A.K. designed the experiments. W.J. did the design, synthesis, and characterization of the supraparticles and studied their chemical and chiroptical properties. S.R.M. designed, carried out, and analyzed the experiments combining time and spectrally resolved fluorescence. Z.Q. performed the MD simulations of the Au-Cys nanosheets. Y.W. and P.K. studied the phase diagram of Au-Cys supraparticles. Y.M. helped W.J. with some synthesis and characterizations. J.H.B. did the FDTD simulations of the CD spectra. K.B., W.R.G., F.M.C., A.L.-B., and A.F.d.M. carried out the DFT MD simulations, calculations of CD spectra, and coarse-grained simulations of nanoparticle assemblies. N.A.K. conceived and calculated the GT models for the characterization of the complexity of different structures. E.M. measured and analyzed the SAXS data. W.J. and N.A.K. co-wrote the paper. All authors contributed to data analysis, discussion, and writing. **Competing interests:** Authors declare no competing interests. Patents: N.A.K. and J.Y., Synthesis of Chiral Nanoparticles Using Circularly Polarized Light, #14/940,845, filed 13 November 2015, granted 29 January 2019. N.A.K., Self-Assembly Methods for Forming Mesoscale Hedgehog-Shaped Particles, application no. 62/563,966, filed 27 September 2017. **Data and materials availability:** All data are available in the main text or the supplementary materials.

SUPPLEMENTARY MATERIALS

science.sciencemag.org/content/368/6491/642/suppl/DC1
Materials and Methods
Figs. S1 to S44
Tables S1 to S5
Movies S1 and S2
References (*41*–*49*)

9 October 2019; accepted 30 March 2020
Published online 9 April 2020
10.1126/science.aaz7949

SYNTHETIC BIOLOGY

Light-powered CO_2 fixation in a chloroplast mimic with natural and synthetic parts

Tarryn E. Miller[1], Thomas Beneyton[2], Thomas Schwander[1], Christoph Diehl[1], Mathias Girault[3], Richard McLean[1], Tanguy Chotel[2], Peter Claus[1], Niña Socorro Cortina[1], Jean-Christophe Baret[2,3]*, Tobias J. Erb[1,4]*

Nature integrates complex biosynthetic and energy-converting tasks within compartments such as chloroplasts and mitochondria. Chloroplasts convert light into chemical energy, driving carbon dioxide fixation. We used microfluidics to develop a chloroplast mimic by encapsulating and operating photosynthetic membranes in cell-sized droplets. These droplets can be energized by light to power enzymes or enzyme cascades and analyzed for their catalytic properties in multiplex and real time. We demonstrate how these microdroplets can be programmed and controlled by adjusting internal compositions and by using light as an external trigger. We showcase the capability of our platform by integrating the crotonyl–coenzyme A (CoA)/ethylmalonyl-CoA/hydroxybutyryl-CoA (CETCH) cycle, a synthetic network for carbon dioxide conversion, to create an artificial photosynthetic system that interfaces the natural and the synthetic biological worlds.

The photosynthetic transformation of inorganic carbon into organic matter is a fundamental biological process that is responsible for most of the stored energy and biomass on Earth. This process is spatially and temporally controlled and highly integrated with other cellular functions. Photosynthesis ultimately converts light energy through membrane-bound protein complexes into the energy-rich chemical cofactors adenosine triphosphate (ATP) and reduced nicotinamide adenine dinucleotide phosphate (NADPH). ATP and NADPH are subsequently used to fuel metabolic processes, particularly the fixation of CO_2 through the Calvin-Benson-Bassham cycle (*1*).

The principle of photosynthesis has been the inspiration for artificial systems that use the energy of light for the controlled capture and conversion of CO_2 into useful compounds (*2*–*9*). Two recent developments in bio- and nanotechnology promise to afford integrated systems of higher efficiency, approaching or rivaling that of natural biological systems. One is the emergence of microfluidics as a technology platform to manipulate and assemble constitutive elements and functions of living systems in miniaturized and confined environments (*4*, *10*–*16*). The second is the successful design and realization of complex biomimetic modules and systems from defined biological parts. Recent examples are metabolically active microcompartments, artificial light-harvesting organelles (*17*–*20*), advanced transcription-translation circuits (*21*, *22*), and complex, in vitro metabolic networks (*23*–*25*). However, the combination of these individual modules into more complex systems remains a challenge (*26*). Here, we developed a platform for the automated assembly of picoliter-sized reaction compartments that enable the light-driven conversion of CO_2 into multicarbon compounds (i.e., glycolate), mimicking the function of chloroplasts.

In photosynthesis, thylakoid membranes provide the energy for CO_2 fixation, and we sought to exploit this ability directly for biocatalytic and synthetic biological applications. To establish a module for the light-driven regeneration of ATP and NADPH, we isolated thylakoid membranes from the chloroplasts of *Spinacia oleracea*. At 100 μmol photons m^{-2} s^{-1}, these thylakoid preparations catalyzed the light-dependent reduction of $NADP^+$ to NADPH (with concomitant oxygen evolution) at a specific activity of 3.41 ± 0.01 μmol min^{-1} μg^{-1} total chlorophyll (Chl, sum of Chl A and B; Fig. 1A), which is comparable to values measured by others (table S1). NADPH regeneration required the addition of external ferredoxin, with an optimum concentration of 5 μM (figs. S1A and S1B). Supply of external ferredoxin:$NADP^+$ reductase (FNR) did not increase activity further (fig. S6A). Addition of superoxide dismutase and catalase to scavenge reactive oxygen species (ROS) resulted in prolonged thylakoid membrane activity (fig. S2D). In the following experiments, we used light intensities between 50 and 60 μmol photons m^{-2} s^{-1} to further minimize the formation of ROS, which would damage the photosynthetic apparatus (e.g., the D1 subunit), while providing sufficient rates of NADPH regeneration (fig. S2E).

Thylakoid membranes also catalyzed the regeneration of ATP from adenosine diphosphate (ADP) both in the light and in the dark. ATP regeneration in the dark was quantified at 1.2 ± 0.2 μM min^{-1} μg^{-1} Chl, attributed to membrane-bound adenylate kinases (*27*), which could be suppressed by using an adenylate kinase–specific inhibitor, diadenosine pentaphosphate (DAPP) (*28*, *29*) (fig. S1C). In the light, ATP production from ADP increased sixfold (6.5 ± 0.5 mM min^{-1} mg^{-1} Chl). Addition of DAPP resulted in a light- (and ATPase-) dependent ATP synthesis rate of 5.4 ± 0.5 mM min^{-1} mg^{-1} Chl (Fig. 1B), comparable to previous studies. The specific activities of thylakoid membranes varied slightly between individual preparations (fig. S1E). Thylakoid membranes were stably maintained in the dark for at least 2 hours at room temperature and for at least 24 hours when maintained on ice, with no observable loss of NADPH productivity upon illumination (fig. S1D). Membrane preparations could be stored at −80°C for >1 year without notable loss of activity (fig. S1E), demonstrating their usability as a thylakoid membrane–based energy module (TEM).

Next, we tested the ability of TEM to energize individual enzyme reactions. We coupled the TEM with two different CO_2-fixing enzymes, crotonyl-coenzyme A (CoA) carboxylase/reductase (Ccr) and propionyl-CoA carboxylase (Pcc), which require NADPH and ATP, respectively (Fig. 1C). In the case of Ccr, product formation was strictly light dependent with a CO_2-fixation rate of 5.2 ± 0.2 μM min^{-1} μg^{-1} Chl (Fig. 1D). Pcc showed a light-dependent CO_2-fixation rate of 5.1 ± 0.2 μM min^{-1} μg^{-1} Chl (Fig. 1D) and a low, light-independent carboxylation rate of 0.8± 0.1 μM min^{-1} μg^{-1} Chl, which was caused by the adenylate kinase activity of the TEM (see above). These carboxylation rates are more than three orders of magnitude higher than recent efforts to couple enzymatic CO_2 fixation to isolated photosystem II (PSII) (~6.9×10^4 molecules h^{-1} per PSII reaction center compared with 34 molecules h^{-1} per PSII reaction center; table S2), highlighting the capability of our TEM to energize catalytic transformations.

We sought to test the capacity of the TEM to not only power individual CO_2-fixing reactions, but a complete metabolic cycle for the continuous fixation of CO_2. To that end, we combined the 16 enzymes of the crotonyl-CoA/ethylmalonyl-CoA/hydroxybutyryl-CoA (CETCH) cycle (version 5.4) (*23*), an artificial pathway for the fixation of CO_2 in vitro, and a glyoxylate/hydroxypyruvate reductase from *Escherichia coli* (Ghr) with the TEM (Fig. 2A). Initial efforts to operate the CETCH cycle together with the TEM failed, indicating a negative interaction of system components (fig. S3). One problem was an intrinsic hydratase activity of TEM converting crotonyl-CoA into

[1]Department of Biochemistry and Synthetic Metabolism, Max Planck Institute for Terrestrial Microbiology, D-35043 Marburg, Germany. [2]University of Bordeaux, CNRS, Centre de Recherche Paul Pascal, UMR 5031, Pessac 33600, France. [3]Institut Universitaire de France, Paris 75005, France. [4]Center for Synthetic Microbiology, Max Planck Institute for Terrestrial Microbiology, D-35043 Marburg, Germany.
*Corresponding author. Email: toerb@mpi-marburg.mpg.de (T.J.E.); jean-christophe.baret@u-bordeaux.fr (J.-C.B.)

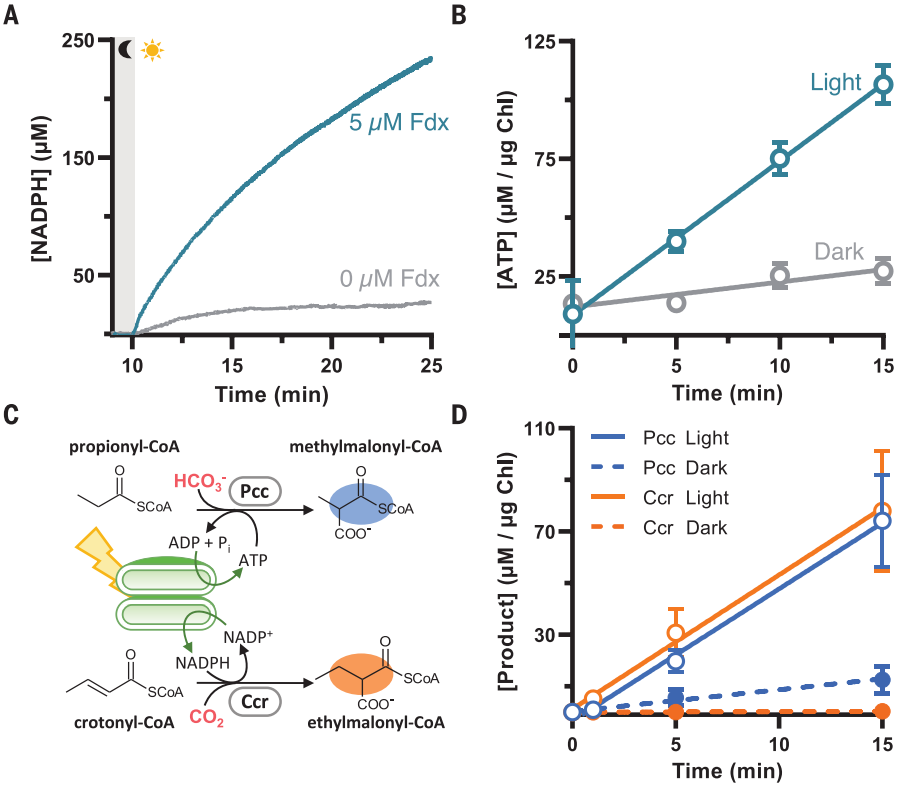


Fig. 1. Light-driven cofactor regeneration by TEM. (**A**) NADPH production is dependent on light and externally added ferredoxin. (**B**) ATP production is dependent on light, with some background reaction in the dark caused by membrane-bound adenylate kinase (fig. S1C). (**C**) Scheme of TEM-driven carboxylation reactions of Pcc and Ccr using light-produced ATP and NADPH, respectively. (**D**) Reactions coupled to TEM (2.5 or 5 μg Chl and 60 μmol photons m^{-2} s^{-1}) (N = 6).

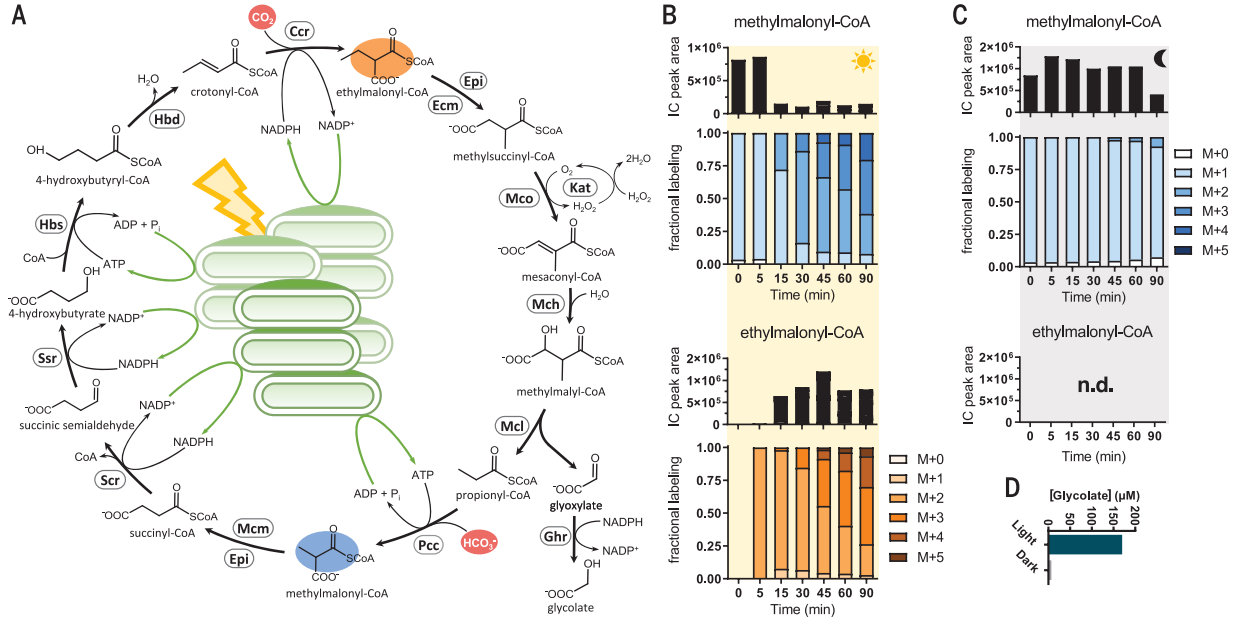


Fig. 2. Light-driven, continuous fixation of CO_2 into organic acids. (**A**) Scheme of CETCH version 6.0 for the conversion of CO_2 into glycolate coupled to TEM. (**B** and **C**) ^{13}C-labeling patterns and total levels of methylmalonyl-CoA (blue) and ethylmalonyl-CoA (orange) over time, starting the CETCH cycle with 80 μM propionyl-CoA. (B) CETCH cycle version 6.0 directly operated by 125 μg Chl ml^{-1} TEM under constant illumination (60 μmol photons m^{-2} s^{-1}). Shown is the extracted ion peak area and the fractional labeling of ethylmalonyl-CoA, as well as methylmalonyl-CoA (in shades of orange and blue, respectively; see fig. S4 for an explanation of the labeling pattern). IC, ion count. (C) Same as (B) but in the dark, showing that light is required to operate the cycle. Ethylmalonyl-CoA is not produced in the dark when starting from propionyl-CoA. n.d., not detected. (**D**) Glycolate production in the light and the dark by CETCH version 6.0.

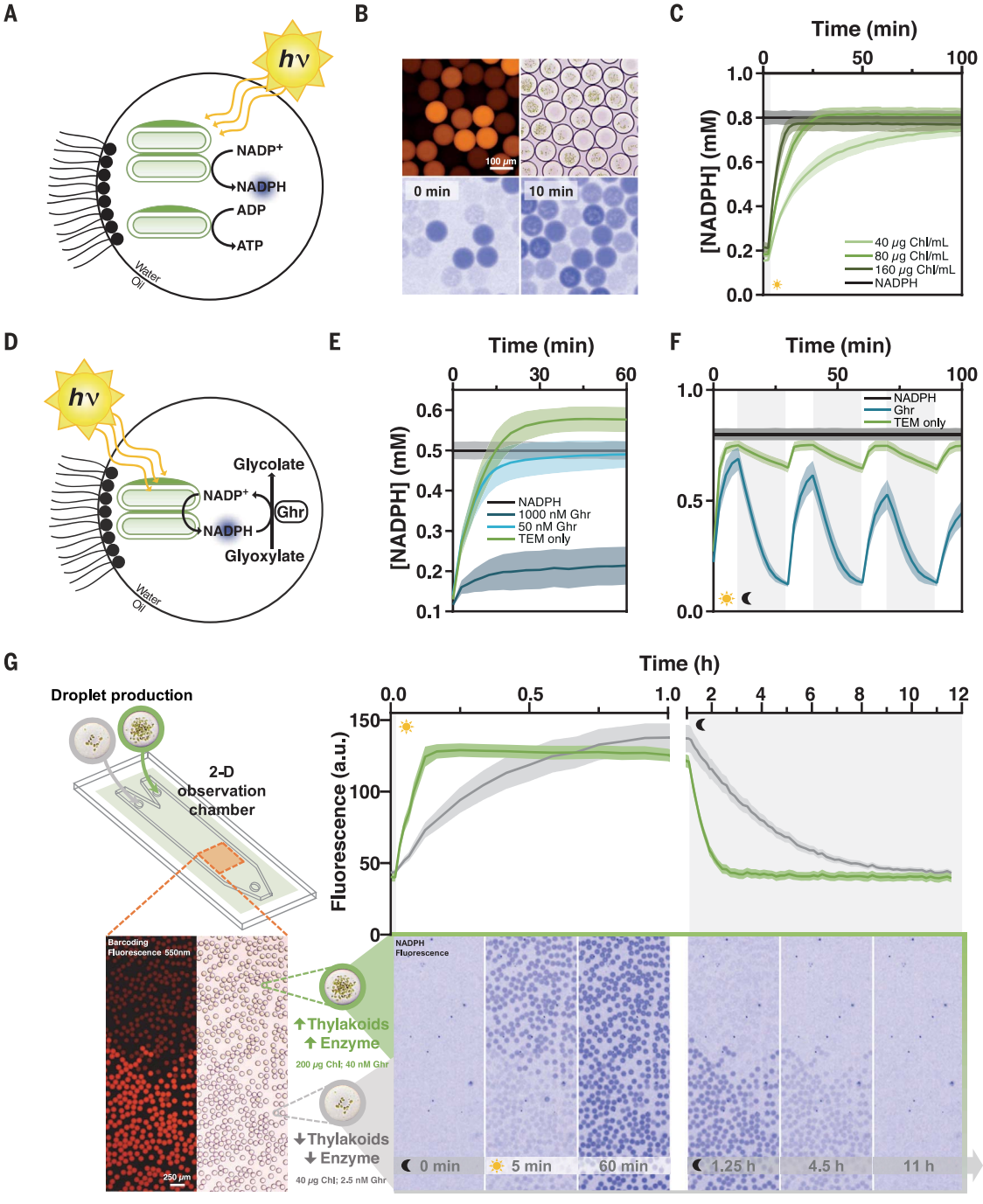


Fig. 3. Encapsulation of a functional TEM in microdroplets and light-driven enzymatic reaction coupled to TEM in microdroplets. (**A**) Scheme of the TEM system encapsulated in microdroplets. Light triggers TEM activity to produce NADPH and ATP. NADPH production is monitored by NADPH fluorescence (365 nm) of individual droplets. Populations of droplets can be distinguished from one another through the addition of a bar-coding dye. hν, photon energy. (**B**) Microscopic photographs of a representative four-bit emulsion of droplets containing four different TEM concentrations. First row, left to right: barcoding fluorescence, bright field. Second row, left to right: NADPH fluorescence at time point 0 and NADPH fluorescence after 10 min of illumination. A time-lapse video of the increasing NADPH fluorescence is available as movie S1. (**C**) NADPH concentration versus time of microdroplets with varying TEM. (**D**) Scheme of the TEM-powered reduction of glyoxylate into glycolate by Ghr encapsulated in microdroplets. (**E**) TEM-driven conversion (65 μg Chl ml^{-1}) of glyoxylate (5 mM) by Ghr in microdroplets (N = 50). The concentration of Ghr changes the steady-state level of NADPH at 50 μmol photons m^{-2} s^{-1}. (**F**) TEM-driven conversion of glyoxylate (120 μg Chl ml^{-1} and 5 mM, respectively) in microdroplets under programmed light-dark cycles. Shown is the photoreduction of $NADP^+$ in droplets (N = 50) with 53.5 nM Ghr (teal line) under alternating cycles of illumination (50 μmol photons m^{-2} s^{-1}) and darkness. Control: Droplets containing no Ghr (green line) and droplets containing 1 mM NADPH (black line). A time-lapse video of oscillations is available as movie S2. In (C), (E), and (F), bold lines indicate the mean of the droplet population. Shaded areas indicate ± SD (N = 50). (**G**) Time and space control of metabolic activity in droplets. A binary emulsion of droplets with two different TEM and Ghr concentrations was created. A spatial pattern was created by filling the droplets into an observation chamber, with each population filling approximately half of the chamber. The plot shows relative NADPH fluorescence over time under fluctuating light conditions (dark, 50 μmol photons m^{-2} s^{-1}) for both droplet populations, with the same color coding. A time-lapse video of NADPH fluorescence is available as movie S3.

3-hydroxybutyryl-CoA (fig. S5), which we addressed by the addition of a crotonase from *Pseudomonas aeruginosa* (PhaJ) (*30*) for metabolite proofreading (*31*). Further analysis suggested that the flavin adenine dinucleotide (FAD)–dependent enzymes methylsuccinyl-CoA oxidase (Mco) and propionyl-CoA oxidase (Pco) interfered with TEM productivity, likely because of the formation of ROS and free FAD in the enzyme preparation (fig. S6). The latter is capable of directly oxidizing NADPH through the interaction with FNR (see also figs. S3, A and B, and S6, B and C). When we replaced Pco with Pcc and added Ghr as an output module (creating CETCH

cycle version 6.0; Fig. 2, A to C), the coupled system produced 156 μM glycolate from 120 μM acceptor molecule (Fig. 2D). Replacing Mco with a methylsuccinyl-CoA dehydrogenase (Mcd), its cognate electron transfer protein (Etf), as well as an Etf-ubiquinone oxidoreductase (creating CETCH cycle version 7.0), further improved glycolate formation from CO_2 and light (fig. S7).

The above results demonstrated that the synthetic CETCH cycle can be functionally coupled to the native energy machinery of photosynthesis in a fully integrated fashion using light energy to form multicarbon compounds from CO_2. Realizing the limitations of individual bulk experiments (e.g., sample volume, self-shading effects, number of parallel assays, and no real-time monitoring), we further envisioned to miniaturize our experimental setup for parallelization, multiplexing, and high-throughput analysis. We therefore developed a droplet-based microfluidic platform for the automated assembly of metabolically active microcompartments that can be controlled and powered by external illumination and analyzed in real time (fig. S8).

In a first step, we encapsulated the TEM into water-in-oil microdroplets (300 pl; 92 μm in diameter; Fig. 3, A and B) and studied their metabolic activity by assessing NADPH fluorescence in single droplets using microscopy (figs. S8 and S9). Encapsulating thylakoid membranes produced droplets with a specifically defined number of TEM granules (~100) with a maximum droplet-to-droplet variation of 20%, which is expected from a random encapsulation process (fig. S10B). We further used orthogonal fluorescent bar coding to multiplex different populations of droplets (*10*), which allowed us to quantify the local chemical and metabolic states of hundreds of individual droplets of different composition in one experiment in parallel.

We then used multiplexing to study and optimize the activity of droplet-encapsulated TEM granules. $NADP^+$ photoreduction in droplets was strictly dependent on illumination and directly correlated to the number of TEM granules, following a correlation with chlorophyll content (Fig. 3C and fig. S11). We observed a maximum photoreduction rate of 2.0 ± 0.1 (95% confidence interval) NADPH μmol min^{-1} μg^{-1} Chl at 50 μmol photons m^{-2} s^{-1}, which is comparable to rates obtained earlier in bulk experiments. Droplet-to-droplet variation in NADPH production was largely determined by statistical fluctuations of the number of encapsulated TEM granules (fig. S10C). We further characterized and optimized the operating conditions of the TEM in microdroplets. Sorbitol at 700 mM increased the stability of the TEM by several hours (fig. S11). $NADP^+$ photoreduction increased with higher light intensities from 50 to 200 μmol photons m^{-2} s^{-1}, above which NADPH production rates decreased again, likely because of photodamage of the TEM (fig. S12). $NADP^+$ photoreduction was operable and stable over light-dark cycles (figs. S13, S14D, and S15B), demonstrating that the TEM could be switched on and off in individual droplets.

We next tested the capability of TEM-containing droplets to power individual enzyme reactions by coencapsulation of enzymes and substrates. First, we tested Ghr, which catalyzes the NADPH-dependent reduction of glyoxylate to glycolate (Fig. 3D). At 120 μg Chl ml^{-1} reaction mixture, 8.2 μg ml^{-1} Ghr, and 50 μmol photons m^{-2} s^{-1}, we observed production of 4.7 mM glycolate (starting from 5 mM glyoxylate and only 0.8 mM $NADP^+$) after 75 min in the light and no production in

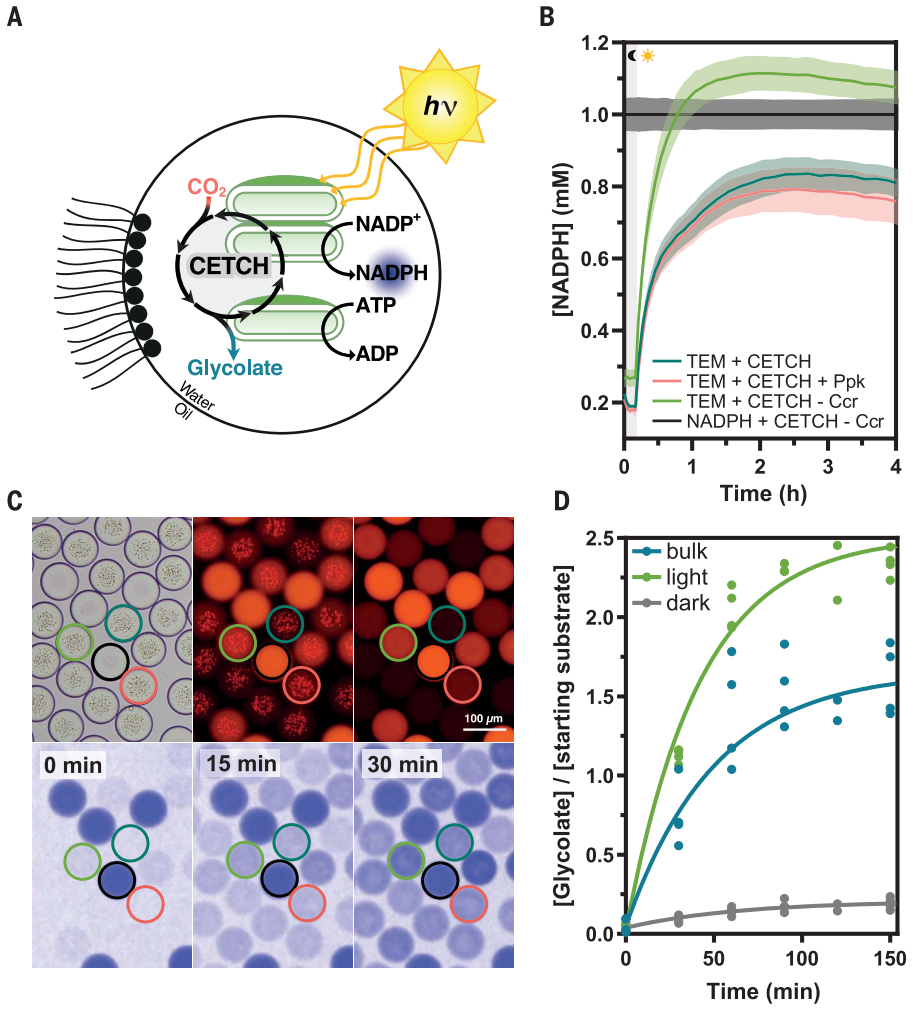


Fig. 4. Light-driven, continuous fixation of CO_2 into organic acids by CETCH version 7.0 coupled to TEM in microdroplets. (**A**) Scheme of the CETCH version 7.0 coupled to TEM operating inside microdroplets. (**B**) Dynamic equilibrium states of NADPH fluorescence of four populations of droplets: (i) Droplets containing TEM (60 μg Chl ml^{-1}), 1 mM $NADP^+$, and CETCH version 7.0 (teal line); (ii) droplets containing TEM, 1 mM $NADP^+$, and an additional ATP regeneration system [polyphosphate kinase (Ppk) and polyphosphate, coral line]; (iii) control droplets containing 1 mM NADPH and all CETCH version 7.0 components except for Ccr (black line); and (iv) control droplets containing TEM, 1 mM $NADP^+$, and all CETCH version 7.0 components except for Ccr (green line). (**C**) Images of the droplets from (B) using the same color coding; first row, left to the right: bright field, thylakoid fluorescence with overlap from the coding dye, and coding dye; second row, left to the right: NADPH fluorescence before illumination, after 15 min of illumination, and after 30 min of illumination. A time-lapse video is available as movie S4. (**D**) Glycolate formed per acceptor molecule (sum of crotonyl-CoA and 3-hydroxybutyryl-CoA) over time in droplets and in bulk solution. The light and dark curves represent droplets maintained in the light and in the dark, respectively. The bulk curve shows an experiment with the same reaction mixture but on the microtube scale, kept in the dark for the duration of droplet manufacture. The bulk solution and the droplets were simultaneously exposed to light for parallel comparison.

the dark control. Varying the number of TEM granules and the concentrations of substrate and Ghr in individual droplet populations resulted in distinct dynamic NADPH equilibrium states (Fig. 3, D to F, and fig. S14), reflecting the real-time cofactor production and consumption rates in the different populations of droplets. Light-dark cycles could be used to temporally regulate cofactor regeneration and enzyme kinetics in droplet populations (Fig. 3F).

The homogeneous behavior of droplet populations enabled us to subsequently program the metabolic activity of reaction compartments in a predictable fashion. To demonstrate this, we created a patterned emulsion of two populations of droplets differing in TEM and Ghr concentration. This binary emulsion was activated by illumination, resulting in distinct NADPH production rates, depending on the TEM concentration in the two droplet populations. In a subsequent dark phase, NADPH was consumed at distinct rates that were correlated to different Ghr loading of the two populations (Fig. 3G and movie S3), demonstrating the high level of spatial, temporal, and synchronized control over individual reaction compartments that can be achieved with our platform. Similar results were also obtained for other droplet-encapsulated enzymes that required ATP and/or NADPH, namely propionyl-CoA synthase (Pcs) and Ccr (figs. S15 and S16). Using Ccr, we measured single-enzyme CO_2-fixation rates of 6.4 μmol min^{-1} mg^{-1} Chl in droplets. Without any further optimization, these rates are more than two orders of magnitude higher than recent reports of coupling PSII reaction centers to pyruvate carboxylase (*18*), comparable to values reached for PSII-coupled photoelectrochemical hydrogen production [notably, without CO_2 fixation (*5*)] and reaching levels measured for isolated chloroplasts (table S2).

Having created photosynthetic microcompartments powering single-enzyme reactions, we ultimately aimed at encapsulating and screening different variants of the CETCH cycle inside TEM-containing droplets (Fig. 4). After further optimizing the preparation of droplets for enzymes and metabolites of the CETCH cycle (fig. S17), we encapsulated different CETCH cycle versions together with TEM and monitored the dynamic equilibrium state of NADPH. This allowed us to directly quantify the behavior of different CETCH variants in hundreds of microcompartments side by side and in real time, which would not have been possible in bulk experiments (Fig. 4, B and C, and fig. S18, A and B). Droplets with CETCH based on Mcd (version 7.0) maintained TEM activity longer than droplets containing CETCH based on Mco (version 6.0) (fig. S18). Supply of an additional ATP regeneration module (Ppk and polyphosphate) did not increase activity further (Fig. 4, B and C), suggesting that cofactor regeneration was not limiting productivity of our integrated photosynthetic system, but rather the concentration, intrinsic properties, and/or interplay of the individual components of our system, such as the stability of CoA-thioester intermediates (fig. S17). Without further optimization, our integrated system was able to produce 47 ± 5 μM glycolate from CO_2 over 90 min in droplets (Fig. 4D). Thus, although the overall productivity of our complex system was lower compared with Ccr alone, it still outperforms other efforts using only single enzymes (*18*). For the full CETCH cycle, we calculated a carbon-conversion efficiency of ~3.5% in our microcompartments (NADPH consumption rate of CO_2 reduction divided by the measured maximum rate of $NADP^+$ photoreduction achieved in droplets). Overall, our results demonstrated that it is possible to interface natural and synthetic biological modules in thousands of cell-sized compartments to create new-to-nature photosynthetic entities that have the potential to outcompete natural photosynthesis (i.e., because of a more efficient CO_2-fixation metabolism that does not suffer from photorespiration).

The technical capability to reconstruct, control, and study complex reaction networks in a cell-like environment will be of use for both top-down and bottom-up synthetic biology. Prototyping complex metabolic reaction cascades in miniaturized compartments has the potential to provide new means for metabolic engineering. Technical advancements, especially the development of combinatorial screening methods (*32*) and bar-coding techniques to encode reaction conditions in microfluidics-based high-throughput screening (*33*) could further enhance multiplexing capabilities and guide future efforts of testing and optimizing the CETCH cycle and other new-to-nature pathways before their transplantation into living cells.

Our efforts also demonstrate how natural and synthetic biological modules can be mixed and matched to create highly integrated systems that show lifelike functions. Our "synthetic chloroplast" has the essential characteristics of photosynthesis that allow the formation of biological building blocks from inorganic carbon, providing the basis to develop a self-sustained, completely synthetic "designer" carbon metabolism in our artificial organelle. Future implementation of other life characteristics such as self-repair and reproduction, as well as information processing and regulatory circuits, will further contribute to the realization of synthetic organelles and cells from the bottom up that approach—or may even exceed—a grade of organization, integration, and functional efficiency comparable to their natural counterparts (*4*).

REFERENCES AND NOTES

1. J. A. Bassham, A. A. Benson, M. Calvin, *J. Biol. Chem.* **185**, 781–787 (1950).
2. C. Liu, B. C. Colón, M. Ziesack, P. A. Silver, D. G. Nocera, *Science* **352**, 1210–1213 (2016).
3. K. Jensen, P. E. Jensen, B. L. Møller, *Trends Plant Sci.* **17**, 60–63 (2012).
4. P. Schwille *et al*., *Angew. Chem. Int. Ed. Engl.* **57**, 13382–13392 (2018).
5. K. P. Sokol *et al*., *Nat. Energy* **3**, 944–951 (2018).
6. J. Guo *et al*., *Science* **362**, 813–816 (2018).
7. K. K. Sakimoto, A. B. Wong, P. Yang, *Science* **351**, 74–77 (2016).
8. W. Zhang *et al*., *Nat. Catal.* **1**, 55–62 (2018).
9. Z. C. Litman, Y. Wang, H. Zhao, J. F. Hartwig, *Nature* **560**, 355–359 (2018).
10. T. Beneyton *et al*., *Nat. Commun.* **9**, 2391 (2018).
11. M. Weiss *et al*., *Nat. Mater.* **17**, 89–96 (2018).
12. S. Deshpande *et al*., *Nat. Commun.* **10**, 1800 (2019).
13. K. Hasatani *et al*., *Chem. Commun.* **49**, 8090–8092 (2013).
14. A. Dupin, F. C. Simmel, *Nat. Chem.* **11**, 32–39 (2019).
15. M. J. Booth, V. Restrepo Schild, S. J. Box, H. Bayley, *Sci. Rep.* **7**, 9315 (2017).
16. R. Booth, Y. Qiao, M. Li, S. Mann, *Angew. Chem. Int. Ed. Engl.* **58**, 9120–9124 (2019).
17. S. Berhanu, T. Ueda, Y. Kuruma, *Nat. Commun.* **10**, 1325 (2019).
18. K. Y. Lee *et al*., *Nat. Biotechnol.* **36**, 530–535 (2018).
19. X. Feng, Y. Jia, P. Cai, J. Fei, J. Li, *ACS Nano* **10**, 556–561 (2016).
20. B. C. Buddingh', J. C. M. van Hest, *Acc. Chem. Res.* **50**, 769–777 (2017).
21. A. M. Tayar, E. Karzbrun, V. Noireaux, R. H. Bar-Ziv, *Proc. Natl. Acad. Sci. U.S.A.* **114**, 11609–11614 (2017).
22. M. Yelleswarapu *et al*., *ACS Synth. Biol.* **7**, 2879–2887 (2018).
23. T. Schwander, L. Schada von Borzyskowski, S. Burgener, N. S. Cortina, T. J. Erb, *Science* **354**, 900–904 (2016).
24. N. Srinivas, J. Parkin, G. Seelig, E. Winfree, D. Soloveichik, *Science* **358**, eaal2052 (2017).
25. Q. M. Dudley, A. S. Karim, M. C. Jewett, *Biotechnol. J.* **10**, 69–82 (2015).
26. M. J. Booth, V. Restrepo Schild, F. G. Downs, H. Bayley, *Mol. Biosyst.* **13**, 1658–1691 (2017).
27. S. Murakami, H. Strotmann, *Arch. Biochem. Biophys.* **185**, 30–38 (1978).
28. D. D. Strand, N. Fisher, D. M. Kramer, *J. Biol. Chem.* **292**, 11850–11860 (2017).
29. G. E. Lienhard, I. I. Secemski, *J. Biol. Chem.* **248**, 1121–1123 (1973).
30. T. Fukui, N. Shiomi, Y. Doi, *J. Bacteriol.* **180**, 667–673 (1998).
31. J. Sun, J. G. Jeffryes, C. S. Henry, S. D. Bruner, A. D. Hanson, *Metab. Eng.* **44**, 150–159 (2017).
32. A. Kulesa, J. Kehe, J. E. Hurtado, P. Tawde, P. C. Blainey, *Proc. Natl. Acad. Sci. U.S.A.* **115**, 6685–6690 (2018).
33. C. M. Svensson *et al*., *Small* **15**, e1802384 (2019).
34. T. E. Miller *et al*., Data and computational codes for: Light-powered CO_2 fixation in a chloroplast mimic with natural and synthetic parts, Zenodo (2020); https://doi.org/10.5281/zenodo.3724502.

ACKNOWLEDGMENTS

We thank J. Zarzycki, D. Strand, and S. Burgener for enlightening discussions and G. Stoffel for providing CoA esters. **Funding:** This work was supported by the Max Planck Society (MaxSynBio), the European Research Council (grant no. ERC 637675 "SYBORG"), and the U.S. Department of Energy Joint Genome Institute, a DOE Office of Science User Facility (contract no. DE-AC02-05CH11231) with T.J.E. as grantee. J.-C.B. acknowledges financial support by the Region Nouvelle Aquitaine and by the French Government's Investments for the Future Programme, University of Bordeaux Initiative of Excellence (IDEX Bordeaux; (ANR)-10-IDEX-03-02). T.E.M. and R.M. were supported by the International Max Planck Research School for Environmental, Cellular and Molecular Microbiology (Marburg, Germany). **Author contributions:** The project was conceived by T.E.M., T.B., T.S., J.-C.B., and T.J.E. Characterization and optimization of thylakoid preparations was done by T.E.M. Couplings of the CETCH cycle to thylakoids in bulk were performed by T.E.M. together with T.S. and C.D. The ETF:QO system as electron acceptor for Etf was developed by T.E.M and R.M. Mass spectrometric analyses were performed by N.C.S. and P.C., and these data were analyzed by T.E.M. The microfluidic

platform to encapsulate thylakoids was developed by T.B. and J.-C.B. Microfluidic experiments were planned, performed, and analyzed by T.B. and T.E.M. with assistance from T.C. The software for light-dark cycles time-lapse fluorescence microscopy, as well as the image-processing software to analyze TEM activity in droplets, was developed by M.G. Experimental data were analyzed by T.E.M., T.B., and T.J.E. The manuscript was written by T.E.M., T.B., J.-C.B., and T.J.E. with contributions from all other authors. **Competing interests:** J.-C.B. is a founder and scientific adviser at Emulseo. The authors declare no other competing interests. **Data and materials availability:** All data are available in the main text or supplemental materials. The LabVIEW code used for image analysis has been deposited to GitHub (*34*).

SUPPLEMENTARY MATERIALS

science.sciencemag.org/content/368/6491/649/suppl/DC1
Materials and Methods
Figs. S1 to S18
Tables S1 to S9
References (*35*–*64*)
Movies S1 to S4

View/request a protocol for this paper from *Bio-protocol*.

30 September 2019; accepted 24 March 2020
10.1126/science.aaz6802

ASTEROIDS

Sample collection from asteroid (162173) Ryugu by Hayabusa2: Implications for surface evolution

T. Morota[1,2]*, S. Sugita[1,3], Y. Cho[1], M. Kanamaru[4]†, E. Tatsumi[1,5,6], N. Sakatani[7]‡, R. Honda[8], N. Hirata[9], H. Kikuchi[7], M. Yamada[3], Y. Yokota[7,8], S. Kameda[10], M. Matsuoka[7], H. Sawada[7], C. Honda[11], T. Kouyama[12], K. Ogawa[9,13], H. Suzuki[14], K. Yoshioka[15], M. Hayakawa[7], N. Hirata[11], M. Hirabayashi[16], H. Miyamoto[17,18], T. Michikami[19], T. Hiroi[20], R. Hemmi[21], O. S. Barnouin[22], C. M. Ernst[22], K. Kitazato[11], T. Nakamura[23], L. Riu[7], H. Senshu[3], H. Kobayashi[2], S. Sasaki[4], G. Komatsu[24], N. Tanabe[1], Y. Fujii[8], T. Irie[2], M. Suemitsu[2], N. Takaki[1], C. Sugimoto[1], K. Yumoto[1], M. Ishida[10], H. Kato[10], K. Moroi[10], D. Domingue[18], P. Michel[25], C. Pilorget[26], T. Iwata[7,27], M. Abe[7,27], M. Ohtake[7,11], Y. Nakauchi[7], K. Tsumura[28,29], H. Yabuta[30], Y. Ishihara[31]§, R. Noguchi[7], K. Matsumoto[27,32], A. Miura[7,27], N. Namiki[27,32], S. Tachibana[1,7], M. Arakawa[9], H. Ikeda[33], K. Wada[3], T. Mizuno[7,27], C. Hirose[33], S. Hosoda[7], O. Mori[7], T. Shimada[7], S. Soldini[7,34], R. Tsukizaki[7], H. Yano[7,27], M. Ozaki[7,27], H. Takeuchi[7,27], Y. Yamamoto[7,27], T. Okada[7,35], Y. Shimaki[7], K. Shirai[7], Y. Iijima[7]¶, H. Noda[27,32], S. Kikuchi[7], T. Yamaguchi[7]#, N. Ogawa[7], G. Ono[33], Y. Mimasu[7], K. Yoshikawa[33], T. Takahashi[7]**, Y. Takei[7,33], A. Fujii[7], S. Nakazawa[7], F. Terui[7], S. Tanaka[7,27], M. Yoshikawa[7,27], T. Saiki[7], S. Watanabe[2,7], Y. Tsuda[7,27]

The near-Earth asteroid (162173) Ryugu is thought to be a primitive carbonaceous object that contains hydrated minerals and organic molecules. We report sample collection from Ryugu's surface by the Hayabusa2 spacecraft on 21 February 2019. Touchdown images and global observations of surface colors are used to investigate the stratigraphy of the surface around the sample location and across Ryugu. Latitudinal color variations suggest the reddening of exposed surface material by solar heating and/or space weathering. Immediately after touchdown, Hayabusa2's thrusters disturbed dark, fine grains that originate from the redder materials. The stratigraphic relationship between identified craters and the redder material indicates that surface reddening occurred over a short period of time. We suggest that Ryugu previously experienced an orbital excursion near the Sun.

Hayabusa2 is a sample-return mission to (162173) Ryugu, a carbonaceous (C-type) near-Earth asteroid (NEA) (*1*). The spacecraft was launched on 3 December 2014 and arrived at Ryugu on 27 June 2018. Initial global observations showed that the asteroid has a spinning-top shape and rubble-pile structure (*2*, *3*). The surface has generally uniform spectra (*4*, *5*). Small variations in surface color are quantified using the spectral slope from the *b*-band (0.48 μm) to the *x*-band (0.86 μm) (hereafter, the *b*-*x* slope) (*2*, *5*, *6*), observed with the telescopic optical navigation camera (ONC-T) (Fig. 1A) (*5*). Two distinct types of material are present on the surface with different colors: bluer material distributed at the equatorial ridge and in the polar regions and redder material in the mid-latitude regions (*5*). However, the cause of these spectral variations is not understood.

On 21 February 2019, Hayabusa2 conducted its first sample collection from Ryugu, performing a touchdown on the surface. During the touchdown operation, Hayabusa2 took images of Ryugu's surface with resolutions reaching ~1 mm per pixel. Those images allow us to observe the surface's response to the physical disturbances generated by the touchdown, including the sampling projectile collision and the firing of the spacecraft's thruster gas jets.

The touchdown site was selected on the basis of established engineering safety criteria and scientific merits (*2*, *6*, *7*). Regional variations in the mixing ratio between redder and bluer materials are measured using the spectral slope (Fig. 1A). Spectral variations between candidate touchdown sites are much smaller than those within each site (*2*), which implies that the surface materials are well mixed locally. A sampling operation at any of the candidate sites should, therefore, collect both redder and bluer components. Safe landing locations were limited by the high surface density of boulders (*5*, *8*). We initially selected the region designated L08-B, one of the lowest–boulder density areas on Ryugu, as the primary landing site (*2*, *6*, *7*) and deployed a target marker (TM) on 23 October 2018 to facilitate navigation. On the basis of the location where the TM settled on the surface and a search for nearby areas with no boulders taller than 65 cm—which could reach Hayabusa2's reaction control system (RCS) during a touchdown—we narrowed the landing site to the location L08-E1 (Fig. 2A and fig. S5).

Hayabusa2 performed multiple low-altitude (~40 m) descent maneuvers near the L08 region, during which we conducted spectral and morphological observations with spatial resolutions reaching 0.01 m per pixel. The touchdown site is generally slightly bluer than the global average, but reddish areas are found within L08-E1 (Fig. 1E and Fig. 2C). These reddish areas are, on average, slightly darker than the bluer areas (fig. S6), a trend that was previously observed globally (*2*, *5*). The reddish areas are limited to parts of individual boulders, with most boulder surfaces in this location being blue (Fig. 2C). These observations are compatible with the interpretation that Ryugu's boulders are originally bluer, with redder materials produced by surface metamorphic processes, such as space weathering (*9*), thermal metamorphism by solar heating (*10*), and/or pulverization by small impacts (*11*). Redder materials may have been shed from boulder surfaces by impact disruption and/or thermal fatigue. The bluer surfaces of boulders remain unreddened, which implies that the time scale for surface reddening is longer than that of

[1]Department of Earth and Planetary Science, The University of Tokyo, Tokyo 113-0033, Japan. [2]Departments of Earth and Environmental Sciences and Physics, Nagoya University, Nagoya 464-8601, Japan. [3]Planetary Exploration Research Center, Chiba Institute of Technology, Narashino 275-0016, Japan. [4]Department of Earth and Space Science, Osaka University, Toyonaka 560-0043, Japan. [5]Departamento de Astrofísica, Universidad de La Laguna, 38206 La Laguna, Tenerife, Spain. [6]Instituto de Astrofísica de Canarias, 38205 La Laguna, Tenerife, Spain. [7]Institute of Space and Astronautical Science, Japan Aerospace Exploration Agency (JAXA), Sagamihara 252-5210, Japan. [8]Department of Information Science, Kochi University, Kochi 780-8520, Japan. [9]Department of Planetology, Kobe University, Kobe 657-8501, Japan. [10]Department of Physics, Rikkyo University, Tokyo 171-8501, Japan. [11]School of Computer Science and Engineering, University of Aizu, Aizu-Wakamatsu 965-8580, Japan. [12]National Institute of Advanced Industrial Science and Technology, Tokyo 135-0064 Japan. [13]JAXA Space Exploration Center, Japan Aerospace Exploration Agency, Sagamihara 252-5210, Japan. [14]Department of Physics, Meiji University, Kawasaki 214-8571, Japan. [15]Department of Complexity Science and Engineering, The University of Tokyo, Kashiwa 277-8561, Japan. [16]Department of Aerospace Engineering, Auburn University, Auburn, AL 36849, USA. [17]Department of Systems Innovation, The University of Tokyo, Tokyo 113-8656, Japan. [18]Planetary Science Institute, Tucson, AZ 85719, USA. [19]Faculty of Engineering, Kindai University, Higashi-Hiroshima 739-2116, Japan. [20]Department of Earth, Environmental and Planetary Sciences, Brown University, Providence, RI 02912, USA. [21]The University Museum, The University of Tokyo, Tokyo 113-0033, Japan. [22]Johns Hopkins University Applied Physics Laboratory, Laurel, MD 20723, USA. [23]Department of Earth Science, Tohoku University, Sendai 980-8578, Japan. [24]International Research School of Planetary Sciences, Università d'Annunzio, 65127 Pescara, Italy. [25]Université Côte d'Azur, Observatoire de la Côte d'Azur, Centre National de le Recherche Scientifique, Laboratoire Lagrange, 06304 Nice, France. [26]Institut d'Astrophysique Spatiale, Université Paris-Sud, 91405 Orsay, France. [27]Departments of Space and Astronautical Science and Astronomical Science, The Graduate University for Advanced Studies, SOKENDAI, Hayama 240-0193, Japan. [28]Department of Natural Science, Faculty of Science and Engineering, Tokyo City University, Tokyo 158-8557, Japan. [29]Frontier Research Institute for Interdisciplinary Sciences, Tohoku University, Sendai 980-8578, Japan. [30]Department of Earth and Planetary Systems Science, Hiroshima University, Higashi-Hiroshima 739-8526, Japan. [31]National Institute for Environmental Studies, Tsukuba 305-8506, Japan. [32]National Astronomical Observatory of Japan, Mitaka 181-8588, Japan. [33]Research and Development Directorate, JAXA, Sagamihara 252-5210, Japan. [34]Department of Mechanical, Materials and Aerospace Engineering, University of Liverpool, Liverpool L69 3BX, UK. [35]Department of Chemistry, The University of Tokyo, Tokyo 113-0033, Japan.
***Corresponding author. Email: morota@eps.s.u-tokyo.ac.jp** †Present address: Institute of Space and Astronautical Science, Japan Aerospace Exploration Agency (JAXA), Sagamihara 252-5210, Japan. ‡Present address: Department of Physics, Rikkyo University, Tokyo 171-8501, Japan. §Present address: JAXA Space Exploration Center, Japan Aerospace Exploration Agency, Sagamihara 252-5210, Japan. ¶Deceased. #Present address: Mitsubishi Electric Corporation, Kamakura 247-8520, Japan. **Present address: NEC Corporation, 1-10 Nisshin-cho, Fuchu, Tokyo 183-8501, Japan.

boulder resurfacing by impact disruption and/or thermal fatigue.

There are two morphological types of submeter-sized boulders around the touchdown site: dark, ragged boulders and bright boulders with smooth surfaces (Fig. 2D and fig. S7A). These types of boulders are observed in the 10-m size range in remote images (*5*) and on smaller scales in images taken on the surface by the Mobile Asteroid Surface Scout (MASCOT) lander (*12*). Images taken during the descent operation show that there is also a submeter-scale heterogeneity in surface reflectance of the bright boulders: The edges of many boulders are brighter than the planar

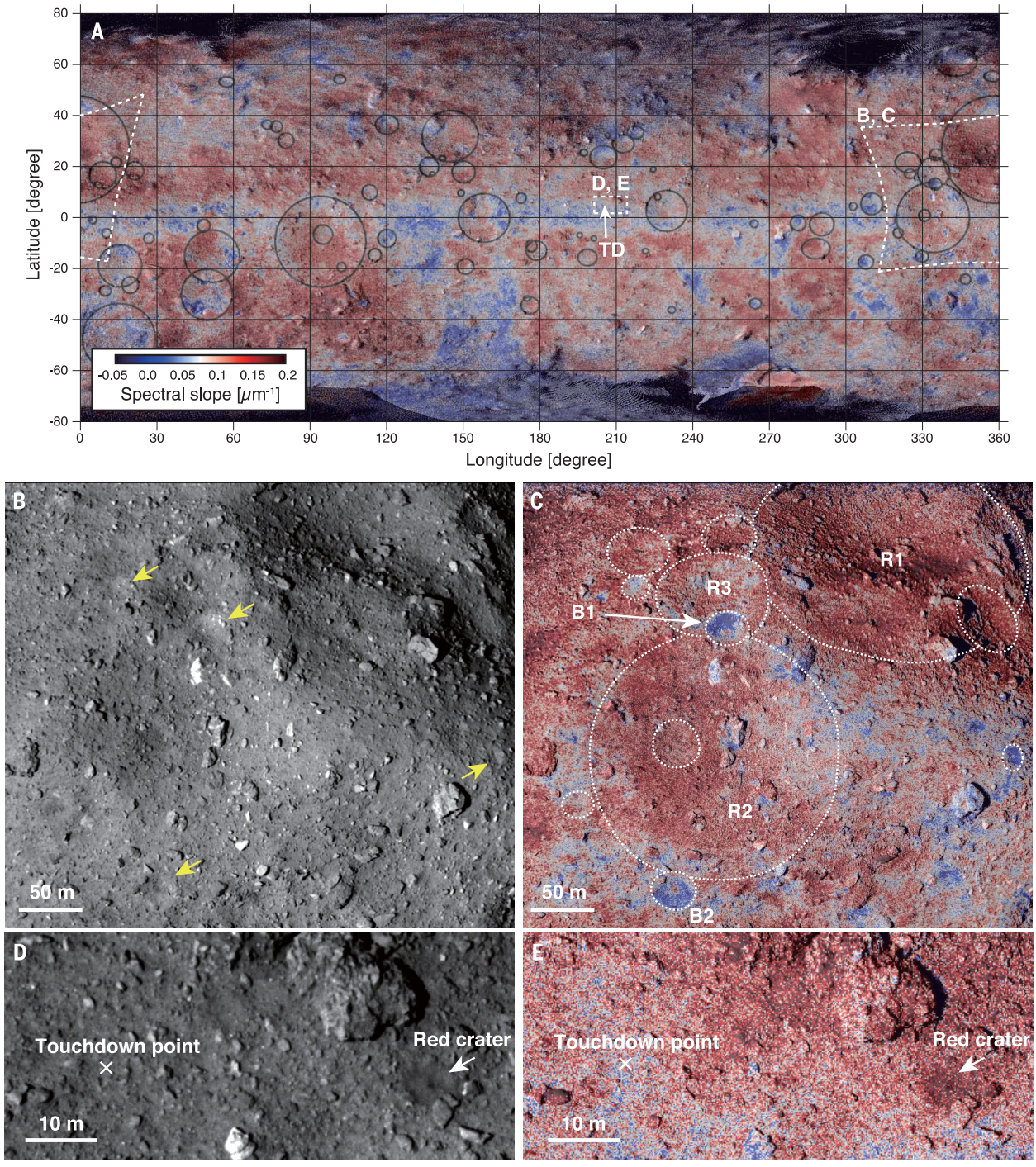


Fig. 1. Spectral slope of Ryugu's surface. (**A**) Global map of the *b*-*x* slope (μm^{-1}), indicated by the color bar, superimposed on a *v*-band image map. The white arrow indicates the location of the first touchdown (TD) point (4.30°N, 206.47°E). Craters >20 m in diameter are shown by black circles. Dashed white lines indicate areas shown in other panels. (**B**) *v*-band image (hyb2_onc_20180801_183933_tvf) obtained from 5.1-km altitude. Yellow arrows indicate craters with bluer interior than the surrounding materials, as shown in (C). (**C**) *b*-*x* slope of the same region as (B). Craters >20 m in diameter are shown with white dashed circles. Blue craters B1 and B2 are higher in the stratigraphy than red craters R1, R2, and R3. There is no blue crater stratigraphically superposed by red craters, which suggests that the blue craters are younger than the red craters. (**D** and **E**) *v*-band image (D) and *b*-*x* slope image (E) showing a 9-m crater with redder interior than the surrounding materials, located close to the TD point, which is marked with a white X. (C) and (E) use the same color scale as (A).

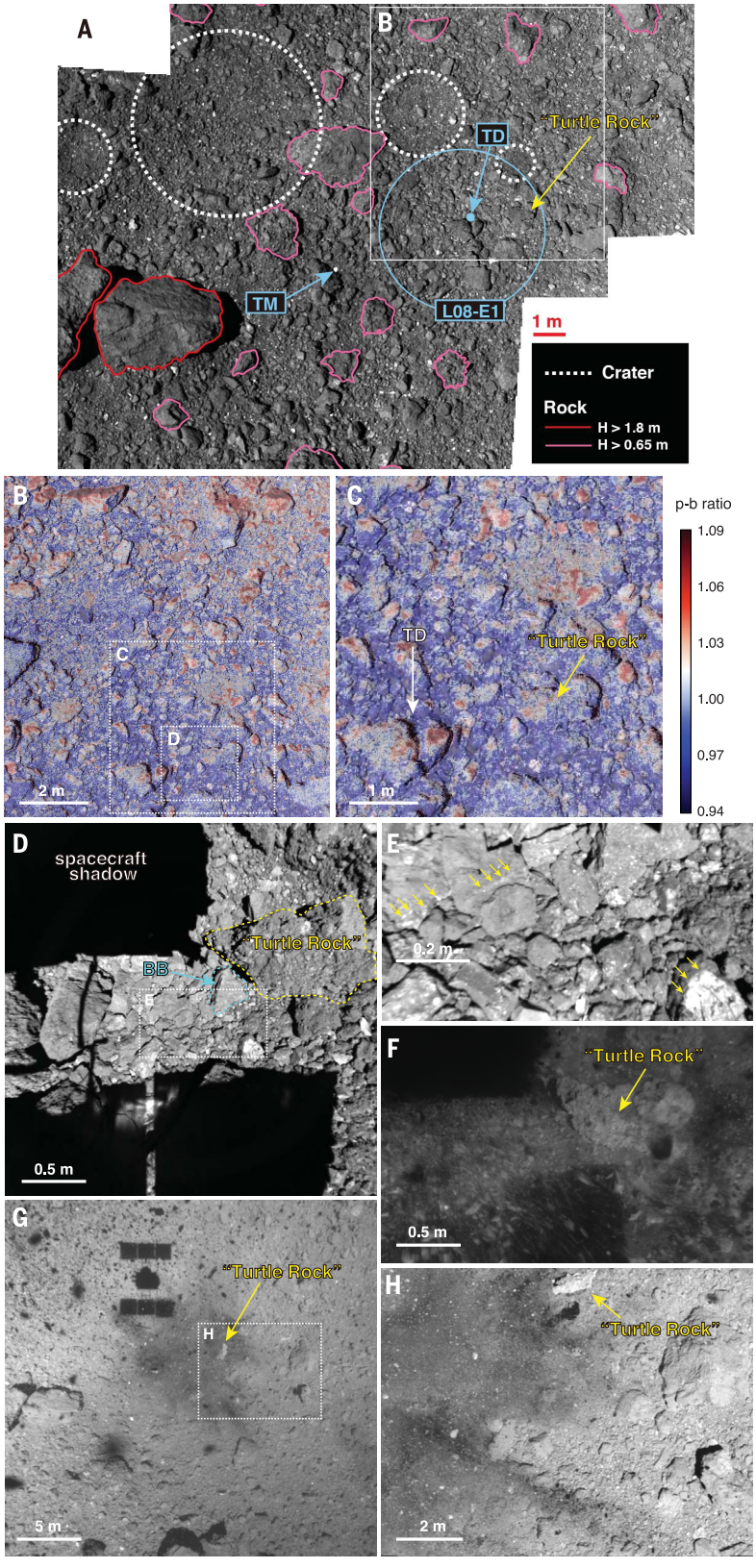


Fig. 2. Touchdown site before, during, and after the touchdown operation. (**A**) Boulder and crater map around the touchdown site L08-E1. The light blue arrows indicate the location of the target marker (TM) (4.04°N, 206.01°E) and the touchdown point of the sampler horn (TD) (4.30°N, 206.47°E) (*7*). The light blue circle indicates the L08-E1 area. The white dashed circles indicate craters. Boulder heights (H) were estimated from their shadow lengths; those with H > 1.8 m are outlined in red and those with H > 0.65 m are outlined in pink. The boulder nicknamed Turtle Rock is indicated by the yellow arrow. The white box indicates the region shown in later panels. (**B** and **C**) *p-b* ratio images (*6*) calculated from *b*- and *p*-band (0.95 μm) images obtained during the touchdown rehearsal operation, from two different altitudes (hyb2_onc_20181015_134707_tbf and hyb2_onc_20181015_134655_tpf). The dashed boxes in (B) indicate regions shown in the other panels. (**D**) ONC-W1 image obtained during the spacecraft's descent before the touchdown (hyb2_onc_20190221_222859_w1f). The dark, ragged Turtle Rock and an example of bright boulders (BB) with smooth surfaces are outlined in yellow and cyan dashed lines, respectively. The white dashed box indicates the area shown in (E). (**E**) Close-up of the image in (D), with yellow arrows indicating fresh bright spots at corners and a possible broken plane of a boulder. (**F** and **G**) ONC-W1 images obtained ~7 and 47 s after the touchdown, showing debris lifted from the surface (hyb2_onc_20190221_222917_w1f and hyb2_onc_20190221_222957_w1f). (**H**) ONC-T *ul*-band (0.39 μm) image obtained at 76-m altitude after the touchdown (hyb2_onc_20190221_223156_tuf). Turtle Rock was lifted clear of the surface by the exhaust from Hayabusa2's RCS thrusters, indicated by the yellow arrows in (F) to (H).

surfaces of the same boulders (yellow arrows in Fig. 2E and fig. S7B). This may be because of a higher abrasion rate at the boulder edges. One boulder in Fig. 2E appears to have broken in two, with the possible broken surface ~1.5 times as bright as the surfaces of the surrounding boulders. Because the interior or less-processed parts of the boulder are exposed on the edges and broken areas, these observations suggest that boulder surfaces are generally darkened by exposure to space.

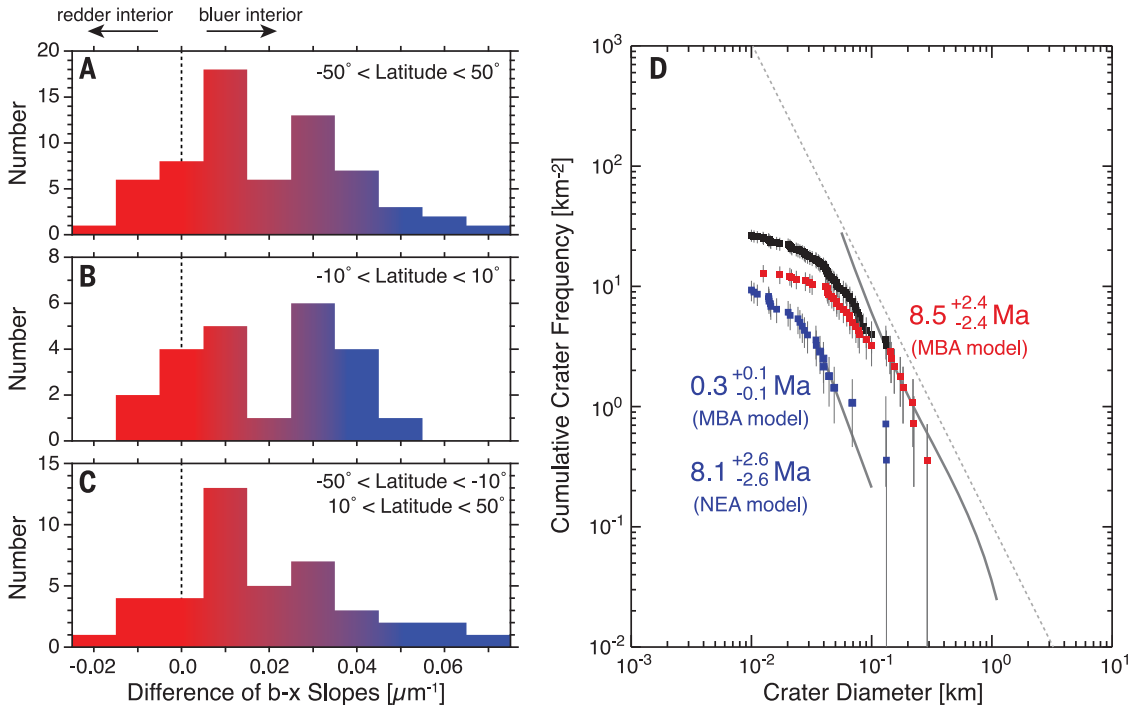


Fig. 3. Crater statistics on Ryugu. (**A** to **C**) Histograms of the differences in the *b*-*x* slopes between the interior and the surroundings of craters >10 m in diameter, in the latitude ranges ±50° (A), ±10° (B), and −50° to −10° and 10° to 50° (C). Bar colors are illustrative only. (**D**) Crater SFDs in the latitude range of ±50°. Black, red, and blue squares indicate crater frequencies of all craters, red craters (defined as having a difference of *b*-*x* slope of <0.025), and blue craters (having a difference of *b*-*x* slope of >0.025), respectively. Gray curves indicate crater chronology models fitted to the data for the red and blue craters. The dashed line indicates the empirical saturation level. Error bars are calculated by $\pm N^{1/2}/A$, where N is the cumulative number of craters and A is the area of the latitude range of ±50°. The resulting model ages for the main belt asteroid (MBA) and NEA impact rates are indicated in red and blue text.

The Hayabusa2 spacecraft has a sampling mechanism (*13*) similar to that of the original Hayabusa spacecraft (*14*). Ejecta are generated by the impact of a 1-cm-diameter tantalum projectile fired at a speed of ~300 m s^{-1} during the first contact with the surface, and they are caught with a sampler horn that is extended from the bottom of the spacecraft (*13*–*15*).

The combination of the impact of the projectile fired from the sampler system and the operation of the RCS thrusters during the touchdown produced a large amount of debris from Ryugu's surface (Fig. 2G and movie S1) (*6*). The video obtained by the nadir-viewing wide-angle optical navigation camera (ONC-W1) indicates that large boulders (up to 1 m in the longest dimension) were moved horizontally by >5 m during the touchdown (fig. S9). However, most of the debris disturbed during the touchdown was small pebbles and fine grains with diameters that are less than the pixel size (which varied from 1 to a few millimeters) of the W1 images (fig. S8) (*6*). This high mobility of fragmented debris deposits (i.e., regolith) during the touchdown indicates that the cohesive forces between boulders and pebbles may be very weak or that the forces depend on the particle sizes. This interpretation is consistent with the observed deficit of small craters (*5*, *16*), mass movement along slopes (i.e., mass wasting) on crater walls (*5*), and the crater formation during Hayabusa2's artificial impact experiment (*17*).

Immediately after the RCS thrust on touchdown, the entire field of view of ONC-W1 was darkened, apparently uniformly. A dark, ragged boulder, which we nicknamed "Turtle Rock," simultaneously became as bright as the surrounding brighter boulders (Fig. 2, F and H) (*6*). Turtle Rock was also moved by the RCS exhaust. These observations suggest that dark, fine grains were originally present on the surfaces (or inside the pores) of darker and redder boulders before being lifted by the RCS thrusting. Such fine grains were not visible in the surface images taken by MASCOT (*12*). The sampling process produced a cloud of dark, fine grains that expanded from the touchdown site and extended over a zone ~10 m in diameter, centered at the touchdown site (Fig. 2, G and H). We estimate the total mass of the fine-grained cloud to be ~12 kg (*6*). The pretouchdown color of this region was slightly bluer than that of the surrounding region, but it became redder after the deposition of the lofted dark, fine grains (Fig. 2G and fig. S11) (*6*). Observations with the Near Infrared Spectrometer (NIRS3) of the region before and after the touchdown showed little change in the hydroxide (OH) band depth, although the NIRS3 spectra after the touchdown are slightly bluer and brighter (fig. S12). This is consistent with the global lack of correlation between the spatial distribution of the OH band depth and the red-blue color variations in the ONC observations (*4*, *5*). We conclude that dark, fine red grains were originally concentrated on the boulder surfaces or in voids on the boulders, that these grains are not compositionally distinct from the subsurface, and that the disruption of the touchdown event produced a more-even distribution of the grains across the affected area.

Globally, the *b*-*x* slope varies with latitude (Fig. 1A). We found that the *b*-*x* slope also correlates with the crater distribution. Fresh and stratigraphically younger craters >20 m in diameter have interiors that are spectrally bluer than their surroundings (Fig. 1C). This implies that the redder materials were covering the bluer materials, with the latter exposed by the crater formation. This is consistent with the stratigraphic relationship between the redder and bluer materials inferred from the global *b*-*x* slope distribution (*5*). On the other hand, stratigraphically older craters tend to have redder interiors, and the color of these crater interiors is similar to that of the surrounding materials (Fig. 1C). We investigated the contrasts in spectral slopes between crater

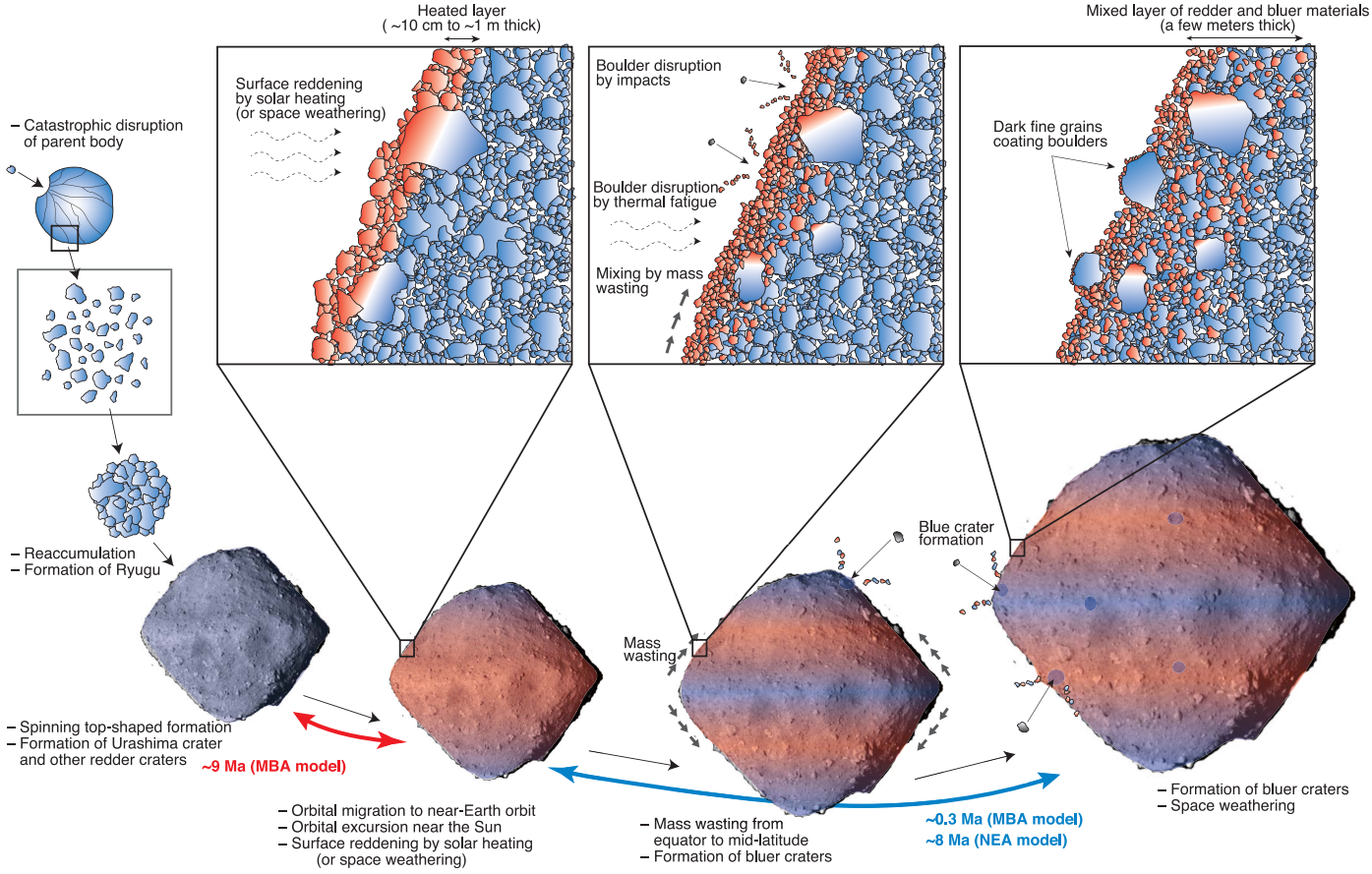


Fig. 4. A schematic illustration of our suggested evolution of Ryugu. Surface reddening occurred within a short period after the emplacement of red craters and before the formation of blue craters. We interpret the cause of the surface reddening as solar heating that occurred while Ryugu came temporarily closer to the Sun than on its present orbit. Between the formation of Ryugu's spinning-top shape and the surface reddening, we estimate a time of 9 Ma on the basis of the SFDs of red craters. From the SFDs of blue craters, the age of the surface reddening is estimated to be 0.3 Ma using the main belt collision-frequency model and 8 Ma using the NEA collision-frequency model. We interpret these estimates as upper and lower age limits for the surface reddening. After the surface reddening event, the redder materials were disrupted and redistributed by impacts, thermal fatigue, and mass wasting from the equator to mid-latitude regions. A layer of mixed red and blue material subsequently formed on Ryugu's surface.

interior surfaces and their surrounding areas, which we define as the area outward from the crater rim within a distance equal to the crater's radius (*6*). The histogram of the contrast in the *b*-*x* spectral slope shows a bimodal distribution (Fig. 3), which indicates that craters on Ryugu can be divided into two groups: red craters whose interior has a *b*-*x* slope similar to that of their surroundings and blue craters whose interior is bluer than their surroundings.

A potential explanation for the latitudinal variation in the *b*-*x* slope is that the exposure of Ryugu's materials to space has led to their reddening, and mass wasting from the equator and polar regions (topographic highs) to the mid-latitude regions (topographic lows) has exposed fresh, bluer subsurface materials (*2*, *5*). The polar regions exhibit bluer spectra than the equatorial ridge (fig. S3), which suggests that the reddening process seems to depend on illumination by the Sun [Ryugu's obliquity is 171.6° (*2*)]. The color variation of crater interiors can be explained by their stratigraphic relations; the craters with redder interiors were formed before surface reddening occurred, whereas the bluer craters were formed after the surface reddening and the underlying bluer materials were exposed by the impacts. The bimodal distribution of the contrast in the *b*-*x* spectral slope (Fig. 3) suggests that the surface reddening has not been active throughout the whole of Ryugu's history and occurred mainly after the formation of redder craters and before the formation of bluer craters. The surface reddening process might not be currently active, or it might be active but slow compared with the resurfacing processes of boulder surfaces, as discussed above (Fig. 2C).

We interpret the crater size–frequency distributions (SFDs) using collision-frequency models derived for the asteroid main belt (*6*, *18*, *19*). From the SFD of red craters >100 m in diameter (Fig. 3D), we estimate the time between the formation of Ryugu and the surface reddening event to be 8.5 million years (Ma). This is much younger than the breakup time of candidate parent asteroids, Eulalia and Polana [several hundred Ma to ~1 Ga (billion years)] (*5*, *20*), which suggests that Ryugu is the product of more than one generation of parent body disruptions and/or global resurfacing processes, and the current spinning-top shape must have formed more than 8.5 Ma ago. The observed number density of blue craters is 3% of the number density of red craters (Fig. 3D). We estimate a model age for the reddening event of ~0.3 Ma, from the observed SFD of blue craters >30 m in diameter on the basis of the main belt collision-frequency model (fig. S14A). Using an alternative NEA collision-frequency model, the age of the reddening event is estimated to be ~8 Ma, because there is a much lower collision frequency for bodies in NEA orbits (*6*, *18*, *19*). We interpret these estimates as upper and lower age limits

on the surface reddening event. The NEA model age is younger than the typical dynamical lifetime of NEAs (~10 Ma) (*21*) and the median orbital lifetime of Ryugu (~40 Ma) (*22*). Therefore, we suggest that the reddening of Ryugu's surface occurred after its orbit shifted from the main belt to its current near-Earth orbit (*5*).

The deficit of craters <100 m in diameter on Ryugu's surface suggests that crater erasure processes have occurred (*5*). Therefore, existing small craters must have formed recently in geological terms. However, smaller craters (<10 m in diameter) do not always exhibit bluer interiors, which would be expected if they were all young. Some small craters exhibit a redder—not bluer—interior than the materials of their surroundings (Fig. 1E). Streaked patterns of redder materials, such as ejecta deposits, are visible across the whole surface (fig. S4B). A streaked pattern of redder materials elongated from a boulder suggests that a mass of redder material collided with the boulder and dispersed (fig. S4F). Redder materials may have been disrupted and redistributed by impacts, thermal fatigue, and mass wasting, which may have resulted in the formation of a mixed layer of redder and bluer materials after the surface reddening event (Fig. 4). This interpretation is supported by the distribution of redder materials on boulder surfaces and the existence of reddish dark, fine grains observed in the touchdown operation. The thickness of the mixed layer of redder and bluer materials is estimated to be a few meters, derived from the minimum crater size (~10 m in diameter) that penetrates to the underlying blue materials. The presence of ejecta rays with a length of a few tens of meters that consist primarily of redder materials (fig. S4F) implies that the redder material layer originally had a minimum thickness of a few tens of centimeters (*6*). Solar heating is more likely than space weathering to be the source of the reddening of Ryugu's surface, because space weathering typically affects only a thin layer of ~100 nm, whereas the diurnal and annual thermal skin depths (the depth at which temperature variations decay to $1/e$ of their value at the surface) are $\lesssim$10 cm and ~1.5 m, respectively (*23*, *24*).

We suggest that a surface reddening event within a short period of time could be explained if Ryugu underwent a temporary orbital excursion near the Sun, causing higher surface heating. Such solar heating is consistent with the apparent deficiency of C-type asteroids with evidence of aqueous alteration (inferred from a spectral band at 0.7 μm) in the NEA population (*25*). However, solar heating on Ryugu during an orbital excursion cannot account for the low abundance of hydrous minerals revealed by global observations (*4*, *5*), because the bluish or brighter areas on Ryugu, which did not experience the intense solar heating, also have a low abundance of hydrous minerals (*4*).

The large local variations in the spectral slope and albedo within the sampling site on Ryugu suggest that both bluer and redder components were likely collected during the touchdown of Hayabusa2. We predict that the returned sample will contain a mix of altered and unaltered materials, with the former recording a solar heating event.

REFERENCES AND NOTES

1. S. Watanabe *et al.*, *Space Sci. Rev.* **208**, 3–16 (2017).
2. S. Watanabe *et al.*, *Science* **364**, 268–272 (2019).
3. M. Hirabayashi *et al.*, *Astrophys. J.* **874**, L10 (2019).
4. K. Kitazato *et al.*, *Science* **364**, 272–275 (2019).
5. S. Sugita *et al.*, *Science* **364**, eaaw0422 (2019).
6. Materials and methods are available as supplementary materials.
7. S. Kikuchi *et al.*, "Design and reconstruction of the Hayabusa2 precision landing on Ryugu," AAS 19-762, paper presented at the 2019 AAS/AIAA Astrodynamics Specialist Conference, Portland, ME, 11 to 15 August 2019.
8. T. Michikami *et al.*, *Icarus* **331**, 179–191 (2019).
9. C. Lantz *et al.*, *Icarus* **285**, 43–57 (2017).
10. T. Hiroi, M. E. Zolensky, C. M. Pieters, M. E. Lipschutz, *Meteorit. Planet. Sci.* **31**, 321–327 (1996).
11. E. A. Cloutis, P. Hudon, T. Hiroi, M. J. Gaffey, *Icarus* **220**, 586–617 (2012).
12. R. Jaumann *et al.*, *Science* **365**, 817–820 (2019).
13. S. Tachibana *et al.*, *Geochem. J.* **48**, 571–587 (2014).
14. H. Yano *et al.*, *Science* **312**, 1350–1353 (2006).
15. H. Sawada *et al.*, *Space Sci. Rev.* **208**, 81–106 (2017).
16. N. Hirata *et al.*, *Icarus* **338**, 113527 (2020).
17. M. Arakawa *et al.*, *Science* **368**, 67–71 (2020).
18. W. F. Bottke Jr. *et al.*, *Icarus* **175**, 111–140 (2005).
19. D. P. O'Brien, R. Greenberg, *Icarus* **178**, 179–212 (2005).
20. W. F. Bottke *et al.*, *Icarus* **247**, 191–217 (2015).
21. B. Gladman, P. Micheal, C. Froeschlé, *Icarus* **146**, 176–189 (2000).
22. P. Michel, M. Delbo, *Icarus* **209**, 520–534 (2010).
23. M. Delbo, P. Michel, *Astrophys. J.* **728**, L42 (2011).
24. D. D. Mazanek *et al.*, "Asteroid redirect mission (ARM) formulation assessment and support team (FAST) final report" (Technical Memorandum NASA-TM-2016-210911, NASA, 2016).
25. S. Marchi, M. Delbo', A. Morbidelli, P. Paolicchi, M. Lazzarin, *Mon. Not. R. Astron. Soc.* **400**, 147–153 (2009).

ACKNOWLEDGMENTS

The Hayabusa2 spacecraft was developed and built under the leadership of the Japan Aerospace Exploration Agency (JAXA), with contributions from the German Aerospace Center (DLR) and the Centre National d'Études Spatiales (CNES), and in collaboration with NASA, Nagoya Univ., The Univ. of Tokyo, National Astronomical Observatory of Japan (NAOJ), Univ. of Aizu, Kobe Univ., and other universities, institutes, and companies in Japan. We thank the many engineers, including N. Inaba at JAXA and T. Masuda, S. Yasuda, K. Matsushima, and T. Ohshima at NEC Corp. for their dedicated work on the Hayabusa2 mission; K. Sato at NEC Corp. for ONC development; and S. Kashima at NAOJ for optical calculations. We are grateful to B. E. Clark and two anonymous reviewers for thoughtful and constructive comments in their review of this paper. We also thank W. F. Bottke for useful comments on the orbital evolution of NEAs. **Funding:** T.Mo., S.Su., N.S., S.Ka., M.M., S.Sa., M.Ab., R.N., A.M., K.W., and S.W. were supported by KAKENHI from the Japan Society for the Promotion of Science (JSPS) (grant nos. 17H06459, 19H01951, 17H01175, 17KK0097, 19H00727, 18H01267, 18K11610, 19K03955, 16H04044, and 19K03958). This study was supported by the JSPS Core-to-Core program "International Network of Planetary Sciences." T.H. acknowledges funding support from NASA's EW and PDART programs. M.Hi. acknowledges support from NASA/Solar System Workings (NNH17ZDA001N/80NSSC19K0548) and Auburn Univ.'s intramural research grant. O.S.B. acknowledges support from OSIRIS-REx under contract NNM10AA11C, issued through the NASA New Frontiers Program. D.D. and C.M.E. acknowledge funding through the NASA Hayabusa2 Participating Scientist Program. P.M. acknowledges funding from the French space agency CNES; from Academies of Excellence: Complex systems and Space, environment, risk, and resilience, part of the IDEX JEDI of the Université Côte d'Azur; and from the European Union's Horizon 2020 research and innovation program under grant agreement no. 870377 (project NEO-MAPP). **Author contributions:** T.Mo. coordinated coauthor contributions, led the ONC data analyses and interpretations, and wrote the paper with contributions from S.Su., N.H. (Aizu), and S.Ka. ONC data acquisitions and reductions: R.Ho., N.S., Y.Yo., M.Ya., S.Su., T.Mo., S.Ka., H.Sa., M.M., T.K., E.T., C.Ho., K.O., H.Su., K.Yoshio., M.Ha., Y.C., Y.Ii., N.Tak., C.S., K.Yu., M.I., H.Ka., K.Mo., and D.D.; Spectral analysis: E.T., D.D., R.Ho., Y.Yo., S.Su., and T.Mo.; Crater statistics and geomorphology analyses: T.Mo., Y.C., M.K., N.H. (Kobe), O.S.B., C.M.E., E.T., and S.Su.; Shape modeling: N.H. (Kobe), N.H. (Aizu), O.S.B., C.M.E., R.N., Y.S., S.W.; NIRS3 data acquisitions and reductions: K.K., T.N., L.R., C.P., T.Iw., M.Ab., M.Oh., Y.N., and K.T.; Landing site characterization: Y.Ts., S.W., T.Sa., S.Ki., T.Y., N.O., Y.Ya., Y.S., K.S., N.H. (Kobe), K.O., K.K., N.H. (Aizu), K.W., H.Yab., Y.Is., R.N., T.Mo., N.S., K.Ma., H.Se., R.Ho., E.T., Y.Yo., C.Ho., T.Mic., M.M., A.M., N.Tan., Y.F., T.Ir., M.S.; Science operations of spacecraft: T.Miz., C.Hi., S.H., O.M., T.Sh., S.So., R.T., H.Yan., M.Ha., T.Iw., M.Ab., H.Sa., M.Oz., H.T., Y.Ya., T.O., Y.S., K.S., Y.Ii., H.N., S.Ki., T.Y., N.O., G.O., Y.M., K.Yoshik., T.T., Y.Ta., A.F., S.N., F.T., S.Tan., M.Yo., T.Sa., S.W., and Y.Ts.; Project administration: S.W., M.Yo., S.Tac., K.K., S.Su., T.O., N.N., M.Ar., M.Ab., H.I., S.Tan., S.N., F.T., T.Sa., and Y.Ts.; and Interpretation and writing contribution: T.Mo., S.Su., R.Ho., E.T., Y.C., Y.Yo., S.Ka., N.S., M.M., M.Ya., N.H. (Kobe), N.H. (Aizu), S.W., T.Mic., M.Hi., T.H., R.He., G.K., S.Sa., T.N., K.W., N.Tan., C.M.E., D.D., and P.M. All authors discussed the results and commented on the manuscript. **Competing interests:** Y.Ya. is also affiliated with Tokyo Metropolitan University. **Data and materials availability:** All images and input data used in this paper, and our derived digital elevation map, are available on the JAXA Data Archives and Transmission System (DARTS) website, www.darts.isas.jaxa.jp/pub/hayabusa2/paper/Morota_2020/. Additional data from the mission are delivered to the DARTS archive at www.darts.isas.jaxa.jp/planet/project/hayabusa2/, and higher-level data products will be available in the Small Bodies Node of the Planetary Data System at https://pds-smallbodies.astro.umd.edu/ 1 year after departure from the asteroid.

SUPPLEMENTARY MATERIALS

science.sciencemag.org/content/368/6491/654/suppl/DC1
Materials and Methods
Figs. S1 to S14
Table S1
References (*26*–*38*)
Movie S1

26 September 2019; accepted 2 April 2020
10.1126/science.aaz6306

3D PRINTING

Controlling interdependent meso-nanosecond dynamics and defect generation in metal 3D printing

Saad A. Khairallah[1]*, Aiden A. Martin[1], Jonathan R. I. Lee[1], Gabe Guss[1], Nicholas P. Calta[1], Joshua A. Hammons[1], Michael H. Nielsen[1], Kevin Chaput[2], Edwin Schwalbach[2], Megna N. Shah[2], Michael G. Chapman[2,3], Trevor M. Willey[1], Alexander M. Rubenchik[1], Andrew T. Anderson[1], Y. Morris Wang[1], Manyalibo J. Matthews[1], Wayne E. King[4]

State-of-the-art metal 3D printers promise to revolutionize manufacturing, yet they have not reached optimal operational reliability. The challenge is to control complex laser–powder–melt pool interdependency (dependent upon each other) dynamics. We used high-fidelity simulations, coupled with synchrotron experiments, to capture fast multitransient dynamics at the meso-nanosecond scale and discovered new spatter-induced defect formation mechanisms that depend on the scan strategy and a competition between laser shadowing and expulsion. We derived criteria to stabilize the melt pool dynamics and minimize defects. This will help improve build reliability.

Laser powder bed fusion additive manufacturing (L-PBF AM) technology uses a laser beam to scan 2D patterns over a flat bed of microscopic (~15 to 100 μm) metal powder. This forms melt pool tracks that fuse with the lower layers. Repeating the layer-wise process thousands of times results in the build of a 3D object. There is a strong need to understand and control the interdependency between laser process parameters and complex powder and melt pool dynamics. This is to help solve the variability problem, where the printed parts do not repeatably meet the standards required to pass the qualification and certification step (*1*, *2*). The variability stems from the accumulation of various defects, such as pores, that are randomly generated at the powder bed layer and in the melt pool during each layer scan.

Investigations at the powder bed layer uncovered chaotic powder dynamics driven by vapor that escapes the melt pool depression at hundreds of meters per second (*3*). This high vapor flux creates a complex gas flow that entrains loose powder particles surrounding the sides of the laser track. This process sometimes results in large denudation zones that lack powder (*4*) and causes 85% of the particle spatter observed as sparks to the naked eye (*5*). X-ray imaging shows that spatter particles can reach speeds of ~15 m/s (*6*–*8*) and that they form at various environmental pressures (*4*, *8*). Therefore, diminishing spatter is a high priority in L-PBF. Producing parts devoid of these defects remains challenging. Mechanical properties are influenced by the presence of a small amount of microscopic pores, even for parts that are more than 99% dense (*9*). Probing the melt pool is accomplished by ultra-high-speed x-ray techniques (*10*, *11*), but these can still lack the spatial and temporal resolution required to fully capture ultrafast dynamics of melt pool morphology and the micropores.

We used a high-fidelity multiphysics model and verified it with in situ x-ray and other diagnostics experiments (*12*–*16*). [See (*17*) for materials and methods.] The modeling delivers 3D temperature, velocity, and other data at a 2-μm scale and is predictive because it uses full laser ray tracing (figs. S1 to 12 and movies S1 to 20). The hydrodynamics is coupled with heat diffusion on the nanosecond scale to accurately capture the highly dynamic and nonlinear laser-powder and laser–melt pool interactions. We then related the variability problem to the transient physical states. Our modeling results present a roadmap for reducing spatter, decreasing voids, and improving the reliability of L-PBF parts.

[1]Lawrence Livermore National Laboratory, Livermore, CA 94550, USA. [2]Air Force Research Laboratory, Wright-Patterson Air Force Base, OH 45433, USA. [3]UES Inc., Dayton, OH 45432, USA. [4]The Barnes Group Advisors, 415 Orchard St., Sewickley, PA 15143, USA.
*Corresponding author. Email: khairallah1@llnl.gov

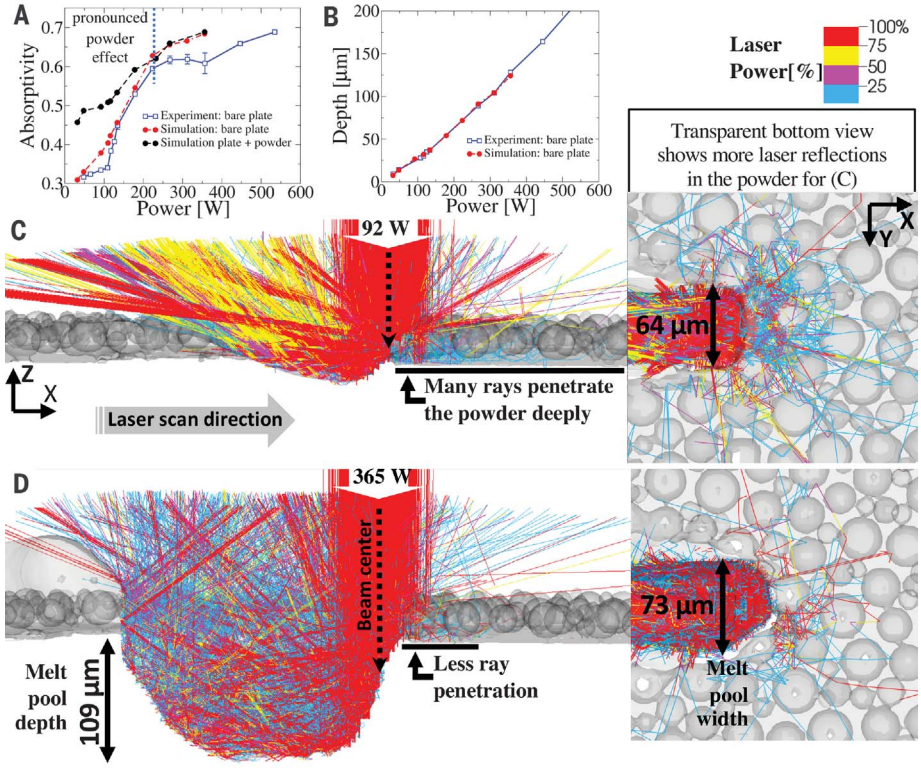


Fig. 1. Complex laser powder absorptivity. (**A**) Absorptivity plot showing the conduction (low power) to keyhole (high power) transition for a bare plate (SS316L, Gaussian laser spot size D4σ = 60 μm, and scan speed 1.5 m/s). Adding 35-μm-thick powder improves absorptivity at low power. That the simulation data overlap at higher power (beyond the dotted vertical blue line) with and without powder indicates that powder becomes less relevant. (**B**) Simulation captures the linear relationship between melt pool depth and power. (**C** and **D**) Laser–powder–melt pool interaction. For clarity, the laser rays are denoted in four discrete colors and represent four power bins. The incoming rays arrive at 100% power (red) and lose energy upon reflection. A blue ray is at a power less than or equal to 25% of the initial power. At low power (92 W), the rays penetrate the powder through multiple reflections. Hence, the absorptivity is higher than a flat plate. At high power (365 W), the beam center is on top of the melt pool and the rays are concentrated inside the depression. The laser-powder interaction becomes less pronounced. The 3D melt pool is sliced in half and made semitransparent for visual clarity. The *X*, *Y*, and *Z* axes act as a frame of reference.

L-PBF is a thermally driven process that requires an accurate laser-material absorptivity for predictive modeling. Unfortunately, absorptivity can vary in a complicated way as a function of the melt pool morphology and temperature. Our modeling differed from previous high-fidelity models (*13*, *14*, *18*) in that the absorptivity was a predicted output rather than an input approximated as a constant value. This capability better captured all L-PBF laser power ranges because it predicted the transition from conduction mode melting at low laser power to the keyhole (deep and narrow melt pool) regime at high laser power and the melt pool depth during steady-state scan over a bare plate (Fig. 1, A and B).

When we added a 35-μm-thick powder bed (monomodal particle distribution peaked at a mean diameter of 27 μm with a half-max width of 15 μm) onto the bare plate, the absorptivity still increased with power, similarly to the bare plate results, because a widening depression (Fig. 1, C and D) at higher power can accommodate more reflections, or equivalently, more energy absorption events. The notable difference from the bare plate was that the powder improved the absorptivity response at lower power. This is because almost half of the incident rays interact with the powder surrounding the front of the melt pool (Fig. 1C); therefore, the additional reflection events within the powder give higher absorption than in the bare plate case. At high power (>200 W), the overlap in absorptivity data (Fig. 1A) indicates that the powder becomes less relevant. Indeed, Fig. 1D shows that the majority of the laser rays are incident on the melt pool surface and interact less with the powder. The model does not include gas dynamics. The vapor recoil pressure that generates deeper melt pools is considered as a boundary condition on the liquid surface and captures the depth well (Fig. 1B). The powder is initialized in a presintered state, so it is fixed. This helps to isolate the effects of spatter and the benefits of presintered powder in minimizing spatter, as suggested in (*8*).

Presintering is a heat treatment applied before the fusion process to make the particles bind with each other and the surroundings rigid. Presintering is already practiced in electron beam AM to prevent powder motion due to electrostatic repulsion caused by an accumulation of negative charges over the powder. Figure 1C shows that laser presintering can be achieved using a low-power laser beam because it can deeply penetrate the powder and deposit energy efficiently owing to high absorption. The particles' contacts with each other and the substrate would then fuse lightly, hence preventing powder motion. A scan with a second high-power laser would fuse the powder. In the absence of gas-entrained spatter, we artificially introduced spatter scenarios in a series of digital experiments to study short–time scale laser-spatter interaction and the benefits of presintering (Fig. 2; (*17*) section 1, figs. S1 to S8, and movies S1 to S8).

The simulations reveal the laser rays' interaction with spatter and the resulting laser expulsion mechanism in fine spatial-temporal detail. In the first scenario (Fig. 2A, figs. S1 to S8, and movie S1), a 300-W laser impinged at 1.8 m/s on a large spatter, made from an agglomerate of particles, suspended 40 μm above the powder bed and expelled it away to the side. The grazing laser rays boiled the agglomerate's surface and accelerated it to ~5 m/s within 40 μs. It is the exponential dependence of vapor recoil pressure on temperature {$P(T) = 0.54P_a\exp[-\lambda/k_B(1/T - 1/T_b)]$, where P_a is the ambient pressure, λ = 4.3 eV per atom is the evaporation energy, $k_B = 8.617 \times 10^{-5}$ eV/K is the Boltzmann constant, T is the surface temperature, and T_b = 3086 K is the boiling temperature of 316L stainless steel} that creates the necessary large impulse force. At 275 μs, the spatter was a 90-μm molten sphere moving away from the laser scan path. The spatter's early trajectory is determined by the large expulsion force (acceleration ~1×10^5 m/s^2). The trajectory may be altered later in time in the presence of gas entrainment at high environment pressure and/or get caught by the vapor plume that exists at all environment pressures [(*17*) section 1].

This laser spatter interaction affects the track quality, as the melt pool depth fluctuations show (Fig. 2F). The depth decreased by 15% without causing lack of fusion pores. However, a laser at a half-power of 150 W (Fig. 2B and movie S2) failed to expel the cluster

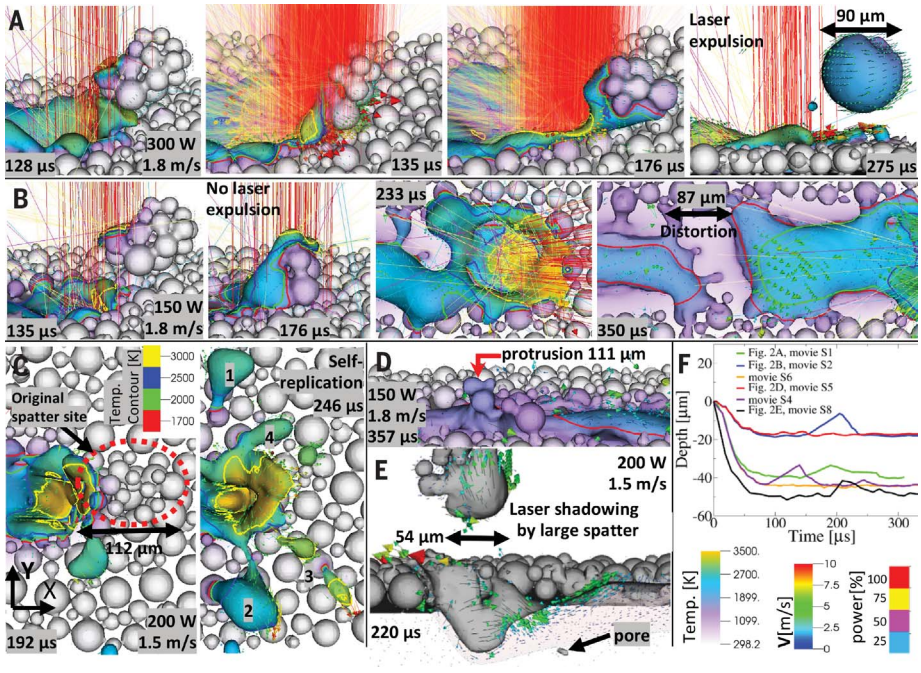


Fig. 2. Spatter defects due to laser expulsion, self-replication, and shadowing mechanisms. (**A**) High laser power (spot size 54 μm) is required to expel a large floating agglomerate (SS316L fused spatter particles). (**B**) A low-power comparison shows that agglomerates can distort laser tracks, which can induce a lack of fusion defects. Fewer rays are displayed for clarity. (**C**) Top planar view of the laser impinging onto an agglomerate site (deposited agglomerate). A self-replicating effect takes place when the agglomerate disintegrates into fragments that generate four new spatter sites, labeled 1 to 4. (**D**) At low power, an off-center agglomerate site melts partially and protrudes 111 μm above the substrate, which can damage the powder recoater. (**E**) 3D mid-slice shows a pore (3 μm) forming because of laser shadowing (blocking the laser) by a floating spatter with a size comparable to the laser's spot size. The liquid melt pool is represented as a semitransparent red surface. The temperature pseudocolor and contours are absent for clarity. In situ x-ray experiments in fig. S7 reveal melt depth change but lack the spatial and temporal resolution to show micrometer pores. (**F**) Melt pool depth rise due to laser shadowing (spatter blocking the laser) varies for different scenarios. The abrupt cooling in (E) resulted in the fastest rise in depth [black in (E)]. Surprisingly, off-center spatter does not affect the depth much (orange and red in (D)]. For all panels, the laser scan direction is to the right (+*X*) except in (E). Temperature contour lines are represented in four discrete colors (1700 K for melting up to 3000 K for close to boiling). The velocity vector fields **V** are represented as colored arrows. See (*17*) section 1 and movies S1 to S8.

because it could not vaporize the vertical sides of the cluster as quickly as the 300-W laser. Instead, the laser boiled the top surface of the cluster (yellow contour line) and the recoil pressure pressed it down into the melt pool at 176 μs, decreasing the melt depth by 90%, distorting the track direction at 233 μs, and creating an 87-μm discontinuity at 350 μs. This outcome is problematic because the location of the discontinuity may not be densely packed during the powder spreading phase, which may prevent a weak laser from fusing the layers. This results in a lack of fusion defects and a low densification, which in turn may undermine the mechanical properties. Hence, a high laser power is necessary to activate the expulsion mechanism that pushes away large spatter and suppresses the associated defects.

Many AM printers use argon cross flow applied a few centimeters above the powder bed to protect the laser optics from metal vapor and vertical spatter; however, the cross flow is not always uniform over the build plate, and a large expelled cluster such as that in Fig. 2A could still land on the laser scan path. We modeled such a head-on collision with the laser (Fig. 2C, figs. S3 and S4, and movie S3) and found a self-replicating effect, whereby the large cluster broke into molten 5- to 10-m/s ejecta that contaminated the surroundings by generating four spatter sites, within 50 μs. Over a nonsintered powder bed, the molten ejecta may coalesce with the loose powder particles and form larger agglomerates. This process may repeat itself and lead to a "snowballing" effect, whereby the agglomerates get uncontrollably large. These can interfere with the powder spreading blade, decrease the uniformity of the powder bed, and lead to a lack of fusion defects (movie S7).

In the case when the cluster is off-center but within the hatch spacing of a scan track (Fig. 2, D and F, and movies S5 and S6), the melt depth did not change at 150 or 300 W, showing that the depth is determined by the hottest spot achieved directly under the Gaussian laser center. The clusters merged into the melt pool with the exception that at low power (150 W; Fig. 2D), with less heat being delivered for complete melting, the cluster partially protruded at a height of 111 μm, which can scratch a hard powder spreading blade and cause nonuniform powder spreading and bad build quality. Laser expulsion and head-on collision events with large clusters should occur regularly (~1 ms; see figs. S4 and S5) because the gas entrainment from the vapor jet continuously sucks loose particles toward the laser spot (*3*) (fig. S6).

In the final scenario, we studied the impact of laser shadowing by blocking the laser beam with a floating agglomerate using simulations (Fig. 2E and movie S8) and in situ x-ray imaging [(*17*) section 2 and fig. S7]. The results show the melt pool's morphology (depth) to be sensitive to laser shadowing. Also, an agglomerate that is as large as the laser beam (Fig. 2E) was not expelled quickly and blocked the center of the Gaussian beam profile, which has the highest laser intensity. Therefore, the depth decrease was the fastest at ~20 μs, compared with ~50 μs for the other scenarios (Fig. 2F). This rapid cooling induced a micropore defect (Fig. 2E). This indicates a spatter size threshold determined by the beam size and the laser power, beyond which laser shadowing may produce pores. Equivalently, for a given spatter size, there is a power threshold beyond which laser expulsion improves. The power threshold is approximately a linear function of scan speed [power is equal to ~157 times the scan speed for stainless steel 316L (SS316L) and 50-μm laser spot size, derived in (*17*) section 3] and defines a process window for efficient expulsion, given spatter of similar size as the beam (fig. S8).

These findings add a physical foundation to certain AM practices (*19*) in that high densification of AM parts (>99%) requires high power while avoiding keyholes. Reliability would also be improved using a multibeam for presintering in L-PBF when powder recyclability and oxidation are addressed. Reduction in spatter has already been noted with a multibeam study (*20*), and presintering has an additional benefit of reducing residual stresses (*21*).

Although high laser power along with presintering can minimize bad spatter effects, we discovered through modeling and in situ x-ray experiments in Ti-6Al-4V [Fig. 3A, (*17*) sections 4 and 5, figs. S9 to S11, and movies S17 to S20] that the laser scan strategy, which dictates the laser power and scan speed along a track, can generate oversized (~200 μm) back-spatter (spatter in the backward direction) at the start of a track. These pose major risks because they are much larger than the beam size and might not be mitigated by laser expulsion. Back-spatter can arise in different AM scan strategies that use the common high-speed galvanometer mirror technology for laser scanning. The mirrors cannot maintain a constant laser scan speed when starting and stopping, respectively, at the start and end of a track owing to inertia, which leads to deposition of nonuniform energy density. The common scan strategy called "skywriting" (*22*) remedies this problem by turning the laser power off during the acceleration and deceleration phases and turning the laser on during the linear constant speed phase. But the issue may persist, because we show that back-spatter is facilitated by a fast laser power ramp up when the laser is turned on. In addition, the fiber laser power may uncontrollably spike before converging to the requested power owing to limitations imposed by the physics of laser generation.

Large and brief changes in laser power, or equivalently of temperature, translate into exponential changes in the applied vapor recoil pressure (*14*). A high pressure can overcome the surface tension and cause a strong flow and spatter. A quick ramp up to a high power of 320 W, in Fig. 3A, generated an 85-μm-deep depression within 25 μs. The maximum of the recoil pressure is exerted below the Gaussian laser center, which is located at the front of the depression (see, for example, Fig. 1, C and D). When the laser started moving, a large pressure difference developed between the front and the back and created the back-spatter. Following the Bernoulli equation and the continuity of mass flow, we idealized the problem's geometry and considered the melt being compressed by the laser at low velocity (~3 m/s) through a large pipe of cross-sectional area $4\pi w^2$, given by the depression ($2w$ is the depression's width, ~100 μm). The melt then flowed backward into a narrow cross section πr^2 (r is the inner radius of the depression and is of similar magnitude as laser beam radius ~25 μm) at high speed (~13 m/s) and low pressure and reached the top boundary condition 40 μs later [(*17*) section 4 and fig. S11].

Based on this ideal picture, we developed a stability criterion to explain and prevent this high-speed backflow (causes back-spatter) by considering the magnitude of surface tension relative to inertial pressure (pressure due to the momentum of the fluid). The large amount of energy deposited during the short ramp up in power (~25 μs) caused the melt to reach boiling temperatures (Fig. 3A), which decreased the surface tension. A high surface tension γ prevents turbulent flow by minimizing the surface energy $\gamma(1/r_1 + 1/r_2)$, where r_1 and r_2 are the radii of the curvature of the depression in two perpendicular directions and are close to the beam's radius, r. Opposite to that, a large inertial pressure with energy defined as $\rho V^2/2$, where ρ is melt density and V is melt velocity, favors a high-speed flow. The ratio of the inertial pressure to the surface tension defines the Weber number $\mathrm{We} = \rho V^2 r/4\gamma$. A critical flow velocity $V_{\mathrm{critical}} = 2\sqrt{\gamma/\rho r}$ can be defined when We = 1. The critical velocities for Ti-6Al-4V and SS316L are 6.1 and 3.8 m/s, respectively. A value $V > V_{\mathrm{critical}}$ (i.e., We > 1) indicates fast melt flow that induces surface turbulence and liquid droplets (*23*). Indeed, Fig. 3A shows speeds two times larger than V_{critical}. When $V < V_{\mathrm{critical}}$ (i.e., We < 1), a steady surface forms. The Weber number sets a reference scale and is not calculated exactly for nonideal problems. We used it to set a maximum limit for $\mathrm{d}z/\mathrm{d}t$ or how fast the melt depth z under the laser should vary without creating spatter (i.e., turbulence) over time t. From the continuity of liquid mass flow, the rate of liquid mass generated in the depression ($\rho\pi w^2 \mathrm{d}z/\mathrm{d}t$) is equal to the amount displaced

backward ($\rho\pi r^2 V$). This leads to $dz/dt < r^2/w^2 V_{critical}$ for steady flow and implies that the power should be ramped up slowly to maintain a slow change in recoil pressure or equivalently in depth. The critical limits, $(dz/dt)_{critical}$, are 1.5 and 0.9 m/s for Ti-6Al-4V and SS316L, respectively. The back-spatter in Ti-6Al-4V (Fig. 3A) was observed for dz/dt = 3.4 m/s, which is about two times higher than the critical limit. To enforce $dz/dt < (dz/dt)_{critical}$, a proportional-integral-derivative (PID) controller was implemented in the simulation to dynamically vary the power and maintain a liquid melt line (liquidus) over a fictitious tracer point located at z below the laser center. When the laser is turned on, the point is lowered at a user defined rate dz/dt to a sufficient melt depth (about two times powder thickness).

The control over the tracer point's trajectory makes this approach generalizable to other scan strategies. We modeled a modified skywriting technique by keeping the laser stationary for 50 μs at the start of a track to achieve a good fusion depth with the previous layer before moving the laser. This is because in skywriting, the power ramps up as the laser moves, which can produce back-spatter and might not achieve a good fusion depth until later ahead of the starting point. A contour laser scan over the endpoints is performed to improve fusion, but it is not always adequate because the surface of printed parts can still be rough and porous. The model gave the

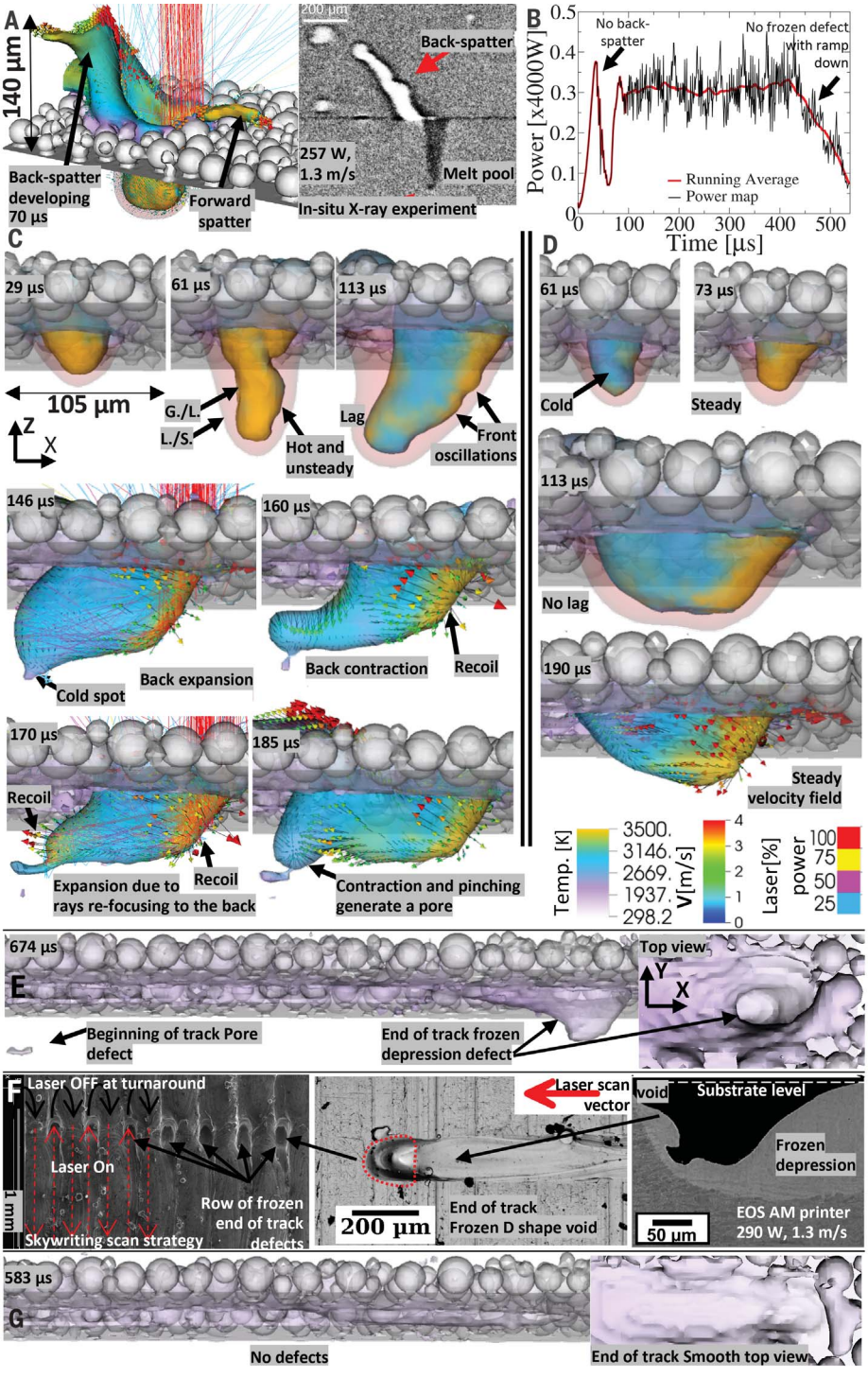


Fig. 3. Stability criterion to control start of track spatter, pores, and end of track frozen depression. (**A**) Simulation and in situ x-ray experiments [(*17*) sections 4 and 5, fig. S10, and movies S17 to S20] show oversized (~200 μm) back-spatter at the start of the track during a skywriting scan of Ti-6Al-4V. Ramping the laser power high and fast sets higher average temperatures (3000 K) and flow velocity (~13 m/s) than in a steady-state melt pool. The magnitude of the velocity vector only in (A) is given by 2.5 times the color scale for **V** (m/s). (**B**) A general stability criterion that is implemented in the simulation, to prevent back-spatter and stabilize melt pool dynamics in a single track of SS316L (laser spot size 54 μm), dynamically assigns (i.e., maps) laser power to scan positions along the track as a function of time (power map). (**C**) For a constant power of 132 W, the melt pool dynamics is unsteady and pores form at the start of the track owing to large temperature variations at the gas-liquid (G./L.) interface. (**D**) In contrast to (C), the power map (B) enables steady melt pool dynamics. (**E**) Start and end of track defects caused by melt pool transient dynamics in (C). (**F**) The frozen depression defect is not system specific. Our skywriting of Ti-6Al-4V with the EOS M280 commercial 3D printer shows that the scan strategy and resulting D-shaped line voids at the end of a scan vector. A 2D slice of a back-scattered electron image shows details of the frozen depression [(*17*) section 6]. (**G**) The power map strategy prevents pore defects and leads to a smooth surface at the end of the track. For all panels, the surface rendering is semitransparent. The liquid melt pool boundary (L./S.) is represented as a semitransparent red surface. The velocity vector field **V** is defined on the gas-liquid (G./L.) interface. See figs. S9 to S11 and movies S9 and S10.

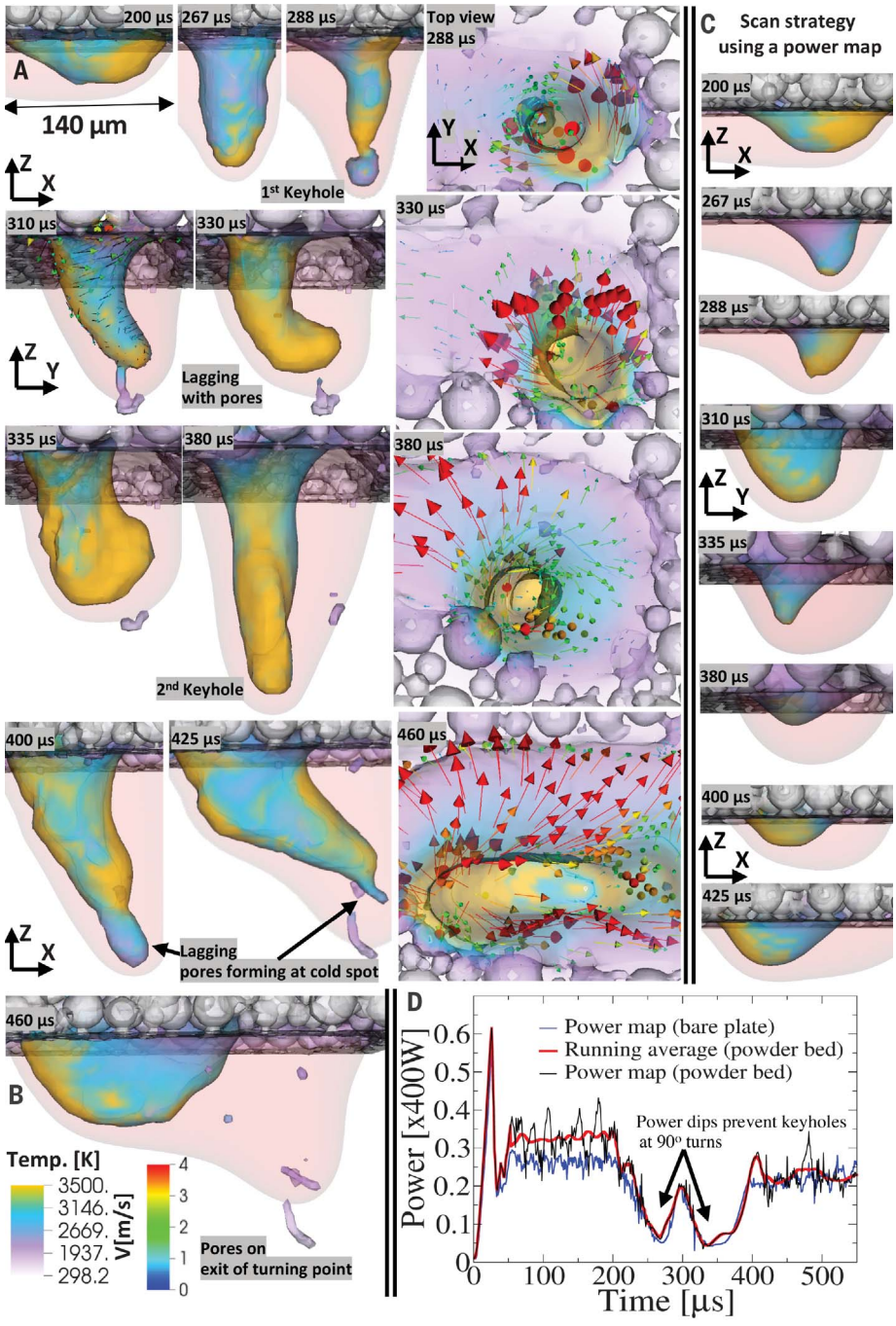


Fig. 4. Controlling transient keyhole defects during a turnaround scan strategy. (**A**) Transition of a Ti-6Al-4V melt pool into two keyholes at constant power during a turn. The laser executes two 90° turns (+*X*, −*Y*, then −*X* directions). The overheating from the extra dwell time at both turning points creates two keyholes. During the turn, the keyhole's opening is circular compared with the oval shape when the laser enters and exits the turnaround. The colored arrows represent the velocity vector on the liquid surface. (**B**) Pores form and freeze after the laser exits the turn owing to rapid melt depth rise. This happens because of transient states generated by a lack of coupling between the power and scan vector. The melt pool lagging shape in (A) is a manifestation of this uncoupling. (**C**) The stability criterion generates a stable melt pool as the laser scans and suppresses keyholes and pores during the turn. (**D**) The power map, generated by the stability criterion, exhibits complex variations due to the nonlinearity of the melt pool dynamics. The powder is less relevant during the turnaround, as the overlap of the blue and black curves show. See (*17*) section 7 and movies S11 to S13.

power map (Fig. 3B and movie S9), which assigns or maps a laser power to positions along the scan track as a function of time, to conduct this scan strategy and showed no back-spatter for dz/dt = 0.13 m/s (10 times lower than the critical limit) during the initial transient state (61 to 113 µs in Fig. 3D). The melt pool morphology remained steady at the start of the scan and afterward during steady state (190 µs) using an average power of 132 W.

For comparison, when scanning at a constant power of 132 W (Fig. 3C), no back-spatter was generated, but dz/dt = 1 m/s was close to the critical limit, which resulted in a hotter, unstable, and deeper melt pool, as well as pore generation during the transient (29 to 113 µs in Fig. 3C, fig. S9, and movie S10).

At the end of the track (Fig. 3, E to J), the power map prescribed a power ramp down and maintained a liquid state in the depression. This gave the surface tension time to smooth the surface (Fig. 3J). Turning the laser off abruptly otherwise lead to a 43-µm frozen depression due to rapid cooling (Fig. 3E) (*14*, *24*). This defect was observed in Ti-Al6-4V parts (Fig. 3F) using the skywriting mode in the EOS M280 AM printer [(*17*) section 6]. Another common alternative to turning the laser off is to perform a turnaround with the laser on. This is done, for example, in the island scan strategy (*25*). However, keyhole pores may arise owing to extra laser dwell time causing overheating. Figure 4A, (*17*) section 7, and movies S11 and S12 detail how applying a constant power generates two keyholes at the turn. Pores (Fig. 4B) form when the laser exits the turn, as reported in (*11*). In comparison, by setting a tracer point at a constant depth along the track [$dz/dt = 0 << (dz/dt)_{critical}$], the model generated a stable depression (Fig. 4C) and a power map (Fig. 4D) that can be adopted in actual AM machines.

Diminishing the variability problem involves controlling random events generated by interdependency dynamics of complex laser–powder–melt pool interactions. This results in a narrow AM process parameter space because the laser power threshold sets a lower bound for efficient laser expulsion of spatter. The stability criterion sets an upper bound on power while eliminating oversized back-spatter and stabilizing melt pool dynamics. Other bounds due to transient physical states in AM and, more generally, other beam welding technologies remain to be set. High-fidelity multiphysics simulations coupled with in situ diagnostics will be indispensable to introduce stability criteria to advance manufacturing and help usher in the industry 4.0 revolution (*26*).

REFERENCES AND NOTES

1. T. DebRoy *et al*., *Nat. Mater.* **18**, 1026–1032 (2019).
2. T. Wohlers, *3D Printing and Additive Manufacturing State of the Industry* (Wholers Associates, 2018).
3. P. Bidare, I. Bitharas, R. M. Ward, M. M. Attallah, A. J. Moore, *Acta Mater.* **142**, 107–120 (2018).
4. M. J. Matthews *et al*., *Acta Mater.* **114**, 33–42 (2016).
5. S. Ly, A. M. Rubenchik, S. A. Khairallah, G. Guss, M. J. Matthews, *Sci. Rep.* **7**, 4085 (2017).
6. C. Zhao *et al*., *Sci. Rep.* **7**, 3602 (2017).
7. C. L. A. Leung *et al*., *Nat. Commun.* **9**, 1355 (2018).
8. Q. Guo *et al*., *Acta Mater.* **151**, 169–180 (2018).
9. T. Voisin *et al*., *Mater. Des.* **158**, 113–126 (2018).
10. R. Cunningham *et al*., *Science* **363**, 849–852 (2019).
11. A. A. Martin *et al*., *Nat. Commun.* **10**, 1987 (2019).
12. Lawrence Livermore National Laboratory, ALE3D for industry (2018); https://ale3d4i.llnl.gov.
13. S. A. Khairallah, A. Anderson, *J. Mater. Process. Technol.* **214**, 2627–2636 (2014).
14. S. A. Khairallah, A. T. Anderson, A. Rubenchik, W. E. King, *Acta Mater.* **108**, 36–45 (2016).
15. J. Ye *et al*., *Adv. Eng. Mater.* **21**, 1900185 (2019).
16. J. Trapp, A. M. Rubenchik, G. Guss, M. J. Matthews, *Appl. Mater. Today* **9**, 341–349 (2017).
17. See supplementary materials.
18. C. Panwisawas *et al*., *Comput. Mater. Sci.* **126**, 479–490 (2017).
19. C. Kamath, B. El-dasher, G. F. Gallegos, W. E. King, A. Sisto, *Int. J. Adv. Manuf. Technol.* **74**, 65–78 (2014).
20. T. Heeling, K. Wegener, *Addit. Manuf.* **22**, 334–342 (2018).
21. F. Abe, K. Osakada, M. Shiomi, K. Uematsu, M. Matsumoto, *J. Mater. Process. Technol.* **111**, 210–213 (2001).
22. A. M. Mancisidor *et al*., *Phys. Procedia* **83**, 864–873 (2016).
23. J. Eggers, *Rev. Mod. Phys.* **69**, 865–930 (1997).
24. M. A. Groeber *et al*., *IOP Conf. Ser. Mater. Sci. Eng.* **219**, 012002 (2017).
25. A. H. Nickel, D. M. Barnett, F. B. Prinz, *Mater. Sci. Eng. A* **317**, 59–64 (2001).
26. K. Schwab, The fourth industrial revolution: What it means, how to respond (2018); www.weforum.org/agenda/2016/01/the-fourth-industrial-revolution-what-it-means-and-how-to-respond.

ACKNOWLEDGMENTS

We thank R. Ferencz and C. Clouse (support); A. Hamza (fruitful discussions); C. Noble (ALE3D-4i); M. Miller and E. Brugger (visIt); S. Weeratunga, D. Miller, and B. Ryujin (ASC laser package); N. Sinclair, P. Rigg, and D. Rickerson (x-ray imaging at DCS); and K. Fezzaa and A. Deriy (Beamline 32-ID APS). **Funding:** Work was performed under the auspices of the U.S. Department of Energy (DOE) by Lawrence Livermore National Laboratory (LLNL) contract DE-AC52-07NA27344. Lawrence Livermore National Laboratory directed research and development, project 17-ERD-042, 18-SI-003. This research used resources from the Advanced Photon Source, DOE User Facility operated for the DOE Office of Science by Argonne National Laboratory under contract no. DE-AC02-06CH11357; and the Dynamic Compression Sector (DCS), operated by Washington State University under (DOE)/National Nuclear Security Administration award no. DE-NA0002442. **Author contributions:** S.A.K.: code development, analysis, and writing; A.A.M., N.P.C., J.A.H., M.H.N., T.M.W., and J.R.I.L.: in situ x-ray imaging; G.G.: spatter optical imaging; K.C., E.S., M.N.S., and M.G.C.: pore optical imaging; A.M.R.: absorptivity; A.T.A.: ALE3D support; and Y.M.W., M.J.M., and W.E.K.: guidance. **Competing interests:** S.A.K. is an inventor on patent US 10,220,471 B2 held by LLNL that covers "Spatter reduction laser scanning strategy in selective laser melting." S.A.K., G.G., W.E.K., and M.J.M. are inventors on patent application 62/647,375 submitted by LLNL that covers "Additive manufacturing: Power map to mitigate defects." **Data and materials availability:** The data in the paper and supplementary materials are available upon request owing to large data size. ALE3D code along with computing resources are available through the High-Performance Computing Innovation Center (*12*). Lawrence Livermore National Laboratory release and review number LLNL-JRNL-774900.

SUPPLEMENTARY MATERIALS

science.sciencemag.org/content/368/6491/660/suppl/DC1
Materials and Methods
Supplementary Text
Figs. S1 to S12
References (*27*–*35*)
Movies S1 to S20
Data S1 and S2

18 July 2019; accepted 1 April 2020
10.1126/science.aay7830

CHEMICAL PHYSICS

Intermolecular vibrational energy transfer enabled by microcavity strong light–matter coupling

Bo Xiang[1], Raphael F. Ribeiro[2], Matthew Du[2], Liying Chen[2], Zimo Yang[1], Jiaxi Wang[2], Joel Yuen-Zhou[2]*, Wei Xiong[1,2]*

Selective vibrational energy transfer between molecules in the liquid phase, a difficult process hampered by weak intermolecular forces, is achieved through polaritons formed by strong coupling between cavity photon modes and donor and acceptor molecules. Using pump-probe and two-dimensional infrared spectroscopy, we found that the excitation of the upper polariton, which is composed mostly of donors, can efficiently relax to the acceptors within ~5 picoseconds. The energy-transfer efficiency can be further enhanced by increasing the cavity lifetime, suggesting that the energy transfer is a polaritonic process. This vibrational energy-transfer pathway opens doors for applications in remote chemistry, sensing mechanisms, and vibrational polariton condensation.

Vibrational energy transfer (VET) is ubiquitous for many molecular processes in the condensed phase, ranging from chemical catalysis (*1*, *2*) to biological signal transduction and molecular recognition (*3*, *4*). Due to through-bond anharmonic couplings, intramolecular and solute-solvent VET is widespread, leading to rapid intramolecular vibrational redistribution (IVR) that competes with other chemical events (*5*, *6*). However, through-space, selective intermolecular (solute-solute) VET is relatively rare. The scarcity of intermolecular VET is a consequence of weak intermolecular forces. Relative to electronic transitions, which readily undergo intermolecular energy transfer [e.g., via the Förster and Dexter mechanisms (*7*, *8*)], vibrational transition dipole moments are smaller by a factor of 10 to 100 (*9*), leading to uncompetitive intermolecular dipole-dipole couplings when compared with their electronic counterparts (Fig. 1A, top). As such, intermolecular VET is usually obfuscated by IVR.

Here we report a state-of-the-art strategy to engineer intermolecular vibrational interactions via strong light–matter coupling. When a highly concentrated molecular sample is inserted into an optical microcavity [e.g., a Fabry-Perot (FP) cavity] or placed onto a plasmonic nanostructure (*10*), the confined electromagnetic modes interact reversibly with the collective macroscopic molecular vibrational polarization such that hybridized light–matter states, known as vibrational polaritons, are formed (*9*–*16*). Owing to the delocalized nature of polaritons, the relaxation kinetics of strongly coupled systems differs substantially from that of their weakly coupled counterparts (*13*). Although pioneering studies have demonstrated such effects in the context of electronic energy transfer (*17*–*21*), intermolecular VET under strong light–matter coupling seems to operate by different mechanisms, as we describe below. Furthermore, given the scarcity of selective intermolecular VET in condensed phases, its polaritonic counterpart introduces a powerful concept that may alter the course of ground-state chemistry in solution (*22*).

To study cavity-assisted intermolecular VET, we designed a strongly coupled system composed of a microcavity and ensembles of two vibrational modes from different molecules. We encapsulated an equimolar solution of $W(CO)_6$ and $W(^{13}CO)_6$ in hexane/dichloromethane (DCM) solvent (total concentration 105 mM, 1/1 volumetric ratio; see supplementary materials and methods for details) in a FP cavity. These molecules are ideal for achieving vibrational strong coupling, as they have degenerate asymmetric stretch modes with high oscillator strength and narrow linewidths. The cavity with thickness L has resonances at wavelengths $\lambda = \frac{2}{n}L$, where n = 1,2,3, … is the cavity mode order. Because the carbonyl asymmetric stretches of $W(CO)_6$ and $W(^{13}CO)_6$ absorb at 1980 and 1938 cm^{-1}, respectively, a cavity with $L = n \times 2.5$ μm has modes that are nearly resonant with both vibrational transitions. In our experiments, unless specifically noted, we kept L at 12.5 μm and strongly coupled the fifth-order cavity modes to the vibrations.

For each molecular subsystem, the light–matter coupling g is proportional to $\sqrt{C}$, where C is the concentration of the absorbers. Given a large enough C, each molecular subsystem satisfies $g > \Gamma_{vib}, \Gamma_{cav}$, where Γ_{vib} and Γ_{cav} are

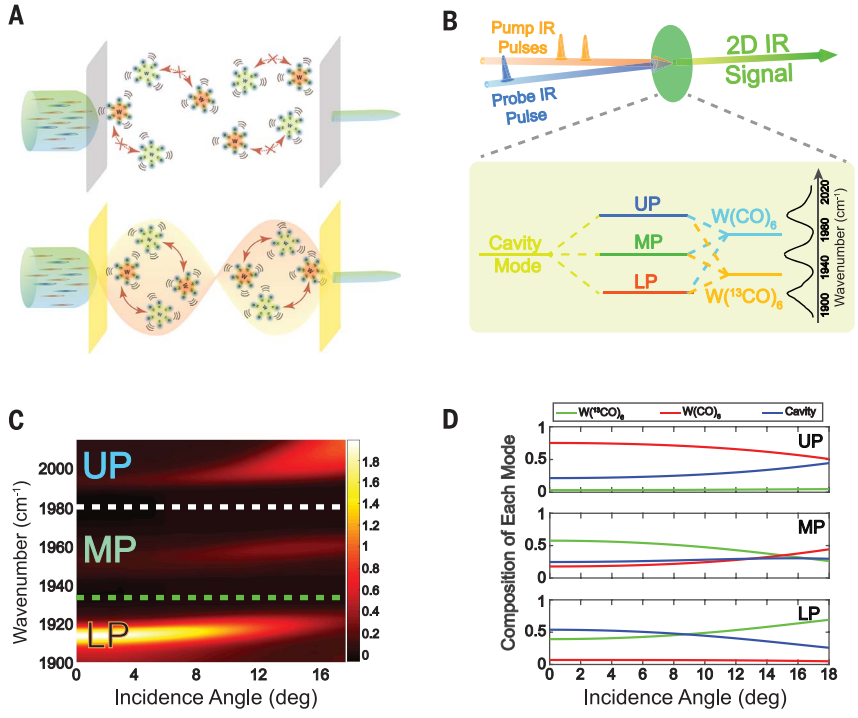


Fig. 1. Strongly coupled system between $W(CO)_6$ and $W(^{13}CO)_6$ in a hexane/DCM mixture and a cavity. (**A**) Schematic illustration showing that VET between vibrational modes of $W(CO)_6$ and $W(^{13}CO)_6$ molecules is unfavorable in solution (top) but is enabled by strong coupling of the molecular system to an infrared cavity mode (bottom). (**B**) Diagram of the 2D IR pulse sequence along with the IR spectrum and energy diagram of the system. (**C**) Transmission spectra of the polaritonic system as a function of incidence angle; white and green dashed lines denote bare $W(CO)_6$ and $W(^{13}CO)_6$ vibrational transitions, respectively. (**D**) Hopfield coefficients for LP, MP, and UP as a function of incidence angle, calculated as described in supplementary materials section 11.

[1]Materials Science and Engineering Program, University of California, San Diego, La Jolla, CA 92093, USA. [2]Department of Chemistry and Biochemistry, University of California, San Diego, La Jolla, CA 92093, USA.
*Corresponding author. Email: joelyuen@ucsd.edu (J.Y.-Z.); w2xiong@ucsd.edu (W.X.)

the full widths at half maximum of the vibrational and cavity modes, respectively. Therefore, the vibrational and cavity modes (hereafter referred to as basis modes) hybridize and form new normal modes, denoted as upper, middle, and lower polaritons (UP, MP, and LP) (*17*, *19*, *23*) (Fig. 1B, bottom). Each polariton consists of a superposition of the basis modes. The polariton resonant frequency and composition, characterized by Hopfield coefficients, can be controlled by changing the incidence angle (Fig. 1, C and D). For example, at 15° incidence angle, the UP consists of 59.4% $W(CO)_6$ carbonyl asymmetric stretch, 4.3% analogous vibration in $W(^{13}CO)_6$, and 36.3% cavity photon, whereas the LP is composed of 5.8, 60.8, and 33.4% of the respective basis modes. As discussed later, this information is essential to investigate the ability of strong coupling to mediate intermolecular VET.

We used two-dimensional infrared spectroscopy (2D IR) (*12*–*14*) to show VET from $W(CO)_6$ to $W(^{13}CO)_6$. In 2D IR, if the UP was pumped and VET occurred, a substantial population of $W(^{13}CO)_6$ excited states would be generated and the intensity of the corresponding cross peak would rise. In Fig. 2, we compare 2D IR spectra of the $W(CO)_6/W(^{13}CO)_6$ mixture inside and outside the microcavity. The 2D IR spectrum of the bare $W(CO)_6/W(^{13}CO)_6$ mixture (Fig. 2A) confirms the absence of energy transfer between vibrational modes. It shows two pairs of diagonal peaks, corresponding to excitations of asymmetric carbonyl modes of $W(CO)_6$ and $W(^{13}CO)_6$, respectively, whose vibrational lifetimes are ~200 ps. There are no cross peaks (dashed black box in Fig. 2A), thus indicating the absence of intermolecular VET (supplementary materials section 2).

The strongly coupled $W(CO)_6/W(^{13}CO)_6$ system provides a substantially different picture. The 2D IR spectrum (Fig. 2B) shows several cross peaks at delay time t_2 = 30 ps, indicating cavity-induced intermolecular correlations. At t_2 = 30 ps (greater than the polariton lifetime), the remaining pumped energy equilibrates to the first excited state of dark modes, as determined in previous studies (*12*, *15*). Furthermore, the $W(^{13}CO)_6$ dark modes have $v = 1 \rightarrow v = 2$ transitions (v, vibrational state) at 1917 cm^{-1}, whereas those of $W(CO)_6$ are at 1961 cm^{-1}. Thus, the transient absorptions at probe frequency $\omega_3 = \omega_{LP}$ (~1920 cm^{-1}) and ω_{MP} (~1959 cm^{-1}) provide an optical window into population dynamics of the $W(^{13}CO)_6$ and $W(CO)_6$ reservoir modes, respectively (supplementary materials section 12). In particular, the cross peak at $\omega_1 = \omega_{UP}$ and $\omega_3 = \omega_{LP}$ (denoted as [ω_{UP}, ω_{LP}] hereafter; see red box in Fig. 2B) suggests that a larger-than-expected (on the basis of Hopfield coefficients) fraction of the energy in UP [dominated by $W(CO)_6$] was transferred to the dark $W(^{13}CO)_6$ modes after 30 ps, a signature of intermolecular VET. We also conducted 2D IR experiments with the pump beam tailored to selectively excite $|UP><UP|$ population states, and a similarly strong cross peak appeared at $\omega_3 = \omega_{LP}$. Thus, the [ω_{UP}, ω_{LP}] and [ω_{UP}, ω_{MP}] cross peaks (Fig. 2B) arise from a UP population, whereas pump-driven coherences such as $|UP><LP|$ and $|UP><MP|$ do not contribute to the observed spectral features (supplementary materials section 5).

We compared the cross-peak intensities at [ω_{UP}, ω_{LP}] ($I_{UP,LP}$; red box in Fig. 2B) and [ω_{UP}, ω_{MP}] ($I_{UP,MP}$; black box in Fig. 2B) to determine the equilibrated excited-state populations of $W(^{13}CO)_6$ and $W(CO)_6$ (supplementary materials section 12) that arise from UP relaxation. On the basis of the Hopfield coefficients (for an incidence angle of 15°), we ascertained that only 4.3% of the UP energy would be stored in $W(^{13}CO)_6$ reservoir modes, whereas 59.4% would be allocated to $W(CO)_6$ dark states. Therefore, in the absence of VET, the average population ratio between these reservoir modes ($I_{UP,MP}/I_{UP,LP}$) must be approximately equal to the ratio of the corresponding Hopfield coefficients: 59.4%/4.3% ≈ 14/1. However, experimentally, $I_{UP,MP}/I_{UP,LP}$ is 2.5/1. This observation suggested that after the UP population was optically generated, its energy was preferentially channeled to $W(^{13}CO)_6$, increasing the relative peak intensity of [ω_{UP}, ω_{LP}]. To further examine this argument, we conducted similar measurements with a blue-detuned cavity mode so that UP had a greater fraction of $W(CO)_6$ (supplementary materials section 7). Even at a Hopfield coefficient ratio of 25/1, there is still a substantial amount of energy transfer ($I_{UP,MP}/I_{UP,LP}$ = 2.6 ± 0.1). Additional evidence supporting intermolecular VET is given by the anisotropy decay of the [ω_{UP}, ω_{MP}] and [ω_{UP}, ω_{LP}] peaks (supplementary materials section 8).

We then used pump-probe spectroscopy to monitor the VET dynamics when only the UP population was excited (Fig. 3A). The intensity

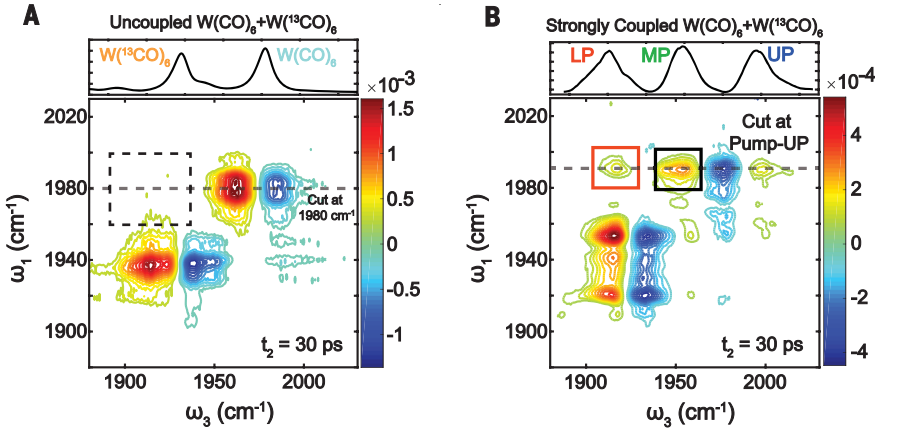


Fig. 2. Comparison of 2D IR spectra inside and outside of the microcavity. 2D IR spectra of (**A**) uncoupled and (**B**) strongly coupled $W(CO)_6/W(^{13}CO)_6$ with a total concentration of 105 mM in binary solvent (hexane/DCM), along with the corresponding linear spectra of the two systems (top panels). The strongly coupled sample was taken at an incidence angle of 15° (Fig. 1D), where the cavity resonance is kept at 1961 cm^{-1}. The dashed box in (A) indicates the absence of cross peaks. The red and black boxes in (B) indicate the [ω_{UP}, ω_{LP}] and [ω_{UP}, ω_{MP}] cross peaks, respectively.

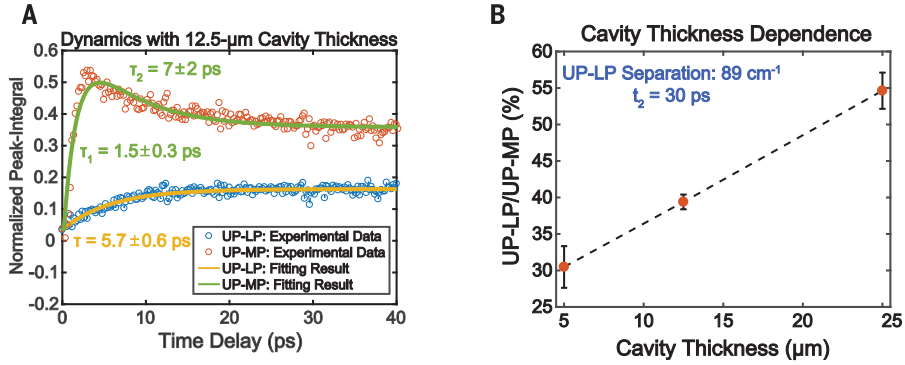


Fig. 3. Dynamics and cavity-thickness dependence of polariton-enabled intermolecular VET. (**A**) Dynamics of [ω_{UP}, ω_{LP}] and [ω_{UP}, ω_{UP}] peak integrals and the fitting results. The sample was taken at an incidence angle of 15° (Fig. 1D). (**B**) Plot of $I_{UP,MP}/I_{UP,LP}$ as a function of cavity thickness at t_2 = 30 ps. Error bars represent the SD of three independent scans.

of the [ω_{UP}, ω_{LP}] peak increased with a time constant of 5.7 ± 0.6 ps. This value represents the time scale for energy transfer from UP to $W(^{13}CO)_6$ reservoir modes. By contrast, the direct relaxation of UP to $W(CO)_6$ happened much faster than VET, with a lifetime of 1.5 ± 0.3 ps, as indicated by the rising dynamics of $I_{UP,MP}$. The decay of $I_{UP,MP}$ is composed of a fast and a slow component. The fast dynamics has a lifetime of 7 ± 2 ps, similar to the rising time of $I_{UP,LP}$. Thus, it implies energy "leakage" from the $W(CO)_6$ mode to the $W(^{13}CO)_6$ mode (see supplementary materials section 13). The slow component, whose decay extends beyond the time range of our scan, should correspond to the population relaxation of reservoir $W(CO)_6$ (*12*, *15*).

To confirm the importance of cavity modes in facilitating polariton VET, we attempted to enhance VET by increasing the cavity thickness L. In Fig. 3B, we present the $I_{UP,MP}/I_{UP,LP}$ ratio for the same molecular mixture in cavities with L = 5, 12.5, and 25 μm, corresponding to 1.12-, 2.80-, and 5.60-ps cavity lifetimes, respectively (supplementary materials section 4). This ratio, which reflects the efficiency of VET at 30 ps, increased with increasing L. Because thicker cavities have longer lifetimes, this dependence suggests that a larger fraction of UP energy was collected in $W(^{13}CO)_6$ modes as polariton decay by photon leakage slowed. This property substantiates that intermolecular VET involves polaritonic intermediate states (supplementary materials section 13). The nature of the ultrafast energy redistribution process requires further study, which suggests that, in contrast to measurements performed on organic microcavities (*17*, *19*), previously unexplored mechanisms dominate the relaxation kinetics reported here. Possible mechanisms include polariton-mediated scattering and interaction of polaritons with other dark modes.

The reported concept of polariton-enabled intermolecular VET could be expanded to the selective promotion or suppression of vibrational energy transport channels. The preferential relaxation to lower energy states is a key process for IR polariton condensation, remote energy transfer (*17*, *18*), and cavity chemistry (*22*, *24*).

REFERENCES AND NOTES

1. D. C. Tardy, B. S. Rabinovitch, *Chem. Rev.* **77**, 369–408 (1977).
2. J. P. Kraack, A. Frei, R. Alberto, P. Hamm, *J. Phys. Chem. Lett.* **8**, 2489–2495 (2017).
3. T. Baumann *et al*., *Angew. Chem. Int. Ed.* **58**, 2899–2903 (2019).
4. R. Gnanasekaran, J. K. Agbo, D. M. Leitner, *J. Chem. Phys.* **135**, 065103 (2011).
5. D. J. Nesbitt, R. W. Field, *J. Phys. Chem.* **100**, 12735–12756 (1996).
6. M. Gruebele, P. G. Wolynes, *Acc. Chem. Res.* **37**, 261–267 (2004).
7. T. Förster, *Ann. Phys.* **437**, 55–75 (1948).
8. D. L. Dexter, *J. Chem. Phys.* **21**, 836–850 (1953).
9. R. F. Ribeiro, L. A. Martínez-Martínez, M. Du, J. Campos-Gonzalez-Angulo, J. Yuen-Zhou, *Chem. Sci.* **9**, 6325–6339 (2018).
10. H. Memmi, O. Benson, S. Sadofev, S. Kalusniak, *Phys. Rev. Lett.* **118**, 126802 (2017).
11. R. F. Ribeiro *et al*., *J. Phys. Chem. Lett.* **9**, 3766–3771 (2018).
12. B. Xiang *et al*., *Proc. Natl. Acad. Sci. U.S.A.* **115**, 4845–4850 (2018).
13. B. Xiang *et al*., *J. Phys. Chem. A* **123**, 5918–5927 (2019).
14. B. Xiang *et al*., *Sci. Adv.* **5**, eaax5196 (2019).
15. A. D. Dunkelberger, B. T. Spann, K. P. Fears, B. S. Simpkins, J. C. Owrutsky, *Nat. Commun.* **7**, 13504 (2016).
16. X. Liu *et al*., *Nat. Photonics* **9**, 30–34 (2014).
17. X. Zhong *et al*., *Angew. Chem. Int. Ed.* **56**, 9034–9038 (2017).
18. M. Du *et al*., *Chem. Sci.* **9**, 6659–6669 (2018).
19. D. M. Coles *et al*., *Nat. Mater.* **13**, 712–719 (2014).
20. X. Zhong *et al*., *Angew. Chem. Int. Ed.* **55**, 6202–6206 (2016).
21. K. Georgiou *et al*., *ACS Photonics* **5**, 258–266 (2018).
22. A. Thomas *et al*., *Science* **363**, 615–619 (2019).
23. M. Muallem, A. Palatnik, G. D. Nessim, Y. R. Tischler, *J. Phys. Chem. Lett.* **7**, 2002–2008 (2016).
24. M. Du, R. F. Ribeiro, J. Yuen-Zhou, *Chem* **5**, 1167–1181 (2019).
25. B. Xiang *et al*., Intermolecular Vibrational Energy Transfer Enabled by Microcavity Strong Light-Matter Coupling, version 1, Zenodo (2020); http://doi.org/10.5281/zenodo.3695870.

ACKNOWLEDGMENTS

The authors thank T. Porter from C. Kubiak's group for his efforts in synthesizing the $W(^{13}CO)_6$ compounds. B.X. and W.X. thank J. Kim for insightful discussion on fluorescence resonance energy transfer. **Funding:** B.X. is supported by a Roger Tsien Fellowship. B.X., L.C., J.W., and W.X. acknowledge support from AFSOR YIP grant FA9550-17-1-0094. Z.Y and W.X. acknowledge support from NSF CAREER award DMR-1848215. The research instrument is supported by AFOSR DRUIP FA9550-18-1-0451. The development of the kinetic model was carried out by M.D. and J.Y.-Z. under funding support from the U.S. Department of Energy, Office of Science, Basic Energy Sciences, CPIMS Program under Early Career Research Program award DE-SC0019188. R.F.R. elucidated signatures of the energy-transfer processes in the nonlinear spectra with funding from Air Force Office of Scientific Research award FA9550-18-1-0289. **Author contributions:** W.X. and J.Y.-Z. conceived the original idea. W.X. supervised the overall research and J.Y.-Z. supervised the theoretical work. B.X. and W.X. designed the experiments. B.X., L.C., Z.Y., and J.W. conducted the experimental work. B.X. and W.X. analyzed experimental data. R.F.R., M.D., and J.Y.-Z. developed theoretical work. B.X., R.F.R., M.D., J.Y.-Z., and W.X. interpreted and discussed the experimental and theoretical results and wrote the final manuscript. **Competing interests:** The authors declare no competing interests. **Data and materials availability:** All data needed to support the conclusions of the main text and supplementary materials have been uploaded to Zenodo (*25*).

SUPPLEMENTARY MATERIALS

science.sciencemag.org/content/368/6491/665/suppl/DC1
Materials and Methods
Supplementary Text
Figs. S1 to S19
Tables S1 and S2
References (*26*–*30*)

25 November 2019; accepted 30 March 2020
10.1126/science.aba3544



Waterless Condenser

The CondenSyn Waterless Air Condenser from Asynt is a proven "green" replacement for water-cooled condensers and suitable for over 95% of all chemical-reflux applications. The CondenSyn is a high-performance glass condenser requiring no cooling water for operation. The elimination of cooling water reduces your lab's environmental impact and water usage cost. Offering clear visibility of ongoing experimental reflux, the unit is easy to clean and maintain, and its nonroll feature helps prevent accidents if it is left on a lab bench. Asynt's range of CondenSyn products can suit different-capacity round-bottom flasks. A typical chemistry laboratory replacing their standard water condensers with CondenSyn units can expect to see a return on its investment in as little as 6 months.

Asynt
For info: +44-(0)-1638-781709
www.asynt.com/product/asynt-condensyn-air-condenser

Phospholipid Removal Microplate

Porvair Sciences announces Microlute PLR, a 96-well microplate that effectively removes more than 99% of phospholipids and proteins from plasma and serum samples with higher levels of reproducibility, while maintaining maximum recovery of target analytes. Phospholipid-based matrix effects are a major source of variability and inaccuracy in bioanalytical MS analysis. Instead of a loose-filled base product, Microlute PLR microplates are composed of a solid, interconnected network of evenly distributed pores that allow biological fluids to flow smoothly and consistently throughout the active media. These microplates enable you to increase the sensitivity and integrity of your UHPLC/HPLC methods. Benefiting from an easy-to-use protocol, they ensure consistent phospholipid removal and analyte recovery from well-to-well and batch-to-batch, first time and every time.

Porvair Sciences
For info: 856-696-3605
www.microplates.com/microlute-plr

Digital Reagent Dispensers

Designed to dispense reagent volumes from 11 pL to 200 µL in any well, the Multidrop Pico 1 and Pico 8 can meet the requirements of a broad array of low-volume applications, including quantitative PCR, dose–response curves, drug screening assays, serial dilutions, genotyping reactions, and enzyme-linked immunosorbent assays. Featuring disposable, noncontact dispensing heads, these units eliminate carryover, protecting sample integrity and further optimizing the accuracy of generated data. They operate on an easy-to-use software platform with application-focused wizards and a highlighted loading guide, allowing for quick, effortless plate setup and operation.

Thermo Fisher Scientific
For info: 800-345-0206
thermofisher.com/digitaldispenser

Single-Tube Scanner

Designed for labs tasked with processing fewer samples, the DataPaq Single-Tube Scanner from Ziath offers easy setup straight out of the box, requiring only a few minutes to install the application software. The large scanning window makes it easy to present your coded sample tubes, even while wearing cryoprotective or contamination clothing. Affordably priced, the compact instrument comes already calibrated and can read all types of 2D datamatrix coded tubes. A single USB connection is all the scanner needs for power and data communication. Durably constructed with a scratch-resistant, mineral glass window, each scanner comes with a no-quibble, 2-year guarantee. Ziath's proprietary Cryoprotection coating is a special option that eliminates condensation and ensures uninterrupted scanning. Our unique method for stopping condensation is cost effective and uses no extra electrical components, removing the risk of accidentally thawing your samples while increasing reliability.

Ziath
For info: 858-880-6920
www.ziath.com

Mini EV Isolation System

The SmartSEC Mini EV Isolation System is used for size exclusion chromatography (SEC)-based isolation of extracellular vesicles (EVs) from small sample volumes—including as little as 10 µL of serum. Leveraging our powerful SmartSEC technology in a spin-column format, SmartSEC Mini delivers high yields of clean EVs with an easy 30-min workflow. It delivers higher purity and yield than ultracentrifugation and is compatible with most downstream applications. SmartSEC Mini is the first commercially available EV isolation kit that's been optimized and validated in a number of developmental biology model organisms, including *Arabidopsis*, *Planaria*, and *Drosophila*.

System Biosciences
For info: 888-266-5066
systembio.com/smartsec-mini

Total Nucleic Acid Extraction

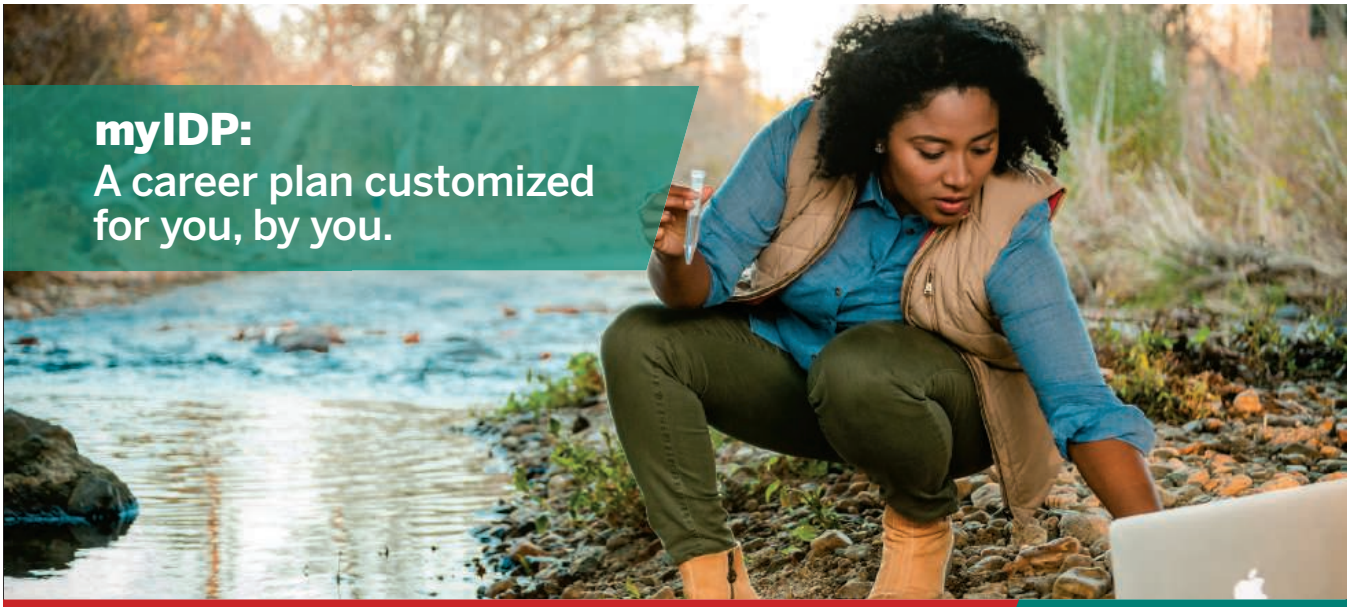
The MagSi-NA Pathogens Kit from AMS Biotechnology enables easy extraction of DNA and RNA from serum, plasma, oropharyngeal swab/nasopharyngeal swab, and any other respiratory samples for pathogen detection. The kit is particularly suitable for total nucleic acid extraction for SARS-CoV-2/COVID-19 detection—currently a major bottleneck in COVID-19 testing. Due to the kit's simple protocol and ready-to-use agents, it is easy to scale to small-, medium-, and high-throughput automation, yielding highly pure nucleic acid in small elution volumes. The MagSi-NA Pathogens Kit utilizes magnetic beads to ensure a consistently high yield, with the proprietary MagSi-PA VII magnetic beads optimized for fast separation even from viscous sample lysates. In less than 30 min, the unit delivers a consistently high yield of total nucleic acids, which can be used for quantitative PCR–based detection or any other enzymatic pathogen detection method. It is compatible with liquid-handling robots, and protocols are available for popular magnetic processors, enabling easy integration into a high-throughput workflow.

AMS Biotechnology
For info: 617-945-5033
www.amsbio.com/magsi-na-pathogen-kit.aspx

Electronically submit your new product description or product literature information! Go to www.sciencemag.org/about/new-products-section for more information.

Newly offered instrumentation, apparatus, and laboratory materials of interest to researchers in all disciplines in academic, industrial, and governmental organizations are featured in this space. Emphasis is given to purpose, chief characteristics, and availability of products and materials. Endorsement by *Science* or AAAS of any products or materials mentioned is not implied. Additional information may be obtained from the manufacturer or supplier.

ScienceCareers online @sciencecareers.org



For your career in science, there's only one Science

Features in myIDP include:

- Exercises to help you examine your skills, interests, and values.
- A list of 20 scientific career paths with a prediction of which ones best fit your skills and interests.
- A tool for setting strategic goals for the coming year, with optional reminders to keep you on track.
- Articles and resources to guide you through the process.
- Options to save materials online and print them for further review and discussion.
- Ability to select which portion of your IDP you wish to share with advisors, mentors, or others.
- A certificate of completion for users that finish myIDP.

myIDP

Visit the website and start planning today!
myIDP.sciencecareers.org

ScienceCareers In partnership with:

FASEB Federation of American Societies for Experimental Biology
UMASS University of Massachusetts Medical School
UCSF University of California San Francisco
UIC
BURROUGHS WELLCOME FUND

Cancer Biology - Assistant Professor Tenure-Track University of Minnesota – Twin Cities

The University of Minnesota's School of Dentistry and Masonic Cancer Center invite applications for a full-time tenure-track Assistant Professor level faculty position in cancer biology, with an emphasis on oral and/or head & neck cancers (e.g., oropharyngeal cancer). Ideal candidates will have a record of compelling research in cancer biology, high promise or demonstrated success in obtaining extramural funding for their research and complement existing strengths that allows contribution to interdisciplinary and collaborative cancer research teams. The successful candidate will join a large and vibrant cancer research community that is associated with the Masonic Cancer Center and the School of Dentistry, faculty in the Medical School, the School of Public Health, and the Institute for Molecular Virology. The Masonic Cancer Center is an NCI-designated Comprehensive Cancer Center that creates a collaborative research environment focused on the causes, prevention, detection and the treatment of cancer. Appointment at the Associate Professor rank will be considered for individuals with appropriate credentials. Salary is commensurate with experience. Position open until filled. Essential

Duties/Responsibilities: The primary role of this new faculty position is to develop a cancer biology research program emphasizing oral and/or head & neck cancers, and to foster collaboration with other supportive fields. The successful candidate will maintain a peer-reviewed research program funded from federal and non-federal sources. Limited teaching and service will be expected. Required: • PhD or equivalent degree. • 2-3 years relevant post-doctoral experience supporting development of a research program in oropharyngeal cancer biology. • High promise or evidence of independent research funding from NIH or other national agency at the time of appointment. • Strong record of research publications in peer-reviewed journals. • Experimental science background. • Demonstrable commitment to equity, diversity and inclusion. Preferred: • Ph.D. degree and research in oral cancer biology or related field. • Training or experience in head and neck cancer research. • Record of peer-reviewed research funding.

To be considered for this position, applicants will submit a cover letter stating their interest in this position, a current CV, a detailed statement of research and career goals, and contact information for three professional references. Go to: **https://humanresources.umn.edu/content/find-job**. Click on "External Applicants." In the Search Jobs field, enter **335920** to locate and apply for the position.

SIMONS FOUNDATION

The Simons Foundation is pleased to announce the appointment of our new class of Junior Fellows of the Simons Society of Fellows, a community of scholars created to encourage intellectual interactions across disciplines and research centers in New York City.

Begüm Aydin, *The Rockefeller University*,
Enteric Nervous System

Philipp Brand, *The Rockefeller University*,
Evolutionary Biology and Neuroscience

Leah Houri-Ze'evi, *The Rockefeller University*,
Neurogenetics and Behavior

Patrick Kennedy, *Columbia University*,
Evolution of Cooperation in Animals

Emily Mackevicius, *Columbia University*,
Systems and Computational Neuroscience

Ashley Villar, *Columbia University*,
Astrophysics

Songtian Sonia Zhang, *Columbia University*,
Condensed Matter Physics Experiments

Jeroen Zuiddam, *New York University*,
Theoretical Computer Science and Combinatorics

For more information:
@Simons_SOF
https://www.simonsfoundation.org/simons-society-of-fellows

JOHNS HOPKINS
BLOOMBERG SCHOOL
of PUBLIC HEALTH

Director of the Johns Hopkins Malaria Research Institute

The Johns Hopkins Bloomberg School of Public Health and W. Harry Feinstone Department of Molecular Microbiology and Immunology seek to recruit an outstanding scientist as **Director of the Johns Hopkins Malaria Research Institute** (JHMRI) and **Professor of Molecular Microbiology and Immunology**.

JHMRI was established in 2001 and supports a broad program of basic research with the goal of generating novel approaches to malaria treatment and control. JHMRI has extensive insectary and core facilities in Baltimore, as well as the JHMRI field site in Macha, Zambia with a molecular lab, insectary and semi-field containment facility. Information on JHMRI faculty, research programs, core resources, and Macha Research Trust can be found at our website: http://malaria.jhsph.edu.

The successful applicant will establish a relevant research program within an interactive environment of investigators interested in the pathogenesis of infectious diseases. Applicants must have a PhD, MD or equivalent degree and appropriate experience.

Applicants should provide curriculum vitae, bibliography, and description of research to **apply.interfolio.com/74933** by **July 1, 2020**.

For more information, contact Genevieve Williams, Program Manager, Johns Hopkins Malaria Research Institute, Department of Molecular Microbiology and Immunology, Johns Hopkins Bloomberg School of Public Health, 615 N. Wolfe St., Baltimore, MD 21205, phone: 410-614-4883, email: genevieve.williams@jhu.edu.

The Johns Hopkins University is an Equal Opportunity/Affirmative Action Employer committed to recruiting, supporting and fostering a diverse community of outstanding faculty, staff and students. All applicants who share this goal are encouraged to apply.

10 ways that *Science* Careers can help advance your career

1. Register for a free online account on **ScienceCareers.org**.
2. Search thousands of job postings and find your perfect job.
3. Sign up to receive e-mail alerts about job postings that match your criteria.
4. Upload your resume into our database and connect with employers.
5. Watch one of our many webinars on different career topics such as job searching, networking, and more.
6. Download our career booklets, including Career Basics, Careers Beyond the Bench, and Developing Your Skills.
7. Complete an interactive, personalized career plan at "my IDP."
8. Visit our Employer Profiles to learn more about prospective employers.
9. Research graduate program information and find a program right for you.
10. Read relevant career advice articles from our library of thousands.



Visit **ScienceCareers.org** today — all resources are free

SCIENCECAREERS.ORG

ScienceCareers
FROM THE JOURNAL SCIENCE AAAS

HIGH-LEVEL GLOBAL TALENTS RECRUITMENT

Welcome back to hometown.
Thousands of academic job vacancies are in fast-developing China.

2020 Global Online Job Fair (www.edu.cn/cv)

May 08, 2020 North Area of East China Doctoral Talents Recruitment
May 09, 2020 Hong Kong, Macao, Taiwan and the China Great Bay Area Doctoral Talents Recruitment
May 15, 2020 High-level Global Talents Recruitment

Qualification for Applicants

Global scholars, Doctor and Post-doctor

Key Disciplines

Life Sciences, Health Sciences and Physical Sciences

Participating Approach

Please send your CV to consultant@acabridge.edu.cn for 2020 Global Online Job Fair

Scan to check the sessions

Job Vacancies in China's Universities and Institutes
Please visit https://www.acabridge.edu.cn/ Contact consultant@acabridge.edu.cn

Overseas *Chinese Scholars'* Visit to Top Chinese Universities

Check the Details from www.edu.cn/zgx

- **10,000+ academic job vacancies in China**
- **Free one-to-one consultation service**

Send your CV to *consultant@acabridge.edu.cn*

海外学者中国行

上海师范大学 中国石油大学 中南民族大学

Scan for application

By **Kara Fikrig**

A Ph.D. on hold—indefinitely

I sat in my apartment in Iquitos, Peru, facing a stark choice between my research and my well-being. I was there to collect data for my dissertation, but my work was on hold because the Peruvian government had declared a national lockdown 9 days earlier as the COVID-19 crisis took hold. At first, my plan was to wait out the pandemic in Peru. But then I learned the country's airports and borders would be closed indefinitely. An evacuation flight for U.S. citizens was departing the next day. It would probably be my last chance to leave, given that Iquitos is a remote city with no road link to the rest of the world. So, in less than 24 hours, I had to decide whether to prioritize the research that means so much to me, or abandon my field season and evacuate.

One month earlier, I had said goodbye to my friends and family, given my dog a final hug, and set off to Peru. I'd spent much of the previous 2 years planning for the field season, and I was excited to finally get started. As the plane descended below the cloud cover and into Iquitos, I peered out at the endless expanse of trees and the winding Amazon River—the region where I planned to spend 6 months studying the mosquito that's responsible for an ongoing dengue outbreak there.

The lockdown came just 2 weeks later. I weighed my options: If I stayed in Peru, my fieldwork would be delayed, but as soon as local restrictions were lifted, I could begin again. On the other hand, if I returned to the United States, I would be surrounded by my support network during a stressful time and could help my parents, both of whom are infectious disease doctors, if needed. But my fieldwork might be delayed by months—or even years—given that international travel restrictions would likely remain in place longer than local restrictions.

I worried about my timeline for graduating. I'm in the third year of my Ph.D. and my department only guarantees 5 years of funding. I felt the pressure of the ticking clock, and it weighed heavily on my mind.

My first impulse was to remain in Peru and get my fieldwork done at all costs. I was willing to make sacrifices to complete the project, which I viewed as important—both for my career and for public health in the region. But as COVID-19 news continued to stream in and the severity of the situation crystalized, my mindset changed. Eventually, I decided that I needed to get home, whatever the cost to my work. So, on the 10th day of the lockdown, I packed my supplies and took a bus with other evacuees to the airport.



"I have no idea when I might be able to return to Peru."

It was a relief when I finally arrived at home in upstate New York on 27 March. But in the weeks since, I've been grappling with what my future might look like. My field season ended before it even began, leaving me with no data and little to show for the years of planning. I have no idea when I might be able to return to Peru. And I am trying to come to terms with the fact that my Ph.D. will take longer than I had originally planned.

Sometimes I wonder whether I shouldn't have left. But then I look at my family and am reminded why I made this decision. I'm currently staying with my parents, which allows me to help with chores as they work with COVID-19 patients. It is a comfort that we won't be half a world apart if any of us get sick. The situation makes it clear to me that my well-being, along with that of my family, is more important than my research. However, repeating this to myself does not erase the stress I feel about my graduation timeline.

My adviser has pledged to support me financially until I finish my dissertation. But other graduate students who are facing similar obstacles to their research may not be so lucky. Some institutions are implementing "stop-the-clock" policies for tenure-track professors. I believe that graduate students deserve similar protective policies—for instance, an additional year of guaranteed funding. Although such a measure would not erase all the anxieties caused by COVID-19, it would at least alleviate some of the financial and logistical stress. ■

Kara Fikrig is a Ph.D. student at Cornell University in Ithaca, New York. Send your career story to SciCareerEditor@aaas.org.

ILLUSTRATION: ROBERT NEUBECKER

Published by AAAS